Santorini Volcano

T. H. Druitt, L. Edwards, R. M. Mellors, D. M. Pyle,
R. S. J. Sparks, M. Lanphere, M. Davies & B. Barriero

Published by the Geological Society

Santorini Volcano

Geological Society Special Publications
Series Editor
A. J. FLEET
R. E. HOLDSWORTH
A. C. MORTON
M. S. STOKER

Dedicated to Peter Nomikos
for his generosity and patience

It is recommended that reference to all or part of this book should be made in the following way.

DRUITT, T. H., EDWARDS, L., MELLORS, R. M., PYLE, D. M., SPARKS, R. S. J., LANPHERE, M., DAVIES, M. & BARREIRO, B. 1999. *Santorini Volcano*. Geological Society, London, Memoirs, **19**.

GEOLOGICAL SOCIETY MEMOIR NO. 19

Santorini Volcano

T. H. Druitt,[1] L. Edwards,[2] R. M. Mellors,[3] D. M. Pyle,[3] R. S. J. Sparks,[2]
M. Lanphere,[4] M. Davies[1] & B. Barreirio[5]

[1] *Laboratoire Magmas et Volcans (UMR6524 et CNRS), Université Blaise Pascal, 5, Rue Kessler, 63038 Clermont Ferrand, France*
[2] *Department of Earth Sciences, University of Bristol, Bristol BS8 1RJ, UK*
[3] *Department of Earth Sciences, University of Cambridge, Cambridge CB2 3EQ, UK*
[4] *Branch of Isotope Geology, MS 937, US Geological Survey, 345, Middlefield Road, Menlo Park, California 94025, USA*
[5] *NIGL, British Geological Survey, Keyworth, Nottingham NG12 5GG, UK*

1999
Published by
The Geological Society
London

THE GEOLOGICAL SOCIETY

The Geological Society of London was founded in 1807 and is the oldest geological society in the world. It received its Royal Charter in 1825 for the purpose of 'investigating the mineral structure of the Earth' and is now Britain's national society for geology.

Both a learned society and a professional body, the Geological Society is recognized by the Department of Trade and Industry (DTI) as the chartering authority for geoscience, able to award Chartered Geologist status upon appropriately qualified Fellows. The Society has a membership of 8600, of whom about 1500 live outside the UK.

Fellowship of the Society is open to persons holding a recognized honours degree in geology or a cognate subject and who have at least two years' relevant postgraduate experience, or not less than six years' relevant experience in geology or a cognate subject. A Fellow with a minimum of five years' relevant postgraduate experience in the practice of geology may apply for chartered status. Successful applicants are entitled to use the designatory postnominal CGeol (Chartered Geologist). Fellows of the Society may use the letters FGS. Other grades of membership are available to members not yet qualifying for Fellowship.

The Society has its own Publishing House based in Bath, UK. It produces the Society's international journals, books and maps, and is the European distributor for publications of the American Association of Petroleum Geologists (AAPG), the Society for Sedimentary Geology (SEPM) and the Geological Society of America (GSA). Members of the Society can buy books at considerable discounts. The Publishing House has an online bookshop (*http://bookshop.geolsoc.org.uk*).

Further information on Society membership may be obtained from the Membership Services Manager, The Geological Society, Burlington House, Piccadilly, London W1V 0JU (Email: *enquiries@geolsoc.org.uk*; tel: +44 (0)171 434 9944).

The Society's Web Site can be found at *http://www.geolsoc.org.uk/*. The Society is a Registered Charity, number 210161.

Published by The Geological Society from:
The Geological Society Publishing House
Unit 7, Brassmill Enterprise Centre
Brassmill Lane
Bath BA1 3JN, UK

(*Orders*: Tel. +44 (0)1225 445046
Fax +44 (0)1225 442836)
Online bookshop: *http://bookshop.geolsoc.org.uk*

First published 1999
Reprinted 2002

British Library Cataloguing in Publication Data
A catalogue record for this book is available from the British Library.

ISBN 1-86239-048-7
ISSN 0435-4052

Typeset by Aarontype Ltd, Unit 47, Easton Business Centre, Felix Road, Bristol BS5 0HE, UK

Printed by
Alden Press, Osney Mead,
Oxford OX2 0EF, UK

Distributors
USA
AAPG Bookstore
PO Box 979
Tulsa
OK 74101-0979
USA
(*Orders*: Tel. +1 918 584-2555
Fax +1 918 560-2652
Email bookstore@aapg.org)

Australia
Australian Mineral Foundation Bookshop
63 Conyngham Street
Glenside
South Australia 5065
Australia
(*Orders*: Tel. +61 88 379-0444
Fax +61 88 379-4634
Email bookshop@amf.com.au)

India
Affiliated East-West Press PVT Ltd
G-1/16 Ansari Road, Daryaganj
New Delhi 110 002
India
(*Orders*: Tel. +91 11 327-9113
Fax +91 11 326-0538)

Japan
Kanda Book Trading Co.
Cityhouse Tama 204
Tsurumaki 1-3-10
Tama-shi
Tokyo 206-0034
Japan
(*Orders*: Tel. +81 (0)423 57-7650
Fax +81 (0)423 57-7651)

Contents

Preface vii

Chapter 1 Previous research 1

Pre-1960 research 1
Discovery of Akrotiri and submarine tephra 1
First International Scientific Congress on the Volcano of Thera, 1969 1
Research from 1969 to 1978 2
Second International Scientific Congress, Santorini, Greece 1978 3
Research from 1978 to 1989 3
Third International Scientific Congress, Santorini, Greece, 1989 4
Research from 1989 to 1998 4
Santorini: a European laboratory volcano 4

Chapter 2 Geological and tectonic setting of Santorini 5

Tectonic setting of the Aegean 5
The crystalline geology of the south Aegean 5
Volcanism in the Aegean area 10
Summary 11

Chapter 3 Development of the Santorini volcanic field in time and space 13

General description of the volcanic field 13
The geological map and radiometric ages 16
The pre-volcanic island (Triassic to Eocene) 16
Early Centres of the Akrotiri Peninsula (650–550 ka) 17
Peristeria Volcano (530–439 ka) 19
Cinder Cones of the Akrotiri Peninsula (450–330 ka) 20
First explosive cycle (*c.* 360180 ka) 20
Second explosive cycle (180–3.6 ka) 27
The minor pyroclastic sequences 48
Kameni Islands (197 BC to AD 1950) 48
The timescale of volcanism 49
The importance of regional tectonics 51
Explosive activity 53
Summary 56

Chapter 4 Compositional zoning and petrology of the Thera pyroclastics 59

Petrology of the Santorini lavas 59
General features of the Thera pyroclastics 60
Eruptions of dominantly silicic composition 60
Eruptions of dominantly intermediate composition 67
Magmatic temperatures 73
Magmatic water contents 73
Magma-chamber zoning and development 74
Origin of the normal-to-reverse zonation 78
Summary 78

Chapter 5 Cumulate nodules in the Thera pyroclastics 79

Nodule occurrences 79
Petrology 79
Comparison between the petrology of the nodules and volcanic rocks 82
Temperature and pressure estimates 85
Whole-rock geochemistry 85
Petrogenesis 87
Summary 87

Chapter 6 Geochemistry, isotopic composition and petrogenic modelling of the Thera pyroclastics 89

Previous research 89
Major units of the Thera pyroclastics 92
Minor pyroclastic sequences 100
Isotopic studies of the Thera pyroclastics 100
Interpretations of the geochemistry 106
Geochemical modelling 109
Assimilation and fractional crystallization models 110
Summary 000

Chapter 7 Studies of short-lived radionuclides in Santorini volcanics 118

Systematics and conventions 118
Magmatic tracers 118
Results 118
The Lower Pumice 2 deposit 124
U–Th disequilibria data for other Thera pyroclastics 125
U–Th disequilibria data from the lava shields 126
Secular evolution of U and Th isotopic indices for the Thera pyroclastics 128
Summary 128

Chapter 8 The evolution of Santorini 129

Geological and tectonic controls 129
History of the volcano 129
Caldera formation 130
Magma evolution mechanisms 130
Causes of secular variations in magma geochemistry 131
Causes of the cycles 132

Appendix 1 Analytical methods and errors 134

K–Ar and $^{40}Ar/^{39}Ar$ dating 134
Electron microprobe analysis 134
XRF analysis 134
Lead, strontium and neodymium isotopes 135
Oxygen isotopes 135
Hydrogen isotopes 135
Uranium, thorium and radium isotopes 136

Appendix 2 Tabulated analytical data 138

Juvenile components of the Thera pyroclastics 138
Plutonic blocks from the Thera pyroclastics 151
Juvenile components of the minor pyroclastic sequences 154

References 158

Index 162

This page intentionally left blank

Preface

Santorini is one of the most spectacular caldera volcanoes in the world. It has been the focus of significant scientific and scholastic interest because of the great Bronze Age explosive eruption that buried the Minoan town of Akrotiri. The recognition of the catastrophic character of this eruption, the realization that the eruption might have had a devastating effect on the ancient civilizations in the eastern Mediterranean and the preservation of exquisite frescoes beneath the pumice deposits at Akrotiri have led to intense research on the geology and archaeology of the islands. Three International Congresses funded by the Thera Foundation have taken place since 1969 and the scientific literature is now replete with contributions on an enormous range of subjects. Santorini has been dormant since 1950, but there have been several substantial historic eruptions. There is a large indigenous population that swells to many tens of thousands during the tourist season. As a consequence of the high potential risk to life and property Santorini has been chosen as one of five European Laboratory Volcanoes by the European Commission. Thus the island is likely to remain a focus of volcanological research for the foreseeable future.

The geology of Santorini has long fascinated geologists. The treatise by Fouqué in 1879 was an early masterpiece in volcanological research, which described the stratigraphy of the caldera wall, recognized the true volcanic origin of the caldera depression and discovered buildings of an ancient civilization beneath the uppermost volcanic layers. The 1936 study of Santorini geology by H. Reck was also a very significant contribution to volcanology and developed a stratigraphy that is still the basis for modern studies. The last three decades have seen numerous studies of various aspects of Santorini geology. A detailed geological map, with further refinements of the stratigraphy, was published by Hans Pichler and colleagues in 1979. Research groups from Denmark, Germany, France, Greece, Holland, Great Britain and the USA have been prominent in developing a modern understanding of the stratigraphy, volcanology, petrology and geochemistry.

One of these groups was based at Cambridge University and later Bristol University where PhD projects on Santorini were instigated in 1980 with the objective of developing a detailed understanding of the pyroclastic deposits and of the overall magmatic evolution of the islands. PhD theses were produced by T. H. Druitt (1983), R. Mellors (1988) and D. M. Pyle (1990) at Cambridge and by R. M. E. Thomas (1993) and L. Edwards (1994) at Bristol University. Although several publications have emerged from this project, a great deal remained unpublished until now. Most of the publications have concerned aspects of the physical volcanology, with one synoptic paper on the stratigraphy (Druitt *et al.* 1989). Since the 1989 paper, significant new information on the geochronology and stratigraphy has been obtained. The volcanic field was remapped in 1994/95 at a scale of 1:10 000 by the group at Blaise Pascal University in Clermont-Ferrand, France. A large suite of lavas were dated radiometrically by M. Lanphere at the US Geological Survey in order to provide an absolute time framework. A substantial amount of petrological and geochemical data has been collected since 1980, but has hitherto remained unsynthesized and largely unpublished.

A remarkable picture of cyclic volcanic activity and magmatic evolution has emerged from this work. This could not have happened without the detailed understanding of the stratigraphy and physical volcanology of the pyroclastic deposits (the Thera pyroclastics) and the integration of this information with a large body of high quality analytical data on the petrology and geochemistry. This Memoir has thus been produced because the time is now right to synthesize all the data on Santorini and to tell the new story. The new data and ideas in this memoir do not solely derive from the PhD theses. There have been other research groups working over the same period on Santorini and our results and ideas have been integrated with other published work. Colleagues from other institutions have collaborated with the Cambridge/Bristol/Clermont group and are thus involved as co-authors because of their substantial contributions.

The Memoir is organized into eight chapters. Chapter 1 provides a synopsis of the history of research and identifies the landmarks in the evolution of knowledge and ideas. Chapter 2 reviews the geological and tectonic setting of Santorini. It also summarizes recent work on the basement geology of the Aegean islands. Chapter 3 describes the latest interpretation of the stratigraphy, geochronology and physical volcanology of Santorini. This chapter includes information on the stratigraphy and structure of the volcano to complement the new geological map, which is included at the back of the memoir. It also describes the new K–Ar and $^{40}Ar/^{39}Ar$ dates. Much of the physical volcanology of the main pyroclastic deposits on Santorini has already been published so this aspect is presented only as a summary of the main facts. However new data are presented on the features of the important sequences of minor pyroclastic deposits that occur between the major units. Chapter 4 presents the petrology, mineral chemistry and compositional zoning of the Thera pyroclastics and provides comparisons with published accounts of the lava sequences. Chapter 5 considers the petrochemistry of plutonic nodules that occur in several pyroclastic horizons, which are predominantly gabbros, but also include diorites and granites. These rocks represent part of the high-level intrusive core of the Santorini system. Chapter 6 describes and interprets the major element, trace element and isotope geochemistry of the Thera pyroclastics. Secular variations in magma chemistry are identified and interpreted. Chapter 6 includes new data on the geochemistry the isotopic compositions of Santorini volcanic rocks and presents modelling of the geochemical and isotopic data which constrains the petrogenesis of the magmas. Isotopic data include radiogenic isotopes (Sr, Pb, Nd) and stable isotopes (O and H) of both whole-rock samples and mineral separates. Chapter 7 discusses results of U-series disequilibria studies on Santorini rocks with new data on U, Th and Ra activities. Chapter 8 summarizes the overall evolution of the Santorini system, discusses the origin of the various kinds of magmatic and volcanic cycles and attempts to elucidate the links between magmatic evolution and volcano behaviour.

Over the years we have enjoyed discussions and collaborations with friends who have also worked extensively on Santorini, in particular Enzo Francaviglia, Walter Friedrich, Mike Fytikas, Grant Heiken, Joep Huijsmans, Jörg Keller, Buffy McClelland, Floyd McCoy and Georgos Vougioukalakis, Christos Doumas often provided access to the Akrotiri excavations and to his limitless knowledge of the Bronze Age world. Permission to work on Santorini has always been provided by the Greek Institute of Geology and Mineral Exploration.

The Memoir could not have come into existence without the generous and enthusiastic support of Peter Nomikos and funding from the Thera Foundation. Funds from the European Community more also contributed to the production of the Memoir and Map. The Natural Environment Research Council (UK) supported research studentships to T. H. Druitt, R. A. Mellors, D. M. Pyle and L. Edwards and analytical costs at the NERC Isotope Geology Laboratory, Keyworth. Completion of the memoir was also supported by the French Centres de Recherches Volcaniques (CRV) to T. H. Druitt and the Leverhulme Trust to R. S. J. Sparks. We also acknowledge Michelle Dance for her help in drafting the diagrams and Tim Brewer for his excellent help in the XRF analytical work and advice to NERC research students. Reviews by Catherine Deniel, Shan DeSilva, Wes Hildreth, Mike Le Bas, Pete Lipman, Mac Rutherford and Olgeir Sigmarsson are acknowledged. We thank our families for their support and encouragement during the preparation of this Memoir.

This page intentionally left blank

Chapter 1
Previous Research

Santorini has fascinated and stimulated explorers and scholars since ancient times. Jason and the Argonauts were apparently visitors to the islands and described a giant called Talos. Molten metal flowed from his feet and he threw stones at them. The island is perhaps best known for the paroxysmal eruption that took place in the Late Bronze Age at the height of the Minoan civilization that dominated Crete and the Aegean region. The legend of Atlantis, in which a whole city sank beneath the sea in a single day and night, is plausibly based on the effects of this eruption on the Minoan Civilization.

The geographer Strabo described the eruption of 197 BC in the following way:

> ...for midway between Thera and Therasia fires broke forth from the sea and continued for four days, so that the whole sea boiled and blazed, and the fires cast up an island which was gradually elevated as though by levers and consisted of burning masses...

This introduction gives a brief synopsis of research on the volcano since this dramatic chronicle was written. Research on Santorini has contributed substantial advances not only in the understanding of Santorini itself but to general principles in volcanology and petrology.

Pre-1960 research

Duke Jacomo I Crispo of Naxos (1397–1418) was the first person to have taken a scientific interest in the island, and it is reported that he studied the volcano and conducted experiments on its crater.

Pègues in 1842 was the first historian to realise that the water-filled depression between Thera, Therasia and Aspronisi formed by the volcanic collapse of the island in prehistoric times. He also documented the historical eruptions, describing them as catastrophic for the people of Santorini. Fouqué (1879) made the first detailed geological and petrological study of Santorini. He distinguished three layers in the deposits that buried Bronze Age buildings, suggesting that the eruption occurred in three separate phases. Due to the fact that the Bronze Age houses were in very good condition, despite the power of the eruption and the proximity of the caldera, he concluded that the Minoan eruption was not preceded by a significant earthquake, but began suddenly with the ejection of pumice and ash that covered the settlements at Akrotiri. During the collapse of the island the settlements were protected by the thick tephra layer. Fouqué (1879) postulated that the whole of the centre of the island, together with part of the western coast (a total area of 83 km^2), sank beneath the sea during the caldera collapse, leaving a central abyss. Fouqué was one of the earliest scientists to come up with an interpretation of calderas with the basic elements of modern understanding. His treatise is therefore a landmark in the history of geology. He presented beautiful cross-sections of the entire caldera wall (Fig. 1.1) which provided the first information on the stratigraphy of Santorini.

The first systematic study of the stratigraphy of Santorini was undertaken by Reck (1936), and remains fundamental to any modern re-appraisal. He recognized two distinct older units that he called the Loumaravi–Archangelo and the Akrotiri Volcanics, and within the younger volcanic successions of Santorini he identified the products of several eruptive centres. Pyroclastic deposits of the southern half of Santorini were envisaged to have erupted from a large stratocone complex, called Stronghyli. Within these deposits Reck recognized two prominent white tuff units: a lower one he called der Bimstein Unterer (**Bu**), and an upper one called der Bimstein Oberer (**Bo**). In this memoir we refer to these as the Lower Pumice (**rp3**) and the Minoan (**rp7**) tephra. Reck (1936) recognized three centres for lava eruptions on Therasia and northern Thera: the Peristeria, Simandiri and Skaros–Therasia Volcanoes.

Other early works include those by Ktenas (1935 and several earlier papers), Neumann van Padang (1936) and Liatsikas (1942). However, apart from the paper by Reck (1936), most research up to the early 1960s was confined to the lavas of Nea Kameni and was not concerned with the deposits of the larger islands. The Catalogue of Active Volcanoes (Georgalas 1962) summarized all that was known about Santorini at that time.

Discovery of Akrotiri and the submarine tephra

Key developments in the history of geological research on Santorini came about as a consequence of the discovery by Marinatos in 1967 of the Bronze Age town of Akrotiri, buried beneath metres of pumice and ash, and the identification of a major deep-sea tephra layer in the Eastern Mediterranean with a major eruption of Santorini (Ninkovich & Heezen 1965). Marinatos (1939) had long speculated that a major volcanic eruption of Santorini had led to the destruction of the Bronze Age Minoan Civilization on Crete. His excavations at Akrotiri were a new Pompeii and drew attention to Santorini as an archaeological site of international importance. Taken together, the observations appeared to confirm Marinatos's dramatic theory and led to a major surge in Santorini research.

First International Scientific Congress on the Volcano of Thera, 1969

In September 1969 the first International Scientific Congress on the Volcano of Thera was held in Athens, on board the *m.v. Knossos*, bringing together geologists, archaeologists and historians from as far away as New Zealand and Japan. Many papers were presented over several days covering both geosciences and archaeology (Kaloueropoulou 1971). The Congress concentrated predominantly on the problems connected with the great Bronze Age Minoan eruption.

Volcanological contributions to the Congress included a comparison of the Minoan eruption with the Indonesian eruptions of Toba, Sunda and Merapi (van Bemmelen 1971). All four eruptions influenced human history and created havoc within the surrounding cultures. Neumann van Padang (1971) compared the Minoan eruption of Santorini with two other Indonesian eruptions: Tambora (1815) and Krakatoa (1883). He stated that, like Tambora and Krakatoa, the current compound island structure of the volcano of Santorini originated after the destruction of an older, pre-historic volcano. At all three centres there was a catastrophic eruption that lasted a few days, generated calderas from 5 to 12 km across, and distributed ash to a distance of 200 km to more than 1350 km from the volcano.

Galanopoulos (1971) addressed the question as to whether the catastrophes that affected Egypt and the eastern Mediterranean in the Bronze Age were due, directly or indirectly, to the Minoan eruption of Santorini. He believed that the Plagues of Egypt, mentioned in the Old Testament (Book of Exodus), can be explained by several factors connected to the eruption. However, since the date of the plagues is believed to be in the thirteenth century BC (reply by Pomerance: *in* Galanopoulos 1971), the eruption could not have caused them. Several contributions (e.g. Galanopoulos 1971; Georgalas 1971; Vitaliano & Vitaliano, 1971 and numerous archaeological papers in the volume) followed up Marinatos' original speculation that the Minoan eruption may have been the cause of the destruction of the Minoan civilization on Crete.

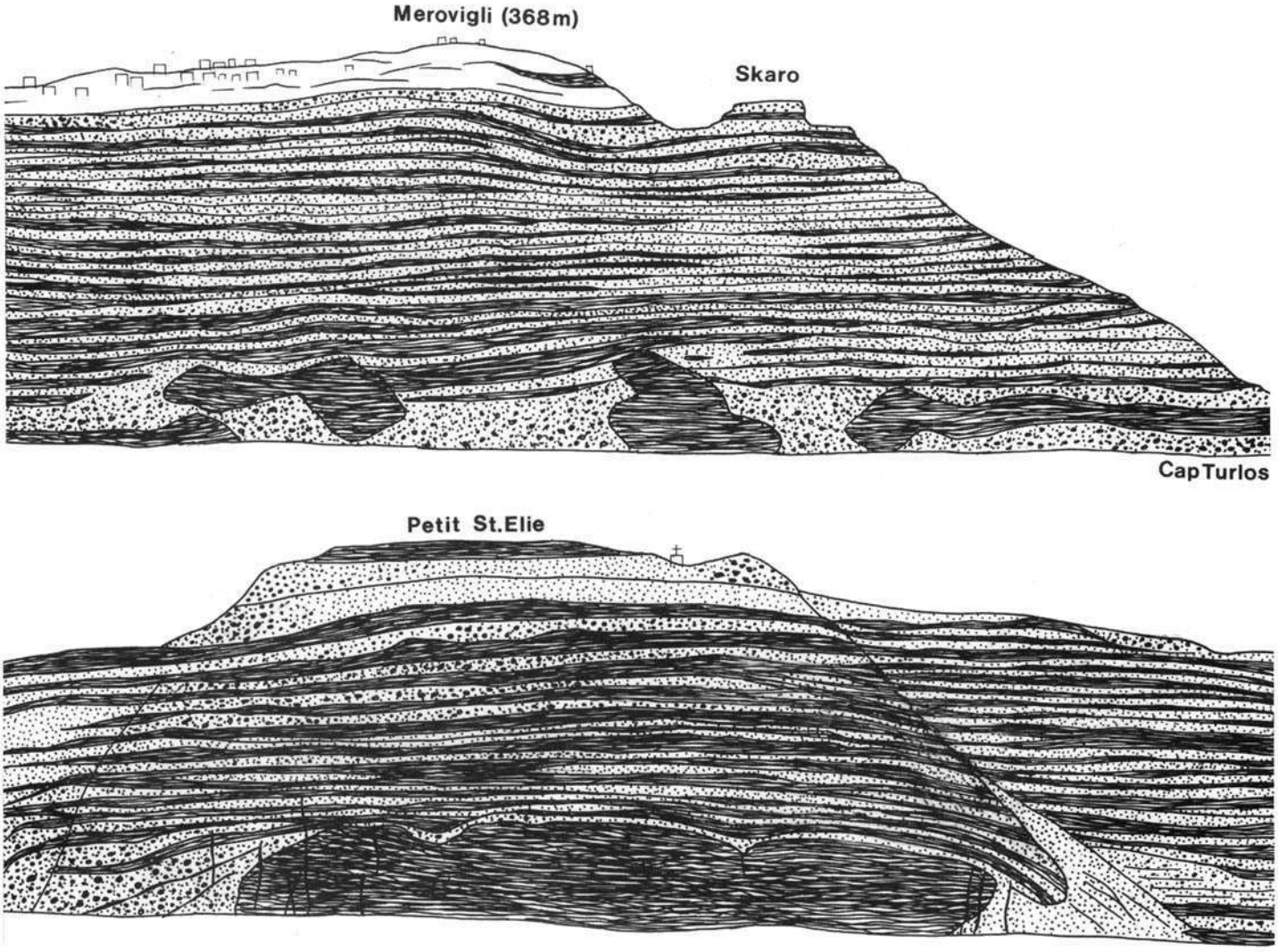

Fig. 1.1. Sketches of the caldera wall geology between Micros Profitis Ilias and Cape Tourlos, reproduced from Fouque (1879). The dark bands are the massive interior parts of lavas and the stippled are mostly brecciated margins of lavas and minor tuff layers.

Other papers presented at the Congress addressed questions relating to tephra falls, the energetics of eruptions and tsunamis, and geochemical and geophysical methods and their application to Santorini, including the first study of the isotopic geochemistry of Santorini rocks (Puchelt & Hoefs 1971).

Research from 1969 to 1978

After the 1969 Congress, several important papers appeared covering many geological aspects of Santorini, providing the first modern and detailed petrological descriptions of the rocks. Nicholls (1971*a*, *b*) presented an in-depth petrological study of the lavas, and divided them into four series: the Loumaravi–Archangelo Series, the Akrotiri–Thira Series, the Main Series and the Modern Series. He found that the lavas of Santorini are compositionally unusual within the Aegean region, and showed that fractional crystallization was important in their magmatic evolution. With the exception of the early hornblende-bearing Loumaravi–Archangelo Series, Santorini magmas rarely contain hydrous minerals. Pichler & Kussmaul (1972) presented a brief outline of the volcanological characteristics of the lava sequences, which they divided into eight volcanic centres. They described and classified the Santorini volcanic rocks and discussed possible petrogenetic processes. Pe & Gledhill (1975) studied the $^{87}Sr/^{86}Sr$ isotopic characteristics of a number of islands in the Aegean, including Santorini.

The physical volcanology of the pyroclastic deposits of the Minoan eruption was examined by Bond & Sparks (1976). They identified four different phases in the eruption: (1) a plinian phase producing a widespread pumice fall deposit; (2) a phreatomagmatic phase represented by interbedded base surge and tephra-fall deposits; (3) an enigmatic third phase consisting of massive pyroclastic deposits including some interpreted as mudflows and (4) a pyroclastic flow phase producing ignimbrite interbedded with coarse breccias and fine co-ignimbrite ash. Bond & Sparks (1976) used data on the variations of thickness and grain size in the plinian deposit to locate the vent 1 to 2 km west of the town of Phira. They found that the volume of the plinian, mudflow and breccia deposits is only a small proportion of the total volume of the eruption products and concluded that most of the volcanic material was ejected as pyroclastic flows which entered the sea, and as fine wind-blown ash associated with these flows.

A study concerning the palaeomagnetism of the Minoan deposits by Wright (1978) indicated that the clasts from the massive phase 3 deposits were deposited cold, whereas those from the phase 4 ignimbrite were deposited hot. Watkins *et al.* (1978) found Minoan volcanic ash in deep-sea sediment cores from the Eastern Mediterranean. This discovery confirmed the large magnitude of the eruption and led to a closer examination of the hypothesis of Marinatos (1939). From the thicknesses of the ash in these cores, Watkins *et al.* (1978) calculated a total minimum volume of submarine Minoan ash in the Aegean, and showed that a considerable proportion of the magma must have been erupted as pyroclastic flows. They also concluded that the volume of ash falling on Crete was probably insufficient in itself to cause a decline of the Minoan civilization, as proposed by Marinatos (1939),

although they stated that this did not preclude a relationship between the eruption and the demise of the culture.

Second International Scientific Congress, Santorini, Greece, 1978

In August 1978 the second International Scientific Congress took place. Again, this was a meeting of minds from a variety of disciplines, and papers were presented in the fields of geosciences, archaeology and related sciences. The proceedings of the Congress were published in two volumes, one before the meeting and one afterwards (Doumas 1978, 1980).

The tectonics of the Aegean region were discussed by a number of authors (e.g. Flemming 1978; Kiskyras 1978; Makris 1980). Makris & Stobbe (1980) used published heat-flow data of the Aegean area and a crustal model deduced from seismic and gravity data to estimate temperature distributions underneath Santorini. A major contribution to the Congress was the publication of a new geological map of Santorini (Pichler & Kussmaul 1980) at a scale of 1:20 000. Pichler & Kussmaul presented a new stratigraphy based on the original scheme of Reck (1936). Friedrich (1980) described several fossil plants found in palaeosols and concluded that the climatic conditions at the time were nearly the same as at present.

Nicholls (1978) presented a paper on the geochemistry of the pre-caldera rocks of Santorini and concluded that the most probable origin of the high-alumina basalts was by fractionation from more mafic, mantle-derived primary magmas. This was supported by the study of Puchelt (1978), who added that large ion lithophile elements (LILE) must have come from the subducted slab or from an additional part of the mantle. Oxygen isotope data were presented by Hoefs (1978), who found that most of the lavas had $\delta^{18}O$ values between +7 and +9. The enrichment in ^{18}O compared to pristine mantle values was attributed to either assimilation of continental crust or to secondary weathering processes.

Several questions about the Minoan eruption still remained unanswered, such as the absolute date of the eruption and its magnitude and effects in the Aegean area. Papers by Wilson (1978, 1980) concerned the energetics of the Minoan eruption. Pichler & Friedrich (1980) suggested that only one tenth of the total tephra of the Minoan eruption was ejected vertically, the remaining nine tenths coming out as lateral base surges and pyroclastic flows. They believed the deposits of the third phase of the eruption were produced by pyroclastic flows, as opposed to the mud-flow interpretation of Bond & Sparks (1976). The postulated tsunami associated with the Minoan eruption was the subject of several papers. Mészáros (1978) suggested that some of the waves could have reached northwestern Cyprus, and may have penetrated inland. Yokoyama (1978) calculated that the height of the tsunami at source was 63 m.

Research from 1978 to 1989

Sparks & Wright (1979) investigated two densely welded pyroclastic rocks exposed in the caldera wall. They demonstrated that the prominent welded black horizon below Phira is the proximal welded facies of the Middle Pumice plinian deposit.

Prior to the study by Heiken & McCoy (1984), investigators had assumed that the Minoan eruption was solely responsible for the whole of the present-day caldera. In order to determine the pre-Minoan palaeogeology and palaeotopography of Santorini, Heiken & McCoy (1984) 'stripped' off the Minoan deposit where its thickness was known, or could be inferred, and noted the elevation and lithology of the rocks below it. From this they concluded that the collapse of the Minoan caldera resulted in the formation of the present-day northern basin, but that the southern basin was already present as a long-lived topographic depression. They speculated that this older caldera was related to the Lower Pumice eruptions. Heiken & McCoy (1984) also suggested that the enigmatic third phase of the Minoan eruption, called a mudflow by Bond & Sparks (1976) and a pyroclastic flow by Pichler & Friedrich (1980), is in fact a phreatomagmatic deposit with multiple facies, including a ballistic facies, a base surge facies (proximal), a mudflow facies (distal), and slump deposits.

The PhD thesis of Druitt (1983) outlined a new stratigraphy for Santorini, calling the pyroclastic succession the Thera Pyroclastic Formation and dividing this succession into two cycles. Twelve major pyroclastic deposits were recognized in the caldera wall and were named. He examined the Middle Pumice and Cape Riva deposits in detail, and also considered the dynamics of caldera collapse. Another PhD thesis by Mellors (1988) studied some of the pyroclastic deposits of the second cycle. Volcanological studies of Santorini pyroclastic deposits provided a significant contribution to the recognition of co-ignimbrite lag breccias as a major facies of proximal localities in caldera walls. Following the initial concept of co-ignimbrite fall deposits (Wright & Walker 1977), Druitt & Sparks (1982) described lag breccias from the Santorini caldera wall and developed interpretations in which the emplacement of lag breccias involved processes of segregation within the collapsing eruption column and pyroclastic flow. Druitt (1985) provided a detailed account of the proximal lag breccias of the Cape Riva eruption. The paper by Druitt *et al.* (1989) summarized the new stratigraphy of Santorini. The emplacement temperatures of pyroclastic deposits on Santorini were investigated by McClelland & Druitt (1989) using thermal remnant magnetism. Their data demonstrated that the co-ignimbrite lag breccias of the Middle Pumice and Cape Riva eruptions were emplaced hot, and that the emplacement temperatures varied from 250°C to more than 580°C.

Several studies concentrated on the petrology and geochemistry of the lavas of Santorini, including Mann (1983), who concluded that the trace element systematics of the calcalkaline, high-alumina, basalt to rhyodacite lavas of Nicholls' Main Series could have originated by crystal fractionation of the phenocrysts observed. The PhD thesis of Huijsmans (1985; summarized in Huijsmans *et al.* 1988 and Huijsmans & Barton 1989) examined the petrology and geochemistry of Santorini lavas. Huijsmans concluded that, although the overall chemical variation in the rocks can be explained by fractional crystallization, together with variable amounts of magma mixing and assimilation, comparison of volcanic products from different eruptive centres reveals variations in magma chemistry that cannot be explained in this way. Such variations may be attributed to progressive depletion of the upper mantle by partial melting. Barton & Huijsmans (1986) discussed the post-caldera dacites of the Kameni islands, and found that these lavas have near-constant composition, even though they span an age range of 2200 years. A study of the alteration of Nea Kameni lavas was carried out by Briqueu & Lancelot (1984), who determined that the fumarolic activity had only affected the external aspect of the rocks. They found no variations in those elements that are mobile as a result of hydrothermal processes. Mitropoulos *et al.* (1987) found that lavas from Santorini have relatively lower Ba and Sr, but higher Th, K and Rb than lavas from elsewhere in the Aegean Island Arc, and concluded that the underlying asthenosphere may be involved in magma production at Santorini.

The first in-depth analyses of $^{87}Sr/^{86}Sr$ ratios of Santorini rocks was the work by Barton *et al.* (1983). They found that the $^{87}Sr/^{86}Sr$ ratios of fresh lavas ranged from 0.70472 to 0.70509 and, as this range was only just greater than analytical uncertainty, the values were considered to reflect those of the parental magmas from which the lavas were derived by fractional crystallization. They attributed the relatively high $^{87}Sr/^{86}Sr$ (compared to mantle values) to the involvement of terrigenous material, either via the subduction zone or by assimilation of lower crustal material during ascent of mantle-derived magmas. Briqueu *et al.* (1986) carried out a detailed isotopic study on the rocks of Santorini, using Sr, Nd, Hf and O systematics to try better to constrain the origins of the lavas. In his PhD thesis, Wyers (1987) also studied magma genesis using Sr and Nd isotopes on Skaros and Micros Profitis Ilias lavas. Information on the petrology and geochemistry of the pyroclastic succession in the PhD theses of Druitt (1983) and Mellors (1988) forms a substantial component of this memoir.

Sullivan (1988) discovered a layer of Minoan tephra in a sediment core taken from a small mountain lake in western Turkey. This provided the first evidence for the dispersal of Minoan tephra well to the northeast of Santorini. The tephra were deposited by the eruption and not by secondary depositional processes as there are no lacustrine muds intercalated with the tephra, and grading is absent. Sullivan (1988) did not re-calculate the total volume of Minoan tephra based on the data in his paper, but concluded that the DRE (dense-rock equivalent) volume would be much greater than 13 km^3 (Watkins *et al.* 1978).

Third International Scientific Congress, Santorini, Greece, 1989

The most recent International Meeting on Santorini took place during September 1989 at the new, purpose-built Conference Centre on Thera itself and was funded, as were all three Congresses, by Peter N. Nomikos. The proceedings of the Congress were published in three volumes (Hardy 1990), devoted to Archaeology, Earth Sciences and Chronology. The Earth Sciences part of the Congress was split into four sessions, covering explosive volcanology of the Theran islands, geology of Thera, Theran environment and comparative volcanology.

Several papers discussed the physical volcanology of Santorini. Heiken & McCoy (1990) found that the Minoan eruption was preceded by phreatic and phreatomagmatic activity, and that this activity may have been what caused people to evacuate the island. Sparks & Wilson (1990) reviewed the Minoan deposits, and calculated that the maximum column height of the plinian eruption was 36 km (±5 km). Pyle (1990*a*) calculated that the minimum volume of erupted material during the Minoan eruption was 30 ± 3 km^3 DRE. From studies of pumice density, Wilson & Houghton (1990) suggested that magma–seawater interaction during the Minoan eruption occurred at very shallow depths. McClelland & Thomas (1990) proposed that the whole Minoan eruption lasted only a few days.

Eriksen *et al.* (1990) examined fossil stromatolites found in calcareous blocks in the Minoan deposits and lying on the surface of fields on Santorini, and deduced that a sea-water filled caldera existed prior to the Minoan eruption. This caldera was even bigger than that proposed by Heiken & McCoy (1984, 1990); its existence was confirmed by the field studies of Druitt & Francaviglia (1990). A detailed study of the pre-volcanic metamorphosed basement around Athinios was presented by Skarpelis & Liati (1990).

A variety of papers were devoted to monitoring the volcanic activity of Santorini, including Fytikas *et al.* (1990*a*), Delibasis *et al.* (1990) and Papazachos (1990), and several others discussed the hydrothermal activity, metallogenesis and marine research of Santorini (e.g. Boström *et al.* 1990*a*, *b*; Perissoratis 1990).

A major controversy of the meeting was the age of the Minoan eruption, with workers having a range of opinions from as early as 1640 BC to as late as 1500 BC. Unfortunately, the inherent uncertainties in radiocarbon dating did not resolve the problem, although there was some tendency for studies to favour an earlier age (e.g. Friedrich *et al.* 1990; Hubberten *et al.* 1990) Evidence on the age of the eruption was presented from tree-ring and ice-core studies (e.g. Baillie 1990). However, there was considerable doubt about the unambiguous recognition of the Santorini event.

Research from 1989 to 1999

A detailed examination of plagioclase phenocrysts from five lavas was undertaken by Stamatelopoulou-Seymour *et al.* (1990). They used Nomarski and laser interferometry techniques to distinguish between different crystals, and found that magma mixing had occurred. The PhD thesis of Pyle (1990*b*) provided further refinements to the stratigraphy and volcanology of the pyroclastic deposits of the first explosive cycle of Santorini. He also studied the petrology and geochemistry of the pyroclastic deposits of the first cycle, and considered the U–Th disequilibrium systematics of the rocks of Santorini, finding that most samples exhibited small but distinctive ^{238}U excesses. Druitt & Francaviglia (1992) studied caldera formation on Santorini and the physiography of the islands in the Late Bronze Age. Through detailed geomorphological studies of the caldera cliffs, they were able to recognize at least four caldera-collapse events at Santorini, and to reconstruct the composite caldera which existed prior to the Minoan eruption. Guichard *et al.* (1993) found Minoan tephra in sediment cores from the Black Sea. The ash was not washed in from Turkey as the thickness of the tephra layer is fairly constant in all cores. Guichard *et al.* (1993) estimated that the total area affected by Minoan ash fallout was 2×10^6 km^2.

The PhD thesis of Thomas (1993) examined the palaeomagnetic properties of Santorini pyroclastic deposits with particular emphasis on the Minoan deposits. The thesis developed further the methodology of temperature determinations from thermal remanent magnetism of lithic and pumice clasts. He established that the emplacement temperatures for the different phases of the Minoan eruption were 250–300°C (plinian), 150–200°C (surge), <300°C (phase 3 deposits) and 300–350°C (phase 4 ignimbrites). He interpreted these deposits as low-temperature ignimbrites transitional to pumiceous mudflows. The PhD thesis of Edwards (1994) examined the minor pyroclastic deposits in between several of the major pyroclastic units. The minor deposits are very similar to deposits documented from Sakurajima volcano in Japan (Kobayashi 1986; Imura 1993). The PhD of Edwards (1994) involved a detailed isotopic study of the pyroclastic deposits of Santorini and the results of this work are presented in this Memoir.

The pyroclastic deposits of Santorini have continued to provide a focus for the investigation of processes in explosive volcanic eruptions. Gardner *et al.* (1996) measured pumice densities from several deposits in the Thera pyroclastics and measured the water contents of melt inclusions in phenocrysts. Their results indicated that the rhyodacitic magmas contained 5–6% water and that the andesitic magmas contained 3–4% water. Cottrell *et al.* (1999) presented experimental investigations of the products of the Minoan eruption. They found that the pre-eruption water content of the rhyodacitic magma of 5–6% was sufficient to stabilise amphibole. Since almost all the Minoan pumice contains no amphibole they inferred that the magma originated at depths where amphibole was stable but had ascended to shallow depths prior to eruption.

Zellmer (1999) considered the time-scales of magmatic processes on Santorini, providing further U-series isotopic data (Zellmer *et al.* 1998) and investigations of the diffusive relaxation of trace elements profiles in plagioclase phenocrysts from Kameni lavas (Zellmer *et al.* 1999).

In 1998, an English translation (by A. R. McBirney) of Fouqué's (1879) book was published (Fouqué 1998).

Santorini: a European Laboratory Volcano

Santorini was declared one of five laboratory volcanoes in the Environment Programme of the European Commission. The EC initiative gave further impetus to reseach on Santorini. The Proceedings of a workshop on Santorini (2–4 May 1996) have been published by the European Commission (Casale *et al.* 1998). Considerable effort has gone into developing montoring networks and baseline data and Casale *et al.* (1998) contains several contributions describing geophysical, geochemical and remote-sensing studies of Santorini. New data were also published on the petrology and geochemistry of Santorini, including studies of the Akrotiri centres (Davis *et al.* 1998; Dietrich *et al.* 1998; Gartzos *et al.* 1998) and geochemical and petrological data on the Thera Pyroclastic Formation (Druitt *et al.* 1998; Tarney *et al.* 1998; Stamatelopoulou-Seymour *et al.* 1998).

Chapter 2
Geological and tectonic setting of Santorini

Santorini lies in an area of complex extensional and subduction-related tectonics in a continental environment (Jackson 1994). The region has had a long geological history with large changes occurring during the Alpine orogeny and in the Late Tertiary as a consequence of post-collisional extension and major re-adjustments of the plate boundaries. The Aegean region is thought to be moving towards the southwest where the Aegean microplate overrides the Eastern Mediterranean sea floor. The collision has created the Hellenic trench to the south of Crete where the eastern Mediterranean sea floor is subducting beneath the Aegean Sea at 5–6 cm a^{-1}. Santorini is one of several Quaternary volcanoes that define the present day active volcanic arc related to this subduction zone (Fig. 2.1). We here provide a synopsis of the broader geological and tectonic context of Santorini within the Aegean area. The geology, isotope geochemistry and geochronology of the crystalline basement of the southern Aegean is of particular relevance as it is likely that the Santorini magmas have interacted extensively with the continental crust. Geochemical evidence presented in Chapters 6 and 7 confirms this prediction. We also give a synopsis of the Quaternary Aegean Island Arc, of which Santorini is the most active centre.

Tectonic setting of the Aegean

The Aegean Sea lies at the confluence of two Alpine mountain chains: the Hellenic chain of Greece and the Pontide–Tauride chain of western Turkey. Alpine rocks form the basement of the Aegean arc. The Aegean is situated on the small, rapidly moving continental Aegean microplate (McKenzie 1970; Jackson 1994), which also incorporates part of mainland Greece, Crete, Rhodes and western Turkey. Tertiary volcanism in the northern Aegean was related to subduction of the African plate beneath the European plate (Fytikas & Marinelli 1976). After the main Tertiary phase of continental collision, lithospheric fragmentation occurred and numerous microplates were formed (Dewey *et al.* 1973). The Aegean microplate stabilized in the mid-Miocene, and the African plate is now subducting in a northeasterly direction beneath the Aegean microplate. Relative to Asia the Aegean microplate is moving southwest at about 3.5 cm a^{-1} and is believed to be partly a response to the westward motion of Turkey along the North Anatolian fault system (Jackson 1994). This subduction began 13 Ma ago (Angelier *et al.* 1982), although Mercier *et al.* (1989) believe that 16 Ma is a better estimate. Extension was initiated in Upper Miocene times. The extension direction changed from WNW–ESE (Late Miocene), to NE–SW (Pliocene–Early Pleistocene) and is currently N–S to NW–SE (Mercier *et al.* 1989).

The present Benioff zone (Figs 2.1 and 2.2) passes south of Crete and dips at an angle of about 30° (Fig. 2.1). The convergence rate is 5–6 cm a^{-1} (Kalogeropoulos & Paritsis 1990; Jackson 1994) and the subduction direction N50E. The associated Hellenic trench system has two main branches (McKenzie 1978; Le Pichon *et al.* 1979). The Ionian trench strikes almost at right angles to the subduction direction and thrust motion is dominant. The Pliny and Strabo trenches strike almost parallel to subduction and the faulting is mainly strike-slip.

Continental crust underlies the entire Aegean region (Makris 1978). Crustal thickness varies from 20 to 32 km. Heat flow is high, and P-wave velocities in the underlying mantle are low (7.5–7.7 km s^{-1}; Kalogeropoulos & Paritsis 1990). As the crust beneath the rest of Greece and Turkey is 40–60 km, McKenzie (1978) estimated that the crustal thickness of the Aegean has been mechanically halved by extension in the last 5 Ma. Stretching has been concentrated in two deep grabens, the Cretan and Anatolian troughs. Between these troughs lies the Central Aseismic Plateau, a relatively stable crustal block characterized by low seismicity. The present-day arc volcanoes lie on the faulted southern boundary of the Central Aseismic Plateau. Regionally the Aegean area has many active faults (Fig. 2.1) which are accommodating active extension. Faulting in the central and northern Aegean is dominated by sets of NE–SW right-lateral strike-slip faults, whereas in the western Aegean and on mainland Greece NW–SE normal faults are most abundant. The latter are believed in part to be ancient faults and structural disconformities reactivated by the present stress regime (Jackson 1994).

Papazachos & Pangiotopoulos (1993) found that epicentres of shallow- and intermediate-depth earthquakes in the southern Aegean form five distinct clusters, which pass through the five volcanic centres of Crommyonia, Methana, Milos, Santorini and Nisyros (Fig. 2.2). The epicentres of the earthquakes and the centres of volcanic activity lie on NE–SW lineaments interpreted as deep rupture zones in the lithosphere. There are similar trends in the geomorphological features such as the grabens between islands. Santorini lies on a NE–SW rupture zone about 70 km long that extends northeast to the island of Amorgos and southwest to the volcanic Christiana Islands (Papazachos & Pangiotopoulos 1993; Mountrakis *et al.* 1998). Details of the local tectonic setting of Santorini are described in Chapter 3.

The crystalline geology of the south Aegean

The crystalline rocks of the Aegean underlie the arc volcanics, and magma rising from the mantle must pass through these rocks. It is probable that some degree of selective assimilation, partial melting or bulk assimilation of the crustal rocks has influenced magma genesis on Santorini. The geology of the crystalline basement rocks is therefore relevant to our later discussion of the geochemistry and isotope systematics of the Santorini magmas (Chapters 6 and 7). The crystalline rocks in this area form the Cycladic Crystalline Complex and link similar rocks of Central Greece with those of the Menderes Massif in Turkey (Fig. 2.3). The rocks are metamorphic with several granitoid intrusions. The sedimentary and igneous protoliths to the metamorphic rocks are believed to be late Palaeozoic/early Mesozoic to post-Mesozoic in age and the granitoid intrusions are Miocene. The metamorphic rocks consist of metabasic rocks, metapelites, metamorphosed intrusive rocks, metasedimentary rocks, metavolcanic rocks and metacarbonates. The sedimentary and volcanic protoliths were laid down on an older, Hercynian basement (Schliestedt *et al.* 1987).

There are two major tectonic units (Jansen & Schuiling 1976; Altherr & Seidel 1977; Durr *et al.* 1978; Van der Maar *et al.* 1981; Henjes-Kunst & Kreuzer 1982; Van der Maar & Jansen 1983; Andriessen *et al.* 1987). Different authors have used different terminologies and so, for clarity, we refer to them as Basement Units A and B (BU-A and BU-B).

Basement Unit A (BU-A)

This comprises schists, gneisses and metamorphosed intrusive rocks of late Palaeozoic/early Mesozoic age. The Basement shows relicts of a Pre-Alpine metamorphic history. There are no exposures of BU-A on Santorini, so we describe briefly the geology of four neighbouring islands to characterise the broad features of the possible upper parts of the continental crust in the area.

There are large exposures of BU-A on Ios and, to a lesser extent, on Naxos and Sikinos. On Ios (Fig. 2.4a) BU-A forms a dome consisting of an augen-gneiss core mantled by garnet-mica schists. Although BU-A has suffered both episodes of Alpine metamorphism, some relicts of an older, high-temperature history

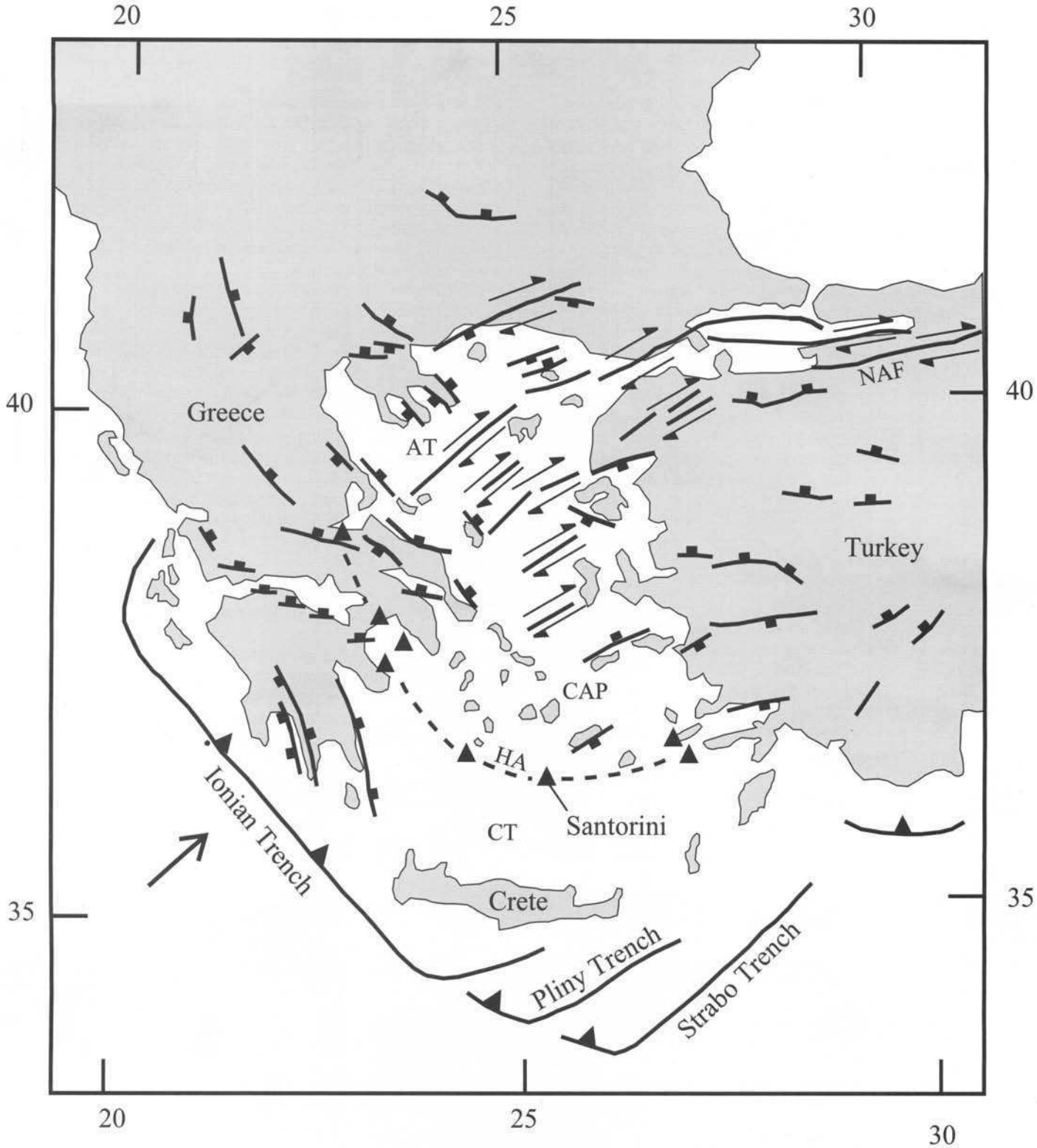

Fig. 2.1. Map of the Aegean region, showing the principal active faults, the three branches of the Hellenic Trench system, and the volcanic island arc (dotted). Boxes mark the downthrow sides of normal faults, and triangles the overriding plates of thrust faults. HA Hellenic Arc, CT Cretan Trough, AT Anatolian Trough, CAP Central Aseismic Plateau, NAF North Anatolian Fault. Individual Quaternary volcanic centres of the arc are shown as triangles. The arrow in the bottom left is the subduction vector. The fault pattern is taken from Jackson (1994).

still remain. Jansen (1973) interpreted the migmatite gneiss dome in the north-central part of Naxos (Fig. 2.4b) as being BU-A, separated from BU-B by a thrust plane characterized by ultramafic lenses. BU-A on Sikinos is exposed in the southeast of the island (Fig. 2.4c) and is a sequence of quartz-chlorite-mica-garnet schists with bodies of metadiorite rocks (Van der Maar *et al.* 1981). The metamorphism affecting the intrusive rocks on Ios is believed to be 268 to 295 Ma (Hercynian: Henjes-Kunst & Kreuzer 1982; Andriessen *et al.* 1987), and so the rocks of BU-A must be older than this. Indeed the intrusive rocks have Rb–Sr whole-rock ages from 462 ± 40 Ma to 520 ± 55 Ma (Henjes-Kunst & Kreuzer 1982), but the age of the country rocks they intrude is unknown. Andriessen *et al.* (1987) found that a metadiorite intrusion on Sikinos has a Rb–Sr date of 275 ± 87 Ma.

For BU-A initial $^{87}Sr/^{86}Sr$ values for Ios are 0.711 to 0.712, for Naxos 0.714 and for Sikinos 0.714 (Altherr *et al.* 1979; Andriessen

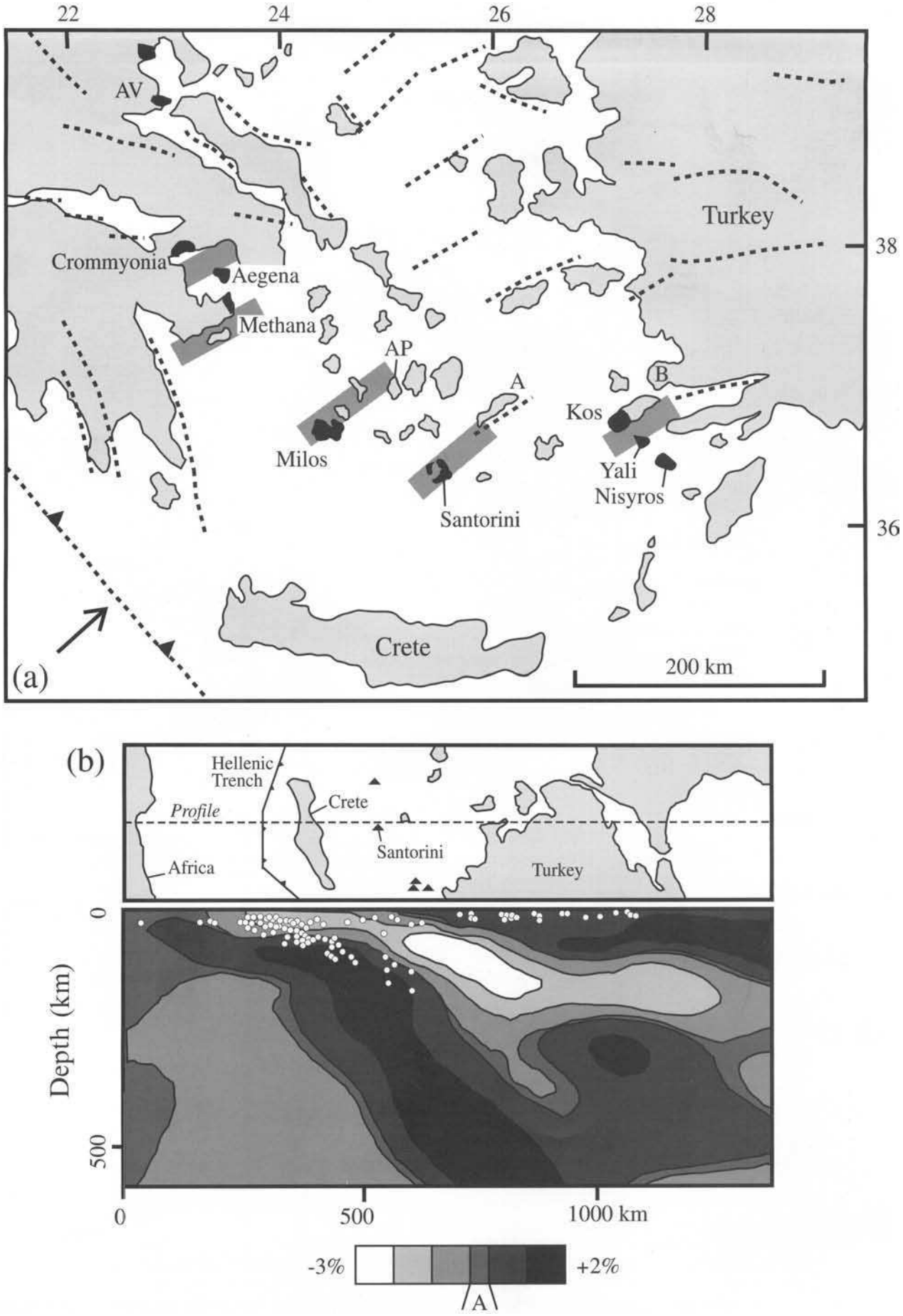

Fig. 2.2. (**a**) Volcanic centres of the Hellenic Arc (in black). The centres lie upon NE–SW-trending fault zones marked by concentrations of shallow to intermediate depth earthquakes (Papazachos & Panagiotipoulos 1993). The dotted lines are active faults of the region, taken from Fig. 2.1. AV, Atlanti–Volos; AP, Antiparos; A, Amorgos; B, Bodrum. (**b**) NNE–SSW cross-section of the crust and upper mantle beneath Santorini, modified from Spakman *et al.* (1988). The upper panel shows the Hellenic trench and volcanoes of the volcanic arc (triangles). The dotted line marks the cross section. The lower panel shows the P-wave heterogeneity calculated from tomographic data, with contours as percentages of the ambient upper mantle velocity, from −3% to +2%. The interval from −0.1% to +0.1% corresponding to the ambient value is marked by the letter A. The dipping positive (black) anomaly is interpreted as the cold subducting plate. Earthquake focii are shown as white dots.

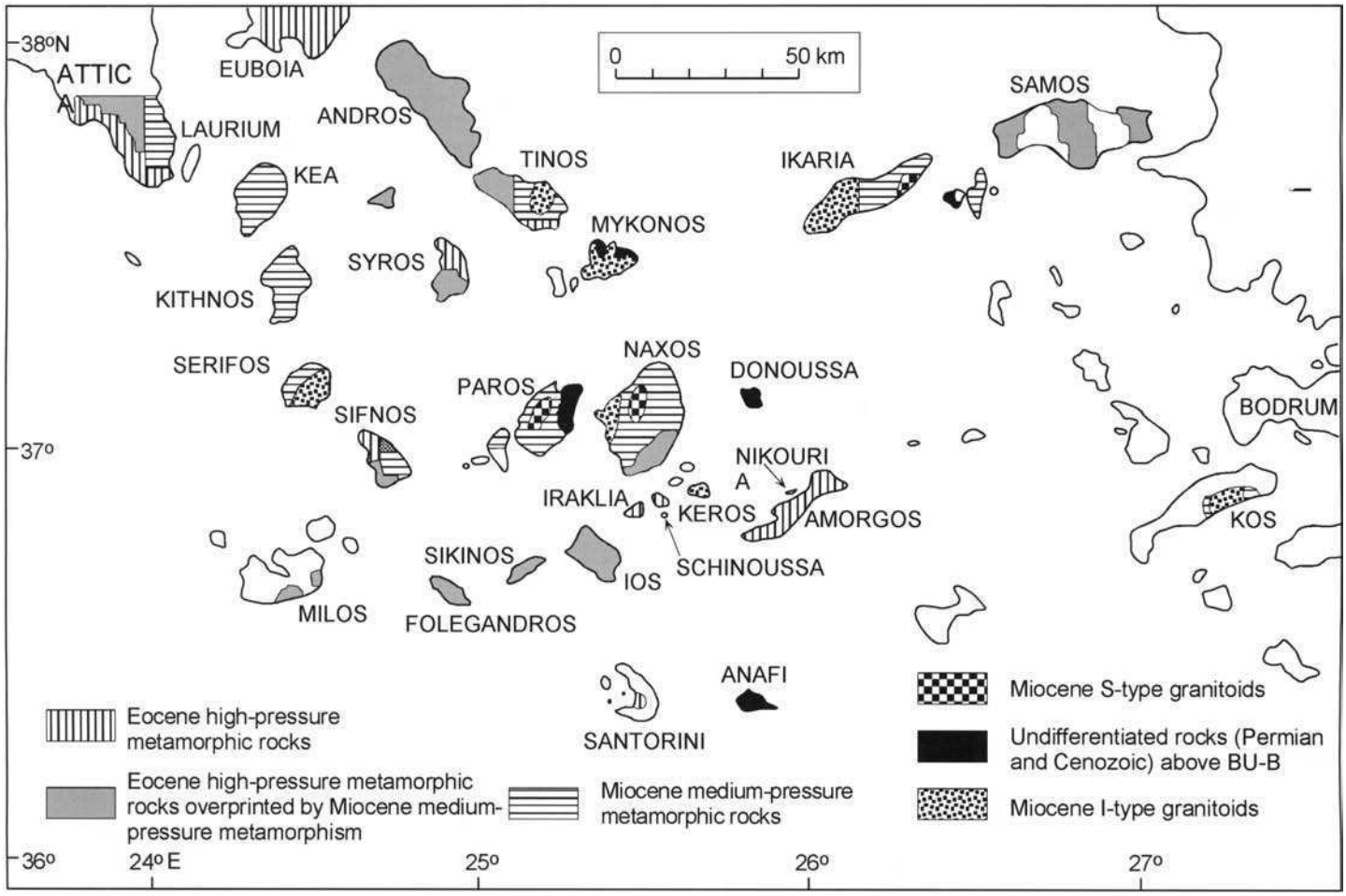

Fig. 2.3. Generalized geological map of the Cycladic Crystalline Complex (after Schliestedt *et al.* 1987).

et al. 1979; Henjes-Kunst & Kreuzer 1982). The elevated values compared to typical mantle indicate a significant component of older crust, and are consistent with a Proterozoic contribution implied by ages reported by Kreuzer *et al.* (1978).

Basement Unit B (BU-B)

Also called the 'Series' by Andriessen *et al.* (1987), this unit comprises alternations of marbles and schists, and isoclinally folded metasediments and metavolcanics. The BU-B unit of Santorini consists principally of schists and crystalline limestones. It is described in detail by Skarpelis & Liati (1990) and by Kilias *et al.* (1998). The schists include metapelites, metapsammites, and metavolcanics. The limestones are of Upper Triassic age and tectonically overlie the schists, which are in part of Palaeocene/Eocene age. BU-B on Ios mainly consists of alternations of isoclinally folded marbles and chlorite, actinolite and glaucophane schists (Fig. 2.4a). The boundary between BU-A and BU-B on Ios is interpreted as a metamorphosed thrust plane due to the presence of ultramafic lenses in the chlorite schists (Van der Maar 1980). Van der Maar & Jansen (1983) considered the ultramafic rocks to be ophiolitic remnants. Schist and marble units surround the migmatite dome on Naxos (Fig. 2.4b), with the metamorphic grade decreasing away from the dome. BU-B on Sikinos and Sifnos is composed of similar rock types to those of Ios and Naxos (Fig. 2.4c and d).

No systematic geochronological studies exist for BU-B. The marble units on Naxos are very similar to emery-bearing marbles of the Menderes Massif in Turkey, and, as Mesozoic fossils have been found in the Turkish marbles, the marbles of Naxos may be of a similar age (Durr *et al.* 1978). A $^{87}Sr/^{86}Sr$ ratio of 0.708 has been determined for the Naxos marbles, which may approach the original Sr isotopic composition of the marine limestone protolith (Andriessen 1978). Marine Sr isotopic values were around this value in the late Palaeozoic/early Mesozoic (Veizer & Compston 1974).

Alpine metamorphism

Both basement units have undergone two main phases of Alpine metamorphism (Altherr *et al.* 1979; Andriessen *et al.* 1979): (i) an Eocene high-pressure event (M1) producing blueschist-facies assemblages; (ii) a Miocene medium-pressure event (M2) producing greenschist-facies assemblages (Fig. 2.3).

Unaltered M1 assemblages appear on several islands including Amorgos, Ios, Milos, Naxos, Sifnos and Syros. Relict assemblages that have been overprinted by the later greenschist facies metamorphism also appear on Santorini, Ios, Folegandros, Naxos, Serifos, Sifnos and Syros (Fig. 2.3). Glaucophane is preserved only very locally in metabasic lithologies on Santorini (Davis & Bastas 1978).

The high-pressure unit in northern Sifnos (Fig. 2.4d) mainly consists of metabasites and metasediments (Okrusch *et al.* 1978; Schliestedt 1980; Matthews & Schliestedt 1984) (Fig. 2.4d). The southeastern part of Naxos and the northern part of Ios contain glaucophane-bearing assemblages, whilst upper greenschist-facies metamorphism has overprinted the blueschist assemblages elsewhere (Van der Maar & Jansen 1983). The age distribution ranges from 32 to 50 Ma. Phengites from the study of Altherr *et al.* (1979) yield a K–Ar date of 42.6 ± 0.5 Ma and a Rb–Sr date of 40.8 ± 6 Ma, putting the M1 metamorphism at around 42 Ma. $^{40}Ar/^{39}Ar$ dates for M1 minerals are around 50 Ma (Wijbrans & McDougall 1988).

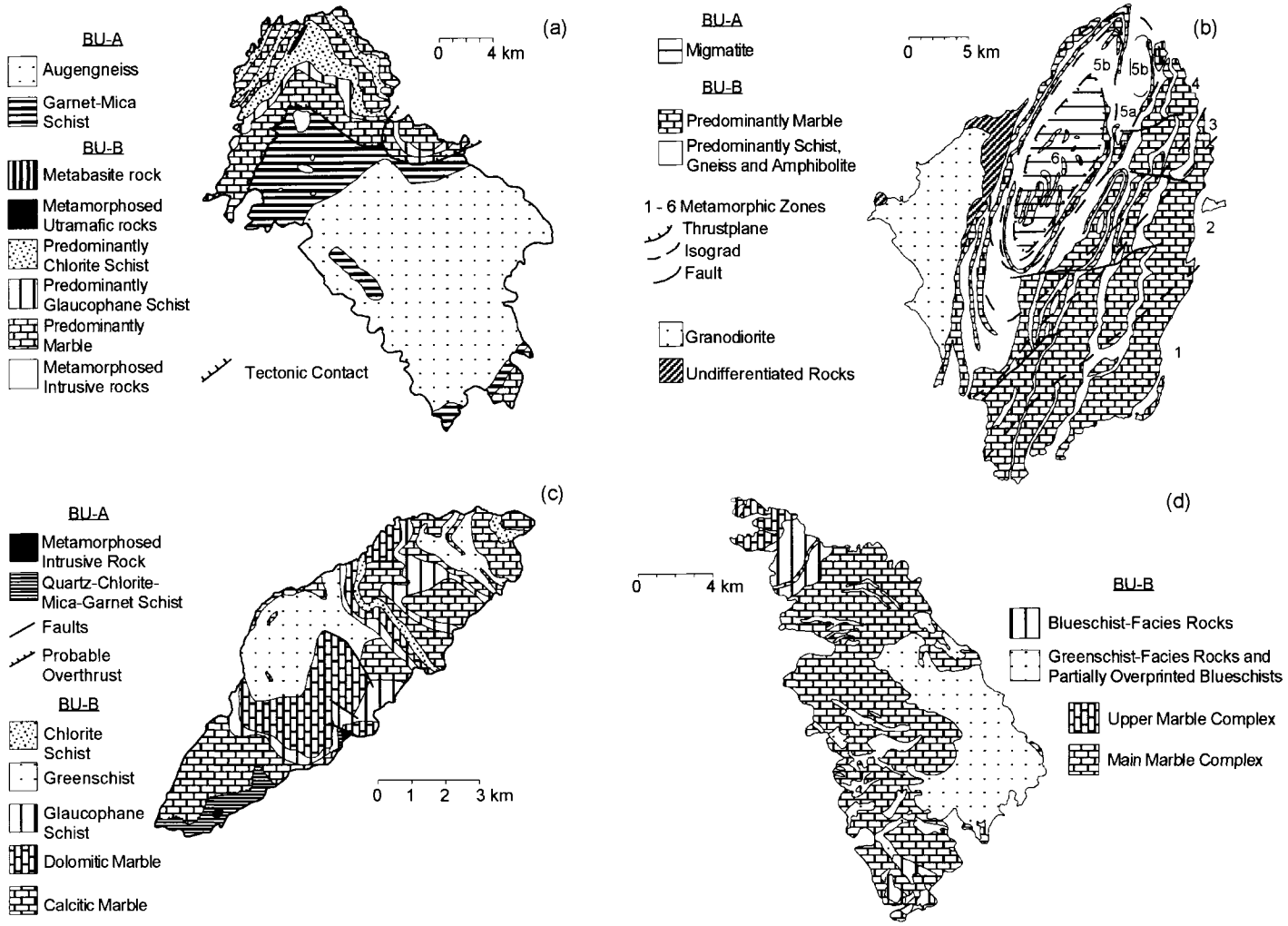

Fig. 2.4. Simplified geological maps of (**a**) Ios (after Van der Maar & Jansen 1983), (**b**) Naxos (after Schliestedt *et al.* 1987), (**c**) Sikinos (after Van der Maar *et al.* 1981), and (**d**) Sifnos (after Matthews & Schliestedt 1984).

Initial $^{87}Sr/^{86}Sr$ values for Sifnos range from 0.705 to 0.710 (Altherr *et al.* 1979; Andriessen *et al.* 1979; Henjes-Kunst & Kreuzer 1982). $\delta^{18}O$ values for the metabasites on Sifnos are $+>10‰$, with a highest value of about +15.5‰ (Matthews & Schliestedt 1984).

Most of the Cycladic islands have been affected by the M2 greenschist metamorphism, which overprinted the earlier blueschists in many places (Fig. 2.3). On Santorini, all of the schists have been strongly overprinted under greenschist facies conditions, and the blue amphibole largely replaced by actinolite (Davis & Bastas, 1978). Greenschist facies rocks are exposed in the southern and central parts of Sifnos (Fig. 2.3d). The temperatures of metamorphism overlap those of the blueschist facies (Matthews & Schliestedt 1984). On Naxos, Jansen & Schuiling (1976) and Jansen *et al.* (1978) identified a series of zones of increasing metamorphic grade towards the centre of the migmatite dome and estimated that the temperature in the centre of the dome was 700°C, whereas in the southeastern corner of the island it was 350°C.

For central Sifnos isotopic dates vary between 21 Ma and 24 Ma. (Altherr *et al.* 1979). On Naxos K–Ar and $^{40}Ar/^{39}Ar$ dates range from 31 Ma to 9 Ma. K–Ar ages decrease with increasing metamorphic grade (Andriessen *et al.* 1979). The hottest temperatures of M2 were in the migmatite dome, where partial melting occurred, and temperatures decrease away from this dome. The radiometric ages increase away from the dome due to more rapid cooling rates, and indicate a smooth cooling over 10–20 Ma.

There is a paucity of isotopic data for M2. Initial $^{87}Sr/^{86}Sr$ data for Sifnos are around 0.707 (Altherr *et al.* 1979). On Sifnos, $\delta^{18}O$ values for non-carbonates are enriched relative to the M1 rocks, and Matthews & Schliestedt (1984) attribute this to the infiltration of large quantities of a fluid phase enriched in ^{18}O that had pervasively re-equilibrated with the metamorphic system. Rye *et al.* (1976) found that M2 $\delta^{18}O$ values on Naxos decrease as the thermal dome is approached, the highest value being +22‰ (zone 3), and the lowest +6‰ (zone 6).

Miocene granitoid intrusions

The distribution of granitoid rocks in the Cyclades is shown in Fig. 2.3. Both S- and I-types are present. The I-types vary regionally in composition, with granodiorites tending to occur in the west (Laurium, Serifos), granites and leucogranites in the centre (Tinos, Mykonos, Naxos, Ikaria), and monzonites in the east (Samos and Kos; Altherr *et al.* 1988). Most of the I-type plutons are composite and mixing between the different magma batches has occurred to some degree, depending on the time interval between successive batches.

A late Miocene I-type granite and its metamorphic halo have been encountered in a borehole at Santorini (Skarpelis *et al.* 1988). The I-type granodiorite to monzonite pluton on Naxos (Fig. 2.4b) caused contact metamorphism and metasomatism of the country rock. Andriessen *et al.* (1979) reported a Rb/Sr whole-rock age of 11.1 ± 0.7 Ma for the pluton, but, as this dates the aplitic and pegmatitic phases, it is probably a minimum age. The date correlates with the final stages of the M2 metamorphism. Wijbrans & McDougall (1988) found a range of K/Ar and $^{40}Ar/^{39}Ar$ dates of 13.6 ± 0.2 Ma, to 11.2 ± 0.1 Ma for the Naxos intrusion, which are slightly older than the date of Andriessen *et al.* (1979).

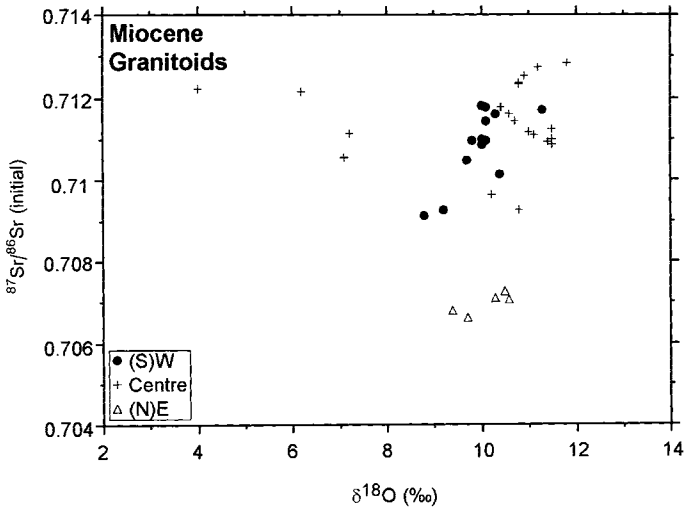

Fig. 2.5. Plot of $^{87}Sr/^{86}Sr$ v. $\delta^{18}O$ for the Miocene granitoids of the Aegean (data from Altherr *et al.* 1988).

Figure 2.5 shows $^{87}Sr/^{86}Sr$ and $\delta^{18}O$ values for Miocene I-type granitoids. The highest values of $^{87}Sr/^{86}Sr$ occur in the central granites of Ikaria, Mykonos, Naxos and Tinos and range from 0.709 to 0.714. The lowest values occur in the eastern monzonites of Kos and Samos and range from 0.706 to 0.708. Intermediate values occur in the western granodiorites of Laurium and Serifos and range from 0.709 to 0.712. $\delta^{18}O$ values are generally in the range +9‰ to +12‰, significantly higher than typical mantle values of +5.5‰ to +6‰.

Deeper parts of the crust

The exposed basement geology in the Aegean only represents upper crustal lithogies. The nature of the deeper crust can only be a matter of speculation. The isotopic data discussed indicates that part of this deeper crust may be Proterozoic gneisses as it is in other deeper parts of the Hercynian crust of southern Europe. The Miocene type granites imply that partial melts have been extracted from the middle and lower crust so it is quite likely that refractory mafic rocks have been left behind. Both the Miocene plutons and more recent arc volcanism since 4 Ma could also have added significant amounts of mafic igneous rocks to the lower parts of the crust as underplated material. Thus the deeper parts of the Aegean crust are expected to be more mafic and less radiogenic than the upper crustal rocks.

Volcanism in the Aegean area

Two main phases of volcanism are recognized in the Aegean region, the first occurring from Oligocene to mid-Miocene times, with the second starting in the late Pliocene and continuing to the present-day (Fytikas *et al.* 1984). The Oligocene–mid-Miocene episode of volcanism mainly affected the north Aegean area, with volcanic activity moving southwards with time. Between the Middle Miocene and the Quaternary, volcanic activity was scattered all over the Aegean area, including Samos and Patmos in the central Aegean (Fytikas *et al.* 1984).

The main episode of volcanism in the south Aegean area began at the end of the early Pliocene, forming the Aegean island arc. The arc has been interpreted as a double structure, with an inner arc stretching from Thebes, through Antiparos, to eastern Kos, and an outer arc from Crommyonia through Methana, Aegina, Poros, Milos and Santorini, to Nisyros and western Kos, with volcanism occurring concurrently along both segments (Fytikas & Marinelli 1976; Innocenti *et al.* 1979; Fytikas *et al.* 1984). Rocks of the inner arc are chemically distinct from those of the active outer arc. According to Innocenti *et al.* (1981) inner arc rocks formed by volcanism along transcurrent faults and are not related directly to subduction.

The Aegean island arc

The width of the Aegean arc does not exceed about 20 km (Keller 1982). Activity at some centres began in the late Pliocene, but the majority is Quaternary (Pe-Piper *et al.* 1983; Fytikas *et al.* 1986). Volcanism at Crommyonia began 3.9 Ma ago and terminated around 2.7 Ma. Aegina became active 4.4 Ma ago and, like Poros, was extinct by the late Quaternary. Methana, Santorini, and Nisyros have each had historic eruptions and are best considered dormant. Methana erupted in 250 BC. Santorini has had numerous historic eruptions, the last in 1950. Nisyros exhibited strong fumarolic activity and phreatic eruptions up to the end of the nineteenth century (Keller 1982). Large composite volcanoes with Quaternary calderas occur in the central and eastern sectors of the arc (Milos, Santorini, Kos, Nisyros), whereas lava dome complexes dominate in the western part (Aegina, Methana, Poros; Innocenti *et al.* 1981).

It was formerly believed that a group of small centres in northeastern Greece, collectively termed the Atlanti–Volos Group (3.5–0.5 Ma; Fytikas & Marinelli 1976) belonged to the Aegean arc. However this volcanism is alkaline in nature and is related to back-arc extension.

The positions of the volcanic centres are strongly controlled by the five NE–SW lithospheric rupture zones recognized by Papazachos & Pangiotopoulos (1993) (Fig. 2.2). Moreover, fault-plane solutions for earthquakes along the arc are normal in character (McKenzie 1978; Jackson *et al.* 1982). Thus despite the compressive stress regime associated with subduction, the arc has developed in an extensional environment.

Rock types in the Aegean arc range from basalt to rhyolite in the eastern sector, and mafic andesite to dacite in the western sector, with andesites and dacites predominating overall. The volcanic rocks of Crommyonia and Poros are dacitic (Pe 1972). In Aegina, there are domes and lava flows with deeply eroded morphologies, and Pe (1973) recognized four lava series ranging from mafic andesites to rhyodacites. Similar rock types are found on Methana (Pe 1974), but they are fresher. On Milos the basement is covered by a basal pyroclastic series laid down by submarine volcanic activity. Above this are complexes of domes and lava flows, more pyroclastics, and the deposits of phreatic activity, all of subaerial

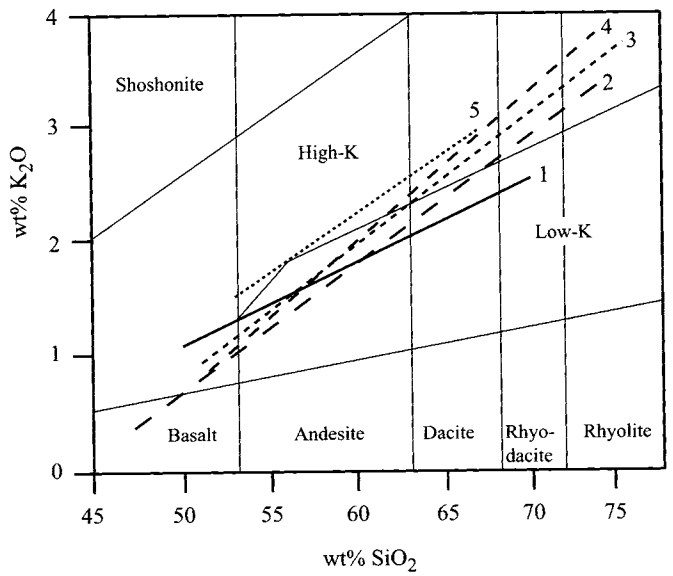

Fig. 2.6. K_2O v. SiO_2 diagram for Aegean arc volcanics. Trends from Innocenti *et al.* (1981) for different volcanic centres are represented by best-fit lines. Classification fields after Peccerillo & Taylor 1976: 1, Methana; 2, Milos; 3, Santorni; 4, Nisyros; 5, Aegina.

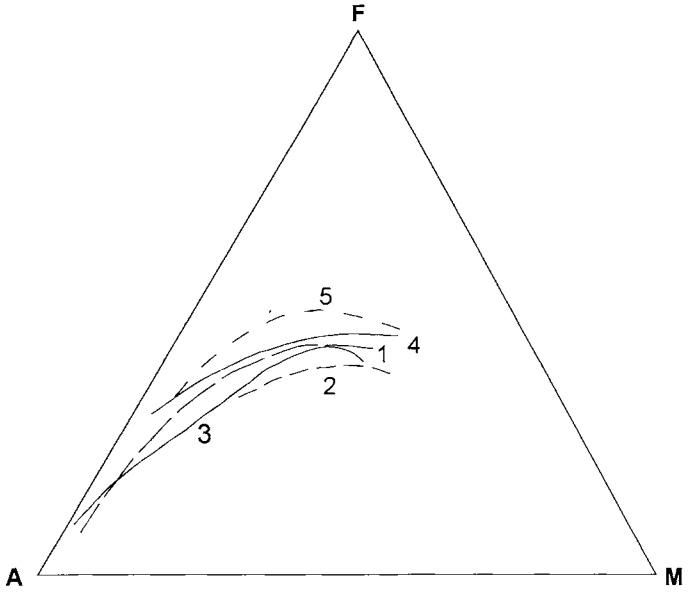

Fig. 2.7. AFM curves for rock suites from different Aegean volcanic centres. $A = Na_2O + K_2O$; $F = FeO + Fe_2O_3$; $M = MgO$. 1, Milos; 2, Methana; 3, Nisyros; 4 & 5, different suites of Santorini lavas recognized by Innocenti *et al.* (1981).

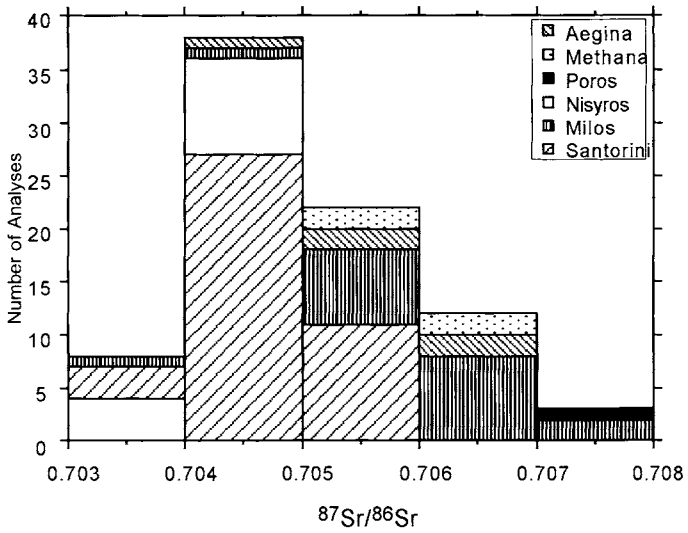

Fig. 2.8. Histogram of $^{87}Sr/^{86}Sr$ for islands of the Aegean arc (data from Pe 1975; Pe & Gledhill 1975; Barton *et al.* 1983; Briqueu *et al.* 1986; Wyers & Barton 1989).

origin (Fytikas *et al.* 1986). The oldest successions on Milos are dominated by andesites and dacites, whilst the younger rocks are mainly rhyolites (Fytikas *et al.* 1986). The volcanic rocks of Santorini range from mafic to rhyodacites. Santorini is the only volcano in the arc with extensive basalts (Keller 1982). The geology of Nisyros has been examined in some detail (Di Paola 1974; Wyers & Barton 1989; Stamatelopoulou-Seymour & Vlassopoulos 1992). Rocks range from mafic andesites to rhyodacites, with rhyolites appearing only on Yali, a small island 5 km north of Nisyros. Caldera formation on Nisyros was accompanied by intense pyroclastic eruptions, producing fallout deposits with pyroclastic flows and surges. Collapse of a submarine caldera occurred during the eruption of a large ignimbrite from the centre of Kos, about 160 000 years ago (Allen & Cas 1998).

In the Aegean arc as a whole the rocks are mainly porphyritic, with the most mafic types dominated by clinopyroxene, partially resorbed olivine, plagioclase and Ti-magnetite. Orthopyroxene occurs only occasionally. In intermediate compositions, clinopyroxene, plagioclase, Ti-magnetite and, to a lesser extent, orthopyroxene occur. Hornblende phenocrysts are found in rocks from Methana, Aegina, Milos and in the oldest products of Santorini. Hornblende and orthopyroxene increase in the more evolved rocks, and biotite, sanidine and rare quartz are found in the rhyolites (Innocenti *et al.* 1981). Detailed descriptions of the petrological features of Aegean arc rocks can be found in Nicholls (1971*a*), Di Paola (1974), Fytikas *et al.* (1986) and Wyers & Barton (1989).

Geochemically, the more mafic rocks of the Aegean arc have high Al_2O_3 (generally higher than 18%), TiO_2 between 0.8 and 0.9%, and relatively low K_2O (Fig. 2.6; Innocenti *et al.* 1981). Intermediate and silicic compositions have medium to high K_2O. Magmas of all the islands have calc-alkaline affinities (Fig. 2.7), although some Santorini lavas and tuffs show more tholeiitic characteristics (Chapter 6). Rocks of most of the islands display negative Eu anomalies, indicating that plagioclase has played an important role in the evolution of the magmas (Innocenti *et al.* 1981). Mitropoulos *et al.* (1987) believe that, although lavas within individual volcanic centres have trace element ratios consistent with fractional crystallisation, between-island variations suggest that the subcontinental lithosphere beneath the southern Aegean is rather complex. Lavas from the eastern (Nisyros, Kos) and western (Milos, Poros, Aegina, Methana) parts of the arc have higher abundances of Ba and Sr, but relatively lower Th, K and Rb concentrations than Santorini in the centre of the arc (Keller 1982; Mitropoulos *et al.* 1987).

Previously published $^{87}Sr/^{86}Sr$ ratios for Aegean arc volcanics are shown in Fig. 2.8. Pe & Gledhill (1975) found values of $^{87}Sr/^{86}Sr$ for the western sector of the Aegean arc to be 0.7041 to 0.7068 (Aegina), 0.7058 to 0.7067 (Methana) and 0.7073 (Poros). In contrast, $^{87}Sr/^{86}Sr$ values for lavas from the eastern part of the arc range from 0.7038 to 0.736 (Santorini), 0.7035 to 0.705 (Nisyros), and 0.7038 to 0.7076 (Milos) (Puchelt & Hoefs 1971; Pe & Gledhill 1975; Barton *et al.* 1983; Briqueu *et al.* 1986; Wyers 1987; Wyers & Barton 1989). However, the higher values of Santorini are thought to be due to alteration, and the range is more likely to be 0.7038–0.7058. It is evident that the eastern part of the Aegean arc has lower $^{87}Sr/^{86}Sr$ values than the western part. Pe & Gledhill (1975) attributed this to variable amounts of selective assimilation of LILE from crustal rocks and/or differences in the mantle source regions. Barton *et al.* (1983) put it down to greater crustal thickness, and thus greater crustal contamination, in the west. They proposed that the high $^{87}Sr/^{86}Sr$ values (relative to MORB) of Santorini and Milos are due to minor amounts of assimilation of crustal material with concurrent fractional crystallization, but that unusual mantle source material may also have been involved. The differences in $^{87}Sr/^{86}Sr$ values for Santorini and Milos reflect different degrees of assimilation. Briqueu *et al.* (1986) found that, in contrast to Santorini, the least evolved lavas of Milos are the most contaminated, and they attributed this to the geodynamic evolution of the Aegean subduction zone. Phases of tectonic extension resulted in the eruption of rhyolites formed by either anatexis of LILE-depleted crust, or by mixing of crustal melts with mantle-derived magmas. Compressive episodes led to the formation of hotter, more mafic magmas that remained in magma chambers in the crust for longer, and so assimilated more crustal material.

Summary

(1) The Aegean region has had a complex geological evolution. Crystalline basement may extend back to Proterozoic age on the basis of isotopic data. The exposed basement consists of metamorphic rocks of Late Palaeozoic to Mesozoic age.

(2) The main episodes of deformation and metamorphism occurred during the Alpine Orogeny with an earlier high pressure and low temperature phase of metamorphism, and a later moderate pressure–higher temperature phase. In the Miocene there was regional emplacement of granite plutons and the region transformed from dominantly compressional tectonics with overthickened crust to extension and substantial crustal thinning and

subsidence. The exposed basement reveals some of the upper crustal lithologies through which Santorini magmas passed on their way to the surface, but deeper unexposed crustal rocks are likely to be more mafic and refractory as a consequence of partial melting events and underplating.

(3) Subduction in the region began between 13 and 16 Ma. Volcanism began in the Oligocene and continued until the middle Miocene, particularly in the northern Aegean.

(4) Subduction is today occurring at 5–6 cm a^{-1} in a N50E direction. Continental crust underlies the entire region, and the thickness varies from 20 to 32 km. The first volcanic activity of the modern arc began about 4 Ma and at least three centres remain potentially active at the present day. The volcanic centres are concentrated on five major NE–SW-trending lithospheric rupture zones and are situated in an extensional tectonic environment.

(5) The volcanic products of the modern arc are calc-alkaine to mildly tholeiitic and have medium to high K_2O contents. Magmas ranging in composition from basalt to rhyolite have erupted from the arc.

Chapter 3
Development of the Santorini volcanic field in space and time

Santorini is one of the largest Quaternary volcanic centres of the Aegean Region. The caldera cliffs preserve well-exposed sequences of lavas and pyroclastic deposits, which record the long development of the volcano in space and time. These include the products of 12 major explosive eruptions and the dissected remains of several ancient lava shields, stratovolcanoes, and lava-dome complexes. The former existence of multiple eruptive centres scattered over the present-day islands shows that Santorini is best considered as a *volcanic field*, which probably also continues under the sea (Heiken & McCoy 1984). Santorini is best known for the Minoan eruption of the late Bronze Age (Bond & Sparks 1976; Heiken & McCoy 1984; Sparks & Wilson 1990), but some of the previous explosive eruptions may have been as large (Druitt *et al.* 1989). The occurrence of repeated explosive eruptions has triggered formation of at least four large calderas, such that the present-day caldera is a composite structure (Druitt & Francaviglia 1992). Santorini is potentially one of the most dangerous volcanoes in Europe, having had numerous eruptions in historic times, some of them with significant explosive components (Fytikas *et al.* 1990*a*).

The evolution of Santorini has been the focus of several detailed studies (Fouqué 1879; Reck 1936; Pichler & Kussmaul 1980; Heiken & McCoy 1984; Huijsmans 1985; Druitt *et al.* 1989; Druitt & Francaviglia 1992) as summarized in Chapter 1. Pichler & Kussmaul (1980) published a geological map of the islands that has been the basis of volcanological studies for the last 20 years. The present chapter describes the development of Santorini in space and time. It is based on a new geological map that accompanies this Memoir and a large set of new radiometric ages, but also draws on previous studies.

The combination of mapping and dating has enabled us to construct a detailed and internally coherent time–stratigraphic framework for the evolution of Santorini and its caldera. This was not straightforward because lavas and pyroclastics interdigitate in complex ways in some parts of the cliffs. Moreover, explosive eruptions have generated a range of depositional facies, even from individual eruptions, thus further complicating field relationships. A key approach has been the use of pyroclastic deposits as marker horizons. Explosive eruptions typically last less than a few days, so that their products act as excellent stratigraphic markers in volcanic successions. Because of our previous studies of the pyroclastic deposits (Druitt *et al.* 1989), we were able to recognize the products of all 12 main explosive eruptions over large areas of the islands, even where only thin erosional remnants remain sandwiched within lava piles. The ability to make correlations enabled us to construct a coherent stratigraphic framework, correlate isolated remnants of individual lava successions, and recognize the remains of ancient calderas. The resulting map differs significantly from that of Pichler & Kussmaul (1980), particularly in the north. The radiometric ages provided a check on field stratigraphy, as well as an absolute time scale. They also gave information on the longevity of the volcanic field as a whole, the longevity of individual shields and stratocones, and the frequency of explosive eruptions and caldera collapse events.

General description of the volcanic field

Santorini lies on the faulted southern margin of the Central Aseismic Plateau on a major NE–SW-trending lithospheric rupture zone (Papazachos & Panagiotopoulos 1993). The regional tectonic framework was described in Chapter 2. The stress regime in this part of the Aegean is extensional. The crust beneath Santorini is about 30 km thick and continental in nature. The sea floor to the northeast is split into alternating horsts and grabens by NE–SW-trending normal faults (Fig. 3.1). Santorini has developed on the northern margin of a basement horst called the Santorini–Amorgos ridge. If extrapolated, the fault defining the northern margin of the

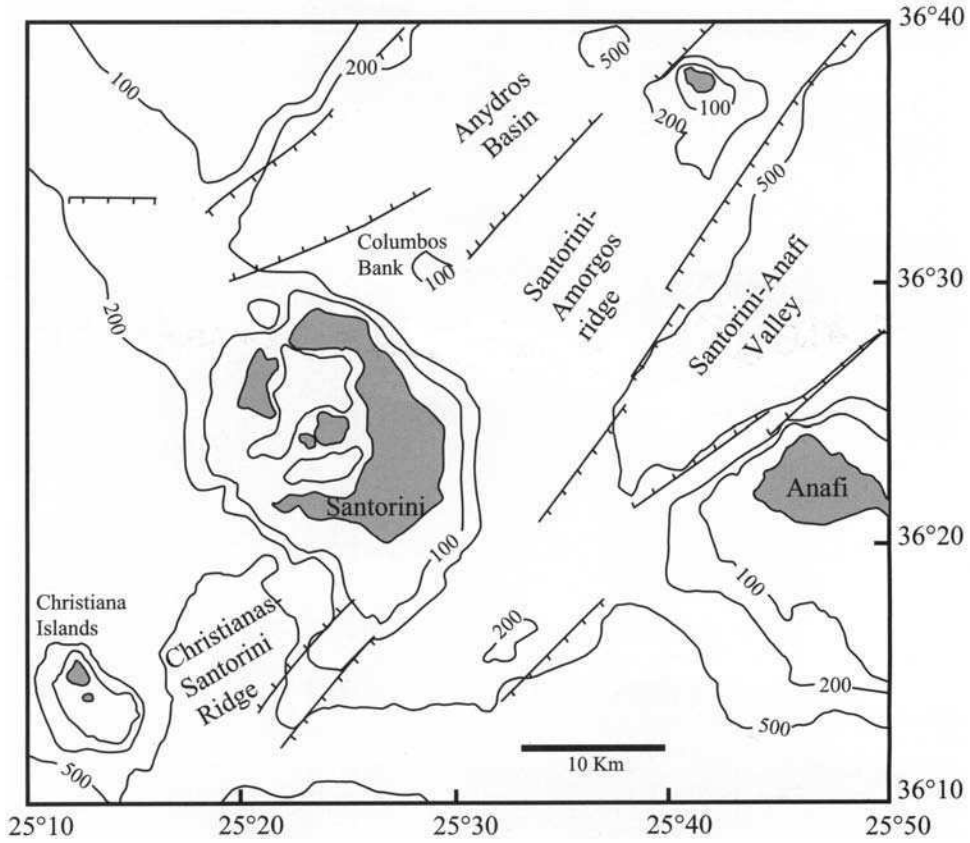

Fig. 3.1. Sea-floor bathymetry and major faults around Santorini, modified after Perrisoratis (1996). The bathymetric contours are in metres. The faults have ticks on their downthrown sides. The extension of the fault defining the northwest limit of the Santorini–Amorgos ridge (a basement horst) appears to cut the Santorini caldera in two. The southern half of Santorini lies on the horst, and the northern half lies in the Anhydros Basin (a tectonic graben).

horst passes through the Santorini caldera. It also passes near the submarine Columbos Bank volcano (last eruption 1650), 6.5 km northeast of Santorini, and the volcanic Christiana Islands to the southwest. Columbos Bank, Santorini, and the Christianas lie on an extension of the same NE–SW fault. On 9 July 1956 the town of Oia was severely damaged by a magnitude 7 earthquake, the epicentre of which lay 60 km to the northeast on a NE–SW fault. NW–SE trends in bathymetric contours south of Anafi and northwest of Santorini may reflect the existence of a complementary set of faults in the region.

Santorini is a complex of five islands (Figs 3.2 and 3.3). Thera, Therasia, and Aspronisi are arranged in a dissected ring around a flooded caldera, in which lie the islands of Palaea and Nea Kameni. The steep caldera cliffs of Thera and Therasia reach more than 300 m above sea level at Cape Tourlos. Southeastern Thera is dominated by two basement massifs, Mount Profitis Ilias and Gavrillos Ridge, which are the protruding peaks of an island that existed prior to volcanism. The original west coast of this island is preserved at Athinios, where it has been exhumed by caldera collapse. Mount Profitis Ilias (552 m) is the highest peak on Santorini. Other peaks include Mounts Loumaravi and Archangelos in southern Thera, Mounts Micros Profitis Ilias and Megalo Vouno in northern Thera, and Mount Viglos on Therasia, all of which are volcanic in origin.

The earliest Quaternary volcanics occur on the Akrotiri Peninsula (Early centres of Akrotiri Peninsula; Fig. 3.3). These and some younger cinder cones (Cinder cones of Akrotiri Peninsula) are covered by a sequence of pyroclastic deposits which in places exceeds 200 m in thickness. These deposits also drape over the basement massif and dominate the cliffs of southern Thera. In contrast, the cliffs of Therasia and northern Thera are dominated by the remains of four effusive centres: the Peristeria Volcano, the Simandiri shield, the Skaros shield, and the Therasia dome complex. The contrast in caldera wall geology between the north (mainly lavas) and south (mainly pyroclastic deposits) is a striking feature of Santorini.

The pyroclastic succession is the product of 12 large explosive eruptions and numerous deposits related to more minor explosive eruptions. We refer to this informally as the *Thera pyroclastics*. The Thera pyroclastics preserve evidence for two cycles of explosive activity, as recognized on the basis of long-term trends in magma composition (Druitt *et al.* 1989). Each explosive cycle commenced with eruptions of mafic to intermediate magmas and terminated with a pair of major silicic eruptions and caldera collapse. The existence of two cycles of explosive eruptions has been used to divide the Thera pyroclastics stratigraphically into two parts.

Thera, Therasia, and Aspronisi are each capped by an essentially continuous layer of white tuff laid down by the Minoan eruption in the late Bronze Age. The broad, gently inclined coastal plains of Thera and Therasia are composed mainly of Minoan ignimbrite. The islands of Palaea Kameni and Nea Kameni lie near the centre of the caldera and are the subaerial expressions of a large, dominantly submarine volcano which post-dates the Minoan eruption.

The caldera is a composite structure resulting from at least four collapse events (Druitt & Francaviglia 1992). It consists of four flat-floored basins (Fig. 3.2): a large, deep northern basin, and three smaller ones in the south (Perisoratis 1996). It is breached by

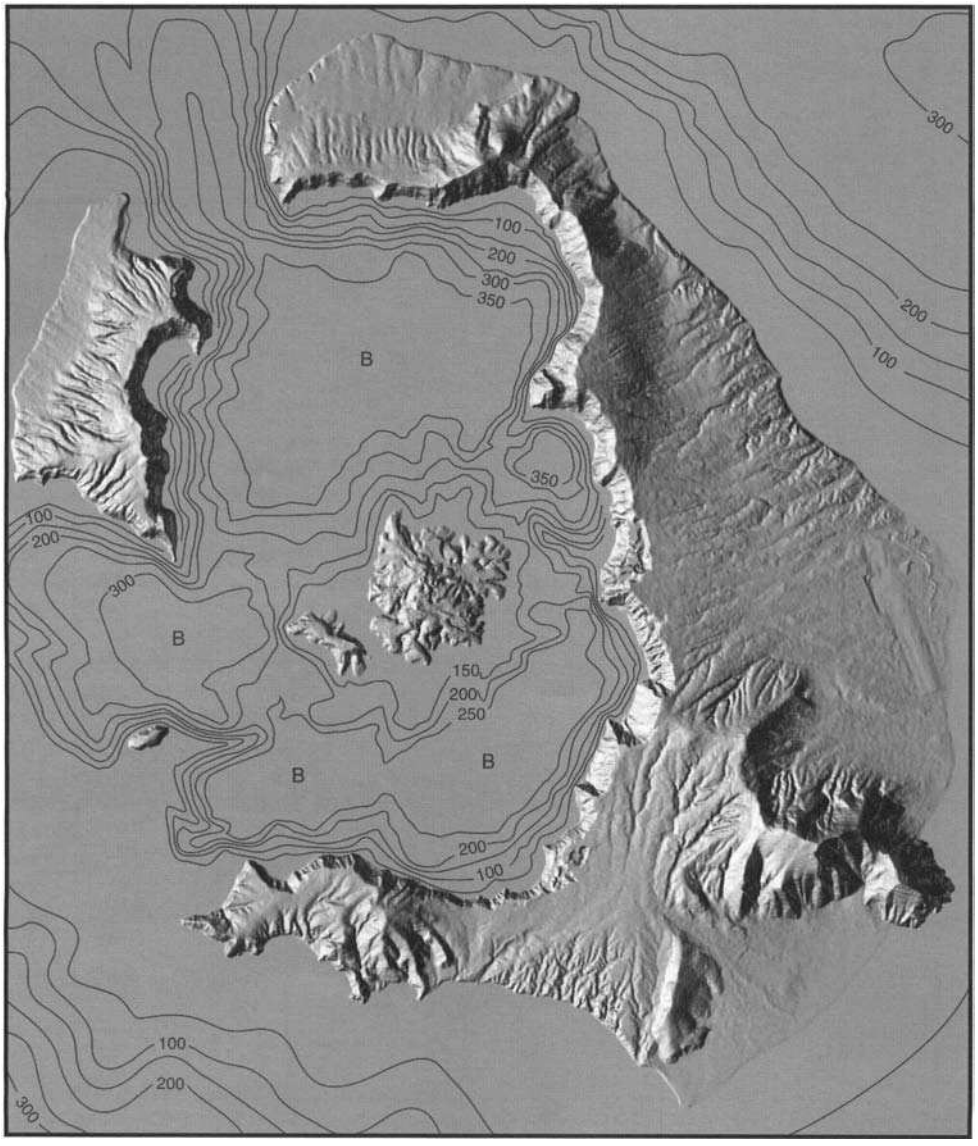

Fig. 3.2. Digital elevation model of Santorini illuminated from the northwest. The rectangular flat area in the east is the airport. Bathymetric contours after Perrisoratis (1996) at 50 m intervals. The four main caldera basins are marked (B).

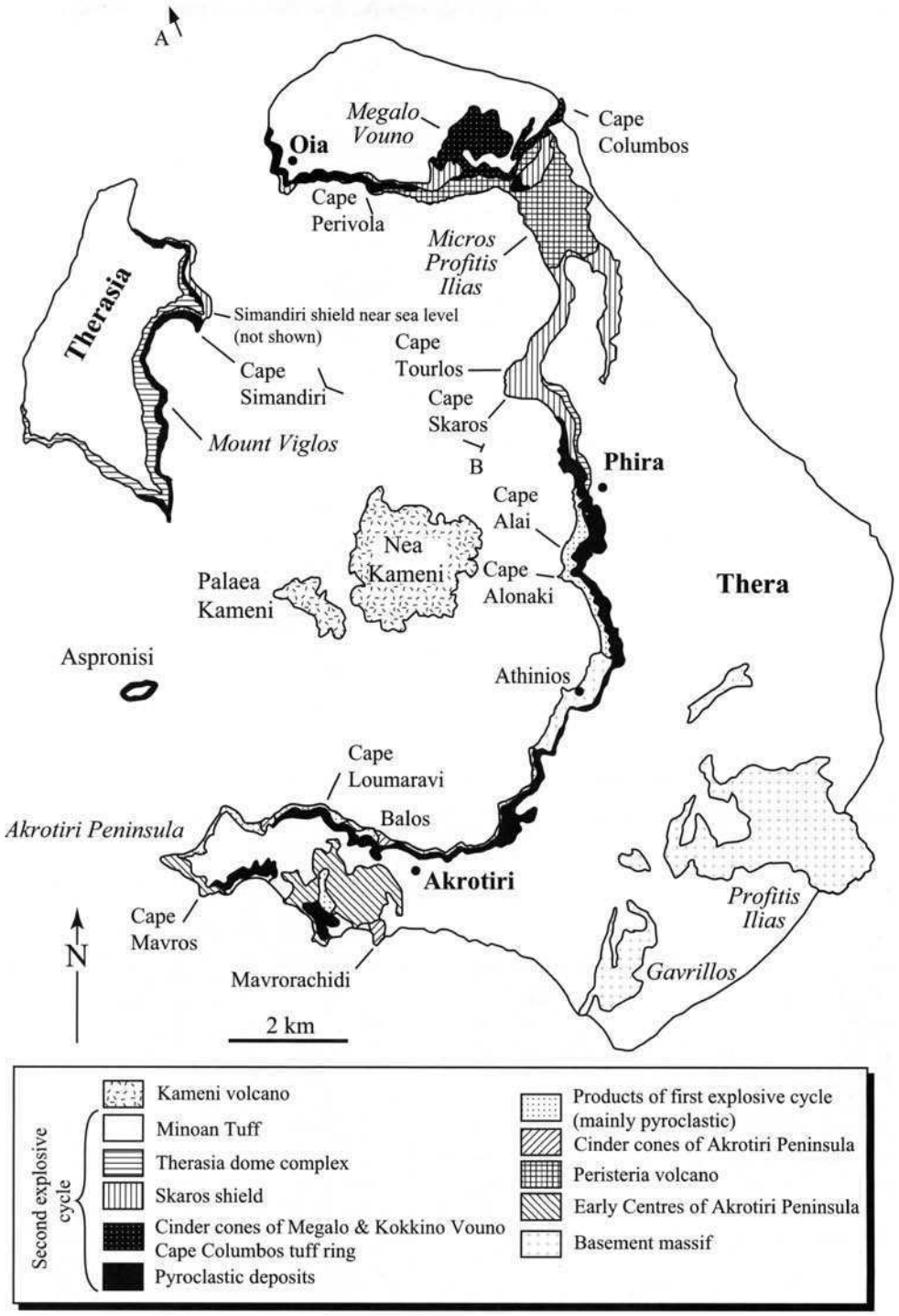

Fig. 3.3. Simplified geological map of Santorini. Lavas of the Simandiri shield crop out in northern Therasia but are too thin in plan view to be distinguished in the legend. Their location is marked on the map.

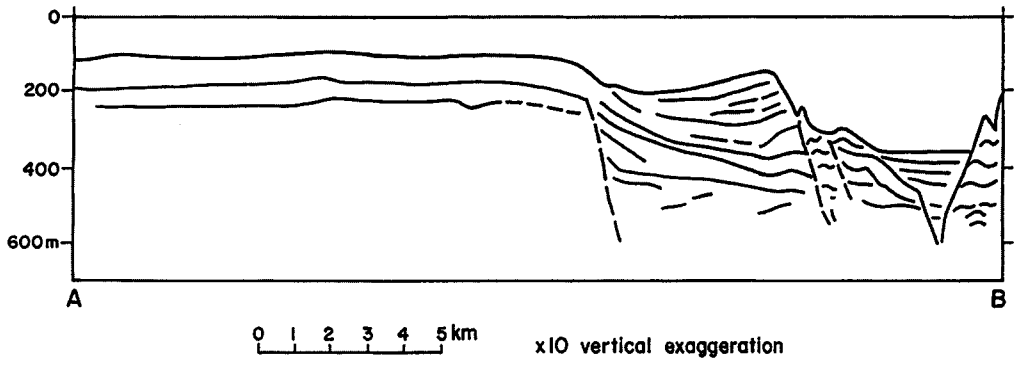

Fig. 3.4. Interpretation of seismic profile through the northwest breach of the caldera, from Heiken & McCoy (1984). Point A lies northwest of the breach and point B on the northern flank of Nea Kameni. A large rotational slump structure is visible on the profile.

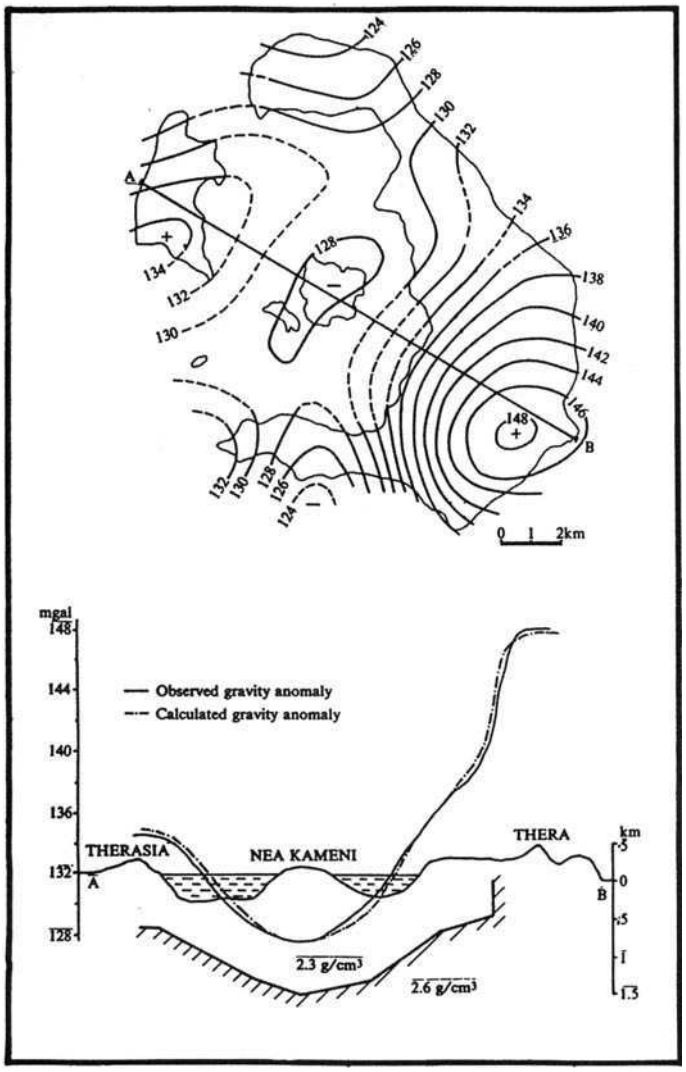

Fig. 3.5. Bouger anomaly map of Santorini, and section showing the interpretation used to model the data, from Fytikas *et al.* (1990*b*). The countour intervals are in mgal. The model invokes the presence of a low-density caldera fill about the kilometre thick.

the sea in three places. The northwest breach formed by a huge rotational landslip visible on seismic profiles (Fig. 3.4; Heiken & McCoy 1984). Steep bathymetric scarps present at the headwalls of the other two breaches suggest that they also formed by rotational slumping. The caldera has a negative Bouger gravity anomaly elongated NE–SW, parallel to the regional tectonic fabric (Fig. 3.5), and is filled with low-density material up to 1 km thick (Budetta *et al.* 1984).

The geological map and radiometric ages

Mapping, stratigraphic framework, and terminology

Field mapping was carried out in the summers of 1994 and 1995 onto 1:10 000 scale Greek topographic maps. The map (enclosure) is presented at a scale of 1:20 000, superimposed on a digital terrain model.

The rocks of Santorini were divided for mapping into **Basement, Volcanic, and Superficial Formations**. Within the Volcanic Formation we recognize six main members. (1) Rocks of the **Early Centres of Akrotiri Peninsula** are confined to southern Thera. They were referred to as the Loumaravi-Archangelo Tuffs by Reck (1936) and were mapped by Pichler & Kussmaul (1980) as the Akrotiri I Volcanics. (2) Lavas and tuffs of **Peristeria Volcano** dominate the caldera wall of northern Thera. Pichler and Kussmaul (1980) distinguished the products of two volcanoes in northern Thera, Megalo Vouno and Micros Profitis Ilias, which they believed to have very different ages. Our data now show that the volcanoes are similar in age, and we have followed Reck (1936) in mapping them as parts of a single edifice (Peristeria Volcano). (3) The remains of three cinder cones, the **Cinder cones of Akrotiri Peninsula**, crop out locally in southern Thera. They are equivalent to Pichler and Kussmaul's (1980) Akrotiri II Volcanics. (4) Products of the **First explosive cycle** consist mainly of pyroclastic deposits from five large explosive eruptions, but also include some intercalated lavas. (5) Products of the **Second explosive cycle** include the deposits from seven major explosive eruptions, as well as the lavas and tephra of the Simandiri shield, the Skaros shield, and the Therasia dome complex (also other miscellaneous lavas and pyroclastic units), which were erupted during the same time period. (6) Lavas of the **Kameni Volcano**.

Each of the six volcanic members were subdivided into a number of stratigraphically coherent units for mapping. The space-time relationships between these are shown in Fig. 3.6. In each unit symbol the first letter denotes the magma composition, recalculated dry: **b** (basalt; <53% SiO_2), **a** (andesite; 53–63%), **d** (dacite; 63–68%), and **r** (rhyodacite; 68–72%) (Huijsmans 1985; Druitt *et al.* 1989; Chapter 6). Where a particular unit contains a range of magma compositions, the letter denotes the dominant one. The letter **p** denotes a pyroclastic unit; the absence of a **p** implies that the main lithology is lava. The 12 main tuffs of the Thera pyroclastics have been grouped into seven units (**ap1, ap2, rp3, ap4, ap5, rp6, and rp7**) on the map. In the following sections, map symbols are written in bold letters.

Radiometric dating

Thirty-eight K–Ar and eight $^{40}Ar/^{39}Ar$ high-precision age determinations were carried out on a total of 22 volcanic rocks and deposits representing the entire volcanic field. Duplicate or triplicate determinations were carried out on 14 samples in order to improve analytical precision. The new K–Ar ages are given in Table 3.1 and the $^{40}Ar/^{39}Ar$ results in Table 3.2. Both plateau and isochron $^{40}Ar/^{39}Ar$ ages are presented. Unless stated, we use the plateau ages, which have lower errors and are considered more reliable. Details of analytical methods are given in Appendix 1. Previous age determinations on Santorini volcanic rocks are summarized in Table 3.3.

The pre-volcanic island (Triassic to Eocene)

The volcanic field was constructed against a pre-existing pre-volcanic island of basement rocks. The basement massif has two principal components: (1) a complex of low-grade metapelites (schists and phyllites) (**Metapelites of Athinios; Mp**), and (2) crystalline limestones (**Limestones of Mount Profitis Ilias; Ml**). A simplified map is shown in Fig. 3.7. The metapelites are exposed along a 2 km stretch of the caldera wall near Athinios, and also in the saddle between Profitis Ilias and Mesa Vouno. The limestones form the massifs of Profitis Ilias, Mesa Vouno, and Gavrillos.

Descriptions of the basement lithologies have been given by Davis & Bastas (1978) and Skarpelis & Liati (1990) and a detailed structural analysis is presented by Kilias *et al.* (1998). The metapelite unit has intercalations of metapsammites, limestones, and metavolcanics. The whole has been metamorphosed to blueschist grade, then overprinted under greenschist to amphibolite conditions in a manner similar to other Cycladic islands (Chapter 2). The occurrence of *Miliolidae* suggests a Palaeocene–Eocene sedimentary age for **Mp** (Tataris 1956). Intrusions of granite porphyry occur locally, and an I-type, late Miocene granite (plus contact aureole) has been intersected in a geothermal borehole 255 m below Megalohorion (Skarpelis *et al.* 1988, 1992). The granite is petrologically and geochemically similar to those of Naxos, Mykonos, and Delos.

The limestones contain *Megalodontidae*, and are of Triassic, probably Upper Triassic, age (Papastamatiou 1956). In the saddle between Profitis Ilias and Mesa Vouno, the metapelite unit is

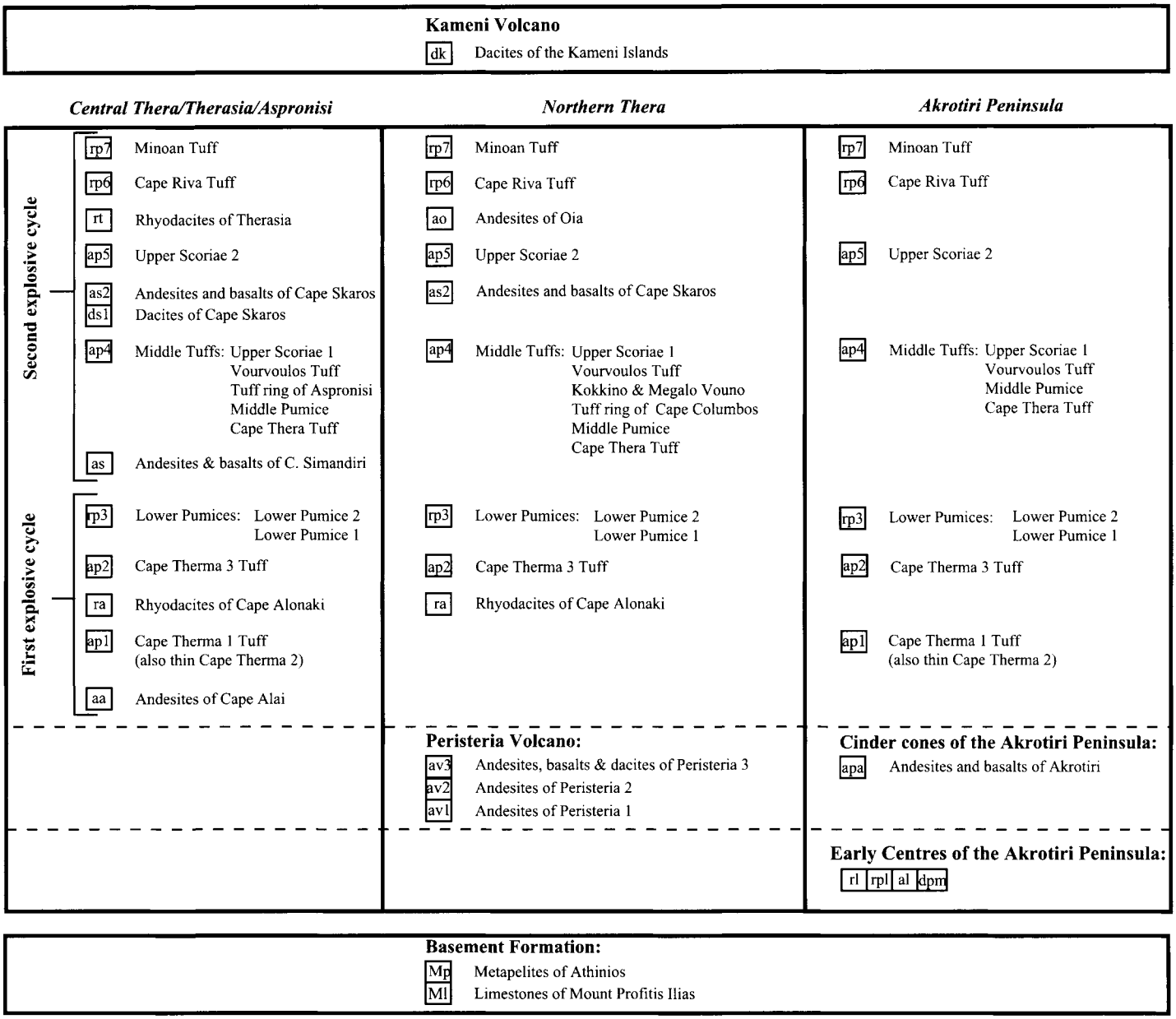

Fig. 3.6. Stratigraphic relationships between the map units, excluding superficial formations.

sandwiched between two southeast-dipping faults. The fault slice consists of chaotically intermixed metapelites, metapsammites, and metavolcanics, with metre-sized blocks of limestone.

The prevolcanic island is reconstructed in Fig. 3.8. Steep topographic gradients and linear palaeocoastlines show that the island's form was controlled by complex block faulting, most of which must have pre-dated volcanism.

Early Centres of the Akrotiri Peninsula (650–550 ka)

The oldest Quaternary volcanic rocks are amphibole-bearing silicic lavas and tuffs forming the hills of Mount Loumaravi, Mount Archangelos, Cape Vounia, and Cape Akrotiri (Fig. 3.9). The presence of abundant amphibole distinguishes these from younger Santorini volcanics, which generally lack amphibole. They are also distinctive chemically (Nicholls 1971*a*; Huijsmans 1985; Davis *et al.* 1998; Dietrich *et al.* 1998; Chapter 6).

In the Loumaravi–Archangelos area the complex is dominated by submarine domes, coulées, and hyaloclastite aprons (**Rhyodacites of Akrotiri; rl**), which interdigitate with water-lain vitric tuffs, pumice breccias and conglomerates (**Tuffs of Akrotiri; rpl**; Figs 3.10 and 3.11). Some lavas at higher elevations may have erupted subaerially. An altered andesite (**Andesite of Mount Loumaravi; al**) of unknown age crops out locally between Loumaravi and Archangelos. Field relationships between these different lithologies are complex and no stratigraphy has been established. Intercalations of marine sediments bearing benthic and planktonic forams occur in vitric tuffs 100 m or more above sea level, providing clear evidence for submarine eruption (Fouqué 1879; Seidenkrantz 1992). A smaller lava mass of similar age forms Cape Akrotiri. Marine deposits rich in siliceous sponge spicules occur near the top of this lava at an altitude of 100 m (Seidenkrantz 1992). The complex lies in faulted contact to the southeast with the mass of dacitic hyaloclastite breccias and tuffs that forms Cape Mavros (**Dacites of Cape Mavros; dpm**).

Prolonged eruption on the sea floor generated a complex of lava domes and flows, hyaloclastite aprons, ash accumulations, and pumice cones on the western submarine flank of the pre-volcanic island. Later stages in the development of the complex were probably subaerial. The presence of amphibole-bearing rhyodacites in drill holes east of Akrotiri village (Fytikas *et al.* 1990*b*) suggests that the original complex was larger than implied by present-day outcrops. The occurrence of fossiliferous marine sediments 100 m or more above sea level implies considerable post-formational uplift of these early centres. Uplift occurred as two fault blocks (Loumaravi–Archangelo and Cape Akrotiri massifs) (Fig. 3.8).

Dating of the rhyodacite from Cape Akrotiri gave 645 ± 92 ka by K–Ar and 582 ± 24 ka by $^{40}Ar/^{39}Ar$ (S90-2; Tables 3.1 and 3.2).

Table 3.1. *K–Ar ages of Santorini rocks*

Sample	Stratigraphic unit	Map unit	Location and comments	K_2O (wt%)	Radiogenic ^{40}Ar (10^{-13} mol/g)	Radiogenic ^{40}Ar (%)	Calculated age (ka)	Average age (ka)
S90-8	Upper Scoriae 2	ap5	Welded spatter, Cape Tourlos	1.557 ± 0.007	2.085	4.6	93 ± 13	
					1.600	4.5	71 ± 10	79 ± 8
S94-3	Cinder cone of Megalo Vouno	ap4b	Welded spatter, 1 km N of Megalo Vouno summit	0.745 ± 0.007	0.5775	1.6	54 ± 23	54 ± 23
S94-2	Cinder cone of Megalo Vouno	ap4b	Andesite spatter under S94-3	0.769 ± 0.007	0.8472	1.3	76 ± 28	76 ± 28
S90-20	Simandiri shield	as	400 m N of Cape Simandiri	2.375 ± 0.11	5.908	2.1	172 ± 33	172 ± 33
S90-25	Lower Pumice 1	rp3	Juvenile obsidian clast, Cape Perivola	3.18 ± 0.008	7.902	15.6	172 ± 6	
					10.53	14.7	230 ± 7	
					9.437	14.2	206 ± 7	203 ± 24
S90-10	Rhyodacite of Cape Alonaki	ra	Basal flow, 200 m S of Phira harbour	3.232 ± 0.01	10.40	13.1	223 ± 7	
					10.50	13.2	225 ± 7	224 ± 5
S90-17	Rhyodacite of NE Thera	ra	1.3 km E of Cape Heptapedio	3.48 ± 0.012	12.52	37.8	250 ± 5	
					10.88	35.3	217 ± 5	
					15.26	36.7	304 ± 5	257 ± 31
S90-11	Andesites of Cape Alai	aa	Flow at sea level, Phira harbour	1.355 ± 0.006	6.736	1.6	345 ± 88	
					2.840	0.9	145 ± 64	
					3.826	1.1	196 ± 69	209 ± 85
S91-26	Andesites of Cape Alai	aa	200 m S of S90-11	2.065 ± 0.002	8.987	3.0	302 ± 40	
					12.63	4.2	425 ± 39	364 ± 62
S94-1	Peristeria 3	av3	Lava below tuff ring deposits, Cape Columbos	3.76 ± 0.001	16.69	12.3	308 ± 10	308 ± 10
S90-19	Peristeria 3	av3	Lava below Lower Pumice, Oia	1.968 ± 0.007	12.22	17.0	431 ± 13	
					12.32	17.2	435 ± 11	433 ± 8
S86-23	Peristeria 3	av3	Topmost lava of Micros Profitis Ilias	3.20 ± 0.015	20.98	27.3	457 ± 7	
					21.72	35.6	472 ± 7	464 ± 8
S90-24	Peristeria 3	av3	Topmost flow of Megalo Vouno succession	3.008 ± 0.005	20.79	34.7	480 ± 7	
					20.80	32.9	480 ± 7	480 ± 5
S90-15	Peristeria 2	av2	Second flow from base, Micros Profitis Ilias	1.856 ± 0.013	13.07	8.5	489 ± 23	
					13.40	8.6	502 ± 23	496 ± 16
S90-18	Peristeria 1	av1	Lowest flow at sea level, Cape Heptapedio	2.275 ± 0.009	18.05	19.3	551 ± 12	
					16.53	20.6	505 ± 11	528 ± 23
S90-1	Cinder cones of the Akrotiri Peninsula	apa	Massive core of cinder cone core, Cape Balos	0.464 ± 0.003	2.276	8.4	340 ± 33	
					2.320	8.1	347 ± 30	344 ± 24
S90-4	Cinder cones of the Akrotiri Peninsula	apa	Lava S of cinder cone core, Cape Mavrorachidi	1.245 ± 0.007	9.364	2.0	522 ± 104	522 ± 104
S90-5	Early Centres of the Akrotiri Peninsula	rl	Lava 300 m NW of Cape Mavrorachidi	2.866 ± 0.005	10.84	2.4	263 ± 43	263 ± 43
S90-3	Early Centres of the Akrotiri Peninsula	rl	Coulée SE of Akrotiri Village	2.206 ± 0.008	18.65	11.4	587 ± 20	
					18.55	9.9	584 ± 23	586 ± 15
S86-19	Early Centres of the Akrotiri Peninsula	dpm	Dacitic clast, deposits of Cape Mavros	1.71 ± 0.014	15.16	5.8	616 + 42	
					15.41	4.1	626 ± 61	619 ± 35
S90-2	Early Centres of the Akrotiri Peninsula	rl	Lava of Cape Akrotiri	2.219 ± 0.009	20.61	2.8	645 ± 92	645 ± 92

Plus-or-minus values are standard deviations of analytical precision (1σ).

The prominent 600 m long ridge of rhyodacite hyaloclastite breccia south of Akrotiri village yielded 586 ± 15 ka by K–Ar (S90-3). An outcrop of rhyodacitic hyaloclastite 400 m northwest of Cape Mavrorachidi (S90-5) gave a K–Ar age of 263 ± 43 ka and an $^{40}Ar/^{39}Ar$ age of 553 ± 10 ka. The K–Ar age is obviously much younger than the other ages for these rocks, and is considered to be spurious. The $^{40}Ar/^{39}Ar$ age is believed to be accurate since the hyaloclastite is directly overlain by scoria of the Mavrorachidi cinder cone, dated at about 450 ka (see below). A juvenile boulder from the Cape Mavros dacites gave a K–Ar age of 619 ± 35 ka (S86-19).

The data suggest that shallow-marine to subaerial volcanism at Santorini began about 650 ka ago. A similar conclusion was reached by Tarney *et al.* (1998). The ages are younger than those that Ferrara *et al.* (1980) obtained using the K–Ar method on the same rocks (Table 3.3), but are consistent with Huijsmans' (1985) observation that the lavas are all normally magnetized and probably younger than the Brunhes–Matuyama reversal (780 ka). The presence of late Pliocene foraminifers in some of the amphibole-bearing ashes has been taken as evidence that the earliest eruptions occurred at that time. Moreover, zircon fission-track ages of 940–1950 ka

Table 3.2. *$^{40}Ar/^{39}Ar$ ages for Santorini rocks*

Sample	Stratigraphic unit	Map unit	Location and comments	Plateau age (ka)	Plateau ^{39}Ar* (%[steps])	Isochron age (ka)	Isochron intercept
S90-8	Upper Scoriae 2	ap5	Welded spatter, Cape Tourlos	54 ± 3	74 [5 of 10]	39 ± 18	309 ± 36
S90-13	Skaros shield	ds1	Basal dacitic domes, Cape Tourlos	67 ± 9	74 [14 of 21]	87 ± 17	294.7 ± 1.0
S90-20	Simandiri shield	as	400 m N of Cape Simandiri	172 ± 4	94 [15 of 19]	177 ± 18	294.8 ± 1.7
S91-26	Andesites of Cape Alai	aa	Flow at sea level, 200 m S of Phira harbour	543 ± 88	64 [9 of 13]	456 ± 138	299.4 ± 4.7
S95-1	Persiteria 3	av3	Topmost lava of Micros Profitis Ilias	478 ± 3	100 [11 of 11]	444 ± 154	295.0 ± 3.9
S90-4	Cinder cones of Akrotiri Peninsula	apa	Lava S of cinder cone core, Cape Mavrorachidi	451 ± 27	85 [6 of 12]	443 ± 217	295.7 ± 4.6
S90-5	Early Centres of the Akrotiri Peninsula	rl	Lava 300 m NW of Cape Mavrorachidi	553 ± 10	91 [6 of 15]	495 ± 34	299.0 ± 1.9
S90-2	Eary Centres of the Akrotiri Peninsula	rl	Lava of Cape Akrotiri	582 ± 24	88 [14 of 16]	659 ± 41	294.1 ± 0.6

Plus-or-minus values are standard deviations of analytical precision (1σ).
* % is proportion of total ^{39}Ar defining plateau. Steps are number of gas increments on plateau.

Table 3.3. *Previously published ages of Santorini volcanic rocks*

Stratigraphic unit	Map unit	Age	Methods	References
Kameni Volcano	dk	AD 197–1950	Historic records	Fytikas *et al.* (1990*a*)
Minoan Tuff	rp7	3.6 ka	^{14}C on plant remains	Friedrich *et al.* (1990)
Cape Riva Tuff	rp6	18.4 (±0.2) ka	^{14}C on wood (3 analyses)	Pichler & Freidrich (1976)
		19 ka	Deep-sea ash stratigraphy	Thunnel *et al.* (1977)
Upper Scoriae 2	ap5	37.9 (±0.2) ka	^{14}C on wood (2 analyses)	Mellors & Sparks (1991)
Upper Scoriae 1	ap4	54.0 (±0.7) ka	^{14}C on plant remains	W. Friedrich (pers. comm.)
Middle Pumice	ap4	*c.* 100 ka	Correlation with W-2 deep-sea ash	Federman & Carey (1980)
Lower Pumice 2	rp3	*c.* 160 ka	Correlation with V-1 deep-sea ash	Keller (1981)
Lower Pumice 1	rp3	67–138 ka	Fission track on obsidian (6 analyses)	Seward *et al.* (1980)
Peristeria 3	av3	79 (+14/−12) ka	U-series disequilibrium	Pyle *et al.* (1988)
Cape Akrotiri rhyodacite and xenolith in tuffs of Cape Mavros deposits	rl, dpm	630–1590 ka	K–Ar (4 analyses)	Ferrara *et al.* (1980)
Thin silicic ashes overlying basement	rpl?	940–1950 ka	Fission-track on zircon	Seward *et al.* (1980)
Sediments interstratified with tuffs of the Early Centres of Akrotiri Peninsula	rpl	<2000 ka	Foram palynology	Seidenkrantz (1992)

have been reported from thin silicic ash layers draping the basement inlier at Athinios (Seward *et al.* 1980). Some of the earliest tuffs may thus predate 650 ka, although the foraminifers may be reworked from older sediments.

Peristeria Volcano (530–430 ka)

Remnants of Peristeria Volcano form much of the Megalo Vouno massif and all of Micros Profitis Ilias (Figs 3.13, 3.14 and 3.15). Pichler & Kussmaul (1980) interpreted Micros Profitis Ilias as much younger than Megalo Vouno, but this is ruled out because (1) they give similar radiometric ages, and (2) both stratigraphically underlie the Thera pyroclastics and predate the first explosive cycle. Peristeria has been subdivided into three units: (1) a core of andesitic lavas and tuffs (**Peristeria 1; av1**) (2) massive silicic andesite lava flows (**Peristeria 2; av2**) and (3) a succession of thin andesitic and basaltic lavas, with subordinate dacites (**Peristeria 3; av3**). A simplified geological map is shown in Fig. 3.16.

Peristeria 1 (**av1**) forms the lower 120–180 m of the cliffs below Megalo Vouno summit. It consists of interdigitated andesitic lava flows, tuffs, breccias, and hyaloclastites, cut by about 50 dykes (Fig. 3.15). Only the widest dykes are shown on the map (enclosure), with the majority trending north to northeast. Dating of a Peristeria 1 andesite from the lowest stratigraphic level (S90-18) yielded 528 ± 23 ka.

There are three occurrences of Peristeria 2 lavas. First, small silicic andesite domes occur sporadically at the contact between Peristeria 1 and Peristeria 3 below Megalo Vouno. Only the largest of these (at Cape Heptapedio) is shown on the map. Second, directly below Megalo Vouno summit there occurs a funnel-shaped mass of silicic andesite lined with tuff. This represents either the remains of a lava-filled vent or a skin of lava adhered to an ancient cliff. Third, massive silicic andesite flows form the base of the caldera wall of Micros Profitis Ilias (Fig. 3.13). Correlation of these three occurrences is based on their similar chemical compositions and stratigraphic positions. The second Peristeria 2 flow from the base below Micros Profitis Ilias yielded a K–Ar age of 496 ± 16 ka.

The products of Peristeria 3 are up to 140 m thick in the cliffs of Megalo Vouno, where they consist of aphyric to plagioclase-phyric lavas and tuffs. Dyke feeders for some of the lavas are exposed in the cliffs. On Micros Profitis Ilias the succession reaches 180 m thick and onlaps the steep southeastern flank of Peristeria 1. The fault along this contact is a much younger feature (see below) with a throw of a few tens of metres. The youngest Peristeria 3 flow on Megalo Vouno (S90-24) yielded a K–Ar age of 480 ± 5 ka. The youngest flow below Oia (S90-19) gave 433 ± 8 ka. The age of the youngest Peristeria 3 flow on Micros Profitis Ilias, a thick pinkish silicic andesite, is 464 ± 8 ka (S86-23). This same rock has been dated by U-Th disequilibrium at about 80 ka (Pyle *et al.* 1988; Chapter 7), but that age is inconsistent with the stratigraphic position of the lava, which predates the Thera pyroclastics. The older age has been confirmed by $^{40}Ar/^{39}Ar$ dating of a second sample of the same lava (S95-1: 478 ± 3 ka). Tarney *et al.* (1998) obtained K–Ar ages of 511 and 517 ka on Micros Profitis Ilias lavas, although no errors were reported on these ages.

Peristeria was a composite stratovolcano 4 km in diameter, whose summit lay about 350 m above present sea level (Fig. 3.8). The subaerial volume was at least 2 km^3. Construction began about

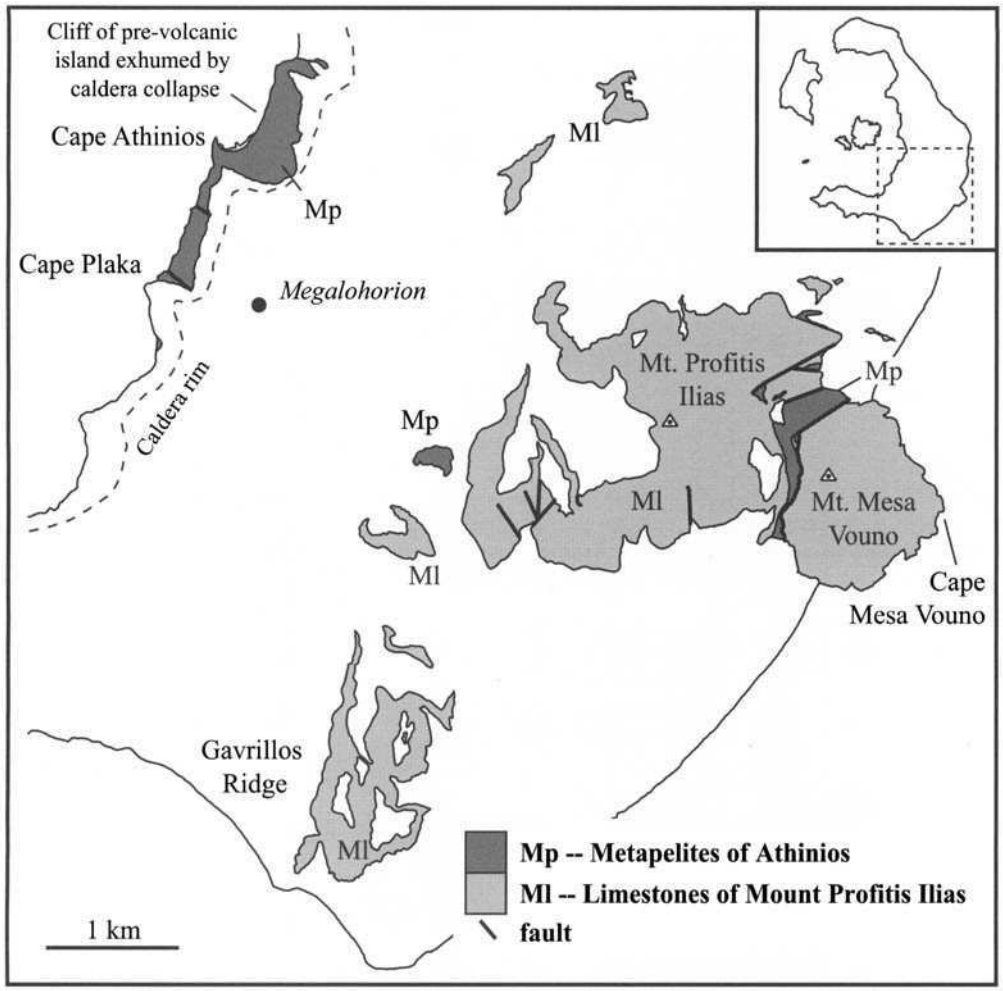

Fig. 3.7. Geological map of the basement complex in the southeast corner of Thera island.

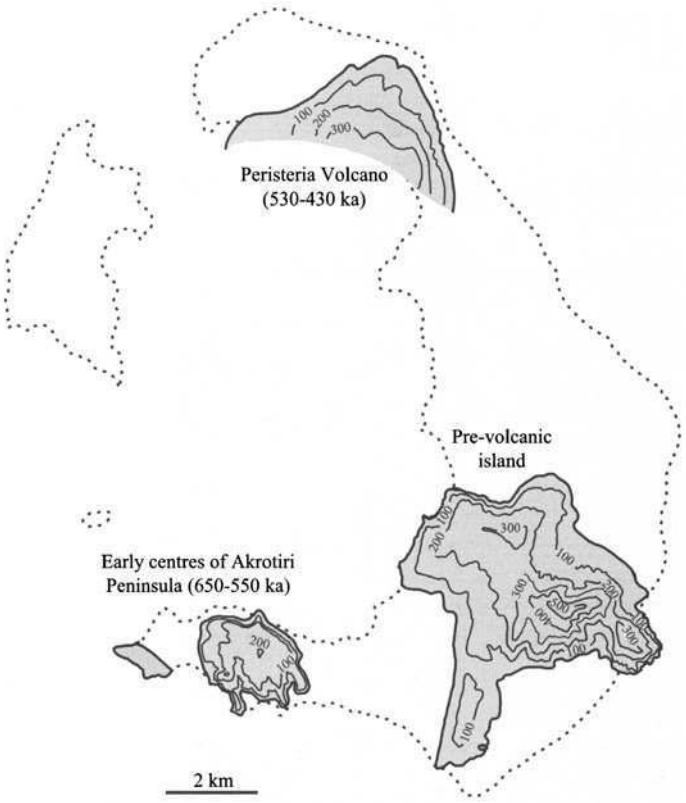

Fig. 3.8. Reconstructions of the pre-volcanic island, the Early Centres of the Akrotiri Peninsula, and Peristeria Volcano. The early centres are shown as two fault blocks after volcano-tectonic uplift. Bore holes show that similar rocks extend to the east towards the basement complex. The outlines of the present-day islands are shown dotted. The topographic contours are in metres.

530 ka and lasted until at least 430 ka. The existence of an andesite flow near Cape Columbos, dated at 308 ± 10 ka (S94-1), may record continued flank eruptions on Peristeria until that time, or may be unrelated. It has been mapped as part of Peristeria 3.

Cinder cones of the Akrotiri Peninsula (450–340 ka)

Commencing around the time of Peristeria 3, strombolian eruptions formed cinder and spatter cones at Capes Balos, Kokkinopetra, and Mavrorachidi (**Andesites and basalts of Akrotiri; apa;** Fig. 3.12). The three centres are shown on Fig. 3.9. Their products overlie tuffs and lavas of the early rhyodacitic centres, but underlie deposits of the first explosive cycle. A thin lava flow, not distinguished on the map, is preserved on the southern flank of Mavrorachidi cone. At Cape Balos, the ascending basaltic magma first interacted with sea water, forming a maar and plastering phreatomagmatic tuffs onto eroded outcrops of **rpl** vitric tuffs 400 m to the west. A change to dry conditions then constructed the cinder cone inside the early maar. The cinder cone was later cut by a NE–SW fault with downthrow to the west.

K–Ar dating of the massive lava-like core of the Balos cone (S90-1) gave 344 ± 24 ka. The thin lava flow at Cape Mavrorachidi (S90-4) yielded a low amount of radiogenic argon and an imprecise K–Ar age of 522 ± 104 ka. However, the $^{40}Ar/^{39}Ar$ plateau age for the Mavrorachidi sample is 451 ± 27 ka, confirming that it is indeed significantly older than Balos.

First explosive cycle (*c.* 360–180 ka)

The explosive activity at Santorini occurred in two cycles (Fig. 3.17). Products of the 12 major eruptions are described in Table 3.4, and their distributions shown in Fig. 3.18. The deposits of these

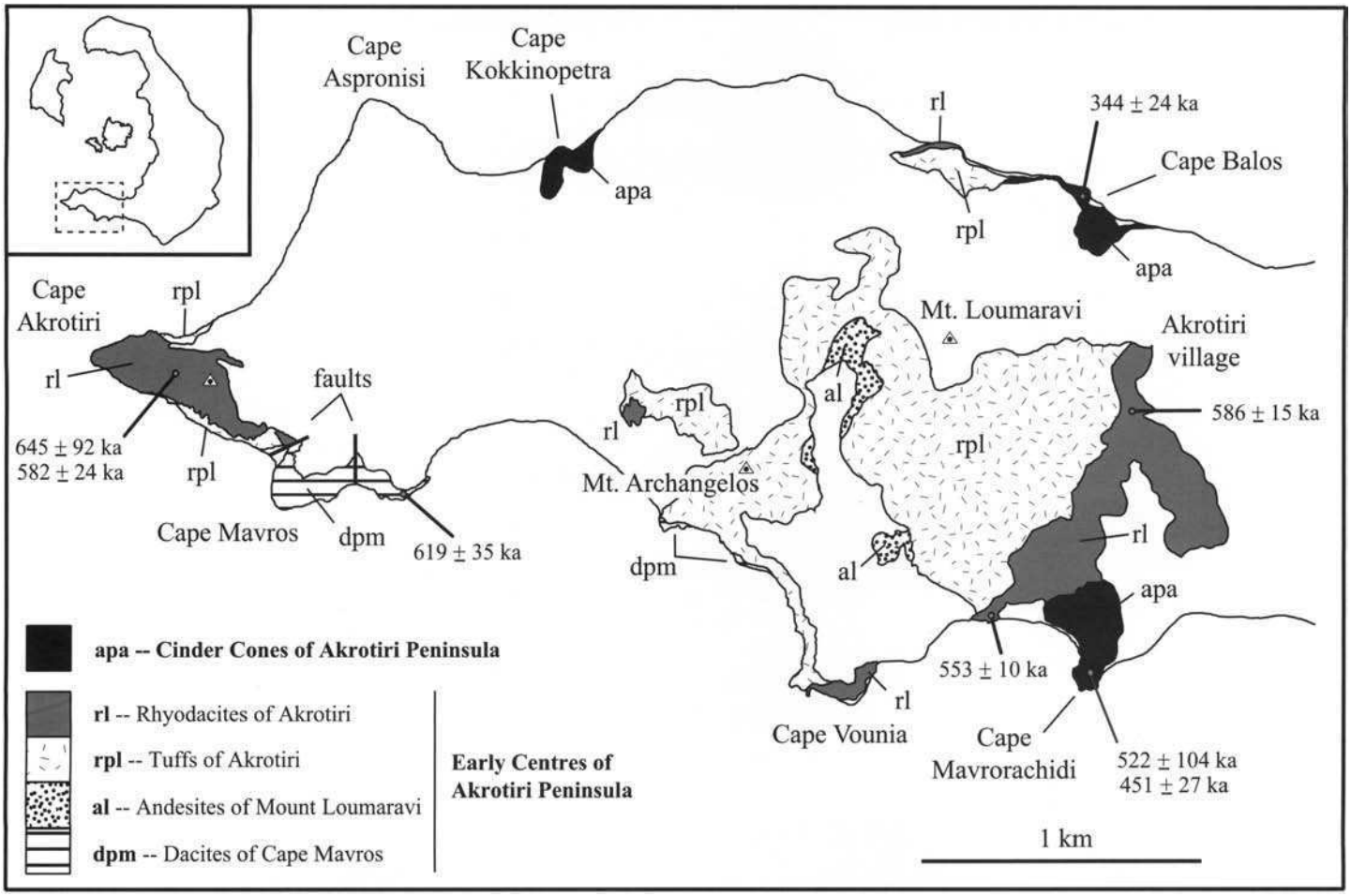

Fig. 3.9. Geological map of the Early Centres of the Akrotiri Peninsula. The Cinder Cones of Akrotiri are also shown. Younger products are shown in white.

Fig. 3.10. View looking west across the Akrotiri Peninsula. Mount Archangelos (A) and most of the foreground consists of submarine tuffs generated by the Early Centres of the Akrotiri Peninsula (**rpl**), which have subsequently been uplifted.

Fig. 3.11. Slump structure in submarine vitric tuffs of the Early Centres of the Akrotiri Peninsula (**rpl**).

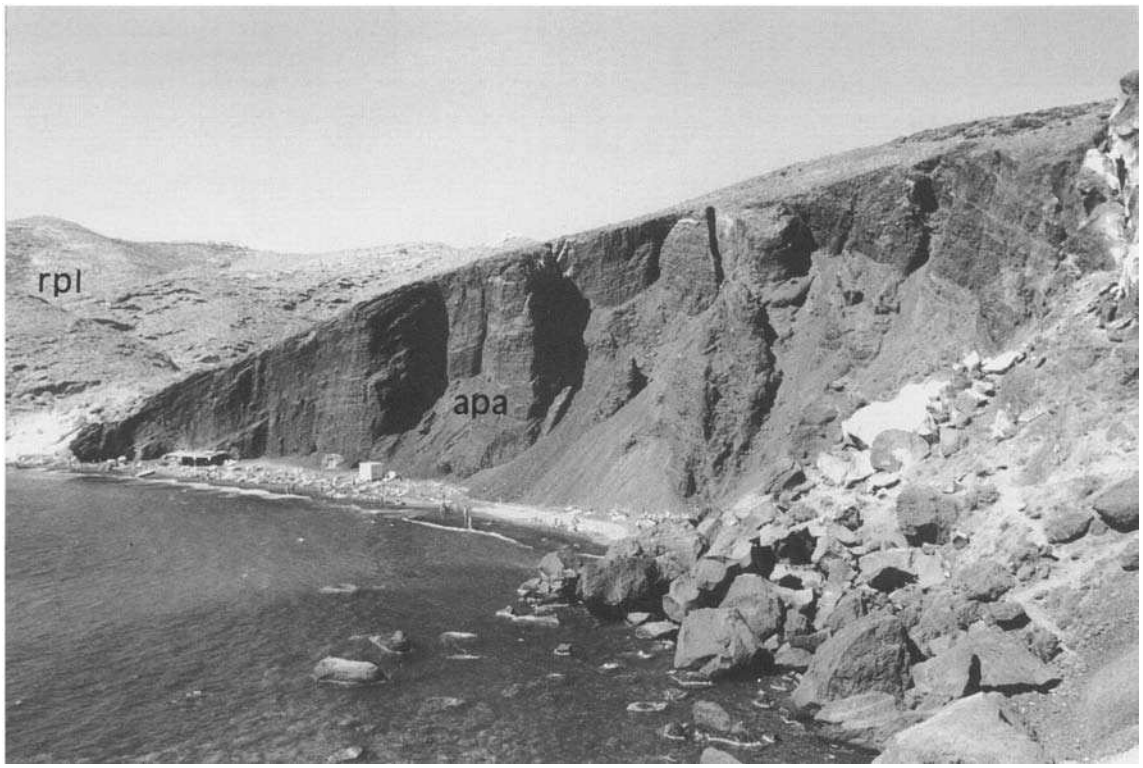

Fig. 3.12. Cinder cone of Cape Mavrorachidi (**apa**), with rhyodacitic tuffs of the Early Centres of the Akrotiri Peninsula (**rpl**) in the background. The cinder cone is younger than the tuffs. The nudists on the beach give the scale.

eruptions have been subdivided into units, each of which is denoted by an upper case letter in Table 3.4. These lettered units are referred to extensively in later chapters. Isopach maps for the fallout deposits of selected explosive eruptions are shown in Fig. 3.19. Sequences of minor pyroclastic deposits and palaeosols between the major units are labelled M1 to M12 (Fig. 3.17). Five large explosive eruptions took place during the first cycle. Two lava successions are preserved from the same time period.

The Cape Alai centre

Andesitic lavas crop out intermittently near sea level for 1 km between Phira harbour and Cape Alai, where they stack to a thickness of 60 m (**Andesites of Cape Alai; aa**). They are mapped as early products of the first explosive cycle because they chemically resemble the Thera pyroclastics that overlie them, but are distinct from the Peristeria lavas further north (Nicholls 1971). The

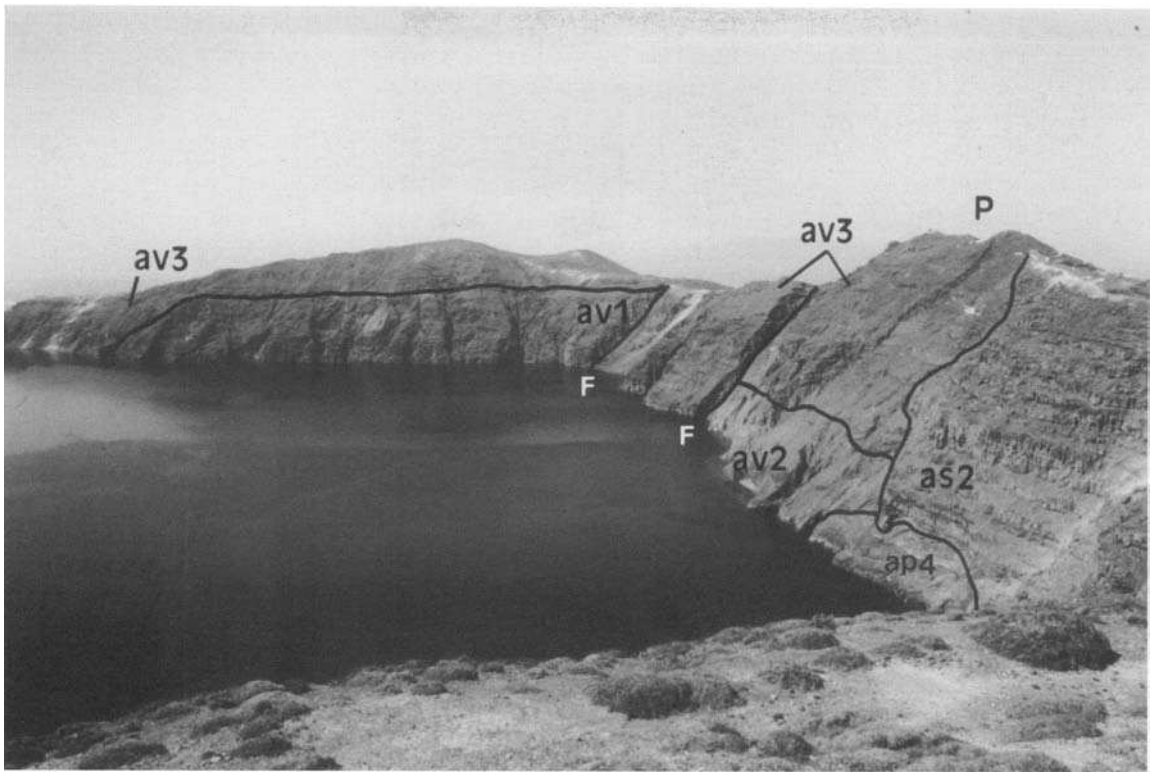

Fig. 3.13. View across the northern caldera basin from Cape Tourlos. The three components of the ancient Peristeria Volcano (Peristeria 1 **av1**, Peristeria 2 **av2**, and Peristeria 3 **av3**) are visible. The remains of Peristeria are onlapped by lavas of the Skaros shield (**as2**), with a small wedge of **ap4** tuffs along the contact. The two faults (F) define a small graben which formed when the Skaros shield collapsed. The peak marked P is Micros Profitis Ilias. The two peaks in the north are Megalo Vouno (left) and Kokkino Vouno (right).

Fig. 3.14. View of the eastern flank of Micro Profitis Ilias (P), showing the steep side of the ancient Peristeria 3 stratovolcano, truncated by the caldera rim.

complex stratigraphic relationships in the caldera wall near Phira are shown in Fig. 3.20.

Two flows near sea level at Cape Alai yielded average K–Ar ages of 364 ± 62 ka (S91-26) and 209 ± 85 ka (S90-11). However, given the poor agreement of the three individual ages for S90-11 (Table 3.1), the age of 345 ± 88 ka calculated from the highest radiogenic Ar extraction is considered most reliable. Together, these samples suggest an age of approximately 360 ka. Sample S91-26 was also dated by $^{40}Ar/^{39}Ar$, which gave a poorly defined plateau age of 543 ± 88 ka and an isochron age of 456 ± 138 ka, the latter agreeing with the K–Ar age of the same sample at the 1σ confidence level. We conclude that the age of the Cape Alai centre is approximately 360 ka, broadly contemporaneous with the cinder cone at Cape Balos.

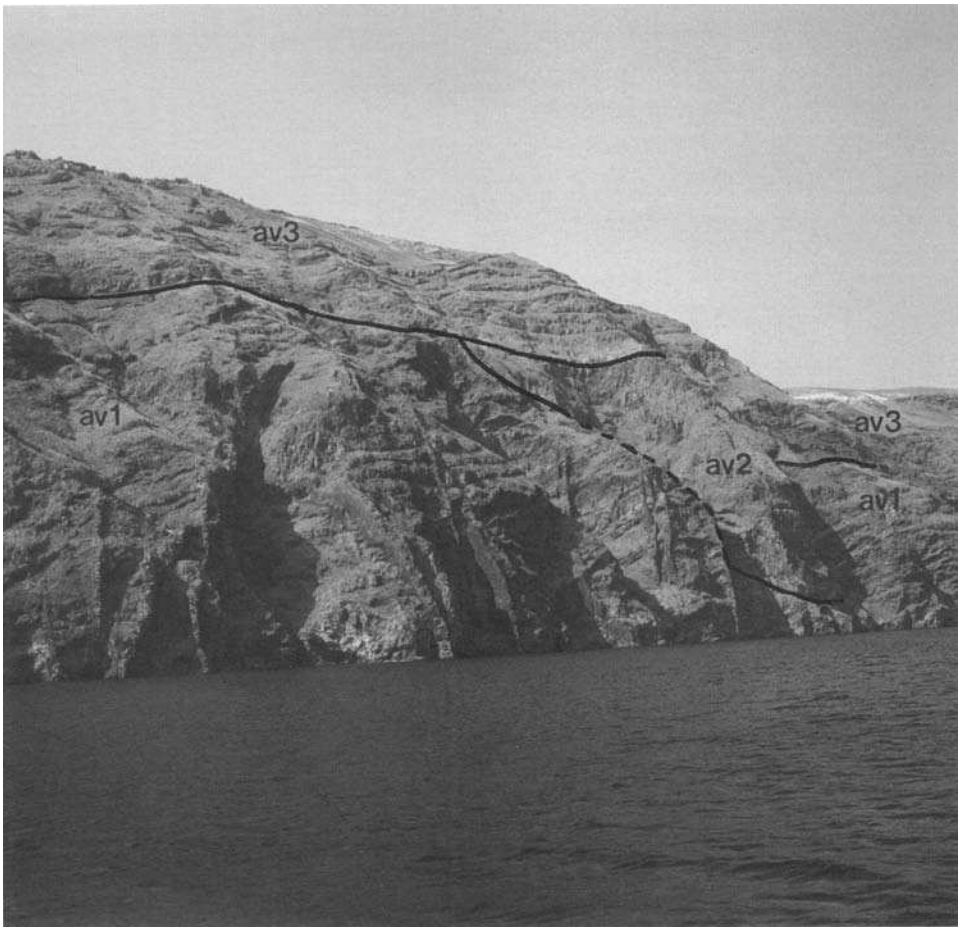

Fig. 3.15. The caldera cliffs below Megalo Vouno summit. Lavas and tuffs of Peristeria 1 (**av1**) are overlain by thin lavas of Peristeria 3 (**av3**). A mass of massive silicic andesite (**av2**) separates the two and lies plastered against a steeply inclined surface, perhaps the wall of an ancient vent. There are numerous dykes cutting **av1**, and some of these also pass up into **av3**.

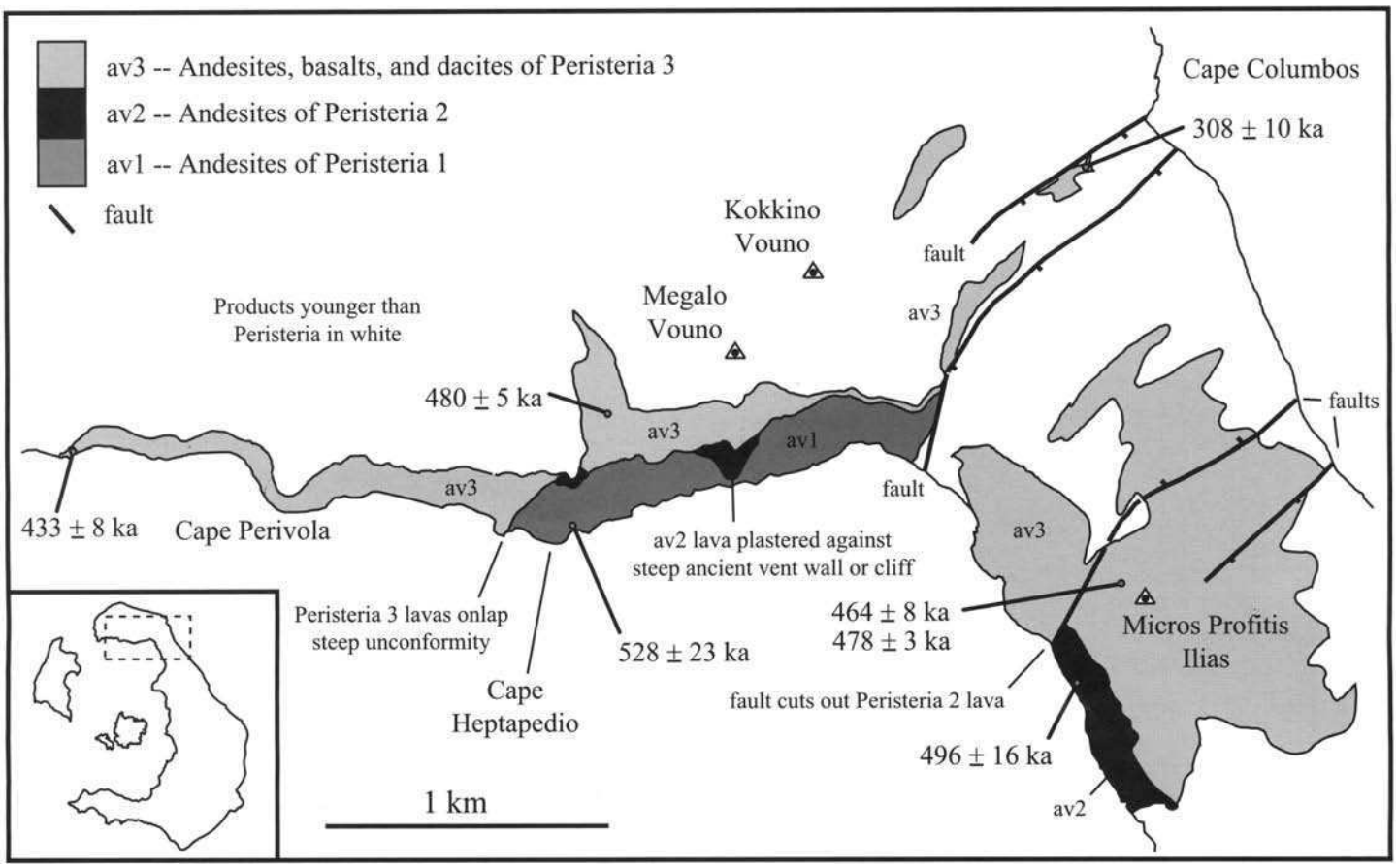

Fig. 3.16. Geological map of the remains of Peristeria Volcano in the northeast corner of Thera. Products younger than Peristeria are shown in white. The downthrown sides of faults are marked by ticks.

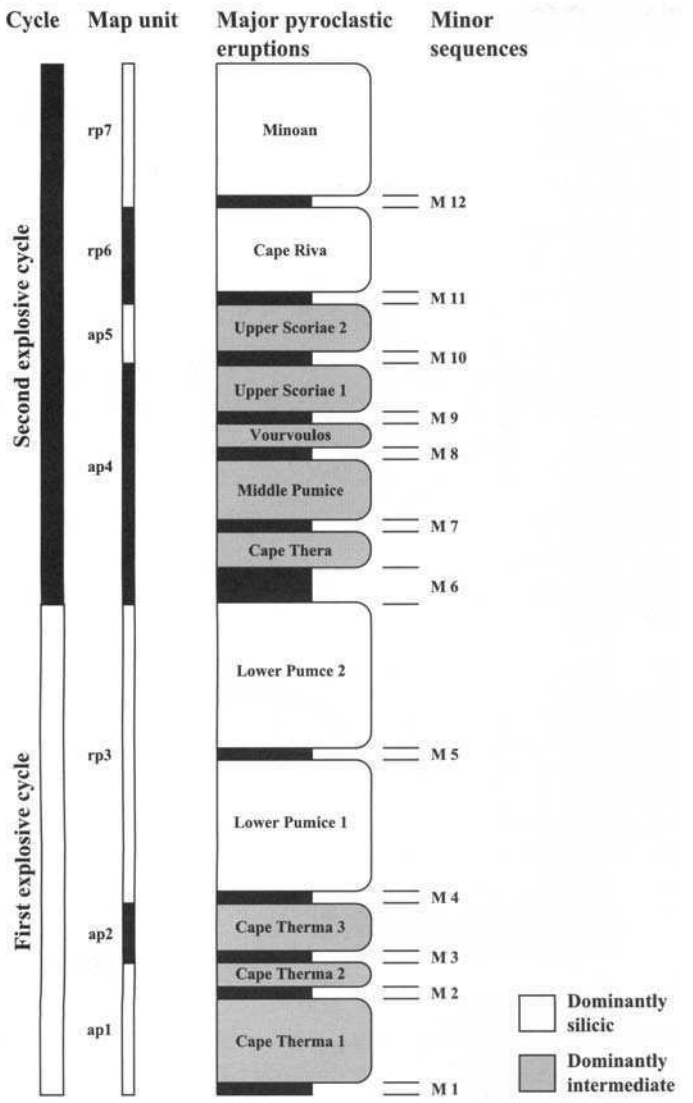

Fig. 3.17. Schematic log showing the products of the 12 major pyroclastic eruptions of Santorini. They are divided into two cycles, as discussed in the text. Sequences of minor tephra and palacosols between the main units are labelled M1 to M12.

Cape Therma 1 eruption

The first major explosive eruption on Santorini generated an andesitic ignimbrite preserved widely in southern and central Thera (Figs 3.18, 3.21, 3.22). The ignimbrite (Unit B; Table 3.4) is most prominent at Cape Therma, where it is about 60 m thick and forms a prominent cliff at the base of the caldera wall (**Cape Therma 1 Tuff; ap1**). The lowest flow units are buff to black and unlithified, whereas the upper units are pink sillar. There is a thin pumice-fall deposit at the base of Cape Therma 1.

Near Cape Alonaki, Cape Therma 1 is underlain by a 30 m thick succession of phreatomagmatic tuffs, which are probably the remnant of a tuff ring. A few metres of alternating pumice fall deposits, surge deposits, and palaeosols then separate these tuffs from Cape Therma 1 (Unit A).

Cape Therma 2 eruption

Cape Therma 1 was followed by the eruption of a prominent, lithic-poor rhyodacitic pumice fall deposit, 2.4 m thick at Cape Athinios, which we call Cape Therma 2. Cape Therma 2 is the thinnest of the named Thera pyroclastics. It is a useful marker horizon in the cliffs of southern Thera. However it is readily confused with white pumice falls in the tuff succession below Cape Therma 1.

The Rhyodacites of Cape Alonaki and NE Thera

Following Cape Therma 2 at least two rhyodacitic lava flows were extruded from vents in the general area of Phira (**Rhyodacites of Cape Alonaki; ra**). They crop out continuously between Phira harbour and 1 km south of Cape Alonaki, where cuts through steep flow fronts or sides are exposed in the cliffs (Figs 3.20, 3.23). The lowest lava (S90-10) yielded a precise K–Ar age of 224 ± 5 ka. Compositional similarity, and the absence of intervening soil, between Cape Therma 2 and the Cape Alonaki lavas suggests that they are probably the products of a single eruption.

Another rhyodacite crops out in the northeast corner of the caldera. It lies at the base of a wedge of Thera pyroclastics preserved at the contact between Megalo Vouno and Micros Profitis Ilias. It has been dated 257 ± 31 ka by the K–Ar method (S90-17). This lava is correlated with the Rhyodacites of Cape Alonaki because (1) they are similar compositionally, (2) both directly underlie Cape Therma 3 (**ap2**), and (3) the K–Ar ages are the same at the 1σ level.

Cape Therma 3 eruption

The Cape Therma 3 eruption generated andesitic deposits preserved extensively in southern Thera (**Cape Therma 3 Tuff; ap2**) (Figs 3.18 and 3.23). The basal pumice fall deposit (Unit A) is stratified, rich in obsidian fragments, and thickest (1.2 m) between Capes Athinios and Alonaki. It is overlain by pyroclastic flow deposits including black, grey or pink scoriaceous ignimbrite, red spatter agglomerates, and lithic-rich breccias up to 20 m thick (Unit B). Grey scoria-flow deposits are the main facies on the Akrotiri Peninsula, while pink sillar-facies ignimbrites and red spatter aggolmerates dominate as far north as Phira. Ignimbrites and spatter agglomerates of Cape Thermas 1 (**ap1**) and 3 (**ap2**) are easily confused, and are also similar compositionally (silicic andesite). They are most readily distinguished where they occur together, separated by Cape Therma 2 and/or the Rhyodacites of Cape Alonaki (**ra**). At Cape Perivola a thin, pink ignimbrite underlying Lower Pumice 1 (**rp3**) is interpreted as Cape Therma 3 (**ap2**). The same ignimbrite occurs between the rhyodacite lava (**ra**) and Lower Pumice 1 (**rp3**) in the northeast corner of the caldera.

Lower Pumice 1 eruption

The first explosive cycle culminated in a pair of rhyodacitic eruptions called Lower Pumice 1 and Lower Pumice 2 (Figs 3.21–3.25). Since the deposits always occur together, we have mapped them as a single unit (**Lower Pumices; rp3**).

Lower Pumice 1 occurs almost continuously in the caldera wall of southern Thera and locally at Cape Perivola in the north (Fig. 3.18). The eruption began with a Plinian phase, generating a pumice-fall deposit up to 5 m thick (Unit A). Isopachs (Fig. 3.19) do not constrain the vent position closely, but are consistent with eruption from a site near Nea Kameni and dispersal to the southwest. The Plinian phase was followed by discharge of voluminous pyroclastic flows. These laid down a distinctive bed of coarse-grained, pinky brown lithic lag breccia, up to 14 m thick, which drapes topography and can be traced widely in the caldera walls (Unit C). The breccia is crudely bedded and cross stratification on a scale of tens to hundreds of metres occurs in the cliffs of the Akrotiri Peninsula. Initial discharge of the pyroclastic flows must have involved a strong ballistic component, because the top of the underlying Plinian deposit is pock-marked with bomb sags (Fig. 3.26). The lithic breccia is also compositionally zoned, the vesicular component changing from rhyodacitic at the base to andesitic at the top. Lenses of non-welded ignimbrite (Unit B) occur below the breccia at many locations. One ignimbrite bed at Cape Perivola is welded and contains black obsidian fiamme. A precise K–Ar age of

Table 3.4. *The major explosive eruptions and their deposits*

Age (ka)	Cycle	Map symbol	Eruption	Unit [8]	Deposit	Thickness (m)
3.6 [1]	2	rp7	Minoan	D	Non-welded ignimbrite and lithic breccia	40
				C	Massive phreatomagmatic tuff	55
				B	Base surges	12
				A	Plinian pumice	6
21 [2]	2	rp6	Cape Riva	D	Incipiently welded ignimbrite	2
				C	Non-welded ignimbrite and lithic-lag breccia	25
				B	Incipiently to densely welded ignimbrite	12
				A	Pumice fall	4
79 ± 8; 54 ± 3 [3]	2	ap5	Upper Scoriae 2	D	Scoria flow with agglomeratic and lithic-rich lag facies	50
				C	Scoria flow and pyroclastic surge	16
				B	Pyroclastic surge	3
				A	Pumice fall	1
	2	ap4	Upper Scoriae 1	D	Scoria flow	1
				C	Agglomeratic and lithic-rich lag facies	12
				B	Scoria flow	4
				A	Scoria fall with base surge	4
	2	ap4	Vourvoulos	B	Ignimbrite and base surge	3
				A	Pumice fall	2
c. 100 [4]	2	ap4	Middle Pumice	C	Pumice fall, in part welded	1
				B	Lithic-rich and agglomeratic lag facies, minor ignimbrite	60
				A	Plinian pumice, in part welded	6
	2	ap4	Cape Thera	B	Scoria flow and base surge	60
				A	Pumice fall	1
c. 180 [5]	1	rp3	Lower Pumice 2	D	Lithic-rich lag breccia	10
				C	Massive phreatomagmatic deposit	20
				B	Base surges	7
				A	Pumice fall	25
203 ± 24 [6]	1	rp3	Lower Pumice 1	C	Non-welded ignimbrite and lithic-rich lag breccia	14
				B	Non-welded ignimbrite	14
				A	Pumice fall	5
	1	ap2	Cape Therma 3	B	Scoria flow with agglomeratic and lithic-rich lag facies	20
				A	Pumice fall	1
	1	ap1	Cape Therma 2		Pumice fall	2
≤ 360 [7]	1	ap1	Cape Therma 1	B	Scoria flow, incipiently welded	60
				A	Pumice fall and base surge	2

[1] Mean of radiocarbon ages on plant remains in tuffs (Freidrich *et al.* 1990).
[2] Mean of radiocarbon ages of plant remains in tuff (Pichler & Freidrich 1977) corrected using the data of Bard *et al.* (1990).
[3] K–Ar and $^{39}Ar/^{40}Ar$ ages of sample S90-8 (Tables 3.2 and 3.3).
[4] Tentative correlation by Federman & Carey (1980) with W-2 deep-sea ash. Age consistent with K–Ar data for rock units stratigraphically above and below.
[5] Constrained by K–Ar and $^{39}Ar/^{40}Ar$ ages for andesites of Simandiri (sample S90-20, Tables 3.1 and 3.2).
[6] K–Ar age of sample S90-25 of Table 3.1.
[7] Constrained by ages of samples S91-26 and S90-1 of Table 3.1 and 3.2 which come from rock units stratigraphically under Cape Therma 1.
[8] Eruption units are from Druitt *et al.* (1989).

203 ± 24 ka was obtained on these fiamme (S90-25), showing that Lower Pumice 1 is older than suggested by fission-track dating of similar material (Table 3.3).

Lower Pumice 2 eruption

Lower Pumice 2 directly overlies Lower Pumice 1, separated only by a single palaeosol. The eruption began with a Plinian phase, which generated a pumice-fall deposit (Unit A) ranging in thickness from more than 25 m to less than a metre (Fig. 3.27). Isopachs suggest dispersal to the east from a vent situated near Nea Kameni (Fig. 3.19). The fall deposit has a relatively thin, white, basal unit overlain by an inversely graded main fall unit. Following the Plinian phase, phreatomagmatic explosions generated dune-bedded surge deposits (Unit B), then a thick, massive, poorly sorted pumiceous deposit up to 20 m thick (Unit C). The eruption terminated with emplacement of lithic breccias laid down by pyroclastic flows (Unit D). The products of Lower Pumice 2 are uniformly rhyodacitic apart from the Plinian deposit, which also contains subordinate scoria of basaltic to andesitic composition.

Lower Pumice 2 forms a prominent marker in the cliffs of southern Thera, from the south side of the Akrotiri Peninsula to Phira (Figs 3.18, 3.23–3.25). In the north, it occurs below Oia and at Cape Perivola (Fig. 3.25). A thin remnant of Lower Pumice 2 is preserved locally at Cape Heptapedio atop the eroded remains of Peristeria Volcano. A white tuff along the contact between Peristeria 1 and Peristeria 3 on Megalo Vouno was interpreted by Huijsmans *et al.* (1988) as Lower Pumice 2 but it is in fact much older.

Lower Pumice 2 is younger than about 200 ka (the age of Lower Pumice 1), but older than the Andesites of Cape Simandiri (**as**; 170 ka) which stratigraphically overlie it. We deduce an age of about 180 ka, which is consistent with the estimated age of deep-sea

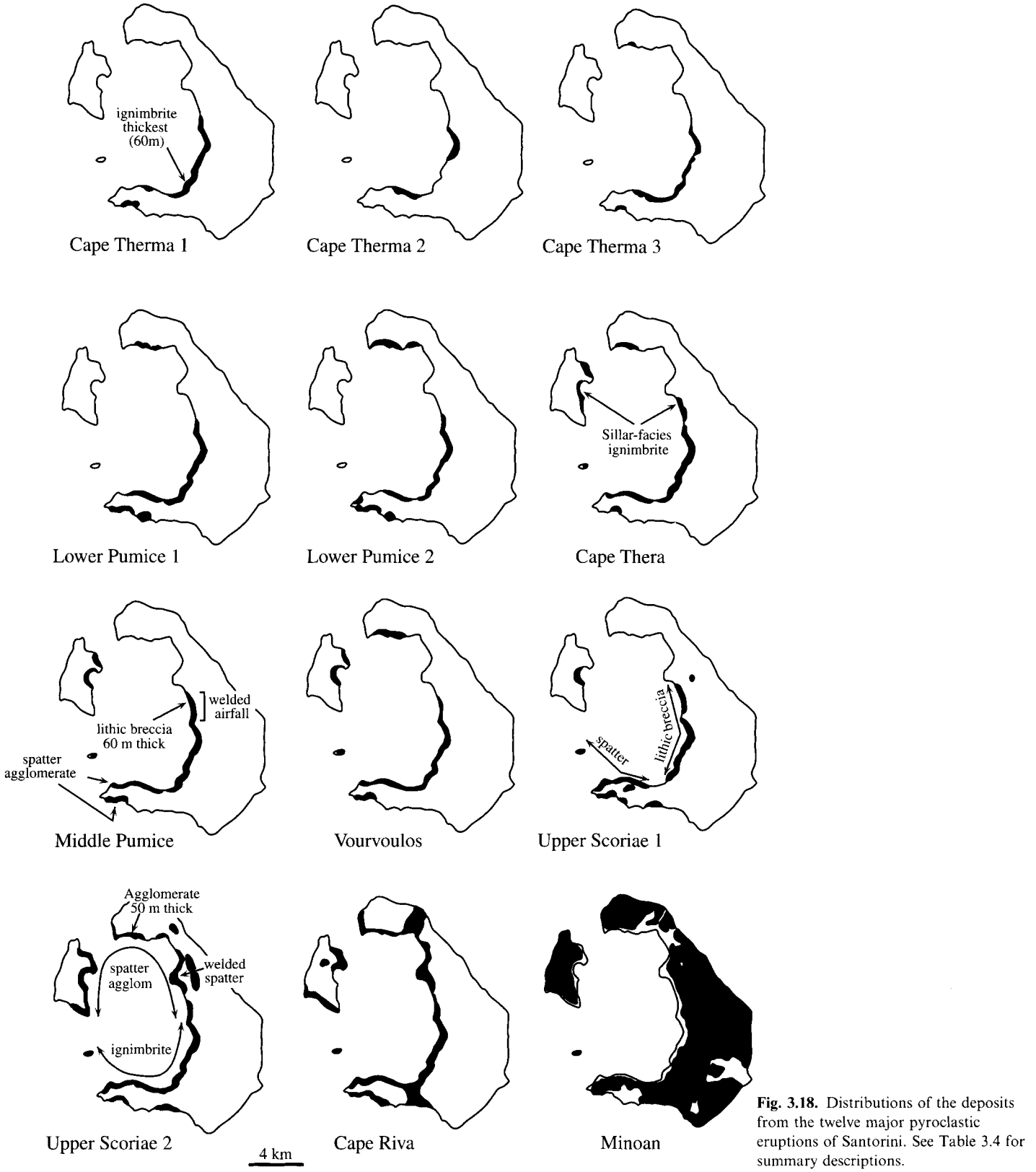

Fig. 3.18. Distributions of the deposits from the twelve major pyroclastic eruptions of Santorini. See Table 3.4 for summary descriptions.

ash layer V-1 (160 ka), which Keller (1981) has correlated with Lower Pumice 2 on compositional grounds (Table 3.3).

Collapse of Caldera 1 (180 ka)

On the south side of Phira harbour, a steep unconformity truncates Lower Pumice 2 and underlying units (Figs 3.20 & 3.28). This ancient cliff line is attributed to caldera collapse during the Lower Pumice 2 eruption. Overlying units drape northwards over the unconformity and thicken dramatically into the old depression, which is called the Lower Pumice caldera, or caldera 1.

Second explosive cycle (180–3.6 ka)

The Simandiri shield

Construction of the Simandiri lava shield commenced after Lower Pumice 2. A remnant of this shield occurs at the base of the Therasia cliffs near Cape Simandiri. Isolated outcrops also occur at sea level on the south side of Manolas Bay (**Andesites and basalts of Cape Simandiri; as**). Founded on stratified phreatomagmatic tuffs and conglomerates, the lavas include thin basalts and thick andesitic domes and coulées. The shield summit must have lain east of Cape Simandiri, in caldera 1, because the lavas dip westwards. A K–Ar

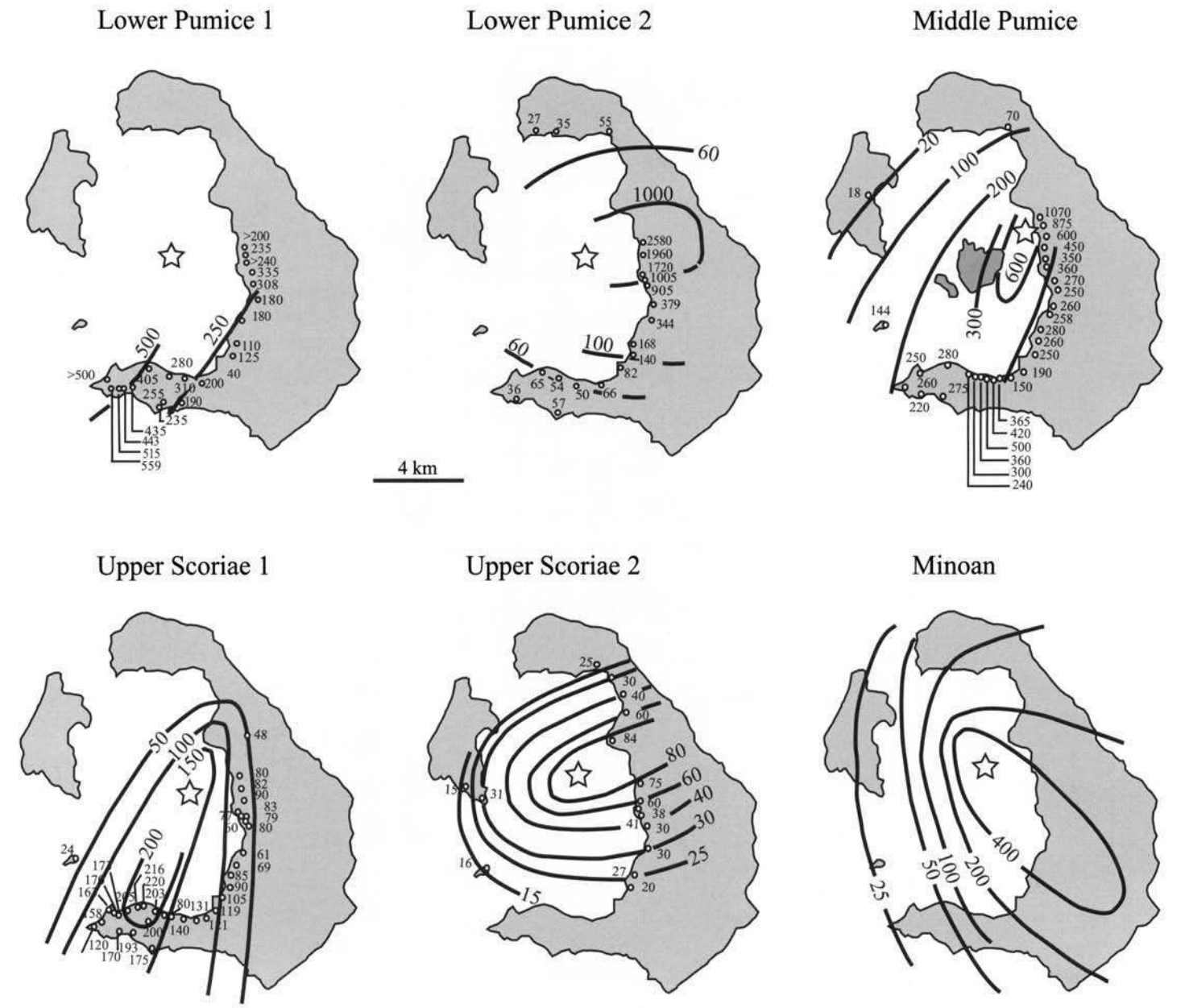

Fig. 3.19. Isopach maps of pumice-fall deposits of six of the major explosive eruptions of Santorini. Data from other eruptions are not of sufficient quality to draw isopach maps. Thicknesses are in centimetres. The Minoan data are taken from Bond & Sparks (1976), and individual data points are not shown.

age of 172 ± 33 ka was obtained on an andesite near the base of the exposed succession (S90-20). An $^{40}Ar/^{39}Ar$ plateau age for the same sample (172 ± 4 ka) is in excellent agreement with the K–Ar age.

The Middle Tuff series of eruptions

There then followed a series of explosive eruptions, four of which discharged at least a few km^3 of andesite or dacite as fallout and ignimbrite and thus are considered as major eruptions (**Cape Thera Tuff, Middle Pumice, Vourvoulos Tuff, Upper Scoriae 1**). Deposits from numerous smaller eruptions occur between the major tuff layers. The entire succession forms a coherent, widely dispersed package we call the Middle Tuff series (**ap4**).

Cape Thera eruption

The Cape Thera Tuff is separated from Lower Pumice 2 by a sequence of minor tephra and palaeosols reaching 13 m in thickness near Phira (M6; Fig. 3.17). The sequence probably records several hundreds to thousands of years of minor activity following collapse of caldera 1. It lies in the same stratigraphic interval as the Simandiri shield, although compositional differences between the two do not favour a direct correlation (Chapter 6).

The Cape Thera eruption generated a thin pumice fall deposit (Unit A), then ignimbrite (Unit B). The pumice fall deposit is 85 cm thick near Phira, but thickness variations do not allow the vent site to be accurately constrained. The ignimbrite is thickest near sea level at Phira, where it ponds to 60 m in caldera 1 and onlaps the old cliff line of that caldera (Figs 3.20, 3.28 & 3.29). A few metres of pink ignimbrite occur on Therasia and above Lower Pumice 2 at Cape Perivola. Elsewhere the ignimbrite is represented by a surge deposit.

Middle Pumice eruption

Following the Cape Thera eruption, there was the accumulation of 5 m of minor pyroclastics and palaeosols. The Middle Pumice eruption then began with a Plinian phase, the pumice fall from

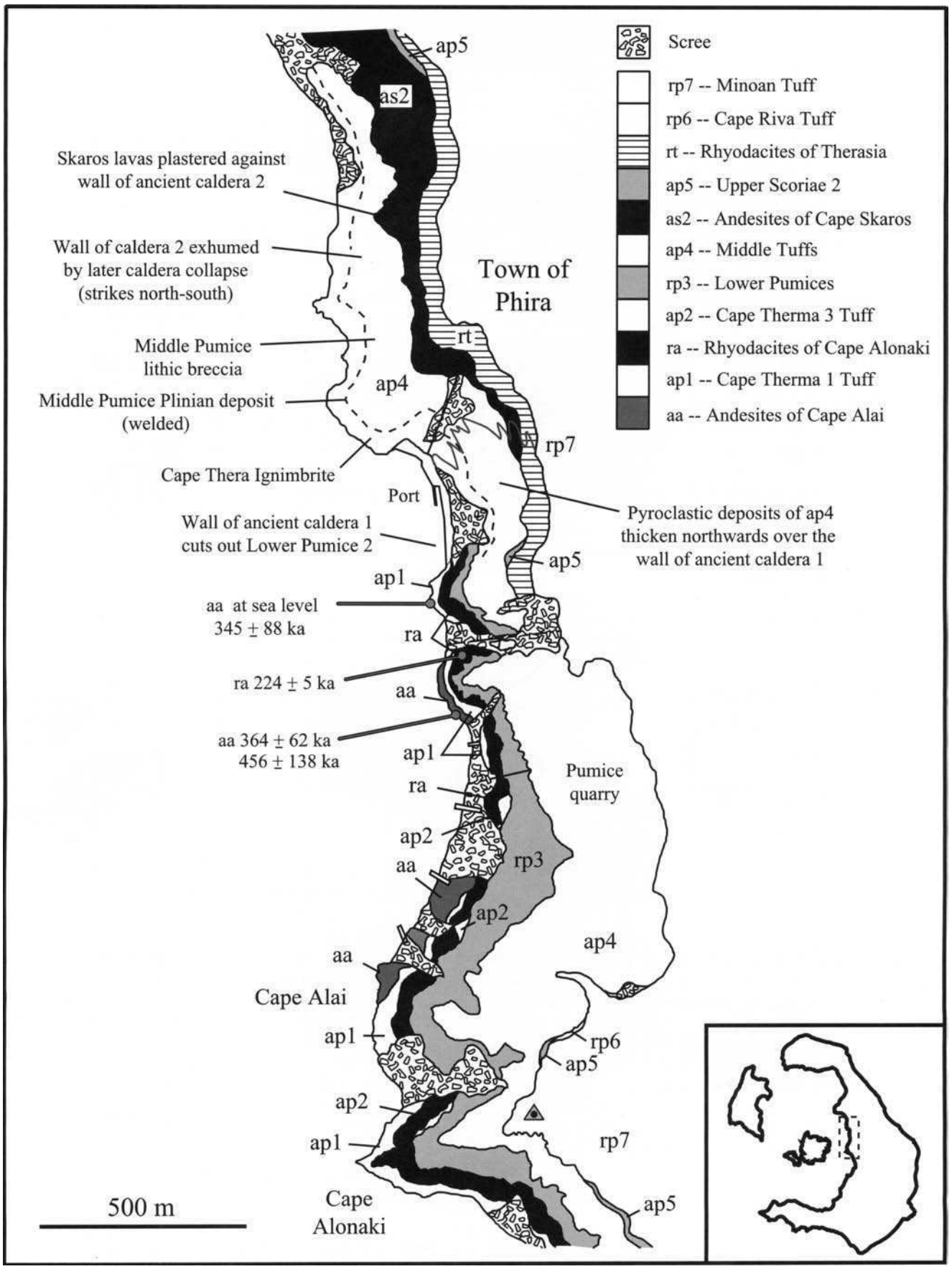

Fig. 3.20. Geological map of the caldera wall near Phira town.

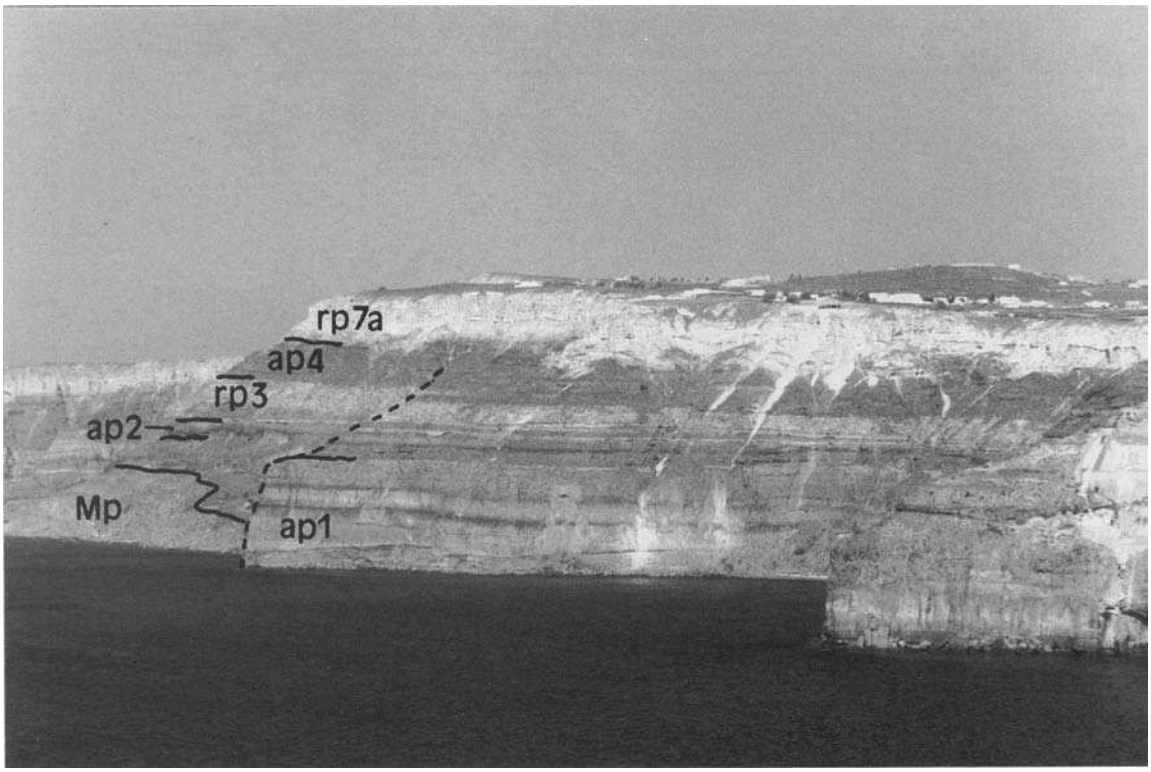

Fig. 3.21. Thera pyroclastic succession of southern Thera. The dotted headland is Cape Plaka, and the one on the right is Cape Therma. **Mp** is the metapelite unit of the basement complex. The main tuff units visible are Cape Therma 1 (**ap1**), Cape Therma 3 (**ap2**), the Lower Pumice Tuffs (**rp3**), the Middle Tuff sequence (**ap4**), and the Minoan Tuff (**rp7a**).

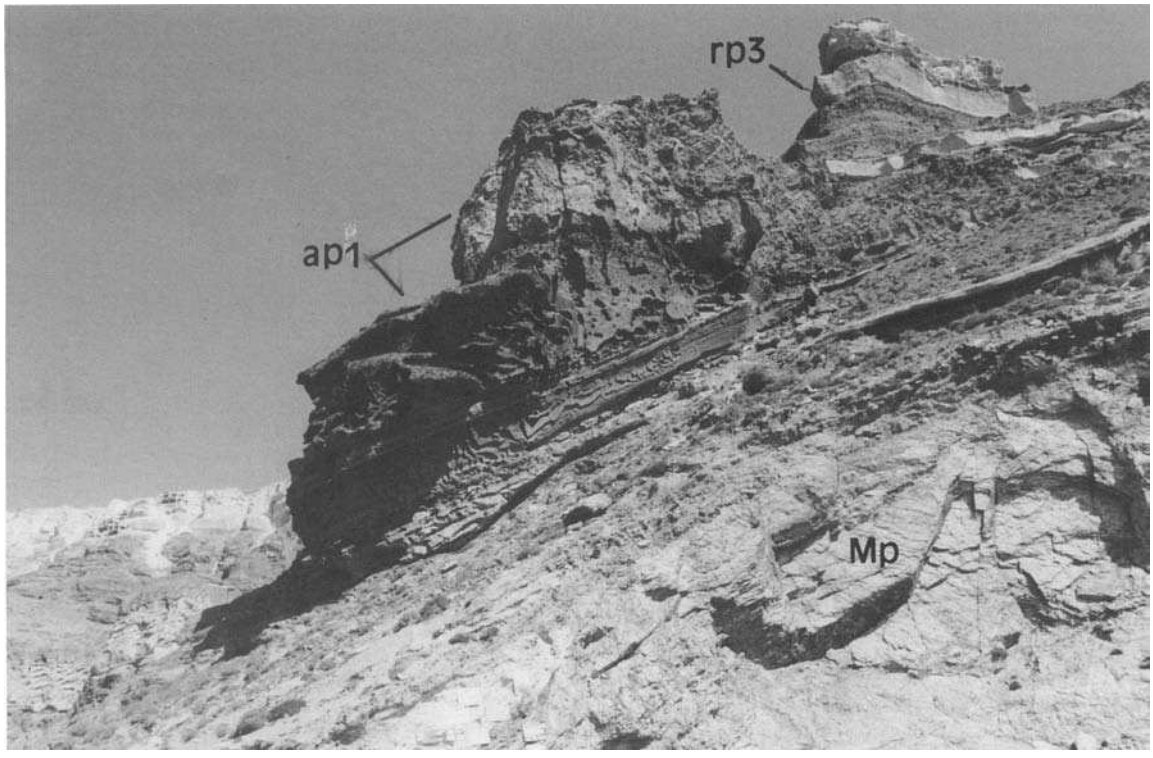

Fig. 3.22. Tuffs of the Thera pyroclastics adhering to the flank of the old pre-volcanic island. **Mp** is the metapelite unit of the basement complex. **ap1** is the Cape Therma 1 Tuff and **rp3** is the Lower Pumice Tuffs. Photograph taken on the road to Athinios harbour.

which forms a prominent, buff-coloured marker bed in the cliffs of southern Thera. Below Phira it occurs as a black, densely welded tuff several metres thick and streaked with layers of orange oxidation (Sparks & Wright 1979) (Figs 3.18, 3.20 & 3.29). The isopach map of this deposit (Fig. 3.19), and the distribution of the welded facies, are consistent with a vent west of Phira. The fall deposit is overlain by grey, greenish, or orange lithic breccias laid down by lithic-rich pyroclastic flows (Unit B; Fig. 3.30. The thickness of the breccias across southern Thera is typically a few metres, but it increases abruptly to 60 m below Phira, where ponded in caldera 1 (Figs 3.18, 3.20 & 3.28). Near Cape Aspronisi the breccias grade laterally into spatter agglomerates resembling those of the two Upper Scoriae eruptions (Fig. 3.31). Deep impact sags with bombs as large as 3 m in the top of the pumice fall record violent ballistic emplacement at

Fig. 3.23. View (looking north) of Cape Alonaki. The town of Oia is in the background. The principal units, from the base up, are the Cape Therma 1 Tuff (**ap1**), the Rhyodacites of Cape Alonaki (**ra**), the Cape Therma 3 Tuff (**ap2**), the Lower Pumice Tuffs (**rp3**), the Middle Tuff sequence (**ap4**), and the Minoan Tuff (**rp7a**). Unit **rp3** comprises Lower Pumice 1 and Lower Pumice 2 separated by the dotted line. The thin white tuff marked T is Cape Therma 2.

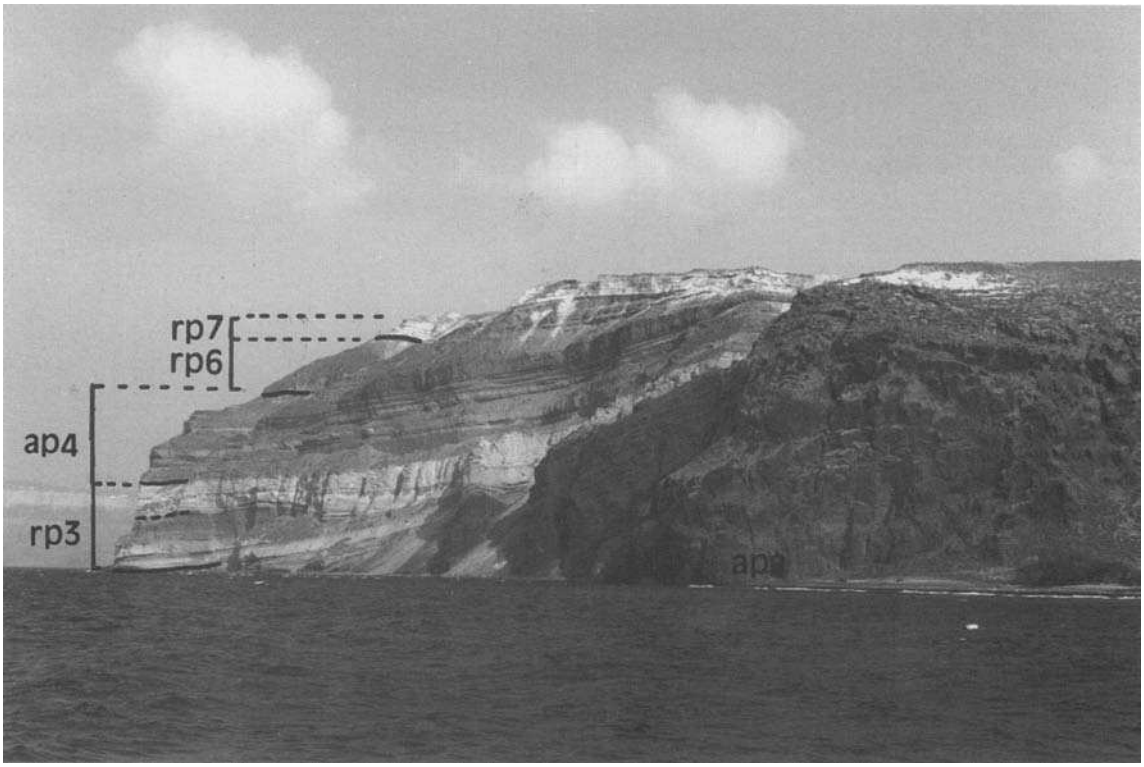

Fig. 3.24. View of Cape Loumaravi, taken from the west. The Thera pyroclastics drape over the cinder cone of Cape Kokkinopetra (**apa**). The main units are the Lower Pumice Tuffs (**rp3**), the Middle Tuff sequence (**ap4**), the Cape Riva Tuff (**rp6**), and the Minoan Tuff (**rp7**). Unit **rp3** comprises Lower Pumice 1 and Lower Pumice 2 separated by the dotted line.

the onset of pyroclastic flow production. The transition from Plinian to pyroclastic flow activity was also marked by extensive vent erosion, since blocks of juvenile welded tuff from the Plinian deposit are abundant in the breccias. The eruption ended with discharge of a second, thinner pumice-fall deposit (Unit C) erupted from the same vent as the first pumice-fall (Druitt 1983).

Federman & Carey (1980) tentatively correlated Middle Pumice with a deep-sea ash layer preserved 450 km ESE of Santorini. They estimated the age of the ash as about 100 ka. This is broadly consistent with the ages of (1) the Simandiri shield (**as**; 172 ka), which predates Middle Pumice, and (2) Megalo Vouno cinder cone (**ap4**; 55–75 ka; see below), which postdates it.

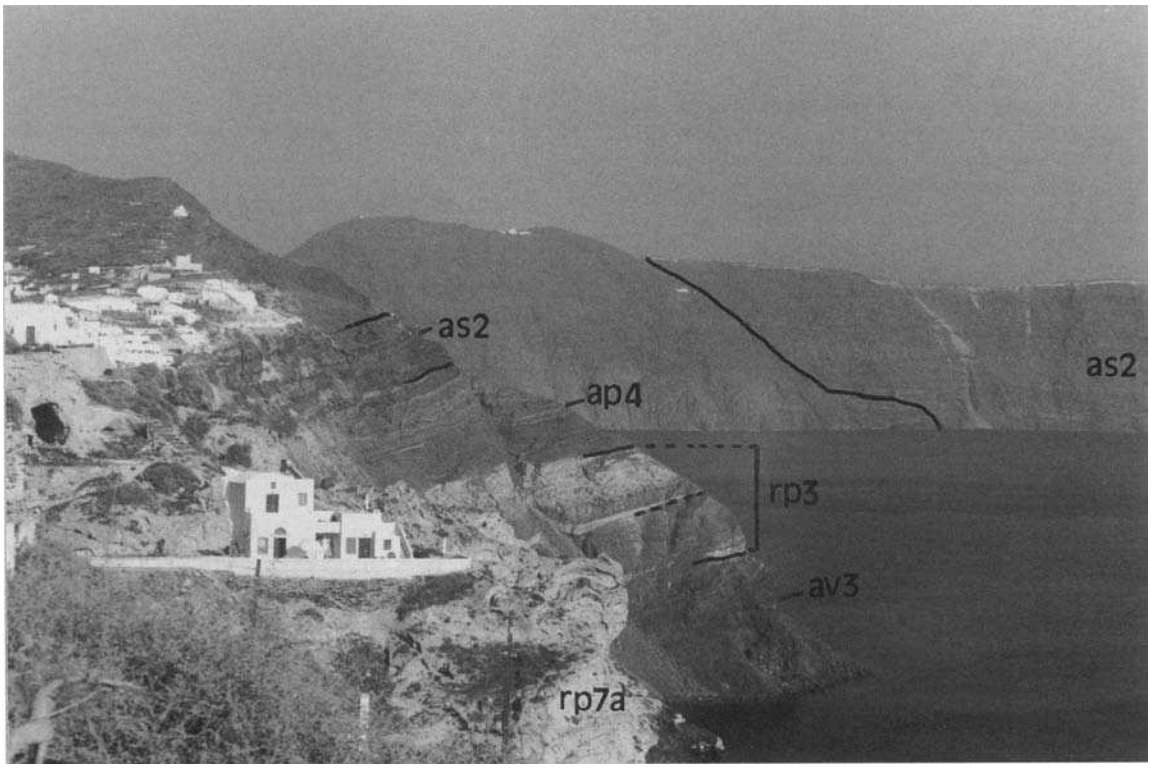

Fig. 3.25. View of Cape Perivola, looking east. The base of the cliff comprises lavas of Peristeria 3 (**av3**). These are overlain by the Lower Pumice Tuffs (**rp3**), the Middle Tuff sequence (**ap4**), then extracaldera lavas of the Skaros shield (**as2**). Unit **rp3** comprises Lower Pumice 1 and Lower Pumice 2 separated by the dotted line. The main mass of Skaros is seen in the background, lapping up against the remains of Peristeria Volcano. The Minoan Tuff (**rp7a**) lies in the foreground.

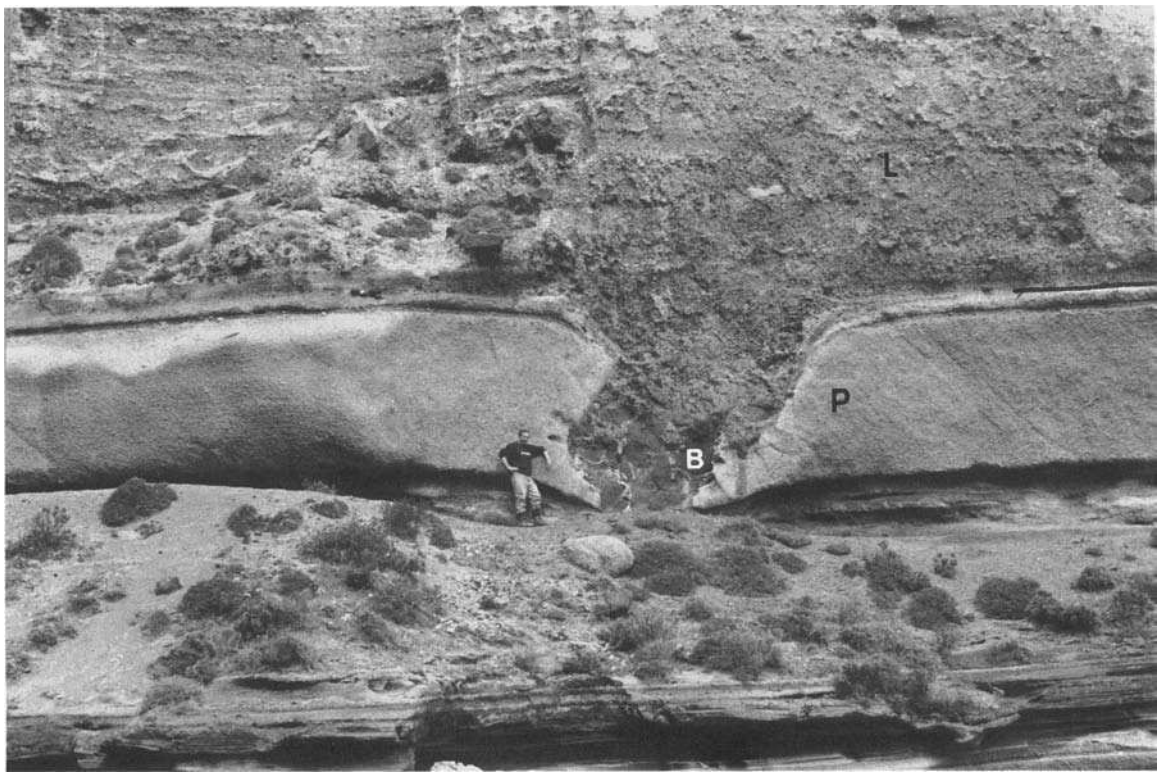

Fig. 3.26. Bomb sag in the Lower Pumice 1 Plinian pumice fall (P) at Cape Balos. Remains of the bomb (B) occur in the sag. Stratified lithic lag breccias overlie the plinian deposit and fill the bomb sag. Man for scale.

Vourvoulos eruption

Up to 9 m of minor pyroclastics and palaeosols then accumulated before the Vourvoulos eruption. These include a prominent scoria fall deposit, 2.5 m thick near Phira, which may correlate with the cinder cones of Megalo and Kokkino Vouno, which erupted around this time. A tuff ring near Aspronisi was also active at this period.

The Vourvoulos eruption laid down thin (few metres maximum), but widespread, deposits comprising a pumice fall layer (Unit A) overlain by cross-bedded surge deposits and ignimbrite (Unit B).

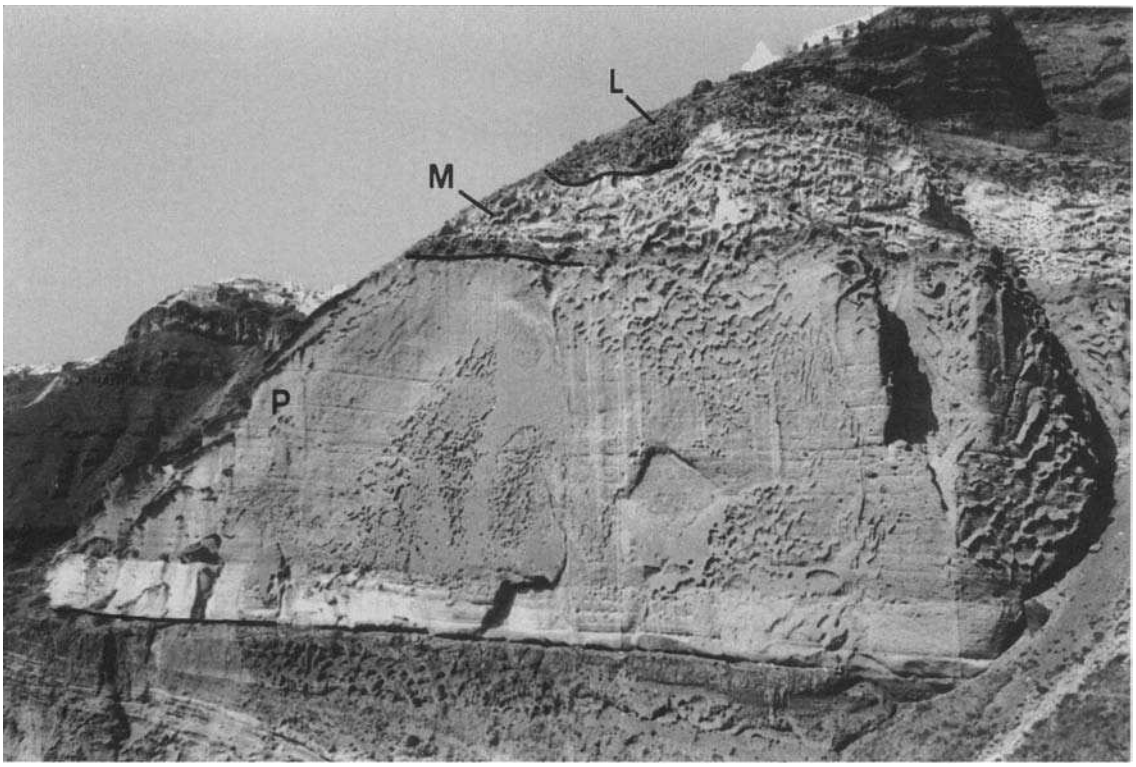

Fig. 3.27. Plinian pumice fall deposit (P) of Lower Pumice 2 on the south side of Phira harbour. The pure white layer is a lithic-poor basal unit of the pumice fall. The entire fall deposit here is 25 m thick and is overlain by massive phreatomagmatic tuffs (M) and lithic lag breccias (L) of the same eruption. The dark deposit underlying the Plinian pumice fall is the lithic breccia of Lower Pumice 1.

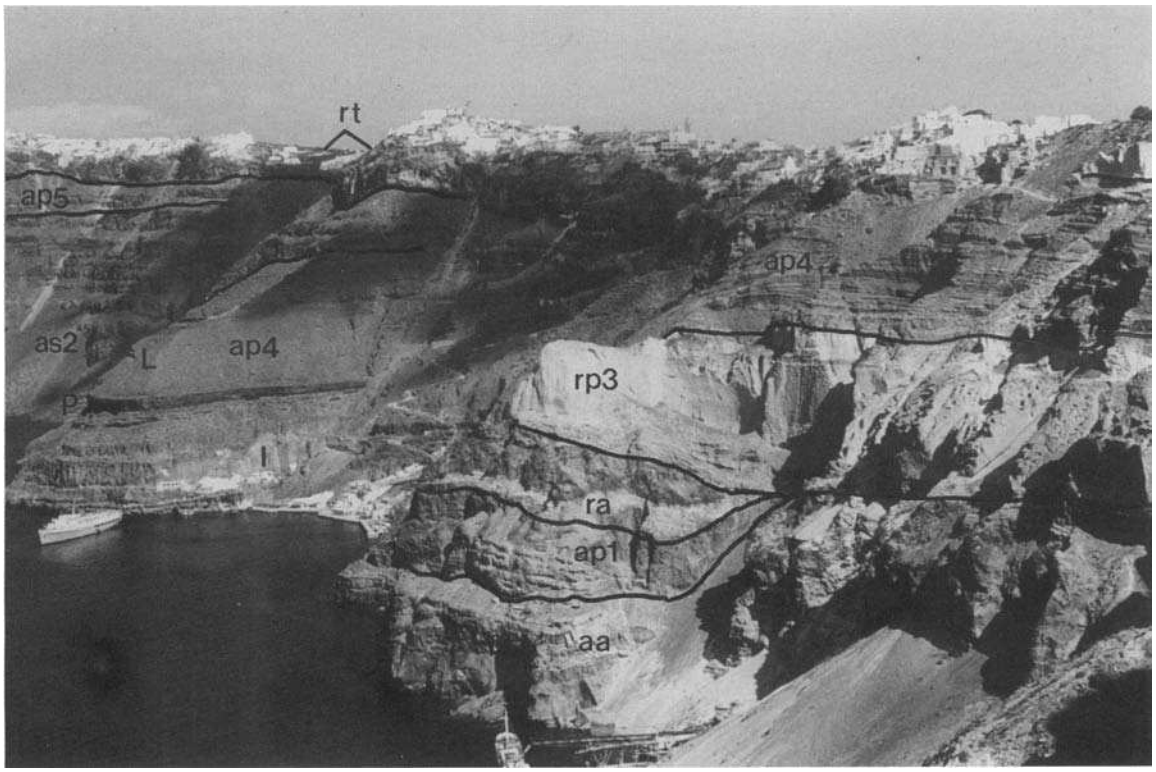

Fig. 3.28. Caldera wall at Phira. On the right (south) lie the Andesites of Cape Alai (**aa**), the Cape Therma 1 Tuff (**ap1**), the Rhyodacites of Cape Alonaki (**ra**), the Lower Pumice 2 Tuff (**rp3**), and deposits of the Middle Tuff sequence (**ap4**). Lower Pumice 2 and units below it are cut out abruptly by an unconformity surface interpreted as the ancient wall of caldera 1. The Middle Tuffs thicken markedly to the north across the unconformity. Prominent layers in **ap4** are the Cape Thera ignimbrite (I), the Middle Pumice welded Plinian deposit (P), and the Middle Pumice lithic breccias (L). A second unconformity is revealed by the dramatic thickening of the Skaros lavas (**as2**) north of Cape Thera, this being the ancient wall of caldera 2. The Skaros lavas are capped by Upper Scoriae 2 (**ap5**) and the Rhyodacites of Therasia (**rt**).

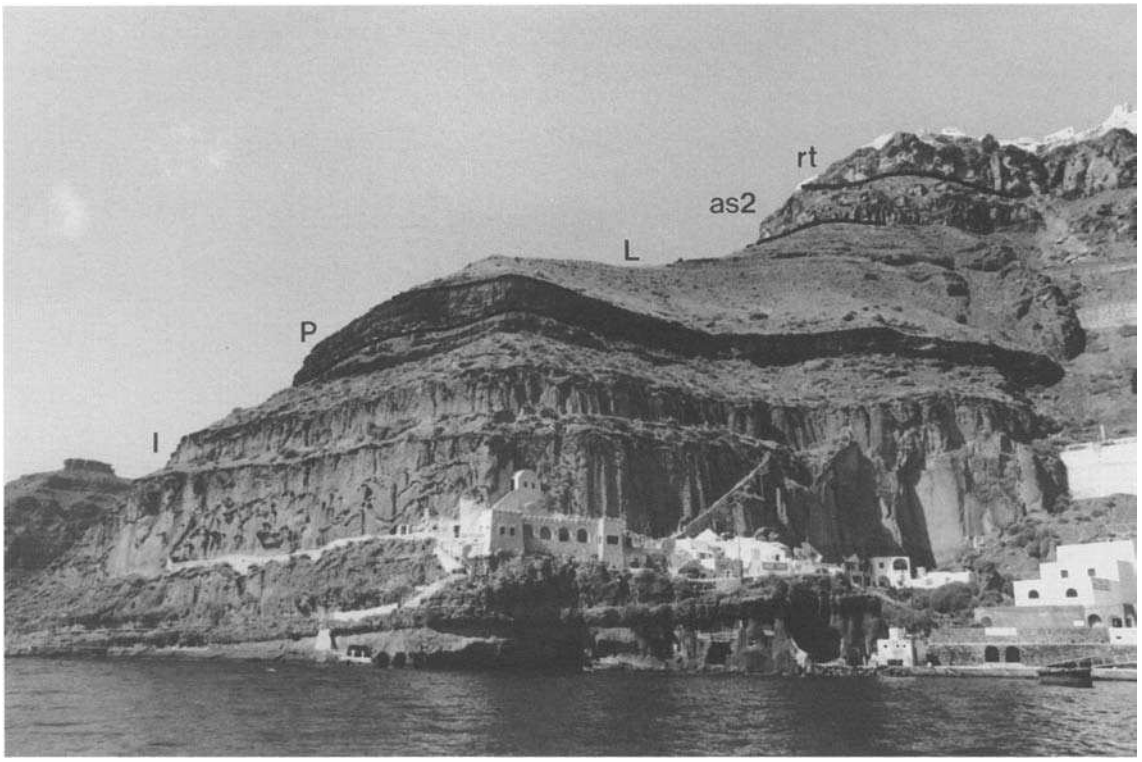

Fig. 3.29. The headland of Cape Thera, on the north side of Phira harbour. Cape Thera ignimbrite (I), welded plinian pumice fall deposit of the Middle Pumice eruption (P), lithic breccias of the Middle Pumice eruption (L), Skaros lavas (**as2**) and rhyodacites of the Therasia dome complex (**rt**).

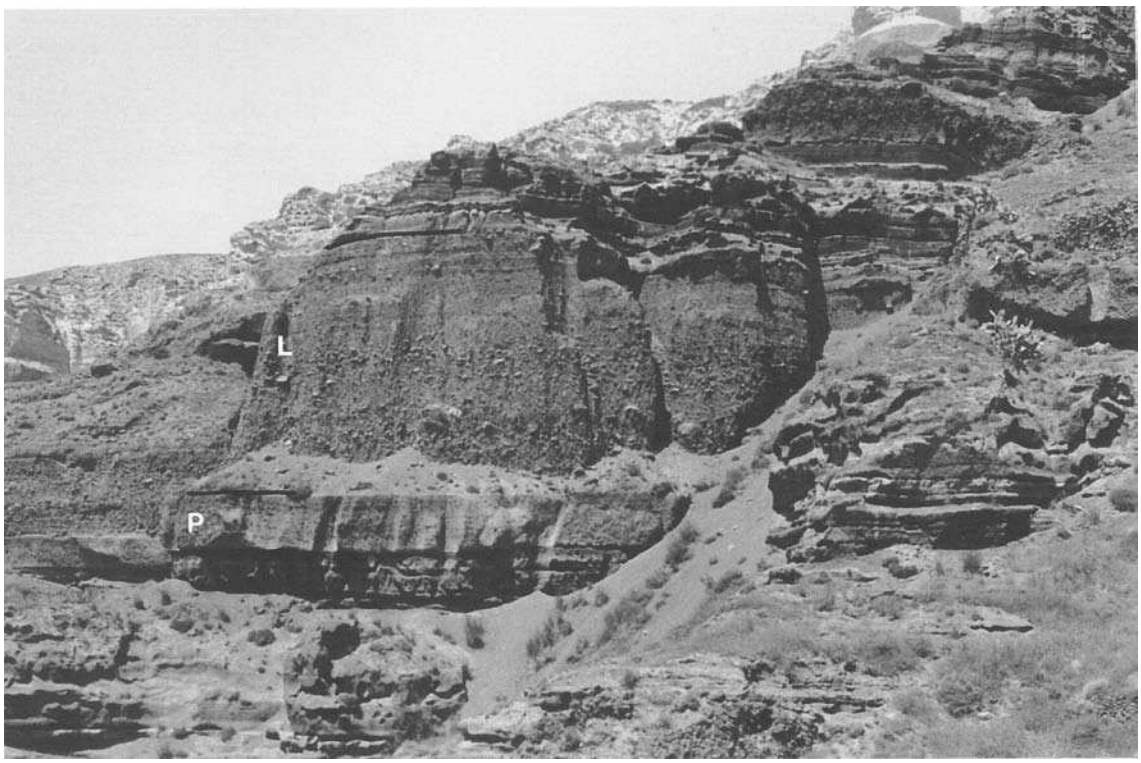

Fig. 3.30. The Middle Pumice near Cape Plaka. Plinian pumice fall deposit (P) overlain by lithic breccias (L). The pumice fall is about 2.5 m thick.

Upper Scoriae 1 eruption

The Upper Scoriae 1 eruption began with emplacement of a black scoria fall deposit containing a pair of ash beds (Unit A). This unit is a highly distinctive marker horizon in southern Thera. The ash beds are less than a metre thick and contain typical base surge climbing-ripple cross stratification and are rich in accretionary lapilli. They cover more than 60 km^2 and, near Cape Aspronisi, fill U-shaped erosional channels. Plastering onto steep slopes, base surge dune structures and the presence of accretionary lapilli suggest a phreatomagmatic origin for the ash beds. Isopach contours for the scoria fall show that the vent lay near present-day Nea Kameni (Fig. 3.19), and this is consistent with flow directions inferred from foreset laminae in the ash beds (Fig. 3.32).

Upper Scoriae 1 culminated with the eruption of pyroclastic flows (Units B to D). These laid down a coarse-grained spatter agglomerate, up to 12 m thick, which is prominent in the caldera wall of the Akrotiri Peninsula. The spatter agglomerate is a type of

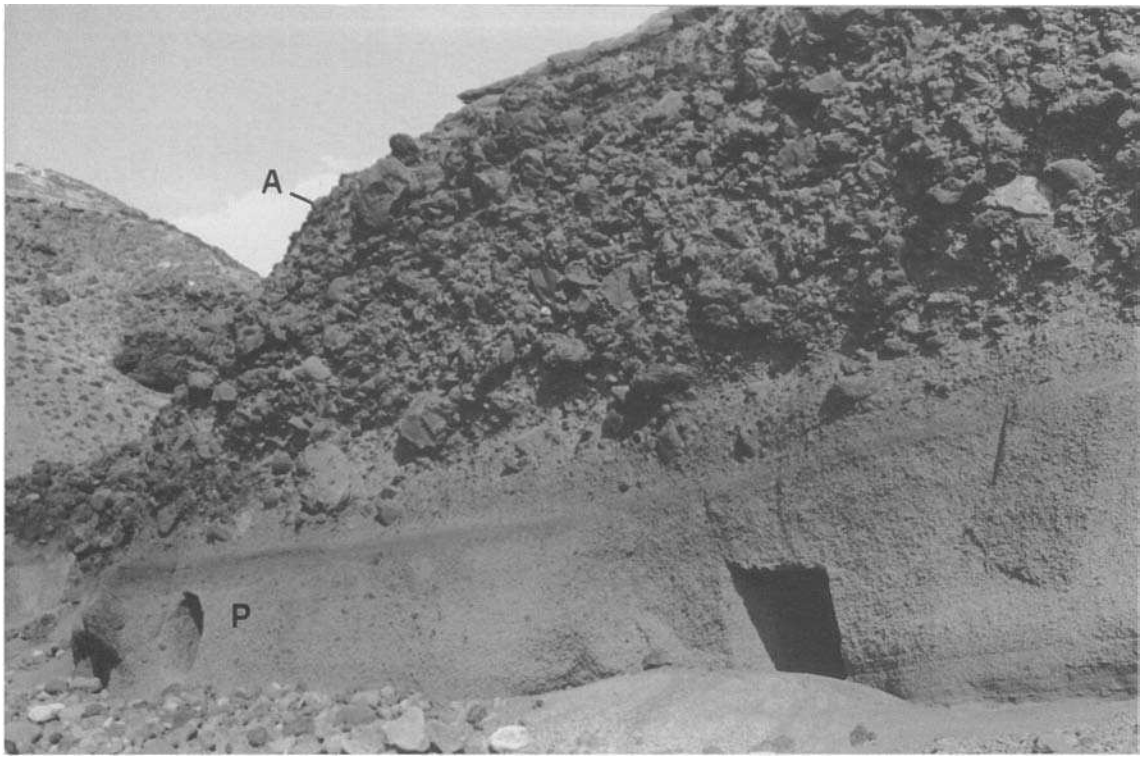

Fig. 3.31. The Middle Pumice near Cape Aspronisi. Pumice fall deposit (P) overlain by spatter agglomerate (A). The spatter agglomerate is the lateral equivalent of the lithic breccias that are the normal pyroclastic flow deposits of this eruption. The pumice fall is 2.5 m thick.

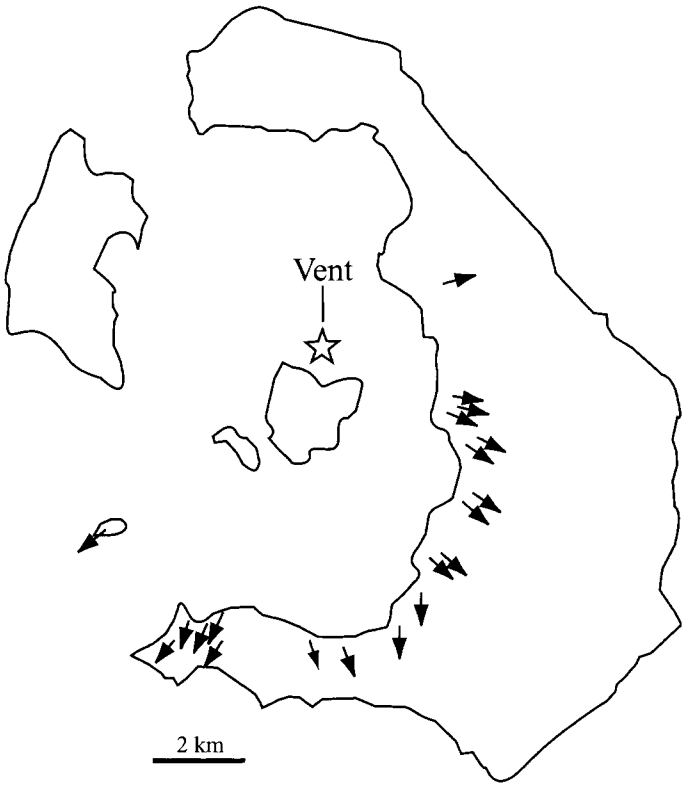

Fig. 3.32. Flow directions of pyroclastic surges of the Upper Scoriae 1 eruption, measured from the orientations of foreset laminae.

lag deposit from pyroclastic flows charged with rags of fluidal andesite (Mellors & Sparks 1991). It is composed of packed red or black andesitic spatter clasts as large as 3 m with subordinate lithic blocks. The spatter clasts are commonly imbricated, showing that the deposit was emplaced by pyroclastic flow (Fig. 3.33; Mellors & Sparks 1991). The agglomerate typically drapes topography, but thickens and coarsens into depressions. Between Phira and Cape Therma lithic blocks are more abundant than spatter rags, and the deposit is best described as lithic breccia (Fig. 3.18).

Friedrich *et al.* (1977) obtained ages of 36.7–44.5 ka from carbon in the palaeosol underlying Upper Scoriae 1. This has been refined to 54.0 ± 0.7 ka using a higher precision ^{14}C technique (W. Friedrich pers. comm. 1984). However Upper Scoriae 1 stratigraphically underlies a Skaros lava dated at 67 ± 9 ka by the $^{40}Ar/^{39}Ar$ technique, suggesting that the ^{14}C method underestimates the true age.

Megalo Vouno and Kokkino Vouno cinder cones. Cape Columbos tuff ring

Construction of two cinder cones (Megalo Vouno and Kokkino Vouno) atop the eroded Peristeria Volcano occurred during the Middle Tuff (**ap4**) period. A tuff ring at Cape Columbos probably also dates from this period. Where deposits of these northern vents dominate **ap4**, we have mapped them separately as **ap4a** (scoria of Megalo and Kokkino Vouno cinder cones), **ap4b** (welded spatter from the cinder cones), or **ap4c** (deposits of Cape Columbos tuff ring). A simplified map of these products is given in Fig. 3.34.

The two cinder cones and the tuff ring lie on a NE–SW lineament, probably due to the presence of a basement fault. The thick andesitic scoria-fall deposit (**ap4a**) from the cinder cones mantles the eroded remains of Peristeria, and dominates the Middle Tuff sequence as far west as Cape Heptapedio and as far southeast as Micros Profitis Ilias. The two cones erupted simultaneously, as their products form a single sheet. Intercalated within the scoria are beds of welded spatter (**ap4b**), which locally remobilized as lava flows. These have all the features of fountain-fed spatter, and are distinct from the agglomerates laid down by pyroclastic flows of the two Upper Scoriae eruptions. The spatter was probably fed by lava fountains from a NNE–SSW fissure separating the two cones, as suggested by (1) thickening of the spatter towards the fissure, and (2) the occurrence of vertically foliated vent agglomerate on the floor of the fissure at its northern end. Several dykes can be traced up the caldera cliffs of Megalo Vouno into the scoria.

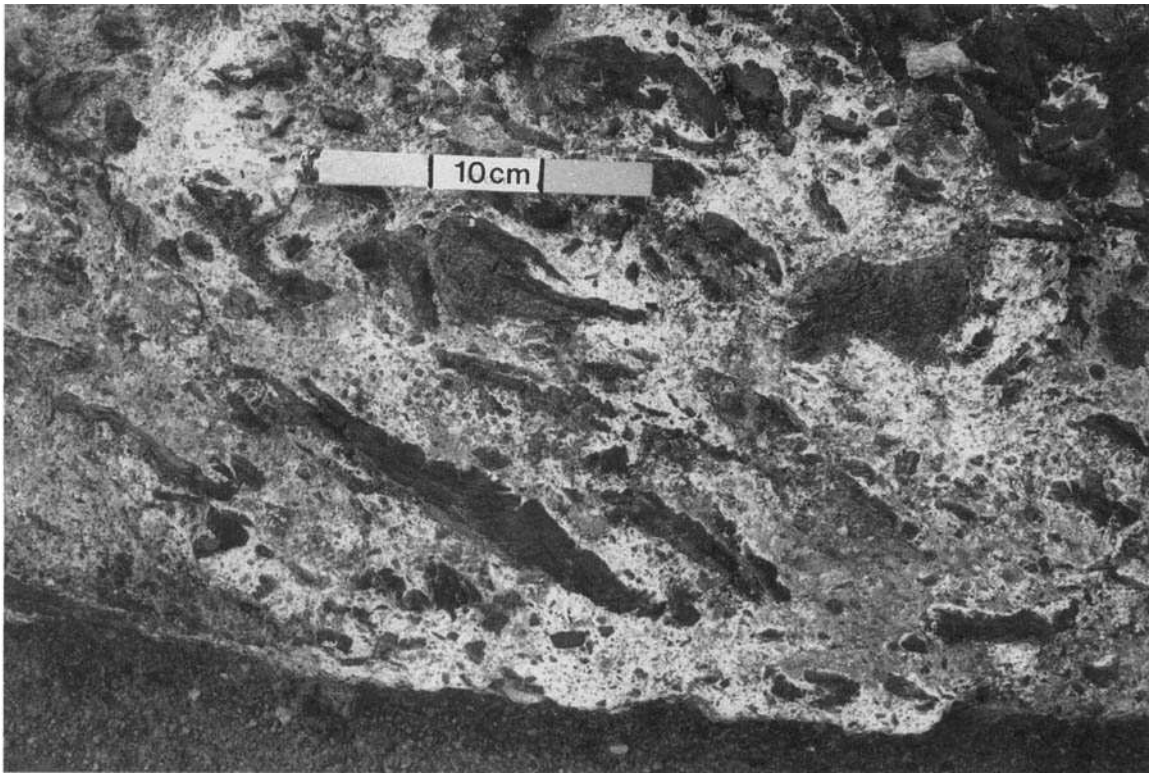

Fig. 3.33. Spatter agglomerate facies of Upper Scoriae 1 showing well developed imbrication of spatter rags. Akrotiri Peninsula.

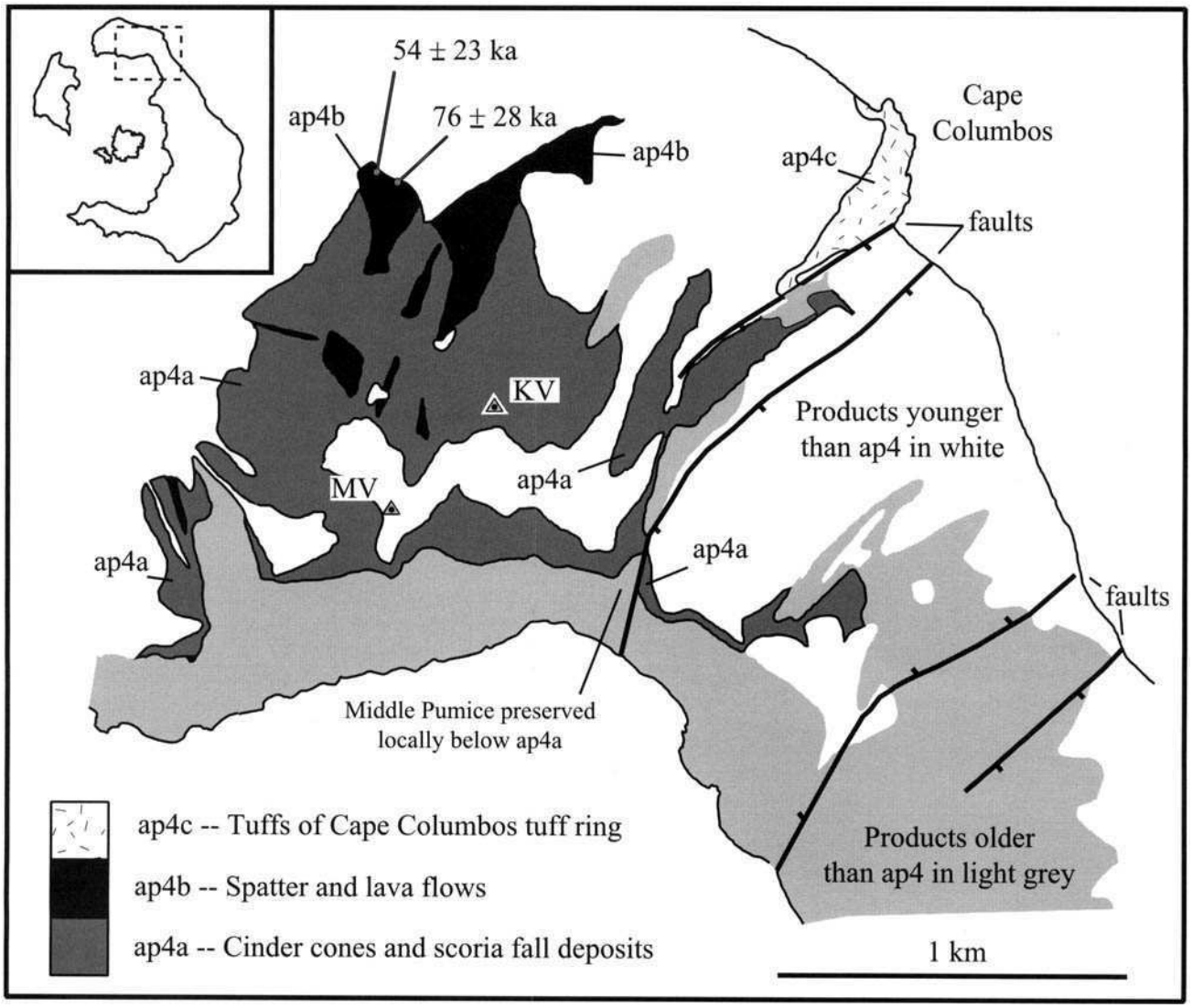

Fig. 3.34. Simplified map of Megalo Vouno (MV) and Kokkino Vouno (KV) cinder cones, and of the tuff ring of Cape Columbos. The downthrown sides of faults are marked by ticks.

The cinder cones postdate Middle Pumice, since a small remnant of Middle Pumice fallout and lithic breccia crops out below **ap4a** in the northeast corner of the caldera (Fig. 3.34). The breccia is recognized by its distinctive fragments of juvenile welded tuff and accidental orange tuff found in no other pyroclastic deposit on Santorini (Druitt 1983). The stratigraphic position relative to Vourvoulos and Upper Scoriae 1 are unknown. K–Ar dating of two superimposed **ap4b** spatter layers on the northern slopes of Megalo Vouno gave ages of 76 ± 28 ka (S94-2; lower layer) and 54 ± 23 ka (S94-3; upper layer), although both samples had low yields of radiogenic argon (Table 3.1).

The deposits of Cape Columbos tuff ring (**ap4c**) overlie a lava 308 ± 10 ka old, and are themselves overlain by Upper Scoriae 2 (**ap5**). Deposits from another tuff ring occur sandwiched between Middle Pumice and Vourvoulos on Aspronisi, but are too thin to be shown on the map. Both tuff rings formed by interaction of andesitic magma with seawater at times when sea level was similar to the present day. Sea level between 125 ka and 80 ka lay less than 25 m below its present-day value (Shackleton 1987), so the tuff rings could have formed during that period.

Caldera 2 and formation of the Skaros shield

The Skaros lava shield grew within, and overtopped, a caldera generated by the Middle Tuff eruptions (Fig. 3.35). This is called the Skaros caldera, or caldera 2. Caldera 2 cannot be linked to any specific eruption. It might relate to Upper Scoriae 1 (the last major eruption before Skaros), or may have formed incrementally as a result of more than one eruption. The shield remnant at Cape Tourlos consists of a basal complex of dacitic domes and coulées (**Dacites of Cape Skaros**; **ds1**) overlain by a succession of gently dipping mafic andesites and basalts (**Andesites and Basalts of Cape Skaros**; **as2**). The entire 300 m thick sequence onlaps an ancient, strongly eroded cliff surface (oriented approximately north–south) which disappears under the Skaros lavas just north of Cape Thera and re-emerges at Micros Profitis Ilias, where ancient talus aprons are preserved near sea level (Figs 3.13, 3.35 & 3.36). Further north, the old wall of caldera 2 has been exhumed (during the collapse of caldera 3), such that its brown, weathered surface makes up most of the present cliffs of Micros Profitis Ilias and Megalo Vouno (Fig. 3.35).

The presence of Upper Scoriae 1 (**ap4**) in the ancient caldera wall shows that this eruption predates the Skaros shield. Huijsmans *et al.* (1988) asserted that Upper Scoriae 1 is intercalated within the Skaros lavas, but the deposits they describe are thin phreatomagmatic ashes of local origin, not Upper Scoriae 1.

Isolated outcrops of **as2** lavas are preserved in the northeast corner of Thera, in the region of Cape Heptapedio, at Cape Ayios Nikolaos, and extensively on Therasia (Figs 3.35 & 3.37). These are interpreted as thin extracaldera successions, preserved where the youngest Skaros lavas overspilled the old caldera rim. Identification of these scattered outcrops as **as2** is based on their stratigraphic position relative to the Middle Tuff (**ap4**) and Upper Scoriae 2 (**ap5**) units, their chemical compositions (Huijsmans 1985), and the presence of distinctive **as2** lithologies with large phenocrysts of olivine and augite. As reconstructed, caldera 2 was comparable in diameter to the northern basin of the present-day caldera (Fig. 3.35). A dacite from sea level near Cape Tourlos (**ds1**; S90-13) gave an $^{40}Ar/^{39}Ar$ plateau age of 67 ± 9 ka.

At its maximum development, the shield was essentially circular with a diameter of 9 km at present sea level (Fig. 3.38). The profile

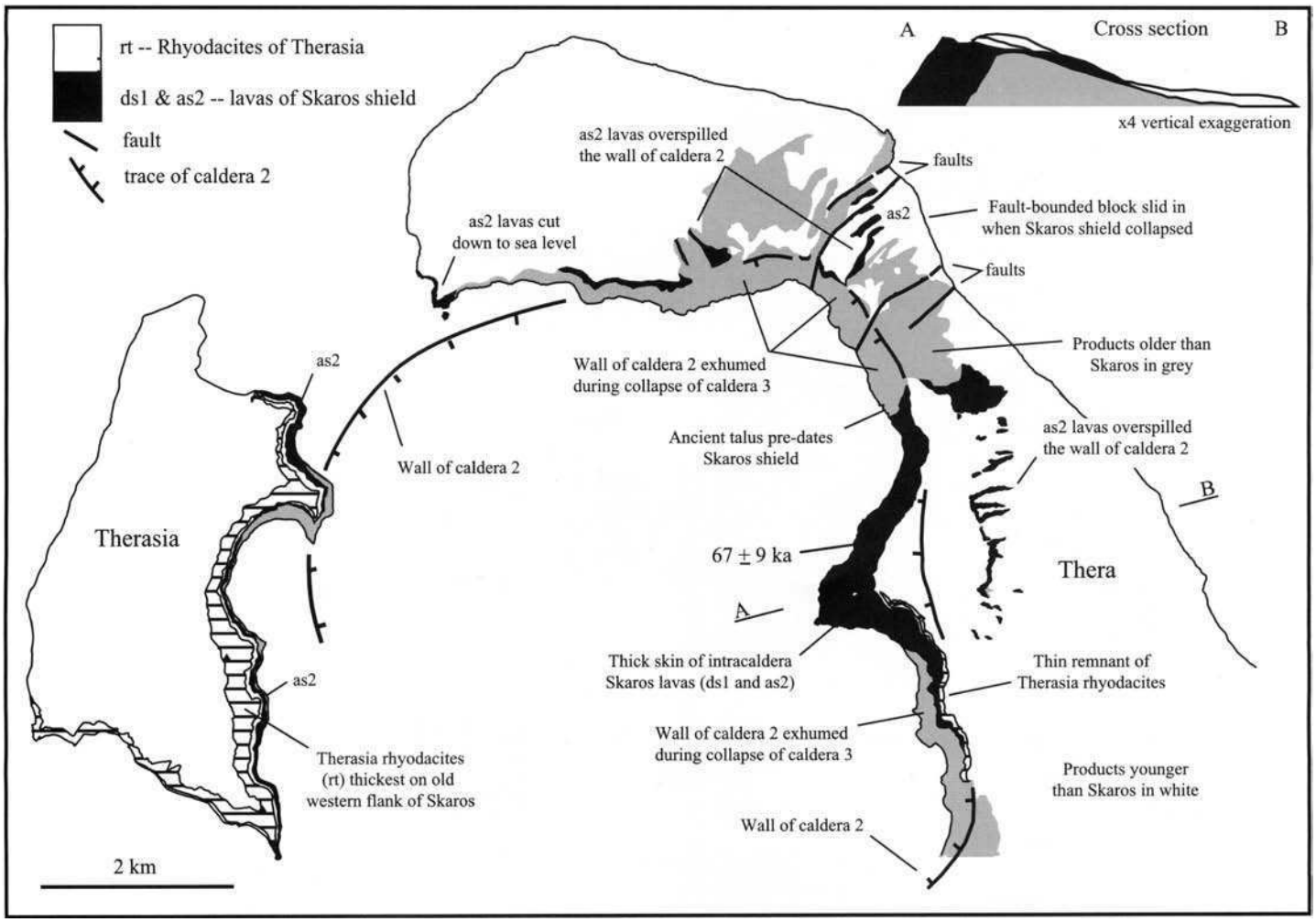

Fig. 3.35. Simplified map of the remains of the Skaros shield and the Therasia dome complex. The Skaros shield was constructed in an extant caldera (Caldera 2), the outline of which is shown. The shield infilled the caldera and overspilled it, as shown on the profile A–B.

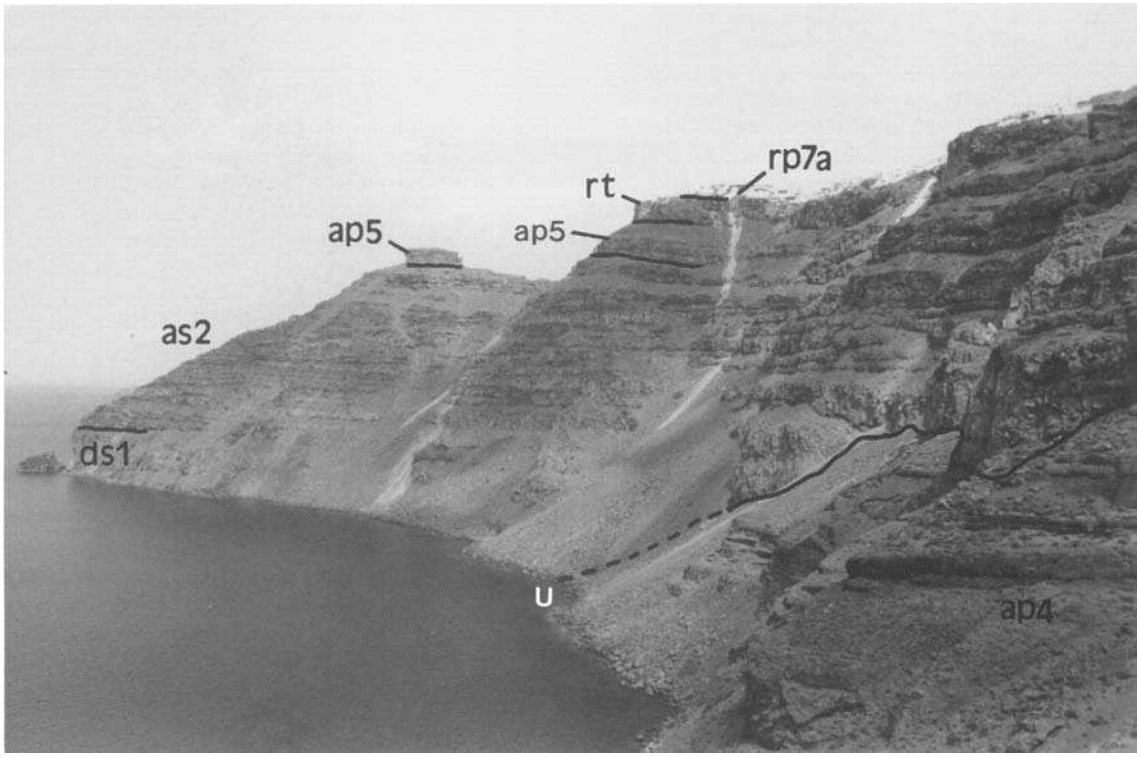

Fig. 3.36. The remnant of the Skaros shield at Cape Tourlos. The unconformity (U) between Skaros and the Middle Tuff sequence (**ap4**) represents the wall of ancient caldera 2. The basal lavas of Skaros are dacites (**ds1**), and the main lavas are thin andesites and basalts (**as2**). The succession is capped by the welded spatter agglomerate of Upper Scoriae 2 (**ap5**), which in turn is overlain by the Therasia rhyodacites (**rt**) and Minoan Tuff (**rp7a**).

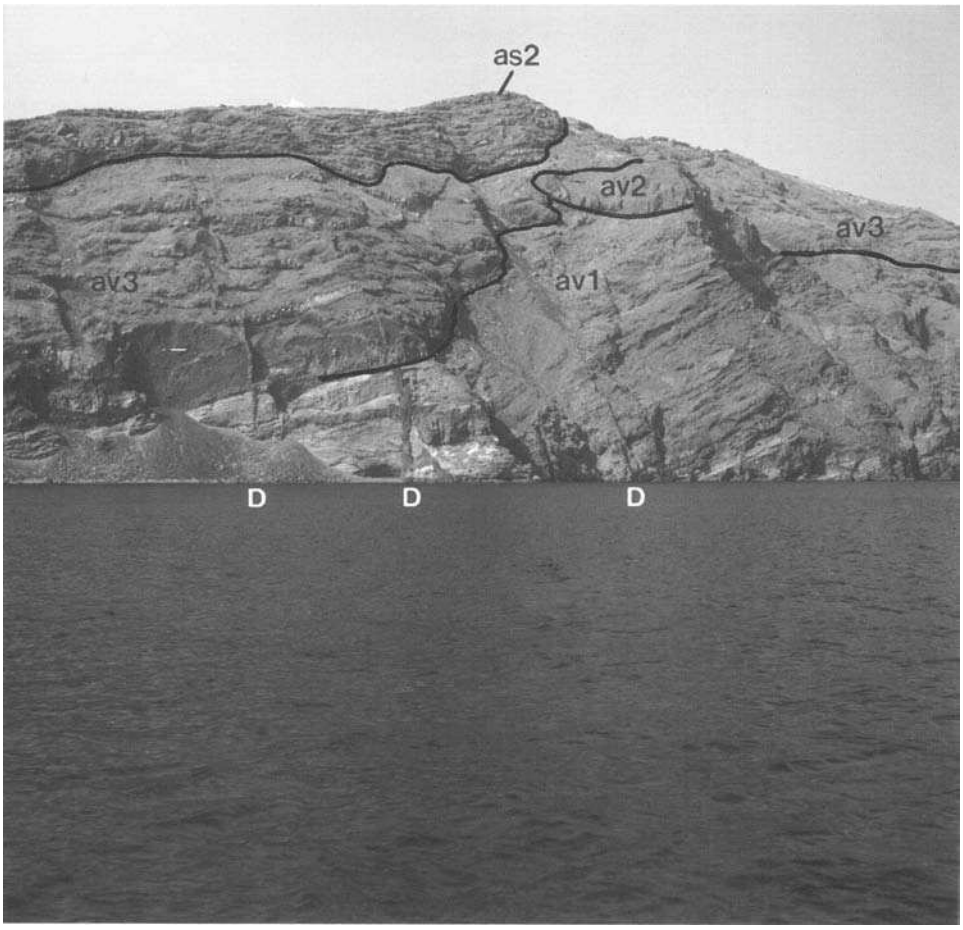

Fig. 3.37. Caldera cliff at Cape Heptapedio. Lavas and tuffs of Peristeria 3 (**av3**) onlap the eroded remains of Peristeria 1 (**av1**) from the west. A small silicic andesite lava (**av2**) lies along the contact. The sequence is capped by extracaldera lavas of the Skaros shield (**as2**). Numerous dykes (D) cut **av1** and **av3**. The one on the left shows beautiful en echelon structure.

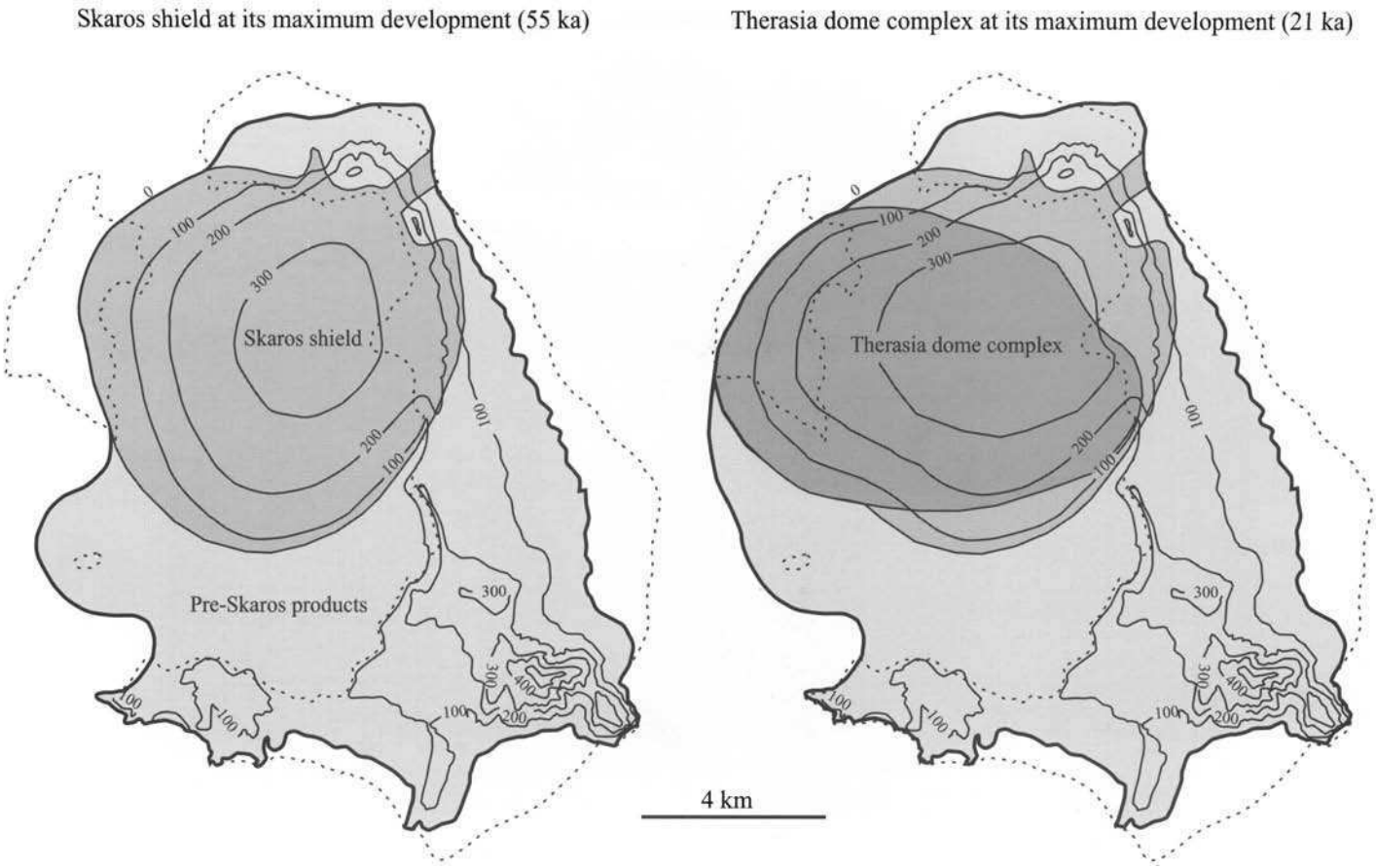

Fig. 3.38. Reconstructions of the Skaros shield and Therasia dome complex at their stages of maximum development. The thick bold line shows the outline of the island at the date indicated, and the thin dotted lines are the outlines of the present-day islands. The contour intervals are in metres.

was convex-up, as typical of shield volcanoes, with a maximum slope of 5°. The summit lay 350–400 m above present sea level a couple of kilometres west of Cape Tourlos. The subaerial volume of the shield was about 10 km^3.

Upper Scoriae 2 eruption

Development of the Skaros shield culminated in a large, dominantly andesitic explosive eruption, the products of which are called **Upper Scoriae 2** (**ap5**). The eruption had a precursory Plinian phase (dacitic) from a vent near Nea Kameni (Fig. 3.19). The thin, white pumice fall (Unit A) is characteristic of the base of Upper Scoriae 2 at most localities, except on the Akrotiri Peninsula. There was little erosion, and no soil development, between this fall and subsequent eruptive phases, so the time gap cannot have exceeded a few years. The main, andesitic eruption began with the emplacement of pyroclastic surges (Unit B). Scoria flows then swept down the southern flanks of the Skaros shield, filling pre-existing stream channels (Unit C). Cross sections through these channels, which strike approximately radial to Skaros (Fig. 3.39), occur widely in the cliffs of southern Thera. In northern Santorini, the scoria flows transported lithic blocks and fluidal spatter rags up to 3 m in diameter, which accumulated as thick, brick red to black spatter agglomerates (Unit D; Mellors & Sparks 1991). The agglomerates are typically are 10 to 20 m thick, but reach 50 m at Oia (Figs 3.18 & 3.40). The prominent knoll capping Cape Tourlos is a highly welded facies of the spatter agglomerates, laid down close to the summit of Skaros shield (Fig. 3.36). Spectacular sections through Upper Scoriae 2 scoria-flow deposits are afforded by the cliffs of southern Therasia, where cross-bedding is visible by boat on a scale of tens to hundreds of metres.

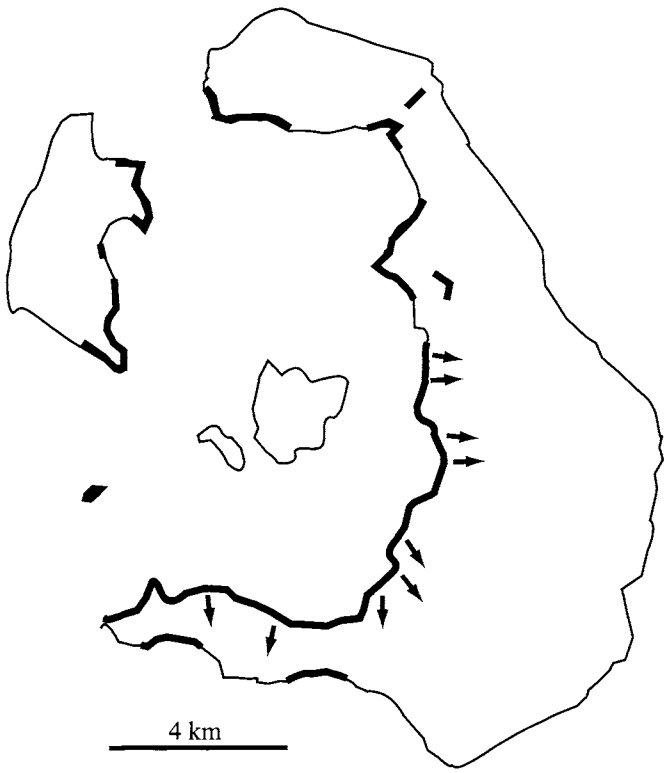

Fig. 3.39. Orientations of erosional channels filled with scoria flow deposits of the Upper Scoriae 2 eruption. Many of the channels are lined with regolith and existed prior to the eruption. The bold black line is the present-day outcrop of Upper Scoriae 2.

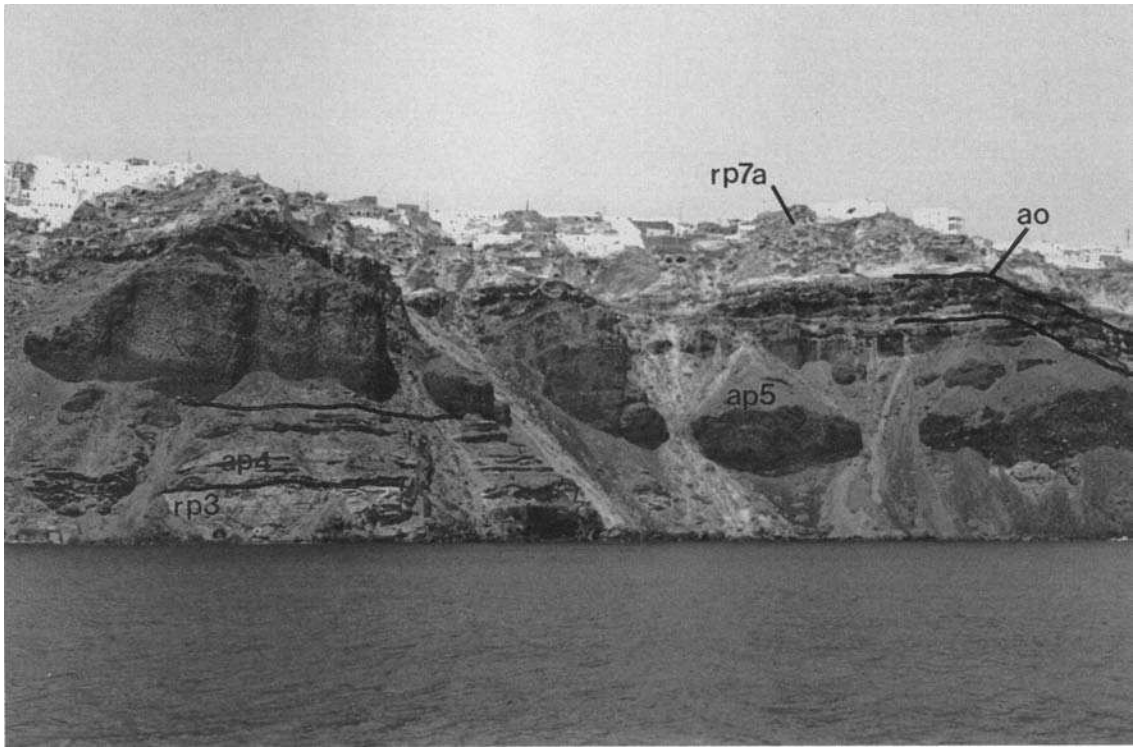

Fig. 3.40. The caldera cliff beneath Oia, showing the Lower Pumice 2 Tuff (**rp3**), the Middle Tuff sequence (**ap4**), 50 m thick spatter agglomerates and lithic breccias of Upper Scoriae 2 (**ap5**), the thin Andesites of Oia (**ao**), and the Minoan Tuff (**rp7a**).

The spatter agglomerates of Upper Scoriae 1 and Upper Scoriae 2 are similar both lithologically and chemically. They are distinguished by their different stratigraphic positions (separated by the Skaros shield), and by the different nature of their underlying tephra: intercalated scoria fall and base-surge ashes in Upper Scoriae 1 and a thin, white pumice fall in Upper Scoriae 2. Only at a few locations do the spatter agglomerates of these two eruptions occur together (Fig. 3.41). Near the summit of Micros Profitis Ilias there occurs a red **av3** scoria bed which superficially resembles Upper Scoriae 2. However the occurrence of an **av3** lava dated 464 ± 8 ka and 478 ± 3 ka above the deposit proves that it is older.

Mellors & Sparks (1991) reported two ^{14}C ages on carbonized wood from Upper Scoriae 2 (Table 3.3). These suggested an age of 38 ka, although this is at the limit of conventional ^{14}C. Our own dating of the densely welded spatter bed capping Cape Tourlos (S90-8) yielded a K–Ar age of 79 ± 8 ka and a more precise $^{40}Ar/^{39}Ar$ plateau age of 54 ± 3 ka. We infer an age of about 55 ka for the eruption, as this is consistent with the ages of (1) the Skaros

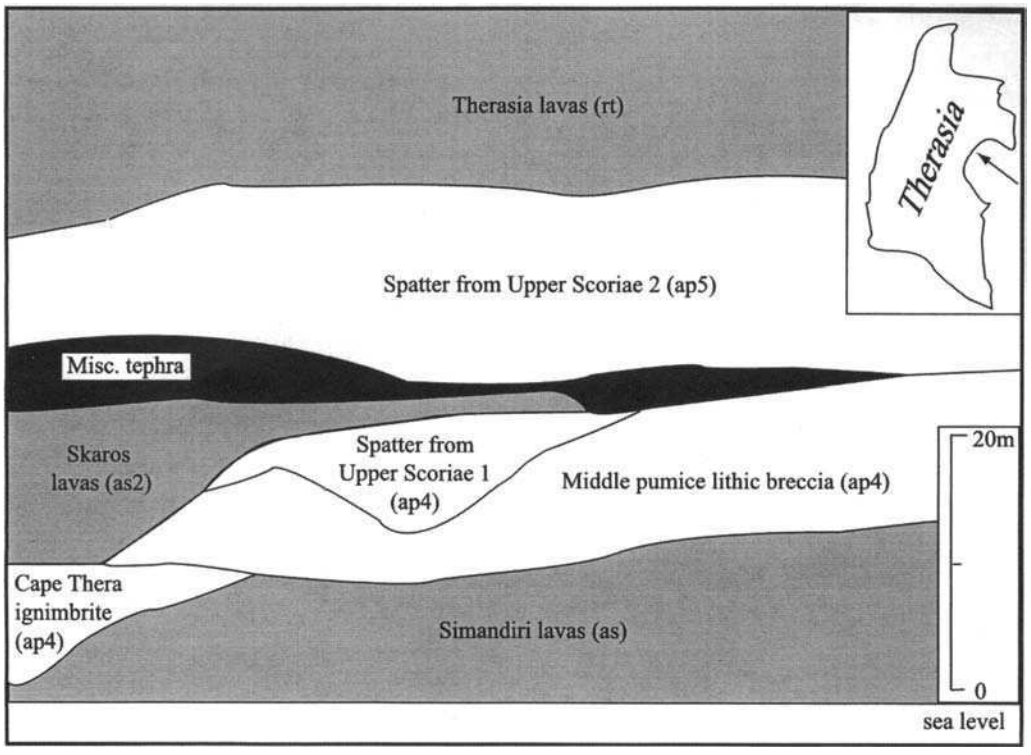

Fig. 3.41. Field relationships in the caldera wall of Therasia, on the south side of the port. Spatter agglomerates of both Upper Scoriae 1 and Upper Scoriae 2 are present at this location.

ds1 lavas and (2) Megalo Vouno cinder cone (**ap4b**), both of which predate Upper Scoriae 2.

Therasia dome complex and the Andesites of Oia

Following Upper Scoriae 2, extrusion of rhyodacites from a number of scattered vents built up a lava-dome complex on the western flank of Skaros (Fig. 3.38). The subaerial volume of this complex is estimated to have been at least a couple of cubic kilometres. Remnants of these domes (**Rhyodacites of Therasia**; **rt**) dominate the caldera cliffs of Therasia, where the succession is over 200 m thick (Figs 3.35 & 3.42). Thin flows of porphyritic andesite cap the succession on Mount Viglos (Druitt 1985). Compositionally similar domes and coulées occur near the top of the caldera wall at Phira, proving that the complex extended across much of the northern basin of the present-day caldera (Fig. 3.38).

Thin flows of sparsely phyric andesite at Oia (**Andesites of Oia**, **ao**) occupy the same stratigraphic level as **rt**, and were probably erupted from flank vents on the Skaros shield.

Cape Riva eruption

The Cape Riva eruption has been described in detail by Druitt & Sparks (1982) and Druitt (1985). The products (**Cape Riva Tuff**; **rp6**) are largely dacitic or rhyodacitic and chemically resemble the lavas of the Therasia dome complex, which were interpreted by Druitt (1985) as precursory leaks from the growing Cape Riva magma chamber. The eruption began with a Plinian phase, the deposit from which is preserved locally near Oia, where it is over 4 m thick (Unit A). Druitt (1985) suggested that the vent for this phase lay in northern Therasia, but new data do not support this. It is more likely that the eruption occurred from somewhere higher on the Therasia dome complex, and that the pumice was distributed by strong winds to the northwest, across Oia. The pumice-fall deposit is compositionally zoned, with subordinate andesitic pumice in its upper half. At the end of the Plinian phase, the eruption column collapsed and a distinctive red-brown welded ignimbrite was discharged (Unit B). This ignimbrite occurs at Cape Tourlos (where it is dune-bedded), around Oia, on Therasia and over much of southern Thera.

The eruption then escalated violently and pyroclastic flows were discharged all over the volcanic field. Segregation of lithic debris from these flows generated a layer of coarse-grained lithic breccia and associated nonwelded ignimbrite up to 25 m thick (Unit C), which occurs intermittantly all over the islands (Figs 3.18 & 3.43). The onset of lag breccia emplacement probably records the beginning of caldera collapse during the eruption (Druitt & Sparks 1984; Druitt 1985).The eruption terminated with the emplacement of a second welded ignimbrite over northern Thera (Unit D).

The Cape Riva eruption is well dated at 18 ka ^{14}C years (Pichler & Friedrich 1976), which corresponds to a calibrated age of 21 ka using the data of Bard *et al.* (1990). An 18.5 ka old deep-sea ash layer has been correlated with the Cape Riva Tuff by Thunnel *et al.* (1977).

Collapse of caldera 3

The Cape Riva eruption triggered collapse of the Skaros lava shield. As collapse occurred, landslides ate back until they hit, and partially exhumed, the ancient wall of caldera 2, which today forms large areas of the cliffs of northeastern Thera (Druitt & Francaviglia 1992). The resulting depression is called the Cape Riva caldera, or caldera 3.

Evidence for caldera 3 is provided by the occurrence of Minoan deposits plastered, apparently *in situ*, on the present-day caldera wall at six locations in northern Thera. These were described in detail by Druitt & Francaviglia (1992). The best example occurs below Phira, where a small patch of Minoan Plinian pumice (and underlying palaeosol) occurs 140 m above sea level on the present cliff face. The evidence shows unambiguously that the Skaros shield (and overlying Therasia dome complex) had already collapsed before the Minoan eruption, and that a caldera already existed when the latter began.

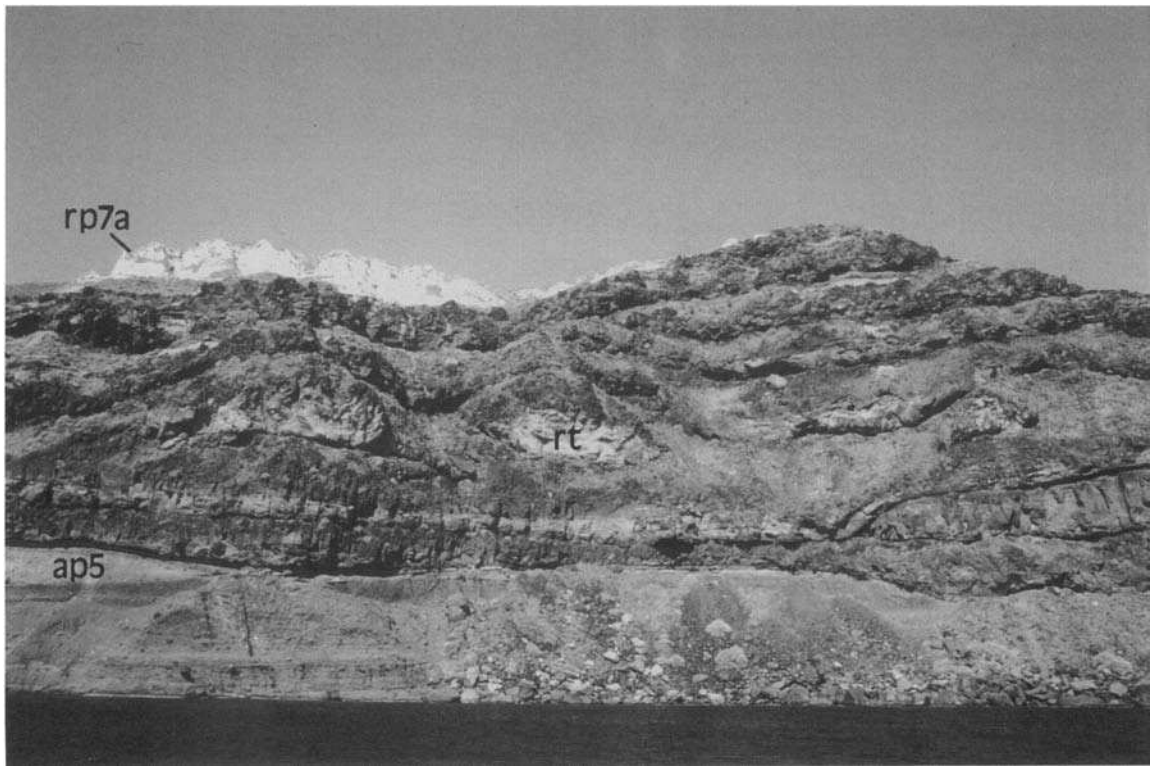

Fig. 3.42. The caldera wall at the southern end of Therasia. Scoria flow deposits of Upper Scoriae 2 (**ap5**) are overlain by the thick rhyodacites of Therasia (**rt**) which dominate these cliffs. The Minoan Tuff (**rp7a**) is visible at the top.

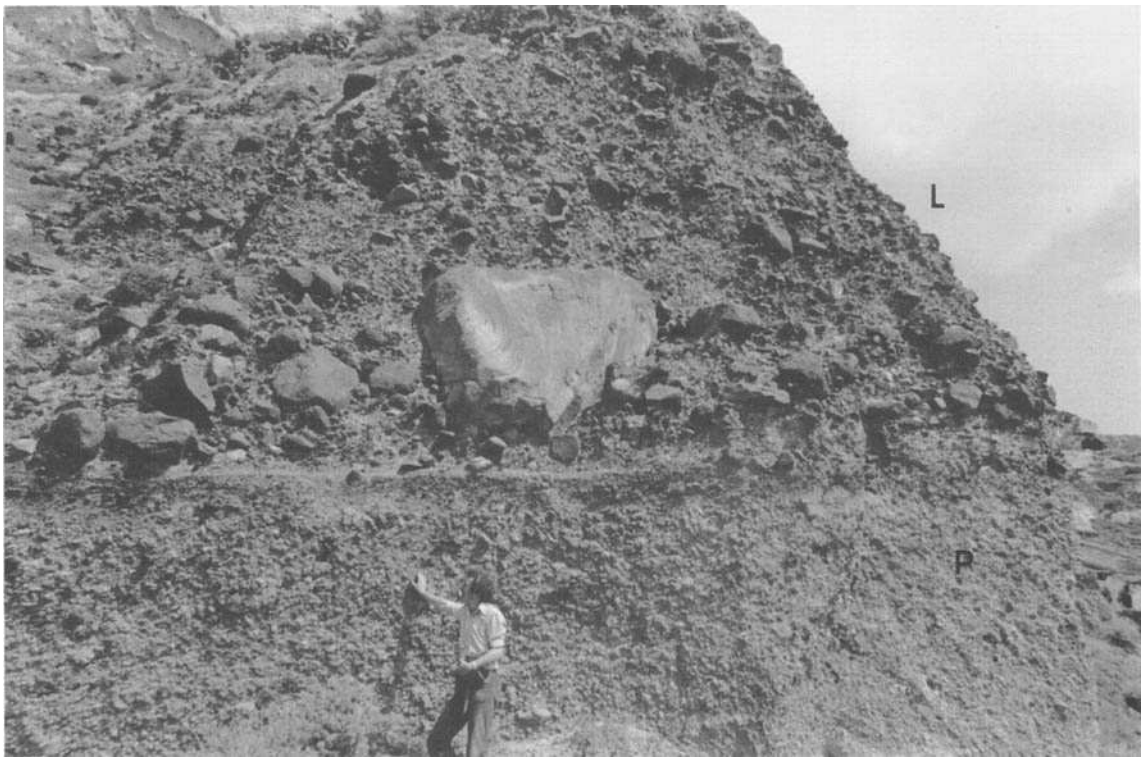

Fig. 3.43. Plinian pumice fall deposit (P) and lithic lag breccia (L) of the Cape Riva eruption at Ammoudi, Oia.

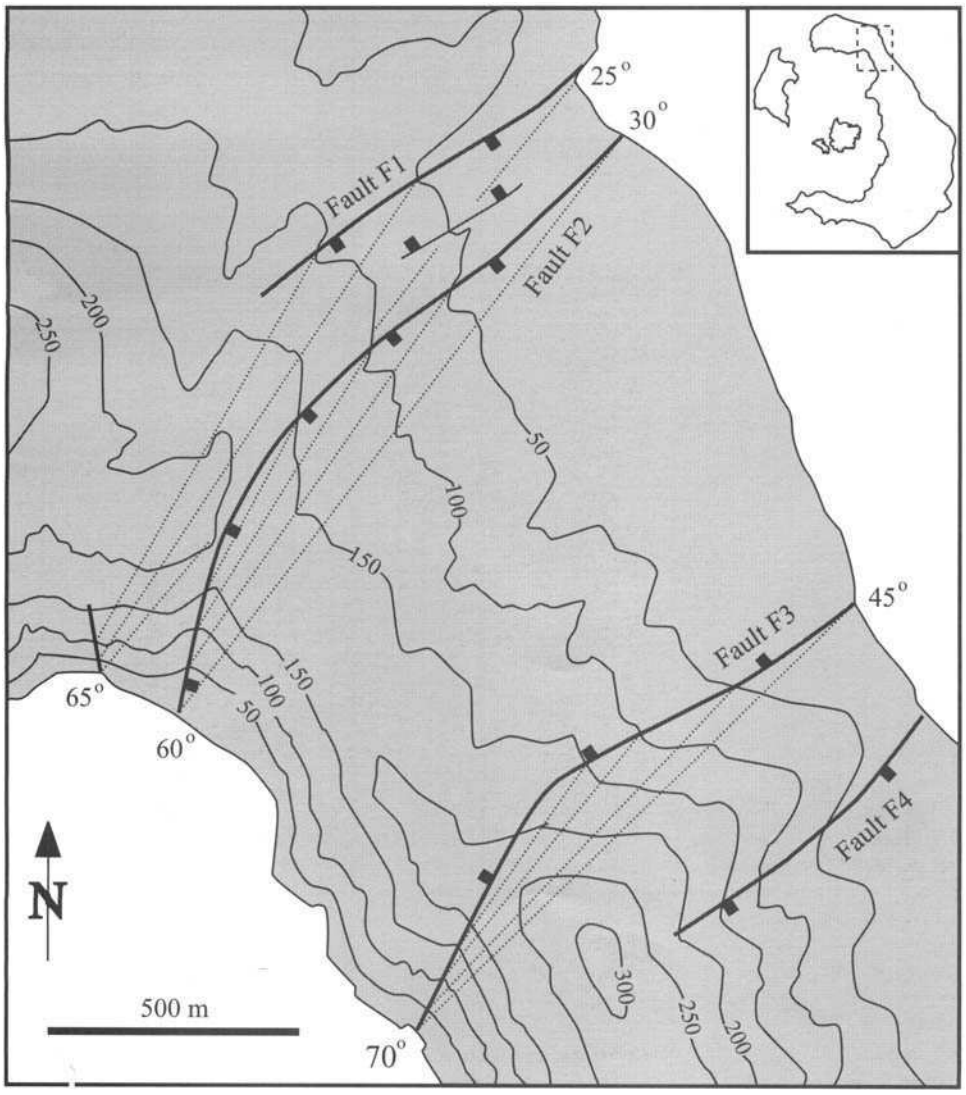

Fig. 3.44. The four faults F1 to F4 in northeastern Thera. Ticks show the directions of downthrow. Dotted lines are structure contours constructed at 50 m intervals on the fault planes. Faults F1, F2 and F3 have curved planes which are steepest at the caldera wall and most shallow at the coast. The angles in degrees are the dips of the fault planes. The fault between F1 and F2 is not shown on the color geological map at the back of this memoir, as it is too small. The topographic contours are given in metres.

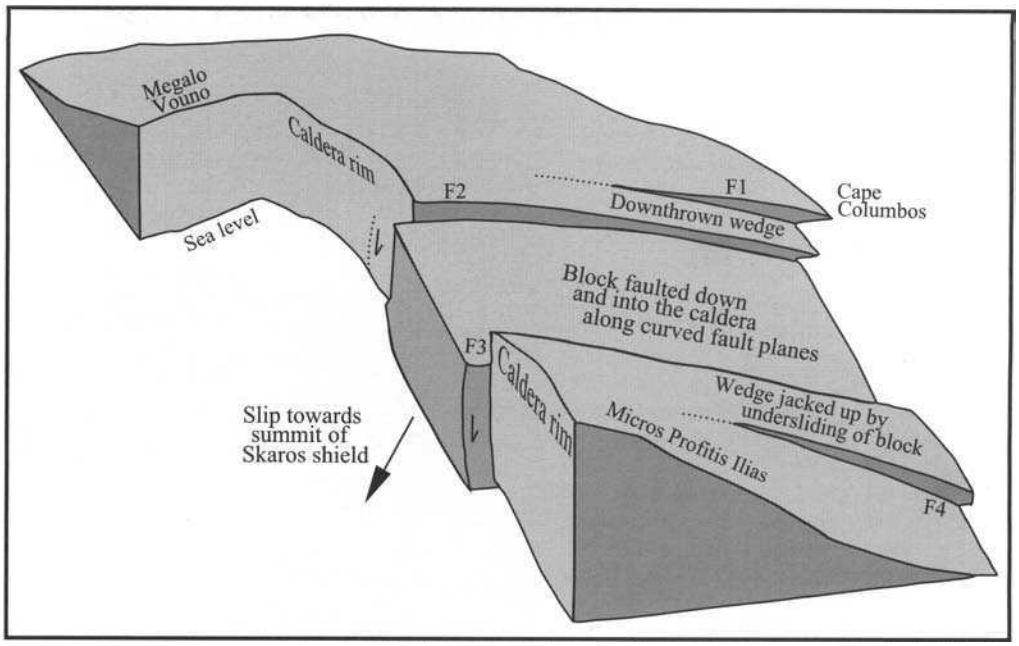

Fig. 3.45. Interpretation of field relationships in northeast Thera, as shown in Fig. 3.44. During the 21 ka Cape Riva eruption, collapse of the Skaros shield triggered insliding of a large block of northeastern Thera. The slip vector (towards the summit of Skaros), and the geometry of main faults F2 and F3, generated a zone of extension at Cape Columbos and the jacking-up of a wedge of Peristeria lavas on the flank of Micros Profitis Ilias.

New evidence relating to the formation of caldera 3 comes from northeastern Thera, where four NE–SW-trending faults (F1 to F4) cut the island (Fig. 3.44). F1 defines the steep margin of the Columbos tuff ring. Downthrow to the southeast here exceeds 20 m, but the displacement decreases towards the caldera. A small fault visible in the caldera cliff is probably an extension of F1. Fault F2 is marked by a prominent NE-trending topographic scarp near the caldera rim, where smeared **ap4** tuffs and rotated blocks of Skaros **as2** lava occur along the fault plane. Near Cape Columbos, F2 downthrows Skaros lavas to the south and linear crush zones are present in these lavas. Fault F3 is visible in the caldera wall below Micros Profitis Ilias, where it downthrows (to the north) the massive Peristeria 2 silicic andesite flow below sea level (Fig. 3.16). The sense of movement is also clear from the smearing of distinctive tuff layers along the fault plane. The same fault, when extrapolated, cuts an outcrop of Upper Scoriae 2 agglomerate on the northeast coast. Fault F4 forms a steep scarp in the Peristeria 3 lavas of Micros Profitis Ilias, but there is no visible displacement in the caldera wall. F1, F2, and F3 have very similar, curved geometries with dips of 60 to 70° near the caldera wall and 25 to 45°E at the coast (Fig. 3.44). Structure contours cannot be constructed for F4.

Fault-plane geometries suggest movement down, and inward to the SSW, of a 800 m wide block along two curved faults (F2 and F3) (Fig. 3.45). Faults F1 and F4 are accommodation structures generated by the SSW slip vector and the shallow, curved shapes of the principal fault planes. Fault F1 downthrows a wedge of rock into the space generated by block motion. Sliding of the main block at an angle of 45° under Micros Profitis Ilias caused the jacking-up of a wedge of rock along fault F4. Insliding of the fault block must have occurred during the Cape Riva eruption, because (1) F3 and F4 cut a coastal outcrop of Upper Scoriae 2 and therefore postdate that eruption, and (2) F1, F2, and F3 are draped by Minoan Plinian pumice, which clearly postdates block movement. As the Skaros shield collapsed, support was removed from the narrow, northeast corner of the island. The large block slid into the collapsing depression (towards the summit of the collapsed shield), but was prematurely arrested, forming a small graben. Mountrakis *et al.* (1998) have interpreted the graben as purely tectonic. However, while it does parallel the regional fault trend, it has a volcanic origin.

Existence of a large caldera prior to the Minoan eruption is also required by volume constraints. The total volume of the present caldera is about 60 km^3, about double the 30 ± 3 km^3 of magma discharged during the Minoan eruption, implying the existence of a large pre-existing depression (Druitt & Francaviglia 1992). The presence, in the Minoan Tuff, of fragments of stromatolites and travertines containing gastropods and forams characteristic of shallow brackish to saline water is also consistent with a flooded pre-Minoan caldera (Eriksen *et al.* 1990). A reconstruction of caldera 3 immediately prior to the Minoan eruption is shown in Fig. 3.46.

The Minoan eruption

The Minoan eruption and its rhyodacitic products have been described extensively in the literature (e.g., Bond & Sparks 1976; Heiken & McCoy 1984, 1990; Sparks & Wilson 1990; Sigurdsson *et al.* 1990; Pyle 1990*a*; Druitt & Francaviglia 1992), and emplacement temperatures have been estimated using the thermal demagnetization method (McClelland & Thomas 1990). Only a summary of these studies is given here. A schematic cross section through the products (**Minoan Tuff; rp7**) is shown in Fig. 3.47. Detailed thickness and facies maps have been presented by Heiken & McCoy (1984). At most locations a single palaeosol separates the Cape Riva and Minoan Tuffs. However a scoria fall deposit is present in this interval at Cape Tourlos, and a thin pumice fall at Oia.

The Minoan eruption took place from a shallow, flooded caldera (Fig. 3.46). A central island was probably present in the caldera (Eriksen *et al.* 1990; Druitt & Francaviglia 1992). Abundant fragments of black, glassy dacite and dacitic hyaloclastite in the Minoan phase 3 deposits are interpreted as pieces of this intracaldera volcano.

Precursory phreatic and phreatomagmatic explosions showered about 10^6 m^3 of ash over southeastern Thera (Heiken & McCoy 1990). The main eruption began with a Plinian phase (phase 1) from a subaerial vent near Nea Kameni (probably on the central island), during which the column reached a height of about 36 km (Sigurdsson *et al.* 1990). Although distributed by wind to the southeast, the Plinian deposit (Unit A) occurs all over Thera, Therasia and Aspronisi to a maximum depth of 6 m (Figs 3.19 & 3.48), and represents a couple of cubic kilometres of magma. The phase had a calculated peak discharge rate of 2.5×10^8 $kg\,s^{-1}$; inverse grading shows that intensity increased with time. The pumice-fall deposit is compositionally zoned, with an andesitic component that increases in abundance upwards.

Subsequent access of sea water to the vent initiated violent phreatomagmatic explosions and the emplacement of base surge deposits, up to 12 m thick (phase 2; Unit B), overlain by massive, white, poorly sorted tuff (phase 3; Unit C). Water access probably occurred as incipient subsidence began and fractures propagated out from the subaerial vent to the sea. The base surge deposits

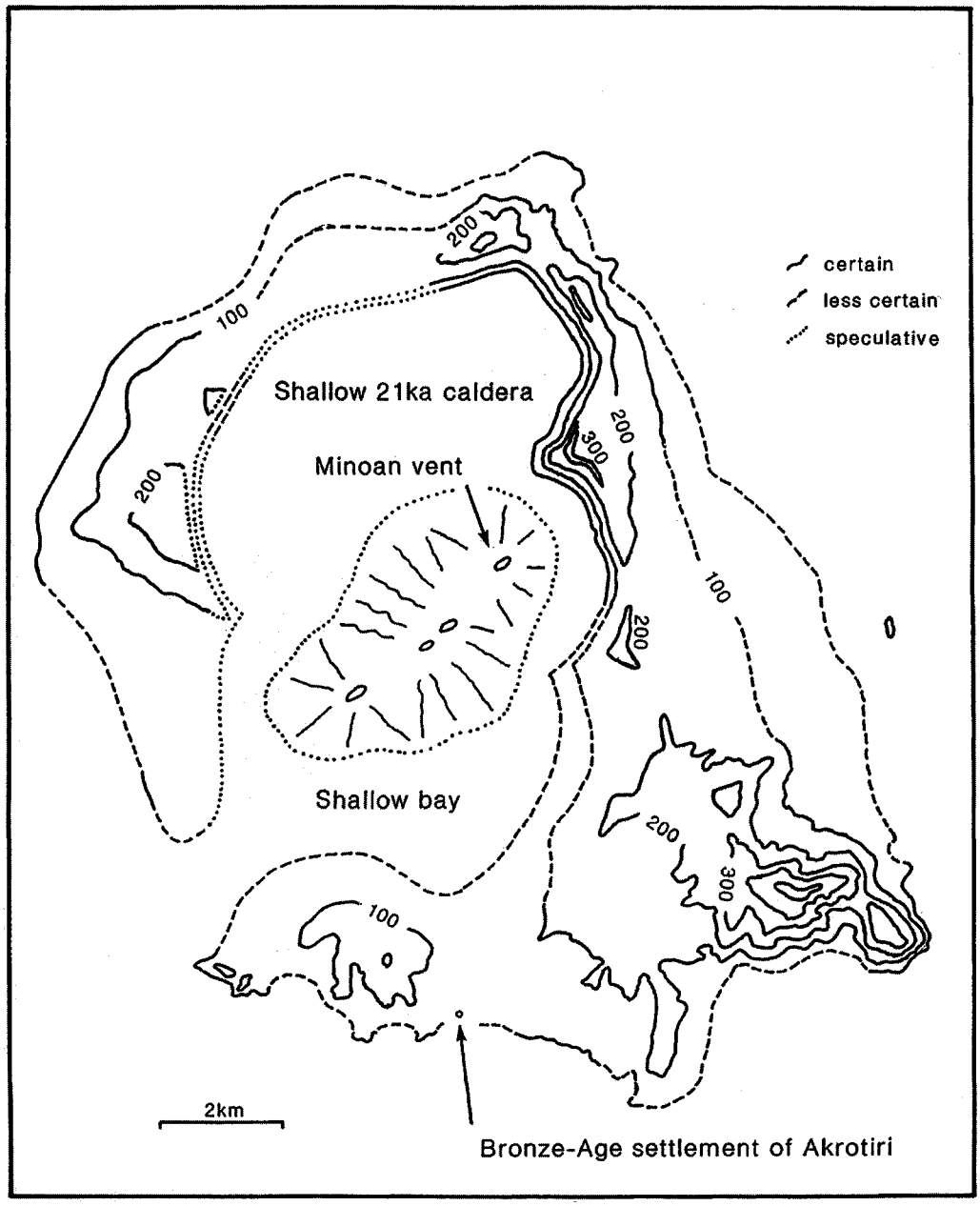

Fig. 3.46. Reconstruction of caldera 3 as it was immediately prior to the Minoan eruption. Evidence for the central island is based on the occurrence of abundant blocks of dacitic lava and hyaloclastite in the Minoan deposits (Druitt & Francaviglia 1992).

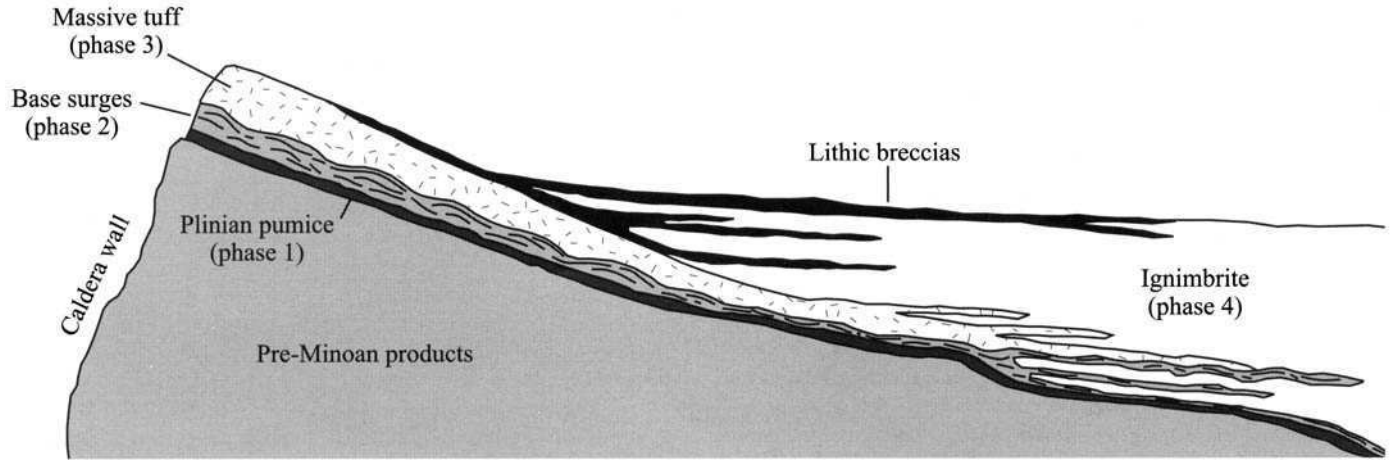

Fig. 3.47. Schematic cross section through the Minoan Tuff (after Bond & Sparks 1976). The diagram is not to scale. The maximum thickness of the Minoan deposits on the caldera rim is about 60 m, and at the coast is 40 m, although at most locations the base is not exposed.

contain spectacular cross-layering, unidirectional bedforms and ballistic impact sags (Fig. 3.48). Thermal demagnetization temperatures of 150–250°C have been obtained from the surge deposits. Plinian fallout must have continued during phase 2 because thin pumice-fall beds occur interstratified in the surges. The massive tuffs of phase 3 are interpreted as the products of hot debris flows and low-temperature (≤300°C), three-phase (solid, liquid, gas) pyroclastic flows (Sparks & Wilson 1990). Their thickness reaches up to 55 m on the caldera rim and decreases rapidly away from the caldera. Abundant blocks of dacite and dacitic hyaloclastite up to

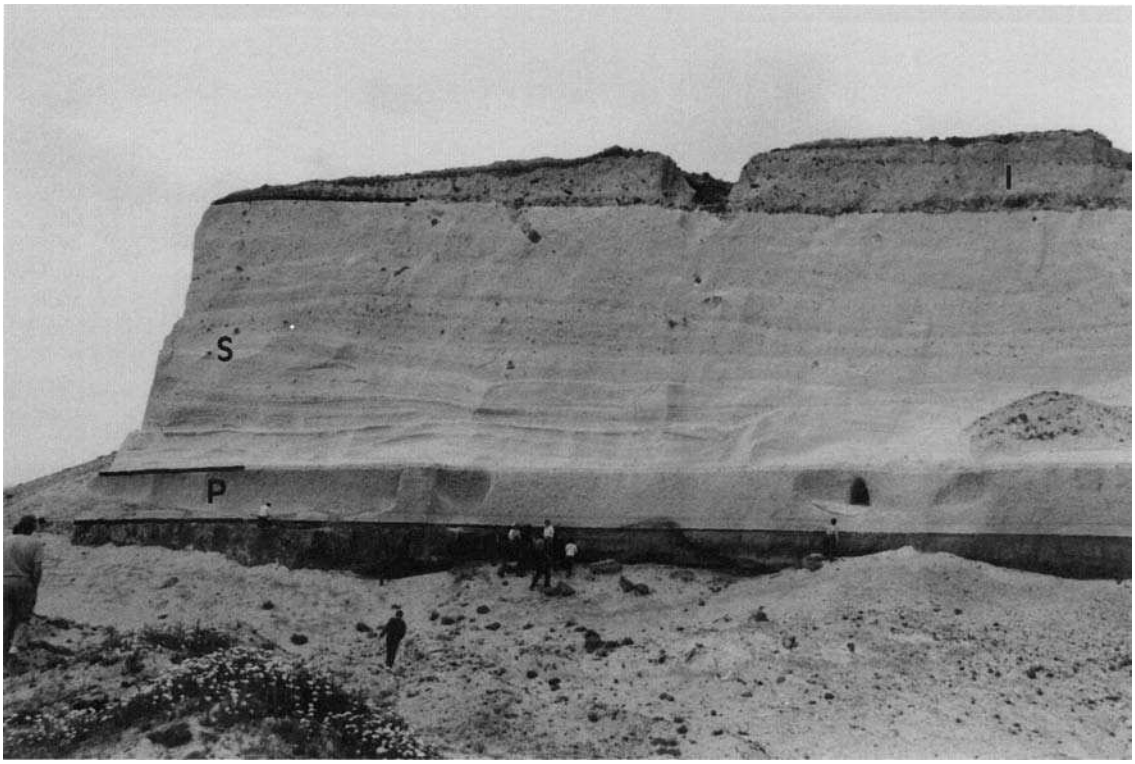

Fig. 3.48. Minoan Tuff in the Akrotiri pumice quarry above Cape Therma. The Plinian pumice fall deposit of phase 1 of the eruption (P) is overlain by dune-bedded base-surge deposits of phase 2 (S). A thin veneer of ignimbrite from the pyroclastic flows of phase 4 (I) caps the sequence. The deposits of phase 3 are absent at this site. People for scale.

10 m in diameter occur in the phase 3 deposits. Deposits from eruptive phases 1 to 3 are combined as unit **rp7a** on the map.

During phase 4 of the eruption, hot (300–350°C) pyroclastic flows were discharged all over the islands (Unit D). The ignimbrite forms a gently sloping apron, up to 40 m thick, all around the outer coasts of Thera and Therasia (Figs 3.47, 3.49 & 3.50). Thin, stratified veneers of ignimbrite also extend to the caldera rim north and south of the basement massif (Fig. 3.48). Coarse-grained breccias occur interstratified within the ignimbrite, and these are interpreted as lithic-rich segregation layers from the pyroclastic flows. The ignimbrite is covered at some locations by a few metres of fluvial gravel due to flash-floods following the eruption. In places the gravels appear to load down into the ignimbrite, suggesting that the latter was still fluidized at the time. The floods may have been

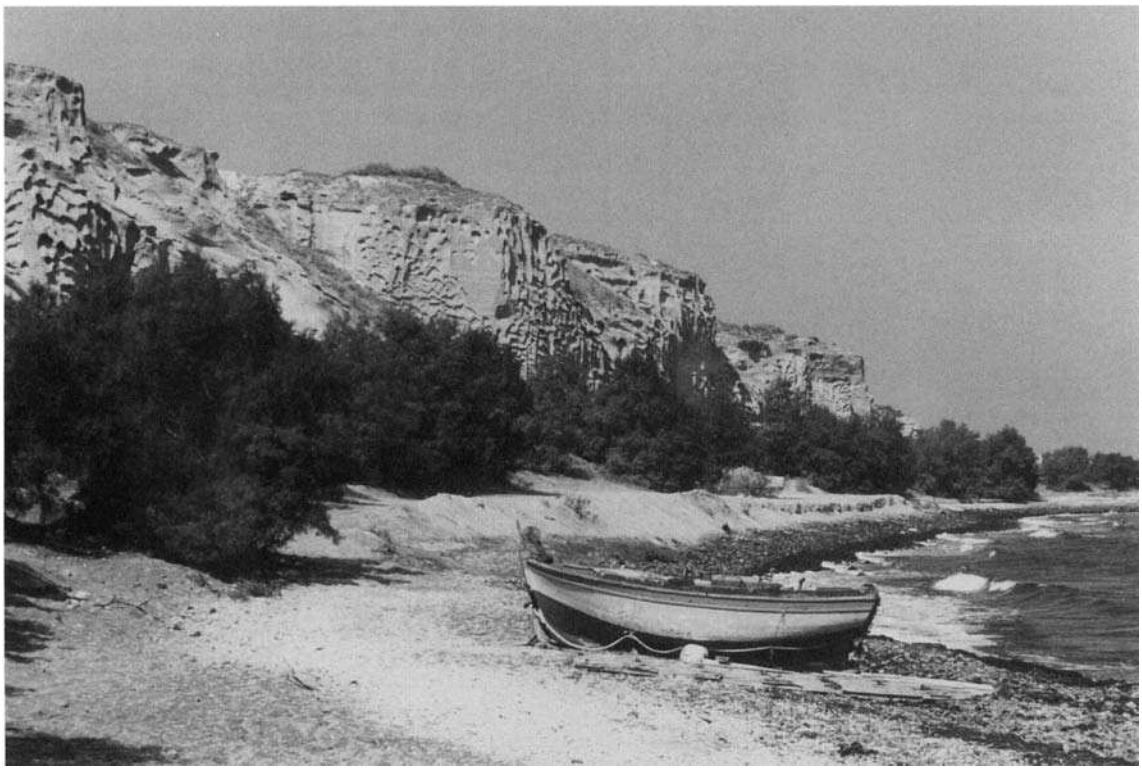

Fig. 3.49. Ignimbrite from the Minoan eruption on the south coast of the Akrotiri Peninsula.

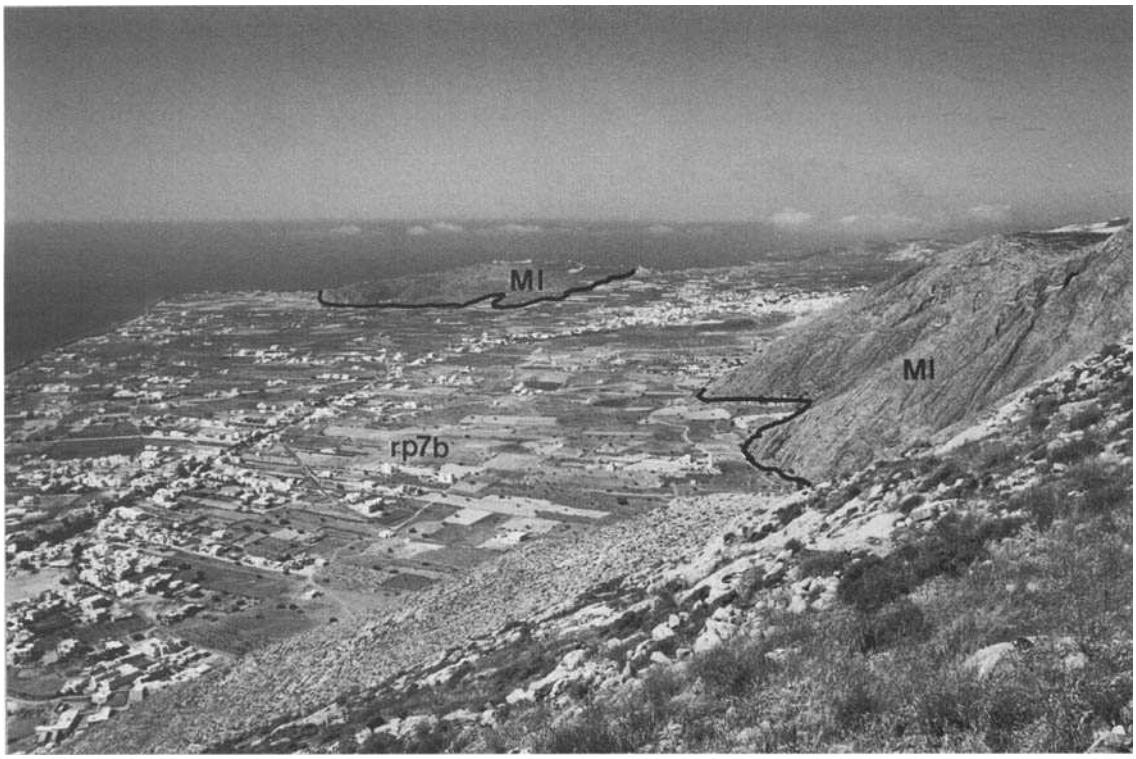

Fig. 3.50. The coastal plain of Minoan ignimbrite (**rp7b**) and the limestone (**MI**) massifs of Profitis Ilias (right) and Gavrillos (left centre). The photo was taken from Mesa Vouno towards the southwest.

due to intense rainfall following the eruption. Another possibility is that tsunamis generated by caldera collapse washed up over the caldera wall and across the island. The ignimbrite, lithic breccias, and fluvial gravels have been mapped together as **rp7b**.

Distal ash drifted to the east and today forms a widespread layer on the sea floor of the eastern Mediterranean. Most of the distal ash is thought to be coignimbritic in origin. The Minoan ignimbrite shows significant crystal enrichment and calculations place the percentage of elutriated ash at almost 60% of the total pyroclastic-flow mass (Pyle 1990*a*). The Minoan ash layer has also been found on the islands of Kos and Rhodes, and in western Turkey. In all the eruption discharged at least 30 km^3 of rhyodacitic magma, most of it as ignimbrite (Pyle, 1990*a*). In addition to the volume of material estimated by Pyle (1990*a*) an unknown and probably substantial volume of pyroclastic deposits must have been trapped within the pre-existing caldera and then down-faulted during caldera collapse associated with the Minoan eruption.

The conventional archaeological age for the eruption is 1450–1500 BC. However, recent studies suggest a possibly earlier date: (1) radiocarbon dating of short-lived material from the Akrotiri excavations gives ages in the second half of the seventeenth century BC (e.g., Friedrich *et al.* 1990); (2) a prominent sulphuric acid peak in a South Greenland ice core has been dated at 1645 ± 20 BC, and this has been tentatively correlated with the Minoan eruption (Hammer *et al.* 1987); (3) high-altitude bristlecone pines in California, as well as some Irish oaks, suffered severe frost damage in the year 1627 ± 2 BC, corresponding to a major eruption in 1628 ± 2 BC (LaMarche & Hirschboeck 1984; Baillie & Munroe 1988). To date it is unclear whether the ice cores and tree rings are recording the same eruption, and whether that eruption is the Minoan. The

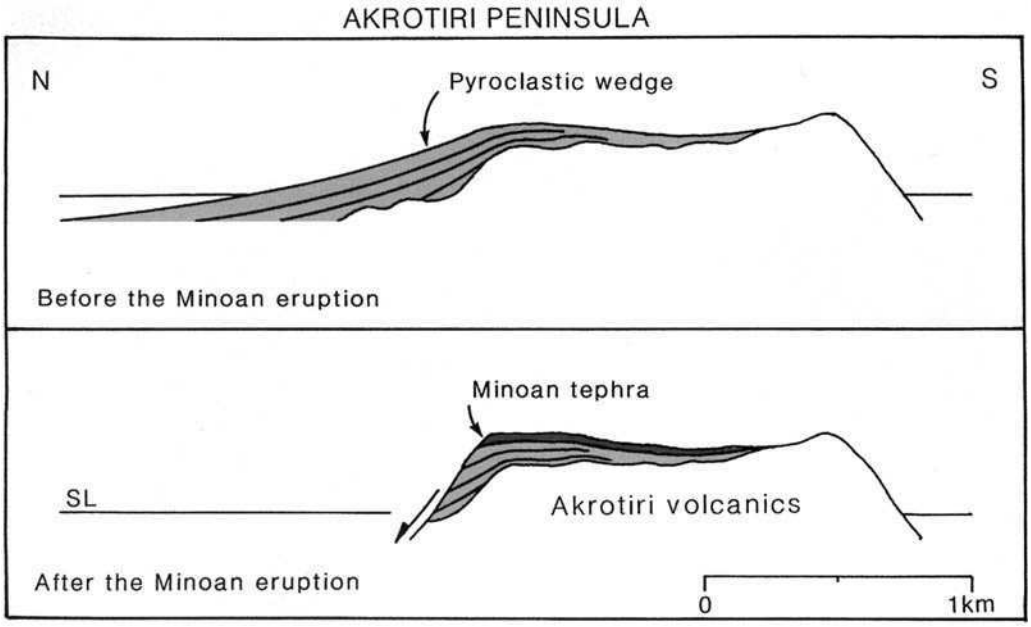

Fig. 3.51. Schematic north-south cross section through the Akrotiri Peninsula before and after Minoan caldera collapse. Before the eruption, a wedge of older Thera pyroclastics was plastered onto the Early Centres of the Akrotiri Peninsula (marked 'Akrotiri volcanics'). Minoan collapse truncated this wedge, so that the older deposits exposed in the cliffs now dip gently into the present caldera.

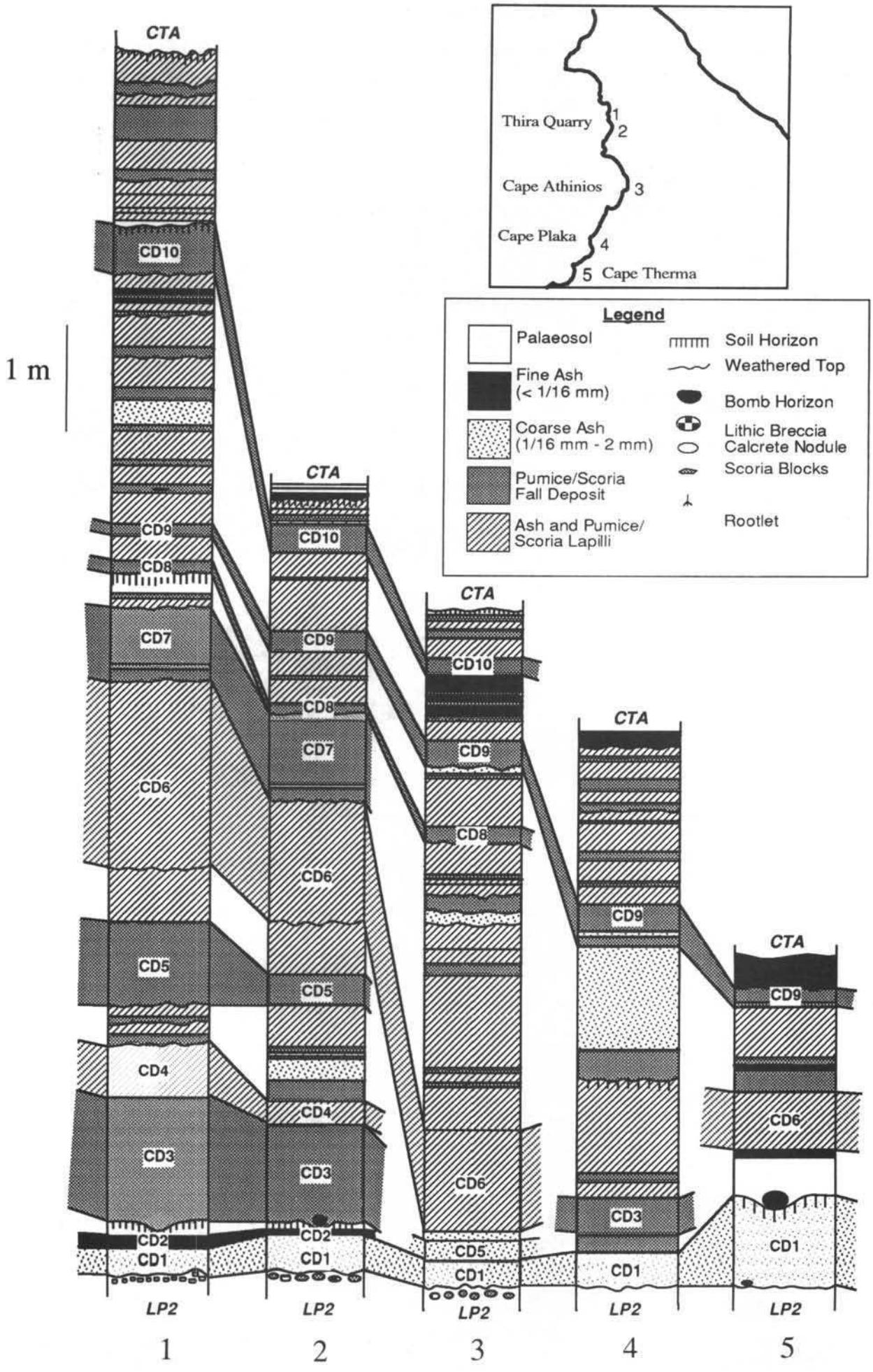

Fig. 3.52. Stratigraphic logs of minor pyroclastic sequence M6 along the caldera wall. The sections are located between Cape Tourlos and Cape Therma on Thera island.

Aniakchak eruption in Alaska (3430 ± 100 BP), the Avellino eruption of Vesuvius (3360 ± 40 BP), and the Mount St Helens Y eruption (3420 ± 50 BP) are alternative candidates for the ice core and tree ring signals.

Collapse of caldera 4

Collapse during the Minoan eruption deepened and enlarged the extant caldera, forming the complex present-day assemblage of four basins (Fig. 3.2). In southern Thera, collapse truncated the wedge of Thera pyroclastics draped over, and plastered up against, the pre-volcanic island and Early centres of Akrotiri Peninsula (Fig. 3.51). This accounts for the widespread inward dip of these units in the cliffs of southern Thera. At Athinios, landsliding during Minoan collapse exhumed the northwest cliff of the pre-volcanic island, leaving isolated remnants of the earliest Thera pyroclastics plastered onto the basement slopes. It seems likely that the three breaches of the present caldera formed during Minoan collapse. These have steep headwall scarps and formed by large rotational landslides into the caldera (Fig. 3.4).

The minor pyroclastic sequences

The twelve major units of the Thera pyroclastics are separated by sequences of minor tephra and palaeosols, each of which is typically a few metres thick, but may reach 13 m. They are labelled M1 to M12 in Fig. 3.17. There are five principal types of deposit: (1) scoria-fall deposits, predominantly of basaltic to andesitic composition, generated by violent Strombolian or sub-Plinian eruptions; (2) ash fall layers generated by weak Strombolian or Vulcanian explosions; (3) thin, fine-grained base-surge layers; (4) deposits of yellowish wind-reworked ash and lapilli similar to deposits documented on Japanese stratovolcanoes such as Sakurajima (Kobayashi 1986) where they are related to long-lived vulcanian or weak strombolian ash emissions over tens or hundreds of years (Imura 1993); (5) yellow-brown palaeosols representing long periods of dormancy. An example of a typical sequence is given in Fig. 3.52 showing stratigraphic and lithological logs of sequence M6 along the caldera wall. Detailed logs of other minor pyroclastic sequences can be found in Edwards (1994). Each minor pyroclastic sequence contains evidence of many pyroclastic events. Several of the minor sequences develop thick paleosols towards the top, suggesting that the volcano went into a period of reduced volcansism or dormancy before the onset of a large magnitude explosive eruption.

The minor sequences accumulated during prolonged periods of effusive and minor explosive activity that occurred between the main pyroclastic eruptions. Some of the minor pyroclastic sequences were broadly contemporaneous with construction of substantial lava shields, notably the Simandiri shield (M6) and the Skaros shield (M10). There may not be a direct correlation between M6 and the Simandiri shield because there are compositional differences between the two (Chapter 6). Although the majority of the minor pyroclastic sequences do not have an equivalent lava sequence preserved, the large number of basaltic to andesitic pyroclastic eruptions within a sequence indicate that there was also associated effusive volcanism. We surmise that the associated lavas have disappeared during periods of caldera collapse. Taken together, the minor pyroclastic sequences preserve a record of more than 100 individual eruptions powerful enough to lay down a few cm or more of tephra over large areas of Santorini.

Kameni Islands (197 BC to AD 1950)

Historic volcanism at Santorini has built the present-day islands of Palaea Kameni and Nea Kameni (**Dacites of the Kameni Islands; dk**). These are the subaerial expression of a 2.5 km^3 intracaldera volcano, 3.5 km in basal diameter, the summit of which rises 500 m above the caldera floor (Fig. 3.53). Construction of the edifice probably began soon after the Minoan eruption. The volcano broke the surface in 197 BC and the last eruption was in AD 1950. Subaerial products are uniformly dacitic (Barton & Huijsmans 1986; Conticelli *et al.* 1998; Francalanci *et al.* 1998). A simplified geological map is provided in Fig. 3.54. Nine subaerial eruptive episodes have been reported or deduced from historic records (Fytikas *et al.* 1990*a*).

Fig. 3.53. View of the caldera taken from the Akrotiri peninsula. Nea Kameni (N) and Palaea Kameni (P).

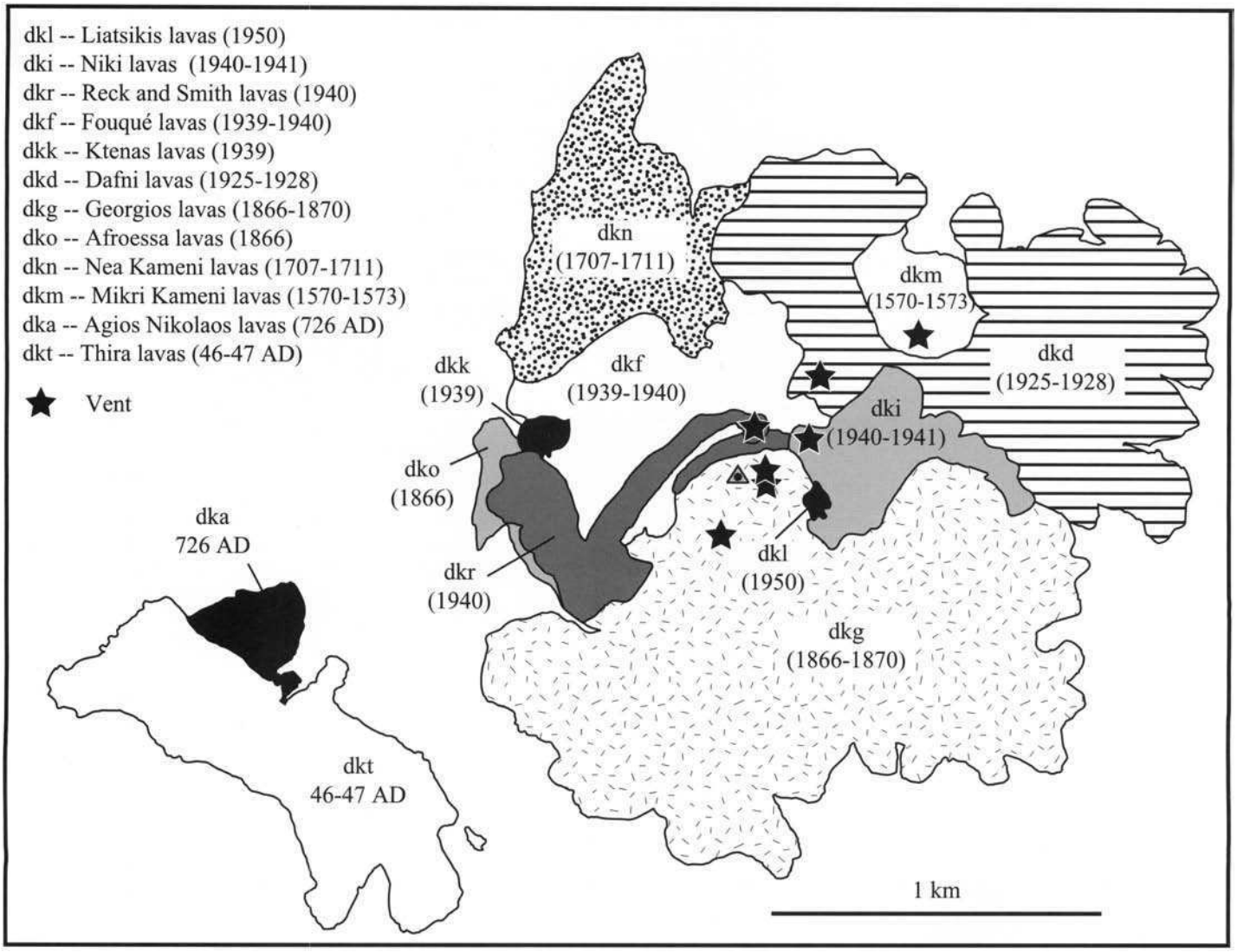

Fig. 3.54. Geological map of the Kameni Islands.

Detailed accounts were given by Fouqué (1879), Washington (1926), Reck (1936), Liatsikis (1942) and Georgalas (1953). Pichler & Kussmaul (1980) interpreted the lavas of Palaea Kameni as being of two ages (197 BC and AD 1866). We have followed Fytikas *et al.* (1990*a*) in assigning the same lavas ages of AD 46–47 and 726 respectively. A brief chronology of the Kameni Volcano now follows.

197 BC. Explosive activity built up a pyroclastic cone called Iera. The remains of this cone are believed to be no longer exposed above sea level (Fytikas *et al.* 1990*a*).

AD 46–47. Extrusive activity formed Thia island, which is believed to be present-day Palaea Kameni.

726. After a repose of seven centuries, explosive activity occurred at a centre near Palaea Kameni, spreading pumice all over Asia Minor. This was probably followed by volcanotectonic collapse, creating the steep northeast cliff of Palaea Kameni, then by extrusion of the 726 Ayios Nikolaos lavas.

1570–73. Activity shifted to the northeast and formed the island of Mikri Kameni.

1707–11. The eruption began on the west flank of Mikri Kameni with very slow lava extrusion. Later alternation of extrusive and explosive eruptions formed Nea Kameni over the next four years.

1866–70. The eruption began with slow lava extrusion. Two days later the first explosions began and the eruption column height reached 2 km. In all there were three eruptive centres: Georgios, which was active continuously, Afroessa, characterized by slow, then rapid lava extrusion, and the centre of May's Islands, which emerged from the sea off the west coast of Nea Kameni.

1925–28. Activity began with jets of water, followed by the first lava and explosions. Soon the eruptions shifted to the northwest to the centre of Dafni. Explosive activity dominated at Dafni, with clouds reaching 3 km. Some small pyroclastic flows were generated from this centre. A long repose period occurred between May 1926 and January 1928, before the extrusive activity that terminated the eruption.

1939–41. The eruption began with a submarine explosion. Activity then shifted to the centre of Nea Kameni, where lava extrusion built up the flows and domes of Ktenas, Fouqué, Smith-Reck, and Niki. In each case the appearance of lava was preceded by phreatic explosions.

1950. After some phreatic activity, extrusion of the Liatsikis lava occurred. The final phreatic phase generated the 'twin-tunnel' crater (Fig 3.55)..

The timescale of volcanism

The evolution of Santorini is summarized in Table 3.5. The radiometric dates are compiled in Fig. 3.56, which also includes previous age determinations (Table 3.3). We have identified in Fig. 3.56 (by dotted bars) all imprecise K–Ar samples with yields of radiogenic argon less than 2.5%. Excluding these less reliable ages, the agreements between the K–Ar and $^{40}Ar/^{39}Ar$ ages, between the radiometric ages and known stratigraphic ages, and between the new radiometric ages and previous age estimates vary from acceptable to

Fig. 3.55. The 'twin-funnel' vent at the summit of Nea Kameni, formed by phreatic explosions at the end of the 1939–41 eruption.

Table 3.5. *Summary of the history of the Santorini Volcanic Field*

Event	Magma [1]	Age
Formation of the Kameni Volcano	D	197 BC to AD 1950 [2]
Caldera collapse		
Minoan eruption	R	3.6 ka [3]
Caldera collapse		
Cape Riva eruption	R	21 ka [4]
Eruption of the Andesites of Oia	A	
Construction of Therasia dome complex	R	
Upper Scoriae 2 eruption	A	79 ± 8; 54 ± 3 ka [5]
Construction of Skaros lava shield	B, A, D	67 ± 9 ka [5]
Caldera collapse (incremental?)		
Upper Scoriae 1 eruption	A	
Vourvoulos eruption	A, D	
Eruption of Megalo Vouno; Columbos tuff ring	A	76 ± 28; 54 ± 23 ka [4]
Middle Pumice eruption	A, D	*c.* 100 ka [6]
Cape Thera eruption	A	
Construction of Simandiri lava shield	A	172 ± 33; 172 ± 4 ka [5]
Caldera collapse		
Lower Pumice 2 eruption	R	
Lower Pumice 1 eruption	R	203 ± 24 ka [5]
Cape Therma 3 eruption	A	
Extrusion of Rhyodacites of Cape Alonaki and NE Thera	R	257 ± 31; 224 ± 5 ka [5]
Cape Therma 2 eruption	R	
Cape Therma 1 eruption	A	
Extrusion of the andesites of Cape Alai	A	456 ± 138; 364 ± 62; 345 ± 88 ka [5]
Eruption of the Cinder Cones of Akrotiri Peninsula	B, A	522 ± 104; 451 ± 27; 344 ± 24 ka [5]
Construction of Peristeria 3	B, A, D	480 ± 5; 478 ± 3; 464 ± 8; 433 ± 8; 308 ± 10 ka [5]
Extrusion of lavas of Peristeria 2	A	496 ± 16 ka [5]
Construction of Peristeria 1	A	528 ± 23 ka [5]
Eruption of the Early Centres of Akrotiri Peninsula	D, R	645 ± 92; 619 ± 35; 586 ± 15, 582 ± 24; 553 ± 10 ka [5]

[1] B basalt: A andesite; D dacite; R rhyodacite.
[2] Historic records.
[3] Mean of radiocarbon ages on plant remains in tuffs (Freidrich *et al.* 1990).
[4] Mean of radiocarbon ages of plant remains in tuff (Pichler & Freidrich 1977), corrected using the data of Bard *et al.* (1990)
[5] K–Ar or $^{40}Ar/^{39}Ar$ age of this study.
[6] Tentative correlation by Federman & Carey (1980) with W-2 deep-sea ash.

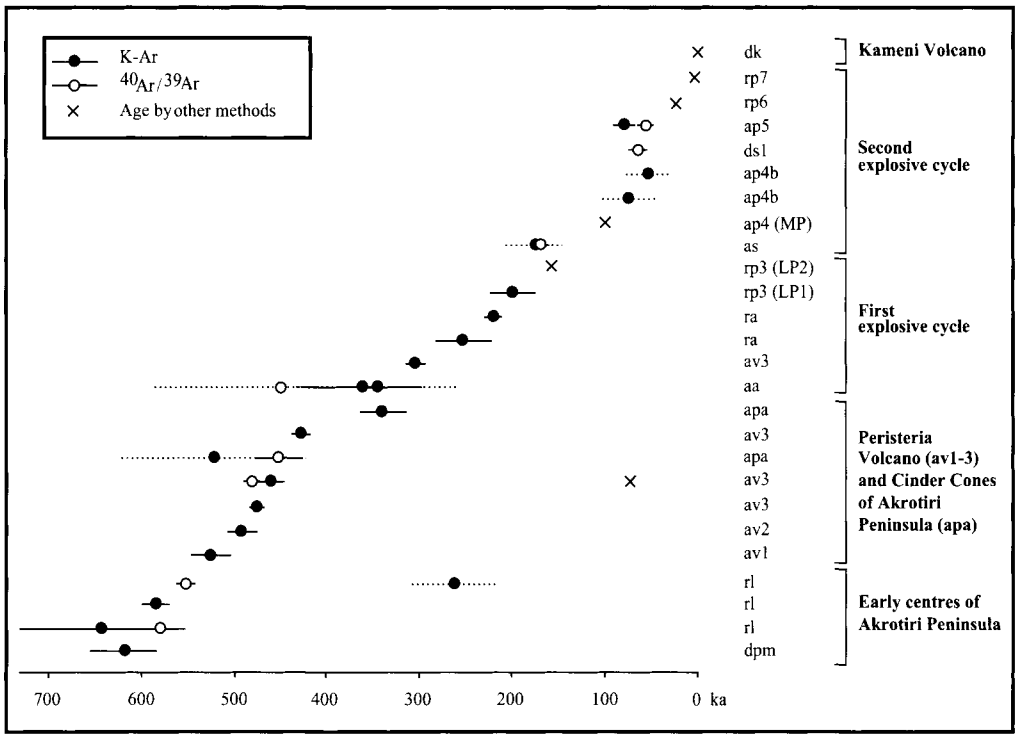

Fig. 3.56. Summary of radiometric dates of the present study, and comparison with dates obtained by other methods (Table 3.3). Bars give the 1σ error on measurements. Imprecise K–Ar ages are shown with dotted error bars where the sample yielded less than 2.5% radiogenic argon.

excellent. Since the dating was carried out on whole-rock samples, there is a possibility that the ages are slightly too old due to xenocrystic contamination.

Effusive activity at Santorini began about 650 ka ago and continued without significant break until the present day. Santorini lavas are all normally magnetized (Huijsmans 1985) because they are younger than the Brunhes-Matuyama reversal (780 ka). Owing to repeated caldera collapse, and to the probable existence of submerged flank vents, it is certain that the record of volcanism is incomplete. Nonetheless, the longest pause in volcanism permitted by the age data amounts to a few tens of thousands of years, and at the 1σ level is essentially zero.

The data constrain the longevities of the different effusive centres. The early rhyodacitic centres remained active for about 100 000 years, from 650 to 550 ka. Peristeria Volcano was constructed over at least 100 000 years, from 530 to 430 ka, which is a typical lifetime for an andesitic stratovolcano. The Skaros shield began its growth around 67 ka and was more than 10 km^3 in volume 12 000 years later. Following construction of the Therasia dome complex on its western flank, the shield finally collapsed 21 000 years ago, some 50 000 years after its inception. Kameni Volcano is already 3600 years old, if we assume that it began growth immediately after the Minoan eruption. In conclusion, the longevity of individual effusive centres on Santorini is typically a few tens of thousands of years, but major growth phases can probably occur on timescales of thousands of years

The onset of major explosive volcanism at Santorini took place about 360 ka. Intervals between the twelve largest eruptions vary between 17 000 and 40 000 years, with an average recurrence time of 30 000 years. In between the large explosive eruptions there were periods of constructive volcanism. The constructive volcansim, as indicated by the compositions of the minor pyroclastic sequences and lava shield sequences, is often basaltic to andesitic. More than 100 minor explosive eruptions are recorded by the minor sequences. Given the total duration of explosive activity (about 360 000 years), the recurrence interval for an eruption of this magnitude is thus of the order of 3000–4000 years.

Each long-term explosive cycle lasted about 180 000 years. The origin of these cycles is unclear, but the data rule out that they are somehow related to sea-level change. It has been suggested that sea-level fluctuations can influence volcanic behaviour by changing the stresses on the plumbing system of an island volcano (Wallman *et al.* 1988). However the total 360 000 year duration of the two explosive cycles at Santorini corresponds to three sea-level cycles (Bassinot *et al.* 1994), ruling out any simple relationship. It therefore appears that the cycles have a deeper origin, as discussed in Chapter 8 and are not related to sea level.

The importance of regional tectonics

Development of the volcanic field has been strongly influenced by regional faults. It is constructed on the northern flank of the Santorini–Amorgos Ridge, a NE–SW-trending basement horst (Fig. 3.1). The basement massif of southeastern Thera is the subaerial expression of this ridge. The northern half of the volcanic field lies in a graben, which is probably the continuation of the Anydros Basin. Basement rocks do not crop out in northern Santorini because they are down-thrown below sea level. Most of the effusive activity since 530 ka has been concentrated in this graben. This includes Peristeria Volcano, the Simandiri shield, the Skaros shield, the Therasia dome complex, and the Kameni Volcano (Fig. 3.57).

Several other features reflect the regional tectonic fabric (Fig. 3.57). Many dykes in northern Thera strike approximately NE–SW, as does the small graben between Micros Profitis Ilias and Megalo Vouno (Heiken & McCoy 1984; Mountrakis *et al.* 1998; Fig. 3.57). Several eruptive vents lie on distinct NE–SW lineaments. One, called the *Kameni Line*, passes through the centre of the caldera and includes the Kameni Islands, Aspronisi tuff ring, and vents for the six Plinian eruptions shown in Fig. 3.19. Extension of this lineament across Thera is marked by a line of enhanced gas emission (Barberi & Carapezza 1994). Moreover, individual vents on the Kameni Islands are confined to a 600 m wide elongated zone oriented NE–SW (Fytikas *et al.* 1990*a*) (Fig. 3.54). A second NE–SW lineament, called the *Columbos Line*, is defined by Megalo Vouno cinder cone, Kokkino Vouno cinder cone, and the Cape Columbos tuff ring. It is clear that regional faults have played a major role in channelling magma to the surface at Santorini.

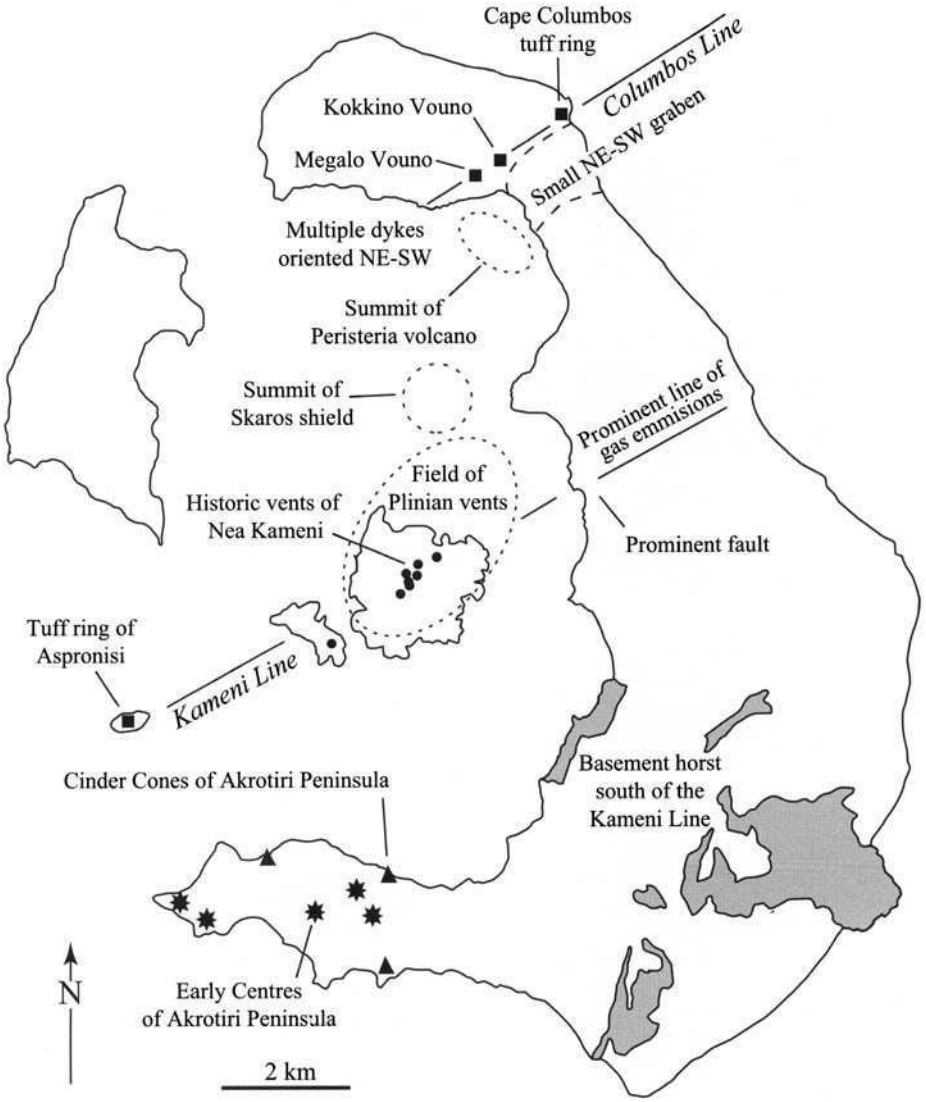

Fig. 3.57. Map showing the strong influence of regional tectonics on the development of the volcanic field. See the text for discussion.

Repeated caldera collapse at Santorini

At least four explosive eruptions at Santorini generated calderas for which direct evidence is preserved (Fig. 3.58). The present-day caldera is a composite structure with several generations of cliff surface (Fig. 3.59).

Caldera 1 (180 ka) formed during the Lower Pumice 2 eruption, the evidence being the steep unconformity that cuts out Lower Pumice 2 south of Phira (Fig. 3.20). Caldera 2 (about 70 ka) formed as a result of one or more of the Middle Tuff series of eruptions. It covered much of the area of the present-day northern basin, and was subsequently filled by the Skaros shield. Caldera 3 (21 ka) formed during the Cape Riva eruption, which collapsed the Skaros shield. Finally, the Minoan eruption deepened and widened the extant depression, forming the present-day caldera 4 (3.6 ka). It is notable that three of these calderas formed during the large silicic eruptions that terminated the two 180 ka explosive cycles.

A typical sequence of events at Santorini is as follows. During a large explosive eruption, a caldera collapses. Over the subsequent thousands to tens of thousands of years, intracaldera volcanoes grow in the caldera, which becomes partially, or totally, filled with lava. At the same time, sequences of minor pyroclastic deposits accumulate all over the islands. The intracaldera volcanoes then themselves collapse when the next major explosive eruption takes place. The Skaros shield is an example of a lava succession which completely filled a pre-existing caldera. In other cases, such as the (hypothetical) central volcano of caldera 3 (Fig. 3.46), the lavas did not succeed in filling the previous caldera before the next collapse occurred. During caldera collapse, rotational landslides eat back until they exhume ancient caldera cliffs and unconformities. This is particularly clear in the case of caldera 3 when collapse of the Skaros shield exhumed the old cliff line of caldera 2. Large areas of the cliffs in northern Thera are interpreted as the ancient walls of caldera 2 exhumed 21 000 years ago during the Cape Riva eruption (Fig. 3.59). A similar process occurred during the Minoan eruption, when landslides exhumed the western margin of the pre-volcanic island at Athinios (Fig. 3.59).

Each collapse at Santorini removes support from the flanks of the volcanic field. In some cases this triggers large-scale rotational slumping into the caldera and forms breaches. The small graben in the northeastern corner of the caldera formed by incipient slumping when the Skaros shield collapsed 21 000 years ago. It is interpreted as a failed breach of caldera 3.

The observations have implications for the mechanics of caldera collapse. Scandone (1990) suggested that collapse at Santorini occurs in a chaotic manner, generating a huge breccia-filled funnel, but the evidence does not support this. All three calderas for which reasonable reconstructions can be made have broadly similar locations and sizes, suggesting that subsidence repeatedly uses the same faults. Another observation is that several explosive eruptions began at vents near Nea Kameni, showing that repeated caldera collapse fails to destroy the plumbing system of the volcano. This is particularly clear in the case of the Minoan eruption, where the main site of post-collapse lava effusion (Nea Kameni) coincides approximately with the site of the initial Plinian vent. We consider it most likely that caldera collapse at Santorini occurs as a series of essentially

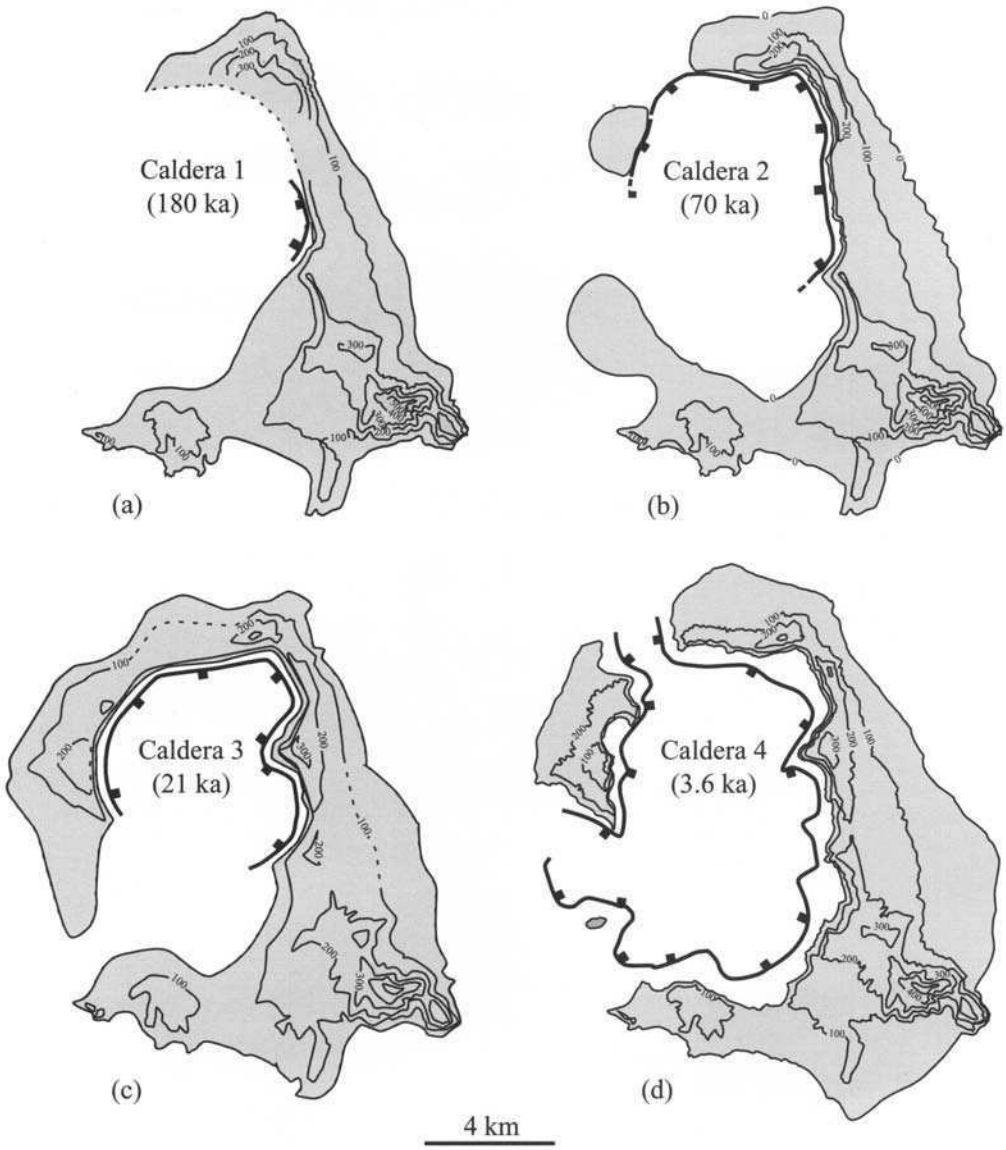

Fig. 3.58. Reconstructions of the four calderas of Santorini for which field evidence is preserved. Contours in metres.

coherent blocks along regional faults. This enables the ascending magmas to re-exploit the same faults (for example, the Kameni Line) once collapse is over.

Explosive activity

Santorini has had 12 major explosive eruptions over the last 360 000 years, making it one of the most explosive arc volcanoes known to the present authors. The eruptions and their deposits are summarized in Table 3.4. Each began with a fallout phase, and all except Cape Therma 2 generated pyroclastic flows. The fall deposits are hard to classify due to limited subaerial extent, but all six shown in Fig. 3.19 are dispersed on a scale typical of Plinian eruptions. In one case, accumulation of pumice close to source was so rapid that welding occurred (Sparks & Wright 1979). Most of the ignimbrite and scoria-flow deposits from the climactic phases of these eruptions is buried on the flanks of the islands or under the sea. Only the Minoan ignimbrite crops out extensively over the islands. In many cases, the passage of pyroclastic flows is recorded only by coarse-grained lag deposits preserved in the caldera walls.

For these reasons it is impossible to calculate accurate volumes for the pre-Minoan eruptions. However, the deposits are in several cases comparable in thickness and dispersal to the Minoan Tuff, which has a DRE (dense-rock equivalent) volume of at least 30 km^3. Moreover, at least two other eruptions, Cape Riva and Lower Pumice 2, were voluminous enough to lay down significant ash layers on the floor of the Aegean Sea (Keller 1981). We conclude that most of the 12 named eruptions discharged between a few cubic kilometres and a few tens of cubic kilometres of magma. Eruptions of several cubic kilometres or more typically trigger caldera formation (Smith 1979), and this is consistent with the field evidence for repeated caldera collapse.

Proximal pyroclastic flow deposits

Proximal lag deposits from pyroclastic flows abound in the caldera walls of Santorini. The main facies are coarse-grained lithic breccias and spatter agglomerates. Recognition that the breccias and agglomerates were laid down by pyroclastic flows has been crucial to unravelling the complex eruptive history of the islands.

The lithic breccias were described by Druitt & Sparks (1982). The best examples occur in Lower Pumice 1, Middle Pumice, Upper Scoriae 1, Upper Scoriae 2 and Cape Riva (Figs 3.26, 3.30 & 3.43). Cape Therma 3, Lower Pumice 2 and Vourvoulos generated breccias of local extent. Lenses of breccia in the Minoan ignimbrite are interpreted as lithic-rich segregation layers from the pyroclastic flows. The breccias consist of blocks too large and too dense to be transported efficiently by the parent pyroclastics flows (Fig. 3.60). They are coarse-grained, clast-supported, and very extensive (Fig. 3.61). For example, breccias of Lower Pumice 1, Middle Pumice and Cape Riva are at least several metres thick all over the islands, and in some places reach 20 m in thickness. As typical of deposits emplaced

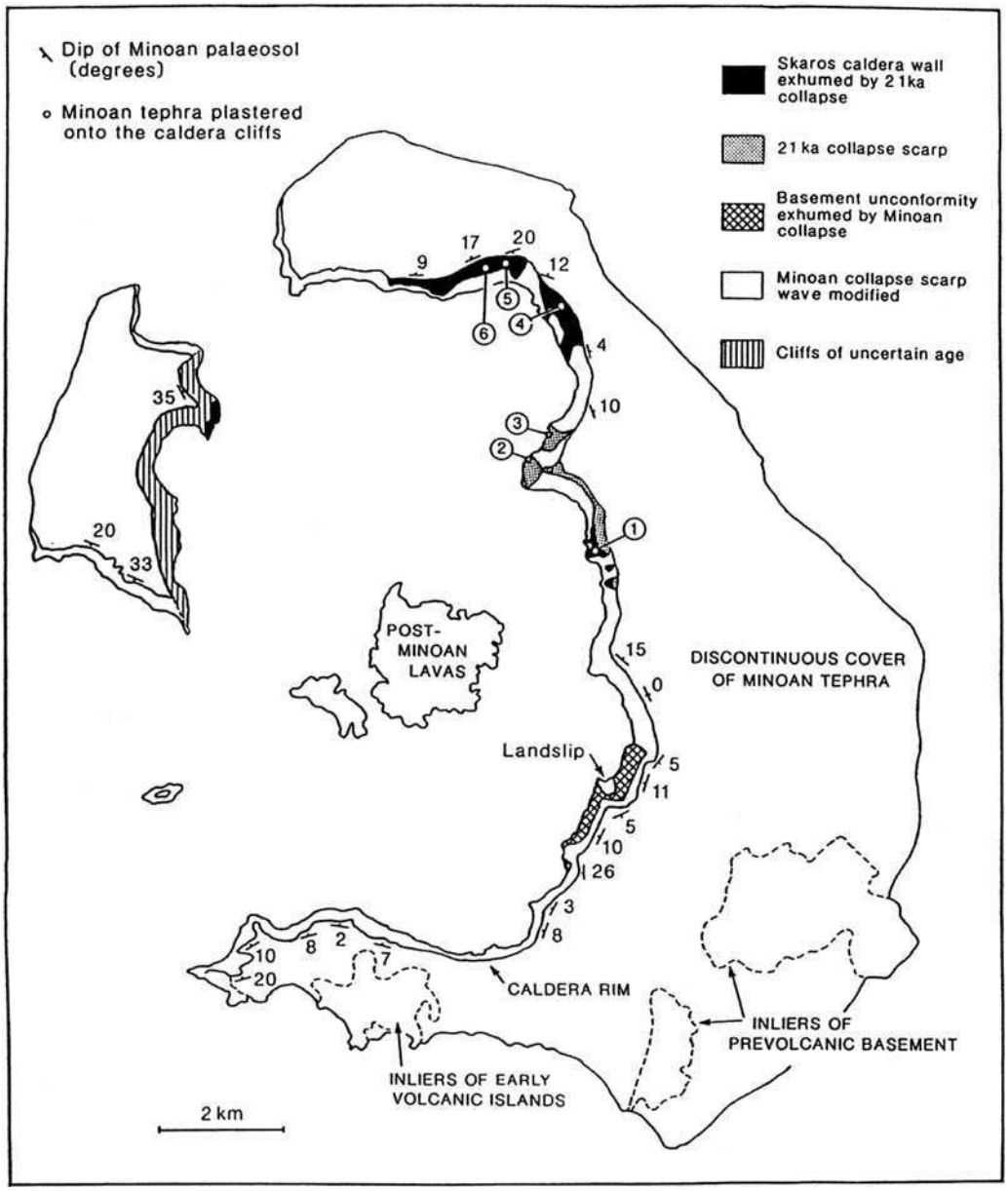

Fig. 3.59. Geomorphological map of the different generations of cliff surface recognized in the present-day caldera walls. Numbers mark the six sites where *in situ* Minoan Tuff lies plastered on the present-day caldera wall, showing that a caldera (Caldera 3) already existed prior to the Minoan eruption (Druitt & Francaviglia 1992).

laterally, the breccias thicken and coarsen into depressions and thin onto highs. They are known to be primary deposits because they grade laterally and vertically into associated ignimbrite and contain segregation pipes, pods and lenses indicative of gas fluidization. Thermal demagnetization studies of lithic blocks in the Cape Riva and Middle Pumice breccias have confirmed that they were emplaced at high temperatures (McClelland & Druitt 1989).

The spatter agglomerates were described by Mellors & Sparks (1991). They are a type of lag deposit from pyroclastic flows rich in large, fluidal rags of andesite (Fig. 3.62). The best examples occur in Cape Therma 1, Upper Scoriae 1 and Upper Scoriae 2, but the Middle Pumice has a similar facies at the end of the Akrotiri Peninsula (Fig. 3.31). In all four cases the agglomerates grade laterally and vertically into lithic breccias and scoria flow deposits, making facies variations in these deposits very complicated. At Cape Tourlos, the spatter agglomerate of Upper Scoriae 2 becomes densely welded, forming the prominent knoll on the headland (Fig. 3.36).

Heiken & McCoy (1984) interpreted the spatter agglomerates as pyroclastic fall deposits. However, thickness and grain size variations are not consistent with fallout. The agglomerates maintain their coarse grain size over the islands and thicken and coarsen into depressions (Fig. 3.63). The Upper Scoriae 2 agglomerate at Oia can be traced radially away from source for a kilometre, without significant fining. Moreover, the internal stratification here dips outwards at only a few degrees, which is not typical of airfall spatter. Another feature is that the agglomerates commonly exhibit imbrication of spatter rags, providing clear evidence for emplacement by flowage (Fig. 3.33). The agglomerate of Upper Scoriae 1 exhibits a particularly well developed imbrication over much of southern Thera. Similar coarse-grained andesitic pyroclastic flow deposits have been recognized on other arc volcanoes such as Lascar in Chile (Gardeweg *et al.* 1998).

Eruption and emplacement of pyroclastic flows

Of the 12 major explosive eruptions, 11 culminated in the discharge of pyroclastic flows. A variety of eruption and emplacement processes are represented by these deposits. In this discussion we distinguish between those eruptions that were *dominantly intermediate* in composition (mainly andesitic), and those that were *dominantly silicic* (mainly dacitic or rhyodacitic).

In three of the dominantly intermediate eruptions (Cape Therma 1, Cape Thera, Vourvoulos), initial fallout phases were followed by emplacement of normal scoria flows with associated pyroclastic surges. The scoria flows from Cape Therma 1 and Cape Thera eruptions ponded locally up to many tens of metres in ancient depressions.

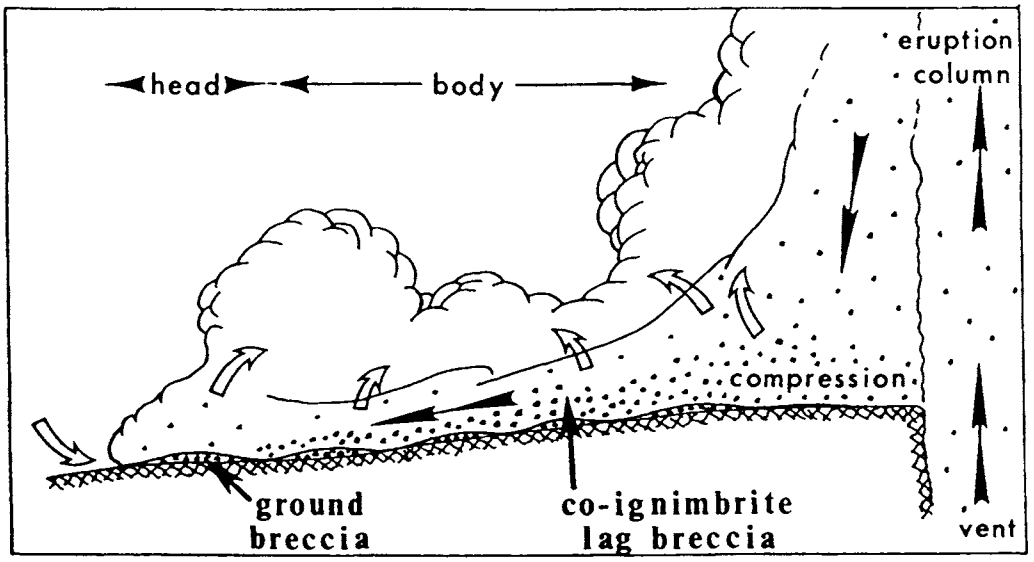

Fig. 3.60. Formation of co-ignimbrite lag breccia from a collapsing eruption column, from Druitt & Sparks (1982). This figure refers specifically to the Cape Riva lag breccias, which commonly have a basal ground layer.

The other four dominantly intermediate eruptions (Cape Therma 3, Middle Pumice, Upper Scoriae 1 and Upper Scoriae 2) appear to have been much more violent. Following initial fallout phases, fast-moving pyroclastic flows sped out radially, laying down widespread lag deposits. The relative proportions of lithics and spatter in these flows varied circumferentially around the caldera, and also with time during each eruption. In some directions the flows were rich in accidental debris, generating lithic breccias, whereas in others they laid down imbricated spatter agglomerates. Initial discharge of the Middle Pumice pyroclastic flows was accompanied by huge explosions and vent widening. Large volumes of accidental debris, including fragments of the welded Plinian deposit, were shed into the flows, and ballistic blocks up to 3 m in diameter were showered over what is now southern Thera. Flows rich in spatter rags were channeled to the southwest, where they deposited the agglomerate facies preserved on the Akrotiri Peninsula (Figs 3.18 and 3.31). Flows of Upper Scoriae 1 that travelled to the southeast were rich in lithic debris, whereas those directed southwest were more spatter-rich (Fig. 3.18). During the Upper Scoriae 2 eruption, the flows were channeled strongly down the northwest flank of Skaros, where 50 m of agglomerate accumulated. On the upper eastern flank the spatter rags were so hot that they welded on deposition. As they travelled progressively away from source, the flows of Upper Scoriae 2 laid down more typical scoria flow deposits, including cross-bedded facies.

A prominent feature of these deposits is the presence of plutonic nodules and hydrothermally altered lithic blocks (Mellors & Sparks 1991; Chapter 5). This suggests the occurrence of deep fragmentation and destruction of mature hydrothermal systems during the eruptions. Moreover, many of the spatter fragments contain abundant chips of rock that had been mixed very efficiently into the magma during eruption. One possibility is that stoping of a hot, fluid-rich hydrothermal system into the magma chamber during eruption caused very violent, deep fragmentation. Another is that the spatter agglomerates formed by huge sprays of degassed andesitic magma due to explosions through lava lakes. Similar associations of spatter agglomerates, lithic breccias, and deep fragmentation occur in pyroclastic flow deposits of the Campanian eruption, Italy (Rosi *et al.* 1996). At least one eruption of this type on Santorini caused caldera collapse (Caldera 2)

Two of the four dominantly silcicic eruptions (Lower Pumice 1 and Cape Riva) also generated widespread lithic breccias, but the associated spatter-rich facies are lacking. As in the other eruptions, the initial Plinian phases were in each case followed by huge explosions, sending ballistic blocks over much of the islands, followed immediately by the generation of pyroclastic flows (Fig. 3.64). This has been attributed to the onset of caldera collapse (Druitt 1985), and at least in the Cape Riva case there is direct evidence for the resulting caldera (Caldera 3). Lower Pumice 1 and Cape Riva resemble certain other well-documented ignimbrite eruptions such as Crater Lake, Oregon (Druitt & Bacon 1986) and Ito, Japan (Aramaki 1984), where the volume of ignimbrite is an order of magnitude or more greater than that of the lag breccias. We therefore infer the existence of large volumes of Lower Pumice 1 and Cape Riva ignimbrite under the sea.

The large silicic eruptions that terminated each 180 ka cycle (Lower Pumice 2 and Minoan) laid down remarkably similar deposits. In each case an initial Plinian phase was followed by phreatomagmatic explosions, then the discharge of ignimbrite. The products of the phreatomagmatic phases include base-surge deposits and thick, massive tuffs interpreted as deposits from mudflows and

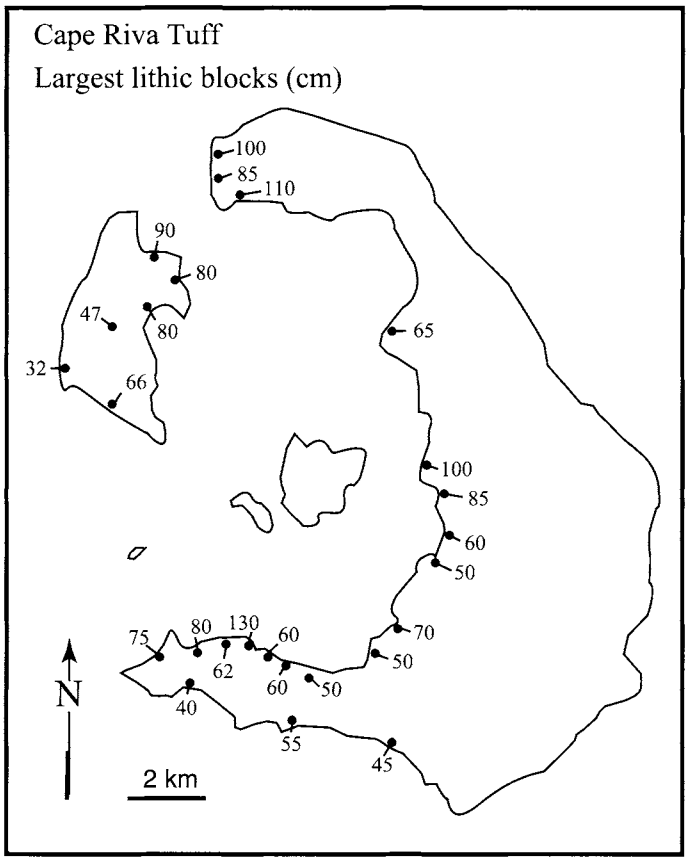

Fig. 3.61. Map of the largest lithic block size in the Cape Riva lag breccias.

Fig. 3.62. Highly fluidal spatter rag in the Upper Scoriae 1 agglomerate facies near Balos.

low-temperature pyroclastic flows. The importance of magma–water interaction is a striking feature of these eruptions. This is well understood in the case of the Minoan eruption, which took place in a flooded caldera. The palaeogeography prior to Lower Pumice 2 is very poorly constrained, but it is possible that a flooded caldera from Lower Pumice 1 also existed at that time.

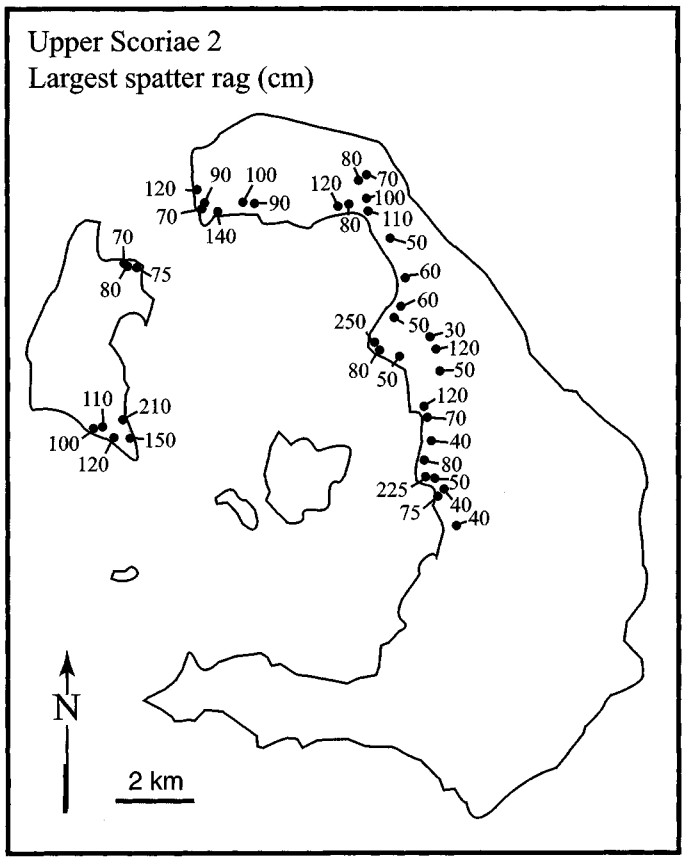

Fig. 3.63. Map of the largest spatter rag size in the agglomerate facies of Upper Scoriae 2.

Summary

(1) A new geological map and 38 new K–Ar and $^{40}Ar/^{39}Ar$ radiometric ages are presented. These, combined with previous studies, have permitted detailed reconstruction of the development of the volcanic field in space and time.

(2) Santorini lies on about 30 km of continental crust, and is founded on the edge of a NE–SW-trending basement horst. The volcanic products are plastered up against, and over, a pre-volcanic island lying on this horst. For the last 530 000 years volcanism has been concentrated in a graben immediately to the northwest of the horst. NE–SW regional faults have played important roles in channelling magma to the surface at Santorini, and probably also during caldera collapse.

(3) Volcanism began about 650 ka and has continued essentially without interruption until the present day. The earliest centres were submarine and located in the south of the volcanic field, where they remained active until at least 550 ka. A $>2\,km^3$ composite andesitic stratovolcano, called Peristeria Volcano, developed in northern Santorini between 530 ka and 430 ka. Major explosive activity began about 360 ka. Since that time twelve large pyroclastic eruptions (km^3 to tens of km^3), and at least a hundred smaller ones have occurred. During the same period several effusive centres, including the $>10\,km^3$ Skaros lava shield and the $>2\,km^3$ Therasia lava dome complex grew, and later collapsed, in the northern half of the volcanic field. The islands of Thera, Therasia, and Aspronisi are today covered by thick white tuffs from the 3.6 ka Minoan eruption. Historic activity has occurred on the Kameni Islands, the subaerial summit of a $2.5\,km^3$ intracaldera volcano, which last erupted in 1950.

(4) Each major explosive eruption began with a fallout (commonly Plinian) phase, and eleven generated pyroclastic flows. In many cases the only record of major pyroclastic flow eruptions is the occurrence of coarse-grained lithic-rich or spatter-rich lag deposits in the caldera walls. The average recurrence time for a major explosive eruption at Santorini is about 30 000 years.

(5) The explosive eruptions can be divided into two 180 000-year cycles on the basis of temporal variations in magma composition. Each cycle terminated with major silicic eruptions and caldera collapse.

(6) The major explosive eruptions of andesitic to rhyodacitic products alternate with sequences of minor pyroclastic deposits and

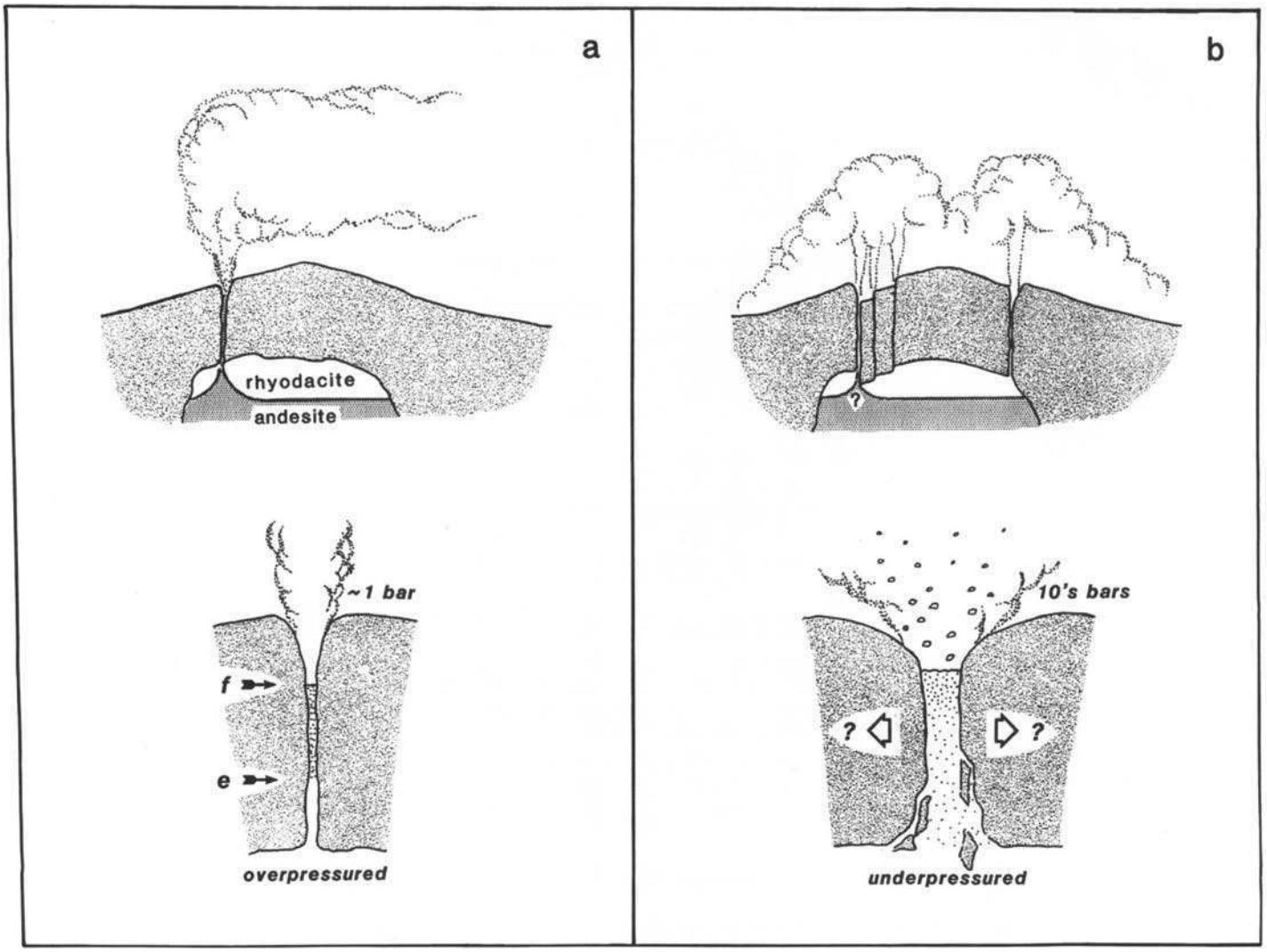

Fig. 3.64. Inferred sequence of events during the Cape Riva eruption. (**a**) Initial stage in which the magma chamber is overpressured and discharge is steady, permitting eruption at atmospheric pressure. This corresponds to the Plinian stage. (**b**) Underpressuring of the chamber causes caldera collapse, escalation of magma discharge rate, and outpouring of pyroclastic flows. Vigorous vent erosion results in the eruption of abundant coarse lithic debris and emplacement of lag breccias.

palaeosols and in some cases lava successions. The minor pyroclastics and associated lavas contain substantial basaltic to andesitic products and represent constructive phases of the volcanic field between the major explosive eruptions.

(7) Explosive eruptions at Santorini have caused the collapse of four large calderas, for which direct field evidence remains. A general sequence of events since about 360 ka has been (a) large explosive eruption and caldera collapse, (b) growth of intracaldera centres and accumulation of sequences of minor tephra, (c) large pyroclastic eruption and collapse of the intracaldera centres. During caldera collapse, landslides eat back until they exhume ancient unconformities and caldera walls. This has resulted in several generations of cliff surface in the present-day composite caldera. Removal of support during collapse triggers insliding of large pieces of the volcano and the formation of breaches.

Chapter 4
Compositional zoning and petrology of the Thera pyroclastics

Compositional zoning is a common feature of pyroclastic deposits erupted from calderas worldwide (Smith 1979; Hildreth 1981; Bacon & Druitt 1988; De Silva 1991; Feeley & Davidson 1994). Compositionally zoned tuffs provide a geologically instantaneous snapshot of the vertical stratigraphy and density stratification in the chamber immediately before eruption. Magma bodies are commonly zoned in density, with light, relatively cool, silicic magma overlying hotter, more mafic magma. Vertical zonation can arise by a number of processes, including crystallization and convective fractionation on the chamber walls, replenishment by mafic magma, which ponds and crystallizes on the chamber floor, and remelting of crustal rocks and ancient plutons.

The Thera pyroclastics provide a record of two cycles of intermediate to silicic magmatism (Fig. 4.1). Within this succession are preserved the deposits of 12 major explosive eruptions, most involving between several and a few tens of cubic kilometres of magma. Many of these deposits are compositionally zoned and preserve evidence for repeated development and eruption of stratified magma bodies beneath Santorini over a period spanning about 360 000 years.

In this chapter we describe the compositional zoning and mineral chemistry of the Thera pyroclastics. We present data on the phenocryst compositions for each deposit, and also use the compositions of interstitial glasses to constrain pre-eruptive water contents. We show that 11 of the 12 major tuffs are compositionally heterogeneous. Three eruptions show an unusual normal-to-reverse (silicic–mafic–silicic) zoning. A more detailed account of the geochemistry and isotope systematics is given in Chapters 6 and 7.

We adopt a chemical classification modified from Gill (1981) and based on dry analyses: basalt (<53% SiO_2), andesite; (53–63%), dacite (63–68%), rhyodacite (68–72%) and rhyolite (>72% SiO_2). We distinguish mafic (53–57% SiO_2) from silicic (57–63%) andesite. For pyroclastic deposits, we analysed fresh, homogeneous pumice or scoria lumps, although in a few cases we included banded or hybrid pumices. Between 7 and 42 individual pumice or scoria clasts were analysed per deposit. Details of analytical methods are given in Appendix 1. Representative microprobe analyses and sample descriptions are given in Appendix 2. For comparative purposes, we begin with a brief account of the petrology of the Santorini lava successions.

Petrology of the Santorini lavas

The lavas of Santorini range in composition from basalt to rhyodacite and rare rhyolite. There has been extensive documentation of their petrology (Nicholls 1971*a*, *b*; 1978; Huijsmans 1985; Huijsmans & Barton 1989; Stamatelopoulou-Seymour *et al.* 1990; Mitropoulos & Tarney 1992; Davis *et al.* 1998; Dietrich *et al.* 1998; Gartzos *et al.* 1998; Conticelli *et al.* 1998; Francalanci *et al.* 1998), and only the main features are reviewed here. The main phenocryst phases are plagioclase, clinopyroxene, orthopyroxene, olivine, magnetite, and ilmenite. Rhyodacites and rhyolites bearing amphibole, biotite and zircon were erupted from the Early Centres of Akrotiri Peninsula. Modal abundances of the phenocryst phases

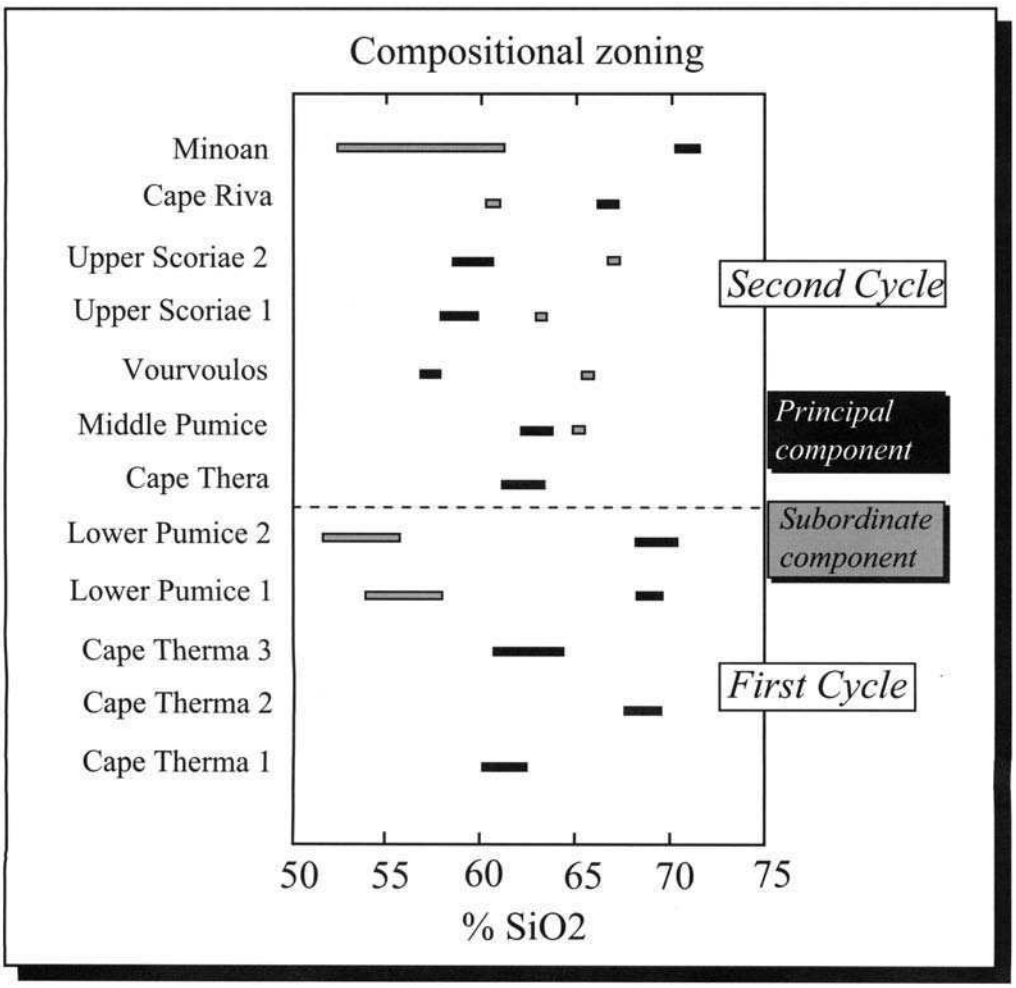

Fig. 4.1. Compositional heterogeneity in the Thera pyroclastics. With the exception of the small-volume Cape Therma 2, each explosive cycle commenced with eruptions of predominantly intermediate magma and terminated with two large silicic ones. The compositional gaps between different components of the same eruption are particularly large in the four dominantly silicic eruptions.

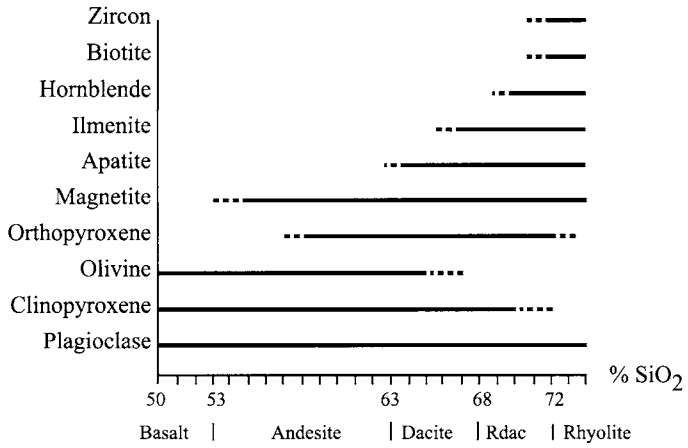

Fig. 4.2. Phenocryst phases in the Santorini magmas, modified from Huijsmans (1985).

show systematic trends as SiO_2 increases (Fig. 4.2). Olivine and plagioclase are the earliest phases to crystallize, followed by clinopyroxene, whilst orthopyroxene replaces olivine and eventually becomes dominant over clinopyroxene in silicic compositions. Phenocrysts or microphenocrysts of magnetite are nearly always present. This order of crystallization is observed at many other island arc volcanoes (Gill 1981). Modal analyses of lavas from the Skaros shield, the Peristeria Volcano and the Kameni islands give phenocryst percentages of 20–38 vol% for basalts and mafic andesites, and 7–17 vol% for silicic andesites, dacites and rhyodacites. Mafic andesites are in general the most phyric lavas. Phenocryst assemblages are nearly always dominated by plagioclase.

Basalts are present in the Skaros shield, occur rarely in Peristeria 3 and are found as cognate inclusions in the rhyodacites of the Early Centres of Akrotiri Peninsula, in the rhyodacites of the Therasia dome complex, and in the dacites of the Kameni islands. The cinder cones of Balos, Kokkinopetra, Megalo Vouno, and Kokkino Vouno are basaltic. The most primitive basalts have about 50% SiO_2, 7.5% MgO, Mg/(Mg + Fe) values of 0.7, 110 ppm Ni and 300 ppm Cr. Santorini basalts have phenocrysts of olivine, plagioclase, clinopyroxene, and minor magnetite. Groundmass phases are plagioclase, augite and/or pigeonite, magnetite and interstitial glass. Plagioclase phenocrysts (An_{93-55}) are predominately bytownite. Olivines have compositions of Fo_{85-53}. Augites have Mg/(Mg + Fe) values of 0.85–0.69. Amphibole occurs abundantly in cognate mafic inclusions in silicic lavas and tuffs of the Early Centres of Akrotiri Peninsula (Davis *et al.* 1998).

Andesites are the most diverse lavas petrologically. Mafic andesites occur abundantly in the Peristeria 1 and Skaros **as2** successions, in the Andesites of Oia and the Andesites of Cape Alai. Some mafic andesites are moderately phyric, with phenocrysts of plagioclase, clinopyroxene, olivine and minor amounts of magnetite. Some highly phyric varieties lack phenocrystic magnetite and contain disequilibrium phenocryst assemblages of orthopyroxene, magnetite, plagioclase, olivine, and clinopyroxene. Features indicative of mineral–melt disequilibrium include (1) resorption and reaction textures, (2) coexisting mineral compositions spanning the entire range of Santorini magmas, (3) the coexistence of normally

Table 4.1. *Analyses of representative juvenile clasts from eruptions of the first explosive cycle*

	Cape Therma									
	1		2	3		Lower Pumice 1			Lower Pumice 2	
Analysis	1	2	3	4	5	6	7	8	9	10
Sample	87-71	87-25	87-88	87-31	79-79	80-170	82-15	79-89	82-9	86-16
Unit*	A	B		A	B	A	C	C	B	A
Code	1	1	1	1	1	2	1	1,3	1	1,4
Major elements (normalized to 100% dry) (wt%)										
SiO_2	62.5	60.5	69.6	63.8	60.8	68.4	58.1	54.4	69.4	55.7
Al_2O_3	16.1	16.4	15.4	15.8	16.4	14.7	17.9	19.7	15.0	17.5
TiO_2	1.06	1.01	0.63	1.01	1.08	0.50	1.04	1.20	0.47	1.10
FeO	6.27	6.88	3.28	5.94	6.88	3.52	6.78	7.50	3.25	7.75
MgO	2.09	2.57	0.69	1.45	2.21	0.83	2.80	3.06	0.65	4.03
CaO	4.83	5.80	2.31	3.95	5.16	2.17	7.24	9.32	2.00	8.25
Na_2O	4.47	4.43	4.58	4.77	4.69	6.21	4.08	3.44	5.56	4.10
K_2O	2.28	2.03	3.34	2.82	2.45	3.48	1.60	0.96	3.47	1.14
MnO	0.20	0.17	0.10	0.15	0.15	0.12	0.15	0.16	0.11	0.18
P_2O_5	0.22	0.21	0.11	0.24	0.27	0.11	0.21	0.32	0.09	0.27
LOI	3.91	0.30	3.78	0.02	0.61	5.53	na	0.40	2.42	1.31
Sum	100.1	99.7	100.3	99.7	100.1	100.0	98.1	99.5	99.0	99.7
Trace elements (raw data) (ppm)										
Ba	417	414	541	484	484	423	321	180	498	267
Ce	32	70	78	63	68	58	33	37	51	18
Cr	25	17	6	14	10	bd	21	18	bd	56
La	33	24	36	38	22	21	25	10	30	16
Ni	12	16	8	10	bd	bd	8	bd	6	15
Nb	11	8	15	13	13	13	9	8	bd	6
Rb	78	66	120	114	90	103	58	32	105	29
Sr	197	210	118	179	198	111	215	283	99	244
Th	15	13	22	19	18	21	12	7	19	bd
V	57	77	26	51	109	13	145	187	15	140
Y	46	44	54	53	53	59	40	33	56	31
Zr	242	223	328	295	272	315	171	104	322	119

Major elements normalized to 100% volatile-free with all Fe as FeO. Loss on ignition (LOI) and oxide sums are taken from the raw analyses. Trace element abundances are from raw analyses. bd, below detection; na, not analysed. Code numbers are as follows: 1, single clast analysed; 2, multiple clasts analysed; 3, contains minor admixed dacitic pumice; 4, grey cauliform scoria.

* Eruption units are listed in Table 3.4.

zoned, reversely zoned, and unzoned crystals, (4) bimodal populations of plagioclase and clinopyroxene cores zoned to rims of similar, intermediate, compositions, and (5) the presence of Fo-rich olivine and An-rich plagioclase. Mixing of mafic and silicic magmas played an important role in generating these hybrid andesites (Huijsmans 1985; Huijsmans & Barton 1989).

The petrology of the silicic andesites, dacites and rhyodacites are somewhat similar to one another. Silicic andesites occur in the Peristeria 2, Simandiri and Skaros lavas. Cape Mavros, the basal Skaros (**ds1**) lavas, and the lavas of the Kameni Volcano are dacitic in composition. Rhyodacites dominate the Therasia dome complex, the Cape Alonaki lavas, and the Early Centres of Akrotiri Peninsula. The phenocryst assemblage in these rocks is typically plagioclase (mostly An_{60-40}), augite, hypersthene, and titanomagnetite. Phenocryst compositions in a given rock are more uniform compositionally than in the mafic andesites. Orthopyroxene typically becomes prominent in dacites and rhyodacites, and is more abundant than clinopyroxene in the rhyodacites. Pigeonite is common as a groundmass phase in some silicic andesites. Some hybrid silicic andesites have mixed crystal populations (Nicholls 1971*a*; Pyle *et al.* 1988) due to magma mixing. Apatite and ilmenite are ubiquitous minor phases in the rhyodacites. Rhyolites and rhyodacites of the Early Centres of Akrotiri Peninsula contain amphibole, biotite and accessory zircon.

General features of the Thera pyroclastics

Juvenile components of the Thera pyroclastics range from mafic andesite to rhyodacite. Scoria of basaltic composition occurs in Lower Pumice 2 (Fig. 4.1; Tables 4.1 and 4.2). Phenocryst contents lie generally in the range 0–30%, but some andesitic and basaltic components of the Minoan and Lower Pumice eruptions are more crystal-rich (Table 4.3). Like Santorini lavas, magmas of the Thera pyroclastics are characterized by the following phenocryst assemblages:

basalts:	Mg-rich ol + plag + cpx + mt
andesites:	plag + cpx ± opx + mt ± xenocrystic Mg-rich ol
dacites:	plag + cpx + opx ± Fe-rich ol + mt + ilm + apat ± xenocrystic Mg-rich ol
rhyodacites:	plag + cpx + opx + mt + ilm + apat ± hb ± zir.

The occurrence of Fe-rich olivine is restricted to dacites of the Middle Pumice and Vourvoulos eruptions, which are the most tholeiitic magmas of the Thera pyroclastics (Chapter 6).

The eruptive styles and chemical compositions of the Thera pyroclastics can be used to recognize two explosive cycles: the first from about 360 to 180 ka, and the second from 180 to 3.6 ka (Chapter 3). Each cycle commenced with explosive eruptions of andesitic or (mafic) dacitic composition and terminated with a pair of large magnitude, strongly bimodal rhyodacitic eruptions with large compositional gaps.

Almost all the 12 main tuffs of the Thera pyroclastics are compositionally heterogeneous, although in Cape Therma 2 the variation is only slightly larger than analytical error. In what follows we neglect Cape Therma 2, which is also much smaller than the other 11 tuffs.

The 11 zoned tuffs can be conveniently subdivided into two types for petrological purposes. (1) Those of *dominantly silicic* composition, which terminate each cycle (Lower Pumice 1 Lower Pumice 2 Cape Riva, Minoan). These are markedly bimodal with large compositional gaps. (2) Those eruptions of *dominantly intermediate* composition. These include eruptions with large compositional gaps (Vourvoulos, Upper Scoriae 2) as well as those with smaller gaps (Cape Therma 1, Cape Therma 3 Middle Pumice, Upper Scoriae 1). Heterogeneity in the Cape Thera Tuff is only detectable as bimodal glass compositions on a thin-section scale. The dominantly intermediate eruptions also generated distinctive deposits with abundant scoria flows, lithic breccias, and spatter agglomerates (Chapter 3).

It is within this framework of two types of differently zoned magma chamber that we describe the petrology and zoning of the Thera pyroclastics.

Eruptions of dominantly silicic composition

The principal juvenile components of the Minoan, Cape Riva, Lower Pumice 2 and Lower Pumice 1 deposits are rhyodacitic pumices of restricted compositional range. Each silicic eruption also has a minor component of andesite or basalt, overall abundances of which vary from $<1\%$ in the Lower Pumice 2, Cape Riva, and Minoan deposits to about 20% in Lower Pumice 1. In Lower Pumice 1 the andesitic component occurs in the lag breccia and increases in abundance with stratigraphic height, as expected from the progressive tapping of a two-layer chamber (Blake & Ivey 1986; Freundt & Tait 1986). In the Lower Pumice 2, Cape Riva and Minoan deposits, scoria appears in the Plinian deposit and increases in abundance upwards. In each of these three cases the scoria abundance reaches a maximum near the top of the Plinian layer, then declines to $\ll 1\%$ in subsequent ejecta (Figs. 4.3 and 4.4). Thus the Lower Pumice 2, Cape Riva, and Minoan deposits display a normal-to-reverse type of compositional zonation.

Silicic components

Each of the four dominantly silicic eruptions began with the venting of rhyodacite or dacite. The compositions are 68.4–69.6% SiO_2 (Lower Pumice 1), 68.1–70.3% (Lower Pumice 2), 66.3–67.7% (Cape Riva), and 70.5–71.4% (Minoan). In each case there is only a small compositional spread beyond analytical precision, suggesting that the silicic magma was well mixed (Table 4.4). The pumices contain 3–20 wt% euhedral to subhedral phenocrysts set in vesicular glass (Fig. 4.5a and b). Glass compositions in Minoan and Cape Riva pumices are uniform (Table 4.5); our data are not detailed enough to tell if this is the case for Lower Pumice 1 and Lower Pumice 2. In order of abundance the phenocrysts are plagioclase, orthopyroxene, clinopyroxene, magnetite, and ilmenite. Small apatite inclusions are common in orthopyroxene and magnetite phenocrysts. Mineral separates from Lower Pumice 2 rhyodacite contains trace amounts of amphibole and zircon.

Plagioclase phenocrysts are typically normally zoned with inclusions of brown rhyodacitic glass (Fig. 4.5a and b). Compositions range from An_{70} to An_{28} (Figs 4.6 and 4.7). Microphenocrysts and phenocryst rims are An_{36-40} in Lower Pumice 1, Cape Riva and Minoan, and An_{28-35} in Lower Pumice 2. Rare bytownite occurs as resorbed cores in some phenocrysts, and as discrete xenocrysts. Orthopyroxenes vary widely in composition ($Wo_3En_{50-68}Fs_{47-29}$) (Fig. 4.8); normal zoning is common but some phenocrysts have weak reverse zoning. Equilibrium (rim) compositions are $Wo_3En_{56-57}Fs_{41-40}$ for Minoan and Cape Riva, $Wo_3En_{53-55}Fs_{44-42}$ for Lower Pumice 1 and $Wo_3En_{50-54}Fs_{47-43}$ for Lower Pumice 2, becoming increasingly Fe-rich in that order. Augite compositions range from $Wo_{44}En_{41}Fs_{15}$ to $Wo_{40}En_{36}Fs_{24}$ (Fig. 4.8). Phenocryst rim compositions are Fs_{17} in the Minoan and Cape Riva, and about Fs_{22} in the two Lower Pumice rhyodacites.

Andesitic components of the Minoan Tuff and Lower Pumice 2

The Minoan and Lower Pumice 2 Plinian deposits contain ellipsoidal to tabular scoria clasts of andesitic to basaltic composition. Maximum abundances are found near the tops of the Plinian deposits (Fig. 4.4): 5% in the case of the Minoan and 30% in Lower Pumice 2. The majority of the Minoan scoria are dark grey and have SiO_2 contents of 56 to 58% and MgO of 3.3–4.4%, but there also occur rare pale grey clasts with 60–61% SiO_2 and about 2.5% MgO. One Minoan scoria with 52% SiO_2 and 4.7% MgO contains dark-grey, chilled inclusions within a lighter grey host. Lower

Table 4.2. *Analyses of representative juvenile clasts from eruptions of the second explosive cycle*

	Cape Thera	Middle Pumice		Vourvoulos		Upper Scoriae 1		Upper Scoriae 2		Cape Riva		Minoan				
Analysis	1	2	3	4	5	6	7	8	9	10	11	12	13	14	15	16
Sample	86-33	82-40	82-105	85-007	86-101	85-014	85-024	86-66	85-069	80-143	80-145	80-28	80-22b	80-24	80-26	80-25a
Unit*	A	A	B	A	B	A	C	A	D	A	A	A	A	A	A	A
Code	1	1	1,3	1	1	2	1	1	1	1,4	1,5	1,4	1,6	1,7	2,7	1,7
Major elements (normalized to 100%dry) (wt%)																
SiO_2	62.9	65.4	63.1	65.7	57.8	63.2	58.6	66.8	59.6	67.1	60.9	71.2	58.5	62.5	58.7	53.7
Al_2O_3	15.5	15.5	16.0	15.1	15.5	15.5	16.1	15.2	16.0	15.3	16.7	14.5	17.1	16.9	17.7	17.4
TiO_2	1.07	0.85	1.02	0.78	1.42	1.01	1.27	0.73	1.20	0.69	0.80	0.41	0.85	0.79	0.83	1.04
FeO	6.64	5.42	5.94	6.20	9.71	7.20	8.69	5.01	8.11	4.55	6.31	2.82	7.34	5.89	7.28	10.2
MgO	1.93	1.30	1.82	1.06	3.03	1.58	2.91	0.97	2.72	1.08	3.01	0.60	3.38	2.10	2.89	4.56
CaO	4.77	3.57	4.45	3.46	6.93	4.48	6.29	3.12	6.08	3.15	6.12	2.21	7.28	5.29	6.66	9.02
Na_2O	4.41	5.09	5.02	4.79	3.68	4.65	4.23	4.76	4.20	5.29	4.29	4.89	3.78	4.30	4.00	2.66
K_2O	2.33	2.57	2.27	2.54	1.51	1.96	1.45	3.09	1.65	2.44	1.61	3.16	1.48	1.91	1.58	1.17
MnO	0.14	0.16	0.15	0.17	0.20	0.18	0.19	0.14	0.19	0.18	0.16	0.08	0.15	0.13	0.15	0.18
P_2O_5	0.24	0.20	0.25	0.20	0.19	0.26	0.20	0.19	0.20	0.18	0.17	0.08	0.12	0.15	0.16	0.09
LOI	2.39	1.48	1.42	2.83	0.40	1.90	1.86	2.21	0.41	2.90	0.82	3.94	1.10	1.91	1.44	0.95
Sum	99.8	98.2	99.3	99.7	100.0	99.8	99.7	99.7	100.0	100.1	100.1	99.9	100.0	99.9	99.5	99.6
Trace elements (raw data) (ppm)																
Ba	387	403	393	420	292	370	239	379	295	451	292	561	405	502	448	334
Ce	63	48	59	55	25	56	57	61	48	53	37	51	39	56	46	45
Cr	bd	8	6	bd	11	bd	7	bd	8	bd	35	3	15	6	8	21
La	35	30	29	30	18	28	11	30	21	23	12	28	16	24	23	19
Ni	bd	9	bd	bd	bd	bd	bd	bd	bd	bd	9	bd	bd	bd	bd	bd
Nb	12	12	11	12	7	10	9	12	8	10	8	10	6	7	7	6
Rb	78	91	84	92	52	70	55	128	65	69	45	88	38	53	42	33
Sr	161	151	168	146	188	177	205	126	177	140	180	98	227	218	264	273
Th	12	19	12	16	10	12	10	18	10	12	12	16	6	14	10	9
V	113	56	82	30	260	69	175	32	176	28	128	21	211	99	168	360
Y	45	62	56	61	43	57	45	58	43	57	41	51	30	36	27	22
Zr	234	300	264	289	181	244	189	319	192	264	185	299	117	167	121	98

Major elements normalized to 100% volatile-free with all Fe as FeO. Loss on ignition (LOI) and oxide sums are taken from the raw analyses. Trace element abundances are from raw analyses. bd, below detection. Code numbers are as follows: 1, single class analysed; 2, multiple clasts analysed; 3, contains few % mm-sized accidental lithic fragments, 4, contains rare andesitic blebs; 5, contains minor admixed dacitic pumice; 6, grey cauliform scoria; 7, crystal-rich pumice.

* Eruption units are listed in Table 3.4.

Table 4.3. *Crystal contents of juvenile components of the Thera pyroclastics*

Eruption	Minoan			Cape Riva		Up Sc 2	Up Sc 1	Vourvoulos		M. Pum	C. Thera	Lower Pumice 2			Lower Pumice 1	
Samples	Rhyodac S79-81	Andesite 8 scoriae	Crystal-rich S80-24	Dacite S80-143	Andesite S80-145	Andesite 85042 85048	Andesite 85019 85022 85024	Dacite 8697	Andesite 861 86101	Andesite S79-30 S79-32b S79-129	Dacite 8647 8638	Rhyodac 8629	Andesite 4 scoriae	Basalt 2 scoriae	Rhyodac S79-88	Andesite S79-89
% Crystals*	10	–	50	15–20	12	10–30	3–14	3	3–25	10–15	13–22	6	–	–	3	45
% Crystals†	–	20–40	–	–	–	–	–	–	–	–	–	–	13–24	68–70	–	–

* Weight %. Calculated by mass balance using whole-rock and glass compositions.
† Volume %. Measured by point counting, vesicle-free.

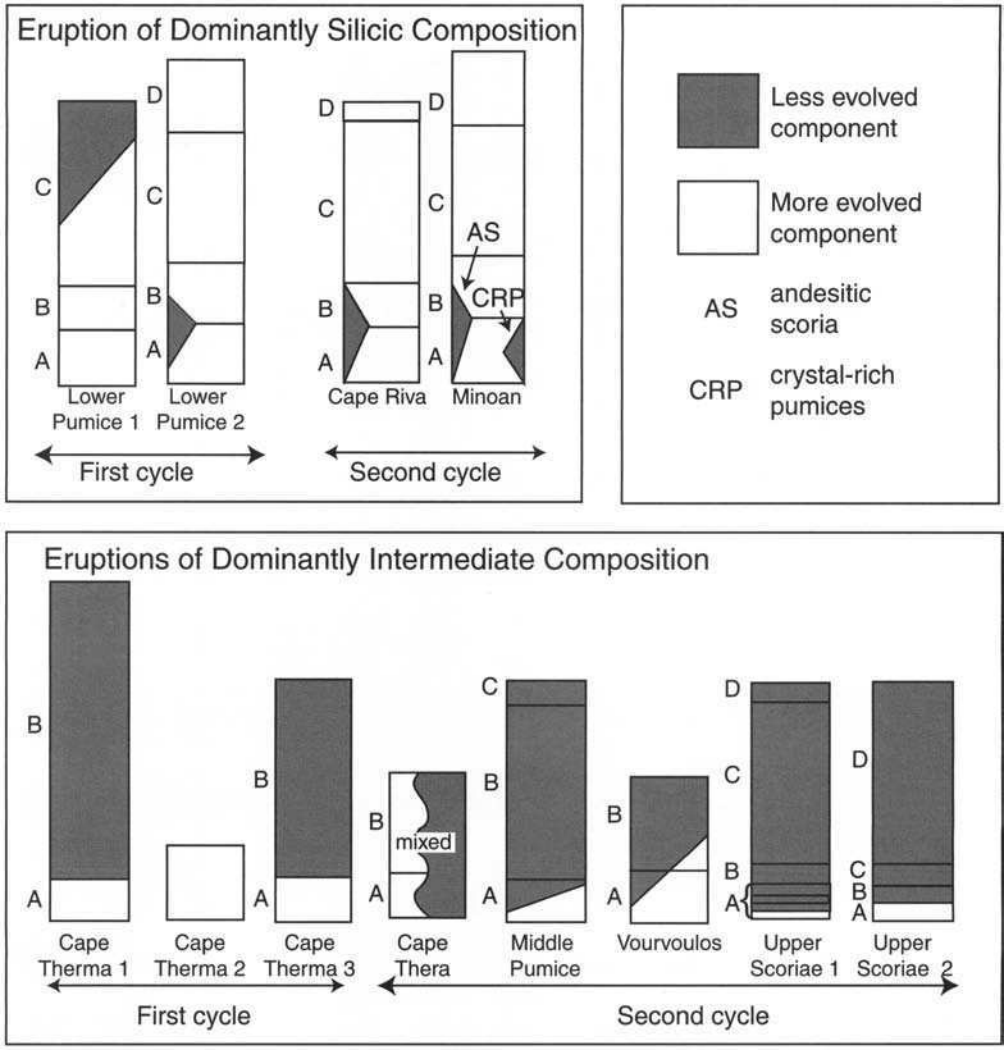

Fig. 4.3. Schematic representation of compositional zoning in the Thera pyroclastics. Each column shows qualitatively the proportions of magma components as a function of position in the sequence.

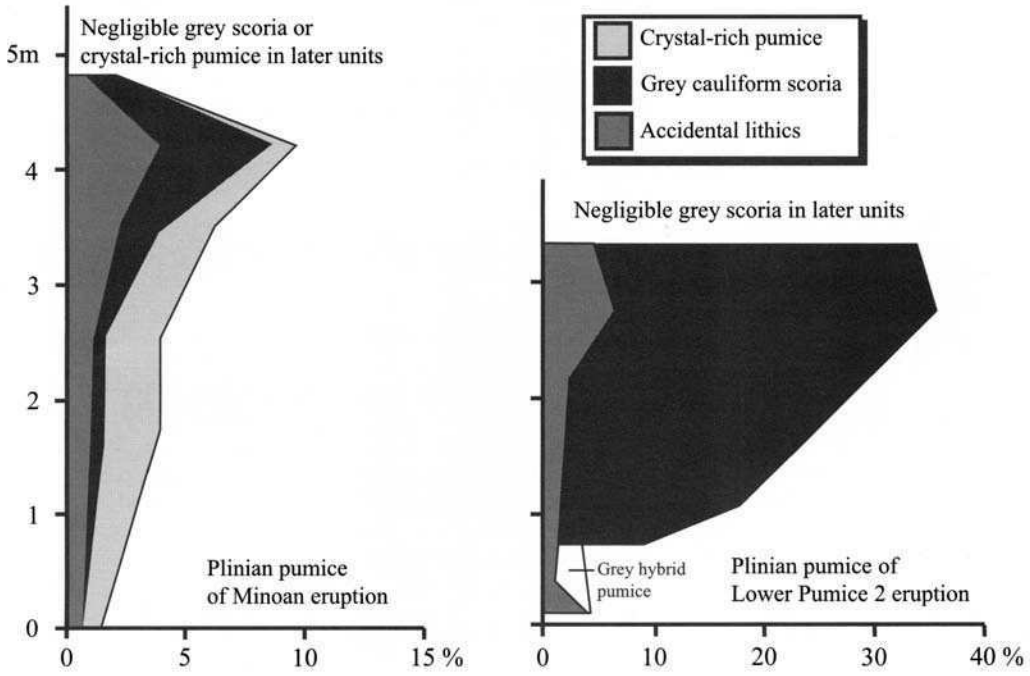

Fig. 4.4. Measured profiles of component abundances in the Plinian deposits of Lower Pumice 2 and the Minoan Tuff. The remaining volume in each case is rhyodacitic pumice. The Lower Pumice 2 profile was measured below the northern end of the Phira pumice quarry, and the Minoan profile at the southern end of the same quarry.

Pumice 2 scoria are dark grey and more primitive, with 47–56% SiO_2 and 4–11% MgO.

The scoria contain macroscopic crystals and crystal aggregates set in a vesicular, glassy andesitic groundmass of plagioclase, pyroxene, and opaques with the acicular, hopper, and branching crystal morphologies characteristic of rapid chilling (Fig. 4.5c). The content of macroscopic crystals is typically between 10 and 40 vol%, although some highly crystalline Lower Pumice 2 scoria contain up to 70 vol% (Table 4.6). Macroscopic crystals have the following three occurrences.

Table 4.4. *Average compositions of silicic pumices from the Minoan, Cape Riva, Lower Pumice 2 and Lower Pumice 1 eruptions*

	Analytical Precision*	Minoan	Cape Riva	Lower Pumice 2	Lower Pumice 1
No. anal.	11	11	18	12	5
Major elements (recalculated to 100% dry) (wt%)					
SiO_2	71.2 (0.1)	70.9 (0.3)	66.8 (0.3)	69.1 (0.6)	68.8 (0.6)
Al_2O_3	14.5 (0.1)	14.6 (0.1)	15.4 (0.1)	15.1 (0.2)	15.1 (0.2)
TiO_2	0.41 (0.01)	0.44 (0.02)	0.73 (0.03)	0.47 (0.03)	0.55 (0.03)
FeO	2.8 (0.0)	2.9 (0.2)	4.7 (0.1)	3.3 (0.2)	3.7 (0.1)
MgO	0.60 (0.02)	0.66 (0.09)	1.1 (0.1)	0.71 (0.12)	0.75 (0.07)
CaO	2.2 (0.0)	2.3 (0.1)	3.1 (0.1)	2.1 (0.3)	2.3 (0.1)
Na_2O	4.9 (0.1)	4.9 (0.1)	5.3 (0.2)	5.8 (0.5)	5.2 (0.8)
K_2O	3.1 (0.1)	3.1 (0.1)	2.5 (0.1)	3.3 (0.1)	3.4 (0.1)
MnO	0.08 (0.01)	0.08 (0.01)	0.15 (0.01)	0.11 (0.01)	0.13 (0.01)
P_2O_5	0.08 (0.01)	0.08 (0.01)	0.18 (0.01)	0.10 (0.01)	0.12 (0.01)
Trace elements (raw data) (ppm)					
Ba	538 (10)	556 (17)	468 (18)	486 (30)	488 (39)
Ce	49 (4)	48 (7)	48 (7)	47 (6)	57 (5)
La	27 (2)	28 (2)	27 (3)	31 (6)	30 (6)
Rb	85 (1)	97 (7)	76 (4)	102 (6)	113 (9)
Sr	95 (1)	98 (5)	141 (6)	100 (8)	109 (2)
Th	16 (1)	19 (3)	13 (3)	18 (3)	22 (4)
V	21 (2)	27 (6)	39 (7)	18 (8)	19 (6)
Y	44 (1)	48 (2)	58 (2)	56 (2)	54 (7)
Zr	287 (2)	307 (16)	272 (10)	316 (17)	332 (16)

* Analytical precision determined by eleven repeated analyses on Minoan rhyodacite pumice sample S80-28. All analyses carried out by XRF at the University of Nottingham and recalculated 100% dry with all Fe as FeO. Figures in brackets are single standard deviations on the averages.

(1) Euhedral to subhedral crystals that occur individually or in small glomerocrysts and are probably true phenocrysts. These include plagioclase, clinopyroxene, olivine, orthopyroxene, and magnetite in the Minoan scoria, and plagioclase, olivine, and clinopyroxene in Lower Pumice 2.

(2) Fragments of cognate gabbro and olivine gabbro up to 5 mm in diameter and containing as many as 100 or more crystals. In the Minoan scoria the fragments are consistently holocrystalline and lack interstitial glass, showing that the gabbros were at subsolidus temperatures prior to disruption. Phase assemblages in the fragments are ol + plag + cpx, plag + cpx, and plag + cpx + mt. At least some of the gabbros were cumulates because they contain up to 60% modal olivine. A weakly developed igneous fabric is also evident in some aggregates. Gabbro fragments in Lower Pumice 2 consist of plag + ol + cpx ± mt. Some have openwork cumulate textures with 65–70% crystals.

(3) Individual xenocrysts formed by mechanical disaggregation of the aggregates.

There are no systematic compositional differences between gabbro fragments and phenocrysts in either of the two deposits. The occurrence of openwork cumulus textures and the absence of visible hydrothermal alteration suggests that the gabbros were cognate in origin.

Olivines in Minoan scoria are Fo_{70-79} and normally zoned. Most occur either in gabbro fragments or as anhedral xenocrysts derived from the disintegration of such fragments. Those occurring in olivine-rich gabbro have higher Fo values than ones in gabbro fragments that are olivine-poor. Clinopyroxenes have compositions of $Wo_{42-43}En_{38-44}Fs_{19-15}$. Orthopyroxene ($Wo_{27-28}En_{68-69}Fs_{29-27}$) occurs as large subhedral bladed phenocrysts, and is rare in the gabbro fragments. Plagioclases in the gabbro fragments range in composition from An_{90} to An_{70} and are unzoned or normally zoned. Skeletal forms with sieved zones crowded with glass and mineral inclusions are common. Clean, unzoned crystals are particularly common in ol-rich gabbro fragments. Euhedral to subhedral crystals that are probably true phenocrysts have cores as calcic as An_{83} and rims of An_{53-55}. Laths of hornblende are conspicuous in the groundmasses of the rare Minoan scoria with about 60% SiO_2.

Minerals in the more primitive scoria of Lower Pumice 2 are consistently less evolved than those in the Minoan. Plagioclases range from An_{90} to An_{94}, with rare examples up to An_{97}. Olivine compositions range from Fo_{82} to Fo_{72}. Clinopyroxenes are magnesian ($Wo_{42}En_{42}Fs_{16}$ to $Wo_{45}En_{45}Fs_{10}$) and have high Al_2O_3 contents (2.5–4 wt%). Orthopyroxene is not present and hornblende is absent from the groundmass.

The diameters of the scoria clasts range from <1 to 26 cm, although a few centimetres is typical of most. Vesicularities range from 36 to 65% and increase with increasing silica content. Clast morphologies are typically ellipsoidal, although tabular shapes are also common. The outer surfaces of the clasts have cauliform, complexly crenulated textures. Some tabular clasts have well developed surface grooves and flow lineations. Others have distinctive rectilinear shapes suggestive of brittle fracturing of thin, chilled melt sheets. Most scoria clasts occur separately, but occasional examples occur with thin adhering skins of silicic pumice, or contained within pumice, suggesting immersion in the silicic host prior to eruption.

We interpret the scoria of the Minoan and Lower Pumice 2 as andesitic magma injected into their respective silicic magma reservoirs shortly before eruption. During injection, the andesites ripped up and entrained pieces of cognate cumulate gabbro from the reservoir floors and sides. The grooved, tabular scoriae may be thin sheets of quenched andesitic magma drawn up into the host rhyodacite and released during eruption and fragmentation.

Quenched blebs of andesite

Millimetre-sized quenched blebs of mafic magma occur dispersed ($\ll$1%) through the pumices of all four dominantly silicic eruptions. They have micro-crenulated surface textures, and many have a single crystal or xenocrystic fragment at their centres (Fig. 4.5d). They are interpreted as small fragments of chilled mafic magma mixed into their rhyodacitic hosts, and provide evidence for the pre-eruptive presence of mafic juvenile components in the magma chambers of the four large silicic eruptions.

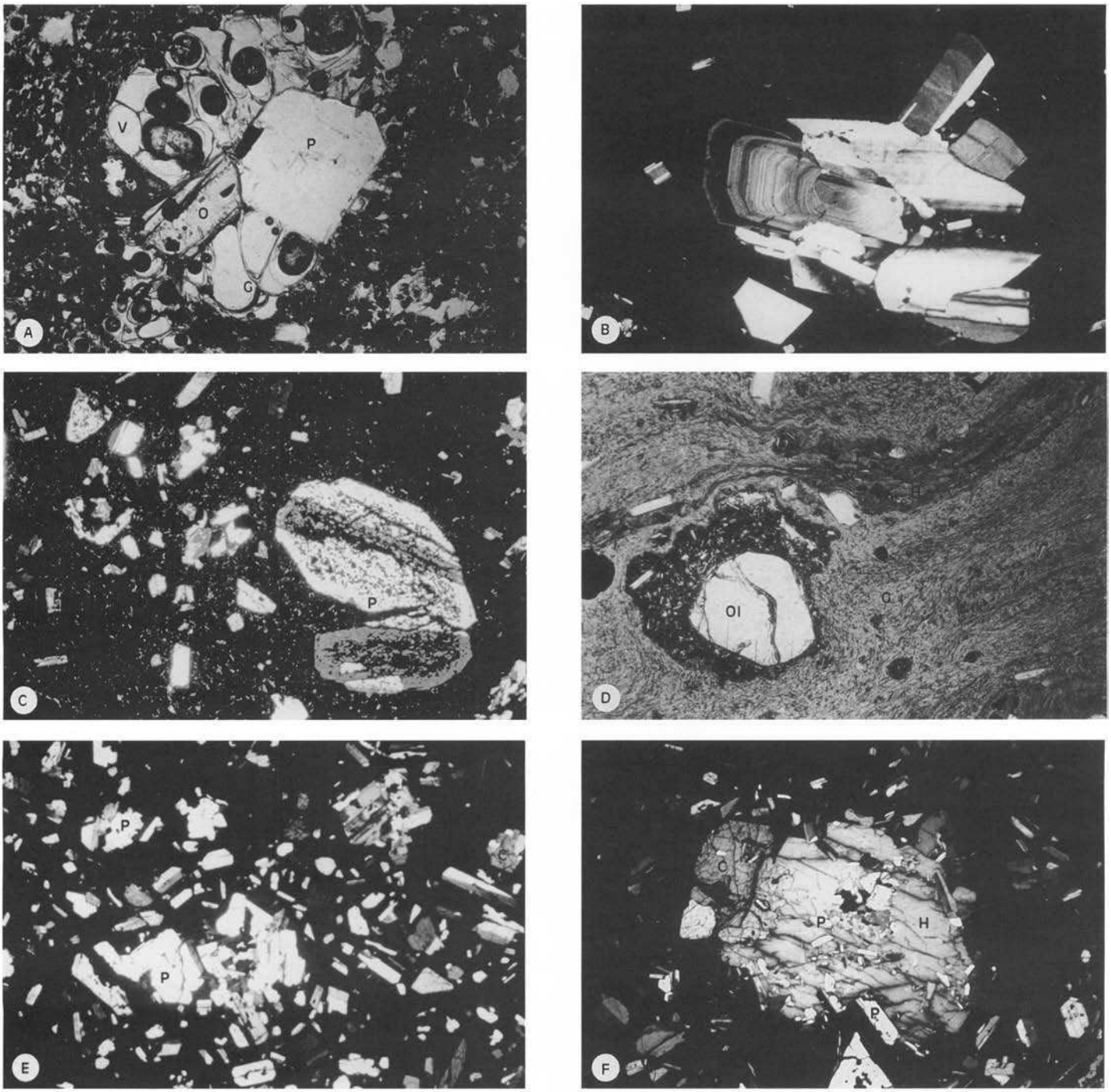

Fig. 4.5. Photomicrographs of samples from the dominantly silicic eruptions. (**a**) Rhyodacitic pumice of the Cape Riva Tuff. Phenocrysts of plagioclase (P) and orthopyroxene (O) set in vesicular glass (G). One vesicle is marked V. Sample S80-144. Plane-polarized light. Width of field 3 mm. (**b**) Cluster of plagioclase phenocrysts in Minoan rhyodacite. Sample 99-5-17. Width of field 5 mm. Crossed polars. (**c**) Sieved plagioclase phenocryst (P) in andesitic scoria of the Minoan Tuff. Sample CS-8. Width of field 5 mm. Crossed polars. (**d**) Quenched andesitic bleb with olivine phenocryst (Ol) in Cape Riva rhyodacite. The sample (S80-82) is a fiamme from a welded ignimbrite, and the glass (G) is non-vesicular. Note the streak of brown hybrid glass (H). (**e**) Minoan crystal-rich pumice with microphenocrysts and crystal aggregates of plagioclase (P), clinopyroxene (C), and oxides set in vesicular glass. Sample S820-27. Width of field 5 mm. Crossed polars. (**f**) Hornblende containing inclusions of plagioclase and attached to a clinopyroxene (C). Minoan crystal-rich pumice S82-27. Width of field 5 mm. Crossed polars.

Andesitic components of the Cape Riva and Lower Pumice 1 eruptions

The andesitic components of Cape Riva and Lower Pumice 1 occur as discrete scoria clasts and as streaks in banded pumices. The scoria are characterized by their glassy nature and lack the microcrystalline groundmasses typical of the chilled cauliform enclaves and blebs of Lower Pumice 2 and the Minoan.

Cape Riva andesite has 61–62% SiO_2 and 3% MgO and occurs as discrete scoria clasts in the upper part of the Plinian deposit and at the base of the welded ignimbrite. It contains 12% crystals of plag + ol + cpx set in brown dacitic glass with 63.5% SiO_2 and 1.4% MgO. Plagioclase compositions range from An_{70} to An_{96} (Fig. 4.6 and 4.7), with a discrete population of euhedral, unzoned grains of An_{90-96}. Olivines are compositionally uniform (Fo_{84}). Augites occur sparsely as microphenocrysts of composition $Wo_{40}En_{41}Fs_{19}$. No orthopyroxene has been observed.

The occurrence of fresh, unzoned anorthitic plagioclase and forsteritic olivine (Fo_{84}) set in dacitic glass is indicative of disequilibrium. Euhedral olivine phenocrysts (Fo_{84}) occur in phenocryst-poor basalts with about 52% SiO_2 and 6% MgO, such as the Balos cinder cone (Huijsmans 1985). Millimetre-sized quenched

Table 4.5. *Representative glass analyses of the Minoan, Cape Riva, Lower Pumice 2 and Lower Pumice 1 eruptions*

	Minoan						Cape Riva									L. Pum 2	Lower Pumice 1		
	Rhyodacite			Crystal-rich			Dacite								Andesite	Rhyodacite	Rhyodacite		Andesite
Sample	S80-28	S82-34b	S79-81	S79-107	S80-24	S80-143	S80-144	S80-145	S80-8	S80-9	S80-11	S80-139	S80-142	S80-186	S80-145a	8629	8663	S79-88	S79-89
Unit*	A	B	D	D	A	A	A	A	B	B	B	C	C	D	A	C	B	C	C
No. anal.	7	12	10	6	8	12	9	5	6	6	6	6	11	5	9	1	15	8	6
SiO_2	73.44(50)	73.44(40)	73.80(44)	74.08(25)	75.02(70)	71.65(30)	71.14(58)	71.00(36)	71.96(30)	71.44(22)	71.59(27)	71.23(26)	71.41(35)	71.70(42)	63.54(40)	71.67	72.62(60)	71.81(36)	61.92(56)
Al_2O_3	14.46(54)	13.98(23)	14.09(21)	13.92(19)	13.71(16)	14.56(29)	15.08(45)	14.41(19)	14.29(13)	14.35(25)	14.61(17)	14.28(20)	14.09(30)	15.03(50)	16.40(37)	14.74	15.37(30)	15.60(17)	16.61(42)
TiO_2	0.31(08)	0.34(06)	0.28(04)	0.32(04)	0.27	0.37(05)	0.37(08)	0.36(05)	0.42(12)	0.42(11)	0.44(08)	0.44(06)	0.42(07)	0.38(06)	0.67(12)	0.29	0.43(05)	0.40(08)	1.00(17)
FeO	2.05(10)	2.14(24)	1.94(21)	2.00(09)	1.19(11)	2.76(18)	3.00(19)	3.10(08)	3.15(22)	2.99(18)	3.09(12)	3.03(17)	3.00(14)	2.79(22)	6.01(22)	2.53	3.05(20)	3.42(16)	6.61(36)
MgO	0.25	0.29(04)	bd	bd	0.40	0.43(02)	0.42(08)	0.75	bd	0.45	0.42	0.49	0.46	bd	1.40(30)	0.32	0.11	0.42	1.69(06)
CaO	1.56(17)	1.46(15)	1.47(14)	1.48(18)	0.95(07)	1.68(15)	1.80(19)	1.83(14)	1.69(14)	1.88(09)	1.33(18)	1.78(06)	1.76(13)	1.76(03)	5.48(24)	1.36	1.89(10)	1.89(12)	5.41(41)
Na_2O	4.81(26)	4.99(15)	5.07(17)	4.96(08)	4.69(62)	5.54(34)	5.28(21)	5.64(39)	5.54(18)	5.53(21)	5.47(35)	5.83(12)	5.92(35)	5.53(10)	4.69(22)	5.63	3.16(30)†	3.03(27)†	5.02(77)
K_2O	3.16(09)	3.36(09)	3.36(12)	3.28(05)	3.77(08)	3.02(09)	2.93(08)	2.92(14)	2.94(07)	2.95(08)	3.05(07)	2.92(08)	2.94(11)	2.80(03)	1.80(10)	3.46	3.37(10)	3.45(26)	1.75(33)

All analyses carried out by electron microprobe except for Lower Pumice 2 glass 8629 which is an XRF analysis of a glass separate. Glass analyses carried out on the University of Cambridge energy dispersive electron microprobe at 20 kV accelerating voltage. Beam current of 10 nA and a 10–15 μm rastered beam. Count time was 80 seconds. Analyses corrected for Na loss. All analyses recalculated 100% dry assuming all Fe as FeO. Figures in brackets are one standard deviation on the average; thus 73.44(50) reads 73.44 ± 0.50.

bd: below detection.

* Eruption units are listed in Table 3.4.

† Low percentages suggest some Na loss in these samples during microprobe analysis.

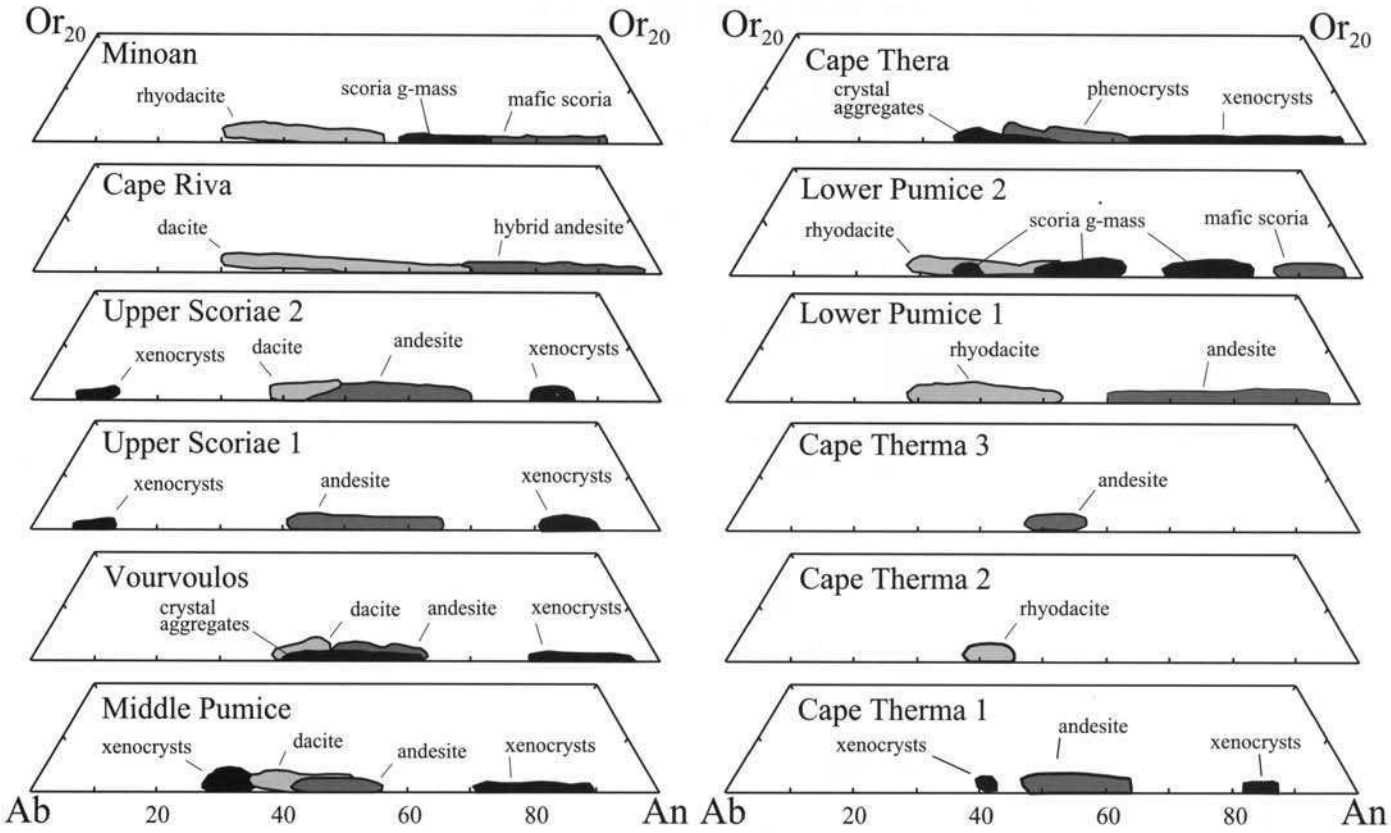

Fig. 4.6. Plagioclase compositions in the Thera pyroclastics.

blebs of mafic magma containing An_{90-96} plagioclase and Fo_{72-84} occur within Cape Riva silicic pumices. We propose that the andesite is a hybrid formed by mixing of basaltic magma with Cape Riva dacite. A mix of 57% dacite plus 43% typical Santorini basalt reproduces well the bulk composition of the hybrid scoria (Table 4.7). Eruption must have occurred some time after mixing since phenocrysts from the dacitic component are not observed (presumed resorbed) and the hybrid glass is homogeneous.

Andesitic scoria occur abundantly at the top of the Lower Pumice lag breccia (Fig. 4.3). They have silica contents of 53.5 to 58%, MgO contents of 2.7 to 3.8%, and glass with 62% SiO_2 and 1.7% MgO (Tables 4.1 and 4.5). Phenocrysts of plagioclase, clinopyroxene, olivine, orthopyroxene, and magnetite make up 45% of the scoriae (Table 4.3). Plagioclase compositions are An_{60-95}, but most lie in the range An_{77-95}. Normal, reverse, and patchy zoning are present. Olivine phenocrysts (Fo_{71-75}) are in equilibrium with the observed whole-rock compositions if a partition coefficient of about 0.30 is assumed (Roeder & Emslie 1970). Clinopyroxenes are mostly of composition $Wo_{46-42}En_{42}Fs_{12-16}$. However, there also occur occasional large cpx crystals that are reversely zoned with cores as Fe-rich as $Wo_{41}En_{39}Fs_{20}$ and rims of $Wo_{47}En_{41}Fs_{12}$. Since the core compositions resemble cpx in the associated rhyodacitic pumice, the scoria are probably hybrid with a small admixed silicic component. Orthopyroxene ($Wo_3En_{67}Fs_{30}$) occurs sparsely in the scoria of Lower Pumice 1.

Crystal-rich pumices

This type of pumice occurs only in the Minoan Plinian deposit. It has a maximum abundance of a few percent in the middle of the deposit and disappears at the top (Figs. 4.3 and 4.4). The pumices contain phenocrysts and abundant microphenocrysts of plagioclase, augite, hypersthene, magnetite and ilmenite, with or without poikilitic hornblende, set in vesicular silicic glass (Figs. 4.5e and f). The bulk-rock silica contents of these pumices range widely (53–63%). A modal and textural gradation exists between the crystal-rich pumices and co-erupted similar granitoid nodules with <1% glass (Druitt 1983). Crystal-rich pumice is interstreaked with typical Minoan rhyodacite in rare banded pumices, showing that the former was molten at the time of eruption.

Druitt *et al.* (1989) interpreted the crystal-rich pumices as samples of the crystallizing boundary layer of the Minoan magma chamber. However, our new data do not support this interpretation. First, the pumices and nodules have trace element signatures, in particular high Ba contents and high Ba/Rb ratios, that clearly distinguish them from Minoan rhyodacite (Chapter 6). Second, uranium-series disequilibrium studies (Chapter 7) suggest that the granitoid nodules, many of which are hydrothermally altered, crystallized more than 100 000 years ago. We interpret the crystal-rich pumices as samples of partially melted granitoid mush from the roof of the Minoan magma chamber, which was stoped into the rhyodacite during the Plinian phase of the eruption. The ability of large reservoirs of silicic magma to partially melt and remobilize their wall rocks is well known (e.g., Bacon & Druitt 1988; Bacon 1992).

Eruptions of dominantly intermediate composition

Cape Thermas 1 and 3

These deposits are petrologically similar and are described together. Both consist of pumice fall horizons overlain by pyroclastic flow deposits and spatter agglomerates. Both eruptions exhibit subtle normal compositional zoning. In Cape Therma 1, pumices in the fall deposit have 61.8 to 62.5% SiO_2 and those in the pyroclastic flows have 59.3–61.0%. In Cape Therma 3 the figures are 62.6–64.8% for the fall deposit and 60.9–61.9% SiO_2 for the pyroclastic flows, lithic breccias and spatter agglomerate. In Cape Therma 1 plagioclase (An_{47-63}) coexists with augite ($Wo_{41}En_{42-41}Fs_{17-18}$), orthopyroxene ($Wo_{3-4}En_{65-62}Fs_{31-34}$), and oxide phases. Cape Therma 3 contains plagioclase (An_{46-55}), augite ($Wo_{40}En_{40}Fs_{20}$), and orthopyroxene ($Wo_3En_{65-61}Fs_{32-36}$), and oxides. Xenocrysts of calcic bytownite and forsteritic olivine occur in both deposits.

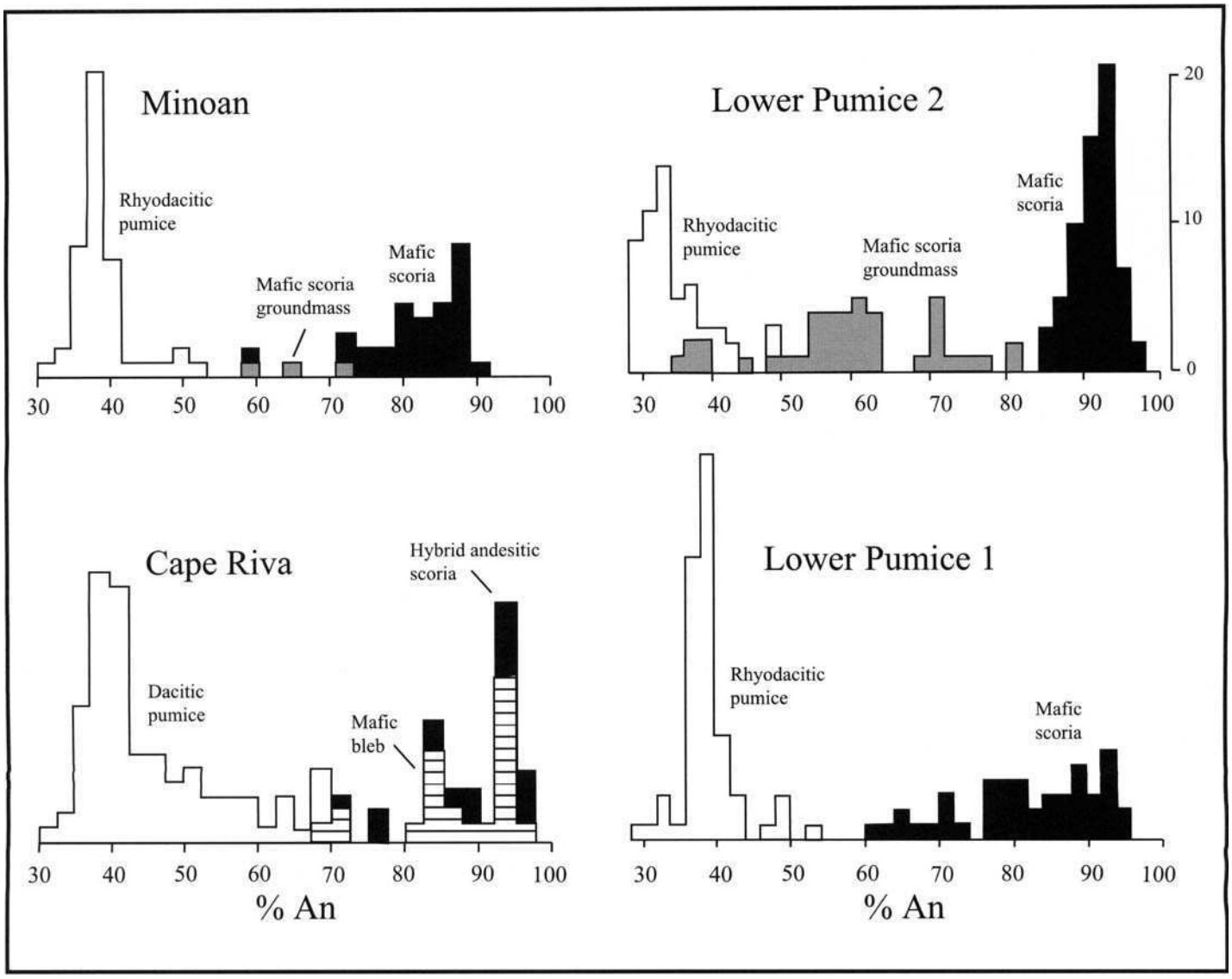

Fig. 4.7. Histograms of plagioclase composition in the four dominantly silicic tuffs of the Thera pyroclastics.

Cape Thera

The Cape Thera Tuff consists of a basal pumice fall deposit overlain by a thick ignimbrite with laterally equivalent surge beds. The base of the fall deposit is dominated by dense, grey pumice, the middle by paler, more vesicular, pumice, and the top by heterogeneous streaky clasts (Fig. 4.9a). The ignimbrite contains abundant pumice and scattered dense scoria clasts. Overall the compositional range is narrow (60.6–62.9% SiO_2), with the less-evolved components in the fall deposit and more evolved ones in the ignimbrite. The phenocryst phases are plagioclase, augite, orthopyroxene, olivine, magnetite and apatite. The glasses are heterogeneous and two types have been identified (Table 4.8). Type 1 is a yellow-brown glass of composition 62–64% SiO_2 containing scattered plagioclase microlites. Type 2 is a paler, more evolved vesicular glass (65–68% SiO_2) containing abundant lava fragments, crystalline inclusions, and flow-aligned microlites. Patchy, turbid areas and streaks of both glasses occur together in juvenile clasts. Type 1 glass is dominant in the grey pumices of bulk composition 61–62% SiO_2 at the base of the fall deposit.

Plagioclase phenocrysts occur as two populations. Isolated, euhedral grains up to 4 mm exhibit minor normal zoning (An_{55} to An_{44}) and are similar in composition to microlites and microphenocrysts in the less evolved (type 1) glass. A slightly more sodic population (An_{38} to An_{45}) of smaller grains exhibits reverse zoning and is particularly common in the more evolved pumices and more silica-rich (type 2) glass. Some xenocrysts with cores of An_{95-89} and rims of An_{61-42} also occur. Augite compositions lie in the range $Wo_{42-37}En_{44-43}Fs_{14-20}$, with both normal and reverse zoning. Orthopyroxenes are in the range $Wo_4En_{67-59}Fs_{27-37}$. Olivines occur as small, euhedral crystals of Fo_{70-71}.

The Cape Thera chamber contained two magmas of slightly different composition: one with glass of about 62% SiO_2 (type 1) and plagioclase of An_{55}, and the other with glass of about 68% SiO_2 (type 2) and plagioclase of An_{38}. Some time before eruption these magmas underwent variable degrees of mixing, generating hybrid and mingled magmas. Both types of plagioclase phenocryst became zoned to a common composition of about An_{45}. Significant mingling probably also occurred during eruption and withdrawal from the chamber. Cape Thera ejecta also contain abundant mm-sized crystal clots of plagioclase (An_{44-37}), augite ($Wo_{41-38}En_{38-37}Fs_{21-25}$), orthopyroxene ($Wo_4En_{54-51}Fs_{42-45}$), magnetite, and apatite set in silicic glass (70% SiO_2; Table 4.7). These clots are probably fragments of cumulate mush from the chamber roof and walls.

Middle Pumice

Middle Pumice contains two juvenile components separated by a small compositional gap: a white to pink, dacitic pumice, which dominates the base of the Plinian deposit, and a greenish scoria of transitional andesite/dacite composition abundant in the upper two thirds of the Plinian deposit and in the overlying lithic breccia. Plots

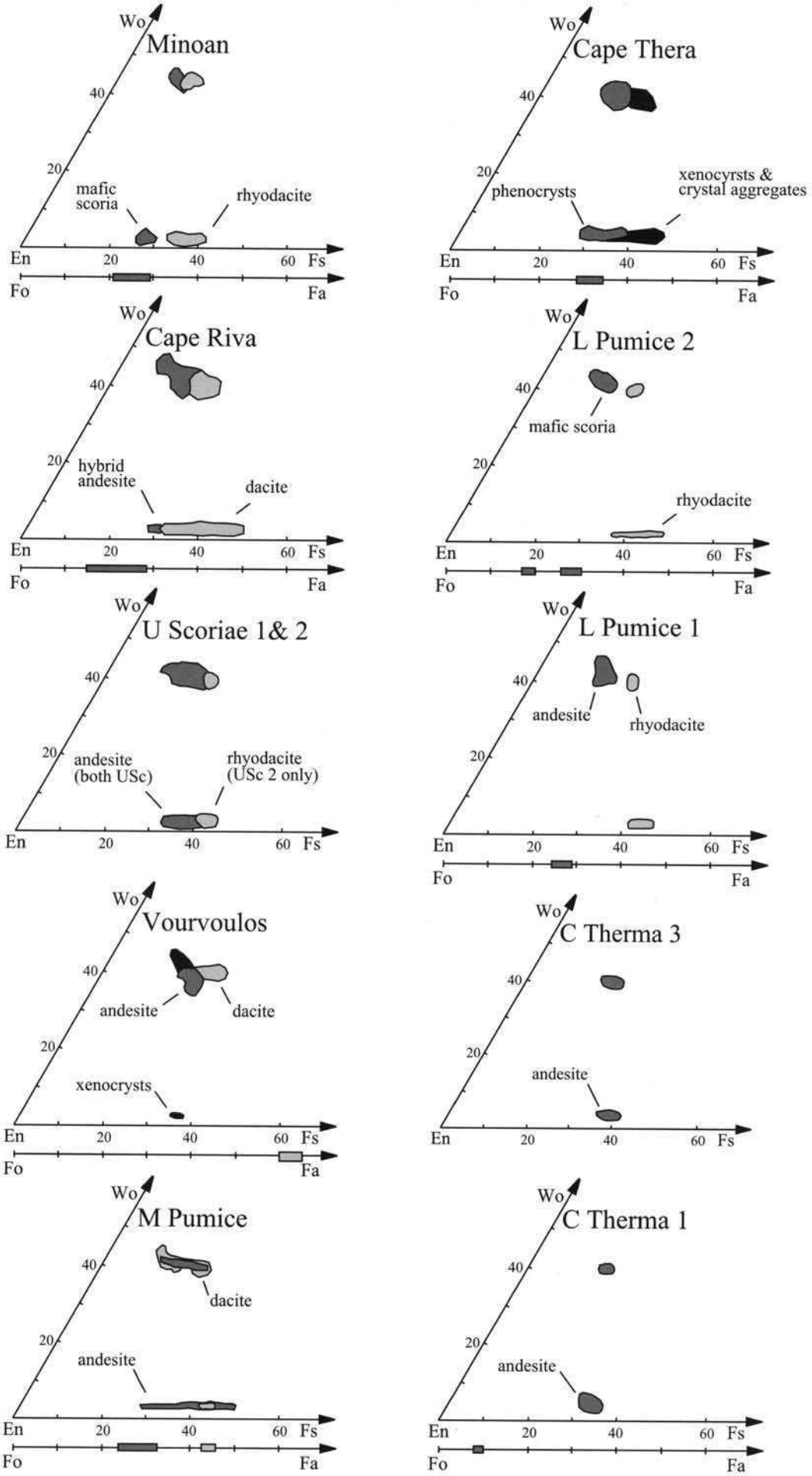

Fig. 4.8. Pyroxene and olivine compositions in the Thera pyroclastics.

Table 4.6. *Modal composition of cauliform scoria clasts of the Minoan and Lower Pumice 2 eruptions*

	Minoan								Lower Pumice 2					
Sample	CS3	CT6	CS2	CT4	CT3	CTI	CT5	CS1	S86-36	S86-16a	S86-59	S86-16b	S86-37	S86-51
Scoria % SiO_2	56.6	56.7	56.7	57.0	57.6	58.1	58.2	60.2	47.4	48.8	54.9	55.7	na	na
Plagioclase	22.9	29.0	16.1	17.8	20.4	16.6	21.0	15.5	67.7	36.4	14.8	9.3	9.6	7.1
Clinopyroxene	5.7	7.5	2.0	7.5	4.7	3.4	2.4	9.0	0.1	19.0	5.8	3.7	2.3	3.6
Olivine	2.3	0.3	2.5	0.7	1.4	1.3	0.3	0.6	3.0	12.3	2.6	1.3	1.2	2.0
Orthopyroxene	–	–	0.5	–	–	–	–	–	–	–	–	–	–	–
Fe–Ti oxides	1.3	2.2	0.4	0.7	0.5	0.8	0.3	0.9	–	–	0.3	0.2	tr	tr
Groundmass	67.8	61.0	78.5	73.3	73.0	77.9	76.0	74.0	29.2	32.3	76.5	85.5	86.9	87.3

na: not analysed.
tr: trace.

Table 4.7. *Least squares mixing calculation of the production of Cape Riva hybrid andesite*

	Cape Riva Rhyodacite	Mafic component	Hybrid andesite	
	Observed (18)*	Sample SI101 (Huijsmans 1985)	Calculated	Observed (3)*
Anal.	A	B	0.566A + 0.434B	
SiO_2	66.8	52.59	60.69	60.7
Al_2O_3	15.4	18.3	16.68	16.6
TiO_2	0.73	0.91	0.81	0.84
FeO	4.7	8.09	6.18	6.5
MgO	1.1	5.84	3.16	3.1
CaO	3.1	10.46	6.31	6.2
Na_2O	5.3	2.83	4.23	4.2
K_20	2.5	0.79	1.76	1.6
MnO	0.15	0.17	0.16	0.15
P_2O_5	0.18	0.12	0.15	0.15
$\sum r^2$			0.15 (majors only)	
Ba	468	147	329	331
Ce	48	22	37	45
Rb	76	25	54	49
Sr	141	231	180	182
Th	13	4	9	12
V	39	250	131	129
Y	58	19	41	44
Zr	272	107	200	189
% crystals†	–	28.5	12	12
Fo obs.	–	85-60	–	84
Fo calc.†	–	83	–	–
An obs.	–	94-75	–	96-70
An calc.†	–	92	–	–

* Figure in brackets gives the number of analyses averaged.
† Crystal content based on observed modal value for mafic component and natural hybrid andesite. Figure for artificial hybrid andesite is calculated. Fo content of olivine in equilibrium with magma composition calculated using $K_d = 0.30$ (Roeder 1974). A content of plagioclase calculated using $K_d = 5.5$ at 2 kbar pressure (Sisson & Grove 1993). 10% of total Fe assumed to be Fe^{2+}.

of ejecta composition against stratigraphic height display a continuous zoning profile (Fig. 4.10). Banded pumice is common and even clasts that are visually homogeneous in the field prove to be subtly banded in composition when analysed with the electron microprobe. Strong compositional zoning occurs in the Plinian deposit, whereas scoria clasts in the overlying lithic breccias are compositionally uniform.

Vertical variations in glass composition are shown in Fig. 4.11 using total FeO content as a differentiation index. Glasses of pumices at the base of the Plinian layer are uniform (4.5% FeO; 68% SiO_2). Those in scoria clasts at the top of the Plinian deposit and in the lithic breccias are similarly homogeneous, but less evolved (5.5% FeO; 65–66% SiO_2). At intermediate levels of the Plinian deposit interstreaked glasses occur with a wide range of compositions from 62% SiO_2 and 7.0% FeO to 71% SiO_2 and 3.5% FeO. These represent andesitic and rhyodacitic liquids with compositions more extreme than those of the two principal juvenile components.

Dacitic (65–67% SiO_2) pumices from the Plinian deposit have 15% phenocrysts of reversely zoned plagioclase (cores An_{38-45}; rims An_{43-53}), compositionally variable augite ($Wo_{40-43}En_{37-46}Fs_{11-23}$), orthopyroxene ($Wo_3En_{55}Fs_{42}$), magnetite, and ilmenite. At the base of the Plinian deposit there also occur abundant chips of dacitic

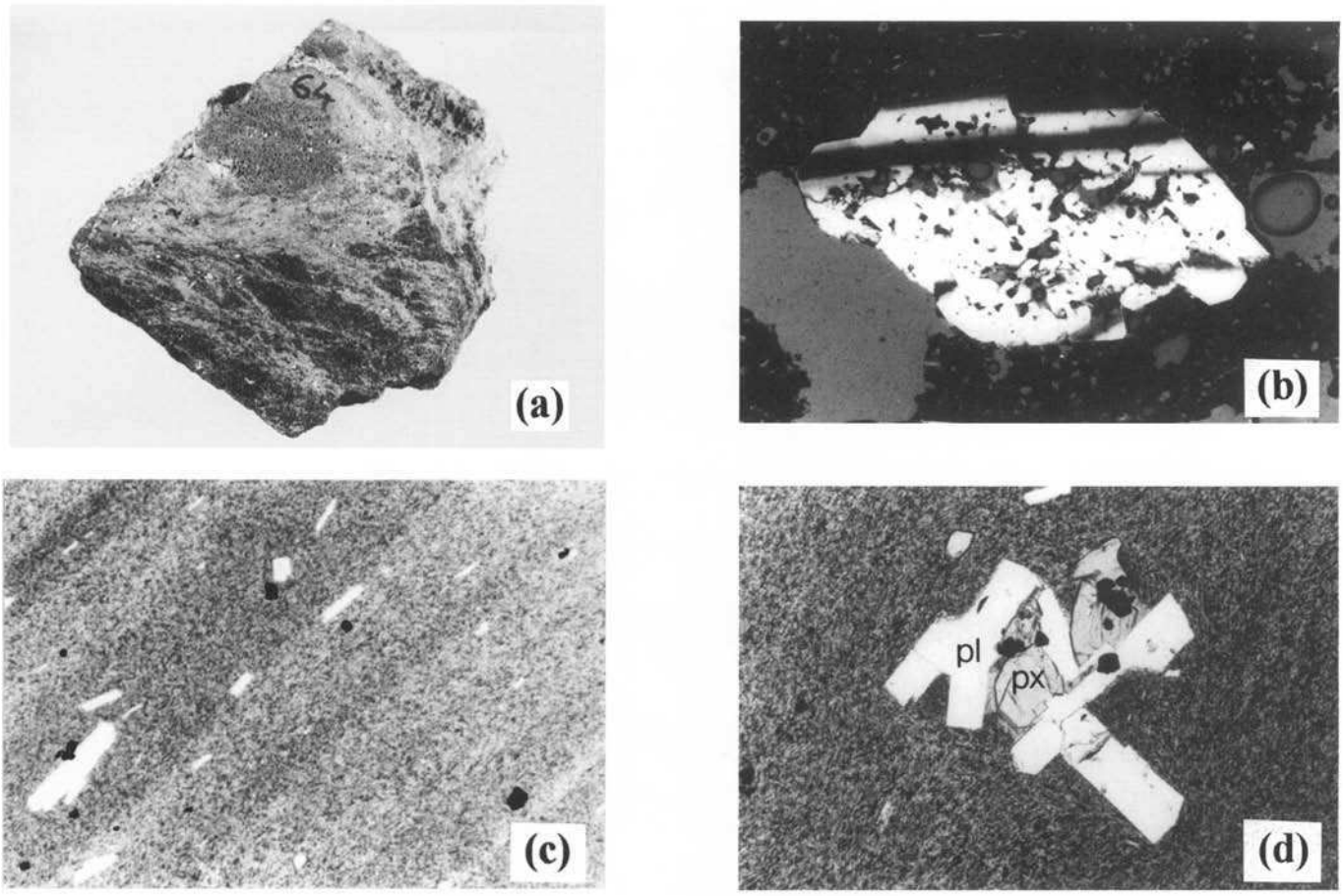

Fig. 4.9. Photomicrographs of samples from the dominantly intermediate eruptions. (**a**) Banded pumice clast from the Cape Thera Tuff. Sample 85064. (**b**) Plagioclase xenocryst in a scoria clast from Upper Scoriae 1. Sample 85023. The crystal is 3 mm long. (**c**) Obsidian clast from the Vourvoulos Tuff, showing subtle flow banding and flow-aligned plagioclase phenocrysts. The field of view is 8 mm. (**d**) Crystal aggregate of plagioclase (pl), augite (px), magnetite, and interstitial glass in an obsidian clast from the Vourvoulos Tuff. Sample 85224. The field of view is 3 mm.

obsidian. These have a similar phenocryst assemblage and glass composition to the dacitic pumices (Table 4.8). They are either chilled samples of Middle Pumice magma or fragments of precursory lavas destroyed by the eruption.

The andesitic scoria from the top of the Plinian deposit and from the lithic breccia have 63–64% SiO_2 and 15 wt% crystals. Plagioclase phenocrysts are normally zoned from cores of An_{55} to rims of An_{43-47}. Augites resemble those in the dacitic pumices ($Wo_{40-43}En_{37-46}Fs_{11-23}$). Orthopyroxene is more diverse compositionally ($Wo_3En_{49-69}Fs_{28-48}$), with a mode at about Fs_{42}. The occurrence of both normally (in the andesite) and reversely (in the dacite) zoned plagioclase phenocrysts with similar rim compositions suggests that some magma mixing preceded eruption. Two xenocryst assemblages occur in the andesite. Glomerocrysts of bytownite (An_{70} to An_{90}), olivine (Fo_{63-77}), and magnesian augite were derived from basalt either by magma mixing or by assimilation of solid rock. Plagioclase (An_{28-35}) and resorbed, olivine (Fo_{34}) were derived from an evolved rhyodacitic liquid.

Vourvoulos Tuff

The Vourvoulos Tuff is bimodal in composition (Fig. 4.1; Table 4.2). The lower part of the pumice fall is composed of dacitic pumice (65% SiO_2) containing phenocrysts of reversely zoned plagioclase with cores of An_{42-44} and rims of An_{48}, augite of composition $Wo_{38}En_{35-38}Fs_{24-27}$, fayalitic olivine ($Fo_{38-39}$), and magnetite. Andesitic scoria from the upper half of the pumice fall and from the surges (56–57% SiO_2) have normally zoned plagioclase with cores of An_{60-63} and rims of An_{55}, augite ($Wo_{34-39}En_{42-43}Fs_{19-23}$), and magnetite. Olivine is absent in the andesite. Reversely zoned plagioclases of composition An_{42-49} also occur in the andesite. These resemble feldspar phenocrysts in the dacite and probably derive from an admixed silicic component.

Chips of degassed juvenile obsidian occur in the pumice fall deposit with whole-rock silica contents (62%), phenocryst compositions (plagioclase An_{52-55}, augite $Wo_{34-38}En_{41-42}Fs_{20-25}$, olivine Fo_{38-39}), and glass compositions (Table 4.8) intermediate between those of the two vesicular components.

Glomeroporphyritic aggregates of plagioclase (An_{43-62}), augite ($Wo_{39-40}En_{40-42}Fs_{18-21}$), rare orthopyroxene ($Wo_3En_{62}Fs_{35}$), magnetite and interstitial glass occur in all juvenile components. Glass compositions in the aggregates are compositionally distinct from those in the host clasts (Table 4.8).The aggregates are probably fragments of cumulate material plucked from the walls of the magma chamber during eruption. Xenocrysts of bytownite are also common.

Upper Scoriae 1 and 2

Upper Scoriae 2 has a basal dacitic pumice fall deposit (65.5–66.5% SiO_2) overlain by andesitic (57.5–60.0%) agglomerates and breccias. The dacitic pumices contain 10–20% phenocrysts of weakly zoned plagioclase (An_{50} to An_{45}), clinopyroxene ($Wo_{41}En_{36}Fs_{23}$), orthopyroxene ($Wo_{3-4}En_{53-56}Fs_{40-44}$), magnetite and ilmenite. The andesite has a similar assemblage but has lower modal plagioclase, a greater proportion of orthopyroxene and magnetite, and lacks ilmenite. Plagioclase is normally zoned (An_{70} to An_{45}). Some strongly zoned phenocrysts with calcic (An_{95-80}) cores and andesine rims also occur. Augite compositions are $Wo_{39-43}En_{35-40}Fs_{13-21}$ and orthopyroxenes $Wo_{3-4}En_{55-64}Fs_{33-41}$.

Table 4.8. *Representative glass analyses of the Upper Scoriae 2, Upper Scoriae 1, Vourvoulos, Middle Pumice, and Cape Thera eruptions*

	Upper Scoriae 2		Upper Scoriae 1		Vourvoulos				Middle Pumice						Cape Thera		
	Dacite	Andesite	Dacite	Andesite	Dacite	Obsidian	Andesite	Crystal aggregates	Obsidian	Dacite	Pale streak	Dark streak	Dacite	Dacite	Glass 1	Glass 2	Crystal aggregates
Samples	8666 85044 85121	85042 85069 85048	85015	85019 85024 85022	85007 8697	85010 8651	861 86101	861	S82-116	S79-24	S82-48	S79-24	S79-27	S79-30 S79-32b S79-129	8638	8635	8634 8642
Unit*	A	C.D	A	AC	A	A	B	B	A	A (base)	A	A	A (top)	B	B	A	A.B
No. anal	6	6	1	6	6	3	3	2	8	5	3	3	31	17	2	2	2
SiO_2	70.61(74)	62.06(28)	64.96	60.32(41)	68.6(51)	63.23(25)	59.81(86)	65.93	68.41(26)	68.46(38)	71.20	62.48	65.25(75)	66.40(57)	66.41	63.05	70.06
Al_2O_3	15.12(21)	16.26(34)	15.66	16.09(42)	14.83(31)	15.59(11)	14.59(41)	14.92	14.97(20)	15.44(59)	14.29	16.15	15.91(35)	15.46(35)	15.28	15.93	14.95
TiO_2	0.57(05)	1.11(16)	0.88	1.32(09)	0.63(07)	1.32(03)	1.73(18)	0.48	0.62(10)	0.53(09)	0.3	1.1	0.91(01)	0.83(07)	0.93	1.26	0.62
FeO	4.12(36)	7.29(31)	6.67	8.33(30)	5.47(23)	7.57(30)	10.19(11)	5.88	4.66(22)	4.83(16)	3.64	6.71	5.69(40)	5.33(22)	5.53	6.75	3.69
MgO	0.39(07)	1.79(22)	1.01	2.17(12)	0.49(06)	1.30(19)	2.06(32)	1.38	0.56(10)	0.44(32)	0.53	1.74	1.24(24)	1.04(17)	1.11	1.72	0.65
CaO	2.41(21)	5.19(15)	4.16	5.84(06)	2.79(16)	4.82(10)	5.96(33)	4.48	3.00(13)	3.04(22)	1.86	4.94	4.01(36)	3.56(32)	3.63	4.85	2.21
Na_2O	4.38(34)	4.33(19)	4.76	4.45(11)	4.70	4.30	4.00	4.33	4.95(21)	4.48(68)	4.87	4.82	4.69(57)	4.88(24)	4.51	4.32	4.53
K_2O	2.41(26)	1.98(12)	1.89	1.47(07)	2.50(17)	1.83(06)	1.65(13)	2.59	2.80(10)	2.78(16)	3.30	2.06	2.30(14)	2.49(14)	2.60	2.11	3.28

Glass analyses carried out on the University of Cambridge energy dispersive electron microprobe at 20 kV accelerating voltage. Beam current of 10 nA, and a 10–15 μm rastered beam. Count time was 80 seconds. Analyses corrected for Na loss. All analyses recalculated 100% dry assuming all Fe as FeO. Figures in brackets are one standard deviation on the average; thus 70.61(74) reads 70.61 ± 0.74.

* Eruption units are listed in Table 3.4.

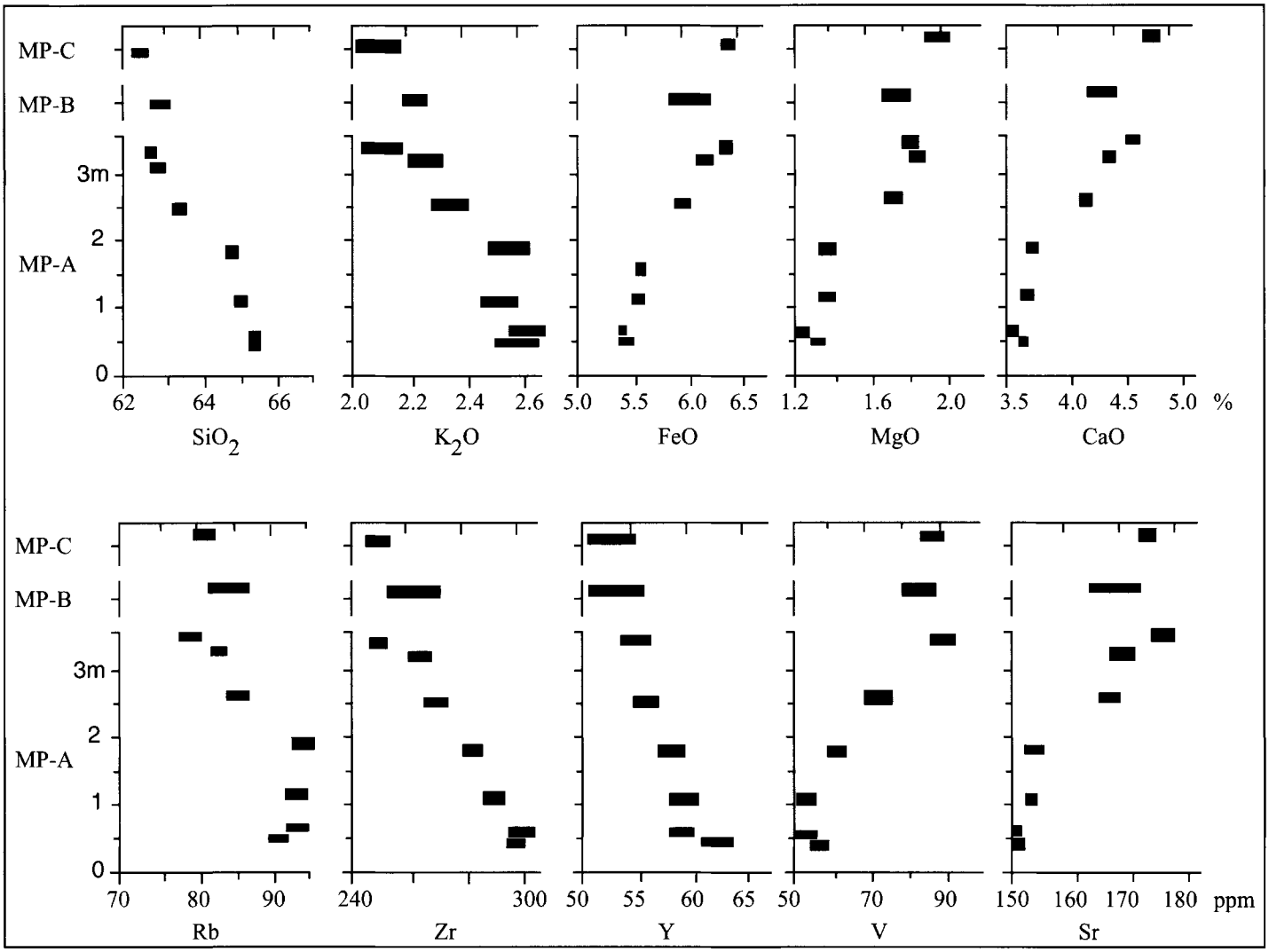

Fig. 4.10. Compositional zoning in the Middle Pumice. MP-A is the main Plinian deposit, MP-B the lithic breccia, and MP-C the upper pumice-fall deposit (see Table 3.4). Each bar in MP-A represents a single analysis. Bars for MP-B and MP-C represent the compositional ranges of 7 and 2 analyses, respectively

The evolved (62.0–63.2% SiO_2) component of Upper Scoriae 1 is confined to the base of the deposit, is volumetrically very minor, and has not been studied. The dominant andesite is compositionally uniform (57.7–59.1% SiO_2). The two Upper Scoriae andesites are similar and the description of Upper Scoriae 2 is also valid for Upper Scoriae 1 (Figs 4.6 and 4.8).

Xenocrysts of calcic plagioclase, quartz, fayalitic olivine, and sodic feldspar (An_{5-15}) are found in both Upper Scoriae units. Abundant plutonic nodules also occur, as described in Chapter 5.

Magmatic temperatures

The most comprehensive discussion of magma temperatures on Santorini is by Huijsmans (1985), based on applying geothermometers to mineral data on lava samples. There are far fewer studies of the pyroclastic ejecta. Many of the mineral analyses available for the Thera pyroclastics for co-existing FeTi oxides and pyroxenes in the theses of Druitt (1983) and Mellors (1988) were made by EDS analysis on the electron microprobe and so lack the precision that can now be achieved in modern microprobe studies. Fe–Ti oxide temperature estimates increase with glass MgO content: 825–830°C for rhyodacites, 835°C for dacites and 985°C for Lower Pumice 1 andesite scoria. These results are systematically lower by 30–60°C for the more silicic compositions in comparison with the more recent results reported by Gardner *et al.* (1996) and Cottrell *et al.* (1999).

For the more mafic rocks (50 to 60% SiO_2) Huisjmans (1985) applied three versions of the olivine-melt geothermometer. The temperature estimates range from 1200 to 980°C, with a systematic decrease in temperature as SiO_2 content increases. Pyroxene geothermometers gave temperatures of 980 to 1030°C for andesites (57 to 63% SiO2) and 923 to 910°C for Kameni island dacites. Cottrell *et al.* (1999) have used analyses of FeTi oxides and pyroxenes to estimate a temperature of 885 ± 7°C for the Minoan magma, using the algorithm of Andersen & Lindsey (1988) for the oxides and the QUILF algorithm for pyroxenes (Andersen *et al.* 1993). Gardner *et al.* (1996) report temperatures of 890°C for the Middle Pumice sample and 1000°C for an Upper Scoriae 1 sample. The experimental phase equilibria data for the Minoan composition also supports high temperatures for the rhyodacite magmas (Cottrell *et al.* 1999).

Magmatic water contents

The explosive nature of the Thera pyroclastic eruptions shows that the magmas were rich in volatiles. The principal volatile species in calc-alkaline intermediate to silicic magmas is water. Water contents can be estimated by two main methods: experimental methods to compare natural mineral assemblages with experimental assemblages and studies of melt inclusions in phenocrysts. Water content

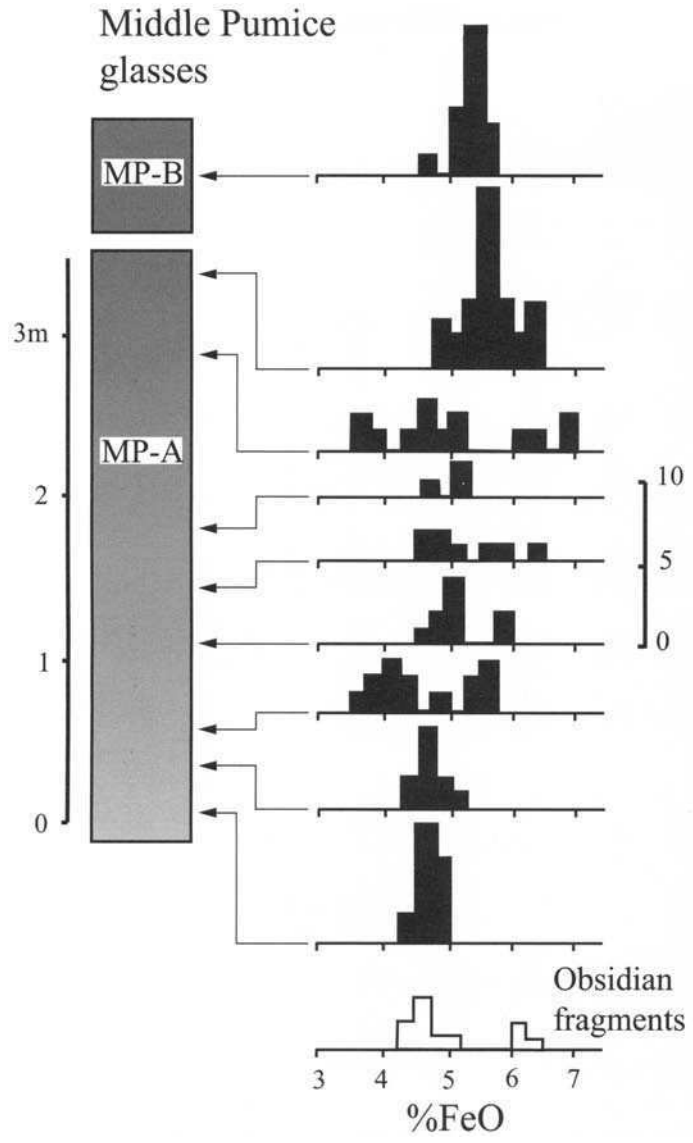

Fig. 4.11. Variation of glass composition with height in the Middle Pumice. The histograms are of total Fe content, as analysed by the electron microprobe and expressed as FeO. MP-A is the main Plinian deposit and MP-B the lithic breccias (see Table 3.4). Glass compositions in obsidian fragments of probable juvenile origin from the base of MP-A are also shown.

estimates can also provide minimum estimates of magma chamber pressure from water solubility relationships.

We have applied the method of Merzbacher & Eggler (1984), who used experimental data to contour the plagioclase–orthopyroxene–clinopyroxene–magnetite cotectic (Fig. 4.12). The method requires co-existence of plag + opx + cpx + mt + glass in the rock. The glass compositions of the Thera Pyroclastics (Tables 4.5 and 4.8) imply dissolved pre-eruptive water contents of 2–4 wt% using this projection. The anomalously high value for the Cape Riva hybrid andesite is artificial, since the minerals and melt were not in equilibrium prior to eruption. Gardner *et al.* (1996) and Cottrell *et al.* (1999) report studies of melt inclusions in phenocrysts, obtaining estimates of about 6% for the Minoan, 5.6% for the Middle Pumice and 3.2% for the Upper Scoriae 1.

The Thera pyroclastics contain almost no phenocrystic hornblende, occurring just as trace amounts in the rhyodacites of Lower Pumice 2 and as a groundmass phase in Minoan andesite. Only the Minoan crystal-rich pumices contain abundant hornblende, but these are interpreted as remobilized plutonic rocks. Experimental studies of rhyolitic melts have shown that at least 4.0% water is required to stabilize amphibole at pressures of about 100 MPa or more (Merzbacher & Eggler 1984; Rutherford & Devine 1988; Cotterell *et al.* 1999). At the rather high temperatures of the Santorini silicic magmas (e.g. 885°C in the Minoan magma) amphibole is only marginally stable even at much higher water pressures. Amphibole stability extends to somewhat lower pressures and higher temperatures as the melt becomes more mafic. For example the experimental studies of Cawthorne & O'Hara (1976) and Allen & Boettcher (1978), and Cottrell *et al.* (1999) on andesite from the Minoan deposit found that water contents of >4 wt% and temperatures of <1050°C are necessary for amphibole crystallization in andesitic melts at pressures in excess of 75 MPa. Water contents 3 to 6 wt% combined with high magma temperatures are thus consistent with the the paucity of hornblende in the Thera pyroclastics. Cotterell *et al.* (1999) have also shown (from phase equilibria experiments) that the Minoan rhyodacite must have contained about 3 wt% water immediately prior to eruption, but contained about 6% water in a deeper chamber at higher pressure.

The occurrence of anorthite (An_{97}) and Fo-rich olivine (Fo_{84}) in the Thera pyroclastics places constraints on the water contents of the mafic magmas that feed the high-level reservoirs at Santorini. Figure 4.13 shows the mineral compositions in the mafic components of the four dominantly silicic eruptions. Also shown are the phase compositions in equilibrium with typical Santorini basalt and mafic andesite at P_{H_2O} values of 0, 100 and 200 MPa, calculated using the distribution coefficients of Roeder & Emslie (1970) for olivine and Wagner *et al.* (1995) for plagioclase. They suggest that the observed phases crystallised from basaltic or mafic andesite magma at P_{H_2O} of 100–200 MPa. These results are comparable to calculations of water pressure made byz Huijsmans (1985) on mafic lavas. These water pressures correspond to water contents of a few percent and minimum chamber depths of a few kilometres.

Magma-chamber zoning and development

The 12 explosive eruptions of the Thera pyroclastics each discharged part or all of a high-level magma body. The deposits display a variety of compositional zoning styles. In this section we discuss the implications of our data for the development and discharge of individual magma bodies. Evolution of the entire plumbing system through time is the subject of Chapter 8. The two types of zoned magma chamber recognized in this study are shown in Fig. 4.14.

The dominantly intermediate type

Seven of the eruptions occurred from magma chambers with a dominant volume of andesite overlain by one or more layers of more evolved magma (dacite, or a more evolved andesite). Each magmatic component in these eruptions has a simple equilibrium phenocryst assemblage, suggesting evolution by crystal fractionation and density stratification from a mafic parent. Mass balance calculations and geochemical modelling show that Santorini andesites and dacites are related principally by low-pressure fractional crystallization of observed phenocryst phases (Mann 1983; Mellors 1988; Edwards 1994; Chapter 6). Santorini magma chambers reside at shallow depths (0.5–2 kbar) in the crust. The relative proportions of andesite and more evolved liquids in the dominantly intermediate chambers seem broadly consistent with a fractional crystallization process. Densities of Santorini magmas decrease monotonically with increasing SiO_2 (Fig. 4.15), so that the observed zoning patterns are consistent with sidewall crystallization and convective fractionation. In this process sidewall crystallization generates buoyant residual liquid which flows in a thin boundary layer to the top of the chamber, where it ponds and stratifies (Huppert *et al.* 1982; Sparks *et al.* 1984; McBirney *et al.* 1985; Nilson *et al.* 1985; Nielson & DeLong 1992; Maaloe & McBirney 1997).

Only in two of the eruptions do the data suggest a more complicated history of chamber development. In Cape Thera and the Middle Pumice, mixing of compositionally disparate magmas occurred some time before eruption. Plagioclase phenocrysts in

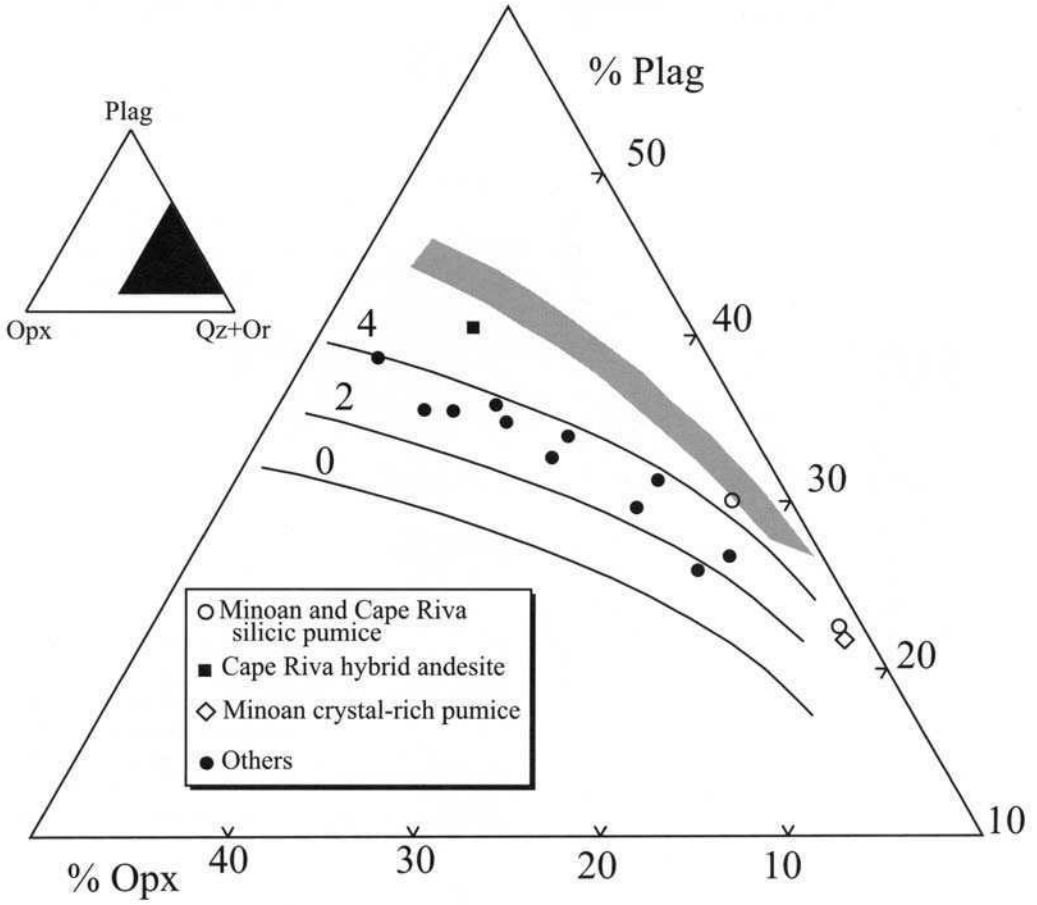

Fig. 4.12. Pre-eruptive water contents of magmas of the Thera pyroclastics estimated using the method of Merzbacher & Eggler (1984). The data points are average glass analyses projected into the system plagioclase–orthopyroxene–(quartz + orthoclase) using an algorithm provided by the authors. The curves are projections of the plag–opx–cpx–mt cotectic based on experimental data at water contents of 0, 2 and 4 wt%. The shaded area is the field of hornblende stability. Estimated water contents range from 2 to 4 wt%, which is in agreement with the general absence of hornblende in the Thera pyroclastics. The anomalously high value for the Cape Riva hybrid andesite is artificial, since the minerals and melt were not in equilibrium prior to eruption.

both deposits include relatively calcic and sodic populations zoned to similar rim compositions. In both examples glass compositions are variable and span a larger range of SiO_2 than the bulk pumice lumps. We suggest that gravitational instability and overturn disrupted zoning with backmixing of different magmas and phenocryst populations. The presence of mineral zoning related to hybridization shows that overturn began before eruption.

Evolution by sidewall crystallization receives support from the abundance of unaltered cognate plutonic debris in the pyroclastic ejecta. Many of the nodules are gabbroic cumulates generated by fractional crystallization of andesitic magma (Chapter 5). They appear to have been derived by syn-eruptive disruption of the margins of the magma chambers. Probable cumulate material also occurs as millimetre-sized crystal aggregates dispersed throughout the magmas. Mineral compositions in these aggregates are indistinguishable from those of individual phenocrysts and the aggregates are probably phenocryst clots similar to those studied by Garcia & Jacobson (1979). However in Cape Thera and Vourvoulos the aggregate crystals and fresh, interstitial glasses are compositionally distinct from those in the host pumice. Such aggregates are regarded as small fragments of cognate cumulate material as inferred by Arculus & Wills (1980) in the Antilles and Scarfe & Fujii (1987) at Mount St Helens. Xenocrysts of sodic plagioclase and/or fayalitic olivine in Vourvoulos, Middle Pumice, and the Upper Scoriae units may be disrupted cumulate debris derived from evolved rhyodacitic liquids. Common xenocrysts of calcic plagioclase and Fo-rich olivine may be derived from disaggregated solid rock or from replenishments of mafic magmas which were not erupted.

The dominantly silicic type

The four dominantly silicic magma chambers developed towards the ends of the two eruptive cycles. In at least three cases (Lower Pumice 2 Cape Riva, Minoan) discharge from these chambers triggered caldera collapse. Each chamber contained a dominant volume of rhyodacite underlain or invaded by basalt or mafic andesite. Thus the chambers were markedly bimodal with well-defined compositional gaps as large as 15 wt% SiO_2.

There is abundant evidence for the mechanical mingling of silicic and mafic magmas in these systems. The blebs and inclusions of andesite, which occur abundantly in silicic pumices of all four eruptions, are interpreted as quenched droplets of mafic magma. Mingling of a small volume of hot, mafic magma with a much larger volume of cool, silicic magma leads to the development of rigid inclusions following thermal equilibrium (Eichelberger 1980; Sparks & Marshall 1986; Bacon 1986). Xenocrysts of calcic plagioclase and Fo-rich olivine with haloes of dark adhering groundmass are also common in the silicic pumices, and may have formed by mechanical disintegration of the blebs (Clynne 1990; Feeley & Davidson 1994). Many cauliform scoriae of the Minoan and Lower Pumice 2 deposits contain inmixed streaks and swirls of pale silicic glass due to incomplete mixing. Only in the Cape Riva chamber did mixing of mafic and silicic components generate significant volumes of homogeneous hybrid. Mixing in this case must have preceded the eruption by a significant period, since the hybrid glass is compositionally uniform. Small amounts of pale grey, hybrid pumices also occur in the Lower Pumice 2 fall deposit (Fig. 4.4). Banded pumices occur abundantly in the ejecta of Lower Pumice 1 and Cape Riva.

The origins of large compositional gaps have been debated widely (e.g. Brophy 1991). Those most relevant to Santorini are now listed. (1) The existence of a density maximum in intermediate magmas generated by fractional crystallization, as observed in some tholeiitic systems. The high density then inhibits eruption of such magmas at the surface (Sparks *et al.* 1984). (2) A phase equilibrium control in which SiO_2 rises rapidly during fractional crystallization through intermediate compositions, thus reducing the volume of such magmas generated (Grove & Donnelly–Nolan 1986). (3) Closed-system sidewall crystallization, stratification, and formation of density interfaces by double diffusive effects (e.g., McBirney

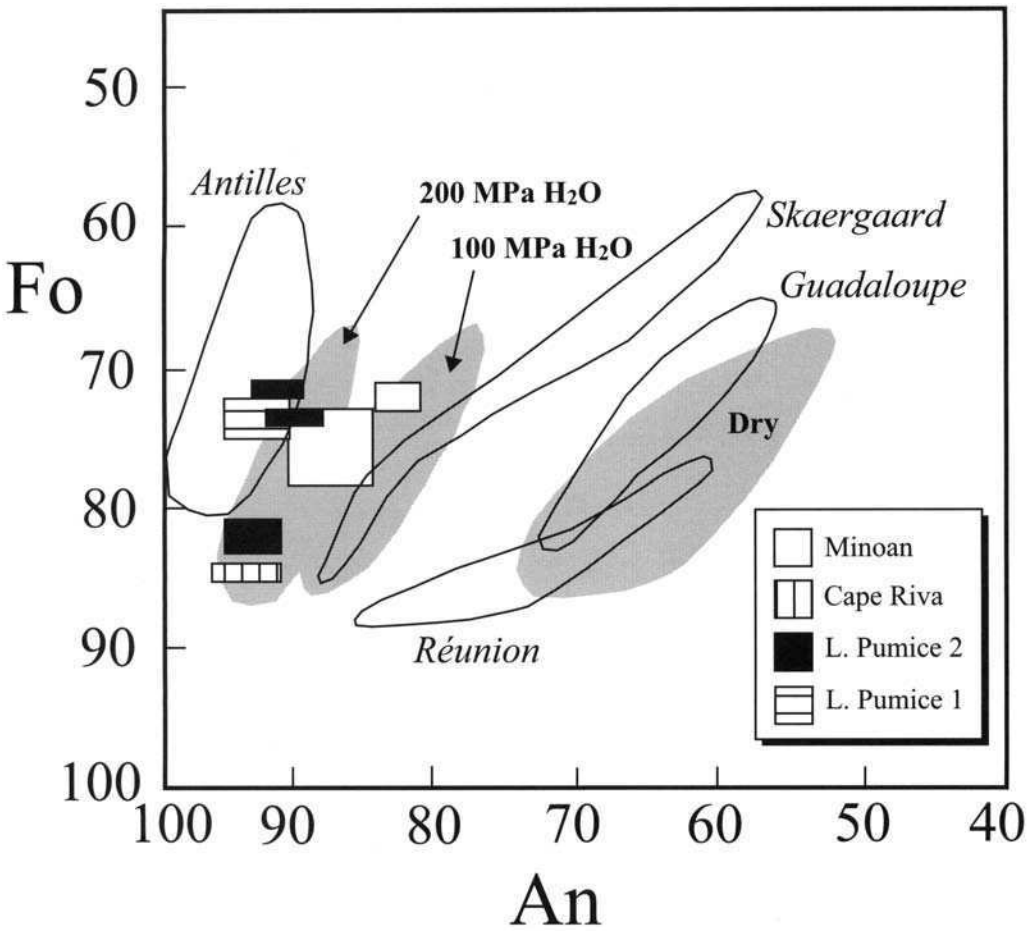

Fig. 4.13. Compositions of coexisting olivine and plagioclase from mafic components of the four dominantly silicic eruptions. Fields for other volcanic regions are from Arculus & Wills (1980). Shaded areas represent coexisting olivine and plagioclase compositions at $P_{H_2O} = 0$, 100 MPa, and 200 MPa calculated using an olivine-melt partition coefficient of 0.30 (Roeder & Emslie 1970) and the plagioclase–melt partition coefficients of Wagner *et al.* (1995) (Kd = 1 dry; 3.1 at 100 MPa H_2O; 5.5 at 200 MPa H_2O).

et al. 1985). (4) Replenishment of a silicic reservoir of magma, generated either by earlier fractional crystallization and/or crustal melting, by dense mafic magma (Bacon & Druitt 1988).

Constraints at Santorini rule out mechanisms 1 to 3. First, the densities of Santorini magmas decrease monotonically with increasing fractionation (Fig. 4.15). There is no density maximum. Second, magmas of intermediate composition generated by fractional crystallization occur in abundance on Santorini, showing that the mechanism of Grove & Donnelly-Nolan (1986) does not apply there (Chapter 6). Third, the eruption of large volumes of differentiated silicic magmas and much smaller volumes of mafic magmas at Santorini appears inconsistent with fractional crystallization and stratification in a closed reservoir.

The bimodal zoning at Santorini is best explained by replenishment of pre-existing silicic magma reservoirs. Chemical and isotopic constraints (Chapters 6 and 7) are consistent with derivation of the silicic magmas by fractional crystallization of basalt with assimilation of continental crust. Alternatively significant volumes of silicic magma could have been formed by the remelting of plutons with similar chemical and isotopic characteristics as erupted Santorini magmas. Blocks of partially melted granitoids, some at least 200 000 years old (Chapter 7), in the Minoan ejecta are consistent with this mechanism.

Intrusion of basalt or mafic andesite into a large silicic magma body immediately prior to (or even during) eruption would generate a bimodal, two layered system. Laboratory experiments have shown that mafic magma injected into a large reservoir of light, silicic magma should spread out at the base, forming a discrete layer (Sparks *et al.* 1984). Gravitational instability and mixing between the two layers might arise if the mafic magma were rich in water. The presence of calcic plagioclase and magnesian olivine in Santorini basalts and mafic andesites is consistent with water contents as high as a few percent. As the injected mafic magma cools it may become vapour saturated and begin to exsolve water. In such a case the density of the mafic layer may fall below that of the silicic volume and overturn might occur (Huppert *et al.* 1982), generating homogeneous hybrid magma such as in the Cape Riva chamber. Another possibility is that the separation and accumulation of gas bubbles at the surface of the mafic layer might generate foam which then becomes unstable, shedding blobs of vesiculated mafic magma up into the silicic host. These would then quench to mafic inclusions (Eichelberger 1980; Thomas *et al.* 1993; Thomas & Tait 1997). Yet another possibility is that thermal convection above the hot replenishment layer entrains blobs and streaks of the mafic magma into the dominant silicic volume (Snyder & Tait 1996).

Mingling of magmas also occurs during eruption by simultaneous withdrawal through the conduit (Blake & Ivey 1986; Freundt & Tait 1986). The banded pumices that occur abundantly in Lower Pumice 1 and the Cape Riva almost certainly formed syneruptively, since the contacts between compositionally distinct streaks are sharp even at the micron scale.

We propose a model for the development of the dominantly silicic magma chambers in which each evolves through a complex history of crystal fractionation, repeated replenishment, reheating and remobilization of plutons, and crustal assimilation (Chapter 8). During evolution, each body is replenished episodically by hot, dense basalt or mafic andesite. Immediately following each replenishment, the mafic magma spreads out across the chamber floor, forming a bottom layer. Rapid heat transfer from this layer to the cool, dominant volume causes vigorous convection and crystallisation of the mafic magma. At the same time vapour saturation causes instability effects and the production of quenched mafic inclusions and hybrid layers. Eventually the mafic layer reaches its crystallinity limit (Marsh 1988; Brophy 1991), and further convection is inhibited. Crystals then settle to form a cumulate layer and the light residual liquid rises buoyantly and mixes into the overlying silicic magma. Each replenishment also reheats the silicic region, remobilizing and assimilating crystal mushes and wall-rocks (Huppert & Sparks 1988). In this way each successive replenishment contributes to the slow growth of the silicic reservoir. A similar interpretation has been proposed for the evolution of the Mount Mazama magma chamber

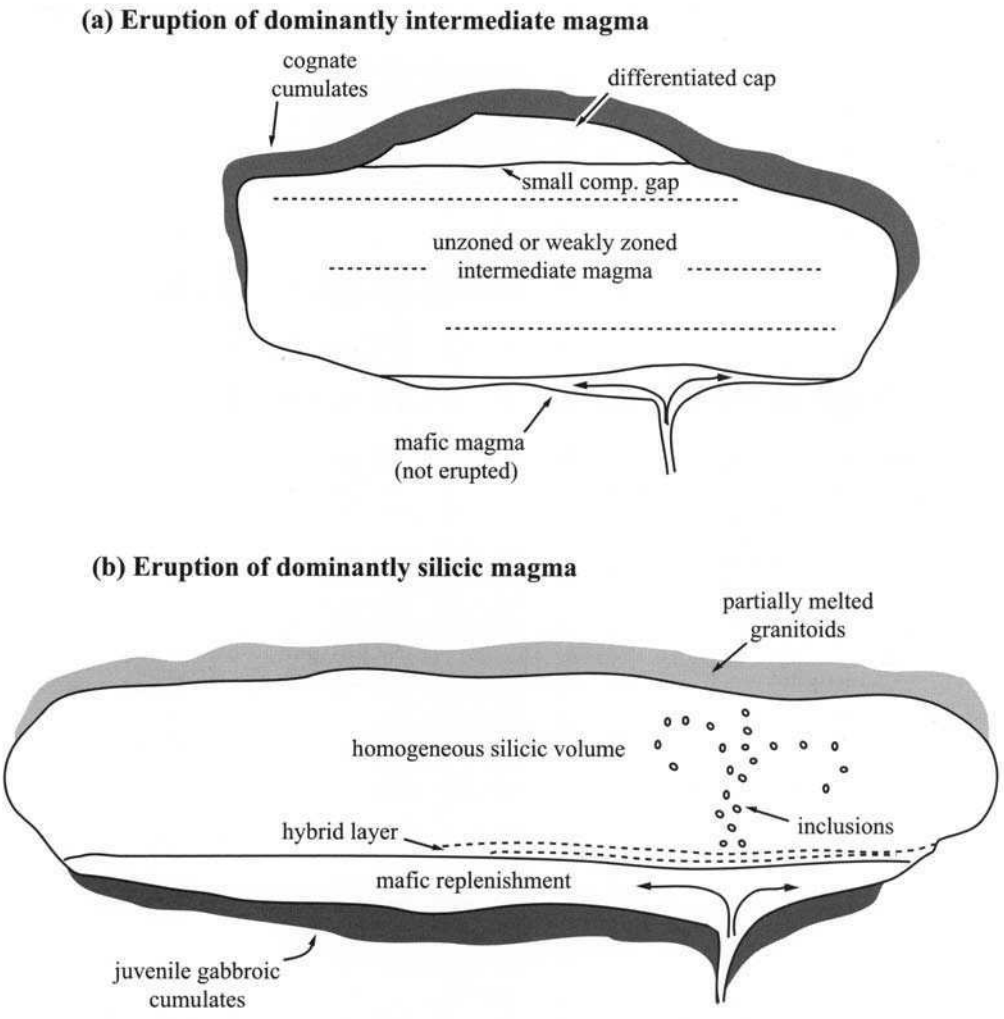

Fig. 4.14. The two main types of compositional zoning present in magma chambers that discharged to form the Thera pyroclastics. (**a**) Upper Scoriae 2, Upper Scoriae 1, Vourvoulos, Middle Pumice, Cape Thera, Cape Therma Scoriae 3, Cape Therma Scoriae 1. Chamber dominated by unzoned or weakly zoned andesite with a volumetrically minor cap of dacite or more differentiated andesite. Blocks of cognate cumulates from the chamber roof and sides are commonly erupted. (**b**) Minoan, Cape Riva, Lower Pumice 2 and Lower Pumice 1. Chamber dominated by essentially homogeneous silicic magma. Replenishment by mafic to intermediate magma, probably shortly before eruption. Entrainment of mafic magma into the silicic volume forms cauliform inclusions and quenched blebs observed in the Minoan and Lower Pumice 2 deposits. Fragments of gabbroic cumulates from the chamber floor are ripped up and erupted in the mafic components of the Minoan and Lower Pumice 2 eruptions. Blocks of partially melted ancient granitoids from the chamber roof are discharged at the start of the Minoan eruption.

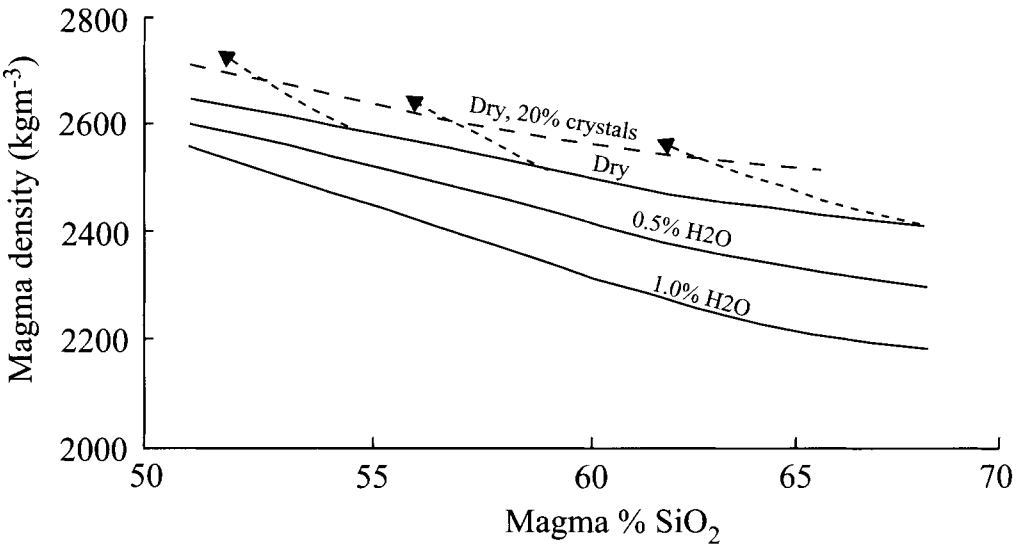

Fig. 4.15. Densities of Thera magmas calculated using the method of Bottinga & Weill (1970). Partial molar volumes from Burnham & Davis (1971) for water at 1 bar and Mo *et al.* (1982) for other oxide components. The calculations are based on the compositions of average Santorini basalt, basaltic andesite, andesite, and rhyodacite. The calculations consider three parental basaltic compositions with 0, 0.5, and 1 wt% water, and assume that more differentiated magmas are produced by fractional crystallization of that parent. H_2O is treated as incompatible, and its abundance in the three differentiated compositions calculated from measured K_2O contents. Addition of crystals to the magma raises the overall magma density and decreases the bulk SiO_2 content of a given magma.

prior to the 6850 BP eruption (Bacon & Druitt 1988; Druitt & Bacon 1989).

This model might explain two further observations. First, during replenishment, the mafic magmas of Lower Pumice 2 and the Minoan ripped up and entrained gabbros forming the floor of the chambers. These gabbros could represent the cumulate beds laid down by successive replenishment volumes during development and growth of these magma chambers. Second, in the four dominantly silicic eruptions the rhyodacite is approximately uniform compositionally. This suggests that each silicic volume was well stirred by convection. A possible explanation is that successive mafic inputs provided the thermal and (through release of plumes of light residual liquid) compositional buoyancy sufficient to keep the main silicic volume well mixed. Plumes of residual liquid released from a crystallising mafic layer would have SiO_2 and thus viscosity close to that of the overlying silicic layer, probably resulting in efficient inmixing and homogenization (Huppert & Sparks 1984).

Recent phase-equilibria and petrological studies by Cottrell *et al.* (1999) and melt inclusion studies by Gardner *et al.* (1996) have

led these authors to propose a more detailed model in the case of the Minoan eruption. The Minoan rhyodacite was initially stored at water pressures of 210–240 MPa, where it contained about 6 wt% dissolved water. The presence of Fo-rich olivine and An-rich plagioclase in gabbro fragments in the andesite show that they originated at comparable water pressures (Fig. 4.13). These results indicate a minimum depth to the source of the Minoan magma of about 8–10 km. The rhyodacite then ascended to be stored at a pressure about 50 MPa (about 2 km). The magma then equilibrated at this lower pressure before being erupted. Andesitic magma is surmised to have been injected into the rhyodacite during magma ascent and eruption.

Origin of the normal-to-reverse zonation

During discharge from compositionally zoned magma chambers, it is common for the light, more silicic component at the top of the chamber to be tapped first (Smith 1979). After a time any lower, denser layers also begin to be drawn up, and compositionally diverse magmas are erupted together. The mechanisms for this process have been demonstrated in laboratory systems (Blake & Ivey 1986; Freundt & Tait 1986). If the eruption continues long enough, deeper mafic magma may discharge alone, even though some silicic magma remains in the chamber. The result is a pyroclastic deposit in which the chamber zonation is preserved, albeit imperfectly, upside-down. At Santorini, several deposits exhibit this type of normal zoning (Cape Therma 1, Cape Therma 2, Lower Pumice 1, Cape Thera, Middle Pumice, Vourvoulos, Upper Scoriae 1, Upper Scoriae 2). However, three (Lower Pumice 2, Cape Riva and Minoan) exhibit an unusual type of normal-to-reverse zonation. In these three cases the base of the fall deposit is exclusively silicic. The mafic or intermediate component then appears above the base and increases in abundance upwards, reaching a maximum near the top of the fall deposit. Mafic components occur in only trace amounts or are absent in overlying flow or surge units, which represent the main volume of erupted material. The silicic component remains compositionally uniform throughout the sequences, indicating derivation from a single magma chamber. There is no evidence for a significant time break at the end of the Plinian phases in these eruptions (Druitt 1985; Druitt *et al.* 1989).

Three models for the normal-to-reverse zoning are considered. First, the layer of dense magma at the base of the chamber was thin and was simply exhausted by the end of the Plinian phase. This model is rejected because it does not readily explain the coincidence of the compositional break with the transition from fallout to surge flow activity.

Second, a change in conduit geometry or discharge rate may have altered the withdrawal dynamics at the end of the Plinian phase, causing the mafic layer to cease being tapped (Blake & Ivey 1986). This model is appealing at Santorini, because there is evidence for changes of the conduit system at the end of the Plinian phases in the Cape Riva (Druitt 1985) and Minoan eruptions (Chapter 3). In the Cape Riva eruption the Plinian column first collapsed, generating welded ignimbrite. Coarse-grained lag deposits were then emplaced as the caldera began to subside. In the Minoan eruption, the end of the Plinian phase was marked by the opening and lateral propagation of fissures and the onset of phreatomagmatic explosions. In each eruption, the transition from initial axisymmetric vent to a fissure vent at the end of Plinian phase may have caused a change in the withdrawal dynamics. Discharge through a fissure results in smaller magma draw-up heights than an axisymmetric vent (Blake & Ivey 1986).

A third model is suggested by the recent experimental work of Snyder & Tait (1996). Replenishment of a reservoir of cool, viscous liquid by a hot, less viscous liquid creates a buoyant plume of hot material above the entry point. When the input ceases, the plume collapses gravitationally. The authors showed that this process could occur in a silicic magma body replenished by hot mafic magma, and applied the mechanism to the 1991 Pinatubo eruption. At Santorini replenishment of each silicic chamber led to the development of a plume of hot, mingled magma, and co-eruption of silicic and mafic components during the initial Plinian phase. When the input supply switched off, the plume collapsed and thereafter only the silicic magma was discharged. A corollary is that, so long as replenishment was taking place the chamber pressure might have been buffered at a high value, maintaining stability of the roof. Once replenishment ceased, but magma continued to discharge, the chamber pressure would have fallen, leading to roof collapse and the onset of caldera subsidence (Druitt & Sparks 1984). This might explain why the disappearance of the mafic components corresponds with the end of Plinian activity.

Summary

(1) Juvenile components of the Thera pyroclastics range from basalt to rhyodacite and have similar phase assemblages Santorini lavas: basalts Mg-rich ol + plag + cpx + mt; andesites plag + cpx ± opx + mt ± xenocrystic Mg-rich ol; dacites plag + cpx + opx ± Fe-rich ol + mt + ilm + apat ± xenocrystic Mg-rich ol; rhyodacites plag + cpx + opx + mt + ilm + apat ± hb ± zir. Hornblende occurs in trace amounts only in the rhyodacites of Lower Pumice 2 and in the groundmass of Minoan andesite. The restriction of Fe-rich olivine to dacites of the Middle Pumice and Vourvoulos deposits is consistent with the particularly tholeiitic character of those eruptions. Phenocryst abundances are mostly between a few percent and 30%, but reach 70% in some magmas contaminated by cumulate material.

(2) Pre-eruptive water contents range from about 2 to 6 wt% in the andesites, dacites and rhyodacites of the Thera pyroclastics. Parental mafic magmas that precipitated feldspar as calcic as An_{97} and olivine as magnesian as Fo_{84} crystallized at P_{H_2O} of 100–200 MPa. The study of Cottrell *et al.* (1999) also indicate that the Minoan rhyodacite magma first evolved at a water pressure of 200 MPa before ascending to a shallower chamber prior to eruption.

(3) Pyroclastic deposits from large explosive eruptions (km^3 to tens of km^3) can be divided into two types. Those that are dominantly intermediate in composition occur in the early to middle stages of each explosive cycle. The main juvenile component is andesite, zoned to subordinate dacite or more silica-rich andesite. In five of these deposits, phenocryst phases appear to be in approximate equilibrium. In each of the Middle Pumice and Cape Thera deposits, bimodal plagioclase assemblages suggest pre-eruptive mixing of different magma types in the chamber. The compositional range of glass compositions in these two eruptions exceeds the whole-rock ranges, and is consistent with incomplete mingling of diverse magmas prior to eruption.

(4) Each explosive cycle terminates with a pair of dominantly silicic eruptions. These are markedly bimodal with compositional gaps as large as 15% SiO_2. The dominant magma in each case is compositionally uniform dacite or rhyodacite and the subordinate magma (<1% to about 30%) basalt or andesite. Mafic components of Lower Pumice 2 and the Minoan contains fragments of cognate gabbroic cumulates, probably ripped up from the chamber floor during replenishment. Nodules and crystal-rich pumices of partially melted granitoids ≥100 000 years old occur at the base of the Minoan deposit.

(5) Magma chambers of dominantly intermediate type evolved principally by fractional crystallization, perhaps by sidewall crystallization. This is consistent with the abundance of cognate cumulate nodules in the ejecta. The zoning in dominantly silicic chambers probably arose by episodic replenishment of silicic reservoirs by mafic magmas. The large volume and uniform composition of the silicic component can be attributed to the repeated additions of heat and mass from the underlying mafic magmas. New mass is added by the fractional crystallization of the mafic magma releasing volatiles and evolved melt into the overlying silicic chamber. Replenishments also resulted in heating, wall rock assimilation, and convective stirring to maintain uniform composition.

Chapter 5
Cumulate nodules in the Thera pyroclastics

Gabbroic and dioritic nodules are common in some horizons of the Thera pyroclastics. These nodules contain pyroxene as the main ferromagnesian phase in contrast to the early Akrotiri centre, which contain nodules with abundant hornblende (Nicholls 1971*a*; Pichler & Kussmaul 1972). Calcsilicate nodules and gabbroic nodules have also been recognized in Santorini lavas (Fouqué 1879; Nicholls 1971*a*). Previous studies of Santorini volcanic rocks indicate that crystal fractionation has played an important role in generating the compositional range basalt–andesite–dacite–rhyodacite (Nicholls 1971*a*; Mann 1983; Huijsmans 1985; Barton & Huijsmans 1986). This interpretation is also consistent with much of the petrological data presented in Chapter 4 and the geochemical data and models presented in Chapter 6. However, disequilibrium phenocryst assemblages in some lavas (Huijsmans 1985; Chapter 4), banded pumice clasts in many pyroclastic deposits (Druitt *et al.* 1989; Chapters 4), isotopic disequilibria in phenocrysts (Pyle *et al.* 1988; Chapters 6 and 7) and complex zoning patterns in plagioclase crystals (Stamatelopoulou-Seymour *et al.* 1990) indicate that magma mixing has also occurred. In addition, trace element and isotopic abundances can be interpreted in terms of assimilation of continental crust during fractionation (Barton *et al.* 1983; Stamatelopoulou-Seymour *et al.* 1990; Chapter 6). The nodules provide information on petrogenetic processes that have influenced the evolution of Santorini magmas. Their petrology is documented in this chapter and compared with that of associated juvenile ejecta. The nodules are identified as cumulates from andesitic and dacitic magmas, confirming the importance of fractional crystallization in the petrogenesis of Santorini magmas. They also demonstrate that mafic plutonic rocks can be formed from intermediate to silicic magmas.

Nodule occurrences

Plutonic nodules are abundant in four of the Thera pyroclastic deposits: Cape Therma 3 Middle Pumice, Upper Scoriae 1 and Upper Scoriae 2. These deposits are predominantly composed of andesitic ejecta. They also occur as minor constituents in the Cape Riva and Minoan deposits. In Cape Therma 3, Upper Scoriae 1 and Upper Scoriae 2 the nodules are particularly abundant in the spatter agglomerates (Chapter 3). Nodules are typically 1–20 cm in diameter and equidimensional. They range from well rounded to subangular. Some show spheroidal weathering. Alteration is variable, ranging from nodules that can be crumbled by hand to fresh hard rocks. The nodules are commonly surrounded by brick red andesitic ejecta indicating strong oxidation during and after emplacement. Individual nodules are texturally homogeneous and mineral layering has not been observed. If they represent fragments of layered intrusions, then the scale of layering is greater than the typical size of the nodules. However gabbro micronodules in Minoan ejecta contain non-cotectic proportions of gabrroic minerals which can be attributed to cumulate processes, such as density or size sorting.

Petrology

Fifty-three nodules were collected for detailed petrological and geochemical study. The nodules typically consist of plagioclase, clinopyroxene, orthopyroxene, titaniferous magnetite and quartz with minor amounts of ilmentite, apatite, alkali feldspar, biotite, amphibole and more rarely olivine, titanite, epidote and opaline silica. Chemical analyses are given in Appendix 2 and modal data in Table 5.1. Mineral compositions are given in Mellors (1988). Most nodules classify as gabbros and quartz gabbros based on their modal mineralogy. A few samples from Middle Pumice and all the Cape Therma 3 nodules classify as diorite. The nodules can be divided into four types based on the presence or absence of olivine and orthopyroxene (Fig. 5.1). 65% of nodules contain orthopyroxene and there are both olivine-bearing and olivine-absent types. Most of the remaining nodules, which do not contain orthopyroxene, are olivine-bearing, but a small number of these also lack olivine, clinopyroxene being the only ferromagenesian phase.

Textures

The nodules are holocrystalline with the exception of one sample containing glass. Textures range from well packed, medium grained and intergranular to subophitic (Fig. 5.2a). Some samples display bimodal grain sizes approaching porphyritic varieties (Fig. 5.2b). Many nodules are readily classified using cumulate terminology (Wager & Brown 1968; Irvine 1982). A framework of unzoned or weakly zoned primocrysts and a pore-filling of intercumulus material usually can be distinguished. The textural range reflects variations in the proportions and packing of primocrysts and the grain size of intercumulus crystals (Fig. 5.2c). Most rocks classify as orthocumulates and mesocumulates using the definitions of Irvine (1982). Interstices are often filled with granophyric intergrowths (Fig. 5.2d).

Plagioclase

Plagioclase typically constitutes 50–60 volume% of nodules with the complete range being 37–70 volume%. A wide variety of plagioclase compositions is observed (Fig. 5.3). They can be divided into three groups on textural and compositional grounds.

(i) Xenocrysts. These are typically fragmented or subhedral and can reach several millimetres in diameter. Xenocryst cores display patchy or irregular zoning (Fig. 5.2b) and the rims show oscillatory normal zoning. Core compositions range from An_{80} to An_{94} and are overgrown by labradorite margins. The calcic cores of these crystals are interpreted as xenocrysts and are similar in texture and composition to cores of some plagioclase phenocrysts observed in the lavas and pyroclastic rocks (Huijsmans 1985; Stamatelopoulou-Seymour *et al.* 1990; Chapter 4).

(ii) Primocrysts (cumulus crystals). The predominant part of the primocryst framework consists of euhedral plates of 1–5 mm in length. Zones of glass and rounded pyroxene inclusions are occasionally present. Core compositions range from An_{73} to An_{50} which are normally zoned to andesine rims (An_{45} to An_{50}). Zoning is sometimes more complex, with some reversals with similarities to the patterns reported by Stamatelopoulou-Seymour *et al.* (1990). Figure 5.3 demonstrates the marked compositional gap between the more calcic xenocrysts and cumulus crystals.

(iii) Intercumulus feldspar. Small euhedral to subhedral plagioclase crystals fill the interstitial spaces. They are strongly zoned ranging from andesine (An_{45}) to albite (An_5) and some zoned crystals have rims of alkali feldspar. Feldspar is commonly intergrown with quartz (Fig. 5.2d) and these are interpreted to have formed by crystallization of trapped intercumulus melt.

Clinopyroxene

Clinopyroxene primocrysts constitute 4–25 volume%. Euhedral to subhedral crystals are up to 4 mm in length and are typically unzoned. Clinopyroxenes are salitic to augitic (Fig. 5.4) ranging

Table 5.1. *Modal composition (volume%) of plutonic nodules from the Thera pyroclastics*

	Cape Therma 3			Middle Pumice																
Sample	86303	86304	86430	8421	8422	8423	8424	8425	8426	8427	8428	8429	84210	84211	84212	84214	84215	84216	84217	84218	84219
Rock	Diorite	Diorite	Diorite	Gabbro	Gabbro	Gabbro	Gabbro	Gabbro	Gabbro	Gabbro	Gabbro	Gabbro	Gabbro	Diorite	Diorite	Gabbro	Gabbro	Gabbro	Gabbro	Gabbro	Gabbro
$\%SiO_2$	60.1	57.6	58.8	55.5	53.3	53.2	52.4	53.6	52.8	57.5	54.8	54.3	54.8	59.3	57.6	54.5	56.2	53.5	54.5	56.0	52.4
Plagioclase	46	50	56	57	47	55	52	44	52	54	57	45	49	54	57	59	62	49	49	56	51
Clinopyroxene	4	4	4	13	19	16	29	22	16	21	21	19	15	5	10	20	14	34	34	13	18
Orthopyroxene	0	0	0	0	0	0	3	0	1	2	2	0	8	0	1	3	4	0	tr	0	7
Oxides	2	3	2	6	4	3	3	5	5	3	4	4	4	7	2	3	3	7	5	5	4
Quartz	12	11	10	4	5	5	4	4	5	3	3	3	11	10	10	9	9	2	5	7	6
Alk feldspar	18	16	13	4	3	2	1	2	2	2	1	1	4	5	6	3	4	3	3	6	2
Amphibole	14	14	11	1	tr	0	tr	1	tr	3	0	tr	0	2	1	0	0	0	4	0	4
Biotite	0	1	4	0	0	0	tr	0	0	0	2	0	tr	tr	1	tr	4	0	0	1	1
Olivine	0	0	0	0	tr	0	1	tr	tr	0	tr	6	0	0	0	0	0	0	0	0	0
Alteration	4	1	0	15	22	19	7	22	19	12	10	22	10	17	12	3	0	5	0	12	7

	Upper Scoriae 1			Upper Scoriae 2									C. Riva
Sample	84130	8513	8645	8401	8405	8407	8409	84010	84014	84015	84016	84023	85041	84921
Rock	Gabbro	Gabbro	Gabbro	Gabbro	Gabbro	Gabbro	Gabbro	Gabbro	Gabbro	Gabbro	Gabbro	Gabbro	Gabbro	Gabbro
$\%SiO_2$	54.9	56.4	55.6	55.5	52.4	52.9	57.5	54.8	54.8	59.3	57.7	52.4	54.9	50.9
Plagioclase	60	59	58	66	52	52	55	54	59	54	58	53	54	55
Clinopyroxene	12	13	12	8	12	21	6	22	13	24	12	13	14	24
Orthopyroxene	8	5	7	2	0	6	1	4	4	1	0	0	4	8
Oxides	5	4	4	3	4	4	3	3	5	9	3	2	3	3
Quartz	13	13	19	8	12	16	10	12	7	1	13	5	13	7
Alk feldspar	0	2	0	0	6	1	4	3	1	0	0	3	2	2
Amphibole	2	3	0	2	2	0	1	1	0	0	0	0	6	tr
Biotite	0	tr	0	2	0	tr	0	1	2	tr	1	0	2	1
Olivine	tr	1	0	0	0	0	0	0	tr	1	0	0	0	0
Alteration	0	0	0	9	12	tr	20	0	9	10	13	24	2	0

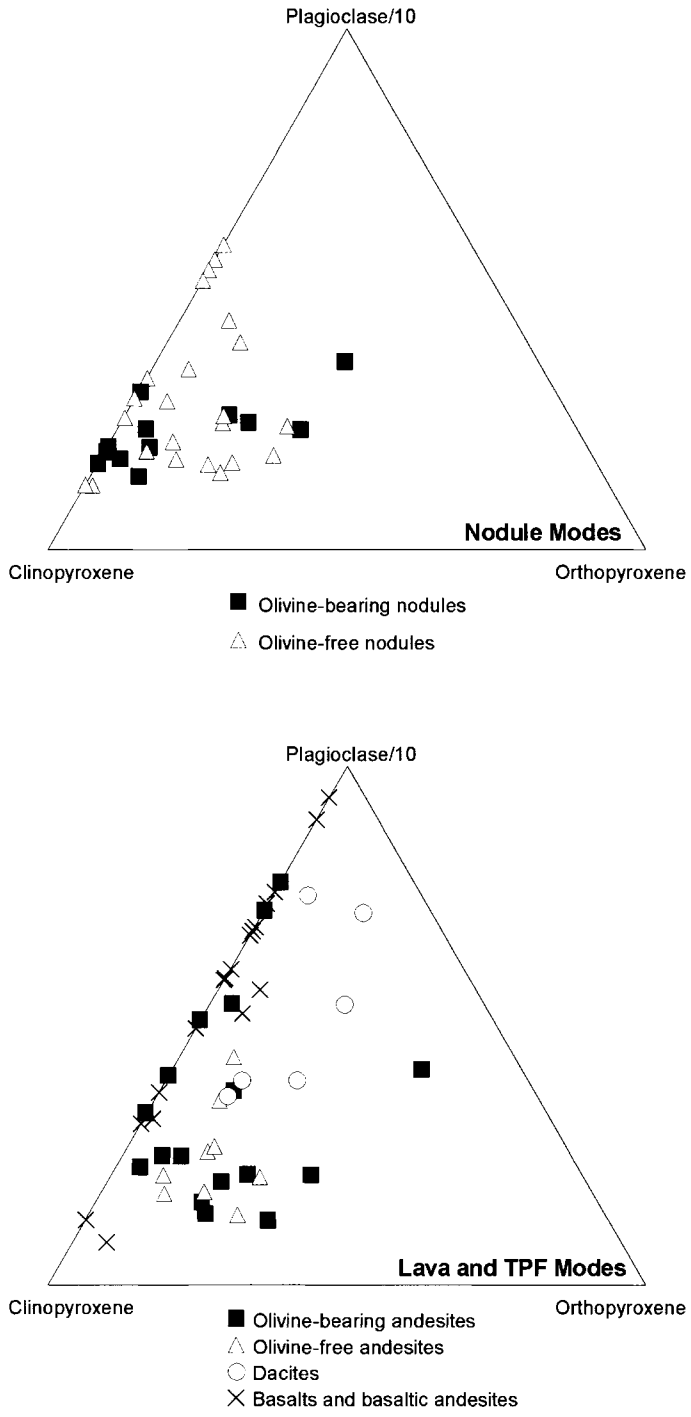

Fig. 5.1. Modal proportions of plagioclase, clinopyroxene and orthopyroxene in triangular plots of Santorini nodules (**a**) and of phenocrysts in Santorini lavas and pyroclastic (TPF) deposits (**b**). The proportion of plagioclase has been reduced by a factor of ten to facilitate

from $Wo_{49}En_{41}Fs_{10}$ to $Wo_{38}En_{41}Fs_{21}$. They have low Na and Al contents. Clinopyroxene encloses plagioclase in a poikilitic texture and more rarely jackets altered olivines. Clinopyroxene is often found in mineral aggregates with orthopyroxene and an opaque phase. Orientated lamellae of alteration products (amphibole and oxide) occur within some clinopyroxenes. Clinopyroxenes are rimmed by, and alter internally to, both actinolitic amphibole and red oxidised hornblende-biotite intergrowths (lamprobolite)

Orthopyroxene

Unzoned subhedral hypersthene primocrysts are present up to 9 volume% in many nodules. The crystals range from En_{69} to En_{41}. Hypersthene can occur at the centre of aggregates with augite and magnetite, and as rims to altered olivine. Rare exsolution lamellae of clinopyroxene have been observed. Orthopyroxenes are commonly partly replaced by orthorhombic amphibole (cummingtonite to anthophyllite) and biotite, with complete pseudomorphs in the most altered nodules. Tie-lines between coexisting clinopyroxene and orthopyroxenes are generally parallel to each other, indicating that the pyroxenes are an equilibrium assemblage (Fig. 5.4).

Olivine

Rounded olivine forms a small proportion (up to 3% by volume) of several nodules. Most are heavily altered to reddish iddingsite and are jacketed by orthopyroxene, usually within aggregates of pyroxenes and oxides. Nodule 8513 (Upper Scoriae 1) contains fresh olivine zoned from a Fo_{57} core to a Fo_{38} rim.

Oxide minerals and apatite

Subhedral to anhedral Ti-bearing magnetite is ubiquitous and is typically associated with pyroxenes. Electron microscopy shows multi-stage exsolution to have occurred, with complex orientated lamellae of ilmenite. Intercumulus magnetite and ilmentite are present. Haematite occurs as an alteration product of pyroxenes. Apatite is present as small acicular crystals within pyroxenes and as granules with intercumulus quartz and plagioclase.

Quartz and alkali feldspar

Quartz is found in most nodules in proportions up to 12 volume%. Anhedral intercumulus grains occur with plagioclase (Fig. 5.2d), and can form granophyric intergrowths with alkali feldspars. Alkali feldspars range from anorthoclase to sanidine ($Or_9An_8Ab_{83}$ to $Or_{76}An_2Ab_{22}$) in composition (Fig.5.3). Nodules from Cape Therma 3 display coarse patches of poikilitic anorthoclase enclosing quartz and plagioclase.

Hydrous phases

Some nodules contain two categories of hydrous minerals: (i) primary amphibole and biotite, and (ii) hydrous alteration products.

(i) Primary amphibole and biotite occur in the intercumulus assemblage with quartz and feldspar as small euhedral to subhedral grains of greenish actinolitic- and magnesio-hornblende and tabular biotite. Actinolitic hornblendes have a fibrous habit whereas magnesio-hornblende forms well-cleaved plates.

(ii) Hydrous alteration products are common. Augites are rimmed or wholly replaced by greenish actinolite (particularly in nodules from Cape Therma 3) or edenitic- to magnesio-hornblendes. Hypersthenes are often partly replaced by fibrous cummingtonite or anthophyllite with brown oxidized rims. In the more oxidized nodules there is partial to wholesale replacement of pyroxenes by bright red material. Single crystal X-ray diffractometry indicates an intergrowth of biotite and oxyhornblende together with minor haematite. Many of the nodules have clearly been affected by hydrothermal metamorphism. They have also been oxidized during eruption and cooling of the pyroclastic deposits.

Epidote, titanite and allanite

Cape Therma 3 nodules contain epidote granules in interstitial regions with compositions ranging from $Ep_{75}Zo_{25}$ to Ep_{65} Zo_{35}. Titanite and, in one example, allanite occur in Cape Therma 3 nodules.

Fig. 5.2. Photomicrographs of coarse-grained nodules. **(a)** Sub-ophitic texture in sample 85041 of Upper Scoriae 2 (plane-polarized light with field of view 8 mm wide) containing predominantly plagioclase and clinopyroxene; **(b)** seriate to glomero-porphyritic texture showing zoned plagioclase primocrysts with calcic bytownite cores in sample 8409 of Upper Scoriae 2 (crossed polars with field of view 5 mm wide); **(c)** mesocumulate texture in sample 8407 of Upper Scoriae 2 (plane-polarized light with field of view of 10 mm) containing plagioclase–augite–hypersthene–magnetite assemblages; **(d)** granophyric intergrowth of quartz and alkali feldspar in orthocumulate textured rock (sample 84921) from the Cape Riva deposit (crossed polars with field of view of 5 mm).

Comparison between the petrology of the nodules and volcanic rocks

The petrology of Santorini lavas has been extensively documented (e.g. Nicholls 1971*a*; Pichler & Kussmaul 1972; Huijsmans 1985; Stamatelopoulou-Seymour *et al.* 1990). These lavas were contemporaneous with the Thera pyroclastics and show a broadly consistent mineralogy over a time period of at least 360 ka (Chapter 3). The petrology of the Thera pyroclastics has been summarized in Chapter 4. Here we provide a distillation of the key features for comparison with the nodules.

Volcanic rocks of the first and second explosive cycles, as well as historic lavas of the Kameni Islands, display a simple mineral paragenesis. Basalt and mafic andesites (<57% SiO_2) are typically porphyritic and contain phenocrysts of plagioclase, augite and olivine (Fig. 5.1b). Orthopyroxene is absent or rare. Most mafic andesites also contain minor amounts of magnetite microphenocrysts. In common with many island arc mafic lavas the plagioclase phenocryst proportions are in excess of those expected from low pressure phase equilibria in many lavas and pyroclastic samples (Fig. 5.1b; Gill 1981). Silicic andesites (56–63% SiO_2) vary from porphyritic to aphyric varieties and always contain phenocrysts of augite, plagioclase and magnetite. Most silicic andesites (80%) contain orthopyroxene phenocrysts and divide into olivine-bearing and olivine-absent varieties (Fig. 5.1b). Most mafic andesites below 57% SiO_2 do not contain orthopyroxene. Orthopyroxene-bearing dacites (63–68% SiO_2) are free of olivine. Orthopyroxene becomes dominant over clinopyroxene in the rhyodacites. Zircon appears as a phenocryst in some rhyodacite lavas with $SiO_2 > 68\%$. Hydrous ferromagnesian phases are absent in even the most evolved rhyodacitic rocks of the Thera pyroclastics, except for rare hornblende in Lower Pumice 2, the groundmass of the Minoan andesite scoria and Minoan crystal-rich pumices. These general features of the mineral assemblages are reflected in the modal

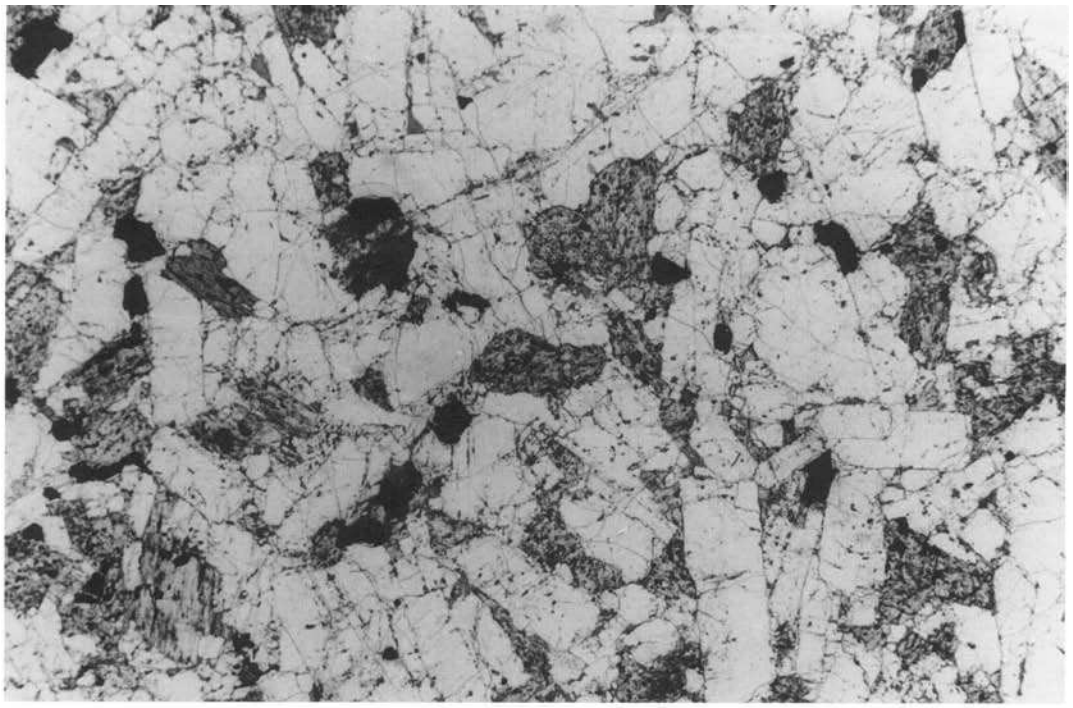

(c)

(d)

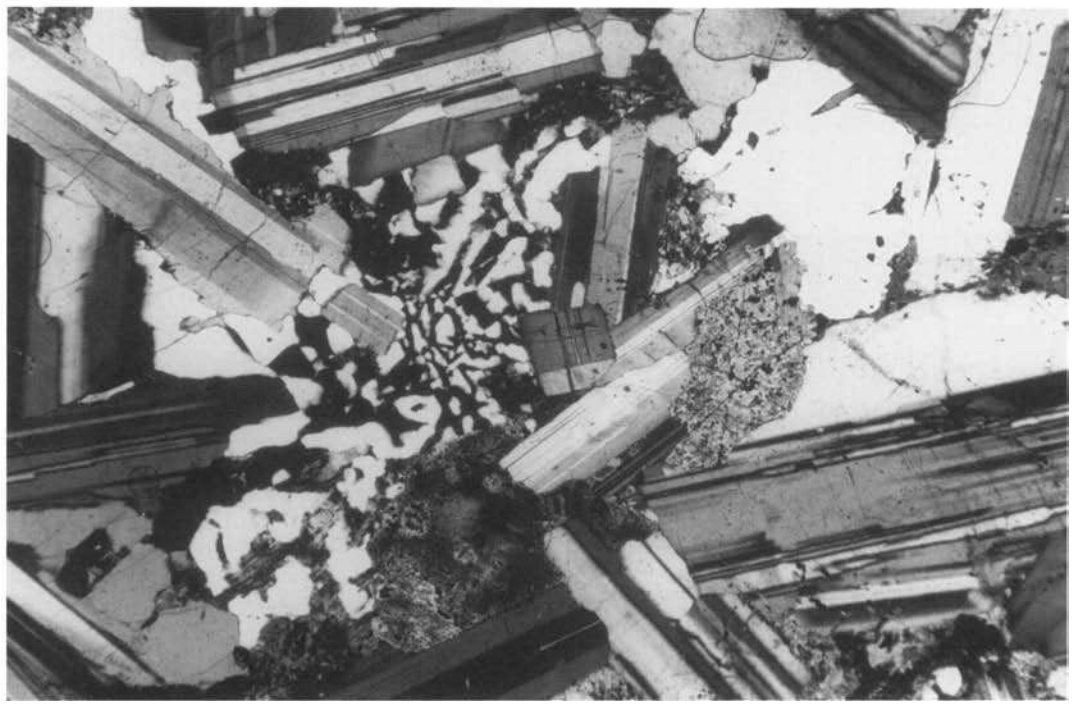

Fig. 5.2. (*continued*).

proportions of phenocrysts (Fig. 5.1b). Thus the nodules broadly divide into a majority (65%), which have orthopyroxene primocrysts and are thus complementary to the phenocryst assemblages in the andesites and dacites, and a minority (35%) which lack orthopyroxene and have primocrysts similar to the phenocryst assemblages in the mafic andesites.

Some lavas show disequilibrium phenocryst assemblages which have been interpreted as the result of magma mixing (Huijsmans 1985; Chapter 4) and magma–cumulate mixing (Pyle *et al.* 1988; Chapter 4). Thus a few mafic andesite lavas contain orthopyroxene and there are silicic andesites containing both olivine and orthopyroxene. Complex zoning patterns in plagioclase and pyroxene and resorption textures are observed in hybrid lavas (Huijsmans 1985; Stamatelopoulau-Seymour *et al.* 1990). Textural and compositional data indicate that there are rare orthopyroxenes in a few lavas with SiO_2 less than 56% and that rare olivines in dacites are xenocrysts (Huijsmans 1985). The gabbro nodules do not show assemblages equivalent to the disequilibrium phenocryst assemblages of the hybrid Santorini andesites, with the exception of calcic plagioclase cores.

The petrology of juvenile ejecta from two main nodule-bearing deposits (Upper Scoriae 2 and Upper Scoriae 1) can be compared with the nodules. Both deposits are dominated by homogeneous andesite ejecta after eruption of dacitic ejecta in initial fallout phases (Chapter 4). The andesites have few vesicles and are crystal-poor, with phenocrysts of plagioclase, clino- and orthopyroxene, and magnetite. Plagioclase falls into two categories (Fig. 5.3). First, fragmental cores of bytownite (An_{90} to An_{79}) are surrounded by mantles of normally zoned labradorite or andesine (An_{70} to An_{43}). Second, smaller rectangular laths of more uniform labradorite-andesine (An_{65} to An_{45}) are observed. Clinopyroxene (salite to augite) and orthopyoxene are granular and the compositions of co-existing pairs

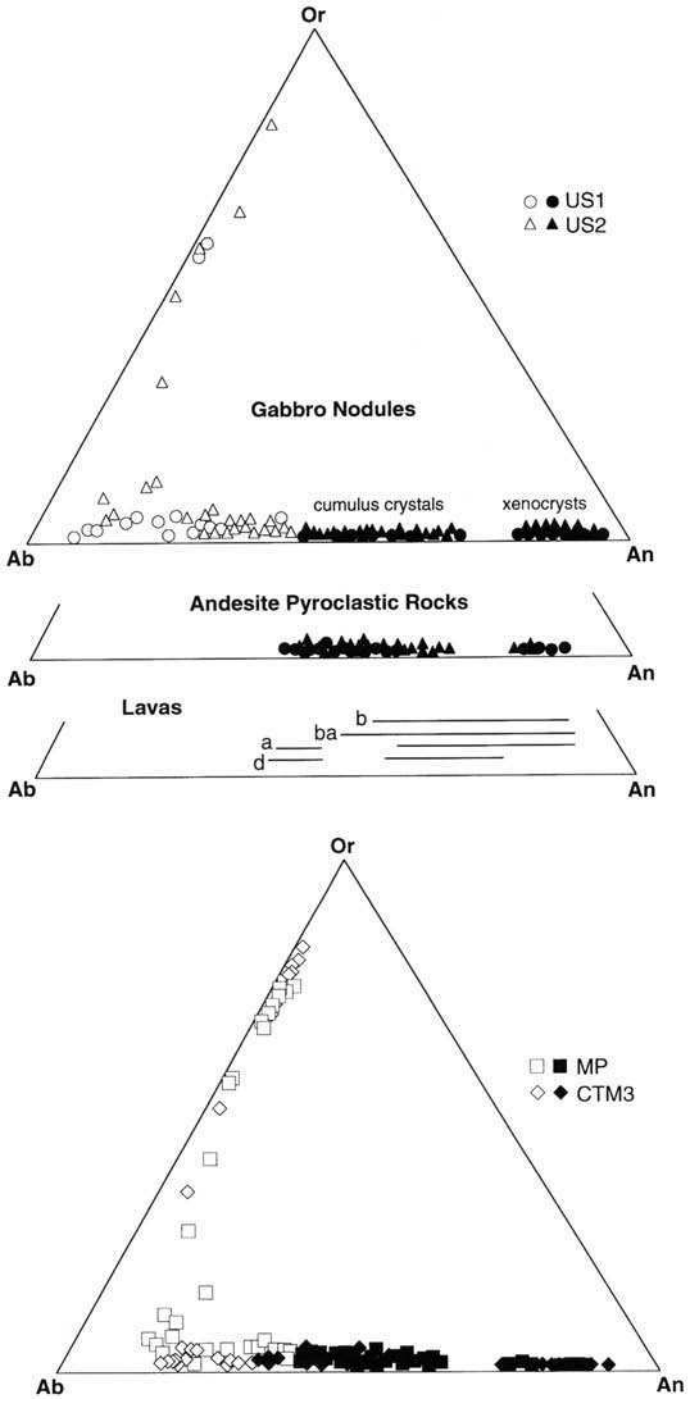

Fig. 5.3. (**a**) Feldspar compositions for Upper Scoriae 2 (US2) and Upper Scoriae 1 (US1) nodules and juvenile ejecta. Ranges of feldspar compositions in lavas from Huijsmans (1985) are shown for comparison (b, basalt; ba, mafic andesite; a, silicic andesite; d dacite). Open symbols, strongly zoned rims of primocrysts and intercumulus material in nodules. (**b**) Feldspar compositions for Cape Therma 3 (CTM3) and Middle Pumice (MP) nodules.

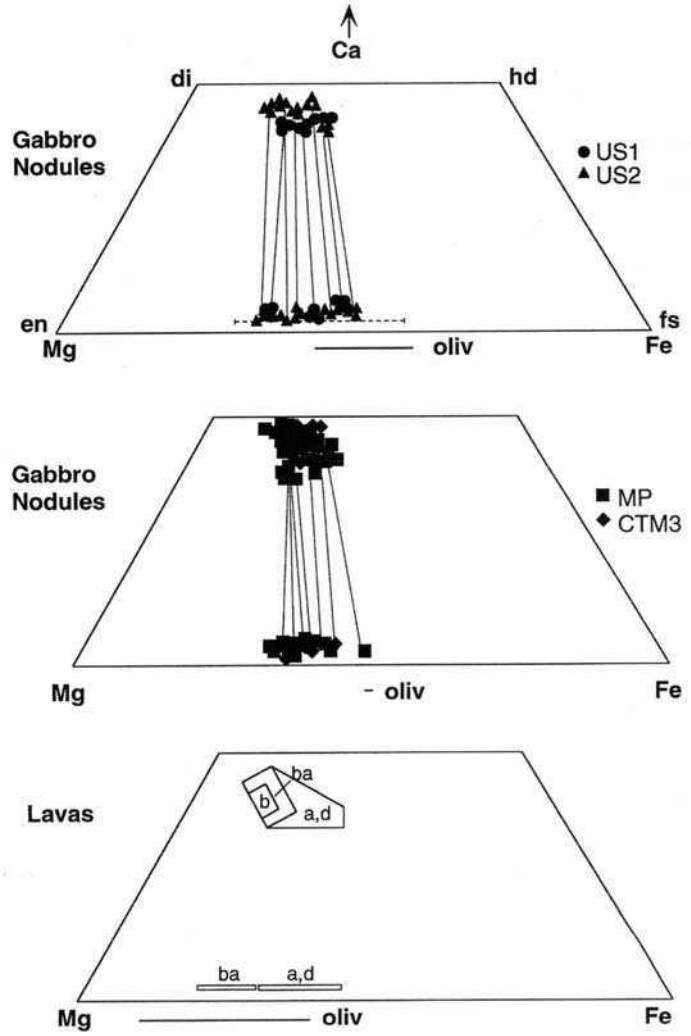

Fig. 5.4. Pyroxene and olivine compositions for Thera Pyroclastic nodules. Fields of pyroxene compositions for lavas from Huijsmans (1985) are shown for comparison (b, basalt; ba, basaltic andesite; a, silicic andesite; d, dacite). Broken line on upper diagram indicates extent of zoning of orthopyroxene in sample 8513 (Upper Scoriae 1).

are consistent with equilibrium. Magnetite can be either euhedral or subhedral. Olivine is present in minor amounts in about half of the Upper Scoriae 2 and Upper Scoriae 1 samples, forming subhedral or rounded grains sometimes jacketed by clinopyroxene.

Primocrysts were distinguished from intercumulus material during modal analysis of the nodules. The modes of the primocryst assemblages were estimated and averaged for nodules from the two Upper Scoriae deposits. The modal proportions of phenocrysts were measured on ten andesite clasts from each of the Upper Scoriae deposits. The average modal composition of the cumulus framework of the nodules and the phenocrysts in andesitic ejecta are compared in Table 5.2. The modal data are similar in each case, although there is a slightly lower magnetite content in nodules of Upper Scoriae 2 compared to the associated andesite and a higher orthopyroxene content in nodules of Upper Scoriae 1 compared to the andesite host.

Clinopyroxene and orthopyroxene phenocrysts in the Thera pyroclastic andesitic ejecta have the same range of compositions as the nodule primocrysts (Fig. 5.4). Clinopyroxene phenocrysts in basalt and mafic andesite lavas are notably more magnesian (Fig. 5.4) with virtually no overlap in composition with the nodules and host ejecta. The single preserved fresh olivine in one nodule in

Table 5.2. *Comparison of nodule modes, phenocryst modes in host andesites and modelled compositions of crystal extract (vol%)*

Computed mode	plag	cpx	opx	Ti-mt
(1) Upper Scoriae 2				
Average cumulate	62.1	25.2	7.2	4.5
Average phenocryst	63.8	20.1	6.8	6.7
Modelled composition	66.8	19.5	7.0	6.7
(2) Upper Scoriae 1				
Average cumulate	62.8	21.7	10.0	5.5
Average phenocryst	68.4	21.3	3.4	6.0
Modelled composition	65.7	17.6	10.5	6.1

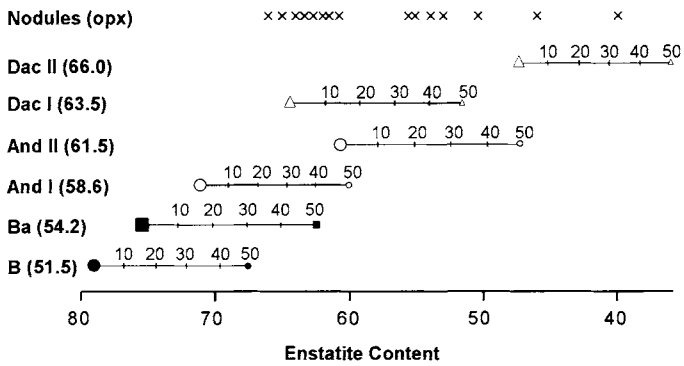

Fig. 5.5. Diagram displays the core compositions of orthopyroxenes in the nodule suite and the range of equilibrium compositions of orthopyroxenes in Santorini magmas as functions of the amount of crystallization. Six Santorini compositions have been taken and their SiO_2 content is indicated in parentheses on the diagram. For each composition the initial composition of equilibrium orthopyroxene has been calculated using the experimentally determined partitioning of Fe and Mg (Baker & Eggler 1987). The change in composition of orthopyroxene as a function of crystallization is then shown in 10% intervals to 50% crystallization. B, basalt; Ba, mafic andesite; And, silicic andesite; Dac, dacite.

Upper Scoriae 1 is significantly more Fe-rich (Fo_{57} to Fo_{38}) than phenocrystic olivine found in basalts and mafic andesites (Fo_{80} to Fo_{65}).

Comparison of the compositions of the ferromagnesian primocrysts in the nodules with phenocrysts in the volcanic rocks is complicated by the possible re-equilibration of the primocrysts with evolving intercumulus melt during solidification, resulting in iron-enrichment. Simple calculations have been carried out to evaluate the extent of iron-enrichment. We estimated the compositions of orthopyroxenes in equilbrium with typical lavas of the Santorini suite. Published experimental and theoretical information (Nicholls 1978; Baker & Eggler 1987; Grove & Baker 1984) indicate that, to a first approximation, partitioning of Fe and Mg between olivine, clinopyroxene, orthopyroxene and melts are similar. We have assumed that (Fe/Mg) crystal/(Fe/Mg) melt = 0.26 following experimental studies by Baker & Eggler (1987) on similar island arc magma compositions. Figure 5.5 displays the results of these calculations and shows that the orthopyroxenes in equilibrium with basalt and mafic andesite lavas would be more magnesian than the primocrysts in most of the orthopyroxene-bearing nodules. Orthopyroxene compositions in the silicic andesites and dacites coincide with those in the nodules.

To evaluate re-equilibration effects, we calculated the expected change in orthopyroxene compositions in each magma type as equilibrium crystallization progresses. We assumed that the proportions of crystallising phases were 60% plagioclase, 25% clinopyroxene, 10% orthopyroxene and 5% magnetite. Figure 5.5 displays the decrease in enstatite content in the orthopyroxene with progressive equilibrium crystallization. The calculations indicate that enstatite content can decrease by about 10–12% by 50% crystallization, but most of the nodules contain orthopyroxenes with core compositions too Fe-rich to be explained by extensive crystallization of basaltic or mafic andesite magmas. Since these more mafic magmas in fact do not contain orthopyroxene, the case for deriving these nodules from magmas with less than 56% SiO_2 by extensive in situ crystallization is unconvincing. For nodules with most Mg-rich orthopyroxene (En_{66} to En_{60}) the calculations also support a cumulate origin rather than in situ equilibrium crystallization of an andesite magma. The later hypothesis would generate significantly more Fe-rich compositions (Fig. 5.5) due to re-equilibration than are actually observed.

Plagioclase from both the andesite/dacite ejecta and nodules display almost identical compositional ranges, with a well-defined compositional gap (Fig. 5.3). Both rock types contain xenocrystic cores of calcic plagioclase. Plagioclases from basaltic and mafic andesitic rocks cover a wide compositional range (Fig. 5.3), but the nodules and andesite/dacite ejecta extend to somewhat more sodic compositions.

In summary, data on modal proportions and mineral chemistry suggest that the nodules were precipitated from magmas covering the compositional range from mafic andesite to silicic andesite and dacite magmas. The majority of nodules contain orthopyroxene which, together with the low abundance or absence of olivine and absence of zircon primocrysts, constrain the silica content of the melts to between 57% and 66% SiO_2. Thus many of the nodules are interpreted to represent the complementary cumulates to silicic andesite and dacite melts. The orthopyroxene-absent nodules which often contain olivine, are interpreted to represent the complementary cumulates to the mafic andesites (<57% SiO_2). However, no nodules have been found with mineral compositions complementary to the basalts. The only cumulates from basaltic magmas known to us from the Thera pyroclastics occur as fragments of olivine gabbro mixed into the Minoan and Lower Pumice 2 andesites.

Temperature and pressure estimates

The mineral assemblages in the nodules provide some constraints on P–T conditions during their formation. Coexisting pyroxenes yield temperatures in the range 850–1000°C using the pyroxene geothermometer of Lindsley (1983) and 830–930°C using the empirical equation of Wells (1977). A value of 1030°C was calculated for a Cape Therma 3 nodule. Diffuse beam analyses of coexisting magnetites and ilmenites yielded temperatures of 850–900°C, but these results should be treated with caution given the pervasive oxidation and exsolution textures observed. These temperatures are substantially lower than the pre-eruptive temperatures of basaltic and mafic andesite magmas. They are plausible for silicic andesite and dacite magmas, although they are likely to be lower than the actual magmatic temperatures if the pyroxenes re-equilibrated at the post-cumulus stage.

The pressure of formation is poorly constrained. Herzberg (1978) showed that the assemblage ol–cpx–opx–plag (such as sample 8513) is unstable at pressures greater than 500 MPa. Coexisting mineral compositions can be used to calculate pressure based on the thermodynamic data set of Wood & Holloway (1982). The following reactions can be used

$$Fo + An = En + CaTs$$
$$Fo + An = Di + MgTs.$$

Both reactions have low dP/dT slopes so are suitable for barometry. Using a temperature of 1000°C, pressures of 0–200 MPa were estimated. The errors propagated are substantial (up to ±100 MPa). However, the semi-quantitative calculations are consistent with low pressure conditions for the formation of the nodules in high level crustal magma chambers.

Whole-rock geochemistry

Fifty-three nodule samples were analysed by XRF using methods described in Appendix 1. The major and trace element compositions of the nodules are listed in Appendix 2.

On variation diagrams (Fig. 5.6) the nodules, including the orthopyroxene-bearing nodules, overlap with Santorini basalt and mafic andesite lavas for many elements. There is more scatter for the nodules than the lavas. The nodules are significantly poorer in SiO_2 than most of the Thera pyroclastics in which they are found. In the TiO_2 and FeO v. SiO_2 diagrams, most of the Upper Scoriae 1 and Upper Scoriae 2 nodules are enriched in TiO_2 and in FeO compared to most basalt and mafic andesite lavas with <57% SiO_2. The lava trend has been interpreted to represent Ti- and Fe-enrichment by fractional crystallization (Huijsmans 1985). K_2O is enriched in most nodules compared to the average lava trend and compared to the associated pyroclastic ejecta at a given SiO_2 value.

Trace element data display considerable scatter for many elements. The nodules broadly overlap with the Santorini mafic lavas (<57% SiO_2) for most elements. Many nodules have higher

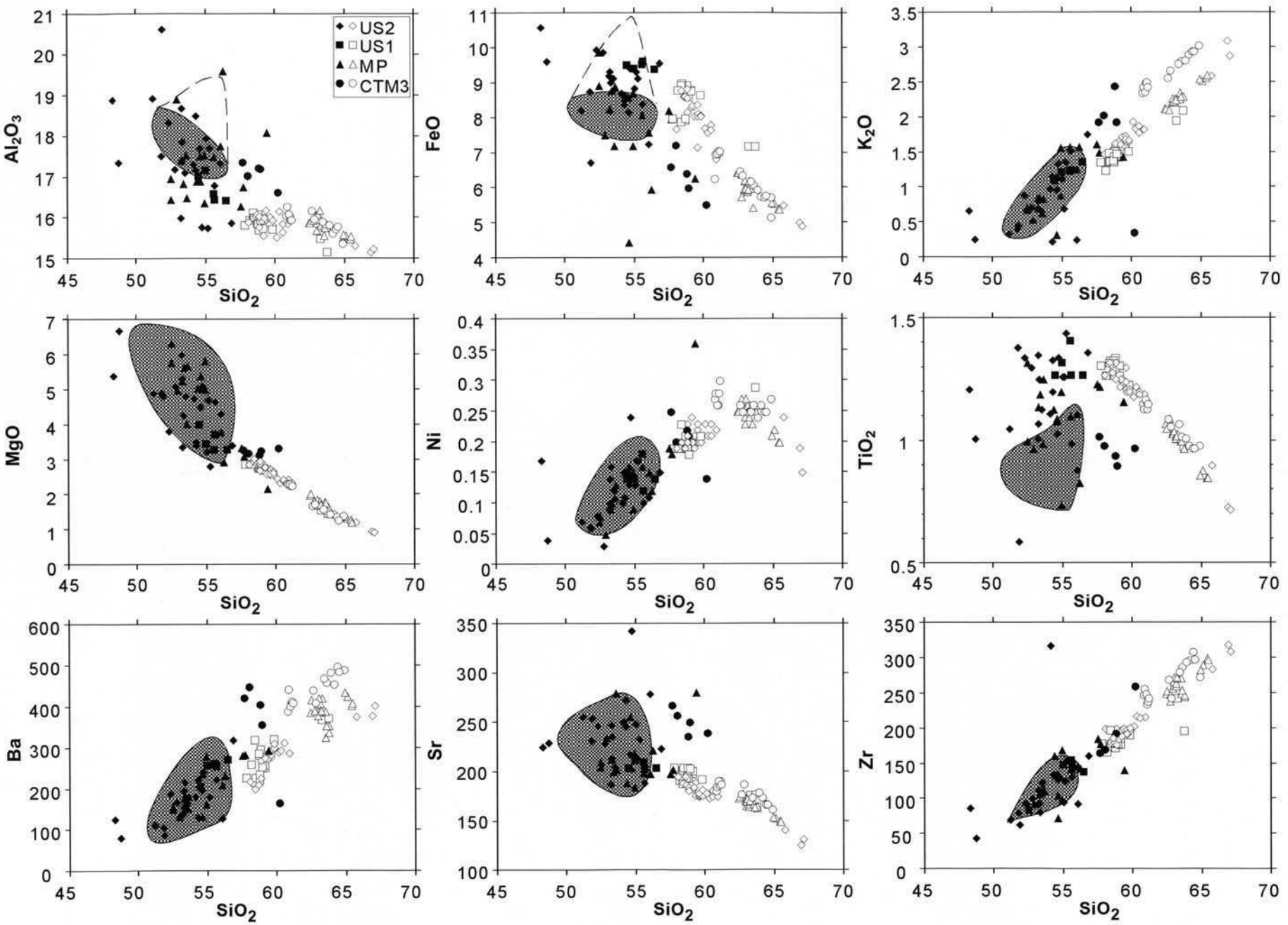

Fig. 5.6. Selected major and trace elements of the nodules and associated volcanic ejecta are plotted against SiO_2. The field of basalt and mafic andesite (<57% SiO_2) lava compositions of Skaros and Peristeria volcanics is shown as a stippled area (data from Huijsmans 1985). For Al_2O_3 and FeO plots most lavas fall in the darker stippled area, with only a small number of samples in the lightly stippled area. Solid symbols are the nodule whole rock compositions and open circles are the compositions of host volcanic rocks.

concentrations of Ni than the pyroclastic ejecta (Fig. 5.6), but lower concentrations than most of the basalt to mafic andesite lavas. Most mafic lavas contain 20–40 ppm Ni whereas nodules with the same SiO_2 contents contain <20 ppm Ni. The diorite nodules from Cape Therma 3 have higher silica contents and are notably enriched in Cr, Ni, Sr and Ce and depleted in V and Y compared to the host Cape Therma 3 andesite ejecta.

As shown in Chapter 6, when geochemical data from the Thera pyroclastics are plotted without discriminating individual deposits, the diagrams appear scattered and incoherent. However, each individual deposit shows a well-defined coherent differentiation trend. Each deposit can be distinguished by distinctive major and trace element contents at a fixed value of SiO_2. The nodules show far less geochemical coherence than the individual Thera pyroclastic deposits.

Petrogenesis

At one extreme the Santorini gabbros and diorites could represent frozen melts of basaltic to mafic andesite composition. The nodules overlap compositionally with lavas of these compositions. However, several lines of evidence suggest that they are, in fact, cumulate rocks derived by fractionation of magmas covering the compositional range from mafic andesite to dacite. First, their textures and mineral compositions can be interpreted as a cumulus framework of usually unzoned pyroxene and weakly zoned plagioclase primocrysts with a pore filling of strongly zoned feldspar and quartz together with minor late-stage minerals. Second, the mineral assemblages of those nodules containing orthopyroxene are found only in lavas with $SiO_2 > 57\%$. Third, the compositions of the minerals are indistinguishable from those found in andesite and dacite lavas. The nodules have basic compositions because they represent the complementary cumulate extract formed by fractionation of the intermediate magmas of Santorini. Fourth the nodule compositions are anomalously low in incompatible elements (e.g. Ni) and enriched in FeO and TiO_2 compared to most lavas of similar SiO_2 content. These geochemical characteristics can be explained if the nodules are crystal extracts from low Ni intermediate magmas and contain abundant FeTi oxides due to accumulation. The variations of modal abundances and compositions of primocrysts indicate that the magmas from which they were formed ranged from mafic andesite through to dacite. They provide direct evidence of differentiation in crustal magma chambers.

In order to test the hypothesis that the nodules are complementary to the fractionation of the intermediate Santorini magmas, fractionation calculations were carried out for the Upper Scoriae deposits. Both deposits are chemically zoned. The proportions of minerals needed to derive the most silica-rich from the most mafic composition were estimated using least-squares techniques. Mineral compositions used were those of observed phenocrysts in the more mafic composition. Results are given in Table 5.3 and are compared to modal abundances of primocrysts in the nodules and of phenocrysts in the andesitic ejecta. The models give low residuals and the mineral abundances are similar to those observed in the nodules and host ejecta, supporting the proposed petrogenetic model.

The poorer geochemical coherence of the nodules compared to the Thera pyroclastics can be attributed to several factors in the formation of cumulate rocks. Conditions of magmatic differentiation on Santorini have varied during the volcano's evolution with magmas showing variations in Fe-enrichment together with hybridism generating for example Fe- and Ti-poor magmas (Chapter 6). The scatter in the nodules can at least in part be attributed to the variations in conditions of magmatic evolution. For example, differentiation trends from low and high TiO_2 content magmas would be complemented by cumulate nodules with low and high TiO_2 contents respectively. Another factor in cumulate rocks that can produce scatter is sorting effects during accumulation. Some of the variation could be attributed to variations in the modal proportions of the main cumulus minerals, resulting from differential settling of crystals of different size and density. Postcumulus processes, such as re-equilibration with melts during compaction could result in chemical modification. Hydrothermal alteration would also have caused variations, particularly in mobile elements.

Table 5.3. *Mass balance calculation on the crystal extracts formed in the fractionation interval from andesite to dacite*

	Initial andesite	Target dacite	Phases removed			
			plag	cpx	opx	Ti-mt
US1						
SiO_2	58.04	62.66	54.19	51.12	51.8	0.79
Al_2O_3	15.78	15.4	28.03	0.87	0.34	2.61
TiO_2	1.29	1	–	0.35	0.37	20.17
FeO(T)	8.74	7.14	1.12	11.56	21.02	69.86
MgO	2.81	1.57	–	14.51	21.63	2.91
CaO	6.36	4.44	11.86	19.4	1.84	–
Na_2O	4.22	4.61	4.89	–	–	–
K_2O	1.4	1.94	0.21	–	–	–
MnO	0.19	0.18	–	0.44	0.89	0.52
Proportion (wt%)		70	17.4	5.7	3.6	3
Recalculated 'cumulate' residue (vol%)			65.7	17.6	10.5	6.1
Sum of residuals ($\sum r^2$)	0.027					
US2						
SiO_2	59.2	66.56	55.78	52.16	52.98	1.06
Al_2O_3	15.93	15.13	28.28	1.63	0.55	2.59
TiO_2	1.23	0.72	–	0.51	0.17	16.78
FeO(T)	8.01	4.94	0.45	10.6	21.69	70.75
MgO	2.61	0.95	–	13.73	21.07	3.29
CaO	6.02	3.07	10.59	19.5	1.68	–
Na_2O	4.34	4.81	5.2	–	–	–
K_2O	1.73	2.97	0.19	–	–	–
MnO	0.16	0.14	–	0.38	0.88	0.44
Proportion (wt%)		60	23.4	8.4	2.5	4.7
Recalculated 'cumulate' residue (vol%)			66.8	19.5	7	6.7
Sum of residuals ($\sum r^2$)	0.067					

US1, Upper Scoriae 1; US2, Upper Scoriae 2.

There is evidence that the nodules are not necessarily genetically linked to the specific andesite ejecta with which they were erupted. The nodules are fully crystallized and some show signs of hydrothermal metamorphism. Consolidation and alteration must therefore have taken place before they were disrupted by the host andesitic magmas. Many nodules also have elemental abundances and ratios of incompatible trace elements which are higher than would be expected if they were precipitated from their host melt. This feature is particularly evident in Cape Therma 3 nodules. In the case of the Upper Scoriae deposits the associated nodules have lower proportions of titanomagnetite than the model fractionation assemblages and the phenocryst abundances in the andesites. Several explanations of this difference can be proposed. One explanation is that the nodules evolved from magmas at higher oxygen fugacities than the associated andesites resulting in earlier precipitation of oxides and lower modal proportions in the cumulate extract. The Upper Scoriae deposits have a tholeiitic character in terms of high FeO/MgO and TiO_2 (Chapter 6). The nodules therefore could be the cumulates from earlier andesitic magma with more calcalkaline affinities and lower FeO/MgO and TiO_2.

Summary

(1) Gabbro and diorite nodules on Santorini are cumulates derived by fractionation of mafic andesite, silicic andesite and dacite magmas in high level (crustal) magma chambers. They are considered to represent samples of the crystal extracts involved in the generation of large volumes (order of 100 km^3) of andesitic, dacitic and rhyodacitic magmas that have been erupted over the last 360 000 years to form the Thera pyroclastics and associated lava sequences.

The data thus support previous studies that have identified fractional crystallization in high-level magma chambers as a major process in the petrogenesis of Santorini magmas (Nicholls 1971*a*; Mann 1983; Huijsmans 1985; Barton & Huijsmans 1986).

(2) Most of the nodules were fully consolidated and had been variably affected by hydrothermal alteration before disruption and ejection by new batches of andesitic magma. Substantial variations in differentiation conditions, from tholeiitic to calcalkaline, and in the concentrations of trace elements are apparent during the evolution of Santorini magmas, resulting in the observed compositional variations in the complementary cumulate nodules. Compositional variation in the nodules also could have been caused by fluctuations in the proportions of cumulus minerals, effects of intercumulus diagenesis and hydrothermal alteration.

(3) Sparks (1990) and Marsh (1990) differed in their views on whether a dichotomy exists between plutonic and volcanic rock. Marsh (1988, 1990) stated that basaltic magma mainly gives rise to gabbroic plutons and silicic magma mainly gives rise to granitic plutons. However the Santorini nodules demonstrate that gabbroic rocks can be formed from intermediate magmas at least up to dacite compositions, provided the residual melts can be separated from the phenocrysts or primocrysts with reasonable efficiency.

Chapter 6
Geochemistry, isotopic composition and petrogenetic modelling of the Thera pyroclastics

This chapter examines the major element, trace element, and isotope geochemistry of the Thera pyroclastics, and places it in the context of the geochemical evolution of the whole volcanic field. Geochemical studies to date have been undertaken predominantly on the lavas, and the pyroclastic succession has been relatively neglected. The data on the pyroclastics are taken from Druitt (1983), Mellors (1988), Pyle (1990*b*), and Edwards (1994). Whole-rock analyses and sample descriptions are given in Appendix 2. Most analyses are of a single pumice or scoria lump, although some are combinations of several small clasts and a few are compositionally banded. The rock classification scheme used throughout the memoir is shown in Fig. 6.1. Previous isotopic studies on Santorini are also largely confined to the lavas, and no detailed studies had been carried out on the pyroclastic rocks. In this chapter we present new $^{87}Sr/^{86}Sr$, $^{143}Nd/^{144}Nd$, $^{206}Pb/^{204}Pb$, $^{207}Pb/^{204}Pb$, $^{208}Pb/^{204}Pb$ and $\delta^{18}O$ isotopic data on 40 samples of the Thera pyroclastics. We also include some measurements of hydrogen isotopes. Methods of geochemical and isotopic analysis are described in Appendix 1. This chapter also presents some quantitative models of fractional crystallization and assimilation of crustal rocks. The geochemical data and models point towards the importance of crystal fractionation, magma mixing and assimilation of continental crust in magma genesis at Santorini. The chapter also documents temporal changes in geochemical features of Santorini magmas.

Previous research

Major and trace element geochemistry

Detailed studies of the lavas have been published by Nicholls (1971*a*, *b*, 1978), Puchelt (1978), Barton *et al.* (1983), Mann (1983), Huijsmans (1985), Barton & Huijsmans (1986), Mitropoulos *et al.* (1987), Huijsmans *et al.* (1988), Huijsmans & Barton (1989) and Arvanitides *et al.* (1990). Some new geochemical and petrological investigations have been completed as part of the EC Laboratory Volcano Project (Davis *et al.* 1998; Dietrich *et al.* 1998; Gartzos *et al.* 1998; Tarney *et al.* 1998). The lavas range from basalt to rhyodacite. On the diagram of Peccerillo & Taylor (1976) most basalts plot in the low-K field, whereas more evolved lavas have medium or high K contents (Fig. 6.1). However some early mafic inclusions of basalt to mafic andesite composition have medium K contents (Davis *et al.* 1998). With the exception of some basalts and mafic andesites, most of the lavas fall just in the tholeiitic field on the standard FeO/MgO–SiO_2 diagram (Fig. 6.2).

Nicholls (1971*a*, *b*) distinguished between four lava series on a chemical and mineralogical basis. We here use the new terminology developed in this memoir, but give the names Nicholls used in italics. Lavas, hyaloclastite breccias and tuffs of the Early Centres of Akrotiri peninsula (*Loumaravi–Archangelo Series*) are mostly

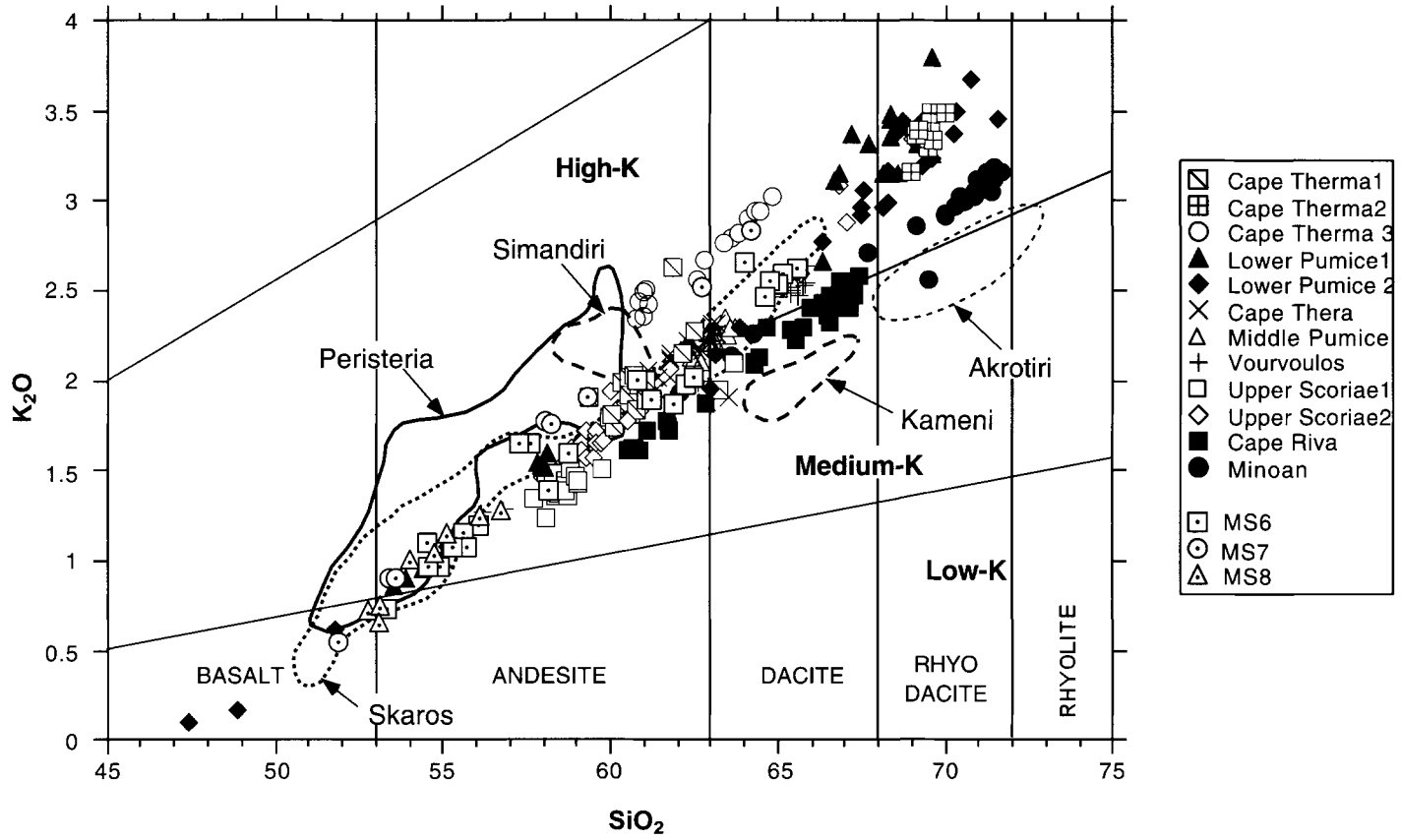

Fig. 6.1. K_2O versus SiO_2 diagram, modified after Peccerillo & Taylor (1976), showing the 12 major Thera pyroclastic units, the three minor successions discussed in the text, and the fields of lavas of the Early Centres of Akrotiri, Peristeria Volcano, the Simandiri and Skaros shields, and the Kameni Islands. Lava analyses are from Huijsmans (1985).

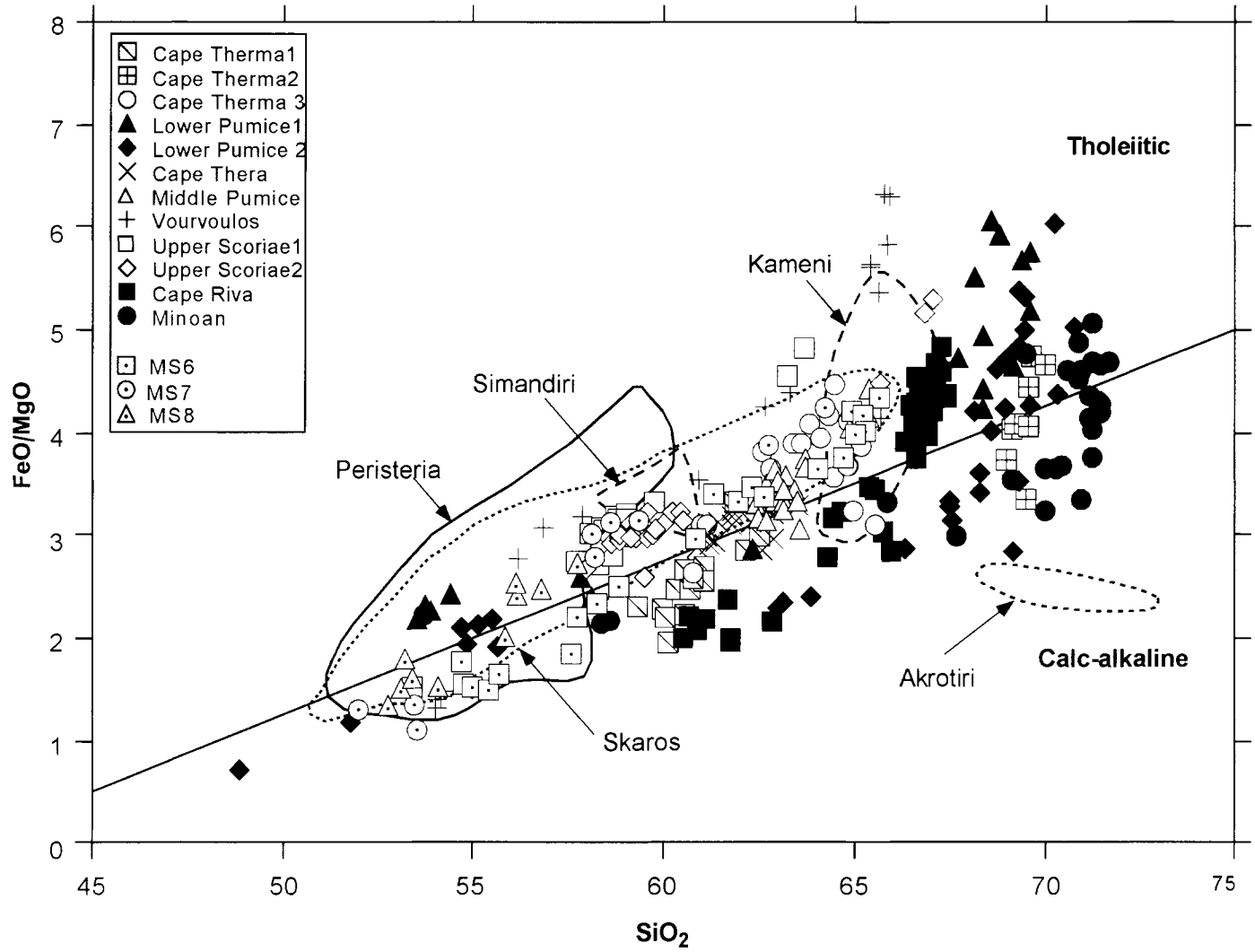

Fig. 6.2. Plot of FeO/MgO versus SiO_2 showing the 12 major Thera pyroclastic units, the three minor successions discussed in the text, and the fields of lavas of the early rhyodacitic centres of Akrotiri, Peristeria Volcano, the Simandiri and Skaros shields, and the Kameni Islands. Lava analyses are from Huijsmans (1985). The solid line divides the tholeiitic and calc-alkaline fields of Miyashiro (1974).

dacites, rhyodacites and rhyolites, but with small flows and intrusions of andesite. The rhyolites and rhyodacites of Akrotiri contain prominent hornblende and magmatic inclusions of hornblende-bearing mafic andesite. Most of the Akrotiri volcanics have calc-alkaline characteristics, although Tarney *et al.* (1998) have documented some rocks from the Akrotiri peninsula with tholeiitic characteristics. In comparison to younger volcanic rocks on Santorini the calcalkaline Akrotiri rocks are richer in CaO and MgO, display enrichments in large ion lithophile (LIL) elements and display higher Rb/Zr, Ba/Zr and K/Zr (Tarney *et al.* 1998). Silicic rocks Akrotiri tend to be poorer in alkalis although the inclusions tend to be enriched in alkalis and incompatible trace elements in comparison to younger mafic rocks (Davis *et al.* 1998). Magmas of the early Akrotiri centres also evolved under more hydrous and oxidizing conditions than the younger lavas. The Peristeria, Skaros, Simandiri, and Therasia lavas (*Main Series*) range from basalt to rhyodacite, lack hydrous phenocryst phases, show moderate enrichment in Fe, Ti, and P in andesitic compositions, and have generally tholeiitic affinities (Fig. 6.2). The *Akrotiri-Thera Series* of Nicholls (1971*a*,*b*) included the mafic Cinder Cones of Akrotiri Peninsula, the Thera pyroclastics, and lavas intercalated in the pyroclastics. These are similar mineralogically and chemically to the Main Series lavas. Some hybrid andesites with disequilibrium phenocryst assemblages and lacking Fe, Ti, or P enrichment occur in this series. Finally, lavas of the Kameni Islands (*Modern Series*) are uniformly dacitic, with magmatic inclusions of andesitic composition (Francalanci *et al.* 1998).

Figure 6.3 shows selected variation diagrams for the Akrotiri, Peristeria, Simandiri, Skaros and Kameni lavas after Huijsmans (1985). The stratigraphy recognized by Huijsmans differs from that presented in this memoir, so care was taken to use only analyses which correspond to the lava sequences defined in Chapter 3. The plotted data also do not include recent results of more comprehensive studies of the early Akrotiri centres (Davis *et al.* 1998). Iron is plotted as total FeO, as it is on all graphs of this chapter. The most primitive basalts plotted have approximately 50% SiO_2, 6.5% MgO, 90 ppm Ni and 200 ppm Cr. Davis *et al.* (1998) report basaltic compositions from the Akrotiri cinder cones with MgO up to 7.5%, and Cr up to 300 ppm. Scatter in the diagrams is partly due to the phyric nature of the samples, with the most pronounced scatter in mafic andesites. Al_2O_3 and Sr show particular scatter, probably due to variations in modal plagioclase. Overall, K_2O, Na_2O, Ba, Rb and Zr increase with increasing SiO_2, and Al_2O_3, FeO(T), MgO, Ni and Cr decrease. FeO(T), TiO_2, P_2O_5, V, Y and Zr reach maxima in andesitic compositions and thereafter decrease (Huijsmans 1985). Sr is very heterogeneous with some very high values in some mafic andesites. This Fe-enrichment trend has been modelled successfully by fractional crystallization of observed phenocryst phases (Mann 1983).

There are systematic differences in the abundances of certain trace elements between the different centres (Huijsmans 1985; Huijsmans *et al.* 1988; Huijsmans & Barton 1989). The early rhyodacitic lavas and tuffs of Akrotiri are relatively rich in Ba and Sr and poor in K, Rb, and Zr (Fig. 6.3). These silicic magmas form

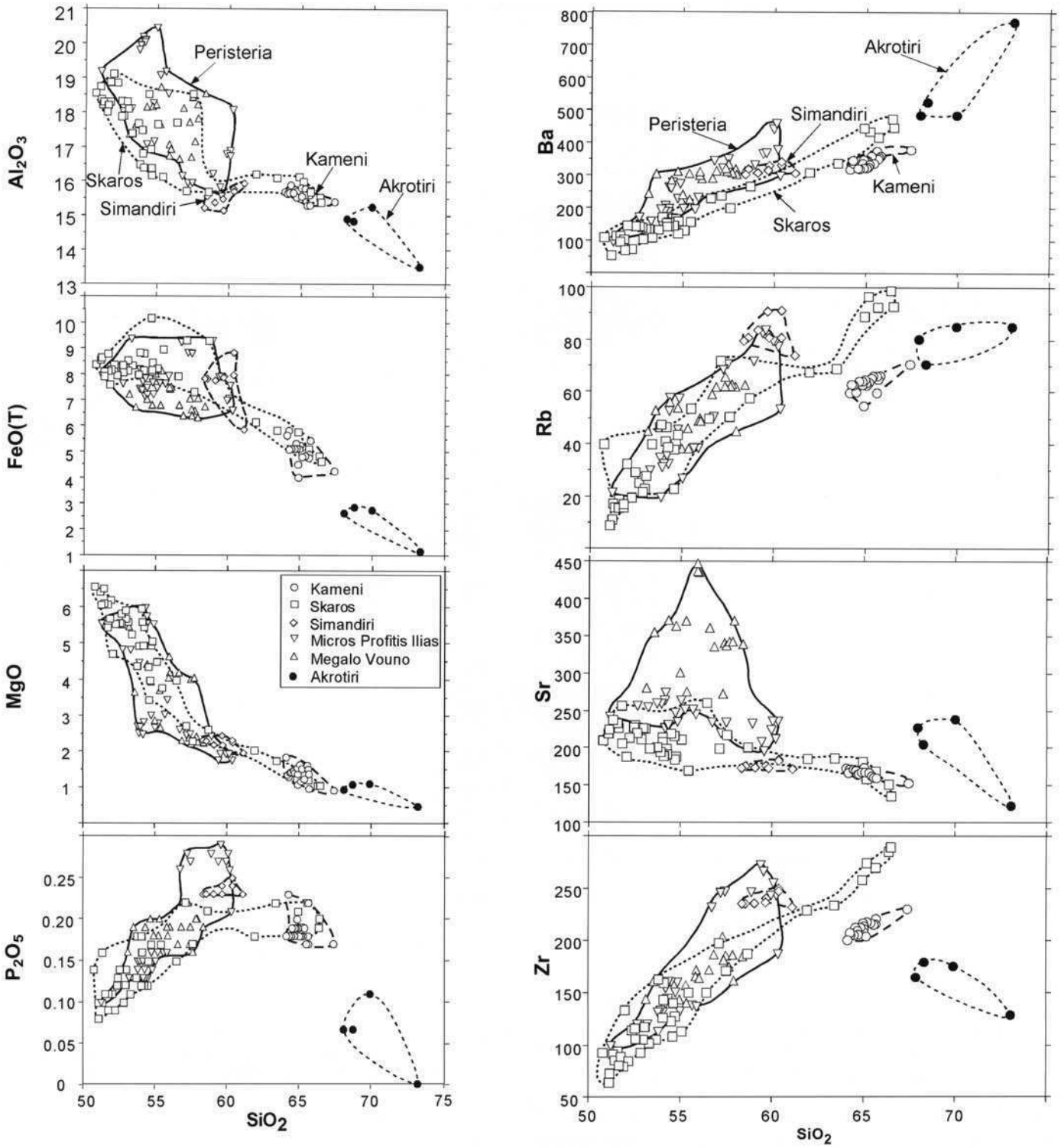

Fig. 6.3. (**a**) Selected major element variation diagrams for lavas of the Early Centres of Akrotiri, Peristeria Volcano, the Simandiri and Skaros shields, and the Kameni Islands. Analyses are from Huijsmans (1985). (**b**) Selected trace element variation diagrams for lavas of the Early Centres of Akrotiri, Peristeria Volcano, the Simandiri and Skaros shields, and the Kameni Islands. Analyses are from Huijsmans (1985).

a negative trend on a Zr–SiO_2 plot, probably due to zircon fractionation. In contrast, mafic inclusions in the same volcanics (not shown) are systematically richer in K, Rb, Ba and Zr than younger mafic rocks (Davis *et al.* 1998). Of the younger lava successions, K, Rb, Ba, and Th are highest in Peristeria and lowest in the Kameni lavas (Fig. 6.3). A similar, but less marked trend is evident for Nb and Zr. Sr is high in many of the predominantly andesitic lavas of Peristeria Volcano in comparison to the younger units. New data on basaltic and intemediate lavas of the early Akrotiri centres (Davis *et al.* 1998) show a tendency to high Sr contents in many samples with similar ranges to the Sr contents of Peristeria volcanics. As noted by Huijsmans (1985), there is a general decrease in the incompatible elements with time at Santorini from 530 ka to the present day when rocks of similar SiO_2 content are compared. This trend can be extended back to the early Akrotiri centres for mafic compositions but not for silicic rocks.

Isotope geochemistry

Previously published isotope ratios for Santorini rocks are listed in Table 6.1. $^{87}Sr/^{86}Sr$ ratios range from 0.7038 to 0.7060 (Pe & Gledhill 1975; Barton *et al.* 1983; Briqueu *et al.* 1986; Wyers 1987).

Table 6.1. *Ranges of previously determined isotopic ratios on Santorini rocks*

Author	$^{87}Sr/^{86}Sr$	$^{143}Nd/^{144}Nd$	$\delta^{18}O$	$^{176}Hf/^{177}Hf$
Puchelt & Hoefs (1971)	0.704–0.736			
Pe & Gledhill (1975)	0.7048–0.706			
Hoefs (1978)			+7.2–13.3	
Barton *et al.* (1983)	0.70472–0.70509			
Briqueu *et al.* (1986)	0.703805–0.705264	0.512718–0.512888		0.282972–0.283142
Wyers (1987)	0.70405–0.70580	0.512542–0.512846		

Puchelt & Hoefs (1971) found values up to 0.736, but these are probably too high (Barton *et al.* 1983). Two Minoan pumices of Briqueu *et al.* (1986) had the highest $^{87}Sr/^{86}Sr$ values (0.70494 and 0.70526) of any Santorini samples analysed by these authors. $^{143}Nd/^{144}Nd$ ranges from 0.51272 to 0.51289 and $^{176}Hf/^{177}Hf$ from 0.28297 to 0.28314 (Briqueu *et al.* 1986). $^{87}Sr/^{86}Sr$ is 0.7046 to 0.7058 in the Peristeria lavas and 0.7041 to 0.7051 in Skaros (Wyers 1987). $^{143}Nd/^{144}Nd$ values are 0.51254 to 0.51274 and 0.51269 to 0.51284 respectively.

The higher Sr isotopic ratios have been variably attributed to contamination by sea water enriched in radiogenic Sr, sea-water altered rocks, and crustal contamination (Puchelt & Hoefs 1971; Pe & Gledhill 1975; Barton *et al.* 1983; Wyers 1987). Another suggestion has been variation in the isotopic composition of the mantle-derived parental magmas. Barton *et al.* (1983), Briqueu *et al.* (1986), and Wyers (1987) concluded that a limited amount of assimilation combined with fractional crystallization (AFC) of the magmas has occurred. However, Barton *et al.* (1983) did not find a correlation of $^{87}Sr/^{86}Sr$ with SiO_2, or other incompatible elements, and so inferred that assimilation happened before much fractional crystallization took place. Briqueu *et al.* (1986) recognized correlations of $^{87}Sr/^{86}Sr$ with incompatible element concentrations and attributed the higher $^{87}Sr/^{86}Sr$ values to limited AFC with continental crust.

Whole-rock $\delta^{18}O$ data fall in the range +7.2‰ to +13.3‰ and plagioclase phenocrysts from two Skaros lava samples +6.6‰ to +8‰ (Hoefs 1978). Hoefs (1978) proposed that low-temperature alteration of whole-rock samples was responsible for the observed highest $\delta^{18}O$ values. $\delta^{18}O$ values of Wyers (1987) for plagioclase phenocrysts from Peristeria are +6.1‰ to +6.4‰ and +5.7‰ to +5.8‰ from Skaros.

Major units of the Thera pyroclastics

Major and trace element data of main units

The Thera pyroclastics span a similar range of SiO_2 as the lavas, but dacitic and rhyodacitic compositions are volumetrically predominant and basalts and mafic andesites are subordinate. The only basaltic components are some cauliform scoriae of Lower Pumice 2. Like the lavas, the pyroclastics have medium to high K contents, although compositions as K-depleted as the Kameni lavas are not observed. Most of the pyroclastic samples are mildly tholeiitic on the FeO/MgO–SiO_2 plot (Fig. 6.2). However, some dacites and rhyodacites, as well as andesites of the Cape Therma 1 and Cape Riva eruptions fall well into the calcalkaline field. A higher proportion of the pyroclastics classify as calcalkaline on an AFM diagram (Fig. 6.4). However, such boundaries are somewhat arbitrary and do not necessarily have genetic significance.

Major and trace element variations for the pyroclastics are shown in Figs 6.5–6.7. Solid symbols depict the dominantly silicic units and open symbols depict the dominantly intermediate units and Cape Therma 2, as distinguished in Chapter 4. While Cape Therma 2 is rhyodacitic, it is much smaller in volume than the other four silicic units and thus is distinguished from them. Only components of the Minoan eruption that are unquestionably juvenile (rhyodacite and andesite) are plotted on these diagrams. The crystal-rich pumices within the Minoan deposit are treated separately below.

The general trends of the Thera pyroclastics resemble those of the lavas and can be correlated with observed phenocryst phases (Chapter 4). Apparent peaks in FeO(T), TiO_2, and V at *c.* 57% SiO_2 correspond approximately to the appearance of magnetite in andesitic compositions. However in each case the left-hand limb of the peak is defined by only three samples. The peak in P_2O_5 corresponds approximately to the appearance of apatite. The small maximum in Y contents at *c.* 65% SiO_2 may be attributed to progressive partitioning of Y into apatite and to the increasing affinity of augite for Y with decreasing temperature (Gill 1981). Some scoria of Lower Pumice 1 and Lower Pumice 2 have $Al_2O_3 > 18\%$. Lower Pumice 2 scoria are contaminated by cumulate gabbro (Chapter 4). Some Lower Pumice 1 andesites have P_2O_5 higher than observed in Santorini lavas.

Collectively the Thera pyroclastics show broad and, for many elements, rather scattered geochemical trends. However, data for each individual zoned deposit tend to have much tighter trends. At a given silica content, Vourvoulos andesites have consistently high contents of FeO and TiO_2, and low Al_2O_3. FeO/MgO ratios are high, making Vourvoulos the most tholeiitic of the pyroclastic units. This is consistent with the occurrence of Fe-rich olivine and the absence of opx in Vourvoulos (Chapter 4). Andesites of the dominantly silicic eruptions Lower Pumice 1, Cape Riva and Minoan have relatively low FeO, FeO/MgO, TiO_2 and P_2O_5. Banded pumices and streaky grey pumices of Lower Pumice 2 fall on the same general trend. These same geochemical features are shown consistently by the andesite of Cape Therma 1.

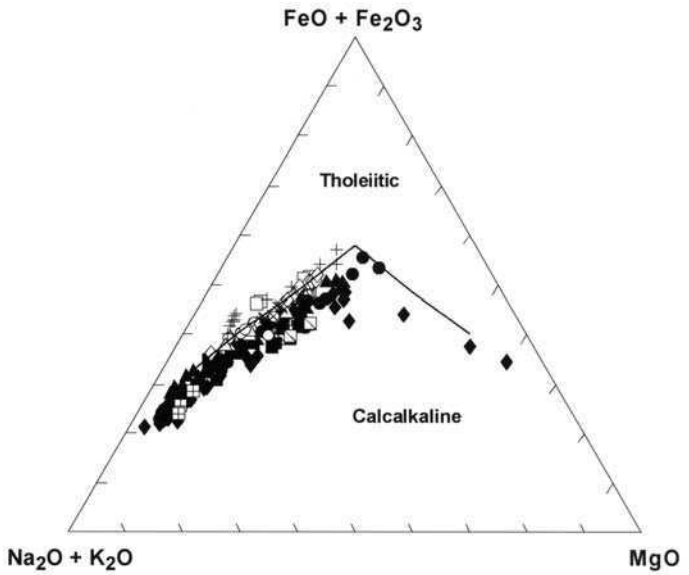

Fig. 6.4. AFM diagram for the Thera pyroclastics (after Irvine & Baragar 1971). Symbols as for Fig. 6.1.

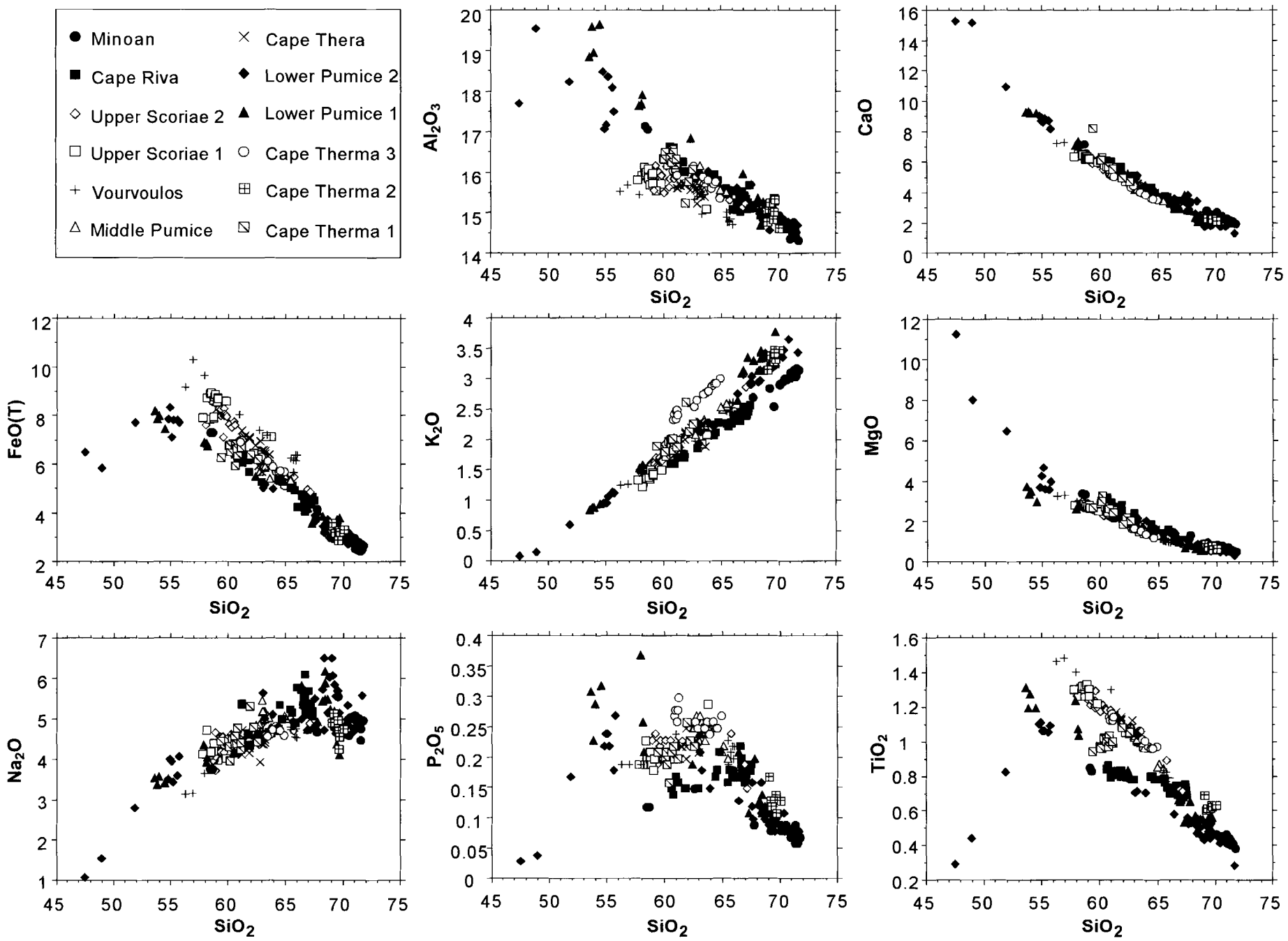

Fig. 6.5. Selected major element variation diagrams for the Thera pyroclastics.

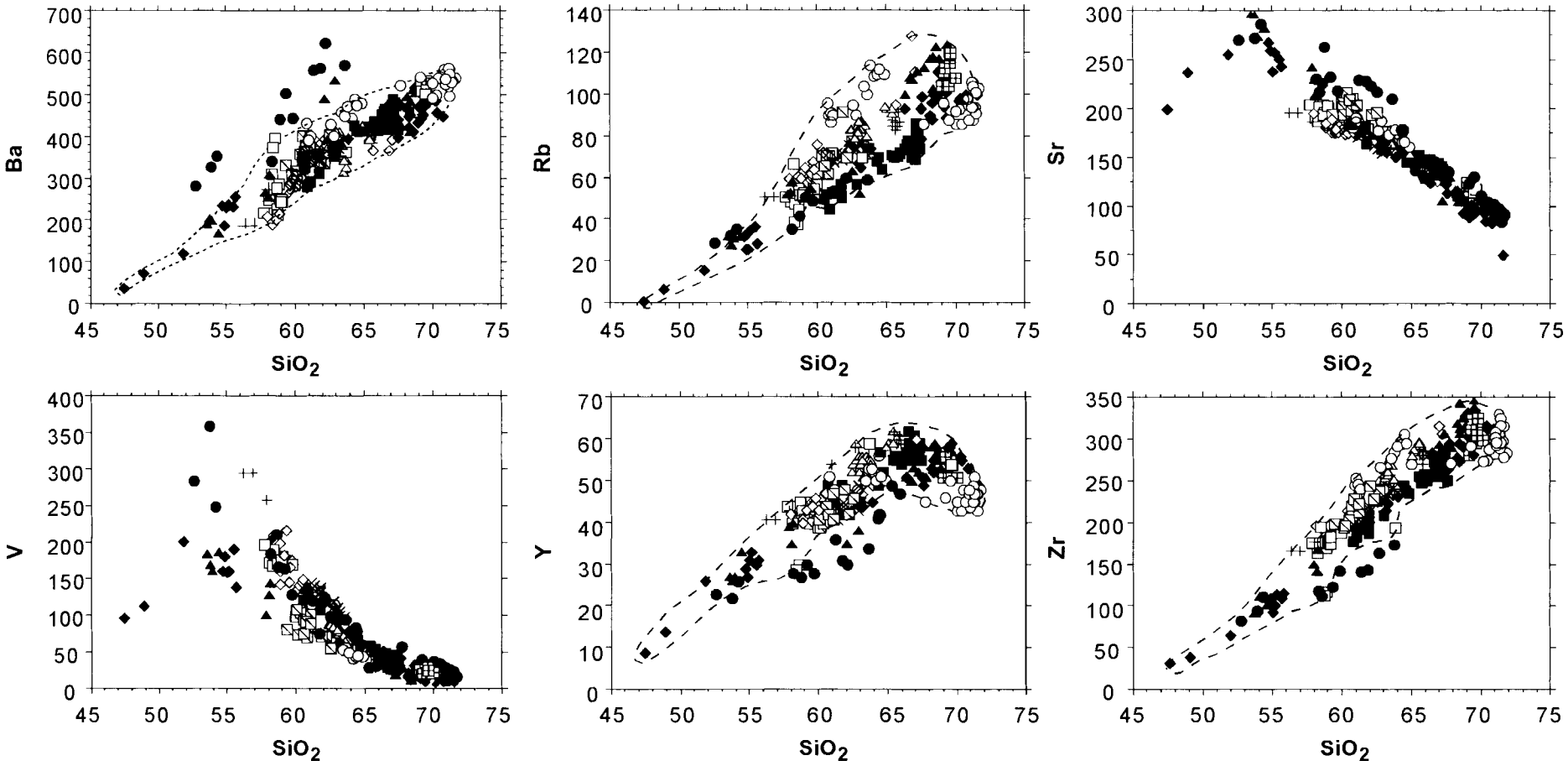

Fig 6.6. Selected trace element variation diagrams for the Thera pyroclastics. The dotted fields encompass all samples apart from the Minoan crystal-rich pumices, and are used on Fig. 6.8. Symbols as in Fig. 6.5.

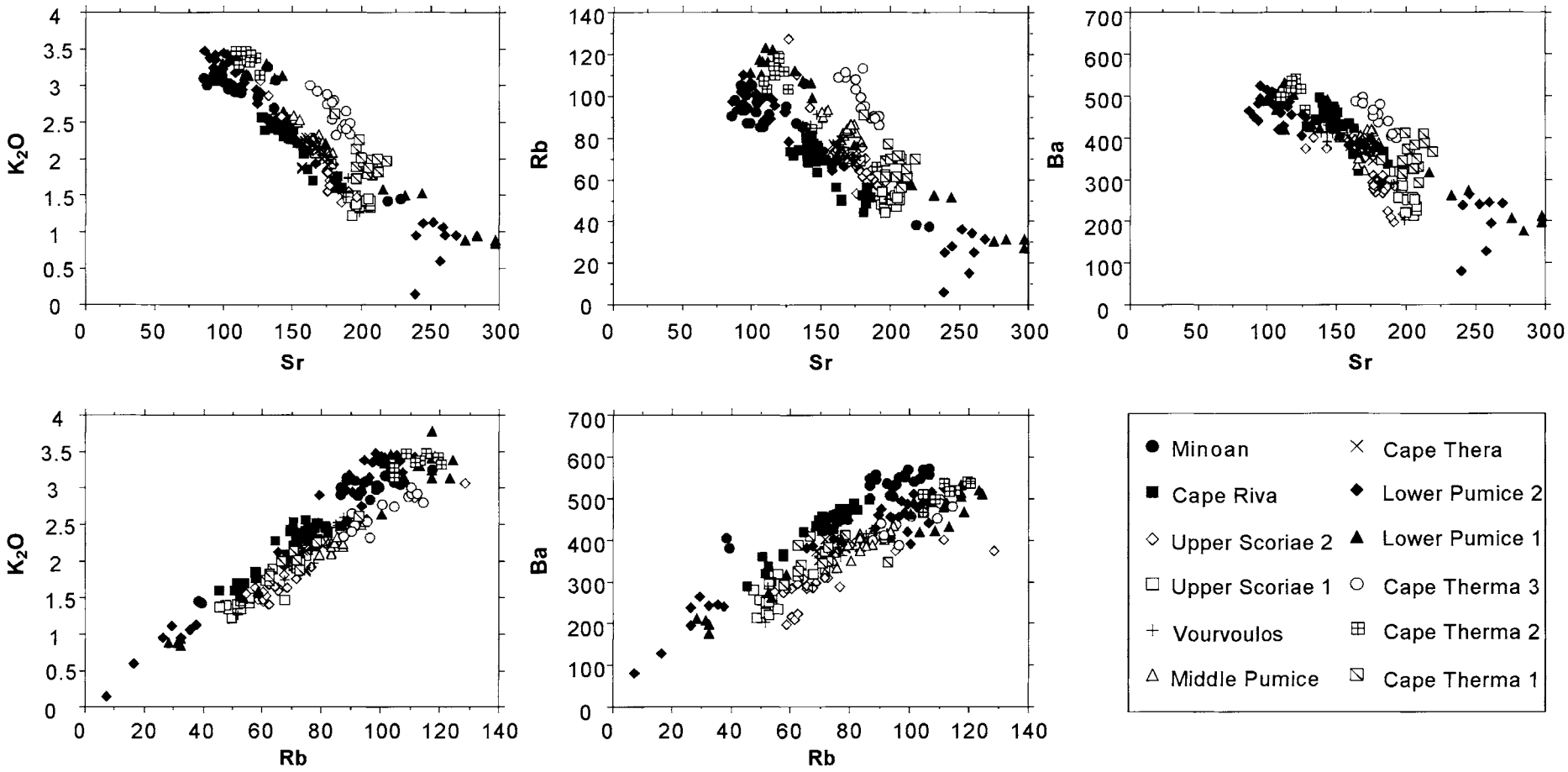

Fig. 6.7. Selected large ion lithophile (LIL) trace element plots for the Thera pyroclastics.

Systematic differences in trace element abundances are also observed. At a given silica content, the andesites of Cape Therma 3 are consistently rich in Rb,Th, Ba, Nb, and Zr, as they also are in K_2O (Fig. 6.1). They also have the lowest K/Rb ratios, showing that enrichment in Rb is greater than that of K. In contrast, the Minoan and Cape Riva magmas have the lowest K_2O, Rb, Th, Nb, and Zr, and the highest K/Rb ratios. Cape Therma 1, Cape Therma 3 and Lower Pumice 1 andesites have the lowest V in their silica range.

Minoan crystal-rich pumices

The geochemistry of the Minoan Tuff is complicated by the presence of a suite of crystal-rich pumices described in Chapter 4. These occur in the Plinian deposit where they are associated with texturally similar granitoid nodules containing < 1% glass, some of which are hydrothermally altered. Selected variation plots for the Minoan components are shown in Fig. 6.8, along with the fields for the entire Thera pyroclastics taken from Fig. 6.6. The crystal-rich pumices range widely in silica content from 53 to 63%. They have low Rb, Zr, and Y, unusually high Ba and Sr and high Ba/Rb ratios when compared with other Thera magmas at comparable SiO_2 content. These geochemical features are also observed in two analysed granitoid samples. The high Ba/Rb ratios in particular seems to rule out that the crystal-rich pumices and Minoan rhyodacite are related by crystal fractionation, particularly since alkali feldspar, mica and amphibole are not phenocryst phases in the main Minoan ejecta. One possibility is that the crystal-rich pumices represent a distinct high-Ba magma batch present beneath Santorini prior to the Minoan eruption. Another is that they are partial melts of older granitoids which formed the walls and roof of the Minoan chamber. The latter interpretation is favoured by U–Th disequilibrium data presented in Chapter 7.

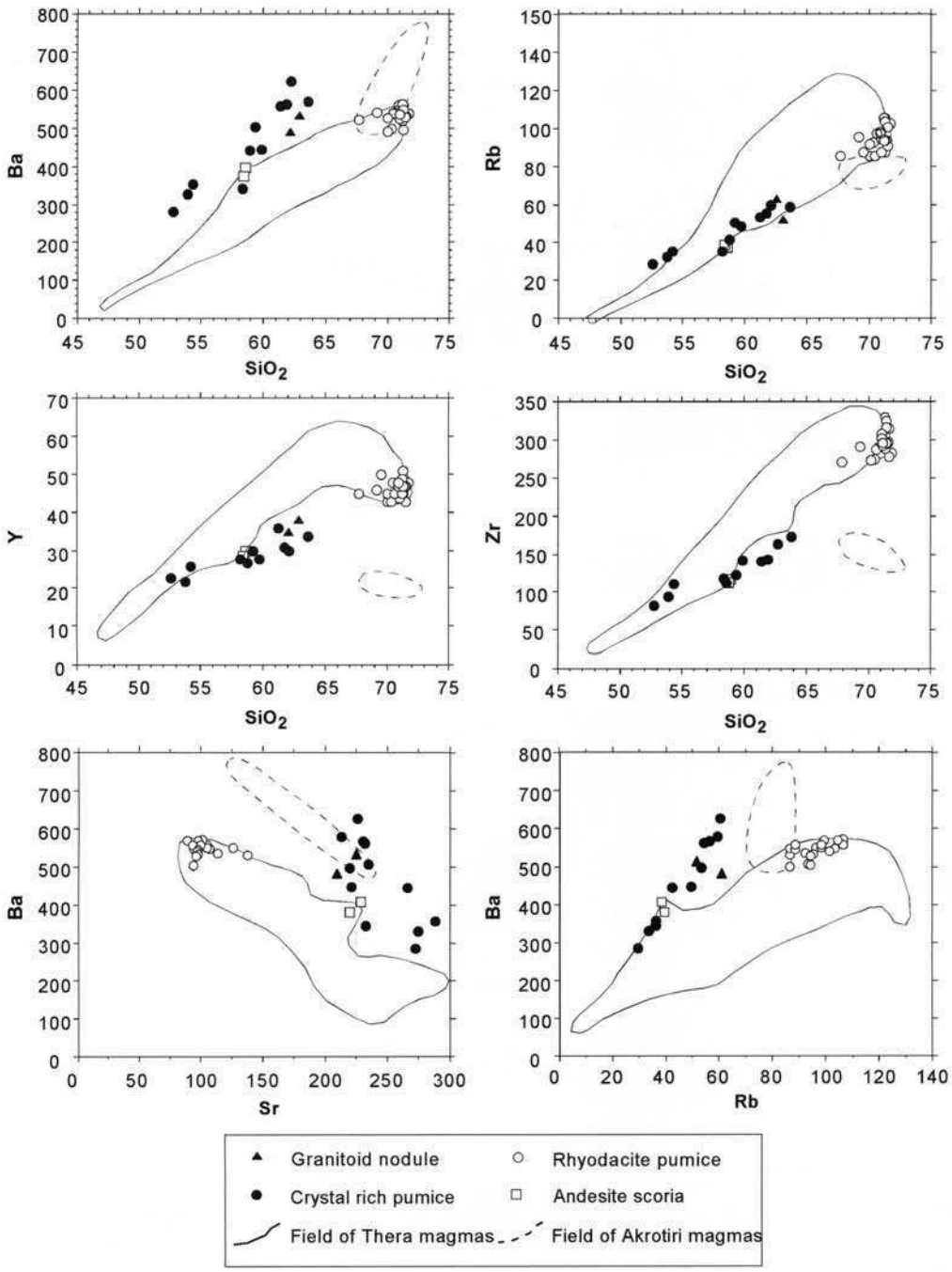

Fig. 6.8. Trace element characteristics of the crystal rich pumices and granitoid nodules of the Minoan Tuff. The main juvenile components of the Minoan (rhyodacite and andesite) are also shown as open symbols. The solid line is the general field of Thera pyroclastics (Fig. 6.6) and the dotted line the field of the early rhyodacitic centres of Akrotiri. The early Akrotiri centres have similar trace element characteristics as the granitoids and crystal-rich pumices. Some crystal-rich pumices probably formed by remobilisation of plutons from the earliest phase of Santorini magmatism.

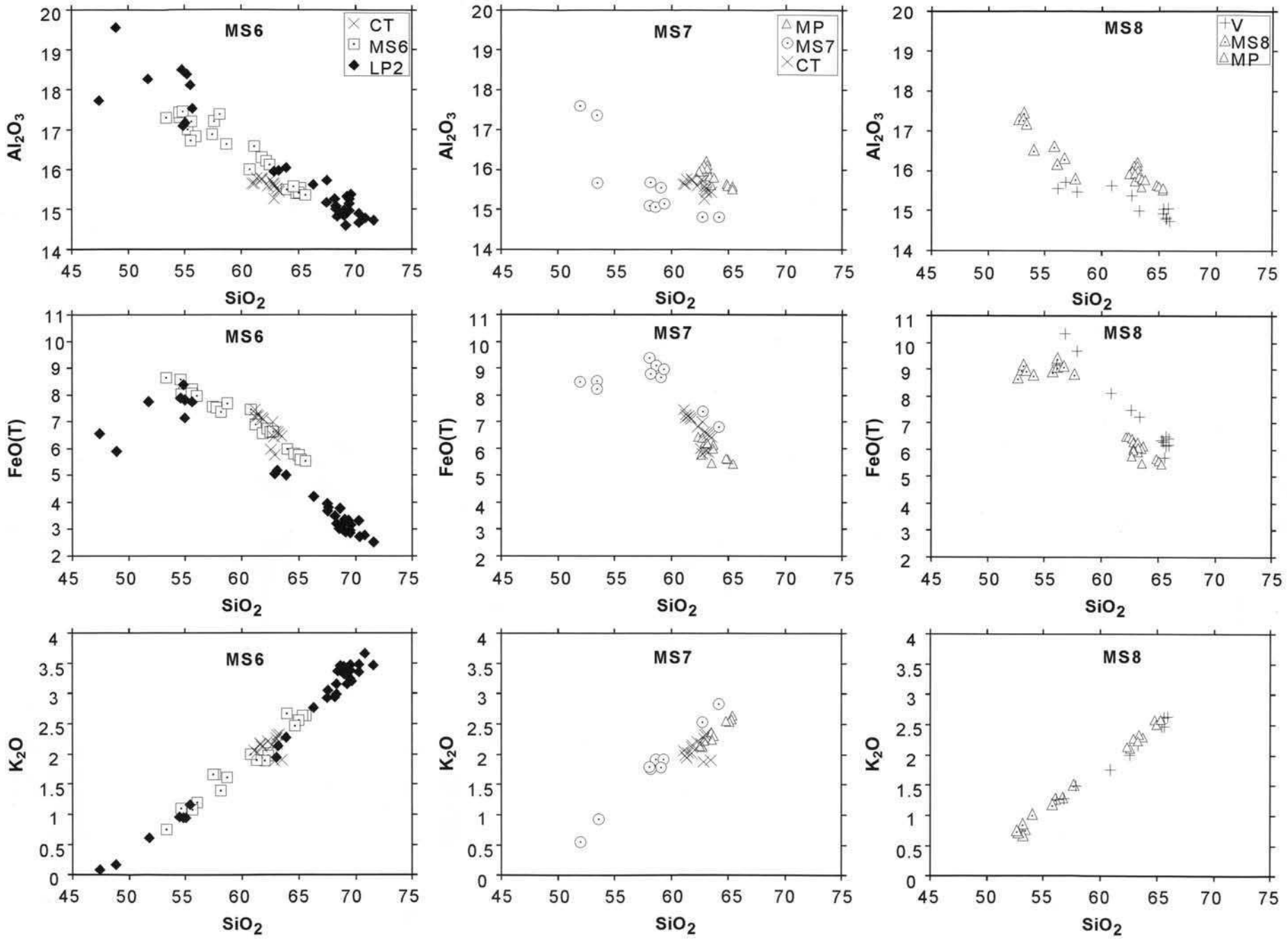

Fig. 6.9. Comparison of the chemical features of the three minor sequences M6, M7, and M8 with those of the major pyroclastic units which immediately bound them above and below. LP2: Lower Pumice 2; CT: Cape Thera; MP: Middle Pumice; V: Vourvoulos.

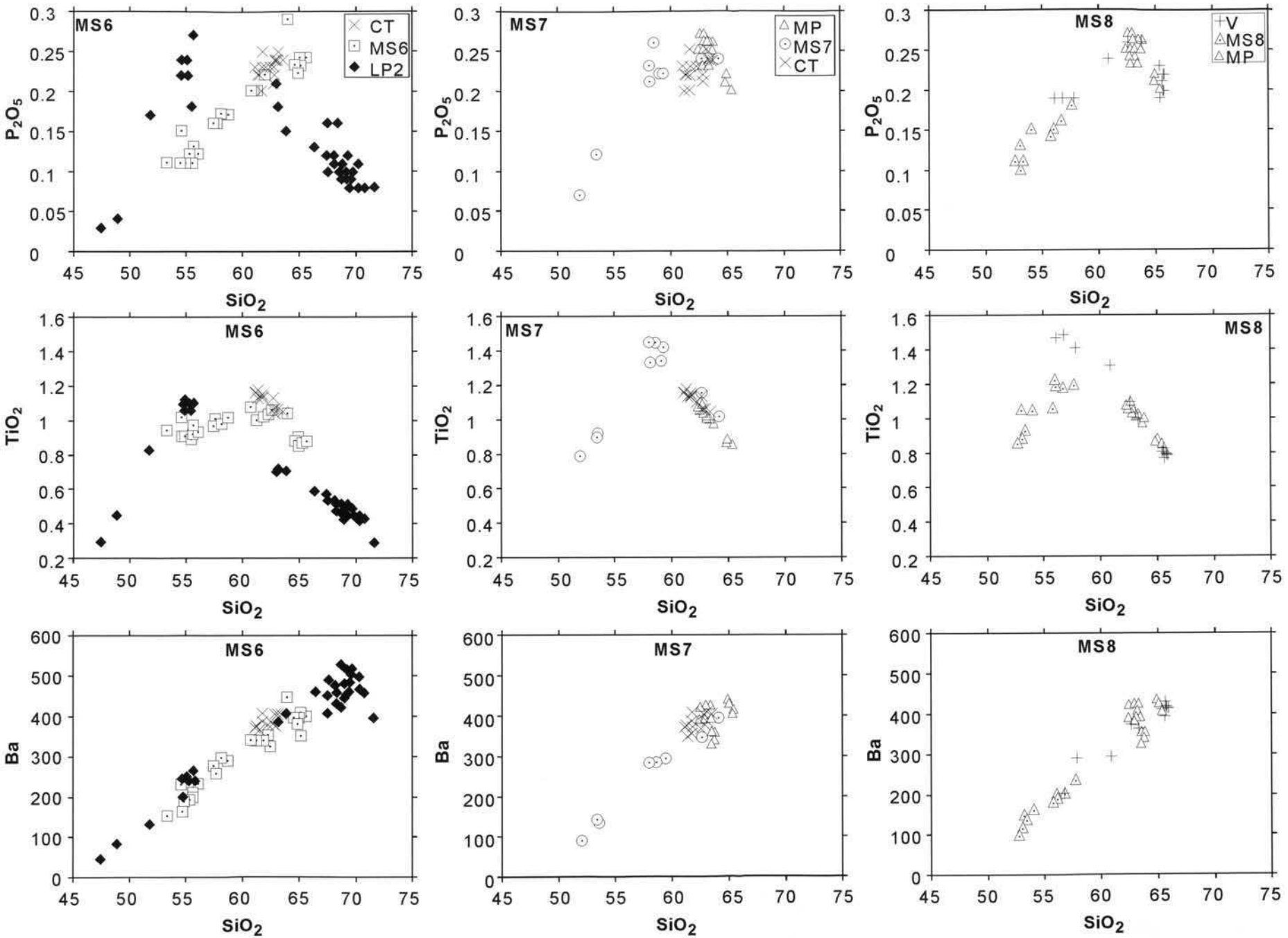

Fig. 6.9. (*continued*).

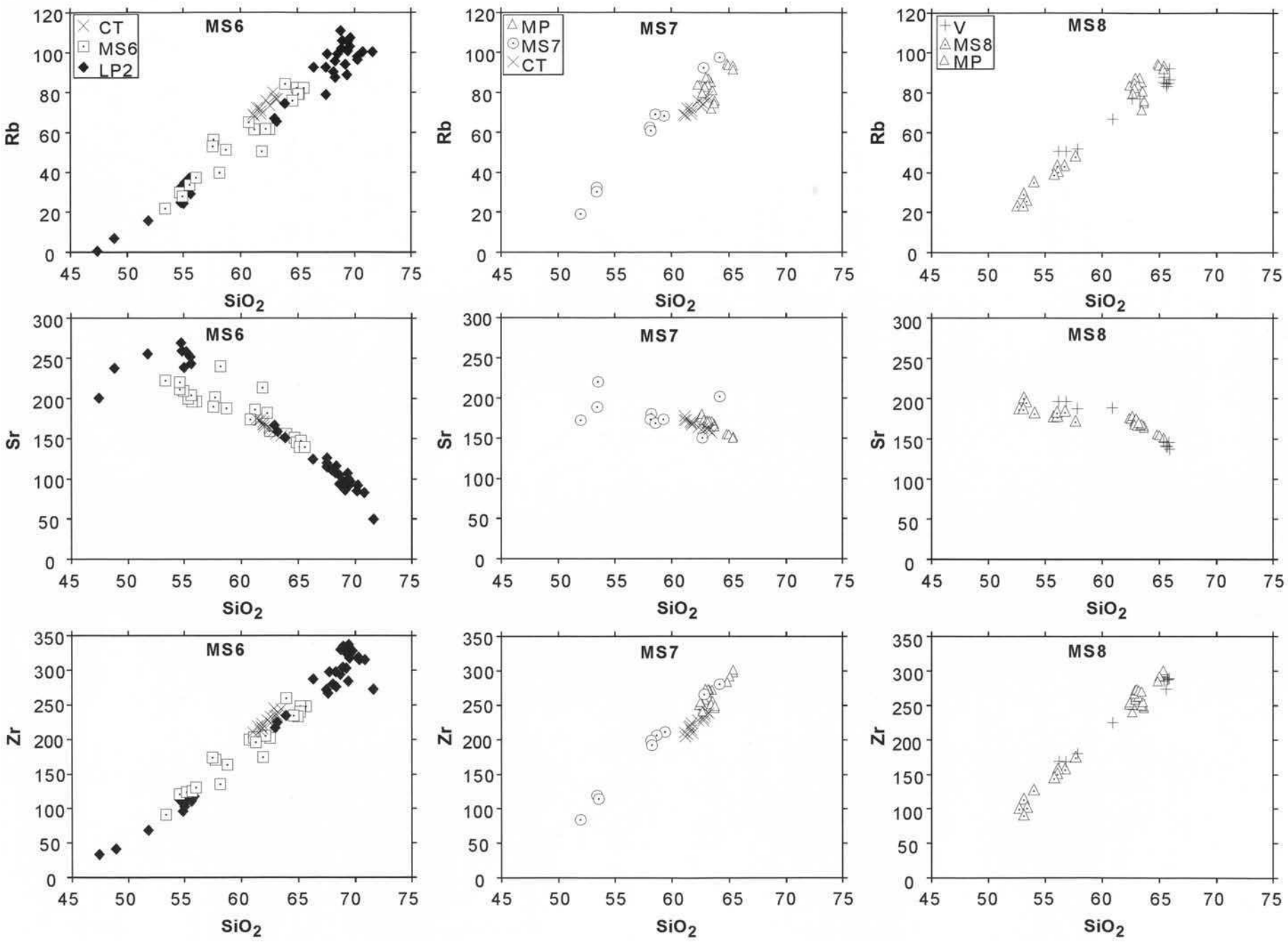

Fig. 6.9. (*continued*).

High-Ba magmas occur at other Aegean centres such as Aegina, Nisyros, and Kos, where Ba reaches nearly 950 ppm at a SiO_2 of 65% (Mitropoulos *et al.* 1987). Only the early Akrotiri centres have trace element characteristics (high Ba and Sr combined with low Rb, Y, and Zr) which resemble those of the Minoan granitoid nodules and crystal-rich pumices (Fig. 6.8; Davis *et al.* 1998). The high Ba/Rb ratios of many Akrotiri rocks are also distinctive and resemble those of the granitoids and crystal-rich pumices (Fig. 6.8). The Minoan crystal-rich pumices also partially overlap with Akrotiri volcanics on a Ba–Sr plot (Fig. 6.8). The abundance of magmatic hornblende in the granitoids and crystal-rich pumices is another similarity to the hornblende-bearing Akrotiri volcanics.

Temporal variations in trace elements

Systematic differences in certain large ion lithophile elements (K, Rb and Th) and high-field strength elements (Zr and Nb) between different eruptions are in agreement with the previously recognised secular variations of these elements at Santorini (Huijsmans 1985; Huijsmans *et al.* 1988; Huijsmans & Barton 1989). The effect is clear in the case of K_2O (Fig. 6.1). Andesites of Cape Therma 3 have the high K contents typical of Peristeria lavas, the andesites of Cape Simandiri and many of the intermediate lavas of the Akrotiri peninsula (Davis *et al.* 1998). Cape Therma 1, Cape Therma 2, Lower Pumice 1, Lower Pumice 2, Cape Thera, Middle Pumice, Vourvoulos, and Upper Scoriae 2 have the K_2O contents of Skaros lavas. The K_2O contents of Upper Scoriae 1, Cape Riva, and the Minoan are systematically lower than Skaros, but higher than the Kamenis. Thus, broadly speaking, potassium decreases with time in the Thera pyroclastics, as in the post-530 ka lava successions (Fig. 6.1). Variations in Rb, Th, Nb, and Zr are similar to those of K. Virtually complete separation of explosive cycle one and explosive cycle two magmas is evident on a plot of K_2O–Rb (Fig. 6.7). In terms of K/Rb the two cycles form parallel trends, implying different parental magmas. Huijsmans (1985) proposed the existence of parents with different trace element signatures.

Minor pyroclastic sequences

The major deposits of the Thera pyroclastics are intercalated with sequences of minor pyroclastic units described in Chapter 3. These sequences are believed to correspond to phases of lava shield and lava cone construction between the main eruptions. Sampling was carried out on the minor successions in the intervals Lower Pumice 2–Cape Thera, Cape Thera–Middle Pumice, and Middle Pumice–Vourvoulos. These intervals are abbreviated MS6, MS7 and MS8 respectively (Fig. 3.17; Chapter 3). The aim here is to document changes in magma chamber chemistry in periods between major explosive eruptions (Fig. 6.9).

SiO_2 in the three minor sequences ranges from 52% to 66% with a higher proportion of mafic compostions than in the major units. M7 and M8 together define a trend of increasing FeO(T), TiO_2 and P_2O_5 to andesite compositions at about 60% SiO_2, and these same components decrease in more evolved rocks (Fig. 6.9). These trends are similar to those observed in many Santorini magmas and are characteristic of fractional crystallization. M6 analyses fall on a trend of higher Al_2O_3 and lower FeO(T), FeO/MgO, TiO_2 and P_2O_5. The trend of slightly increasing TiO_2 from mafic andesite to dacite in M6 contrasts in particular with M7 and M8 rocks. This geochemistry is more reminiscent of magma mixing trends.

Figure 6.9 compares the chemistry of each minor sequence with that of the respective bounding major units. Deposits of M6 change in composition from silicic andesite and dacite at the base to mafic andesite at the top. M6 appears to form a linear mixing trend between a mafic andesite component resembling Lower Pumice 2 scoria and an evolved dacite intermediate in composition between the Cape Thera dacite and the Lower Pumice 2 rhyodacite. Five of the samples of M6 are slightly more evolved than Cape Thera. Although these samples have TiO_2 contents consistent with fractionation from Cape Thera-like magma, they are slightly poorer in Ba, Rb and Zr than Cape Thera. These geochemical features are closer to those observed in Lower Pumice 2. In summary, M6 dacite magmas have features consistent with derivation from magmas similar in trace characteristics to the Lower Pumice 2 rhyodacite. The lower half of M7 is mafic andesite and the upper is silicic andesite or dacite. Samples from M7 define a curved fractionation array and have higher FeO and TiO_2 than either of the bounding major units. K_2O and Rb are also consistently higher than in the two major units. M8 consists of mafic andesite, which falls on a similar evolutionary trend as the more evolved bounding units, although Rb, Sr and Zr appear to be lower than Vourvoulos. Detailed comparison with the bounding units is difficult in the case of M8 owing to its restricted compositional range.

The M6 minor sequence occupies the same stratigraphic level as the Andesites of Cape Simandiri (Chapter 3). Surprisingly Simandiri lavas have significantly higher K_2O and Rb than M6, so that the latter cannot have been erupted from Simandiri, but from another centre of similar age, remnants of which no longer survive.

Isotopic studies of the Thera pyroclastics

Isotopic analyses were carried out on samples from the major units of the Thera pyroclastics at the NERC Isotope Geosciences Laboratory, Keyworth, UK. See Appendix 1 for the analytical techniques. Details of the internal stratigraphy of individual deposits of the Thera pyroclastics are listed in Table 3.4 (Chapter 3). As the Thera pyroclastics are young, and the half-lives of the radioactive parents are so long, no age correction is required when discussing the radiogenic isotope data. The data are given in Tables 6.2 and 6.3.

Isotopic variation with stratigraphic height

The $^{87}Sr/^{86}Sr$ ratios in the Thera pyroclastics range from 0.70433 to 0.70542 and $^{143}Nd/^{144}Nd$ from 0.51263 to 0.51279. Differences in both ratios are significant if they exceed 0.00003. $^{87}Sr/^{86}Sr$ decreases and $^{143}Nd/^{144}Nd$ increases with time up through the first cycle and the earlier stages of the second (Fig. 6.10). $^{87}Sr/^{86}Sr$ reaches the lowest values in Upper Scoriae 1 and Upper Scoriae 2, and then increases in the Cape Riva and Minoan (Fig. 6.10). The andesites of Cape Therma 1 and Cape Therma 3 have elevated $^{87}Sr/^{86}Sr$ and lower $^{143}Nd/^{144}Nd$ compared to the equivalent predominantly intermediate deposits of the second cycle. Isotopic heterogeneity outside analytical uncertainty is apparent in Cape Therma 3, Lower Pumice 1, Lower Pumice 2, Upper Scoriae 1, Cape Riva and Minoan. Also plotted on Figure 6.10 are $^{87}Sr/^{86}Sr$ and $^{143}Nd/^{144}Nd$ data for lavas. Peristeria lavas show a wide range of $^{87}Sr/^{86}Sr$ and $^{143}Nd/^{144}Nd$, with some samples having higher values than any sample of the Thera pyroclastics. The Skaros lavas have similar values to Upper Scoriae 1 and Upper Scoriae 2, with several samples falling to lower $^{87}Sr/^{86}Sr$ and higher $^{143}Nd/^{144}Nd$, defining a minimum in $^{87}Sr/^{86}Sr$ and a maximum in $^{143}Nd/^{144}Nd$. The Rhyodacites of Therasia have higher $^{87}Sr/^{86}Sr$, similar to Cape Riva and Minoan. This is consistent with the interpretation of Druitt (1985) that the rhyodacites represent precursory leaks from the Cape Riva magma chamber. The Kameni lavas have lower $^{87}Sr/^{86}Sr$ and higher $^{143}Nd/^{144}Nd$ than the Minoan.

The ranges in Pb isotopes in the Thera pyroclastics are $^{206}Pb/^{204}Pb$ 18.71–18.95, $^{207}Pb/^{204}Pb$ 15.65–15.73, and $^{208}Pb/^{204}Pb$ 38.74–39.08. The Pb isotopes display less coherence with stratigraphic height and magma type than the other isotopic systems. There is a crude decrease in radiogenic Pb with time (Fig. 6.11) until the Minoan deposit, which has a few samples with elevated radiogenic Pb and three samples with the lowest values of $^{206}Pb/^{204}Pb$.

Table 6.2. *Whole-rock isotope data for the Thera pyroclastics (eruption units in Table 3.4)*

Unit	Sample	$^{87}Sr/^{86}Sr$	$^{143}Nd/^{144}Nd$	$^{206}Pb/^{204}Pb$	$^{207}Pb/^{204}Pb$	$^{208}Pb/^{208}Pb$	$\delta^{18}O$	δD
Cape Therma 1B	LS 155-91	0.704939	0.512701	18.896	15.655	38.858	7.97	–
Cape Therma 2	LS 100-91	0.705106	0.512687	18.951	15.711	39.040	12.34	–
Cape Therma 3A	8635	0.704810	–	18.941	15.728	39.083	8.09	–
Cape Therma 3B	LS 166-91	0.704939	0.512687	18.914	15.688	38.947	7.27	–
Lower Pumice 1A	LS 159-91	0.705087	0.512630	18.906	15.689	38.940	11.90	–
Lower Pumice 1C	S82-34b	0.704848	0.512702	18.829	15.660	38.805	10.94	−81.29
L. Pumice 2A Andesite	LS 99-91	0.704579	0.512767	18.883	15.678	38.896	9.34	–
Lower Pumice 2A	LS 55-91	0.704979	0.512724	18.879	15.659	38.847	13.53	–
Lower Pumice 2A	LS 13-91	0.705065	0.512712	18.902	15.670	38.894	13.22	–
Lower Pumice 2A	LS 103-91	0.705011	0.512726	18.878	15.667	38.863	12.74	–
Lower Pumice 2B	S82-10	0.704710	0.512727	18.847	15.681	38.873	9.89	−66.98, −63.61
Lower Pumice 2C	LS 58-91	0.704896	0.512729	18.930	15.688	38.970	12.80	–
Lower Pumice 2C	LS 61-91	0.705025	0.512720	18.920	15.683	38.941	12.27	–
Cape Thera A	LS 125-91	0.704660	0.512744	18.916	15.670	38.906	8.45	–
Cape Thera B	8642	0.704632	0.512745	18.846	15.650	38.805	7.44	−75.79
Middle Pumice A	8245	0.704461	0.512779	18.837	15.647	38.782	7.70	−70.11
Middle Pumice B	LS 177-91	–	–	–	–	–	8.81	–
Vourvoulos A	LS 131-91	–	–	–	–	–	9.04	–
Vourvoulos B	861	0.704664	0.512788	18.815	15.651	38.772	7.39	–
Upper Scoriae 1A	85022	0.704494	0.512794	18.841	15.670	38.837	6.04	–
Upper Scoriae 1A	LS 134-91	–	–	–	–	–	6.29	–
Upper Scoriae 1C	S82-101	0.704331	0.512780	18.854	15.670	38.853	5.81	–
Upper Scoriae 1C	LS 9-91	–	–	–	–	–	8.48	–
Upper Scoriae 2B	LS 174-91	0.704332	0.512782	18.904	15.658	38.866	8.43	–
Upper Scoriae 2C	85048	0.704333	0.512794	18.854	15.657	38.817	7.86	–
Upper Scoriae 2D	LS 184-91	–	–	–	–	–	8.33	–
Cape Riva A	LS 66-91	0.704930	–	18.890	15.672	38.895	10.60	–
Cape Riva A	LS 76/183-91	0.704732	–	18.878	15.649	38.820	7.57	–
Cape Riva A	LS 77-91	–	–	–	–	–	8.07	–
Cape Riva B	LS 149-91	0.704882	0.512732	18.741	15.666	38.763	9.30	–
Cape Riva C	S82-62	0.704833	0.512733	18.751	15.660	38.741	9.23	−53.93
Minoan A Andesite	LS 124-91	0.705425	0.512631	18.937	15.662	38.901	8.81	–
Minoan A	LS 104-91	0.705168	0.512701	18.941	15.684	38.951	8.81	–
Minoan A	LS 108-91	0.705216	0.512702	18.925	15.665	38.898	9.10	–
Minoan B	LS 112-91	0.705299	0.512673	18.943	15.679	38.935	10.91	–
Minoan B	S82-34b	0.705192	0.512705	18.708	15.708	38.798	10.23	−66.82, −68.89
Minaon C	LS 118-91	0.705339	0.512716	18.927	15.663	38.890	10.95	–
Minoan C	LS 121-91	0.705191	0.512697	18.919	15.659	38.884	11.22	–
Minoan D	LS 172-91	0.705190	0.512701	18.921	15.659	38.883	9.86	–

Table 6.3. *Isotopic data for mineral separates (eruption units from Table 3.4)*

Unit	Sample	$^{87}Sr/^{86}Sr$ CP*	$^{87}Sr/^{86}Sr$ IP*	$^{206}Pb/^{204}Pb$ CP*	$^{206}Pb/^{204}Pb$ IP*	$^{207}Pb/^{204}Pb$ CP*	$^{207}Pb/^{204}Pb$ IP*	$^{208}Pb/^{204}Pb$ CP*	$^{208}Pb/^{204}Pb$ IP*	$\delta^{18}O$ CP*	$\delta^{18}O$ IP*
Cape Therma 1B	LS 155-91	–	–	18.334	–	15.662	–	38.331	–	–	–
Cape Therma 2	LS 100-91	0.704870	0.704813	18.771	18.896	15.658	15.697	38.772	38.943	6.60	–
Lower Pumice 1A	LS 159-91	0.704863	0.704845	–	18.915	–	15.692	–	38.952	6.86	6.92
Lower Pumice 2A	LS 103-91	0.704687	0.704694	–	–	–	–	–	–	6.61	6.85
Lower Pumice 2C	LS 61-91	0.704664	0.704739	–	–	–	–	–	–	7.43	6.94
Cape Thera A	LS 125-91	0.704688	0.704674	18.701	18.892	15.645	15.694	38.671	38.935	–	–
Upper Scoriae 2B	LS 174-91	0.704383	0.704439	–	–	–	–	–	–	–	6.36
Cape Riva A	LS 66-91	–	–	18.896	18.896	15.677	15.678	38.906	38.927	7.30	6.73
Minoan A	LS 108-91	0.704996	0.704999	18.969	18.968	15.711	15.712	39.029	39.041	7.50	6.94
Minoan B	LS 112-91	0.704972	–	18.909	18.865	15.684	15.673	38.926	38.872	7.08	6.99
Minoan C	LS 118-91	0.704966	–	18.887	18.798	15.693	15.689	38.930	38.846	6.58	6.50
Minoan C	LS 121-91	0.704995	0.704960	–	–	–	–	–	–	6.52	6.84
Minoan D	LS 172-91	0.705004	0.704993	–	–	–	–	–	–	6.98	6.01
		ST P*	CT P*	ST P*	CT P*	ST P*	CT P*	ST P*	CT P*	ST P*	CT P*
Lower Pumice 2A	LS 13-91	0.704662	0.704690	18.907	18.929	15.645	15.678	38.864	38.939	7.08	6.65

* IP, Plagioclase with inclusions; CP, clear plagioclase; ST P, simply-twinned plagioclase; CT P, complexly-twinned plagioclase.

$^{207}Pb/^{204}Pb$ values overlap, with silicic magmas of Lower Pumice 2, Cape Riva and the Minoan showing slightly greater range, than the other deposits. Cape Therma 3 has the highest $^{207}Pb/^{204}Pb$.

Whole-rock $\delta^{18}O$ ranges from +5.8‰ to +13.5‰ (Fig. 6.12). The extraction error is ±0.1‰. Later discussion will show that the whole-rock data are strongly modified by low-temperature alteration effects with low density silicic pumice clasts being more affected than scoria of the predominantly intermediate units. Six samples were analysed for hydrogen isotopes. δD ranges from −81.29‰ to −53.93‰ and falls mainly in the mantle range (Fig. 6.12).

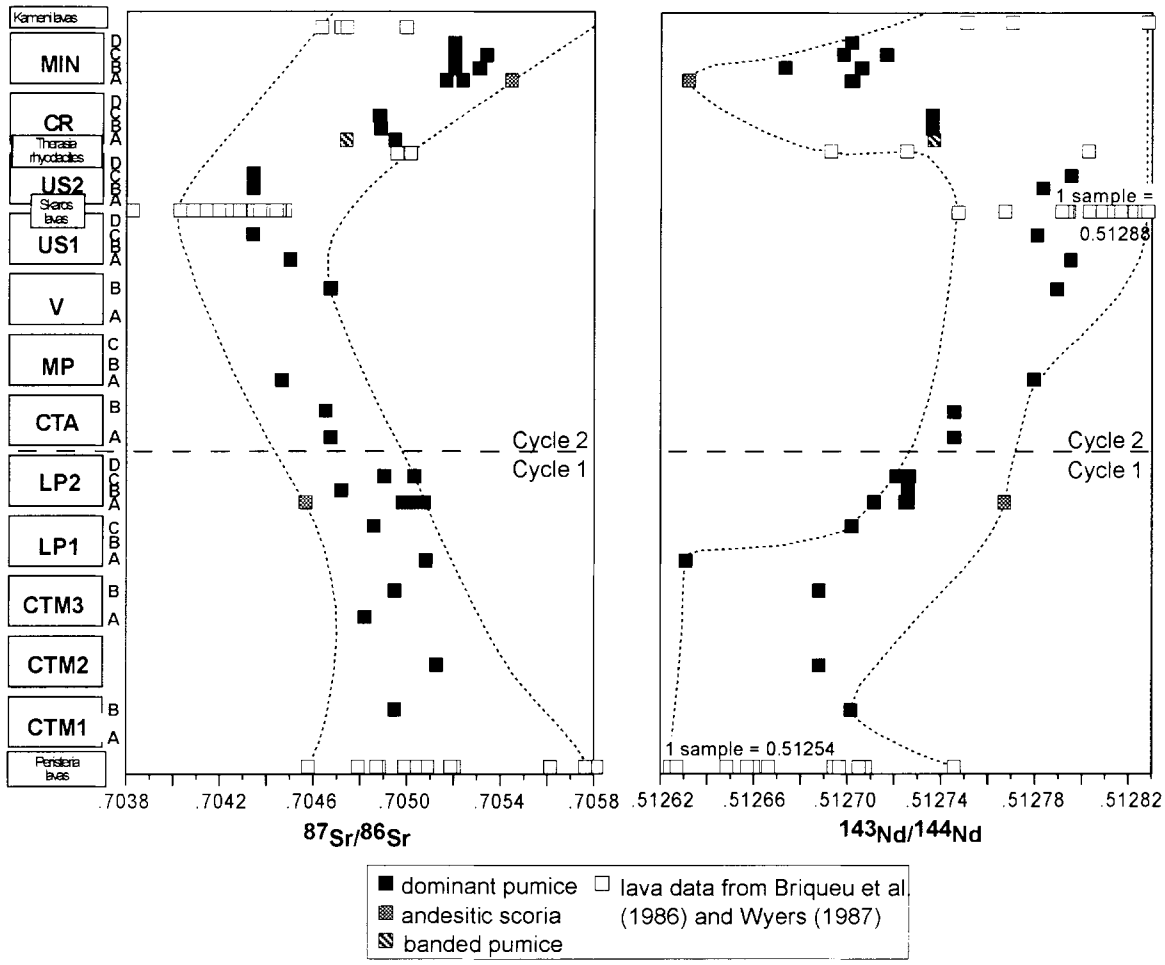

Fig. 6.10. $^{87}Sr/^{86}Sr$ and $^{143}Nd/^{144}Nd$ versus stratigraphic height in the Thera pyroclastics. Letters adjacent to the Thera pyroclastics names correspond to sub-divisions of those units listed in Table 3.4.

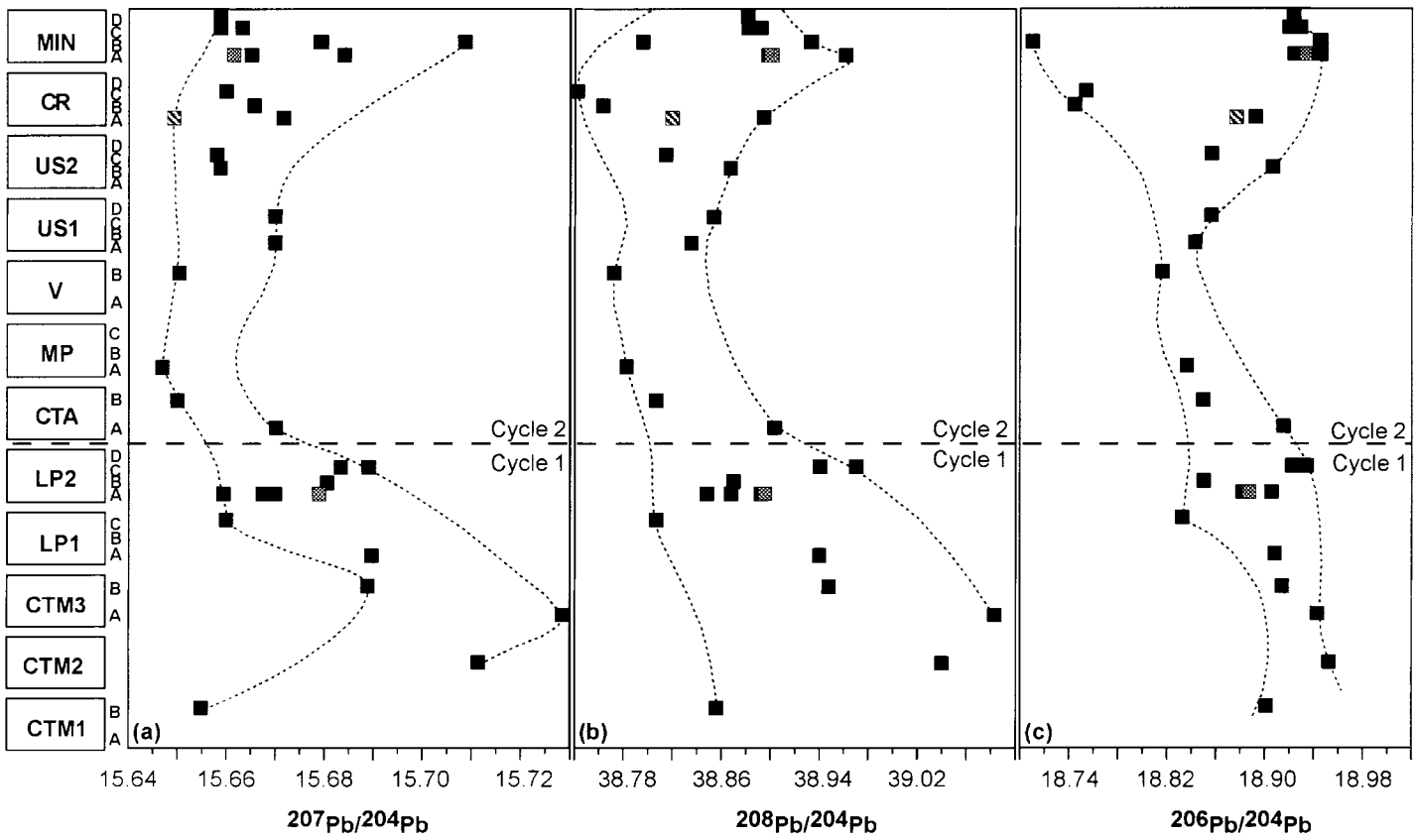

Fig. 6.11. $^{206}Pb/^{204}Pb$ (a) $^{207}Pb/^{204}Pb$ (b) and $^{208}Pb/^{204}Pb$ (c) versus stratigraphic height in the Thera pyroclastics. Letters adjacent to the Thera pyroclastics names correspond to sub-divisions of those units listed in Table 3.4.

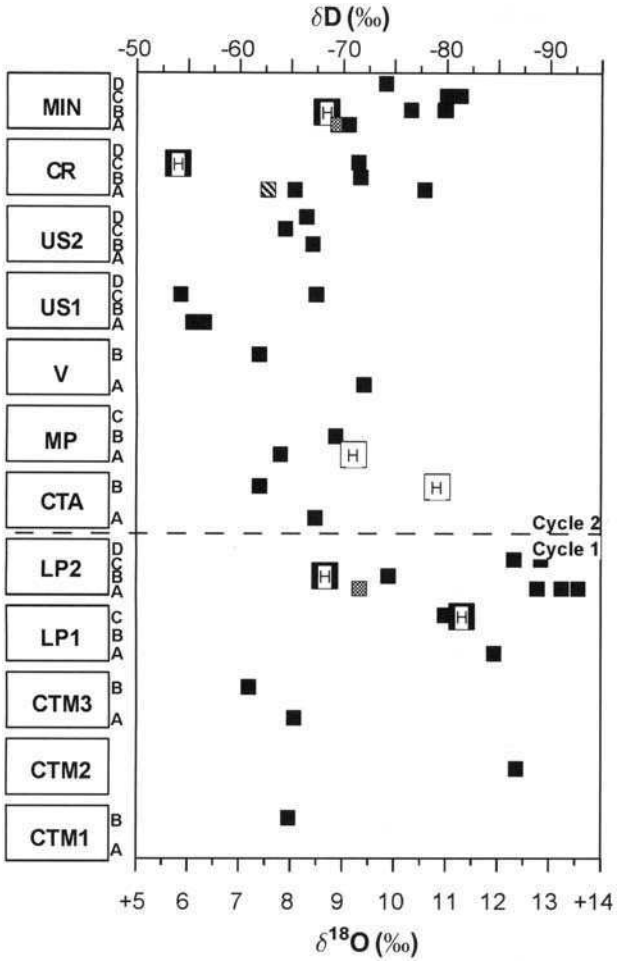

Fig. 6.12. $\delta^{18}O$ (squares) and δD (larger squares marked 'H') versus stratigraphic height in the Thera pyroclastics. Letters adjacent to the Thera pyroclastics names correspond to sub-divisions of those units listed in Table 3.4.

Global comparisons

Figure 6.13 shows $^{87}Sr/^{86}Sr$ plotted against $^{143}Nd/^{144}Nd$ for the Thera pyroclastics and for rocks from other geological settings. The Santorini data form a negative trend and plot well below the Mid Ocean Ridge Basalt (MORB) field, as is common for other arc rocks. Santorini lavas (Barton *et al.* 1983; Briqueu *et al.* 1986) overlap the pyroclastics field, but extend to lower $^{87}Sr/^{86}Sr$ and higher $^{143}Nd/^{144}Nd$, in accordance with their less evolved average compositions (Fig. 6.13b). The pyroclastics have Sr and Nd isotopes similar to the Northern Volcanic Zone (NVZ) of the Andes, the Mexican Volcanic Belt, some Patagonian rocks, and the Sunda Arc. The second-cycle, predominantly intermediate deposits have lower $^{87}Sr/^{86}Sr$ and higher $^{143}Nd/^{144}Nd$, plotting either on, or close to, the mantle correlation line (Fig. 6.13b). The dominantly silicic samples from the Thera pyroclastics and first-cycle deposits are displaced from the mantle array towards higher $^{87}Sr/^{86}Sr$, with less variation of $^{143}Nd/^{144}Nd$. This trend to higher $^{87}Sr/^{86}Sr$ puts these samples close to the field for rocks from the Lesser Antilles (Fig. 6.13b). Hawkesworth & Powell (1980), White & Patchett (1984), De Paolo (1988) and White (1984, 1989) attribute the Lesser Antilles trend to the involvement of oceanic crust or sediment in magma genesis. The high $^{87}Sr/^{86}Sr$ ratios could be due to hydrothermal alteration of oceanic crust (which does not affect $^{143}Nd/^{144}Nd$ ratios), or to an alkali-element enriched, with the REE depleted, component being introduced from the slab. Alternatively, the magmas may have interacted with pre-existing crust during fractionation. Banda arc rocks are also displaced to higher $^{87}Sr/^{86}Sr$ and this has been attributed to the involvement of subducted sediments (White & Patchett 1984).

Co-variation of Sr and Nd isotopes and displacement away from the MORB field is consistent with involvement of continental crust. Isotopic values for several samples of Aegean basement are plotted on Fig. 6.13a. From this diagram these possible contaminants or other, deeper, crustal lithologies could have been involved in magma evolution.

In Pb isotope diagrams the Thera pyroclastics fall on trends between the MORB field and the field for upper continental crust (Figs 6.14 and 6.15). The Thera pyroclastics have similar Pb isotope characteristics to the Andes, the Lesser Antilles Arc and some rocks from Lipari. Rocks from these provinces plot towards the domain of upper continental crust, so that their isotopic features have been attributed to crustal contamination or crustal anatexis (Barreiro 1983; Hawkesworth *et al.* 1993; Harmon *et al.* 1984; James 1984; Wilson 1989; Esperança *et al.* 1992). Similarly, the Pb isotopes of Santorini magmas indicate contamination by upper crustal material. Several samples of Aegean basement are plotted on Fig. 6.14a and confirm that radiogenic Pb in Santorini magmas resembles that of upper crustal lithologies.

Another possibility is that the isotope data record involvement of subducted sediment. To our knowledge there are no published Pb isotope data for Aegean sediments. The Thera pyroclastics plot at higher $^{207}Pb/^{204}Pb$ than oceanic sediments from the Pacific, ruling out a major role for such material. However, the Pb isotope characteristics of Aegean sediments are more likely to resemble those of the local basement from which the sediment is derived. The data are thus also consistent with contamination by subducted sediment.

Combined isotopic studies

In this section we describe how the Sr, Nd and Pb isotopes vary with respect to each other in the Thera pyroclastics. There is a good correlation between $^{87}Sr/^{86}Sr$ and $^{143}Nd/^{144}Nd$ (Fig. 6.16). The deposits also divide into groups with distinctive isotopic signatures. For example, the dominanly intermediate deposits of the second cycle are the least radiogenic group and are isotopically distinct from the equivalent deposits of the first cycle. The Minoan magmas are systematically enriched in radiogenic Sr compared with those of Lower Pumice 1, suggesting different assimilant compositions or contamination processes. Co-variation of $^{87}Sr/^{86}Sr$ and $^{143}Nd/^{144}Nd$ with Pb isotopes are less systematic (Fig. 6.17). Two samples of Cape Riva and one of the Minoan are significantly less radiogenic in Pb in comparison to the main body of data. If these samples are excluded then weak correlations are indicated that are consistent with increases of radiogenic crustal Pb with increase in $^{87}Sr/^{86}Sr$ and decrease of $^{143}Nd/^{144}Nd$.

Isotopic variation with element abundances

Correlations of isotopic ratios with major and trace elements also occur. Overall $^{87}Sr/^{86}Sr$ correlates positively with SiO_2, Rb/Sr and 1/Sr (Fig. 6.18) with the exception of a sample of andesitic scoria from the Minoan, which has anomalously high $^{87}Sr/^{86}Sr$. These results contrast with previous studies of the lavas where no correlation of $^{87}Sr/^{86}Sr$ and SiO_2 was found (Pe & Gledhill 1975; Barton *et al.* 1983). A negative correlation of $^{143}Nd/^{144}Nd$ with SiO_2 is also observed with the present data.

The temporal trends in isotopic composition in the Thera pyroclastics (Fig. 6.10) match trends in some elements. notably K, Rb, Th, Nb, Zr, Ba, and Sr. However there is a reversal at the end of the second cycle, with the Cape Riva and the Minoan ejecta having higher radiogenic Sr and lower radiogenic Na than earlier products of the same cycle (Fig. 6.10).

Phenocryst/whole-rock disequilibria

Figure 6.19 shows differences between the $^{87}Sr/^{86}Sr$ ratios of plagioclase separates and whole-rocks from the Thera pyroclastics

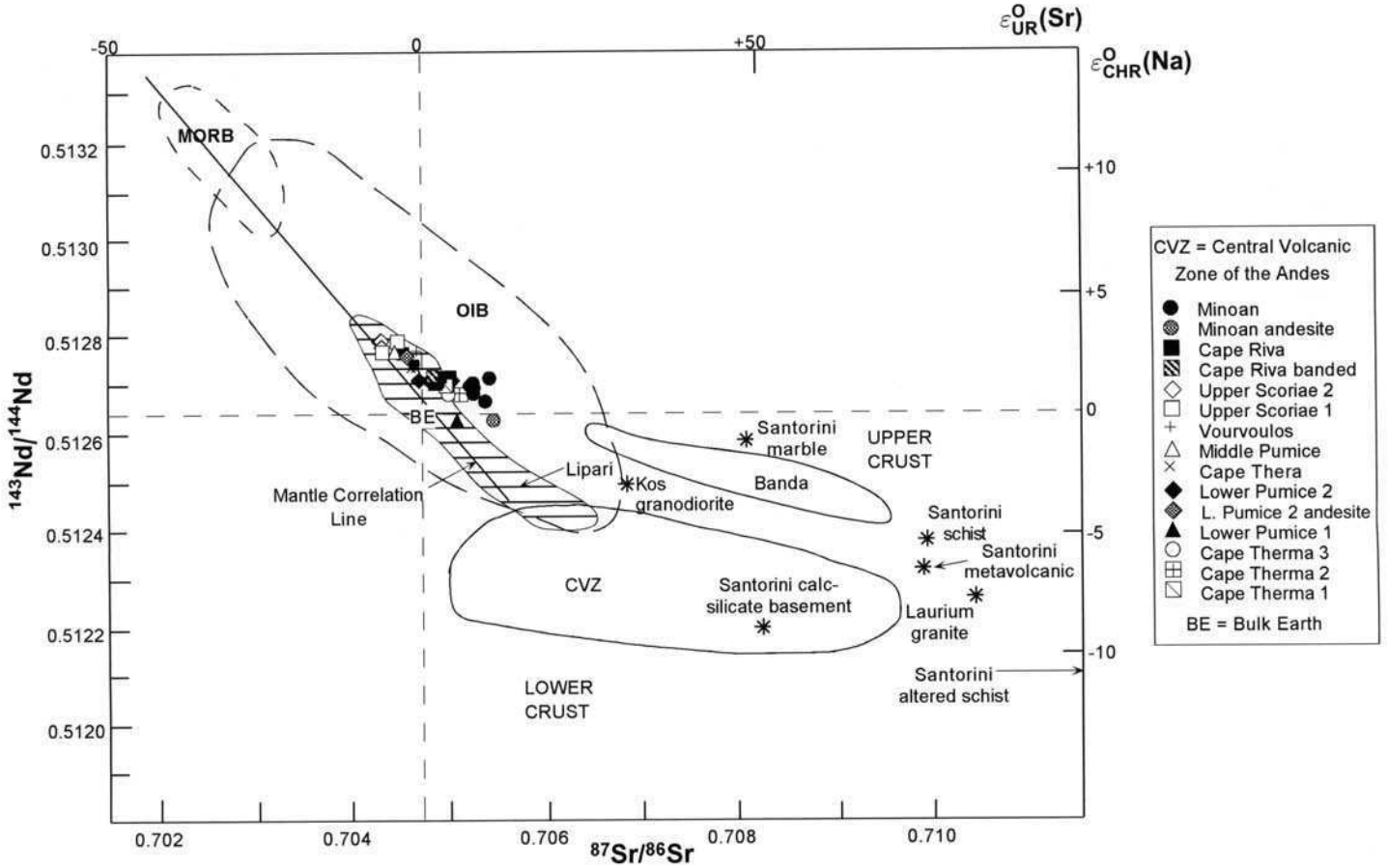

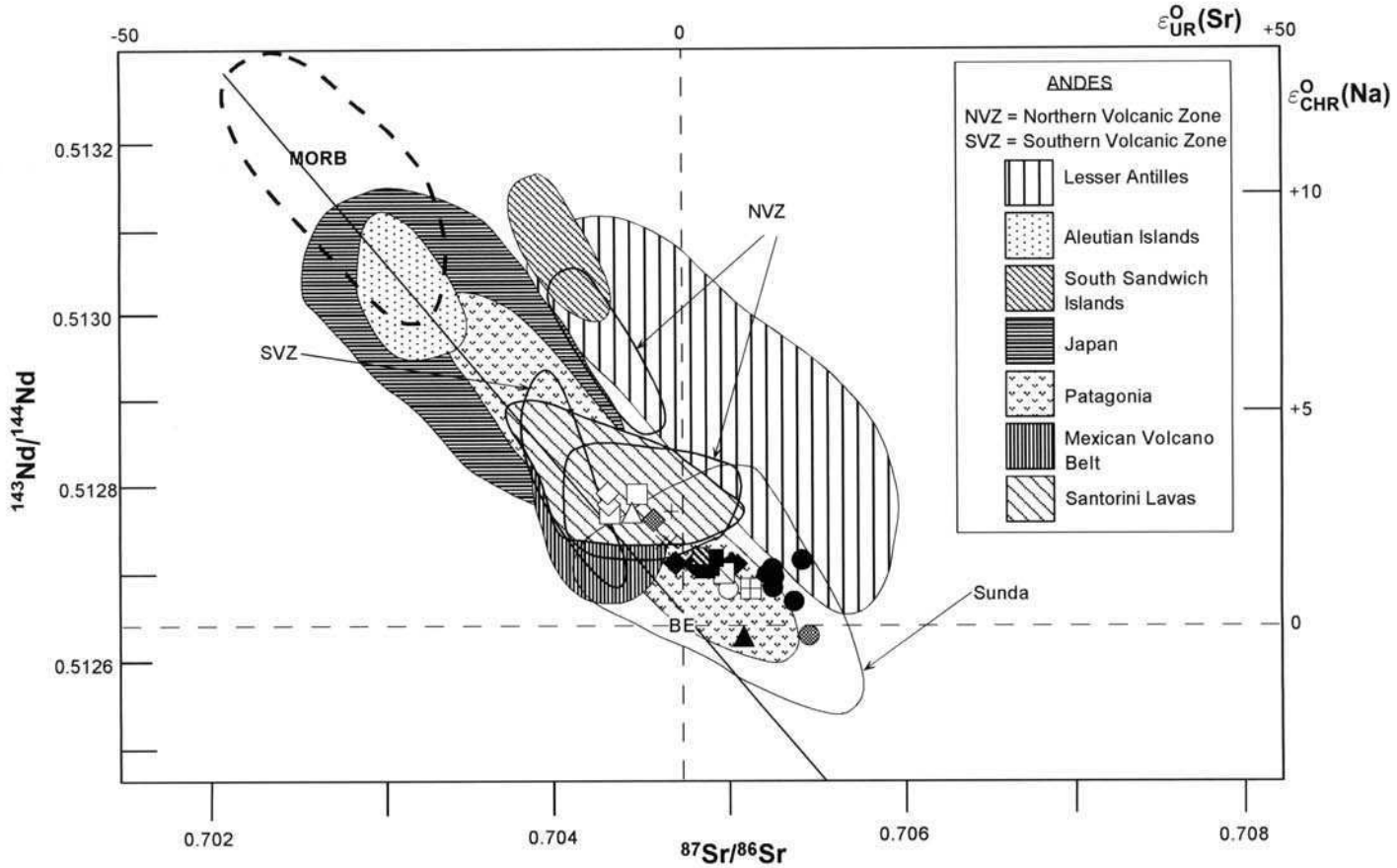

Fig. 6.13. (**a**) $^{87}Sr/^{86}Sr$ versus $^{143}Nd/^{144}Nd$ plot showing the Thera pyroclastics in relation to other arcs and various mantle sources (data from Hawkesworth & Powell 1980; Hawkesworth *et al.* 1983; Briqueu *et al.* 1986; Wilson 1989; Esperanca *et al.* 1992). CHUR(Nd): Chondrite uniform reservoir for Nd. UR(Sr): uniform reservoir for Sr. The present-day value of CHUR(Nd) is 0.512638 (Faure 1986; Rollinson 1993). The present-day value of UR(Sr) is not known accurately, ranging from 0.7045 to 0.7052 (references in Rollinson 1993). For our purposes, the UR(Sr) value at the present time is taken to be 0.7047 (Taylor & McLennan 1985). BE represents bulk earth composition. (**b**) Close-up view of the Thera pyroclastics and other geological settings on the $^{87}Sr/^{86}Sr$ v. $^{143}Nd/^{144}Nd$ plot.

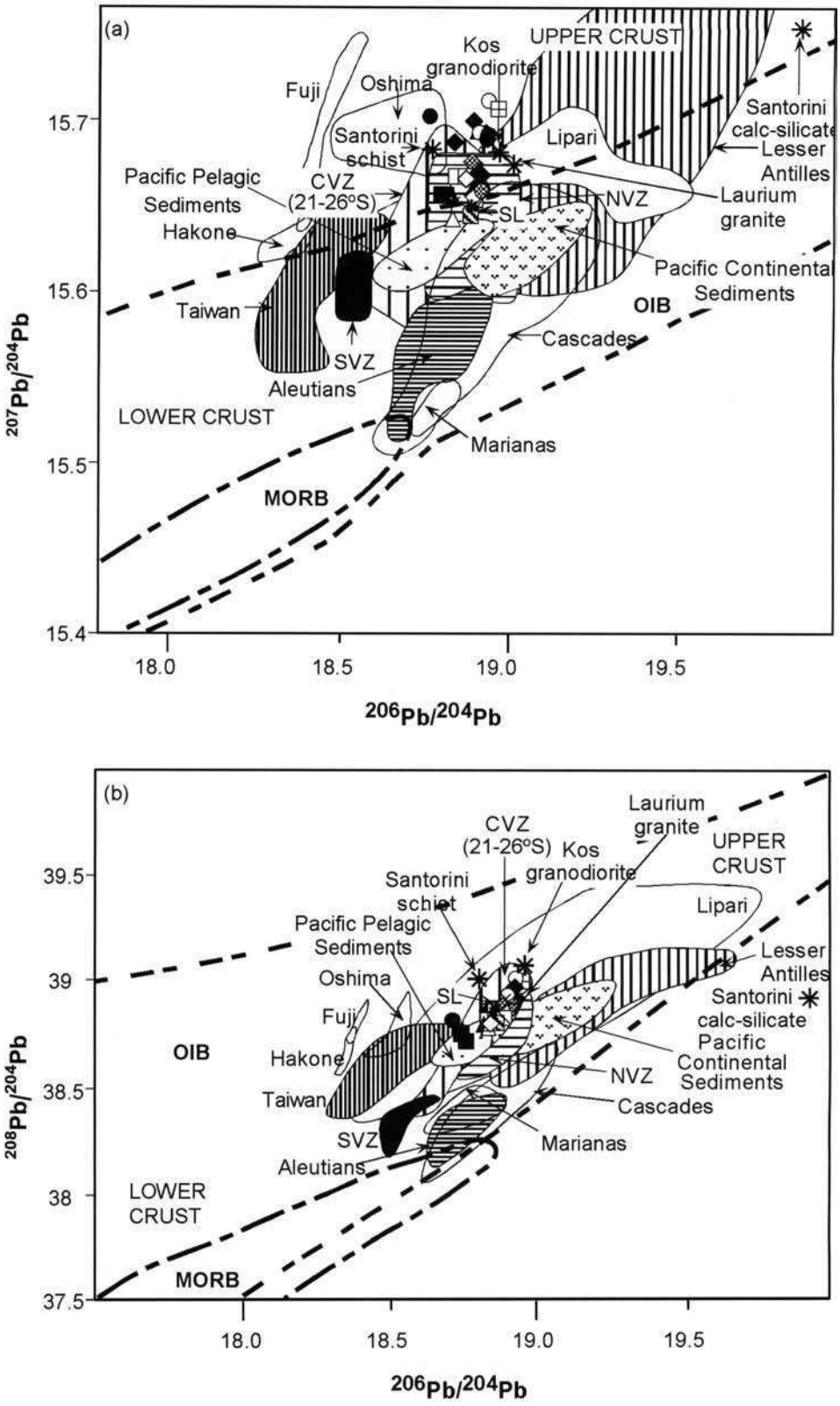

Fig. 6.14. Diagrams of $^{207}Pb/^{204}Pb$ (**a**) and $^{208}Pb/^{204}Pb$ (**b**) versus $^{206}Pb/^{204}Pb$, showing the Thera pyroclastics in relation to other arcs (data from Sun 1980; Hawkesworth *et al.* 1980; Barreiro 1983; Woodhead & Fraser 1985; White & Dupre 1986; Wilson 1989; Arculus *et al.* 1991; Esperanca *et al.* 1992). SL: Santorini Skaros lava.

that are as high as 0.0004, an order of magnitude above analytical error. The majority of plagioclase separates are less radiogenic than whole-rocks, but overall the secular variations of $^{87}Sr/^{86}Sr$ are confirmed, with a decrease in radiogenic Sr in plagioclase with time to Upper Scoriae 2 and a subsequent increase in Cape Riva and the Minoan. The greatest differences between plagioclase and whole-rock are observed in the dominantly silicic units, while one sample from Upper Scoriae 2 exhibits only a small contrast and in Cape Thera there appears to be isotopic equilibrium. In some units there is a small disequilibrium between plagioclase phenocrysts that contain glass inclusions and those which do not. With the exception of the Upper Scoriae 2 sample, the data indicate that melt phases in the magma chambers were more radiogenic than associated plagioclase phenocrysts immediately prior to eruption. This implies that contamination by a radiogenic component occurred after or during crytallization and confirms that at least some of the isotopic variations are related to processes in high-level magma chambers.

Oxygen isotope data

Whole-rock samples show a wide range of $\delta^{18}O$. Unfortunately secondary processes such as hydration and weathering can also be

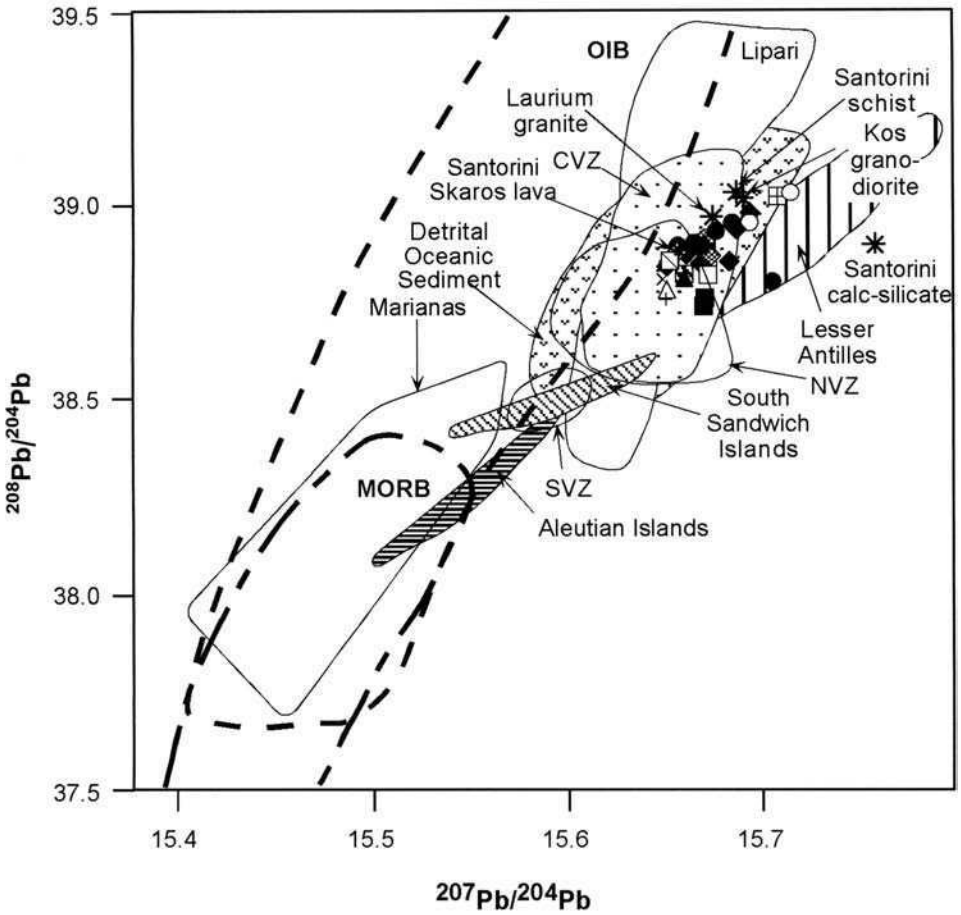

Fig. 6.15. ^{208}Pb ^{204}Pb versus ^{207}Pb ^{204}Pb for the Thera pyroclastics and other arcs (data from Harmon *et al.* 1984; Woodhead & Fraser 1985; Hickey *et al.* 1986; White & Dupre 1986; Esperanca *et al.* 1992)

responsible for substantial increases in $\delta^{18}O$ of porous glassy rocks. There is a strong correlation of $\delta^{18}O$ with loss on ignition and intrinsic water content (Fig. 6.20). This observation suggests hydration and exchange of oxygen between ground waters and the glass in the pumice. Alteration cannot be caused by simple weathering as the materials are perfectly fresh with no clay peaks on X-ray Diffraction patterns (Fig. 6.21). Taylor (1968) and Taylor & Turi (1976) showed that extreme ^{18}O enrichments of silicic material can occur due to low-temperature hydrothermal exchange or hydration by meteoric ground waters. Oxygen isotope analyses were made on plagioclase phenocryst separates from the same rocks, as plagioclase is not as susceptible to secondary alteration as glass. Figure 6.22 shows $\delta^{18}O$ of plagioclase separates plotted against stratigraphic height and compared to $\delta^{18}O$ in the corresponding whole-rocks. There are large differences in $\delta^{18}O$ between plagioclase and whole-rocks, with the greatest differences occurring in the silicic samples and the smallest in andesitic ones. If rocks are unaltered, with groundmass in equilibrium with phenocrysts, then the maximum difference between whole-rock and plagioclase should be only about 0.2 to 0.5‰, the whole-rock having the higher values (Taylor & Turi 1976). The results are best explained as the consequence of hydration of glass in pumiceous silicic samples. If so, only oxygen isotope data from plagioclase separates can be used to make inferences about magma genesis.

The plagioclase phenocrysts from the evolved magmas of the Thera pyroclastics show $\delta^{18}O$ values (+6.0 to +7.5‰) above typical mantle values. $\delta^{18}O$ values for the mantle are usually in the range +5.5 to +6.5‰ (Taylor 1968; Kyser *et al.* 1982). Previous analyses of oxygen isotopes from plagioclase in more mafic Santorini lavas fall in the range +5.7‰ to +6.4‰ (Wyers 1987). Fractional crystallization from basalt to rhyolite produces about a +1‰ change in $\delta^{18}O$ (Matsuhisa 1979; Muehlenbachs & Byerly 1982). Thus the oxygen isotope data are consistent with simple crystal fractionation, although the slight increases of many samples with respect to mantle values is also consistent with some crustal contamination.

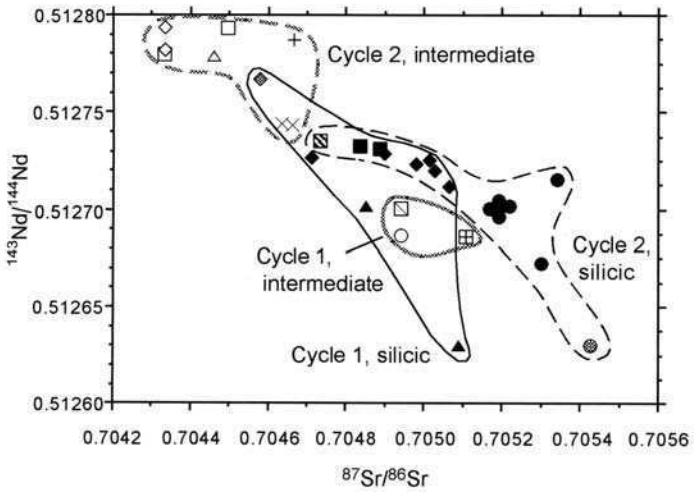

Fig. 6.16. $^{143}Nd/^{144}Nd$ v. $^{87}Sr/^{86}Sr$. Legend as in Fig. 6.1. The grey points are andesitic scoriae of Lower Pumice 2 and the Minoan. The striped square is a banded pumice from Cape Riva.

Interpretations of the geochemistry

The major and trace element variations observed in the Thera pyroclastics can be explained by a combination of three main effects: namely crystal fractionation, magma mixing and assimilation of crustal rocks. Geochemical models to test these ideas are also presented below. Variations in the compositions of parental basaltic magmas is certainly a possible additional factor. Mantle processes are almost certainly a factor in causing geochemical heterogeneity (Huijsmans 1985; Tarney *et al.* 1998), but the Thera pyroclastics are evolved rocks where crustal magmatic processes have masked the effects of deeper mantle processes.

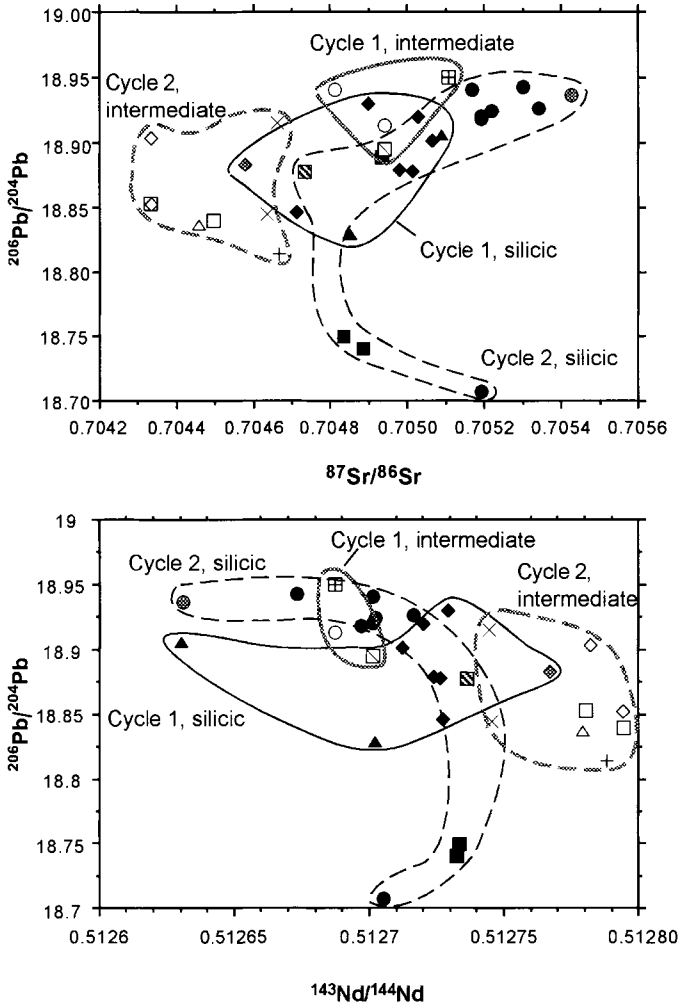

Fig. 6.17. (**a**) $^{87}Sr/^{86}Sr$ and (**b**) $^{143}Nd/^{144}Nd$ versus $^{206}Pb/^{204}Pb$. Legend as in Fig. 6.1. The grey points are andesitic scoriae of Lower Pumice 2 and the Minoan. The striped square is a banded pumice from Cape Riva.

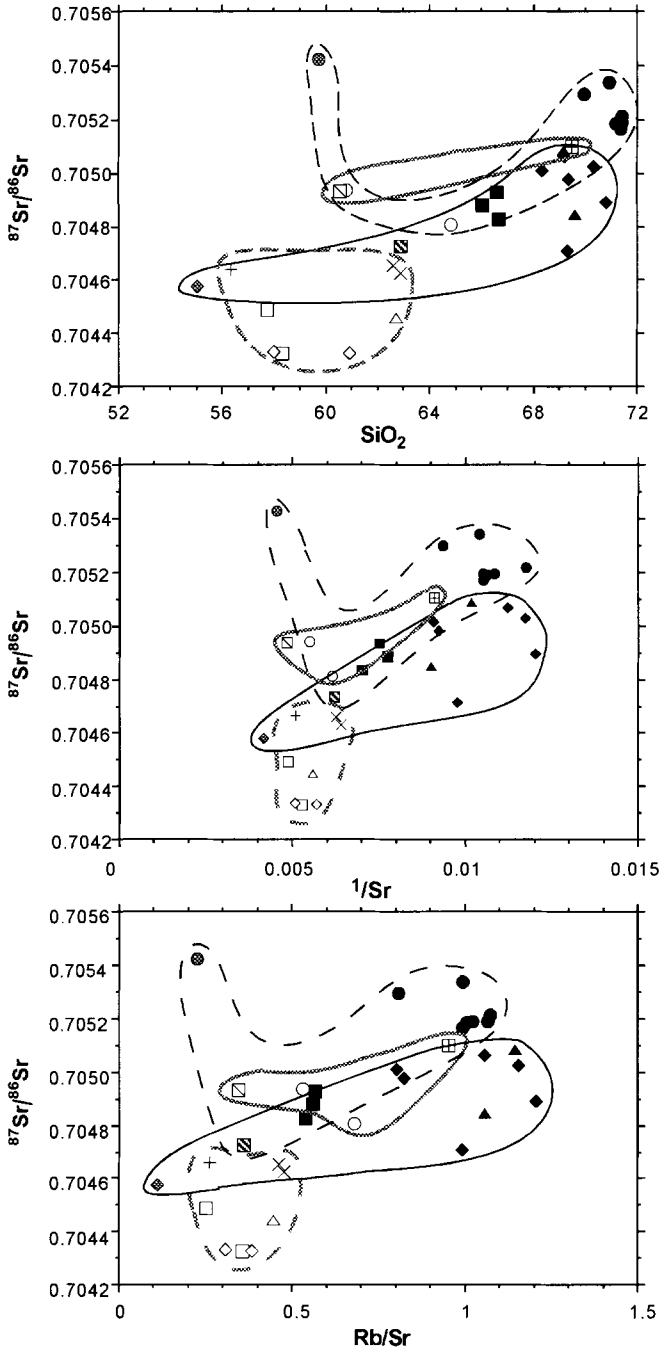

Fig. 6.18. $^{87}Sr/^{86}Sr$ versus SiO_2 (**a**),1/Sr (**b**) and Rb/Sr (**c**) for the Thera pyroclastics. Legend as in Fig. 6.1. The grey points are andesitic scoria of Lower Pumice 2 and the Minoan. The striped square is a banded pumice from Cape Riva. The data are grouped according to eruptive cycle and according to whether they are predominantly intermediate or dominantly silicic, as in Figs 6.16 and 6.17.

Crystal fractionation. Much of the compositional variation in the Thera pyroclastics can be explained by fractional crystallization as previously recognised for the lavas (Nicholls 1971*a*; Mann 1983; Huijsmans 1985). Several of the deposits show non-linear variations in composition with respect to evolution. Geochemical plots of several elements (Figs 6.6 to 6.9) display the non-linear trends that characterise fractionation where elements change from being compatible to incompatible as different phases appear and disappear. Plots of Cr and TiO_2 versus Zr (Fig. 6.23) illustrate plots that are diagnostic of fractional crystallization. We have also described petrological data on the zoned Thera pyroclastic deposits (Chapter 4) and the cumulate gabbros (Chapter 5) that support crystal fractionation as a major factor in magma genesis.

Magma mixing. Andesitic components of the dominantly silicic eruptions Lower Pumice 1, Cape Riva, and Minoan appear to have been influenced by magma mixing. The low FeO, TiO_2, and P_2O_5 contents, low FeO/MgO ratios and mildly calcalkaline chemistries are consistent in each case with the chemical mixing of a silicic component with a more mafic component of basaltic or mafic andesite composition. Cape Therma 1 andesite exhibits identical features, suggesting that it too formed by mixing. Trends for FeO(T), TiO_2, and P_2O_5 against SiO_2 show peak concentrations in intermediate compositions when fractional crystallization is the predominant process. Each of these elements behaves as an incompatible element in the early stages of fractionation and then becomes compatible in the later stages when certain minerals (oxides and apatite) become stable. Mixing of mafic and silicic end members which have lower concentrations of these elements than the intermediate products of fractionation generates intermediate hybrid magmas with anomalously low concentrations of these elements. This is clear on a plot of TiO_2–Zr (Fig. 6.23). Mixing also generates intermediate magmas with anomalously low FeO/MgO ratios and more calcalkaline nature than the endmembers (Sakuyama 1983). Magma mixing is also evident on a diagram of a highly compatible element versus an incompatible one, such as Cr–Zr (Fig. 6.23). Cr enters strongly into augite and olivine, and falls rapidly in residual liquids during initial fractionation from basalt. Zr content then increases with further crystallization, but Cr remains low. This generates a strongly curved fractionation trend. The anomalously high Cr contents of Cape Riva and Cape Therma 1 andesites on Fig. 6.23 are consistent with mixing.

This interpretation is supported by the following observations. First, Minoan scoria commonly have wispy inmixed streaks of pale

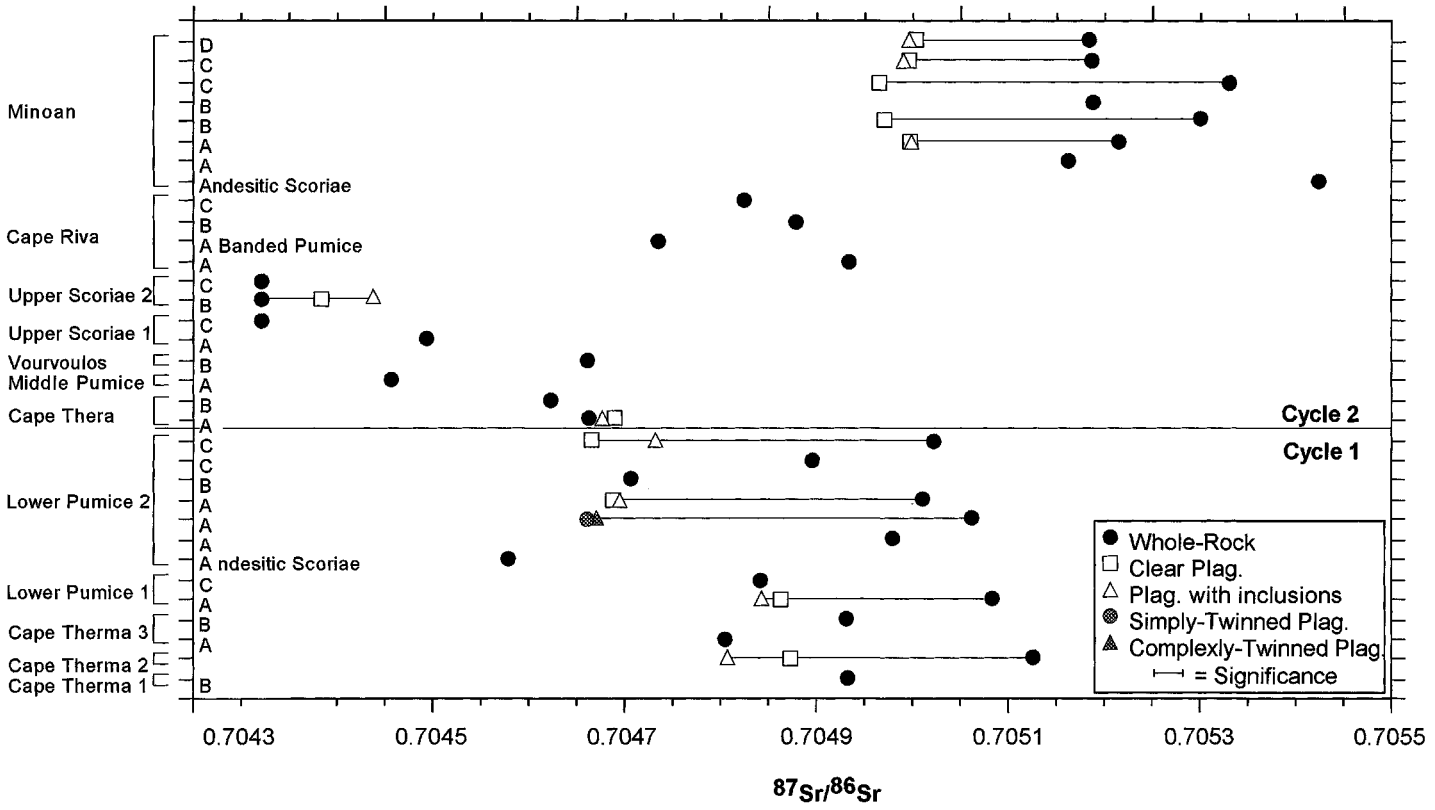

Fig. 6.19. Diagram of $^{87}Sr/^{86}Sr$ against stratigraphic height in the Thera pyroclastics, showing the disequilibria between plagioclase mineral separates and their associated whole-rocks. The letters correspond to eruption units listed in Table 3.4.

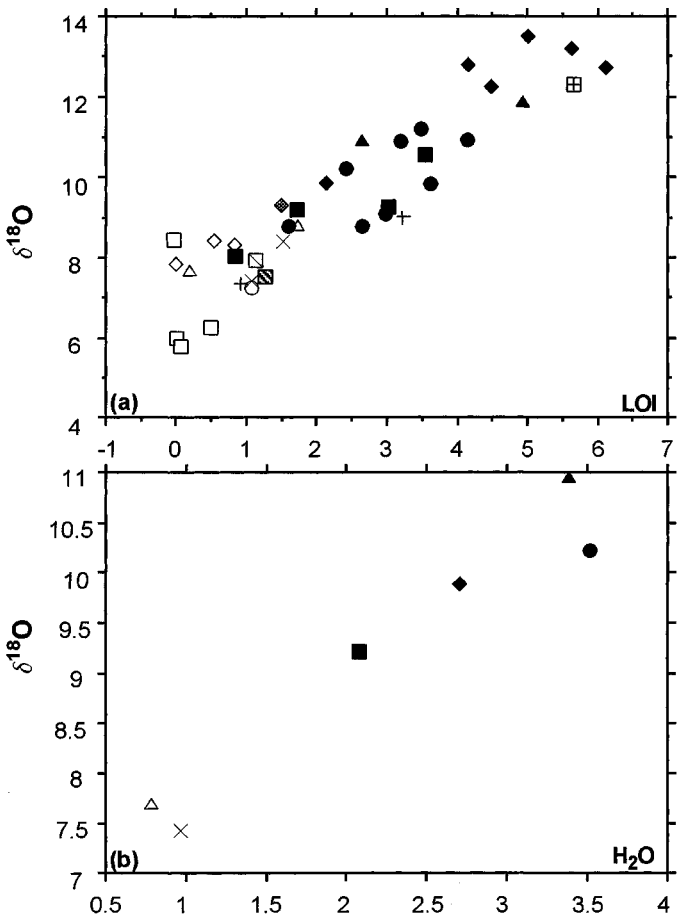

Fig. 6.20. (**a**) $\delta^{18}O$ versus loss on ignition (LOI) and (**b**) $\delta^{18}O$ v. H_2O. Legend as in Fig. 6.1. The grey points are andesitic scoriae of Lower Pumice 2 and the Minoan. The striped square is a banded pumice from Cape Riva.

pumice suggestive of the physical mingling of two components. Second, the Cape Riva andesite has a disequilibrium phenocryst assemblage and its composition can be modelled successfully by the mixing of 57% Cape Riva rhyodacite and 43% typical Skaros basalt (Chapter 4). Third, rare banded pumices and streaky grey pumices from Lower Pumice 2 (silica contents of 63–67%), which are unambiguously chemical mixtures of two components fall on the same trend as the Lower Pumice 1, Lower Pumice 2, Cape Riva, and Minoan andesites. It thus appears that mingling and mixing of magmas of contrasting compositions took place in all four dominantly silicic magma chambers. The andesite of Cape Therma 1 also appears to have a hybrid origin. Huijsmans (1985) also recognized that many andesite lavas of Santorini have involved magma mixing.

Interpretation of the Minor units

The minor sequences do not have any simple relationship to the magmas of the bounding units (Fig. 6.9). In the cases of M7 and M8 there are differences in incompatible element abundances between the minor sequence and bounding units, suggesting the ascent of different magma batches and independent magma evolution. The data provide no evidence that the minor sequence magmas evolved in the same large reservoirs as the major units. We propose that the minor sequences represent the growth of lava shields and lava cones from small magma chambers in the periods between large explosive eruptions. The present-day Kameni Volcano is an example of such a process. Kameni magmas are significantly depleted in incompatible elements compared with the Minoan. They appear not to be remnant magmas from the Minoan chamber, but an independent magma batch.

Implications of the isotope data

Sr, Nd, and Pb isotope compositions are consistent with contamination of Santorini magmas by Aegean crust. The correlations

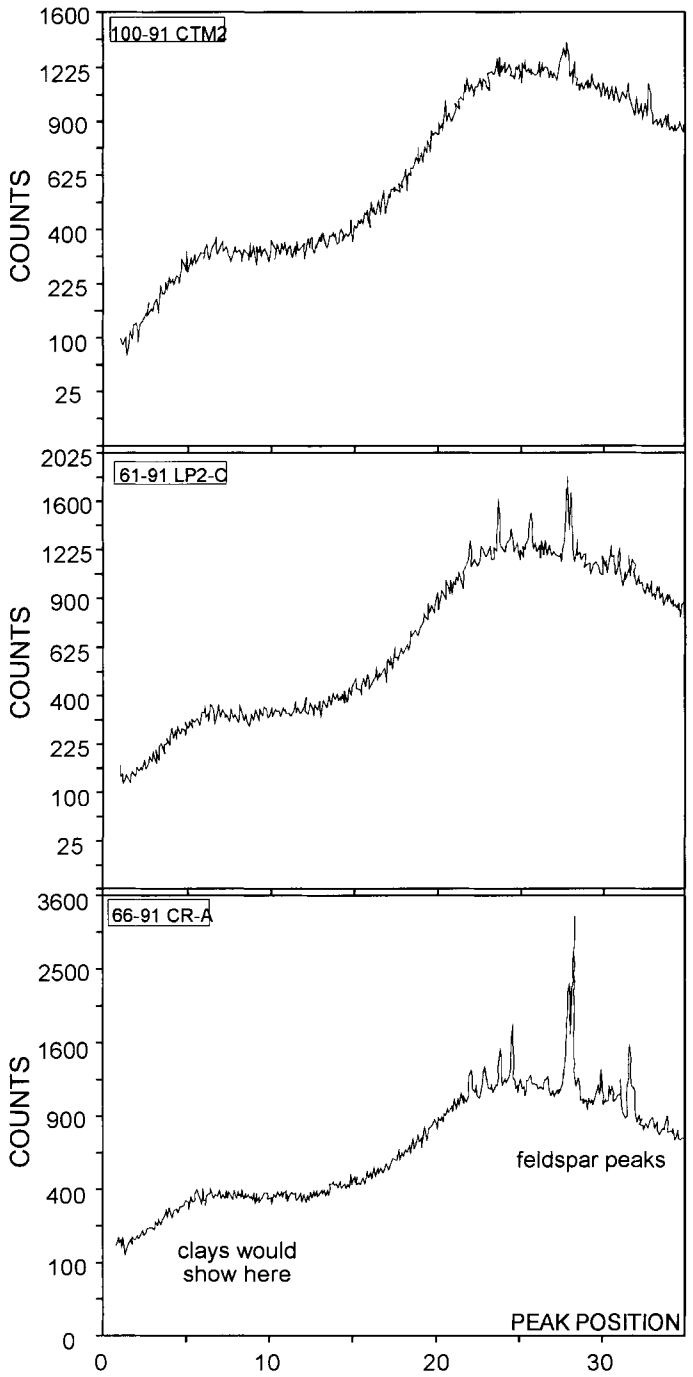

Fig. 6.21. X-ray diffraction plots for selected Thera pyroclastic deposits (note differences in scales).

of $^{87}Sr/^{86}Sr$ and $^{143}Nd/^{144}Nd$ with silica provide further evidence and are suggestive that contamination accompanied fractional crystallization. Some contamination occurred in high-level magma chambers because the melt phases of silicic magmas are mostly more radiogenic than plagioclase phenocrysts. The temporal decrease in incompatible elements through the first cycle and the early part of the second cycle may be related either to decreasing crustal contamination or to changes in the composition of the assimilant, because it is associated with a decrease in $^{87}Sr/^{86}Sr$ and a corresponding increase in $^{143}Nd/^{144}Nd$. Like elemental Ba and Sr, $^{87}Sr/^{86}Sr$ is anomalously high at the end of the second cycle. The oxygen isotope signature of whole-rock pumice samples has been strongly affected by low-temperature hydration. Magmatic values of $\delta^{18}O$ given by feldspar separates are consistent with fractional crystallisation and provide no information on contamination processes.

Geochemical modelling

The evidence presented in Chapters 4 and 5 and this chapter indicate that compositional variations in the Thera pyroclastics can be largely attributed to a combination of crystal fractionation, magma mixing and assimilation of continental crust. In this section we develop quantitative models to test hypotheses and to give further insights into petrogenesis. Objectives of such modelling can only extend to demonstrating that models are quantitatively consistent with observations.

Rayleigh fractionation models

Mann (1983) showed by quantitative fractionation models that the observed major and trace element variations in the lavas can be generated by extraction of the observed mineral assemblages. Similar models are developed here for the Thera pyroclastics. The equation of perfect Rayleigh fractionation is

$$F^{(D-1)} = \frac{C_L}{C_{0,L}} \tag{6.1}$$

where C_L and $C_{0,L}$ are concentrations of the trace element in the daughter liquids and parent liquid, respectively, F is the fraction of liquid remaining, and D is the bulk distribution coefficient of the trace element. $(1 - F)$ is the fraction of magma crystallized.

Basaltic lavas from Peristeria and Skaros (SI 140 and SI 181, respectively; Huijsmans 1985) were chosen as mafic parents to test whether fractionation of typical Santorini basalt can explain the incompatible element contents of the Thera pyroclastics. The major and trace element contents of these lavas are shown in Table 6.4. SI 140 is enriched in incompatible trace elements relative to SI 181, reflecting the secular decrease in incompatible elements observed in lava compositions of Santorini. These particular lava compositions were chosen as they have low silica contents, fall on the primitive end of differentiation trends, and are relatively phenocryst-poor. The two parents were used to derive more evolved liquid compositions represented by the Thera pyroclastic samples. The incompatible elements used to model fractionation were K, Rb, Ba, Y and Zr. D values used were 0.01 for K, Rb and Zr (Gill 1981), 0.2 for Ba (Gill 1981) and 0.1 for Y (Rollinson 1993). Model results were not sensitive to the exact value of D. If the two representative basalts are consistent as parents to the evolved magmas by crystal fractionation, then all the trace elements should give approximately the same values of $(1 - F)$. Differences between calculated $(1 - F)$ values can be accounted for either by changing the compositions of the parents or by invoking other petrogenetic processes such as crustal assimilation. Results are presented in Table 6.5 and in the following account are compared with the major element fractionation models of Mann (1983).

Major element models by Mann (1983) give best fits of about 60% fractional crystallization for the interval basalt to silicic andesite. The models for silicic andesitic compositions (Table 6.5) show agreement with Mann's models for Zr and Y provided that the appropriate parental basalt is chosen. For first-cycle silicic andesites (Cape Therma 1 and 3) the more incompatible-element-rich SI 140 gives the best agreement. If SI 181 is used then the amount of fractionation (69–74%) required by these elements is not consistent with the major element models. For some second-cycle andesites (Vourvoulos and Upper Scoriae 1) SI 181 also provides results consistent with the major element models for Zr and Y. Results for cycle 2 andesites are much more erratic using SI 140 as a parent, underestimating degree of fractionation compared to major element models. The models of Mann (1983) indicate that 75% fractional crystallization would be required to derive rhyodacite from basalt. Models for the silicic compositions (Lower Pumices 1 and 2, Cape Riva and Minoan) are consistent with Mann's results using SI 181 as parent. The results for Zr and Y indicate that, although first-cycle evolved magmas were derived from enriched parents similar to Peristeria basalts, relatively depleted parents resembling Skaros basalts became progressively more important over the 360 000 years represented by the Thera pyroclastics.

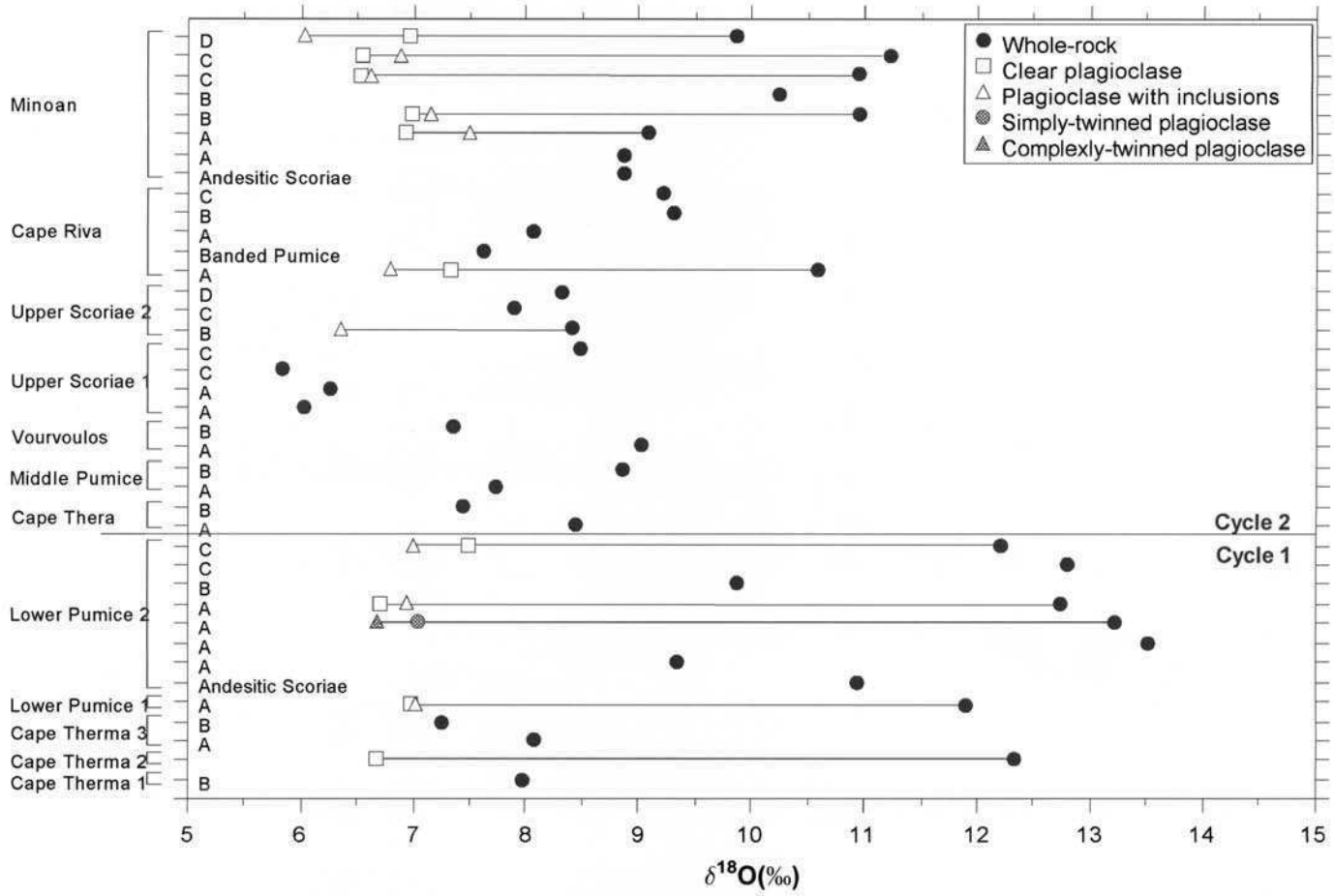

Fig. 6.22. Diagram of $\delta^{18}O$ against stratigraphic height in the Thera pyroclastics, showing the disequilibria between plagioclase mineral separates and their associated whole rocks. The letters correspond to eruption units listed in Table 3.4.

Rb, K and Ba typically give values of $(1-F)$ significantly greater than Mann's major element models and 15 to 20% higher than Zr and Y. One possible explanantion is that the mafic parents from which the evolved magmas were derived either had higher initial concentrations of Rb, K and Ba or lower concentrations of Zr and Y than the magma compositions chosen for modelling. Zr contents of the parental basalts would have to be 30–70 ppm to get similar $(1-F)$ values to Rb, K_2O and Ba. Zr concentrations as low as these are not common in Santorini basalts. Further, the modified models would then give degrees of fractional crystallization from basalt to andesite which are inconsistent with major element models. Alternatively, the parental magmas might have had the observed Zr content but higher contents of K_2O, Rb and Ba. This would require that the parents had K_2O contents of between 0.7 and 1.1. Santorini basalt with such high K_2O contents at comparable SiO_2 and MgO contents are uncommon. Although a few basalts with appropriately high K_2O are known from the Akrotiri peninsula (Davis *et al.* 1998), these same samples have elevated Zr. None of the basalts sampled on Santorini have combinations of elemental abundances that allow a simple fractionation model to be formulated. We conclude that the differences in $(1-F)$ are not a consequence of inappropriate choice of basalt parent, but must be attributed to some other process that enriches Rb, K and Ba relative to Zr and Y.

Assimilation and fractional crystallization models

Simple fractional crystallization models using compositions of Santorini basalts are inconsistent with the trace element and isotopic systematics in the Thera pyroclastics. In this section we test whether the data are consistent with concomitant assimilation and fractional crystallization (AFC). The basis AFC equations were derived by De Paolo (1981).

For any trace element:

$$C_L = C_{0.L} f + \frac{r}{(r-1+D)} C^*(1-f) \tag{6.2}$$

$$f = F^{-K} \tag{6.3}$$

where

$$K = \frac{(r-1-D)}{(r-1)} \tag{6.4}$$

where C_L, $C_{0.L}$, and C^* are the trace element concentrations in the contaminated magma, original magma, and assimilant respectively, r is the ratio of the mass of assimilant to mass crystallized, D is the bulk distribution coefficient for the fractionating assemblage, and F is the fraction of magma remaining.

For any radiogenic isotope:

$$\varepsilon_L = \varepsilon_{0.L} + (\varepsilon^* - \varepsilon_{0.L})1 - \frac{C_{0.L}}{C_L} f \tag{6.5}$$

where ε_L is the isotopic ratio in the contaminated magma, $\varepsilon_{0.L}$ the isotopic ratio in the original magma, and ε^* the isotopic ratio in the assimilant.

For mixing processes for any trace element:

$$C_L = F(C_{0.L} - C^*) + C^*. \tag{6.6}$$

For any radiogenic isotope:

$$\varepsilon_L = \varepsilon_{0.L}(C_{0.L}F/C_L) + \varepsilon^*(C^*(1-F)/C_L) \tag{6.7}$$

Feasible contaminants for Santorini magmas include average upper continental crust, average lower crust, glaucophane schist, and metavolcanic rock (Barton *et al.* 1983; Briqueu *et al.* 1986;

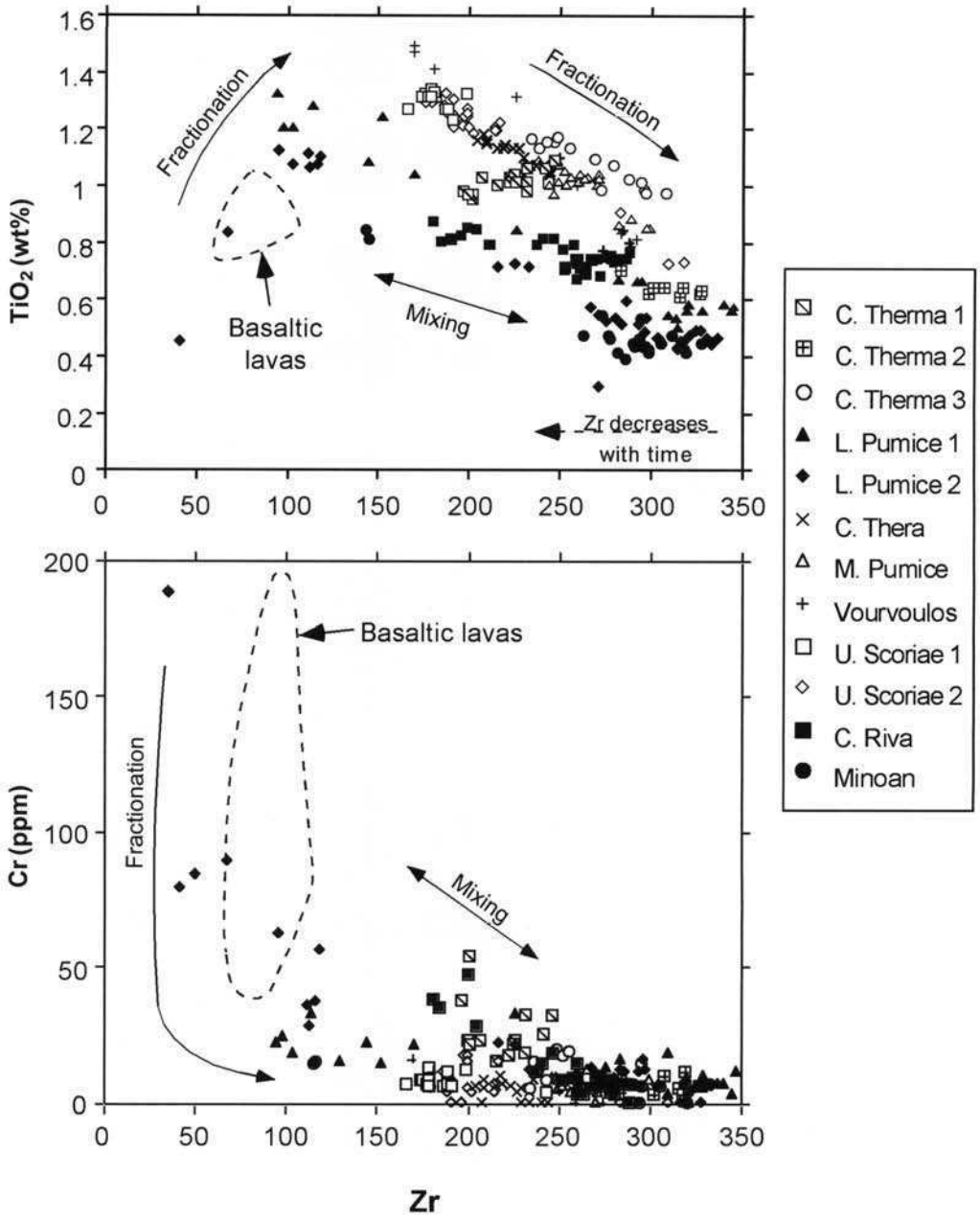

Fig. 6.23. Plots of TiO_2 and Cr versus Zr, summarizing the interpretations for the chemical variations in the Thera pyroclastics. Crystal fractionation from basaltic parents generates curved trends on these diagrams. Zr contents of evolved magmas decrease crudely with time, as discussed in the text. Mixing of compositionally disparate magmas across the fractionation trend generates intermediate magmas with anomalously low TiO_2 and high Cr. The andesites of Cape Therma 1, Lower Pumice 1, Cape Riva, and the Minoan fall on mixing trends, as do banded pumices and streaky grey pumices of Lower Pumice 2.

Wyers 1987). Calculations for the Thera pyroclastics were therefore carried out using a range of rock types from the Aegean (Chapter 2). Values of D are reasonably well-constrained (with D_{Sr} and D_{Nd} being slightly higher in evolved magmas) and therefore the modeller's task is to select values of r and end-member compositions. A valid model must be in agreement with all observations for the elements chosen. In this study the elements Rb Sr, K, Ba, Zr and the isotopes $^{87}Sr/^{86}Sr$, and $^{143}Nd/^{144}Nd$ are used. A good fit between a model and observations does not in itself prove a hypothesis, but a bad fit can demonstrate that a hypothesis is not possible. The AFC equations have too many degrees of freedom to give a unique answer. Other evidence must therefore be used to provide support

Table 6.4. *Mafic lava samples from Peristeria and Skaros (corrected to 100% anhydrous)*

Sample	SiO_2	TiO_2	Al_2O_3	FeO(T)	MnO	MgO	Ca_2O	Na_2O	K_2O	P_2O_5	Ba	Rb	Sr	Zr	Nd	$^{87}Sr/^{86}Sr$	$^{143}Nd/^{144}Nd$
Peristeria																	
SI 140	51.65	0.86	19.56	7.27	0.16	5.65	11.49	2.59	0.65	0.10	103	22	243	101	13	0.704570	0.512740
SI 137	52.91	1.02	18.01	9.34	0.19	4.80	9.54	3.18	0.88	0.13	164	30	256	120	18	0.704890	0.512696
SI 138	52.93	0.99	18.10	9.31	0.20	4.89	9.59	2.99	0.81	0.12	177	28	258	120	–	–	–
SI 135	54.64	0.92	20.23	7.52	0.15	2.56	9.14	3.54	1.14	0.15	197	32	262	134	–	0.705020	0.512648
Skaros																	
SI 181	51.35	0.76	18.94	8.12	0.17	6.51	11.49	2.27	0.31	0.08	60	9	221	65	9	0.704240	0.512846
SI 180	52.10	0.77	18.35	7.98	0.16	6.24	11.35	2.45	0.48	0.09	76	17	207	80	13	–	–
SI 179	52.34	0.80	18.90	8.00	0.17	5.55	10.99	2.56	0.60	0.09	79	20	214	85	13	–	–
SI 182	52.81	0.82	18.00	8.22	0.18	5.89	10.76	2.57	0.66	0.10	108	22	212	93	–	0.704140	0.512805
SI 150	54.44	0.94	19.99	8.79	0.19	4.94	7.07	2.54	0.97	0.11	152	33	189	134	–	–	–

Major and trace element contents from Huijsmans (1985). Isotopic analyses from Wyers (1987)

Table 6.5. *Results of fractionation calculations using SI 140 (Peristeria) and SI 181 (Skaros) mafic lavas as parents*

	CL	SI 140 1-F	SI 181 1-F		CL	SI 140 1-F	SI 181 1-F
Cape Therma 1 155				*Vourvoulos* 147775			
Rb	71	0.69	0.88	Rb	51	0.57	0.83
K	1.93	0.67	0.84	K	1.28	0.50	0.76
Ba	335	0.77	0.88	Ba	206	0.58	0.79
Zr	223	0.55	0.71	Zr	170	0.41	0.62
Y	43	0.62	0.69	Y	41	0.60	0.67
Cape Therma 3 166				*Upper Scoriae 1* 147759			
Rb	96	0.77	0.91	Rb	51	0.57	0.83
K	2.35	0.73	0.87	K	1.36	0.53	0.78
Ba	391	0.81	0.90	Ba	229	0.63	0.81
Zr	248	0.60	0.74	Zr	179	0.44	0.64
Y	51	0.69	0.74	Y	44	0.63	0.70
Lower Pumice 1 159				*Upper Scoriae 1* 145606			
Rb	112	0.81	0.92	Rb	67	0.68	0.87
K	3.32	0.81	0.91	K	1.49	0.57	0.80
Ba	493	0.86	0.93	Ba	322	0.76	0.88
Zr	314	0.68	0.80	Zr	199	0.50	0.68
Y	55	0.71	0.76	Y	42	0.61	0.68
Lower Pumice 2 58				*Upper Scoriae 2* 174			
Rb	88	0.75	0.90	Rb	67	0.68	0.87
K	2.99	0.79	0.90	K	1.83	0.65	0.83
Ba	432	0.83	0.92	Ba	290	0.73	0.86
Zr	276	0.64	0.77	Zr	216	0.54	0.70
Y	52	0.69	0.75	Y	47	0.66	0.72
Cape Thera 125				*Cape Riva* 149			
Rb	73	0.70	0.88	Rb	72	0.70	0.88
K	2.18	0.71	0.86	K	2.41	0.73	0.87
Ba	368	0.80	0.90	Ba	428	0.83	0.91
Zr	233	0.57	0.72	Zr	253	0.60	0.75
Y	47	0.66	0.72	Y	54	0.70	0.76
Middle Pumice 145561				*Minoan* 121			
Rb	79	0.73	0.89	Rb	94	0.77	0.91
K	2.1	0.69	0.86	K	3.1	0.79	0.90
Ba	392	0.81	0.90	Ba	509	0.86	0.93
Zr	233	0.57	0.73	Zr	298	0.66	0.79
Y	59	0.73	0.78	Y	45	0.64	0.70

D values are 0.01 for Rb, K and Zr, 0.2 for Ba, and 0.1 for Y. Sample numbers are given. K in % of K_2O and all other element concentrations as ppm.

Table 6.6. *Major and trace element analyses, and isotopic ratios of Santorini basement rocks used in AFC modelling*

Sample	201-91	SAN 129	SAN 125
SiO2	59.21	–	–
TiO_2	1.13	–	–
Al_2O_3	19.87	–	–
FeO(T)	6.97	–	–
MnO	0.06	–	–
MgO	3.85	–	–
Ca_2O	2.04	–	–
Na_2O	1.69	–	–
K_2O	5	–	–
P_2O_5	0.18	–	–
Ba	622	–	–
Rb	170	260	152
Sr	42	65	72
Y	31	–	–
Zr	224	–	–
Nd	–	22.5	17.7
$^{87}Sr/^{86}Sr$	0.720212	0.709908	0.709940
$^{143}Nd/^{144}Nd$	0.512101	0.512320	0.512391
$\delta^{18}O$	13.3	–	–
$^{206}Pb/^{204}Pb$	19.875	–	–
$^{207}Pb/^{204}Pb$	15.758	–	–
$^{208}Pb/^{204}Pb$	38.863	–	–

Samples SAN 129 and SAN 125 from Briqueu *et al.* (1986). Sample 201-91 from this study.

for a particular petrogenetic model. The models require choices of a mafic end-member and an assimilant, made on geological grounds.

There is now a large amount of data on the mafic rocks of Santorini, including the Peristeria and Skaros Lavas (e.g. Huijsmans 1985; Wyers 1987), and our new data on minor pyroclastic sequences MS6, MS7 and MS8. We assumed that the basaltic lavas of Santorini provide the most plausible mafic end-member compositions. Models have been carried out by choosing a single assimilant end-member and then adjusting the mafic end-member for each element and isotopic ratio until the best fit is achieved at a single value of r for all elements and isotopes. This requires a trial-and-error approach and only the successful results are presented. The only constraint placed on the mafic end-member is that each element or isotopic value must fall within the natural range of observed Santorini mafic lavas. Mafic lava compositions for Peristeria and Skaros are shown in Table 6.4. No single composition could be used to provide a 'best-fit' solution to an individual evolved composition. Data in Table 6.4 were used as a guide to the range of trace element and isotopic compositions of the mafic end-member. As documented below, calculated parental compositions are very similar to these observed compositions.

The nature of the assimilant is much more problematic given the large variation in rock types in the Aegean basement and the largely unknown character of the deeper parts of the crust (Chapter 2). Preliminary AFC modelling was carried out using basement rock types from various Aegean islands as contaminant, and mafic lava samples from Peristeria and Skaros as mafic end-members. It was found that the Rb and Sr contents of Naxos basement rocks would

Table 6.7. *Parameters used in AFC modelling calculations*

	Cape Therma 1	Cape Therma 2	Cape Therma 3	Lower Pumice 1	Lower Pumice 2	Cape Thera	Middle Pumice	Vourvoulos	Upper Scoriae 1	Upper Scoriae 2	Cape Riva	Minoan
Element concentrations in parent liquid												
Ba	190	160	200	180	180	180	180	120	150	200	140	130
Rb	30	20	35	25	25	24	29	20	25	42	9	9
K	6500	5000	8000	7000	7000	6000	6500	3700	5000	9000	2500	2573
Sr	250	221	250	221	221	210	221	250	250	210	200	215
Nd	22	14	17	12	15	15	15	15	14	12	11.5	11.5
Zr	110	95	130	110	100	100	110	80	100	140	70	60
ε Sr	0.7047	0.7042	0.7043	0.7042	0.7042	0.7042	0.7042	0.7042	0.7042	0.7042	0.7042	0.7042
ε Nd	0.51274	0.51283	0.51274	0.51283	0.51283	0.51283	0.51283	0.51283	0.51283	0.51283	0.51283	0.51283
Element concentrations in contaminant												
Ba	622	622	622	622	622	622	622	400	400	622	622	622
Rb	170	170	170	170	170	170	170	72	100	170	170	170
K	41 500	41 500	41 500	41 500	41 500	41 500	41 500	25 000	30 000	41 500	41 500	41 500
Sr	42	42	42	42	42	42	42	150	150	42	42	42
Nd	22	22	13	22	22	22	22	18	18	22	17	17
Zr	224	224	224	224	224	224	224	150	150	224	224	224
ε Sr	0.7202	0.7202	0.7202	0.7202	0.7202	0.7202	0.7202	0.7100	0.7100	0.7202	0.7202	0.7202
ε Nd	0.51210	0.51210	0.51210	0.51210	0.51210	0.51210	0.51210	0.51239	0.51239	0.51210	0.51210	0.51210
Crystal–liquid distribution coefficients												
Ba	0.20	0.20	0.20	0.20	0.20	0.20	0.20	0.20	0.20	0.20	0.20	0.20
Rb	0.01	0.01	0.01	0.01	0.01	0.01	0.01	0.01	0.01	0.01	0.01	0.01
K	0.01	0.01	0.01	0.01	0.01	0.01	0.01	0.01	0.01	0.01	0.01	0.01
Sr	1.20	1.50	1.20	1.50	1.70	1.25	1.20	1.20	1.30	1.20	1.25	1.50
Nd	0.10	0.30	0.10	0.30	0.30	0.10	0.10	0.10	0.10	0.10	0.10	0.30
Zr	0.01	0.01	0.01	0.01	0.01	0.01	0.01	0.01	0.01	0.01	0.01	0.01
Assimilation fractionation ratio (r)												
	0.15	0.20	0.20	0.15	0.15	0.15	0.10	0.15	0.15	0.15	0.15	0.15

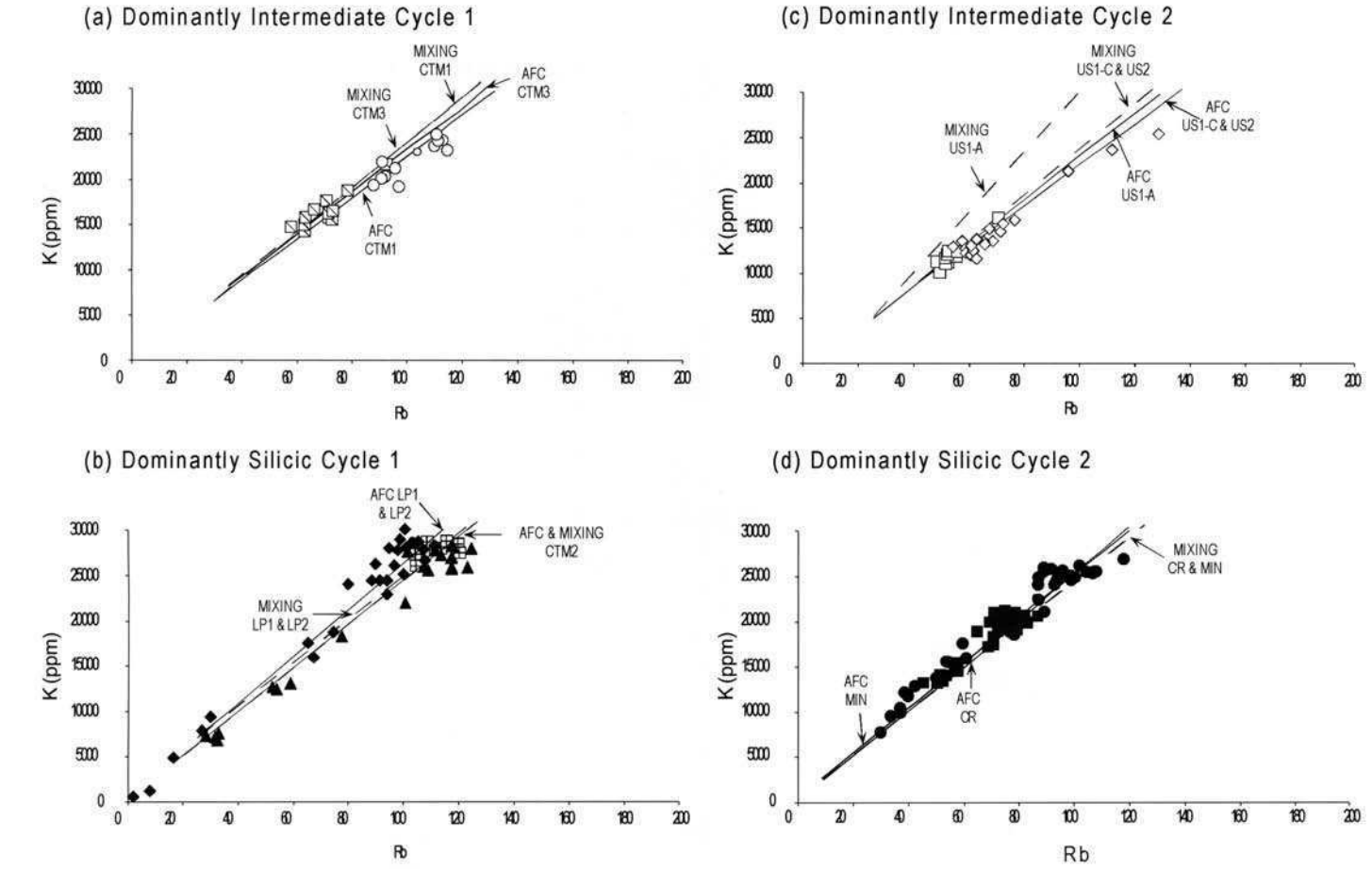

Fig. 6.24. Results of AFC and mixing calculations for K versus Rb for the Thera pyroclastics divided up into four groupings based on the explosive cycles and the dominant magma type. Cape Therma 1 (CTM1), Cape Therma 2 (CTM2), Cape Therma 3 (CTM3), Lower Pumice 1 (LP1), Lower Pumice 2 (LP2), Upper Scoriae 1 (US1), Upper Scoriae 2 (US2), Cape Riva (CR) and Minoan (MIN). Details of end members are given in Tables 6.4 to 6.7. Symbols as in Fig. 6.1.

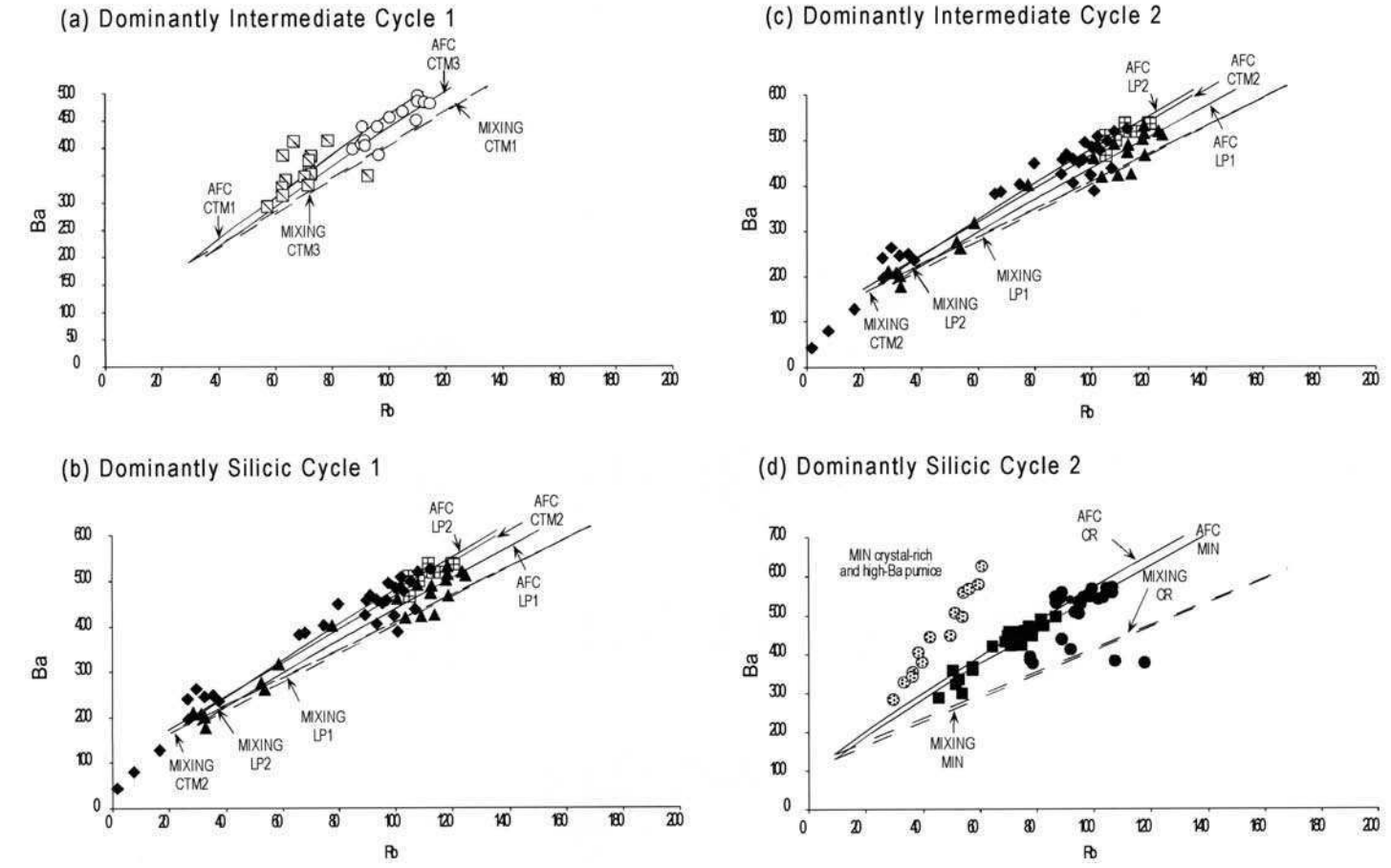

Fig. 6.25. Results of AFC and mixing calculations for Ba v. Rb. Cape Therma 1 (CTM1), Cape Therma 2 (CTM2), Cape Therma 3 (CTM3), Lower Pumice 1 (LP1), Lower Pumice 2 (LP2), Upper Scoriae 1 (US1), Upper Scoriae 2 (US2), Cape Riva (CR) and Minoan (MIN). Details of end members are given in Tables 6.4 to 6.7. Symbols as in Fig. 6.1.

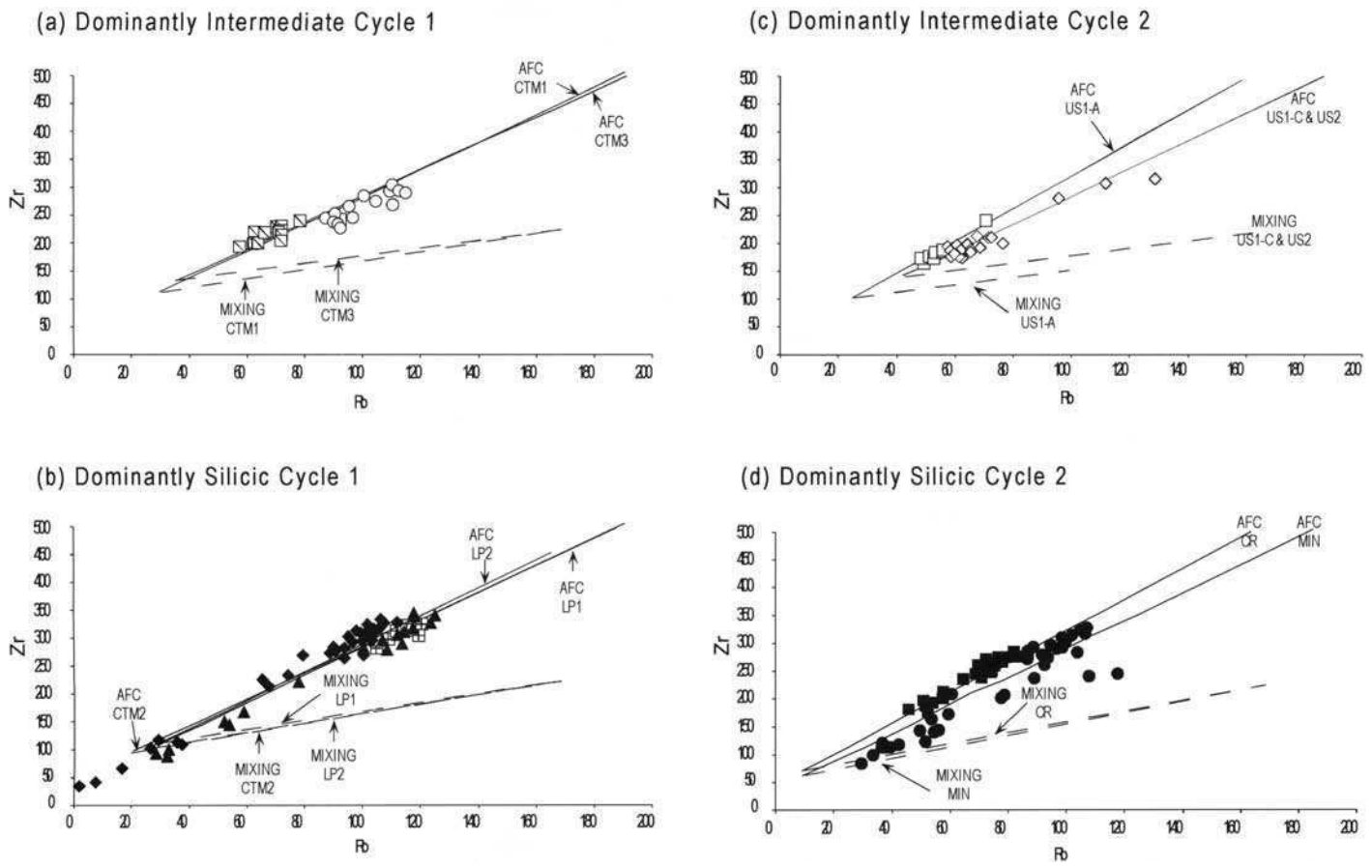

Fig. 6.26. Results of AFC and mixing calculations for Zr v. Rb. Cape Therma 1 (CTM1), Cape Therma 2 (CTM2), Cape Therma 3 (CTM3), Lower Pumice 1 (LP1), Lower Pumice 2 (LP2), Upper Scoriae 1 (US1), Upper Scoriae 2 (US2), Cape Riva (CR) and Minoan (MIN). Details of end members are given in Tables 6.4 to 6.7. Symbols as in Fig. 6.1.

not provide results compatible with the Thera pyroclastics data. Miocene granitoids from Laurium, Serifos, Mykonos/Delos, Naxos, Kos and Samos all have Sr contents far too high. The values for upper and lower continental crust given by Barton *et al.* (1983) also do not work due to high Sr. Therefore it appears that a contaminant is needed that has lower Sr than all of these rock types.

Briqueu *et al.* (1986) obtained quite a good match between an AFC model and their data by using a Mesozoic metavolcanic rock from Santorini itself (their sample SAN 129: Table 6.6). This has a Sr content of only 65 ppm. An andesitic metavolcanic rock collected for this study from Santorini also has low Sr (42 ppm: sample 201-91: Table 6.6). Further evidence for the presence of low-Sr lithologies is the basement of Sikinos, where Sr values vary from 42 to 78 ppm. The contaminant requires high K_2O (5 wt%) and Zr (224 ppm). The problem with these rocks as a choice of assimilant is that, while they have appropriate contents of the chosen incompatible elements and isotope ratios to fit the observations, at least one is an andesite. Thus magmas more mafic than andesite with $SiO_2 = 60\%$ could assimilate such a rock type, but dacites and rhyodacites could not assimilate a rock more mafic than themselves. The requirement for the assimilant to have high Rb, K and Ba, and commensurately low Sr, strongly points to the contaminant being a highly-evolved igneous composition, such as leucogranite or rhyolitic partial melt. Since leucogranites are not a major component of the Aegean crust then the observations suggest involvement of a partial melt.

Given the difficulties of identifying an assimilant, the trace element and isotopic compositions of the three compositions of Table 6.6 have been used to generate AFC models. These were found to give very good fits to the observations. The models constrain the relative abundances of the trace elements quite well, but not the absolute abundances. However the values in Table 6.6 are consistent with the compositions that might be expected by partial melting of common rock types of the Aegean crust. The modelling results are now presented and the best-fit models shown in Table 6.7. Many combinations of r values and end-member compositions were investigated but were discarded because they failed to match all the observed variations. Data for all the Thera pyroclastics are shown on the diagrams so that specific models and observed data may be compared.

Results for models that satisfy simultaneously all trace element and isotopic features of each of the Thera Pyroclastic eruptions are presented in Table 6.7. Some examples of the models are shown in Figs 6.24 to 6.27, showing the good agreement between the models and data. To a first approximation, partition coefficients can be kept constant with the exception of minor variations in D_{Sr} and D_{Nd}. The AFC models have been compared with simple bulk mixing models between the end members (Figs 6.24–6.27). Mixing models always fail to reproduce at least one of the elements or isotopic ratios, and we were unable to find mixing end members that would simultaneously satisfy compositions within the range of Santorini basalts and within the range of common crustal rocks and their partial melts. The results provide evidence that the principal contamination process was AFC, not MASH. In the MASH process basalts assimilate bulk crustal rocks and then fractionate without any further asimilation (Hildreth & Moorbath 1988). The positive correlation of isotopic composition and whole-rock silica content is compatible with AFC, but not with MASH (Fig. 6.18).

For the mafic end-member most results give K_2O in the range 0.78–1.08, Rb 25–35 ppm, Ba 150–200 ppm, and Zr 95–140 ppm. The Sr and Nd isotopic compositions of the mafic end members can be kept almost constant and achieve satisfactory results. The trace element and isotopic ratio ranges are similar to those of the most mafic lavas of Peristeria and Skaros. Models for Cape Riva and the Minoan require significantly lower concentrations of incompatible

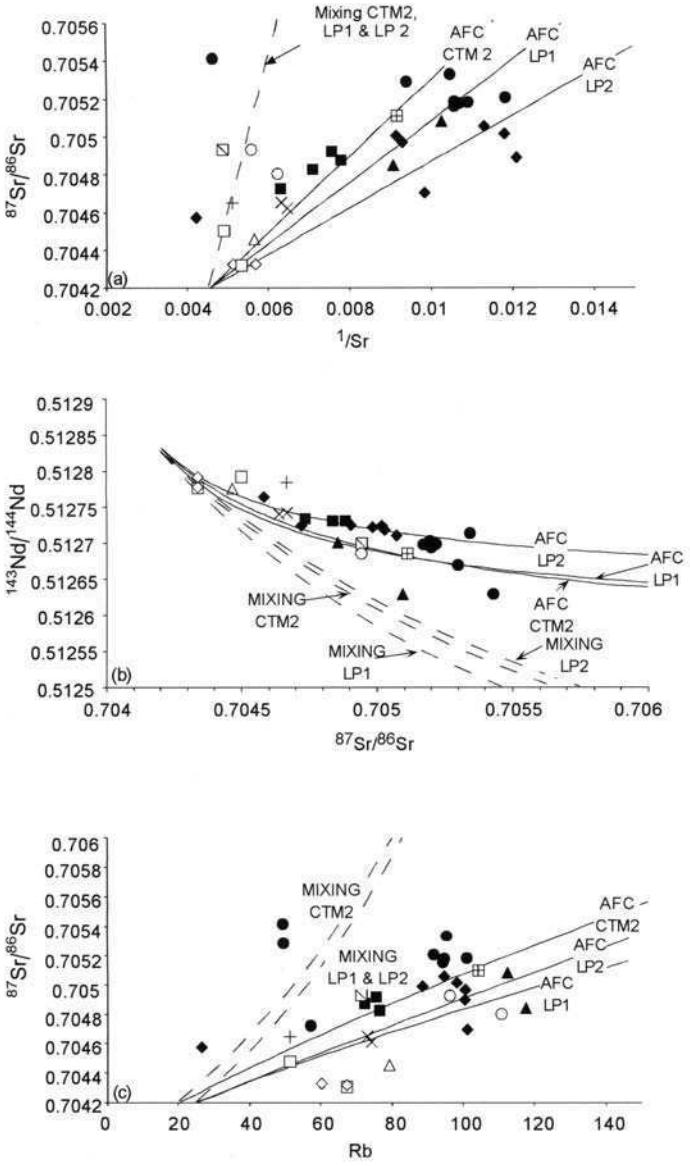

Fig. 6.27. Results of AFC and simple mixing calculations for $^{87}Sr/^{86}Sr$-$^{143}Nd/^{144}Nd$, Rb and 1/Sr. Models are presented for Lower Pumice 1 (LP1), Lower Pumice 2 (LP2) and Cape Therma 2 (CTM2). Data from all the Thera pyroclastics are shown for comparison and details of end members are given in Tables 6.4 to 6.7. Symbols as Fig. 6.1.

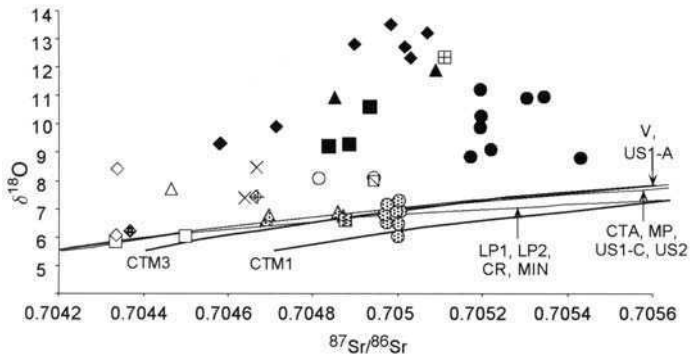

Fig. 6.28. Plot of $\delta^{18}O$ versus $^{87}Sr/^{86}Sr$ showing four AFC models discussed in the text. The mafic endmember had an assumed $\delta^{18}O$ value of +5.5‰ and the assimilant +13.3‰. Whole-rock data are shown by the black and white symbols and plagioclase separates by grey symbols. The legend for whole-rock samples is given in Fig. 6.1. Cape Therma 1 (CTM1), Cape Therma 2 (CTM2), Cape Therma 3 (CTM3), Lower Pumice 1 (LP1), Lower Pumice 2 (LP2), Cape Thera (CTA), Middle Pumice (MP), Vourvoulos (V), Upper Scoriae 1 (US1), Upper Scoriae 2 (US2), Cape Riva (CR) and Minoan (MIN).

trace elements (Table 6.7). This is consistent with the overall depletion of incompatible trace element concentrations with time on Santorini. AFC models thus provide a plausible mechanism for enriching elements such as Rb, K and Ba relative to other incompatible elements such as Zr and Y. Most eruptions can be modelled using a single assimilant with K = 41 500 ppm, Zr = 224, Sr = 42, Rb = 170, Ba = 622, $^{87}Sr/^{86}Sr = 0.7202$ and $^{143}Nd/^{144}Nd = 0.51210$. This is consistent with assimilation of rhyolitic partial melts of igneous lithologies of the continental crust. Vourvoulos and Upper Scoriae 1 are anomalous in requiring a less evolved assimilant with higher Sr and $^{143}Nd/^{144}Nd$ and lower Rb, Zr and $^{87}Sr/^{86}Sr$. A striking feature of the models is the very consistent values of r (0.1–0.2). Values of r much greater or much less than this range always gave poor fits.

Oxygen isotopes are inconclusive with regard to the occurrence of AFC. Figure 6.28 shows whole-rock and plagioclase data with a variety of superimposed AFC models run using a mafic endmember $\delta^{18}O$ of + 5.5‰ and an assimilant $\delta^{18}O$ of + 13.3‰ (Table 6.6). It is clear that the whole-rock samples have $\delta^{18}O$ much higher than required by AFC, supporting the interpretation that they have been affected by low-temperature hydration. The plagioclase separate $\delta^{18}O$ data are consistent with the AFC model.

Summary

(1) Major element, trace element, and isotopic variations in the Thera pyroclastics and Santorini lavas can be explained by a combination of fractional crystallization, crustal assimilation, and magma mixing. Fractional crystallization generates trends of Fe, Ti, and P enrichment and derivative magmas of mainly tholeiitic character. Mixing of compositionally disparate magmas in large, dominantly silicic chambers generates mingled and homogeneous hybrid magmas with anomalously low Fe, Ti, and P and more calcalkaline affinities.

(2) Correlations of Sr, Nd, and Pb isotopic systems suggest contamination of Santorini magmas by upper Aegean continental crust. Pb isotopes fall outside the fields of the main mantle reservoirs and indicate that Santorini magmas contain crustal radiogenic Pb. At least some contamination took place in high-level magma chambers because there is abundant isotopic disequilibrium between coexisting plagioclase phenocrysts and melt in the predominantly silicic units. In contrast, plagioclase/whole-rock pairs from one dominantly intermediate unit are close to isotopic equilibrium. Correlations of $^{87}Sr/^{86}Sr$ and $^{143}Nd/^{144}Nd$ with SiO_2, 1/Sr and Rb/Sr show that crustal contamination at Santorini took place either by an AFC process or a mixing process.

(3) Santorini has close isotopic similarities to other arcs in continental margin environments, such as the Northern and Southern Volcanic Zones of the Andes and the Lesser Antilles Arc. Crustal interaction has also been invoked as an important process in these systems.

(4) Whole-rock oxygen isotope data vary widely from + 6.0‰ to + 14‰. High values are largely attributable to low temperature hydration of glass, because there is a strong correlation of $\delta^{18}O$ with H_2O content and because plagioclase separates have a much lower and more restricted range of $\delta^{18}O$. Plagioclase separates have $\delta^{18}O$ values (+ 6.0‰ to + 7.5‰) only slightly above mantle values.

(5) Santorini magmas show marked secular variations in trace element and isotope compositions. For a given silica content K, Rb, Ba, Th, Nb, Zr, and Sr decrease crudely with time through the first and second cycles as far as Upper Scoriae 2. A similar decrease in incompatible elements is observed in the post-530 ka lava successions. $^{87}Sr/^{86}Sr$ also decreases (and $^{143}Nd/^{144}Nd$ increases) with time in the lavas and pyroclastics, suggesting that the trace element variations are due to temporal changes in the extent of crustal interaction and perhaps the composition of the assimilant.

(6) Cape Riva and Minoan magmas have anomalously high $^{87}Sr/^{86}Sr$ and low $^{143}Nd/^{144}Nd$ values. They are also subtly enriched

in Ba and Sr compared with other second-cycle magmas. The Minoan ejecta contain crystal-rich pumices and nodules of hydrothermally altered hb-bearing granitoids with high contents of Ba and Sr and high Ba/Rb ratios. These chemically resemble lavas of the Early Centres of Akrotiri and are believed in part to be remobilized plutonic rock from the first phase of Santorini volcanism. The trace element and isotopic signatures of the Minoan, and perhaps Cape Riva, magmas may be due to assimilation of such material.

(7) Modelling calculations support the interpretation that crustal assimilation has been important at Santorini and provide quantitative constraints. Rayleigh fractionation models fail to give consistent results when compared with major element fractionation models and K, Rb and Ba are typically enriched by between 15% and 20% compared to other incompatible trace elements such as Zr and Y. AFC models, using analysed Santorini mafic lavas and crustal rocks as end members, can satisfy all the trace element and isotopic trends simultaneously, provided the assimilant has a composition expected for a rhyolitic partial melt. Models involving simple mixing of end members fail to reproduce the observed trends. The modelled ratio of mass assimilated to mass crystallized is consistently 0.1–0.2.

Chapter 7
Studies of short-lived radionuclides in Santorini volcanics

Disequilibria between the short-lived radioactive nuclides ^{226}Ra, ^{230}Th and ^{238}U in young volcanic rocks can be used both for dating the time of crystallisation of a rock, and as isotopic tracers of the sources of magmas and the chemical evolution of volcanic systems. The principles of these methods have been reviewed extensively elsewhere (Condomines *et al.* 1988; Gill *et al.* 1992; Gill & Condomines 1992; Macdougall 1995). In this chapter, we present new ^{238}U–^{230}Th–^{226}Ra disequilibria data for the Thera pyroclastics and for selected lavas. These data complement the radiogenic isotopic data presented in Chapter 6 on the compositional evolution through time of the pyroclastic ejecta. In particular, we find that the $(^{230}Th/^{232}Th)$ isotopic ratio corrected to the time of eruption varies in a systematic way with time through the second cycle of the Thera pyroclastics and variations in this ratio are correlated with the variations of $^{87}Sr/^{86}Sr$, $^{143}Nd/^{144}Nd$ and Pb isotopes.

Systematics and conventions

The contents of different U- and Th-decay series nuclides as measured by alpha-counting are conventionally expressed as activities (with units of 'disintegrations per minute per gram of rock'), and activities and activity ratios are given in parentheses to distinguish them from weight ratios. ^{238}U–^{230}Th disequilibria in a suite of cogenetic rocks or minerals may be used to date young (< 300 ka old) volcanic deposits by isochron methods (Allègre 1968), as the 75 ka half-life ^{230}Th decays towards equilibrium with ^{238}U. For any system, the ratio $(^{230}Th/^{232}Th)$ at time t is given by:

$$(^{230}Th/^{232}Th)_t = (^{230}Th/^{232}Th)_i \exp(-\lambda^{230}t) + (^{238}U/^{232}Th)_t\{1 - \exp(-\lambda^{230}t)\} \quad (7.1)$$

where λ^{230} is the decay constant of ^{230}Th, and $(^{230}Th/^{232}Th)_i$ is the initial thorium activity ratio of the system. As with any isochron system, the isochron slope depends on the time elapsed since the system closed. The $(^{230}Th/^{232}Th)$ intercept also varies with time, as

$$(^{230}Th/^{232}Th)_t = (^{230}Th/^{232}Th)_i \exp(-\lambda^{230}t). \quad (7.2)$$

A system which has not been disturbed for more than 200 000 years will be at secular equilibrium, with $^{230}Th = ^{238}U$, and an isochron for this system will have a slope of 45°. This line is termed the equiline.

^{226}Ra has a half-life of 1602 years, and is the immediate daughter of ^{230}Th. The Ra–Th pair is potentially a powerful complementary tool for understanding the age significance of radioactive disequilibria in young lavas and pyroclastics. ^{226}Ra–^{230}Th disequilibria in a suite of cogenetic rocks or minerals may be used to date young (<8000 years old) volcanic deposits by isochron methods. In principle the dating method is exactly the same as for ^{230}Th–^{238}U dating. The isochron equation can be written down, with the additional assumption that Ba is a close geochemical analogue of Ra, so that the analyses of ^{226}Ra and ^{230}Th can be normalized:

$$(^{226}Ra)_t/Ba = (^{226}Ra)_i/Ba \exp(-\lambda^{26}Rat) + (^{230}Th)_t/Ba\{1 - \exp(-\lambda^{226}Rat)\} \quad (7.3)$$

where $\lambda^{226}Ra$ is the decay constant of ^{226}Ra, and the subscripts i and t refer to the initial and present conditions respectively. Analyses of mineral separates from Mount St Helens and Erebus (Volpe & Hammond 1991; Reagan *et al.* 1992) confirm that successful dating is possible using this technique, and thus that the assumption that Ba is a close homologue of Ra can be appropriate.

Magmatic tracers

As well as being used as a dating tool, U–Th disequilibria in young igneous rocks can be used as isotopic tracers. $(^{230}Th/^{238}U)$ measures the degree of Th–U fractionation during melting, provided that the source was at secular equilibrium on melting. Modelling (e.g. McKenzie 1985; Williams & Gill 1989; Spiegelman & Elliott 1993) has illustrated the sensitivity of $(^{230}Th/^{238}U)$ to the precise style of melting and the timescales of melt formation, separation and extraction. In principle, in a well-constrained system, precise disequilibria data can severely constrain the melting process. However, the geochemical complexity of subduction-related systems is such that, at present, the conclusions that one may draw about the melting process and the precise components involved are not unique (see Hawkesworth *et al.* 1993; Pearce & Peate 1995).

The variation of the thorium initial activity ratio $(^{230}Th/^{232}Th)_i$ with time is another useful index of the magmatic evolution of volcanoes (Allègre & Condomines 1976; Condomines *et al.* 1982). For the Thera pyroclastics we find significant correlations between the secular behaviour of this index and other chemical and isotopic ratios which place important constraints on the origin of the major pyroclastic units on Santorini.

Results

Samples were analysed for U and Th series nuclides by alpha-counting in laboratories at UKAEA Harwell, Oxford using methods described in Appendix 1. Analyses of whole-rocks, glasses and mineral separates from eleven of the main Thera pyroclastics and four lava successions are presented in Tables 7.1 to 7.4.

The Minoan Tuff: ^{238}U–^{230}Th

Three types of juvenile material were erupted simultaneously during the Minoan eruption.

(i) Homogeneous, rhyodacite pumice is the single most abundant (>99 vol%) juvenile component (Chapter 4).
(ii) Conspicuously crystal-rich pumices, previously interpreted as samples of cumulate mush from the cooling sidewall of the Minoan magma chamber (De Silva 1989; Druitt *et al.* 1989). There is a textural gradation between these crystal-rich samples and the granitoid nodules with <1% glass that are also found in the Minoan deposits.
(iii) Dense grey scoria interpreted as andesite contaminated by cognate gabbro.

Examples of each pumice type, and glass and minerals from a crystal-rich pumice (sample 8763) were analysed for U, Th and Ra isotopes (Table 7.1). There is also one analysis of a glassy block of dacite tfrom the Minoan Tuff that probably represents part of the intracaldera volcano of caldera 3 (Fig. 3.46). Most samples show $(^{228}Th/^{232}Th)$ and $(^{234}U/^{238}U)$ close to equilibrium. The only outlier is sample 5660, a partly altered granitoid nodule from the pumice fall deposit which has $(^{234}U/^{238}U) \approx 0.7$ (Table 7.1).

Analyses of Minoan samples are plotted in Fig. 7.1. In general, whole-rock and glass samples show <10% enrichment of ^{238}U over ^{230}Th. Approximately half of the samples fall within 1σ of $(^{230}Th/^{238}U)$ equilibrium (Fig. 7.1). The $(^{238}U/^{232}Th)$ ratio varies by over

Table 7.1. *U, Th, Ra data for samples from the Minoan Tuff*

Sample no	Notes	Th (ppm)	U (ppm)	(^{226}Ra) (dpm g^{-1})	(^{230}Th/^{232}Th)	(^{238}U/^{232}Th)	(^{230}Th/^{238}U)	(^{226}Ra/^{230}Th)	(^{234}U/^{238}U)	Ba (ppm)	(^{226}Ra) 3.5 ka (dpm g^{-1})
5612	8022b WR: andesite scoria	7.91 ± 0.23	2.41 ± 0.07	2.10 ± 0.10	0.84 ± 0.03	0.92 ± 0.04	0.91 ± 0.04	1.29 ± 0.09	0.95 ± 0.03	405	3.7 ± 0.5
5613	8023 WR: crystal-rich pumice	7.71 ± 0.36	2.51 ± 0.09	1.98 ± 0.13	0.77 ± 0.11	1.00 ± 0.06	0.76 ± 0.12	1.38 ± 0.23	0.97 ± 0.03	349	3.9 ± 0.6
5614	8025b WR: crystal-rich pumice	10.7 ± 0.4	3.43 ± 0.09	2.3 ± 0.3	0.88 ± 0.04	0.97 ± 0.05	0.90 ± 0.05	1.0 ± 0.14	0.96 ± 0.03	583	2.3 ± 1.4
5615	8025a WR: crystal-rich pumice	6.18 ± 0.20	1.67 ± 0.06	1.21 ± 0.10	0.83 ± 0.04	0.83 ± 0.04	1.01 ± 0.05	0.98 ± 0.10	1.00 ± 0.04	334	1.0 ± 0.5
5616	8026 WR: crystal-rich pumice	7.87 ± 0.31	2.49 ± 0.09	1.47 ± 0.03	0.85 ± 0.04	0.96 ± 0.05	0.89 ± 0.05	0.89 ± 0.04	0.96 ± 0.04	448	0.85 ± 0.14
5617	8227 WR: crystal-rich pumice	5.5 ± 0.6	1.36 ± 0.06	0.71 ± 0.03	0.83 ± 0.10	0.75 ± 0.08	1.11 ± 0.13	0.63 ± 0.11	0.99 ± 0.05	288	–
5618	8230 WR: rhyodacite pumice	17.0 ± 0.5	5.16 ± 0.17	3.9 ± 0.2	0.91 ± 0.03	0.92 ± 0.04	0.98 ± 0.05	1.03 ± 0.06	1.02 ± 0.03	554	4.3 ± 0.9
5655	8763 WR: crystal-rich pumice	10.6 ± 0.6	2.71 ± 0.08	2.19 ± 0.15	0.75 ± 0.05	0.77 ± 0.05	0.96 ± 0.07	1.12 ± 0.11	1.06 ± 0.03	571	3.0 ± 0.7
5660	8762 WR: granitoid nodule	9.1 ± 0.4	2.43 ± 0.05	2.25 ± 0.28	0.86 ± 0.04	0.81 ± 0.04	1.06 ± 0.06	1.17 ± 0.16	0.70 ± 0.02	630	3.1 ± 1.3
5642	8763 glass I	17.4 ± 0.7	–	4.3 ± 0.3	0.79 ± 0.03	–	–	1.28 ± 0.10	–	–	7.6 ± 1.4
5643	8763 glass II	18.5 ± 0.7	5.21 ± 0.17	4.0 ± 0.2	0.79 ± 0.03	0.85 ± 0.04	0.93 ± 0.05	1.11 ± 0.07	1.01 ± 0.03	–	5.4 ± 0.9
5640	8763 plagioclase	2.98 ± 0.25	0.95 ± 0.04	0.73 ± 0.11	0.87 ± 0.08	0.97 ± 0.09	0.90 ± 0.08	1.14 ± 0.20	1.00 ± 0.04	–	1.0 ± 0.5
5679	8763 magnetite I	2.24 ± 0.15	0.68 ± 0.03	–	0.93 ± 0.09	0.93 ± 0.08	1.00 ± 0.08	–	0.99 ± 0.06	–	–
5680	8763 magnetite II	1.80 ± 0.16	0.95 ± 0.07	–	1.47 ± 0.10	1.60 ± 0.18	0.95 ± 0.09	–	1.03 ± 0.09	–	–
4765	8699 magnetite	0.95 ± 0.07	0.60 ± 0.03	–	1.57 ± 0.13	1.93 ± 0.15	0.81 ± 0.06	–	1.04 ± 0.06	–	–
5686	MNC 1 WR: glassy dacite	15.6 ± 0.5	4.44 ± 0.20	–	0.91 ± 0.03	0.87 ± 0.05	1.04 ± 0.06	–	1.00 ± 0.04	–	–

All U, Th data determined by alpha counting. Uncertainties are 1σ errors due to counting statistics alone. ^{226}Ra activities determined by radon emanation, and represent the weighted mean of 3 to 5 repeat emanations. Ba–XRF analysis of aliquot from same powdered sample. WR: whole rock.

Table 7.2. *Radiochemical data for the Thera pyroclastics older than 21 ka, and for selected lavas*

Sample no.	Unit	Notes	Th (ppm)	U (ppm)	(^{230}Th/^{232}Th)	(^{238}U/^{232}Th)	(^{230}Th/^{238}U)	(^{234}U/^{238}U)
5628	Cape Riva-A	WR	17.4 ± 0.6	5.80 ± 0.15	0.93 ± 0.03	1.01 ± 0.04	0.92 ± 0.04	0.98 ± 0.04
5630	Cape Riva-A	WR	12.1 ± 0.4	4.20 ± 0.15	0.95 ± 0.03	1.06 ± 0.04	0.89 ± 0.04	0.98 ± 0.03
4743	Upper Scoriae 2	RM 8623 WR	17.0 ± 0.8	5.45 ± 0.21	1.01 ± 0.03	0.97 ± 0.06	1.05 ± 0.06	1.01 ± 0.02
4749	Upper Scoriae 1	RM 023 WR	8.96 ± 0.29	2.87 ± 0.08	1.01 ± 0.03	0.98 ± 0.04	1.03 ± 0.06	1.01 ± 0.03
5685	Middle Pumice	WR	13.6 ± 0.4	4.63 ± 0.08	1.01 ± 0.03	1.05 ± 0.04	0.97 ± 0.04	1.00 ± 0.02
5623	Middle Pumice	WR	14.9 ± 0.5	5.33 ± 0.13	0.99 ± 0.03	1.10 ± 0.05	0.90 ± 0.04	1.04 ± 0.04
4738	Lower Pumice 2-C	8629 WR	16.6 ± 0.5	5.4 ± 0.2	0.95 ± 0.01	0.99 ± 0.05	0.96 ± 0.05	0.99 ± 0.01
4737	Lower Pumice 2-C	8629 glass	16.9 ± 0.4	5.59 ± 0.27	0.97 ± 0.02	1.00 ± 0.05	0.97 ± 0.05	1.00 ± 0.02
4766	Lower Pumice 2-C	8629 mag	1.32 ± 0.07	0.47 ± 0.02	1.49 ± 0.09	1.08 ± 0.07	1.43 ± 0.08	1.06 ± 0.05
4764	Lower Pumice 2-C	8629 ilm	1.20 ± 0.06	0.92 ± 0.03	1.86 ± 0.11	2.34 ± 0.14	0.79 ± 0.04	1.00 ± 0.05
4759	Lower Pumice 2-C	8629 plag	0.84 ± 0.04	0.35 ± 0.01	1.35 ± 0.10	1.27 ± 0.08	1.06 ± 0.06	0.98 ± 0.04
5661	Lower Pumice 2-C	8629 opx	0.58 ± 0.03	0.35 ± 0.02	1.45 ± 0.12	1.82 ± 0.13	0.90 ± 0.05	0.90 ± 0.06
4768	Lower Pumice 2-A	8616 WR	0.46 ± 0.05	0.20 ± 0.01	1.29 ± 0.15	1.31 ± 0.15	0.98 ± 0.10	1.06 ± 0.09
5663	Lower Pumice 2-A	8743A WR	5.20 ± 0.24	1.98 ± 0.05	1.08 ± 0.06	1.15 ± 0.06	0.94 ± 0.05	0.89 ± 0.02
4740	Lower Pumice 1-D	8697 WR	6.66 ± 0.29	2.27 ± 0.12	1.03 ± 0.03	1.04 ± 0.07	0.96 ± 0.07	1.02 ± 0.02
4762	Lower Pumice 1-D	8697 glass	9.9 ± 0.4	-	0.94 ± 0.04	-	-	
4763	Lower Pumice 1-A	8696 glass	16.8 ± 0.4	5.40 ± 0.26	0.96 ± 0.02	0.98 ± 0.05	0.99 ± 0.05	1.01 ± 0.03
4739	Lower Pumice 1-A	8696 WR	19.0 ± 0.6	6.66 ± 0.29	0.98 ± 0.02	1.06 ± 0.06	0.92 ± 0.05	0.98 ± 0.02
5683	Cape Therma 3-A	WR	15.2 ± 0.5	4.76 ± 0.17	0.93 ± 0.03	0.95 ± 0.05	0.98 ± 0.05	1.00 ± 0.03
4776	Cape Therma 3-A	8611 WR			0.95 ± 0.03	-		
5682	Cape Therma 2	8821 WR	18.3 ± 0.6	5.86 ± 0.19	0.93 ± 0.03	0.97 ± 0.05	0.96 ± 0.05	1.03 ± 0.03
5684	Cape Therma 1-B	8812 WR	13.3 ± 0.7	3.85 ± 0.17	0.87 ± 0.04	0.89 ± 0.063	0.98 ± 0.07	1.00 ± 0.04
5681	Minor sequence M1	8818 WR	13.6 ± 0.4	3.48 ± 0.09	0.83 ± 0.02	0.78 ± 0.03	1.07 ± 0.05	1.02 ± 0.02
5687	Minor sequence M1	8831 WR	16.8 ± 0.5	4.53 ± 0.22	0.92 ± 0.03	0.82 ± 0.05	1.12 ± 0.07	1.08 ± 0.05
4726	Therasia rhyodacite	WR			0.93 ± 0.02			
4736	Skaros andesite	8661 groundmass	16.4 ± 0.4	5.16 ± 0.20	0.95 ± 0.01	0.96 ± 0.05	0.99 ± 0.05	1.00 ± 0.01
4728	Skaros andesite	8661 WR	8.13 ± 0.34		0.97 ± 0.03	-		
4754	Cape Alonaki rhyodacite	8618 WR	19.9 ± 0.8	6.73 ± 0.25	0.99 ± 0.02	1.03 ± 0.06	0.96 ± 0.05	1.00 ± 0.03

All isotopic data determined by alpha counting. Uncertainties are 1σ errors due to counting statistics alone. Key: WR, whole rock; ilm, ilmenite; mag, magnetite; plag, plagioclase; opx, orthopyroxene. The eruption units denoted by letters are listed in Table 3.4.

Table 7.3. *Summary $(^{230}Th/^{232}Th)_i$ data for the Thera pyroclastics and the Kameni lavas*

Eruption	Age (ka BP)*	$(^{230}Th/^{232}Th)_i$
Kameni, AD 1940	0	0.96 ± 0.02
Kameni, AD 1925	0	0.95 ± 0.03
Kameni, AD 1570	0.4	0.95 ± 0.03
Kameni, AD 726	1.2	0.93 ± 0.04
Minoan	3.5	0.83 ± 0.05
Cape Riva	21	0.92 ± 0.04
Upper Scoriae 2	55	1.04 ± 0.05
Upper Scoriae 1	(80)	1.03 ± 0.05
Middle Pumice	(100)	0.86 ± 0.10
Lower Pumice 2	(180)	0.87 ± 0.17
Lower Pumice 1	203	0.9 ± 0.3
Cape Therma 3	(220)	0.8 ± 0.3
Cape Therma 2	(230)	0.6 ± 0.4
Minor sequence M1	(250)	1.3 ± 0.3

* Brackets indicate an assumed age.

25%, and is accompanied by a 10% variation of $(^{230}Th/^{232}Th)_i$. Both variations are outside analytical error, with a 4σ difference between $(^{230}Th/^{232}Th)_i$ for the glasses (solid triangle, Fig. 7.1) and the rhyodacite whole-rock, which is itself at ^{230}Th–^{238}U equilibrium. A 3.5 ka isochron, representing the approximate eruption age, is shown for reference. The isotopic variability observed cannot relate to ingrowth of ^{230}Th since eruption.

Figure 7.2 shows the covariation of Th and U concentrations, and $(^{230}Th/^{232}Th)$ with SiO_2 for the whole-rock samples. U and Th increase strongly with increasing SiO_2, reflecting their incompatible behaviour in these samples. The [Th/U] weight ratio varies between about 3 and 4, but does not depend systematically on the Th content. There is no significant pattern to the $(^{230}Th/^{232}Th)$ variation with SiO_2.

Analyses of the whole-rock, glass and mineral separates from crystal-rich pumice 8763 are shown in Fig. 7.3. The glass, whole-rock and plagioclase analyses show a small range of $(^{238}U/^{232}Th)$, from 0.77 to 0.97, and fall along a steep array. This has an apparent crystallization age of at least 200 ka, but within the errors could be interpreted as having infinite age. The magnetite separates have widely differing $(^{238}U/^{232}Th)$, but both are close to ^{230}Th–^{238}U equilibrium. This disequilibrium pattern, with mineral analyses trending sub-parallel to the equiline, is similar to that reported for impure mineral concentrates from the 1980 dacites erupted from Mount St Helens (Bennett *et al.* 1982). The data suggest that some of the crystal-rich pumices may contain mixtures of crystals that are significantly older than the actual eruption age, and these same pumices may also have Th-isotopic compositions which are significantly different from the host magma.

Table 7.4. *U–Th disequilibrium data from selected Kameni island lavas and mineral separates*

Sample no.	Notes	Th (ppm)	U (ppm)	$(^{230}Th/^{232}Th)$	$(^{238}U/^{232}Th)$	$(^{230}Th/^{238}U)$	$(^{234}U/^{238}U)$
4701	AD 1940 whole rock	10.3 ± 0.5	3.22 ± 0.14	1.00 ± 0.02	1.04 ± 0.06	0.96 ± 0.06	0.98 ± 0.02
4703	AD 1940 groundmass	12.4 ± 0.4	4.24 ± 0.15	0.96 ± 0.02	1.05 ± 0.05	0.92 ± 0.05	1.03 ± 0.03
4702	AD 1940 plagioclase	0.47 ± 0.02	–	1.15 ± 0.07	–	–	–
4704	AD 1940 magnetite	1.07 ± 0.05	0.48 ± 0.02	0.96 ± 0.06	1.38 ± 0.09	0.70 ± 0.04	1.06 ± 0.05
4705	AD 1940 clinopyroxene	0.64 ± 0.04	0.30 ± 0.03	1.84 ± 0.14	1.42 ± 0.17	1.30 ± 0.15	1.13 ± 0.14
5645	Inclusion, magnetite	0.54 ± 0.10	0.42 ± 0.02	1.2 ± 0.3	2.4 ± 0.5	0.5 ± 0.1	0.97 ± 0.07
8606	AD 1925 whole rock	–	–	0.96 ± 0.03	–	–	–
8604	AD 1570 whole rock	–	–	0.95 ± 0.03	–	–	–
8607	AD 726 whole rock	–	–	0.93 ± 0.04	–	–	–

All isotopic data determined by alpha counting. Uncertainties are 1σ errors due to counting statistics alone.

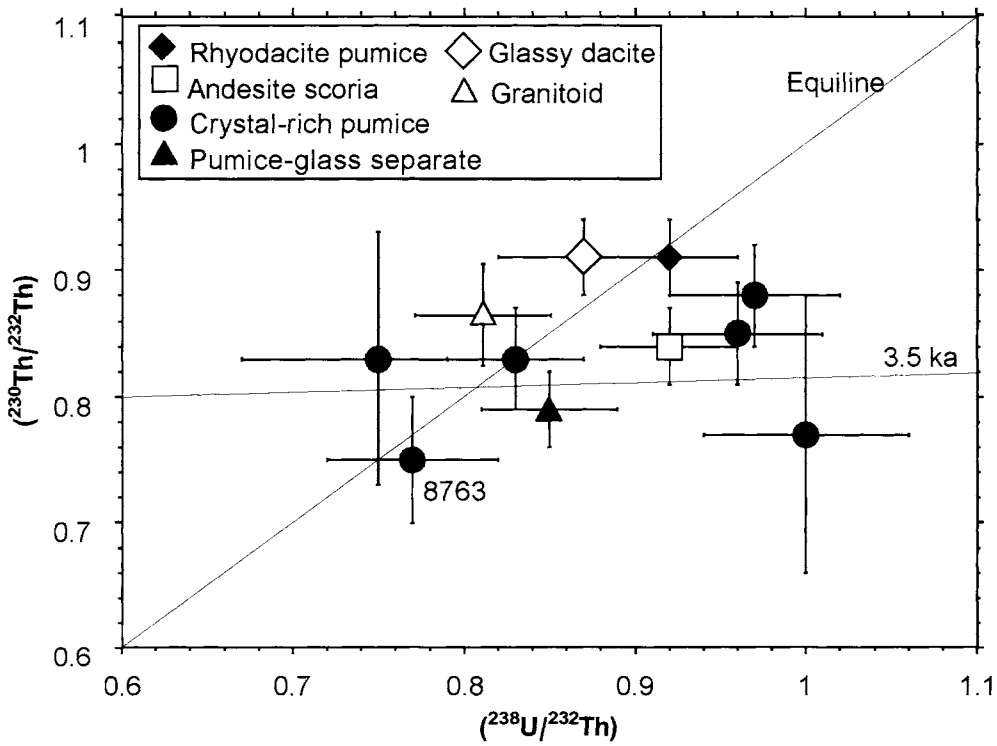

Fig. 7.1. Whole rock and glass analyses for the Minoan samples plotted on a $(^{230}Th/^{232}Th)$–$(^{238}U/^{232}Th)$ isochron diagram. A reference line with a slope equal to that for a 3.5 ka isochron is also plotted. The scatter in the data is outside analytical error and does not reflect ^{230}Th ingrowth since eruption. The crystal-rich pumice from which mineral separates were obtained (8763) is labelled.

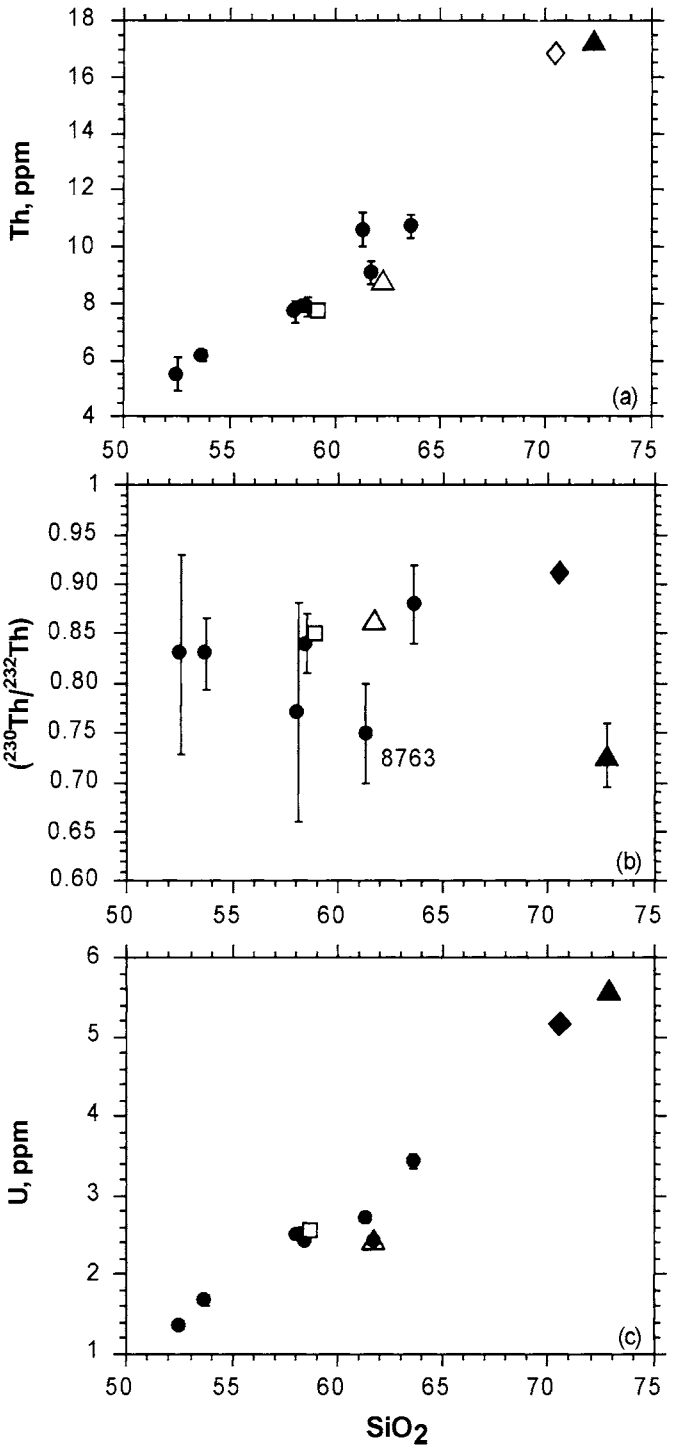

Fig. 7.2. Variation of (**a**) Th concentrations, (**b**) (^{230}Th/^{232}Th) activity ratio, and (**c**) U concentrations (in ppm) with SiO_2 (wt%) for Minoan whole rock samples. Th and U are strongly positively correlated with SiO_2, due to their incompatible behaviour during crystallisation. Symbols as in Fig. 7.1.

The Minoan Tuff: ^{230}Th–^{226}Ra disequilibria

The Minoan is the only pyroclastic deposit which is sufficiently young that it might exhibit ^{226}Ra–^{230}Th disequilibria. ^{226}Ra analyses, measured by radon emanation, are given in Table 7.1. The calculated radium activity at the time of eruption (3.5 ka) and the Ba contents of appropriate samples are also given.

The ^{226}Ra, ^{230}Th, and Ba data are combined on a (^{226}Ra/Ba)–(^{230}Th/Ba) isochron diagram in Fig. 7.4. This plot should behave in the same fashion as the (^{230}Th/^{232}Th)–(^{238}U/^{232}Th) isochron plot, as long as Ra and Ba behave coherently. At zero age, samples with constant (^{226}Ra/Ba), but a range of (^{230}Th/Ba) ratios will fall on a horizontal array. Over 8000 years this array will decay towards the equiline. Whole-rock data reveal a range of (^{230}Th/Ba) ratios for these samples. Four crystal-rich pumices and the granitoid nodule cluster close to equilibrium, with (^{230}Th/Ba) ≈ 3–4×10^{-3} dpm μg^{-1}. The rhyodacite pumice falls close to the equiline at (^{230}Th/Ba) $\approx 7 \times 10^{-3}$ dpm μg^{-1}. If all of these five samples experienced ^{230}Th–^{226}Ra fractionation at the same time, without ^{226}Ra–Ba fractionation, this fractionation occurred over more than 5400 years before present. This model is not favoured because the crystal-rich pumices form a group that is geochemically and petrologically unrelated to the main rhyodacite pumice (Chapters 4 and 6). Three further samples are plotted on Fig. 7.4. One crystal-rich pumice sample falls well below the (^{226}Ra/Ba)–(^{230}Th/Ba) equiline. This pumice with a ^{226}Ra/Ba of 0.002 must have experienced some ^{226}Ra loss after eruption because the ratio ^{226}Ra/Ba would be 0.003 by ingrowth even if the sample had no initial ^{226}Ra. Explanations for the ^{226}Ra loss include leakage in the laboratory, or weathering. The cauliform andesitic scoria shows clear (^{226}Ra/^{230}Th) disequilibrium at the 2σ level. This had (^{226}Ra/Ba) at 3.5 ka of $c.\ 10 \times 10^{-3}$ dpm μg^{-1}, and (^{230}Th/Ba) of $c.\ 4 \times 10^{-3}$ dpm μg^{-1}. This sample cannot be in equilibrium with the rhyodacite pumice, since this would require the last mutual fractionation event to have occurred between 700 and 2000 years after the eruption.

^{238}U–^{230}Th–^{226}Ra disequilibria data, decay-corrected to 3.5 ka, are presented in Fig. 7.5. Most samples fall in the quadrant with (^{226}Ra/^{230}Th) and (^{238}U/^{230}Th) both greater than 1, although most samples are also within 2σ of both ^{226}Ra–^{230}Th and ^{230}Th–^{238}U equilibrium. The plagioclase separate from crystal-rich sample 8763 is within 1σ of ^{226}Ra–^{230}Th equilibrium, and has ^{226}Ra, ^{230}Th and ^{238}U activity ratios close to the whole-rock and glass for the same sample. Given that plagioclase significantly fractionates Ra from U and Th during crystallisation (e.g. Volpe & Hammond 1991) these data suggest that the mineral age of this separate could be >5 ka.

One method of resolving the nature of the original ^{226}Ra–^{230}Th–^{238}U pattern is to use the stable chemical homologues of Ra. If ^{226}Ra was followed closely by Ba during mixing or fractionation, then the signature of this event should still be preserved. Figure 7.6 shows that the (Ba/^{230}Th) ratios of crystal-rich pumices varies little with increasing (^{238}U/^{230}Th). Assuming that Ra and Ba behaved coherently during magmagenesis then the difference between the present-day (^{226}Ra/^{230}Th) and (Ba/^{230}Th) patterns in Figs 7.5 and 7.6 must reflect the variable periods of time elapsed between fractionation and eruption for different samples. If ^{226}Ra–^{230}Th fractionation is assumed to have occurred at 3.5 ka for the most highly disequilibrated sample, then the initial (^{226}Ra/^{230}Th) ratio of the magma from which the crystal-rich pumices formed can be calculated to have been 2.3–2.4. This implies that, if the crystal-rich pumices crystallized from the same melt, the remainder of the crystal-rich samples last experienced a ^{226}Ra–^{230}Th fractionation event some from >3000 to >6000 years before eruption.

Discussion

The Minoan eruption discharged about 30 km^3 of rhyodacitic magma, which was close to ^{226}Ra–^{230}Th–^{238}U equilibrium. It also discharged a considerably smaller volume of chemically heterogeneous high-Ba crystal-rich pumices, related hydrothermally altered granitoid nodules and quenched andesitic scoriae. The available data suggest that these latter samples were isotopically heterogeneous on eruption, exhibiting varying degrees of ^{226}Ra and ^{238}U enrichment and variable (^{230}Th/^{232}Th) activity ratios. The (^{230}Th/^{232}Th) and Th concentration data are consistent with the crystallization of these materials significantly prior to eruption. The data for the mineral separates from one crystal-rich pumice are consistent with an origin of the pumices by remelting of a source older than 200 ka.

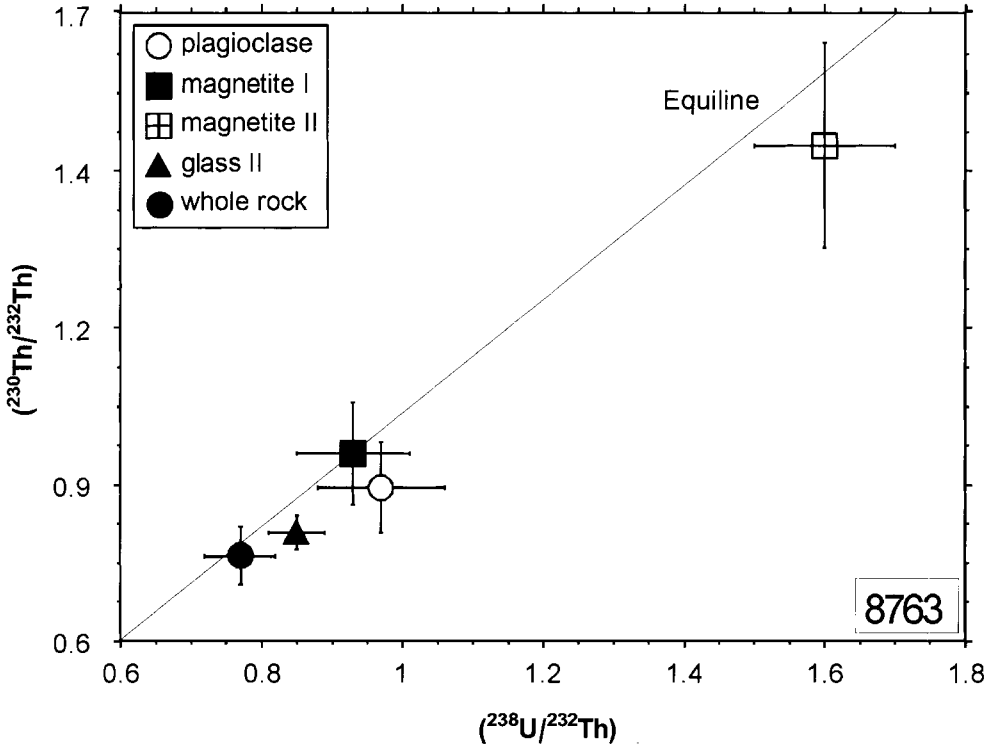

Fig. 7.3. (^{230}Th/^{232}Th)–(^{238}U/^{232}Th) isochron diagram for the crystal-rich sample 8763 and mineral separates. The samples fall along a trend with a slope close to that of the equiline and all analyses are within 2σ of ^{230}Th–^{238}U equilibrium, suggesting that the crystallization age of the sample is >200 ka. See Fig. 7.1 for the whole rock isotopic composition of sample 8763.

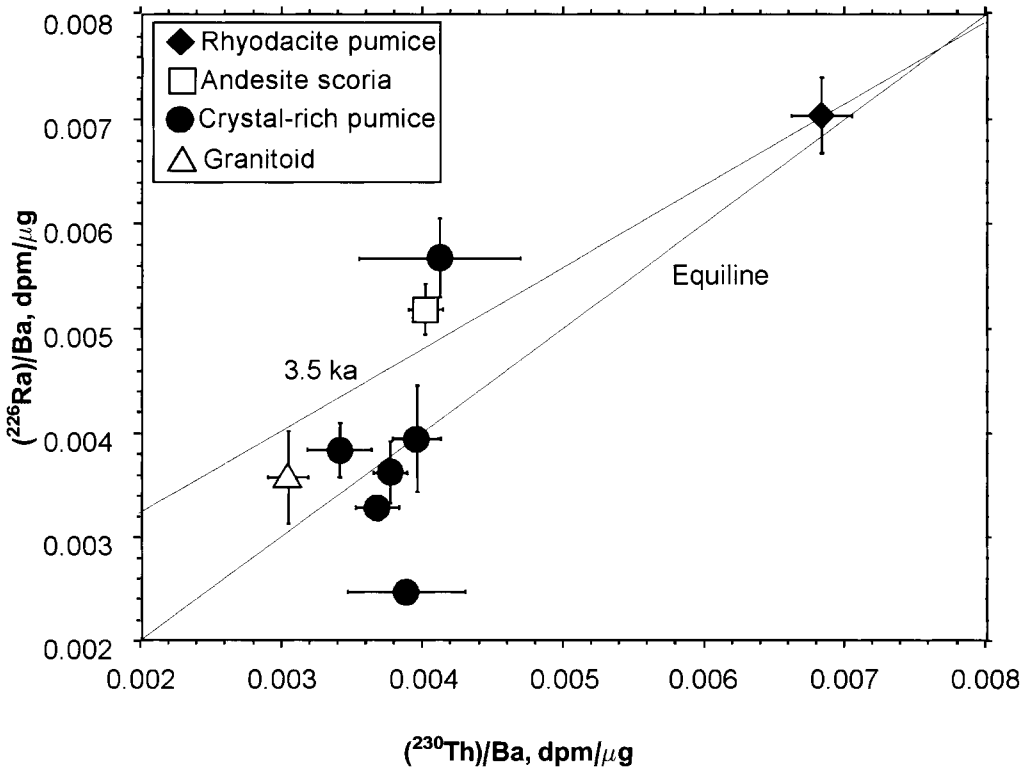

Fig. 7.4. (^{226}Ra)/Ba–(^{230}Th)/Ba isochron plot for the Minoan samples. A 3.5 ka isochron is shown for reference. The (^{226}Ra)–(^{230}Th) fractionation between the crystal-rich pumices and the rhyodacite whole rock was not caused by crystallization coincident with the time of eruption. The sample of crystal-rich pumice that falls below the equiline has experienced substantial ^{226}Ra loss since eruption.

Three explanations are considered to interpret the observed range of disequilibria in the Minoan samples. First, the crystals in at least some of the crystal-rich pumices are old, and remained part of a closed chemical system until just before eruption, when they became intermixed with rhyodacite. Geochemical data presented in Chapter 6 indicated that the compositions of the crystal-rich pumices are consistent with an origin by the remelting of high-level intrusive rocks associated with the Early Centres of the Akrotiri Peninsula. Second, the phenocrysts crystallized recently from a Th-isotopically heterogeneous magma, or crystallized from several magma batches of different isotopic composition. The partial mixing (< 30–50%) of rhyodacite magma close to ^{226}Ra–^{230}Th–^{238}U equilibrium into crystal-rich pumices with variable (^{238}U/^{232}Th) can explain some of the U–Th isotopic variability, and is allowed by the scatter in observed (^{226}Ra, Ba)/(^{230}Th) ratios. The crystal-rich pumices may have crystallized piecemeal from different melt batches over a period of >2500 to >200 000 years prior to eruption. This model is hard to rationalize with the geochemical coherence of the crystal-rich pumices documented in Chapter 6. Third, the rocks have been variably hydrothermally altered by an oxidizing fluid which has mobilized U. U is much more mobile than Th under conditions of hydrothermal alteration. Evidence for U redistribution and associated U–Th disequilibrium has been observed in other young volcanic systems (Sturchio *et al.* 1987). Thus some rocks may be U-enriched, and others depleted. This model is supported by anomalous ^{234}U/^{238}U in the co-genetic

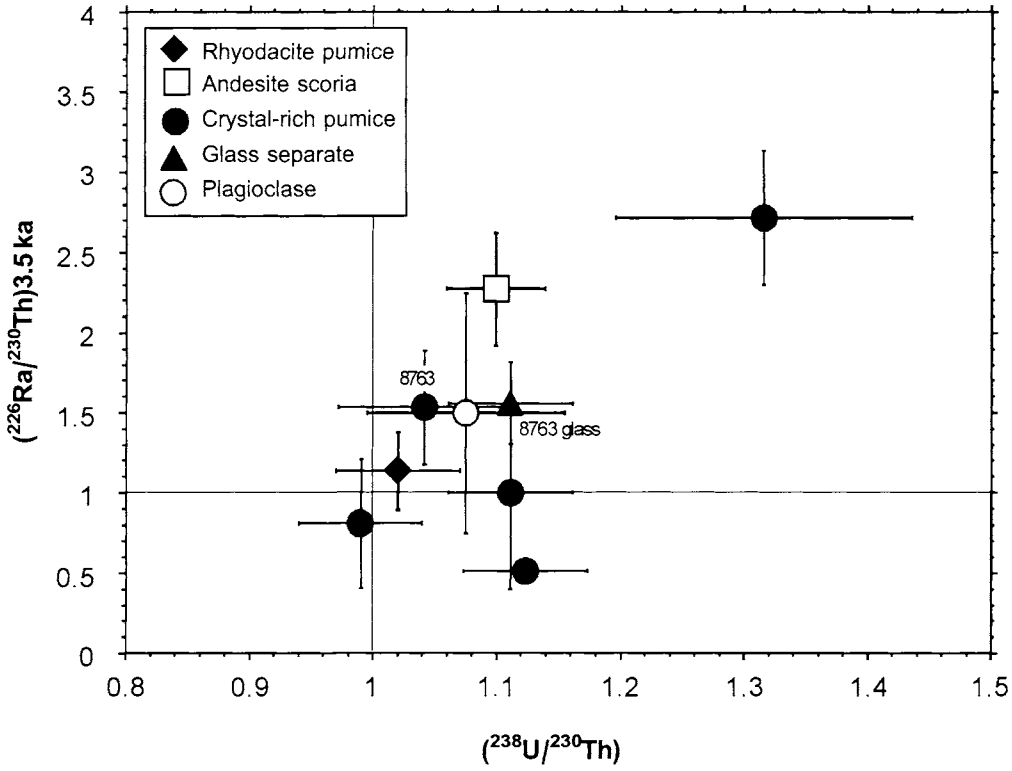

Fig. 7.5. (^{226}Ra/^{230}Th)–(^{238}U/^{230}Th) plot for the Minoan samples, corrected to the 3.5 ka eruption age. Only one sample falls more than 2σ away from (^{226}Ra)–(^{230}Th) equilibrium. The majority of samples had both slight (^{238}U) and (^{226}Ra) excesses (over ^{230}Th) on eruption.

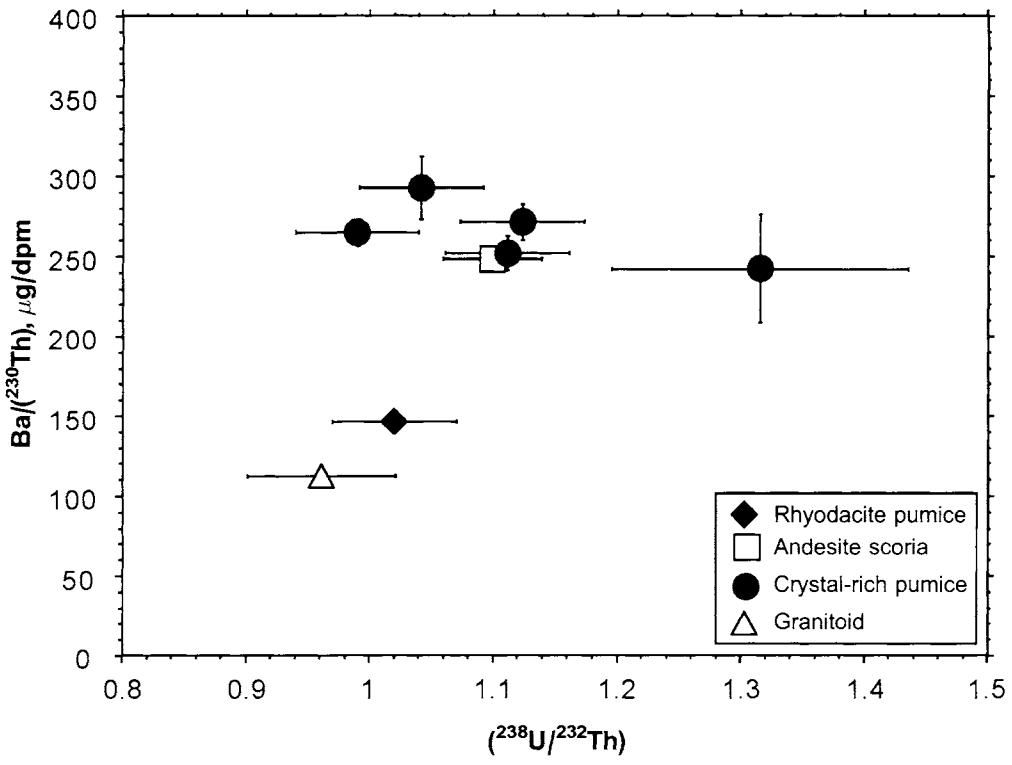

Fig. 7.6. Ba/(^{230}Th)–(^{238}U/^{230}Th) plot for the Minoan samples. The crystal-rich pumices and plutonic granitoid and the andesitic scoria show a weak negative correlation between Ba and ^{238}U. Since Ra should behave as a close analogue of Ba, the difference between the patterns observed in Figs 7.5 and 7.6 may reflect the time elapsed between Ra (or Ba) and ^{238}U fractionation.

granitoid sample, which implies some kind of interaction with a fluid phase, by the variation in Th/U ratio and by the broad spread of ^{238}U/^{232}Th to values either side of the equiline. The horizontal spread of data indicates a young age for the U mobility. It is also possible that disequilibria of ^{226}Ra reflect its greater mobility with respect to Th. Both Ra and Ba can be redistributed during hydrothermal alteration and concentrated in zeolite minerals (Sturchio *et al.* 1989). If this explanation is correct then the Minoan data require Ra and Ba to be transported independently.

On the basis of these arguments, and the data presented in Chapter 6 we propose that the crystal-rich pumices and granitoids represent shallow level plutonic and hypabyssal rocks related to the Early Centres of the Akrotiri Peninsula (650–550 ka) and that the rocks were derived from the hydrothermal system that existed prior to the Minoan eruption.

The Lower Pumice 2 deposit

The two rhyodacitic Lower Pumice eruptions marked the culmination of the first explosive cycle. Our best estimates for their ages are 200 ka (Lower Pumice 1) and about 180 ka (Lower Pumice 2) (Chapter 3).

Radiochemical analyses of mineral separates from a rhyodacite pumice from Lower Pumice 2 are given in Table 7.2 and plotted in Fig. 7.7. Five of the eight analyses (two whole-rock, glass, ilmenite,

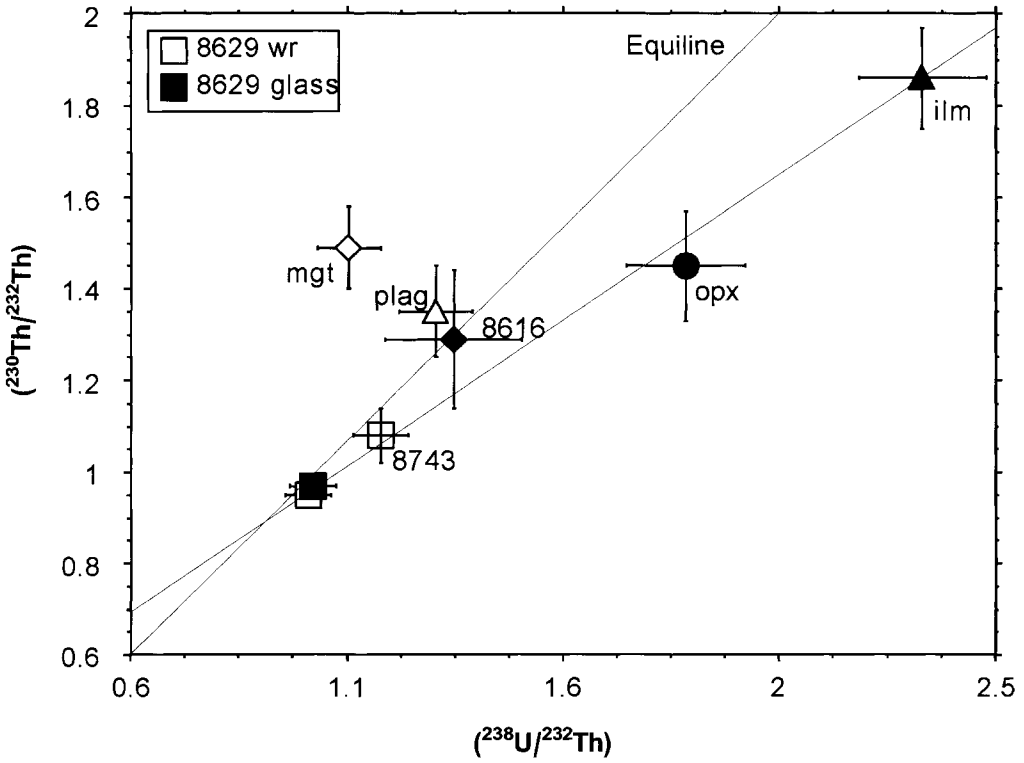

Fig. 7.7. ($^{230}Th/^{232}Th$)–($^{238}U/^{232}Th$) isochron diagram for Lower Pumice 2. Key: plag, plagioclase; mgt, magnetite; opx, orthopyroxene; ilm, ilmenite. Numbered points refer to sample numbers in Table 7.2. A five point isochron (shown) gives an apparent age of $107 + 17$ ka. The presence of samples that fall significantly away from this 'isochron' makes the age interpretation uncertain.

orthopyroxene) fall along an isochron with an apparent age of 107 ± 17 ka. However, since since several separates show evidence for isotopic heterogeneity, and there are large errors associated with the (U/Th) ratios, in particular of the orthopyroxene and ilmenite separates determined by alpha counting, the age significance of this 'isochron' remains unclear. Laboratory fractionation can be ruled out in the case of the magnetite separate that shows 40% excess ^{230}Th over ^{238}U since both ($^{228}Th/^{232}Th$) and ($^{234}U/^{238}U$) ≈ 1. Microprobe analyses of the Mg and Mn contents of coexisting magnetite and ilmenite grains from this same sample show that these oxides are in chemical equilibrium (Bacon & Hirschmann 1988). A plagioclase separate, which falls close to ^{230}Th–^{238}U equilibrium, is isotopically similar to mafic scoria 8616 from Lower Pumice 2. Sample 8616 is composed predominantly of magnesian olivine ($Fo_{73.4 \pm 0.2}$) and calcic plagioclase ($An_{90 \pm 2}$) and is believed to be andesitic magma heavily contaminated by gabbroic crystal mush (Chapter 4).

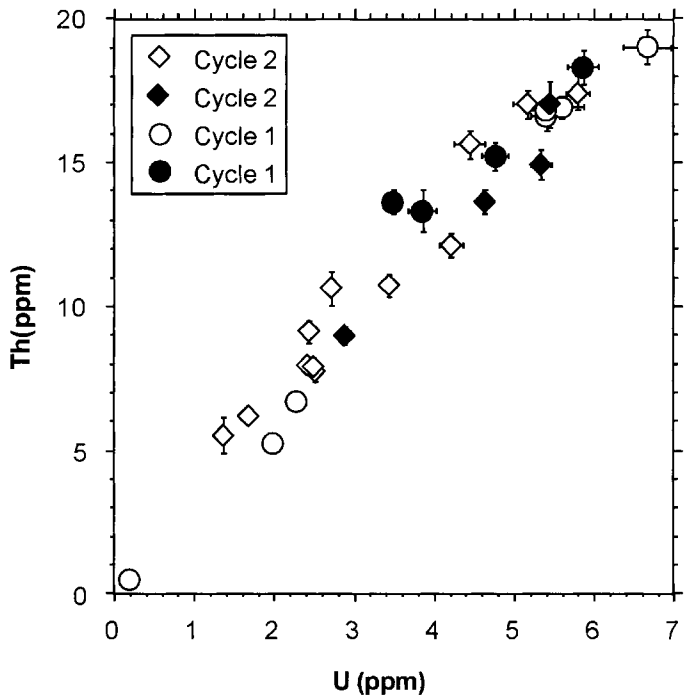

Fig. 7.8. U–Th covariation plot for the Thera pyroclastics. The data define an array with [Th/U] ≈ 3.1. Open symbols are dominantly silicic deposits and filled symbols are dominantly intermediate deposits. Cycle 1 Intermediate magmas from the first explosive cycle have higher Th concentrations at a given U content than second-cycle intermediate magmas.

U–Th disequilibria data for other Thera pyroclastics

^{238}U–^{230}Th disequilibria data for the remaining Thera Pyroclastic deposits are given in Table 7.2. Age-corrected ($^{230}Th/^{232}Th$) ratios are summarised in Table 7.3, and data are plotted on Figs 7.8 and 7.9. The Thera pyroclastics define a broadly coherent series on a U–Th covariation plot (Fig. 7.8), defining a trend with [Th/U] $\approx$ 3.1. The spread in Th concentrations at any given U content is real, and reflects the chemical variability that characterizes the differences between deposits of the two explosive cycles (Chapter 6). In view of the evidence of crustal assimilation during fractionation (Chapter 6), and involvement of some hydrothermally altered roof rocks, the spread in Th/U might also be related to assimilation. In Fig. 7.8 there is a broad tendency for Th/U to decrease in more evolved rocks that is consistent with increasing proportions of crustal assimilant relatively enriched in U during magmatic evolution.

Disequilibria in Santorini samples are similar to other island arcs founded on continental crust, which are characteristically close to ^{238}U–^{230}Th equilibrium (Gill & Williams 1990; Condomines & Sigmarsson 1993). Slightly more samples exhibit a ^{238}U excess than those that do not. Only three of the eleven deposits studied in this chapter show a ^{230}Th excess (Fig. 7.9a, b); these samples are from the more tholeiitic and dominantly intermediate deposits.

Most data today (Fig. 7.9a) exhibit ($^{230}Th/^{238}U$) ≈ 1.1–0.9. This ratio should be corrected for ^{230}Th decay or ingrowth since eruption. This correction leads to considerable uncertainties in the initial ($^{230}Th/^{232}Th$) ratios for all samples older than about 150 ka due to the uncertainties in the ($^{238}U/^{232}Th$) ratios determined by alpha counting (*c.* 5%; Table 7.3; Fig. 7.9b). Many Santorini magmas may have had ($^{230}Th/^{238}U$) between 1.1 and 0.8 on eruption, with only a few exceptions.

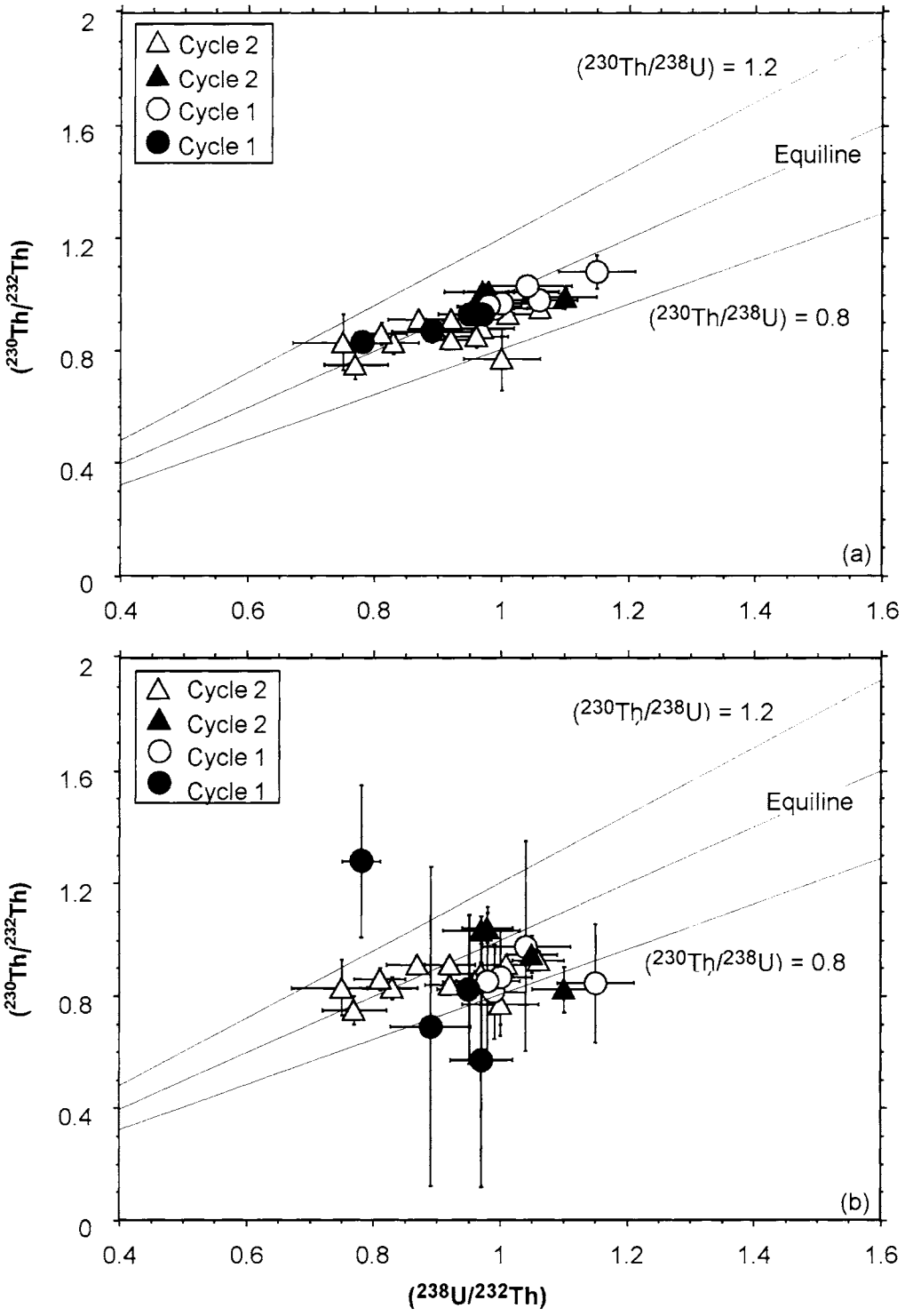

Fig. 7.9. (^{230}Th ^{232}Th)–(^{238}U ^{232}Th) plot of whole rock U and Th decay-series data from the Thera pyroclastics. Filled symbols are dominantly intermediate deposits and open symbols are dominantly silicic deposits. Diagrams are contoured in terms of (^{230}Th ^{238}U). The equiline represents (^{230}Th ^{238}U) = 1.0. (**a**) Data without an age correction: (**b**) age corrected data.

U–Th disequilibria data from the lava shields

Historical lavas from the Kameni Islands

The Kameni islands have erupted chemically homogeneous dacite magma intermittently since at least 197 BC. Lava was last erupted in 1950. The dacite lavas from the Kameni islands contain abundant phenocrysts, glomerocrysts and xenoliths. Plagioclase feldspar is the dominant phase, forming both euhedral, unzoned phenocrysts, and coarser, complexly zoned xenocrystal fragments (e.g. Nicholls 1971*a*; Huijsmans 1985). Isotopic analyses of mineral separates from the 1940 lava, and (^{230}Th/^{232}Th) activity ratios for the AD 1925, AD 1570 and AD 726 lavas are presented in Table 7.4.

The 1940 lava, groundmass and magnetite all have similar $(^{230}\mathrm{Th}/^{232}\mathrm{Th})_i$, confirming the existence of a degree of Th-isotopic homogeneity on crystallization. The 1940 lava is within 1σ of isotopic equilibrium, with $(^{230}\mathrm{Th}/^{238}\mathrm{U}) \approx 0.96$. There is slight U–Th fractionation between the whole-rock and groundmass. While the plagioclase $(^{230}\mathrm{Th}/^{232}\mathrm{Th})_i$ is only marginally outside the whole-rock $(^{230}\mathrm{Th}/^{232}\mathrm{Th})_i$, the clinopyroxene ^{230}Th is unsupported by ^{238}U, so this enrichment must be recent. The origin of this ^{230}Th enrichment is not yet clear, but one possibility is that it reflects the incorporation of altered minerals (e.g. altered oxide grains or amphiboles) within the separated sample or magmatic contamination by altered material. Altered plutonic blocks in other deposits on Santorini have been found to have unsupported (^{230}Th/^{232}Th) as high as 0.9 (Pyle 1990*b*). Xenolithic blocks of many kinds are found

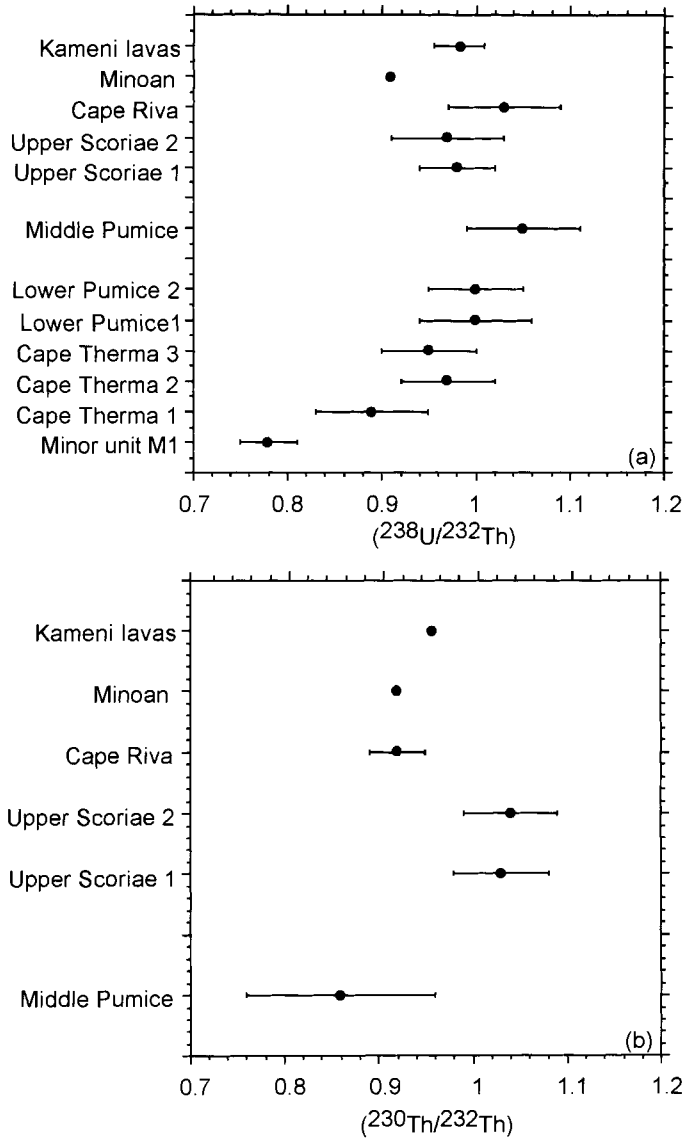

Fig. 7.10. (**a**) Variation of ($^{238}U/^{232}Th$) with stratigraphic height for the Thera pyroclastics. (**b**) Variation of ($^{230}Th/^{232}Th$), corrected to the age of eruption, with stratigraphic height for the second cycle of the Thera pyroclastics.

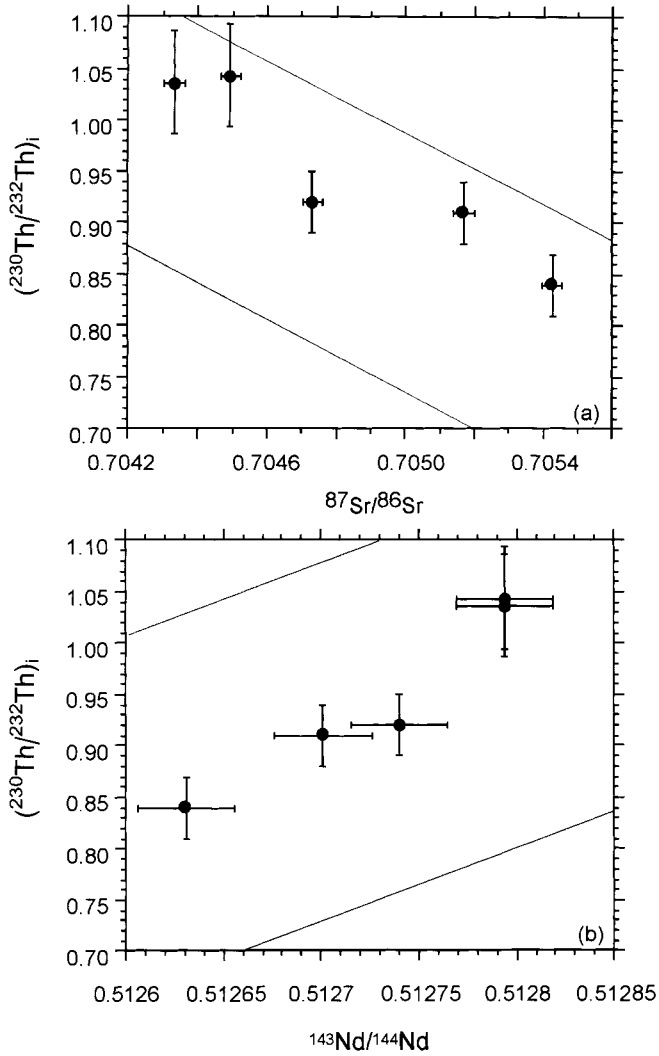

Fig. 7.11. (**a**) $(^{230}Th/^{232}Th)_i$–$^{87}Sr/^{86}Sr$ data, for samples of the second cycle of the Thera pyroclastics. The data show a significant negative correlation, which lies subparallel to the global Th–Sr isotopic array (shown as two solid lines) defined by MORB and OIB magmas first recognized by Condomines *et al.* (1981). This array is shown for reference (from Gill *et al.* 1992; Gill & Condomines 1992 and refs therein). The array is bounded by $Th_i = c - 170(^{87}Sr/^{86}Sr)$ where $c = 120.59$ (lower bound) and 120.84 (upper bound). (**b**) $(^{230}Th/^{232}Th)_i$–$^{143}Nd/^{144}Nd$ data for the second cycle of the Thera pyroclastics. The data show a significant positive correlation; again the global Th–Nd array as defined by MORB and OIB compositions is shown for reference (from Gill *et al.* 1992, and references therein). The array is defined by $Th_i = 700(^{143}Nd/^{144}Nd) - d$, where $d = 358.16$ (lower bound) and 357.81 (upper bound).

within the Kameni lavas (Nicholls 1971*a*; Huijsmans 1985), indicating that the magmas has interacted with older, altered crystalline material.

The $(^{230}Th/^{232}Th)_i$ data for the Kameni lavas (Table 7.4) show no significant change over the past 1200 years. This lack of variability matches the chemical and petrological homogeneity of these same lavas (Chapters 4 and 6), which suggests that the Kameni magma chamber has been thermally and chemical buffered over this same time period (Nicholls 1971; Huijsmans 1985; Barton & Huijsmans 1986).

Peristeria Volcano

The dating of one of the youngest Peristeria 3 lavas on Micros Profitis Ilias was reported elsewhere (Pyle *et al.* 1988). Radiochemical data appeared to define two subparallel isochrons of 79^{+14}_{-12} ka and 93^{+29}_{-22} ka. The two arrays were interpreted as representing the products of a dacitic melt (<20 vol% crystals) and a basaltic crystal mush (>50 vol% crystals), which mixed prior to eruption to generate the hybrid andesite. This interpretation has been corroborated by laser interferometry studies of zoning of plagioclase phenocrysts from Thera (Stamatelopoulou-Seymour *et al.* 1990). This age is significantly at odds with the K–Ar and $^{40}Ar/^{39}Ar$ ages reported in Chapter 3 since the same lava gives 464 ± 8 ka and 478 ± 3 ka. Tarney *et al.* (1998) reported K–Ar ages of 511 and 517 ka on Micros Profitis Ilias lavas. The reason for the discrepancy between the K–Ar and U–Th methods is not clear. The K–Ar and $^{40}Ar/^{39}Ar$ dates are all in accordance with the field stratigraphy (Chapter 3), which suggests that the discrepancy lies with the interpretation of the U–Th disequilibrium data. The disequilibrium data were determined by alpha counting; this technique requires considerable amounts (*c.* 0.5 g) of sample for the analysis of most mineral separates, and has relatively limited precision (± 3–5% relative). As the analyses of Minoan and Lower Pumice materials has shown in this chapter, subsequent alpha-counting work on other mineral separates has also not yielded simple isochrons. Resolution of this problem awaits mass spectrometric analysis of considerably smaller samples (see Chen *et al.* 1992; McDermott *et al.* 1993). This has been shown to significantly improve the resolution of age determinations in other volcanic systems (e.g. Volpe & Hammond 1991).

Secular evolution of U and Th isotopic indices for the Thera pyroclastics

Figure 7.10 shows the activity ratios ($^{238}U/^{232}Th$) and ($^{230}Th/^{232}Th$), corrected to the time of eruption, plotted against stratigraphic height for the Thera pyroclastics. ($^{238}U/^{232}Th$) varies systematically with eruption age (Fig. 7.10a). ($^{238}U/^{232}Th$) increases during the first cycle, and decreases with the chemically heterogeneous Minoan eruption. During the second cycle of the Thera pyroclastics $(^{230}Th/^{232}Th)_i$ (Fig. 7.10b) appears to change broadly sympathetically with the character of the deposit (Chapter 6). Two of the dominantly intermediate magmas erupted during cycle two have $(^{230}Th/^{238}U) > 1$.

The secular trends in the $(^{230}Th/^{232}Th)_i$ ratios of the Thera pyroclastics are similar to those observed for the radiogenic isotopic ratios (Chapter 6). In particular, increasing ($^{230}Th/^{232}Th$) correlates with increasing Nd isotopic ratios, and decreasing Sr-isotopic ratios. Figure 7.11 shows the variation of $(^{230}Th/^{232}Th)_i$ with $^{87}Sr/^{86}Sr$ and $^{143}Nd/^{144}Nd$ for second-cycle magmas. The negative correlation of $(^{230}Th/^{232}Th)_i$ with $^{87}Sr/^{86}Sr$, and the positive correlation with $^{143}Nd/^{144}Nd$ are closely similar to the patterns observed globally for young MORB and OIB basalts, as well as for the majority of subduction-related magmas (e.g. Condomines *et al.* 1988; Gill & Williams 1990; McDermott & Hawkesworth 1991; Gill *et al.* 1992). There are no comparable examples of a single subduction-related volcano where such striking correlations have been observed.

The $(^{230}Th/^{232}Th)_i$–$^{87}Sr/^{86}Sr$ and $(^{230}Th/^{232}Th)_i$–$^{143}Nd/^{144}Nd$ covariation is consistent with the mixing of two isotopically distinct components, one with $(^{230}Th/^{232}Th) > 1.05$, $^{143}Nd/^{144}Nd > 0.5128$ and $^{87}Sr/^{86}Sr < 0.7043$, the other with $(^{230}Th/^{232}Th) < 0.8$, $^{143}Nd/^{144}Nd < 0.5126$ and $^{87}Sr/^{86}Sr > 0.7054$. Crustal contamination of mantle-derived melts is a plausible explanation for these coupled variations. Typical crust with a [Th/U] weight ratio of about 4 would act as source of Th-rich material with $(^{230}Th/^{232}Th) \approx 0.76$, and would also be characterized by relatively radiogenic Sr and unradiogenic Nd (Chapter 6). Progressive contamination of basic melts, derived from depleted mantle with [Th/U] < 3 would therefore generate negative Th–Sr and positive Th–Nd arrays. Thus the U series data provide further support for assimilation of radiogenic crust into the magmas.

Summary

(1) The ^{238}U–^{230}Th disequilibria observed in the Thera pyroclastics are similar to those from other continental margin systems, with the majority of samples lying within 20% of equilibrium.

(2) Crystal-rich pumices from the Minoan eruption are isotopically heterogeneous, with ^{238}U–^{230}Th and ^{226}Ra–^{230}Th disequilibria that indicate that they were not chemically in equilibrium with the host rhyodacite magma at the time of eruption. Analyses of mineral separates from one crystal-rich pumice sample suggest a crystallization-age of >200 ka, and are consistent with the proposal that the crystal-rich pumices represent plutonic rock related to the early Akrotiri centres stoped into the Minoan chamber. Other Minoan samples show disequilibria in ^{238}U–^{230}Th and ^{226}Ra–^{230}Th which indicates young fractionation events. The data are consistent with their piecemeal crystallization over many thousands of years prior to eruption, or to the effects of variable hydrothermal alteration of rocks, prior to assimilation, by oxidizing fluids which mobilized U, Ra and perhaps Ba. We favour the hydrothermal explanation.

(3) Striking coupled Th, Sr and Nd isotopic variations are recognised from the second explosive cycle of the Thera pyroclastics. These observed correlations are consistent with the assimilation of crust with low $^{230}Th/^{232}Th$ into high $^{230}Th/^{232}Th$ mantle-derived magmas.

Chapter 8
The evolution of Santorini

There now follows a synthesis of the main results of this study. We interpret the observations in terms of the interplay between magmatic, tectonic and volcanic processes and place these processes within a global context. Santorini has displayed a wide variety of igneous and volcanic phenomena over a period of at least 650 000 years of almost continuous and focused volcanism. Perhaps the most intriguing issues are the causes of volcanic and magmatic cyclicity, the secular variations in magma composition and the way in which magmatic processes have influenced the style of volcanism.

Geological and tectonic controls

Santorini is part of a continental volcanic arc that developed in the late Pliocene on thinning continental lithosphere (Chapter 2; Jackson 1994). The exposed Aegean crust is composed principally of Mesozoic metamorphic and sedimentary rocks, Tertiary plutonic rocks, and late Tertiary to Quaternary volcanics. There are also local remnants of Hercynian basement of Precambrian to Palaeozoic age, which may be widely present at depth, providing the crystalline foundation to the Mesozoic cover. The Mesozoic rocks were strongly deformed and metamorphosed during the Alpine orogeny, with at least two major episodes of deformation and metamorphism, namely an Eocene high-pressure blueschist-facies event and Miocene greenschist-facies event. The tectonic regime became extensional towards the end of the Miocene, with emplacement of post-collisional granitoids followed by development of the modern arc system in the late Pliocene. The crust roughly halved in thickness during extension and collapse of the Aegean region (Jackson 1994). The deeper unexposed parts of the Aegean crust are likely to contain more refractory mafic rock types. Miocene and late Tertiary magmatism would be expected to form more mafic rocks in the lower crust either by extraction of silicic partial melts or by underplating.

Santorini is located on a 70 km long NE–SW rupture zone associated with the large-scale fault systems that are accommodating regional extension (Heiken & McCoy 1984; Jackson 1994; Mountrakis *et al.* 1998; Chapters 2 and 3). The volcanic centres of Christiana and Columbos to the SW and NE respectively suggest a tectonic control to the location of Santorini. The regional fault system has had a major influence on the volcano during its evolution, with many vents and dykes being located predominantly along the same NE–SW trend (Chapter 3). Much of the volcanism has been along the Kameni Line, which coincides with the boundary between a structural horst to the southeast, where the basement rocks and uplifted submarine volcanics outcrop, and a graben to the northwest. The occurrence of submarine tuffs and hyaloclastite breccias on the Akrotiri Peninsula demonstrates absolute uplift of southern Santorini, whereas northern Santorini has been the focus of both tectonic subsidence and caldera collapse. The predominantly NE–SW vent and dyke alignments indicate a strong influence of regional extension in a graben bounded by major regional faults.

History of the volcano

Effusive volcanism on Santorini began in the period 650–550 ka (Chapter 3). Only small remnants of these early centres are still preserved on the Akrotiri Peninsula. The lavas and tuffs includes andesites, dacites, amphibole-bearing rhyodacites and basaltic products in the form of amphibole-bearing mafic inclusions. The sequence includes submarine pyroclastic rocks, hyaloclastite breccias and lavas which have been uplifted by at least 100 m. The silicic lavas of the early Akrotiri centres have distinctive high Ba and Sr, and high values of Ba/Rb compared to later products (Chapter 6; Davis *et al.* 1998; Tarney *et al.* 1998). Plutonic rocks with strong geochemical similarities to the early Akrotiri centres were stoped into the top of the Minoan magma chamber immediately before its discharge 3.6 ka ago. This requires them to have extended under the volcanic field well to the north of present-day outcrops of the cogenetic volcanics, which represent a small remnant of a much larger area of these early volcanics.

The Peristeria Volcano (mainly 530–430 ka) developed in the northern part of the field and was a composite, steep-sided stratocone. The sequence is composed of lavas and numerous pumice and scoria fall deposits with a compositional range from basalt to dacite. In this study (Chapter 3) we have shown that Micros Profitis Ilias massif and the lower parts of Meagalo Vouno are remnants of the Peristeria Volcano. Volcanism in this period also occurred in the south to form the isolated basaltic and andesitic cinder cones of the Akrotiri Peninsula.

The history of Santorini from approximately 360 ka onwards (Chapter 3) is recorded in the spectacular caldera walls which expose a complex sequence of pyroclastic ejecta (the Thera pyroclastics) and intercalated lava sequences. The Thera pyroclastics constitute the products of a large number of explosive eruptions. Twelve major deposits have been recognized that represent the products of substantial explosive eruptions estimated to be in the 1–30 km^3 magnitude range. These deposits were large enough to be preserved over significant areas of the island and include Plinian pumice or scoria fall deposits, various proximal ignimbrite facies and pyroclastic surge deposits. Deposits from at least 100 minor explosive eruptions are preserved. We surmise that explosive eruptions over the 360 000 years are likely to have numbered in the many hundreds, even thousands, with only the most significant events being preserved. Historic explosive eruptions of the Kameni Volcano demonstrate that more minor explosive eruptions are usually not preserved in the geological record. The vulcanian explosive activity associated with the lava extrusions on the Kameni islands are too small to produce sufficient ash to leave primary deposits. Some of the minor mafic to intermediate ash beds of the Thera pyroclastics are interpreted as Sakurajima-type deposits which accumulated from large numbers of small eruptions that might characterize decades or even centuries of explosive activity (Kobayashi 1986).

Two kinds of cyclic behaviour characterized by different timescales can be recognized in the post-360 ka sequences. First, the major deposits of the Thera pyroclastics define two major cycles which lasted from about 360 to 180 ka and from 180 to 3.6 ka. Second, there have been 12 major explosive eruptions of intermediate to silicic magma over the 360 ka and each major eruption alternates with eruptions of generally more mafic magmas with the volcanism being predominantly extrusive. These latter cycles occur on a time-scale of about 20 000–40 000 years.

Each of the major (180 000 year) cycles was characterized by a period of explosive eruptions of predominantly intermediate (silicic andesite and dacite) magma from zoned magma chambers and culminated in two large eruptions of dominantly silicic magma from homogeneous magma bodies into which minor amounts of more mafic magma had been admixed. There are many similarities between the two cycles in terms of field characteristics of the deposits, petrological characteristics and geochemistry. For example, in both cycles the dominantly intermediate eruptions produced andesitic deposits which include coarse-grained scoria and spatter-rich pyroclastic flow deposits, containing abundant plutonic nodules (Chapter 5). The dominantly silicic eruptions (Lower Pumices 1 and 2 in the first cycle and Cape Riva and Minoan in the second cycle) produced remarkably similar Plinian deposits and pumiceous ignimbrites and lag breccias, compositionally bimodal products including normal-to-reverse chemical zoning patterns in three of them, and

large volumes of homogeneous rhyodacitic magma (Chapter 4). At least three of these eruptions were associated with the formation of large calderas (calderas 1, 3, and 4), although one or more of the dominantly intermediate eruptions also caused collapse (caldera 2). One striking similarity between the second major silicic eruptions of each cycle (Lower Pumice 2 and Minoan) is the eruption of large volumes of phreatomagmatic surge deposits and low-temperature ignimbrite following the initial Plinian phase. In each case these phreatomagmatic facies may be explained as the consequence of eruption from vents situated in the sea-flooded caldera of the previous silicic eruption (Lower Pumice 1 and Cape Riva).

Large silicic magma chambers developed only during the final 50 000 years of each cycle (Chapter 3). In the first cycle, the Rhyodacites of Cape Alonaki were discharged at approximately 225 ka and the cycle terminated with Lower Pumice 2 around 180 ka. In the second cycle, the andesitic Upper Scoriae 2 eruption took place about 55 ka at the end of the construction of the Skaros shield. Thereafter activity was dominated by silicic magmatism with extrusion of the Therasia dome complex, the Cape Riva eruption, then the Minoan eruption. The Therasia lavas are petrologically very similar to the Cape Riva rhyodacite and are inferred to be precursory leaks from the same body. The period of about 35 000 years between the eruption of Upper Scoriae 2 and the Cape Riva eruption at 21 ka indicates the kind of time required to evolve large volumes of silicic magma in the crust. This concentration of large-magnitude explosive silicic volcanism in the final quarter or so of each major cycle is a fundamental feature of Santorini.

The shorter time-scale cyclic pattern can be recognized based on the compositions and stratigraphic organisation of pyroclastic deposits and lava sequences. There are significant packages of mafic to intermediate minor pyroclastic deposits between most of the major pyroclastic deposits, except for the twin silicic eruptions (Lower Pumices 1 and 2; Cape Riva and Minoan). Some of these packages can be correlated with periods of substantial outpouring of lava, the best example being the Skaros lavas between Upper Scoriae 1 and Upper Scoriae 2. The predominance of basalt and mafic andesite scoria and ash in these minor pyroclastic units implies their derivation from periods of constructional volcanism even when the associated lavas are not exposed. Several of the sequences of minor mafic to intermediate pyroclastic deposits show increasing development of soil horizons towards the top of a sequence, consistent with a slowing down of volcanism prior to a major explosive eruption of more evolved magma. This alternation of dominantly mafic to intermediate constructive volcanism with large and destructive explosive volcanism occurred on time scales of 20–40 ka.

Caldera formation

Caldera collapses have been a major feature of the evolution of Santorini. At least four major collapses have occurred, associated with major explosive eruptions of Lower Pumice 2, one or more of the Middle Tuff eruptions, Cape Riva and the Minoan. Collapse related to Lower Pumice 1 has also been inferred. Some of the other major explosive eruptions of the Thera pyroclastics were large enough that it is very likely that they also caused collapse. The calderas are clearly strongly influenced by the regional tectonic structure, the Kameni Line being a key boundary and line of weakness. The origin of the southern basin of the caldera (between the Kameni islands and Akrotiri) is less clear. Heiken & McCoy (1984) attributed the southern depression to caldera collapse during the Lower Pumice eruptions. The >300 m height of the Skaros lava shield however makes it hard to imagine that Skaros lavas did not spread south into this area which is now at over 300 m water depth (Fig. 3.38), implying that deepening of this area is related to significant collapse in post-Skaros eruptions.

Calderas have had a major influence on the distribution of eruptive products. After the formation of a large caldera subsequent products infill the depression. The Cape Thera and Middle Pumice deposits were partly ponded in the caldera formed by the Lower Pumice 2 eruption. In the case of periods of effusive volcanism the lavas were trapped and gradually filled up the caldera. The best example of this process is the development of the Skaros shield, but ponding would probably have happened after other major caldera-forming events with either only small remnants of the lava shields remaining (e.g. the Simandiri shield) or only indirect evidence of the intracaldera volcano's existence in the form of the minor pyroclastic sequences. The Kameni Islands are the latest example of the early stages of this process.

Down-faulting of volcanic rocks during caldera formation must have a profound effect on the structure of the upper crust below Santorini. The combined subsidence of Cape Riva and Minoan eruptions can probably account for several hundred metres of subsidence. Most of the Skaros shield dissappeared by collapse, a minimum of 300 m. Comparable collapse of several hundreds of metres can reasonably be inferred for each of the collapses associated with older major explosive eruptions such as Lower Pumice 1 and Lower Pumice 2. Gravity data show that a layer of low density caldera over a kilometre in thickness lies below Santorini, giving a minimum depth of total subsidence. Cottrell *et al.* (1999) estimated that the magma chamber for the Minoan eruption resided at about 2 km (50 MPa pressure) on the basis of mineral equilibria and petrological observations. Geochemical data on Minoan ejecta are also consistent with assimilation of hydrothermally altered high-level intrusive rocks with geochemical affinities to the early Akrotiri centres at the roof of the chamber (Chapters 6 and 7), which also supports substantial downfaulting. The accumulative subsidence is estimated to be 2 to 3 km based on these various observations and constraints.

Magma evolution mechanisms

Geochemical and petrological variations at Santorini can largely, if not entirely, be explained by processes within crustal magma chambers (Chapters 4 and 6). Along with previous studies (Nicholls 1971*a*; Mann 1983; Huijsmans 1985), much of the chemical variation can be accounted for by fractional crystallisation of mantle-derived island-arc basaltic magma. The occurrence of cumulate-textured gabbroic and dioritic nodules with mineralogical and chemical signatures of fractionation from mafic andesite to dacite (Chapter 5) demonstrates the development of complementary plutonic complexes in the crust. Data from the Thera pyroclastics and nodules suggest that physico-chemical conditions in the magma chambers have varied. For example, intermediate magmas vary significantly in their degree of Fe-enrichment, with some examples in the middle of the second cycle of quite strongly tholeiitic andesites and dacites containing Fe-rich olivine (the Vourvoulos and Upper Scoriae 1 deposits). These differences in magmatic evolution could be related to either different oxidation states of the magmas or to differences in the amounts of crustal assimilation. Assimilation of crust, together with fractional crystallisation, accelerates silica enrichment and suppresses Fe-enrichment (Grove & Kinzler 1986).

Compositional zoning and low phenocryst contents in the dominantly intermediate units of the Thera pyroclastics suggests that fractionation occurred probably by sidewall crystallization in high level magma chambers. Lava sequences such as Peristeria (Micros Profitis Ilias) and Skaros, which show systematic chemical trends with time, also provide evidence of zoned chambers (Huijsmans 1985). There is a marked contrast between the dominantly intermediate deposits and dominantly silicic deposits of the Thera pyroclastics. The former tend to develop more continuous chemical stratification whereas the latter are characterized by large volumes of rather compositionally uniform magma, minor amounts of intermediate to mafic magma and large compositional gaps.

Another important process is magma mixing in open-system magma chambers. Magmatic mafic inclusions are commonplace in several of the major silicic pyroclastic deposits and lavas, notable

examples being the Minoan and Lower Pumice 2 Plinian deposits, the Kameni lavas and the rhyodacite lavas of the early Akrotiri centres. These mafic inclusions have the typical textural features of mafic magma rapidly emplaced into cooler silicic magma with resulting quenching and solidification (Sparks *et al.* 1977; Sparks & Marshall 1986; Bacon 1986; Cottrell *et al.* 1999). Mafic inclusions can be interpreted as due to the break up of basaltic to mafic andesite magma emplaced into middle to upper crustal magma chambers. Compositionally banded pumice is also common. Hybridism in Santorini lavas and pyroclastics produces rocks with disequilibrium crystal assemblages, heterogeneties in glass compositions, and distinctive chemical features such as low FeO, FeO/MgO, and TiO_2, and high Ni and Cr (Huijsmans 1985; Pyle *et al.* 1988; Chapters 4 and 6). Hybrid rocks are particularly common in the dominantly silicic pyroclastic deposits, giving the suite of erupted magmas distinctive calcalkaline trends.

There is abundant evidence for the involvement of crustal rocks in magma genesis. Isotope data are definitive in demonstrating heterogeneity that cannot be ascribed to fractional crystallization (Chapters 6 and 7). Sr, Nd and Th co-vary in ways that are expected from variable amounts of crustal assimilation. $^{230}Th/^{232}Th$ shows a range from high mantle values to lower values typical of continental crust. $^{230}Th/^{232}Th$ also decreases with increasing $^{87}Sr/^{86}Sr$. There is an overall increase in $^{87}Sr/^{86}Sr$ with increasing SiO_2 consistent with progressive assimilation during fractionation. Pb isotopes fall outside the mantle field, with ratios typical of radiogenic upper crust. Oxygen isotope ratios of plagioclase separates range from typical mantle values up to $+7.5\ \delta^{18}O$. The oxygen data are consistent with fractional crystallization with modest amounts of crustal assimilation. Incompatible trace element abundances cannot be modelled by fractional crystallization from basaltic magmas with the range of compositions observed on Santorini. Large-ion lithophile elements are enriched relative to other strongly incompatible elements such as Zr. However good agreement can be found for both trace element trends and isotopic trends using AFC models involving typical Santorini basalts as mafic end members and crustal assimilants with the compositions of Aegean basement rocks. Satisfactory fits can be achieved with a crustal assimilant that has the low Sr and high Rb and K expected of a rhyolitic partial melt of the crust.

An interesting feature of the AFC models (Chapter 6) is that values of the parameter r (the ratio of the mass of assimilant to mass crystallized) is in a rather narrow range of 0.1–0.2. These values can be considered in terms of the broad thermal effects of emplacing basaltic magma into continental crust. The heat supplied by fractional crystallization and cooling heats the surrounding rocks to form the partial melts which are then assimilated into the basalt as it fractionates to produce more silicic magmas. A heat balance can be defined as

$$M_c S_c(T_e - T_c) + M_c x_c L_c = M_b S_b(T_b - T_e) + M_b x_b L_b$$

where S_c and S_b are the specific heats of the crust and basalt, T_e is a typical equilibrium temperature at which rhyolitic partial melt is liberated to mix with the fractionating magma, T_c is the original temperature of the crust at the chamber depth prior to be being perturbed by the onset of volcanism, and T_b is the original temperature of the basalt. M_c is the total mass of crust involved in melting and x_c is the mass fraction of partial melt. M_b is the total mass of basalt and x_b is the mass fraction crystallized from the basaltic magma in cooling to the equilibrium temperature T_e. L_c and L_b are respectively the latent heats of melting of the crust and crystallization of the basalt. The value of r in the AFC model can be equated with the value $M_c x_c / M_b x_b$. Typical parameter values are $S_c = S_b = 1250\ J\,kg^{-1}\,K^{-1}$, $L_c = 2.5 \times 10^5\ J\,kg^{-1}$, $L_b = 4.2 \times 10^5\ J\,kg^{-1}$, $T_b = 1200°C$ and T_c at a depth of 5 km = 200°C. T_e is chosen as about 850°C since this is a suitable temperature to produce significant amounts of silicic partial melt in typical crustal rocks. A result of the above heat balance equation can be obtained by assuming that values of $r = M_c x_c / M_b x_b$ falls in the range 0.1–0.2. To generate rhyolitic melt from basaltic magma requires fractional crystallization in the range 0.7–0.85. This simple calculation implies that for $r = 0.1$ to 0.2 the mass ratio of crust to basalt (M_c/M_b) is about 0.85–0.95, i.e., that a slightly greater amount of basalt is required to partially melt a given mass of the crust. Such calculations neglect the dynamics and complexities that in reality must exist when basalt magma interacts with the crust, but demonstrate that the heat supplied by fractionation of basalt is sufficient to partially melt crustal rocks and supply the composition and masses of rhyolitc melt that are suggested by the geochemical models.

In the case of the Minoan magma body, crystal-rich pumices and granitoid nodules are observed as xenoliths within the rhyodacitic ejecta. These amphibole-bearing rocks have unusual trace element chemistry (high Ba and Sr and low Zr, Rb and K) and are similar chemically and mineralogically to lavas and tuffs of the early Akrotiri centres. Disequilibria of ^{238}U–^{232}Th–^{226}Ra in these crystal-rich pumices (Chapter 7) can be interpreted in terms of relatively recent U and Ra mobility in a hydrothermal system affecting the roof-rocks of the Minoan chamber which were being actively assimilated into the chamber prior to eruption. The study of Cottrell *et al.* (1999) indicate a chamber at a depth of about 2 km. Magmas of all four large, dominantly silicic eruptions, including the Minoan, show $^{87}Sr/^{86}Sr$ isotopic disequilibria, with whole rock compositions having higher $^{87}Sr/^{86}Sr$ than plagioclase. These observations also imply that progressive assimilation of radiogenic crustal melts into the magma chambers as they crystallized.

Causes of secular variations in magma geochemistry

Underlying the geochemical variations related to shallow-level fractionation and assimilation there is an overall decline in the contents of certain incompatible elements (K, Rb, Ba, Th, Nb, Zr) and Sr with time. Up to the eruption of Upper Scoriae 2 at about 55 ka the decrease in abundance of incompatible elements correlates with systematic decreases in $^{87}Sr/^{86}Sr$ and increases in $^{144}Nd/^{143}Nd$ and $^{230}Th/^{232}Th$. The same progressive depletion can also be seen in the lava successions, from the Peristeria volcanics, through the Skaros lavas, to the Kameni lavas (Huijsmans 1985). The Early Centres of Akrotiri do not fit this simple trend, implying more complicated processes during that initial phase of magmatism. AFC models suggest that the mafic parents of Cape Riva and Minoan magmas are more depleted in many incompatible elements and radiogenic isotopes than the lavas of Skaros and the first-cycle Thera pyroclastics, but are less depleted than the Kameni lavas. The dominantly intermediate deposits of the first cycle are enriched in ^{87}Sr compared to those of the second cycle. Elevated $^{87}Sr/^{86}Sr$, Ba and Sr in the Cape Riva and Minoan appear to reverse the trend. However these magmas are highly evolved and, in the Minoan case, have assimilated radiogenic granitoids with high $^{87}Sr/^{86}Sr$, Ba and Sr possibly related to the early Akrotiri centres.

The progressive depletion could be produced by melting of different mantle sources and/or different degrees of melting of a single source. Huijsmans (1985) proposed that the mantle source region underneath Santorini became depleted in Sr and incompatible elements with time. In subduction settings the addition of slab-derived fluids influences the source composition as well as the degree of melting. In the Stolper & Newman (1994) model of arc magmatism, the effect of slab fluids is to increase the amount of melting due to the fluxing effect of water, thus diluting incompatible trace element contents in the resulting water-rich partial melts which then evolve on more calc-alkaline trends. This model could apply to Santorini, with the degree of partial melting increasing with time due to increasing input of input of slab fluids. However there is no evidence that the mafic magmas became more water-rich with time and those deposits showing calcalkaline trends can be explained by hybridism. This hypothesis is also rather ad hoc as there is no compelling reason why subduction processes and magma production should change on a time-scale (about 650 ka)

that is short compared to that of a subduction zone (order of 10 Ma for the Aegean arc).

Another possibility is that the primary magmas were derived by similar degrees of partial melting of different mantle sources. This hypothesis is difficult to evaluate on Santorini due to the strong overprinting of magma chamber processes, in particular AFC. A possible candidate for an enriched source is the continental lithospheric mantle, which becomes progressively depleted with time. Alternatively the subduction zone primitive magmas could assimilate trace-element-rich, low-melting-fraction components from the lithospheric mantle and lower crust as they pass through to feed higher level crustal chambers where they then fractionated. In the MASH process (Hildreth & Moorbath 1988) primitive basaltic magmas rising through the lithospheric mantle and into the base of the crust undergo complex interactions.

We propose that the key factor in understanding the evolution of Santorini is the large amount of basalt magma that has passed through and been emplaced within the crust. Since any model that invokes variations in the mantle as a cause for magmatic diversity is highly speculative, a model which assumes a constant composition primitive basalt magma provides the simplest working hypothesis. On Santorini, basalt parental magmas have passed repeatedly through a relatively small cross-sectional area of continental lithosphere (about 60 km^2) for at least 650 000 years. There are only limited constraints on magma production rate on Santorini. The Kameni Islands have a volume of 2.5 km^3 and have been erupted over 3500 years (0.7 km^3 per ka). The Minoan magma chamber grew to at least 30 km^3 over a period of 17 500 years (1.7 km^3 per ka) and the Skaros shield developed a volume of at least 10 km^3 over about 12 000 years (0.8 km^3 per ka). These rates bracket magma production rates typical of island arc volcanoes (Crisp 1984). On the basis that the average erupted composition is silicic andesite then there must be at least an equivalent volume of plutonic cumulate material at depth. The existence of large plutonic masses is supported by the occurrence of cumulate nodules (Chapter 5) and the dominance of evolved volcanic rocks generated by fractionation. Thus, since the age of volcanism is 650 ka, a conservative estimate of total magma that has passed into or through the crust is 300–600 km^3. Over an area of 60 km^2 the amount of plutonic material is thus 5–10 km, implying that a significant proportion of the 30 km crust beneath Santorini has been replaced by young igneous material. Above we estimated that the crust has been partially melted and assimilated into the magmas with 0.1–0.2 being the estimated value of r. This suggests that a column of crust several kilometres thick beneath Santorini has been depleted of low-melting-temperature components. Removal and eruption of partial melt cryptically in the form of contaminated magmas could perhaps account for a significant proportion of the missing volume of crust.

We propose the following model based on the focused flux of mantle-derived basalt into the crust over a period of 650 ka. The basaltic flux has resulted in the surrounding crustal rocks becoming partially melted. The basaltic magmas have been contaminated by trace-element-rich silicic partial melts as they fractionated to andesites and rhyodacites. The crustal rocks have been progressively stripped of incompatible trace elements and radiogenic components. This is one factor in the evolutionary trend to more depleted compositions. Mid to upper crustal compositionally zoned magma chambers have developed in which fractional crystallization, replenishment, and assimilation of crustal wallrock have occurred. Progressive amounts of continental crust have been stripped of minimum melt components, metasomatized, and/or replaced by young plutonic intrusions. A major factor in the decrease in incompatible elements and radiogenic isotopes with time may be the progressive isolation of rising magmas from the crust. As plutonic intrusions progressively replace the crust and more labile components are removed by partial melting, rising magmas are less affected by assimilation. At the end of the most recent cycle it appears that the Minoan system (and perhaps Cape Riva) started to assimilate plutonic and volcanic rocks from the first phase of Santorini volcanism.

Causes of the cycles

A final question concerns the origin of the two types of cycle, one on a 20 000–40 000 year timescale (the time between the major explosive eruptions) and the other on a 180 000 year timescale. One possibility is that the cycles relate to fluctuations in the supply rate of mantle-derived basalt. However we prefer to explore models which are based on a constant flux of basaltic magma as they are inherently simpler. We hypothesize that the main features of the cycles can be explained in terms of thermal and physical interactions between basalt and the crust and influences of constructive and destructive volcanic processes. In passing through the crust the amount of crustal heating and melting depends on the relative balance between intrusion and extrusion and on the respective temperatures of the magma and of the crust at the level of intrusion. At one extreme, eruption of undifferentiated basalt lava will supply little heat to the crust. At the other extreme, if basalt magma is intruded into the crust then heating of the crust is maximized. Development of large magma chambers containing fractionated magmas also implies the transfer of substantial amounts of heat to the crust. Thus the relative changes in proportions of mafic to silicic magmas erupted in different phases of the cycles implies different heating rates of the crust at depth, even if the underlying mafic magma supply is constant.

Each of the 12 large explosive eruptions of Santorini is interpreted as recording the slow growth, partial or complete discharge, then cooling and crystallization of a shallow magma body over a period of 20–40 ka. Early during a cycle basalt magma or mafic andesite can pass easily through the crust. Some limited fractionation must take place in small chambers since none of the mafic rocks on Santorini are primary and all have differentiated to some extent. Eruption of such magmas constructed lava cones and shields and built up sequences of minor tephra and dissipates much of the heat at the earth's surface. As small magma bodies coalesced and enlarged, mafic magmas were increasingly trapped at depth where the magmas stagnated, surface activity declined and the heat input to the crust increased. This process then led to formation of a large differentiated magma chamber. The low-density, evolved magma then acted as an effective trap preventing denser mafic magma from reaching the surface: a kind of positive feedback effect. The zoned magma body eventually erupted explosively, sometimes resulting in caldera collapse. Either the whole magma body was erupted or the remnants were too insubstantial to prevent denser mafic magmas reaching the surface, so that a new cycle of constructive mafic volcanism could began.

The 20 000 to 40 000 year cycles could also be modulated by high-level volcanic processes. As a volcano increases in height and mass it becomes increasingly hard for dense, mafic magma to reach the surface. The growth of the edifice favours intrusion at depth and the development of high-level magma chambers. During the second 180 000 year cycle, the Skaros shield filled in and overspilled an older caldera. Following the Upper Scoriae 2 explosive eruption about 55 ka, surface volcanism declined, perhaps because the Skaros shield was too high for mafic or even intermediate magmas to reach the surface easily. If this were the case, then the time scale for these cycles might be controlled by the time necessary to build up an edifice sufficient to inhibit magma reaching the surface so that conditions for development of a substantial shallow chamber started to develop.

The longer (180 000 year) cycles are postulated to relate to deeper and larger scale thermal maturation of the crust. We envisage that in the middle crust passage and intrusion of basaltic magmas progressively warms the rocks and eventually a zone of partial melting begins to develop. The ductile character and low density of this deeper zone eventually prevents dense magmas reaching the surface and the volcano moves into a period of dormancy, even if the supply of basalt continues at depth. We suggest that this was the situation after Upper Scoriae 2 in the second 180 000 year cycle, causing development of the large magma bodies that eventually erupted in the Cape Riva and Minoan events. The stagnation of basaltic magma leads to an enhanced rate of heating of the crustal

rocks and fractionation of the basalt. The combination of advanced fractionation and partial melting of the crustal rocks leads to generation of the large volumes of silicic magma required to form the large magma bodies. As noted by Huppert & Sparks (1988) this model involves positive feedback in that the more the basalt is intruded and fractionated the more rapidly and effectively the crust is heated.

Geochemical and petrological evidence (Chapters 4 6 and 7; Cottrell *et al.* 1999) provide support for this concept. The large silicic magma bodies show geochemical features consistent with incorporation of substantial amounts of crustal rocks. The crustal components are not sufficiently radiogenic to be the main upper crustal metamorphic cover rocks, but are more consistent with moderate degree partial melts from rather less radiogenic crystalline basement (Chapter 6). In the case of the Minoan, isotopic disequilibria suggest that the contaminant was progressively mixed into the silicic magma as it fractionated. Experimental studies and analyses of water contents in glass inclusions from the Minoan ejecta (Cottrell *et al.* 1999) also support a two-tier magmatic system. Water contents in glass inclusions and mineral equilibria data indicate that the Minoan magma was initially stored at a water pressure of at least 210 MPa, implying a minimum depth of 8 km. This magma was then fed into a shallow magma storage chamber at about 2 km where it equilibriated prior to eruption.

The culmination of a major cycle could relate to the rise of the silicic magma from the deeper source zone to shallow levels. Cottrell *et al.* (1999) have proposed on the basis of heat transfer arguments that the Minoan magma ascended from its deep source to the shallow magma chamber only a few hundred years before eruption. Our isotopic data (Chapters 6 and 7) also indicate that the magma was out of isotopic equilibrium and had interacted with shallow hydrothermally altered rocks over the last few thousand years. One possibility is that it takes a long time for the magma in the deep source to become large enough to become unstable and start rising due to its buoyancy. The zone of deep silicic magma would grow in thickness in time until it became unstable by a Rayleigh–Taylor instability. This process would account for the long period of dormancy and relatively recent arrival of the silicic magma at shallow levels.

We suggest that the cycles could represent a progressive zone refining of the crust. For an individual cycle, the volumes of silicic magma only require a relatively thin partial melting and magma collection zone. For example, if the Minoan magma had a volume of 30 km^3 collected from an area of 60 km^2 of crust, then the magma body would only need to be about 500 m thick. Assuming that the magma is an equal mixture of 20% partially melted crust and basaltic magma fractionated by 80%, the resulting cumulates and crustal rocks from which partial melt has been extracted would each be 1 km thick. Although these are rough and ready illustrative calculations, they indicate that the concept of a developing magma accumulation and partial melting zone can explain the 180 000 year cycles.

The concept of cyclic zone refining of the crust can be developed into a more general model for crustal magma chambers building on previous ideas of continental arc magmatism and dynamics of the interaction of basalt magma with crustal rocks (Hildreth 1981; Huppert & Sparks 1988). Continental crust is known to be chemically zoned due to repeated episodes of partial melt extraction and additions of underplated mafic magmas from the mantle. In general, the upper crust is more silicic and therefore prone to further melt extraction whereas the lower crust is more mafic and refractory. This is likely to be the case in the Aegean crust where previous episodes of magmatism, such as the post-collisional Miocene granite magmatism, will have contributed to chemical zonation. When a new episode of arc magmatism initiates, the geothermal gradient is perturbed as arc magmas pass through, leaving some heat behind, and crustal magma chambers develop. Extensive partial melting of the crust can be expected to occur as the geotherm rises. We suggest that the first region to melt extensively will be in the middle crust at the deepest level of fertile upper crustal basement rocks, essentially the boundary between the upper and lower crust. A zone of basalt fractionation, partial melting and silicic magma generation develops and culminates in large magnitude silicic eruptions. This process of removing fertile components from the crust essentially converts the zone of magma generation into lower crust, a mixture of cumulate gabbros and refractory crustal rocks. As a consequence, the next cycle might develop such a zone at a shallower level or would extract crustal melts from depleted crustal rocks. The next stage of research on Santorini may be able to test this hypothesis.

Appendix 1
Analytical methods and errors

K–Ar and $^{40}Ar/^{39}Ar$ dating

Thirty eight K–Ar and eight $^{40}Ar/^{39}Ar$ high-precision age determinations were made at the US Geological Survey, Menlo Park, on a total of 22 rocks from the entire volcanic field. Duplicate or triplicate determinations were carried out on 14 samples in order to improve analytical precision. All ages were measured on whole-rock samples selected after thin-section examination. Most of the samples meet the usual criteria for whole-rock dating (Mankinen & Dalrymple 1972), but some contain minor amounts of glass and a few samples are very glassy. The samples selected for dating were crushed to 0.5–1mm (−18 to +35 mesh). For K–Ar dating aliquots weighing *c.* 25 g were used for the Ar measurements. A 10 g aliquot was ground to −200 mesh and splits of the powder were used for K_2O measurements, which were made in duplicate on each of two separate splits of sample powder by flame photometry after lithium metaborate fusion and dissolution (Ingamells 1970). Ar analyses were by isotope-dilution mass spectrometry using a high-purity (>99.9%) ^{38}Ar tracer and techniques and equipment described previously (Dalrymple & Lanphere 1969). All samples for Ar extraction were baked overnight at 280°C. Mass analyses were done on a 22.68 cm radius, multiple-collector mass spectrometer with a nominal 90° sector magnet, using automated data collection (Stacey *et al.* 1981).

Errors given for the calculated K–Ar ages of individual measurements are estimates of the standard deviation of analytical precision. The errors were calculated using formulae derived by Cox & Dalrymple (1967) and Dalrymple & Lanphere (1969). For eight of fourteen duplicate or triplicate K–Ar determinations the calculated ages agree within the uncertainty assigned to each age. For these samples, weighted mean ages were also calculated; weighting is by the estimated variance of individual age measurements (Taylor 1982). The calculation of weighted mean ages allows data of different quality to be combined without poorer data having a disproportionate effect on the result. For the six samples where the error envelopes around each age do not overlap, simple arithmetic ages and standard deviations were calculated.

In the $^{40}Ar/^{39}Ar$ technique the sample is irradiated with fast neutrons to induce the reaction $^{39}K(n,p)^{39}Ar$. Aliquots of −18 +35 mesh material weighing between 100 and 120 mg were placed in Cu foil packets. These packets were stacked vertically in a fused-silica vial. Splits of a sanidine separated from the 27.88 Ma Taylor-Creek Rhyolite of New Mexico (Duffield & Dalrymple 1990) were used as a flux monitor and occupied each fourth position in the sample array. The samples were irradiated for 2 hours in the core of the US Geological Survey TRIGA reactor in Denver. The procedures for irradiating samples for $^{40}Ar/^{39}Ar$ dating are described by Dalrymple *et al.* (1981). The age of a sample is calculated from the measured $^{40}Ar/^{39}Ar$ ratio after determining the fraction of ^{40}Ar converted to ^{39}Ar by analysing a monitor mineral of known age to measure the neutron flux. Corrections for interfering isotopes produced from K and Ca and for atmospheric Ar were also made. The $^{40}Ar/^{39}Ar$ analyses were made using a low-blank resistance-heated furnace attached to a clean-up system and a sensitive rare-gas mass spectrometer equipped with a Baur-Signer source and electron multiplier. The system has been described in detail by Dalrymple (1989).

The incremental-heating analyses were done by heating the sample to a given temperature and calculating the age for that temperature increment. One assumes in calculating an age that nonradiogenic Ar is atmospheric in composition. Evaluation of the array of ages for different temperature increments is done using graphical techniques. In an age spectrum the calculated ages are plotted versus the size of the gas increments as given by the amount of ^{39}Ar in each increment. Contiguous increments whose ages agree within analytical uncertainties define what is called the plateau age. The $^{40}Ar/^{39}Ar$ data may also be plotted on an isotope correlation diagram. Measured ratios are plotted; no assumptions are made about the composition of nonradiogenic Ar. On a plot of $^{40}Ar/^{36}Ar$ versus $^{39}Ar/^{36}Ar$ an isochron is fitted to the data points; the age is calculated from the slope of the isochron. The intercept of the isochron on the ordinate gives the composition of non-radiogenic Ar in the rock, and this serves as a test of the assumption made in calculating ages for gas increments on an age spectrum diagram.

Electron microprobe analysis

Mineral and glass phases were analysed using an energy dispersive (EDS) electron microprobe designed and constructed at the University of Cambridge. The system employs a Li-doped Si detector with a specimen-detector distance of 270 mm and a take-off angle of 40°. All analyses were performed at 20 kV accelerating potential with a count time of 80 seconds. Data was processed using the iterative peak stripping of Sweatman & Long (1969).

All mineral analyses were carried out with a focused electron beam and a beam current of either 45 or 50 nA. Analyses of glasses were performed under conditions suitable to avoid alkali loss (Lineweaver 1963) but also to permit analysis of small areas of individual glass shards. The analyses were done using a 10–15 μm rastered beam and a beam current of 10 nA. In some cases the beam was defocussed. Test analyses of two glass standards, a rhyolite obsidian (Los Posos; LP) and a comendite obsidian (KN18) containing 4.4 and 5.7% Na_2O respectively, indicate that a 10% depletion in Na_2O, but no detectable loss of K_2O, occurs under these conditions. The range of Na_2O values have therefore been increased by a factor of 1.1 in order to correct for this effect. Corrected analyses for the two standards are given in Table A1.1, along with reported analyses. Also shown is a corrected average analysis of Minoan pumice S79-81. The result is in excellent agreement with an analysis of Minoan glass published by Federman & Carey (1980). These authors corrected for Na in their sample by monitoring Na counts with time and extrapolating back to zero using a polynomial regression technique (Nielson & Sigurdsson 1981).

XRF analysis

Analyses were performed at the University of Nottingham using a fully automated Phillips PW1400 X-ray spectrometer system with rhodium X-ray source. Major element analyses were done on fusion discs prepared using the method of Harvey *et al.* (1973). Volatile abundances were determined by loss on ignition at 1000°C for 15 minutes. Trace element determinations were carried out on pressed powder discs, prepared using rock powder which had passed through a 200 mesh sieve.

Analytical precision was determined by eight repeat analyses of a single sample of Minoan rhyodacite pumice (S80-28). Absolute and relative standard deviations for the eight results are given in Table A1.2. Table A1.3. compares reported major and trace element concentrations for three analytical standards: peridotite PCC-1, granodiorite GSP-1 and granite NIM-G (Abbey 1980) with analyses of the same rocks obtained on the Nottingham PW1400. Agreement is generally excellent. There are two discrepancies. First, the determined concentration of La in GSP-1 (150 ppm) is significantly lower than that reported (195 ppm). This is probably due to the fact that the value is outside the normal calibration range for the Nottingham system. Although all Santorini rocks have La contents well within this range, La is not discussed in the text. Second, the determined concentration of Zr in NIM-G (272 ppm) is somewhat lower than the reported value of 300 ppm.

Table A1.1. *Comparison of glass analyses performed on the Cambridge EDS microprobe with previously reported analyses of the same material (R. MacDonald pers. comm. 1983)*

	Los Posos, LP		KN 18		Minoan glass	
	Analysed	Reported	Analysed	Reported	Analysed	Federman & Carey (1980)
No. anal	10	–	10	–	10	6
SiO_2	77.33 (0.26)	76.91	75.35 (0.16)	75.22	73.80 (0.44)	73.56 (0.18)
Al_2O_3	12.47 (0.26)	12.66	10.63 (0.08)	10.62	14.09 (0.21)	14.17 (0.06)
TiO_2	–	–	–	–	0.28 (0.04)	0.27 (0.02)
FeO	0.77 (0.12)	1.05	3.40 (0.14)	3.48	0.28 (0.04)	0.27 (0.02)
CaO	0.30 (0.07)	0.31	0.21 (0.05)	0.15	1.47 (0.14)	1.41 (0.01)
Na_2O	4.42 (0.24)	4.36	5.70 (0.14)	5.73	5.07 (0.17)	5.28
K_2O	4.59 (0.06)	4.61	4.44 (0.04)	4.43	3.36 (0.12)	3.25 (0.01)
Cl	0.12 (0.01)	na	0.27 (0.02)	0.37	0.25 (0.25)	–

na, not analysed.
Figures in brackets are single standard derivations.

Lead, strontium and neodymium isotopes

Radiogenic isotope ratios, and Nd and Sm concentrations, were analysed at the NERC Isotope Geosciences Laboratory. Pb, Sr and Nd for isotope analysis were separated from common dissolutions of 100–150 mg powdered samples, or hand-picked mineral separates, using ultra clean reagents and conventional cation and HBr–HCl anion exchange columns. Procedural blanks for Sr, Nd and Pb averaged 1670 pg, 230 pg, and 230 pg respectively. All Sr and Pb isotopic compositions were measured in static mode on a Finnigan MAT 262 multicollector mass spectrometer; the Nd isotopic compositions were measured in dynamic mode on a VG 354 multicollector mass spectrometer. $^{87}Sr/^{86}Sr$ was normalized to $^{87}Sr/^{86}Sr = 0.1194$, $^{146}Nd/^{144}Nd$ was normalized to $^{146}Nd/^{144}Nd = 0.7219$. Within-run precision for Sr and Nd isotope ratios, expressed as one standard error of the mean, was always better than 10 ppm of the measured ratio, i.e. 0.000007 and 0.000005 for $^{87}Sr/^{86}Sr$ and $^{146}Nd/^{144}Nd$ respectively. Results for isotope standards during the periods of these measurements were: NBS 987 $^{87}Sr/^{86}Sr = 0.710240 \pm 0.000024$ ($n = 182$), Johnson–Matthey Nd

$$^{146}Nd/^{144}Nd = 0.511113 \pm 0.000012 \quad (n = 135),$$

La Jolla Nd $^{146}Nd/^{144}Nd = 0.511845 \pm 0.000005$ ($n = 8$, all errors: one standard deviation). Internal errors on individual measurements were always much smaller than the standard reproducibility reported here and therefore the ability to reproduce the standards should be taken as the limiting factor in interpreting the uncertainty of any given analysis. Pb isotopic compositions were corrected for mass fractionation by 1 per mil per amu, in accordance with multiple analyses of the NBS 981 Pb standard.

Table A1.2. *Precision of major and trace element analyses determined by eight runs on Minoan rhyodacite S80-28*

	Mean (wt% or ppm)	1 std. dev.	1 std. dev. (% relative)
SiO_2	68.14	0.05	0.1
Al_2O_3	13.90	0.06	0.4
TiO_2	0.39	0.01	2.0
FeO	2.70	0.01	0.4
MgO	0.57	0.02	3.5
CaO	2.12	0.01	0.4
Na_2O	4.68	0.13	2.7
K_2O	3.02	0.06	0.2
MnO	0.08	0.01	9.0
P_2O_5	0.08	<0.01	<10
LOI	3.94	nd	nd
Sum	99.91	0.15	0.2
Ba	538	10	2
Ce	49	4	8
Cr	3	1	30
La	27	2	6
Ni	1	–	–
Nb	10	1	10
Rb	85	1	2
Sr	95	1	1
Th	16	1	8
V	21	2	10
Y	44	1	3
Zr	287	2	0.8

Oxygen isotopes

O isotope ratios in whole-rock samples and mineral separates were determined at the NERC Isotope Geosciences Laboratory employing the oxygen liberation techniques of Clayton & Mayeda (1963). Whole-rock powders (6 mg) were reacted with BrF5 at 525°C overnight after outgassing at 250°C and a pre-fluorination reaction with BrF_5 for 30 seconds at 250°C. Mineral separates were reacted with ClF_3 at 525°C overnight after outgassing at 250°C and a pre-fluorination reaction with ClF_3 for 20 minutes at 250°C. The oxygen yields were converted to CO_2 by reaction with a platinized graphite rod heated at 675°C by an induction furnace. CO_2 yields were measured by a capacitance manometer. Yields were generally in the range 98–102% relative to the theoretical oxygen yields. The CO_2 isotopic ratios were measured on a CJS Sciences Ltd Phoenix 390 mass spectrometer (re-built VG 903 automatic triple collector machine) and are reported here in the usual δ notation as permil (‰) deviations relative to the SMOW standard for $^{18}O/^{16}O$ ratios (R) where:

$$\delta_{sample} = ((R_{sample}/R_{std}) - 1) \times 10^3.$$

The $^{18}O_{SMOW}$ results are normalized through the NIGL laboratory standard quartz (LQS-Loch Aline Glass Sand) and quoted relative to the international standard quartz NBS #28 (African Glass Sand) at a value of 9.63. During the overall course of this work monitoring through various comparable laboratory standards gave a mean reproducibility of ±0.3 (1σ for 20 determinations). Eight replicate analyses of one typical whole-rock sample gave a reproducibility of ±0.2 (1σ). The overall determinative error for this work is taken to be ±0.2‰ and the interpretations made accordingly.

Hydrogen isotopes

Samples for D/H analysis were held under vacuum for several hours at 110°C to remove adsorbed water. The water subsequently evolved

Table A1.3. *Major and trace element analyses of standard rocks PCC-1, GSP-1, and NIM-G (Abbey 1980) obtained on the Nottingham PW1400 XRF*

	Reported (Abbey 1980)			Nottingham PW1400		
	PCC-1	GSP-1	NIM-G	PCC-1	GSP-1	NIM-G
SiO_2	42.10	67.32	75.70	41.96	67.51	75.94
Al_2O_3	0.73	15.28	12.08	0.91	15.08	12.22
TiO_2	0.01	0.66	0.09	0.01	0.66	0.09
Fe_2O_3	8.28	4.28	2.04	8.40	4.24	2.01
MgO	43.50	0.97	0.06	43.66	1.02	0.07
CaO	0.55	2.03	0.78	0.58	1.96	0.77
Na_2O	0.01	2.81	3.36	0.02	2.73	3.39
K_2O	na	5.51	4.99	na	5.46	5.04
MnO	0.12	0.04	0.02	0.13	0.05	0.02
P_2O_5	0.01	0.28	0.01	0.02	0.30	0.01
H_2O	4.70	0.58	0.49	4.31	0.99	0.44
Ba	–	1300	120	na	1277	120
Ce	–	360	200	na	326	202
Cr	–	12	12	2523	11	13
La	–	195	105	na	150	116
Ni	–	9	8	2287	9	10
Nb	–	23	53	1	27	55
Pb	–	54	40	17	54	28
Rb	–	250	320	na	250	301
Sr	–	240	10	1	238	11
Th	–	105	52	na	105	53
V	–	54	2	23	58	na
Y	–	29	145	4	30	146
Zr	–	500	300	16	515	272

na, not analysed.

by induction furnace heating, up to melting, was passed over a uranium furnace and the hydrogen yields measured manometrically before D/H analysis on a SIRA II mass spectrometer.

Uranium, thorium, and radium isotopes

Sample preparation

Whole-rock samples were crushed in a tungsten carbide jaw crusher, and taken to −300 mesh in a WC tema mill.

Mineral separates were obtained from jaw-crusher granules, with 0.5–3 kg of samples reduced in a stainless steel ball mill for 30–40 minutes. Mineral concentrates were obtained by sieving this granulated fraction, and by use of a Wilfley table. Concentrates were then reduced to −90 mesh by hand-crushing with an agate pestle and mortar. The −90 mesh samples were washed repeatedly in water to remove the fine powder, and then rinsed in distilled water and filtered and dried. Rough separation of plagioclase, glass and groundmass ($\rho < 2900\,kg\,m^{-3}$) was obtained by using either tetrabromoethane (TBE), or the non-toxic sodium polytungstate (SPT). Plagioclase was purified by successive passes through a Frantz isodynamic separator at increasing currents. The plagioclase obtained at 1.7 amps was then crushed to −200 mesh, washed, dried and purified with TBE or SPT at the selected density required ($2700 < \rho < 2800\,kg\,m^{-3}$). The sample obtained in this fashion was purified at 1.7 amps in the isodynamic separator. Oxides, Fe–Mg silicates, zircon and apatite were purified from the −90 mesh dense fraction, after this had been crushed to −200 mesh, washed and dried. For some samples, magnetite was obtained from the 90–200 mesh split before crushing. Mineral phases were concentrated with Clerici's solution ($\rho < 4200\,kg\,m^{-3}$), and again purified in the isodynamic separator. Magnetite, ilmenite and zircon were all obtained from the $\rho > 400\,kg\,m^{-3}$ concentrate, and silicates from the 3200–3600 $kg\,m^{-3}$ fraction. All separates were washed thoroughly in acetone (TBE) or distilled water after preparation, dried and examined with a microscope for purity. Better than 99% purity could be obtained for most minerals in this fashion.

For sample dissolution, 2–3 g size samples measured into teflon dishes were spiked with $^{229}Th/^{236}U$ and equilibrated in conc. HNO_3 overnight, under an infra-red lamp. Samples were then dried and attacked three times in 10 ml perchloric acid (70%) and 30 ml HF. Samples were then dried out twice after addition of 5 ml conc. HNO_3 (all reagents were analar grade). Samples were then transferred to a teflon bomb, and attacked in 5 ml perchloric acid/5 ml HF in the sealed container, in an oven heated to *c.* 160°C. One such dissolution was effective for most samples. Bombed samples were redissolved in conc. HNO_3, dried twice under an IR lamp, and then dissolved finally in conc. HCl HNO_3, and transferred to yield a mixed aluminous/ferric hydroxide precipitate. Excess Al was removed by dissolution in conc. NaOH, after which precipitated samples were washed thoroughly in distilled water ready for analysis (below).

Uranium and thorium analysis

Three separation columns A–C were prepared using a Bio-rad AG1-X8 100–200 mesh anion exchange washed with distilled water. Columns were of glass and washed in boiling conc. HNO_3 and rinsed in distilled water, prior to use.

Since several of the U and Th (particularly ^{234}U and ^{23}Th) isotopes emit alpha particles of similar energies, which cannot easily be resolved spectrometrically, it is necessary to separate these nuclides chemically. U and Th were separated and purified in two stages using anion exchange columns prior to electrodeposition and alpha spectrometric analysis. (1) The iron hydroxide precipitate was dissolved in 8 M HCl, and transferred through column A, washed through with 8 M HCl. The effluent (Th) was reserved for the second stage, while the iron and U were eluted from the column with 0.2 M HCl. (2) After evaporating down to approximately

10 ml, the eluate was transferred to a centrifuge tube, and U co-precipitated with ferric hydroxide. The precipitate was dissolved in 7 M HNO_3, before passing through the second set of columns (B and C). The resin, with absorbed nuclides, was washed once prior to elution in either 0.2 M HCl (Th). The eluate was reserved in a crystallizing dish with 1 ml of sodium hydrogen sulphate solution, before evaporating to dryness under a heat lamp.

After nitrification and evaporation the crystals were dissolved in sulphuric acid, and made up to 50 ml at the correct pH (2.2 for Th, 2.4 for U) for electrodeposition onto a clean stainless steel disc. The ammonium sulphate electrolyte was transferred to a disposable cell, and current of 1 A passed for 3 (U) or 5 (Th) hours. The prepared source was finally washed in ethanol, dried over a bunsen to remove any traces of organics and placed in an alpha spectrometer for counting. Optimal recoveries were in the range of 70–90% for Th and U, with acceptable counting statistics reached after around 240 ks for U, Th concentrations greater than 1 ppm.

Samples were analysed by alpha spectrometry. Details of analytical procedures and techniques are found in Ivanovich & Harmon (1982). Detectors were dedicated to U or Th analysis, to minimise unwanted background in regions of interest. Typical sample counting rates for whole-rock samples were in the order of 800–1000 counts (per peak) in 150 ks (thousand seconds). Mineral separate counting rates fell as low as <100 counts per 150 ks. The combined blank and background could be as low as 1 count per peak in 150 ks, but were typically <10 counts per 150 ks in any given peak area. Blanks were monitored regularly, and were kept low by washing glassware in boiling conc. HNO_3 and rinsing in distilled water. Platinum electrodes used on the electroplating rig gave negligible blanks after immersion in boiling aqua regia solution.

Radium analysis

Radium was assayed by allowing the daughter ^{222}Rn to grow in to equilibrium in a sealed dreschel bottle. The dissolved sample was washed into a clean 500 ml dreschel and the container sealed. The system was prepared for analysis by bubbling He through the sample, the container resealed and allowed to stand for >15 days to allow the ^{222}Rn to decay back into equilibrium with the Ra.

After the requisite delay, the ^{222}Rn was purged from the system by bubbling through with He for approximately one hour, and was collected on a chilled (−70°C) activated charcoal trap. The radon was then released to a sealed counting cell by heating to 400°C, the cell left for three hours to allow the daughters to reach equilibrium, and then alpha counted for >1000 minutes. Counting efficiencies and background levels were determined by counting standards and blank solutions. These blank solutions were run during every analytical session and typically ranged between 0.2–0.5 cpm for each board. This compares to typical count rates of 2–5 cpm. The blanks are considered to be mainly derived from the system: running a bottle which had just been purged with He gave a very similar result to a bottle which had been allowed to equilibrate. Reagent and bottle were negligible, even for bottles which had previously held a high activity solution, as long as they had been cleaned by standing first in 7 M nitric acid.

Appendix 2
Tabulated analytical data

Details of analytical methods and errors are given in Appendix 1. **bd** means below detection and **na** not analysed. Samples numbers which begin with the letter S are from Druitt (1983) and those that begin with LS are from Edwards (1994). Sample numbers which begin with the number 8 are either from Mellors (1988) or Pyle (1990*b*). Subunits of each major tuff of the Thera pyroclastics are denoted by upper case letters (A to D). These are listed in Table 3.4. In the case of the minor sequences (Appendix 2.3), the sequence abbreviations (M6 to M8) are shown in Fig. 3.17 and the individual unit abbreviations (CD1 to CD10) are from Edwards (1994).

Appendix 2.1 Juvenile components of the Thera pyroclastics

Cape Therma

1	8747	Oxidized scoria. Scoria-flow deposit (B), Cape Therma.
2	8813	Black scoria. Scoria-flow deposit (B), Cape Alonaki.
3	8773	Scoria. Scoria-flow deposit (B), Athinios.
4	8772	Grey pumice. Scoria flow deposit (B), Athinios.
5	8726	Oxidized scoria. Scoria-flow deposit (B), Caldera beach.
6	8725	Oxidized scoria. Scoria-flow deposit (B), Caldera beach.
7	LS155-91	Scoria. Spatter agglomerate (B), Balos.
8	8611	Black scoria. Scoria-flow deposit (B), Cape Plaka.
9	8748	Oxidized scoria. Spatter agglomerate (B), Caldera beach.
10	8749	Black scoria. Scoria-flow deposit (B), Cape Therma.
11	8613	Black scoria. Scoria-flow deposit (B), Cape Plaka.
12	8830	Grey pumice. Pumice fall (A), Cape Loumaravi.
13	8812	Five grey pumices. Pumice fall (A), Cape Alonaki.
14	8771	Several grey pumices. Pumice fall (A), Athinios.

Cape Therma 2

15	8820	Three white pumices. Middle fall unit, Cape Alonaki.
16	87105	Pumices, Athinios.
17	87104	Several grey pumices. Lowest 50 cm, Athinios.
18	LS100-91	Pumice, Athinios.
19	8776	Several white pumices. Upper fall unit, Athinios.
20	8787	Several white pumices. Lowest fall unit, Cape Katofira.
21	8789	Several white pumices. Middle fall unit, Cape Katofira.
22	8788	Several grey and banded pumices. Lowest fall unit, Cape Katofira.
23	8821	Two white pumices. Upper fall unit, Cape Alonaki.

Cape Therma 3

24	LS166-91	Scoria. Spatter agglomerate (B), Cape Plaka.
25	8646	Scoria. Scoria-flow deposit (B).
26	8751	Black scoria. Scoria-flow deposit (B), Cape Therma.
27	8784	Black scoria. Scoria-flow deposit (B), Cape Perivola.
28	8739	Black scoria. Scoria-flow deposit (B), Balos.
29	8734	Black scoria. Scoria-flow deposit (B), Caldera Beach.
30	8791	Black scoria. Lithic breccia (B), Cape Katofira.
31	8723	Grey pumice. Scoria-flow deposit (B), Cape Mavros.
32	8729	Two grey scoriae. Fall deposit (A), Caldera Beach.
33	8643	Grey scoria. Fall deposit (A), Cape Vounia.
34–36	8728	Grey scoria. Fall deposit (A), Caldera Beach.
37	8731	Black scoria. Scoria-flow deposit (B), Caldera Beach.
38	8640	Grey scoria. Fall deposit (A), Alonaki quarry.
39	87107	Obsidian chips. Fall deposit (A), Athinios.
40	8681	Obsidian clast. Fall deposit (A), Athinios.
41	8635	Grey scoria. Fall deposit (A), Athinios.

Lower Pumice 1

42	8642	Black scoria. lithic breccia (C), Alonaki quarry.
43	8736	Three scoria. Lithic breccia (C), Balos.
44	8676	Black scoria. Lithic breccia (C), Phira quarry.
45	S79-89	Scoria with admixed pumice. Lithic breccia (C) 100 m NE of Cape Mavros.
46	S82-14	Scoria. Lithic breccia (C) 800 m NE of Cape Mavros.
47	8697	Black scoria. Lithic breccia (C), Mavros Bay.
48	8692	Black scoria. Lithic breccia (C), Cape Loumaravi.
49	S82-15	Scoria. Lithic breccia (C) 800 m NE of Cape Mavros.
50	8684	Banded pumice. Lithic breccia (C), Athinios.
51	8649	Single grey pumice. Top of Plinian deposit (A), Cape Vounia.
52	8801	White pumice. Ignimbrite (B), Caldera Beach.
53	8691	White pumice. Ignimbrite (B), Cape Loumaravi.
54	8781	Obsidian chips. Base of ignimbrite (B), Cape Perivola.
55	S79-49	Pumice lapilli with rare mafic blebs. Plinian deposit (A) 100 m west of Cape Balos.
56	S82-8	White pumice. Plinian deposit (A) 100 m NE of Cape Mavros.
57	S80-170	Several white pumice lapilli. Base of Plinian deposit (A)100 m west of Cape Balos.
58	8662	Obsidian clast; Ignimbrite (B), Cape Perivola.
59	8696	Several white and banded pumices. Top of Plinian deposit (A), Mavros Bay.
60	LS159-91	Pumice. Plinian deposit (A), Balos.
61	S82-13	White pumice. Lithic breccia (C) 400 m NE of Cape Mavros.
62	S82-12	White pumice with mafic blebs. Lithic breccia (C) 400 m NE of Cape Mavros.

Lower Pumice 2

63	8636	Grey scoria. Top of Plinian deposit (A), Athinios.
64	8616A	Several grey scoriae. Top of Plinian deposit (A), Cape Plaka.
65	S80-276	Several grey scoria clasts. Top of Plinian deposit (A), Athinios.

66	8742	Scoria. Lithic breccia (D), Cape Plaka.
67	8659	Several grey scoriae. Top of Plinian deposit (A), Cape Katofira.
68	LS99-91	Grey scoria. Plinian deposit (A), Athinios.
69–70	8743	Scoria. Lithic breccia (D), Cape Plaka.
71	8616B	Several grey scoriae. Top of Plinian deposit (A), Cape Plaka.
72	8655	Grey scoria. Top of Plinian deposit (A), Cape Katofira.
73	8660	Banded pumice. Top of Plinian deposit (A), Cape Katofira.
74	S82-107	Banded pumice. Middle of Plinian deposit (A), Athinios.
75	S82-109	Banded pumice with abundant mafic blebs. Middle of Plinian deposit (A), Athinios.
76	8656	White pumice. Middle Plinian deposit (A), Cape Katofira.
77	8673	Grey pumice. Top of Plinian deposit (A), Phira quarry.
78	S80-273	Several white pumice lapilli. Base of Plinian deposit (A), Athinios.
79	S82-106	White pumice with abundant mafic blebs. Top of Plinian deposit (A), Athinios.
80	8654	White pumice. Middle Plinian deposit (A), Cape Katofira.
81	8650	White pumice. Top of Plinian deposit (A), Cape Vounia.
82	LS103-91	Pumice. Plinian deposit (A), Athinios.
83	8666	White pumice. Ignimbrite (B), Cape Perivola.
84	S82-111	Cream-coloured pumice. Massive tuff unit (C), Athinios.
85	S82-112	Cream-coloured pumice with obsidian streaks. Massive tuff unit (C), Athinios.
86	8652	White pumice. Top of ignimbrite (B), Cape Vounia.
87	LS13-91	Pumice. Upper part of Plinian deposit (A), Cape Plaka.
88	S82-10	White pumice with rare mafic blebs. Surge deposit (B) 400 m NE of Cape Mavros.
89	LS55-91	Pumice. Base of Plinian deposit (A), Cape Plaka.
90	S82-9	White pumice. Surge deposit (B) 400 m NE of Cape Mavros.
91	S82-110	Cream-coloured pumice. Massive tuff unit (C), Athinios.
92	8629	White pumice. Massive tuff unit (C), Balos.
93	S82-108	White pumice with rare mafic blebs. Middle of Plinian deposit (A), Athinios.
94	S79-69	Cream-coloured pumice. Top of surge deposits (B), 100 m west of Cape Balos.
95	LS61-91	Pumice. 1 m from top of massive tuff unit (C), Cape Plaka.
96	LS58-91	Pumice. Massive tuff unit (C), Cape Plaka.

Cape Thera

97	8632	Grey pumice. Lower part of pumice fall (A), Phira quarry.
98	85074	Dark pumice. Upper part of pumice fall (A), Armeni, Oia.
99	87075	Scoria. Upper part of pumice fall (A), Armeni, Oia.
100	8640	Scoria. Top of upper flow unit of scoria flow deposit (B), Cape Thera.
101	85073	Pumice. Lower part of pumice fall (A), Armeni, Oia.
102	86352	Dark pumice. Top of pumice fall (A), Phira quarry.
103	8637	Scoria. Upper part of scoria flow deposit (B), Phira quarry.
104	86351	Pumice. Top of pumice fall (A), Phira quarry.
105	8647	Scoria. Welded scoria flow deposit (B), Oia.
106	S79-126	Pink pumice. Scoria-flow deposit (B), Cape Thera.
107	8641	Scoria. Base of upper flow unit of scoria flow deposit (B), Cape Thera.
108	85063	Scoria. Scoria flow deposit (B), Armeni, Oia.
109	8638	Scoria. Upper part of scoria flow deposit (B), Phira quarry.
110	8633	Pumice. Pumice fall (A), Phira quarry.
111	LS125-91	Pumice. Pumice fall deposit (A), Thera quarry.
112	8636	Scoria. Scoria flow deposit (B), Phira quarry.
113	8634	Pumice. Pumice fall (A), Phira quarry.
114	8642	Scoria. Scoria flow deposit 10 m above sea level, Cape Thera.

Middle Pumice

115	S82-103	Black scoria with included lithic fragments. Pumice fall (C), Phira.
116	S82-102	Black scoria with included lithic fragments. Pumice fall (C), Phira.
117	S82-45	Black scoria. Top of Plinian deposit (A) (330 cm from base), Phira quarry.
118	S82-104	Black pumice. Lithic breccia (B), Athinios.
119	S82-92	Red scoria with lithic fragments. Agglomerate (B) 400 m east of Cape Akrotiri.
120	S82-44	Black scoria with mafic blebs. 310 cm from base of Plinian deposit (A), Phira quarry.
121	S82-114	Black scoria. Lithic breccia (B), Athinios.
122	S82-115	Black scoria. Lithic breccia (B), Athinios.
123	S82-105	Black scoria with lithic fragments. Lithic breccia (B), Phira.
124	S82-113	Black scoria. Lithic breccia (B), Athinios.
125	S82-93	Black scoria with lithic fragments. Lithic breccia (B) 400 m east of Cape Akrotiri.
126	S82-43	Black scoria with mafic blebs. 250 cm from base of Plinian deposit (A), Phira quarry.
127	S80-244	Red scoria. Spatter agglomerate (B) 400 m east of Cape Akrotiri.
128	S80-41	Greenish pumice. Ignimbrite (B), Cape Kokkinopetra.
129	S80-240	Black scoria with lithic fragments. Lithic breccia (B), Athinios.
130	LS177-91	Pumice. Top of lithic breccia (B), Akrotiri quarry.
131	S82-42	Brown pumice with banding. 180 cm from base of Plinian deposit (A), Phira quarry.
132	S82-41	Brown pumice with banding. 110 cm from base of Plinian deposit (A), Phira quarry.
133	S82-40	Brown pumice. 30 cm from base of Plinian deposit (A), Phira pumice quarry.
134	S82-39	Brown pumice with banding. 60 cm from base of Plinian deposit (A), Phira quarry.

Vourvoulos

135	861	Scoria. Lithic breccia (B), south of Manolas.
136	86101	Scoria. Scoria flow deposits (B), Phira quarry.
137	85010	Obsidian fragments. Top of pumice fall (A), Phira quarry.
138	8651	Obsidian fragments. Top of pumice fall (A), Phira quarry.
139	8698	Brown pumice. 30 cm above base of pumice fall, Cape Perivola.
140	85008	Pumice. Central part of pumice fall (A), Phira quarry.
141	85068	Pumice. Central part of pumice fall (A), Oia.
142	LS131-91	Pumice. Pumice fall deposit (A), Thera quarry.
143	8697	Pumice. Base of pumice fall, Cape Perivola.

144	85007	Pumice. Basal 10 cm of pumice fall (A), Phira quarry.
145	8652	Grey pumice. 50 cm from base of pumice fall, Oia.
Upper Scoriae 1		
146	85233	Scoria. Agglomerate (C), Cape Mavros.
147	85020	Scoria. Upper part of fall deposit, Phira quarry.
148	85022	Scoria. Top of fall deposit, Phira quarry.
149	LS134-91	Scoria. Upper part of fall deposit, Thera quarry.
150	LS9-91	Scoria. Spatter agglomerate, Akrotiri quarry.
151	85024	Scoria. Scoria flow deposit (C), Phira quarry.
152	8303	Scoria. Agglomerate (C), Cape Kokkinopetra.
153	860	Scoria. Scoria flow deposit (B) 1 km east of the Akrotiri excavations.
154	S79-10	Red scoria. Agglomerate (C) 400 m east of Cape Akrotiri.
155	85023	Scoria. Lithic breccia (B), Phira quarry.
156	85110	Scoria. Lithic breccia (C), Alonaki quarry.
157	85019	Grey pumice. Upper part of fall deposit, Phira quarry.
158	85016	Grey pumice. Lower part of fall deposit, Phira quarry.
159	85014	Pumice. Fall deposit (A), Phira quarry.
Upper Scoriae 2		
160	S82-101	Red scoria. Welded agglomerate (D), Cape Tourlos.
161	85106	Scoria. Lithic breccia (D), Alonaki quarry.
162	85048	Scoria. Lithic breccia (C), Phira quarry.
163	85196	Scoria. Unit C.
164	84004	Oxidized spatter. Top of agglomerate (D), Ammoudi.
165	8621	Scoria. Scoria deposit (B), Aspronisi.
166	85241	Scoria. Scoria flow deposit (D), Oia.
167	85038	Scoria. Lithic-rich deposit (B), Alonaki quarry.
168	S79-113	Green scoria. Scoria fall (B), Akrotiri quarry.
169	85138	Scoria. Welded agglomerate (D), Cape Tourlos.
170	84001	Oxidized spatter. Base of agglomerate (D), Ammoudi.
171	8622	Scoria. Base of scoria deposit (B), Aspronisi.
172	84002	Oxidized spatter. 10 m above base of agglomerate (D), Ammoudi.
173	85069	Dark spatter, base of agglomerate (D), Oia.
174	85052	Scoria. Lithic breccia (C), Phira quarry.
175	LS184-91	Scoria. Spatter agglomerate (C), Oia.
176	8667	Scoria. Nonwelded base of welded agglomerate (D), Cape Tourlos.
177	84003	Oxidized spatter. 20 m below top of agglomerate (D), Ammoudi.
178	8668	Scoria. 50 cm above base of welded agglomerate (D), Cape Tourlos.
179	85042	Scoria. Lithic breccia (C), Alonaki quarry.
180	LS174-91	Scoria. Scoria flow deposit (B), Akrotiri quarry.
181	8623	Pumice. Base of pumice fall deposit (A), Aspronisi.
182	8666	Pumice. Centre of pumice fall deposit (A), Cape Tourlos.
183	85044	Pumice. Pumice fall deposit (A), Phira quarry.
Cape Riva		
184	S82-73	Scoria. Plinian deposit (A), Therasia quarry.
185	S82-54	Green scoria with admixed white pumice. Plinian deposit (A), Ammoudi.
186	S80-145	Green scoria with admixed white pumice. Plinian deposit (A), Ammoudi.
187	S82-53	Banded pumice. 240 cm from base of Plinian deposit (A), Ammoudi.
188	S82-55	Banded pumice. Plinian deposit (A), Ammoudi.
189	LS77-91	Scoria. Pumice fall deposit (A).
190	LS183-91	Banded pumice. 5 m from top of pumice fall deposit (A), Oia.
191	S82-72	Banded pumice with lithic fragments. Plinian deposit (A), Therasia quarry.
192	S82-67	Banded pumice. Base of welded ignimbrite (B) 1 km east of Cape Balos.
193	S80-11	Several brown pumice lapilli. Welded ignimbrite (B) 1 km east of Cape Balos.
194	S82-69	Brown pumice with mafic blebs. Welded ignimbrite (B) 1 km east of Cape Balos.
195	S82-66	White pumice with mafic blebs. Welded ignimbrite (B) 1 km east of Cape Balos.
196	S82-68	Brown pumice with mafic blebs. Welded ignimbrite (B) 1 km east of Cape Balos.
197	LS149-91	Pumice. Ignimbrite (B), Balos.
198	S82-23	Brown pumice. Welded ignimbrite (D) 600 m SW of Cape Colombos.
199	S82-65	Brown pumice. Top of welded ignimbrite (B) 600 m east of Cape Balos.
200	S82-60	Brown pumice. Welded ignimbrite (D), Oia.
201	S82-24	Brown pumice. Welded ignimbrite (D) 600 m SW of Cape Colombos.
202	LS66-91	Pumice. Pumice fall deposit (A), Oia.
203	S82-62	Brown pumice. Thin ignimbrite lens in lithic breccia (C), Ammoudi.
204	S82-21	Several brown pumices. Welded ignimbrite (B), Cape Tourlos.
205	S82-50	White pumice. 200 cm from base of Plinian deposit (A), Ammoudi.
206	S82-52	White pumice. 290 cm from base of Plinian deposit (A), Ammoudi.
207	S80-142	Several brown pumices. Lithic breccia (C), 1 km north of Cape Ayios Nikoloas.
208	S80-185	White pumice. Welded ignimbrite (D), Megalo Vouno.
209	S80-278	Two pink pumices. Base of welded ignimbrite (B) 1 km east of Cape Balos.
210	S82-51	White pumice. 340 cm from base of Plinian deposit, Ammoudi.
211	S80-143	Pink pumice with mafic blebs. Plinian deposit (A), Ammoudi.
212	S82-49	White pumice. 70 cm from base of Plinian deposit (A), Ammoudi.
213	S82-84	White pumice. Ignimbrite (C), Cape Loumaravi.
214	S82-88	White pumice. Lithic breccia (C), Cape Loumaravi.
215	S82-75	Brown pumice. Lithic breccia (C), 700 m west of Cape Tinos.
216	S80-136	Several white pumice lapilli. Lithic breccia (C), 1 km north of Cape Ayios Nikoloas.
Minoan		
217	S82-27	Crystal-rich pumice. Plinian deposit (A), Phira quarry.
218	S80-25a	Crystal-rich pumice. Plinian deposit (A), Phira quarry.
219	S82-33	Crystal-rich pumice. Plinian deposit (A), Phira quarry.
220	S80-23	Crystal-rich pumice. Plinian deposit (A), Phira quarry.
221	S80-22a	Three grey cauliform scoria clasts. Plinian deposit (A), Phira quarry.

222	S80-22b	Grey cauliform scoria. Plinian deposit (A), Phira quarry.
223	S80-26	Two crystal-rich pumice clasts. Plinian deposit (A), Phira quarry.
224	S82-26	Crystal-rich pumice. Plinian deposit (A), Phira quarry.
225	LS124-91	Grey scoria. Plinian deposit (A) Cape Plaka.
226	S82-34a	Crystal-rich pumice. Plinian deposit (A), Phira quarry
227	S80-24	Crystal-rich pumice. Plinian deposit (A), Phira quarry.
228	S80-25b	Crystal-rich pumice. Plinian deposit (A), Phira quarry.
229	S82-31	White pumice with banding. Plinian deposit (A), Phira quarry.
230	S82-3	White pumice. Ignimbrite (D) 1 km west of Monolithos.
231	LS112-91	Pumice. 60 cm below top of surge deposit (B), Cape Plaka.
232	S82-28	White pumice. Base of Plinian deposit (A), Phira quarry.
233	S80-29	Two white pumice lapilli with mafic blebs. Top of Plinian deposit (A), Phira quarry.
234	S82-30	White pumice. Middle of Plinian deposit (A), Phira quarry.
235	S82-11	White pumice. Ignimbrite (D) 1 km west of Monolithos.
236	S82-2	While pumice. Ignimbrite (D) 1 km west of Monolithos.
237	S79-101	Several pumice lapilli. Ignimbrite (D) 600 m east of Cape Mavrorachidi.
238	LS118-91	Pumice. 12 m above base of massive tuff (C), Cape Plaka.
239	S82-78	White pumice. Massive tuff (C), Therasia quarry 500 m east of Cape Kiminon.
240	LS172-91	Pumice. Ignimbrite (D), Akrotiri excavations.
241	S80-119	White pumice. Surge deposit (B), Cape Therma.
242	S80-28	White pumice with mafic blebs. Basal 1 m of Plinian deposit (A), Phira quarry.
243	S82-1b	White pumice. Ignimbrite (D) 1 km west of Monolithos.
244	LS121-91	Pumice. 18 m above base of massive tuff (C), Cape Plaka.
245	LS104-91	Pumice. 75 cm above base of Plinian deposit (A), Cape Plaka.
246	S82-34b	White pumice. Top of surge deposit (B), Phira quarry.
247	LS108-91	Pumice. 280 cm above base of Plinian deposit (A), Cape Plaka.

Table A2.1. *Chemical analyses of juvenile components of the Thera pyroclastics*

Eruption	Cape Therma 1													
Analysis	1	2	3	4	5	6	7	8	9	10	11	12	13	14
Sample	8747	8813	8773	8772	8726	8725	LS155-91	8611	8748	8749	8613	8830	8812	8771
Unit	B	B	B	B	B	B	B	B	B	B	B	A	A	A
Major elements recalculated dry (wt%)														
SiO_2	59.3	60.0	60.0	60.1	60.3	60.5	60.5	60.7	60.7	61.0	61.0	61.8	62.1	62.5
Al_2O_3	15.6	16.4	16.4	16.5	16.2	16.4	16.4	16.3	16.6	16.4	16.2	15.3	15.8	16.1
TiO_2	0.95	0.98	0.97	0.97	1.03	1.01	1.03	0.98	1.04	1.01	1.00	1.09	1.06	1.06
FeO(T)	6.35	6.83	6.84	6.59	6.93	6.88	5.99	6.72	6.46	6.75	6.76	6.45	6.51	6.27
MgO	2.74	2.97	3.07	3.32	2.78	2.57	2.67	2.70	2.48	2.50	2.64	1.94	2.27	2.09
CaO	8.32	6.19	6.23	6.43	5.92	5.80	5.83	5.81	5.72	5.65	5.73	5.05	4.82	4.83
Na_2O	4.49	4.53	4.35	3.99	4.54	4.43	4.61	4.43	4.82	4.45	4.29	5.35	4.84	4.47
K_2O	1.92	1.80	1.82	1.75	2.00	2.03	1.93	2.04	1.84	1.90	2.01	2.64	2.16	2.28
MnO	0.17	0.17	0.14	0.14	0.15	0.17	0.16	0.16	0.12	0.17	0.13	0.14	0.18	0.20
P_2O_5	0.21	0.20	0.21	0.19	0.16	0.21	0.21	0.22	0.20	0.20	0.20	0.26	0.23	0.22
Trace elements (ppm)														
Ba	344	296	331	317	370	414	335	379	391	388	354	352	349	417
Ce	40	27	61	51	64	70	78	51	56	41	46	58	37	32
Cr	21	37	23	54	23	17	30	32	21	23	15	32	18	25
La	32	24	31	24	27	24	24	23	16	23	31	23	17	33
Ni	13	7	2	17	19	16	9	13	15	11	14	12	9	12
Nb	11	12	9	10	8	8	10	11	10	8	9	4	7	11
Rb	63	57	62	62	71	66	71	71	62	72	72	92	70	78
Sr	195	207	203	195	217	210	207	199	211	204	205	180	195	197
Th	15	11	11	8	9	13	16	14	9	13	11	17	14	15
V	82	100	110	75	106	77	96	93	71	90	103	73	73	57
Y	40	39	41	39	40	44	43	42	42	41	47	48	42	46
Zr	202	197	200	202	207	223	223	232	225	226	216	247	232	242

Eruption	Cape Therma 2						Cape Therma 3							
Analysis	15	16	17	18	19	20	21	22	23	24	25	26	27	28
Sample	8820	87105	87104	LS100-91	8776	8787	8789	8788	8821	LS166-91	8646	8751	8784	8739
Unit										B	B	B	B	B
Major elements recalculated dry (wt%)														
SiO_2	69.0	69.1	69.2	69.4	69.5	69.5	69.5	69.6	69.9	60.8	60.8	60.9	61.0	61.0
Al_2O_3	14.8	15.1	15.3	14.9	15.1	15.4	15.1	15.4	14.6	16.1	16.3	16.1	16.1	16.0
TiO_2	0.70	0.61	0.62	0.62	0.64	0.64	0.65	0.63	0.64	1.15	1.13	1.17	1.16	1.13
FeO(T)	3.65	3.19	3.24	2.93	3.26	3.34	3.32	3.29	3.36	6.25	6.97	6.99	7.05	6.98
MgO	0.97	0.79	0.79	0.87	0.73	0.82	0.74	0.69	0.72	2.35	2.32	2.31	2.26	2.34
CaO	2.54	2.43	2.35	2.41	2.33	2.37	2.17	2.31	2.18	5.27	5.30	5.21	5.26	5.34
Na_2O	4.94	5.15	4.93	4.99	4.74	4.28	4.89	4.58	4.77	4.72	4.33	4.51	4.40	4.30
K_2O	3.17	3.37	3.40	3.31	3.50	3.44	3.42	3.34	3.49	2.35	2.44	2.36	2.49	2.51
MnO	0.11	0.13	0.08	0.12	0.13	0.10	0.10	0.10	0.14	0.14	0.13	0.14	0.16	0.14
P_2O_5	0.17	0.13	0.12	0.13	0.11	0.14	0.12	0.11	0.13	0.27	0.28	0.26	0.26	0.28
Trace elements (ppm)														
Ba	472	540	522	515	523	544	517	541	503	391	443	403	409	416
Ce	52	53	54	76	66	79	36	78	43	58	65	60	56	58
Cr	8	5	6	10	3	10	11	6	3	23	19	20	5	12
La	30	23	17	37	31	35	36	36	34	26	36	30	19	27
Ni	12	7	11	5	8	9	9	8	13	4	0	12	9	11
Nb	5	14	13	14	16	14	12	15	3	12	10	16	12	12
Rb	104	111	113	104	115	119	116	120	108	96	90	87	91	91
Sr	125	116	122	110	115	119	111	118	108	181	185	191	187	191
Th	18	21	18	18	24	13	19	22	22	16	14	14	20	14
V	28	21	23	24	31	22	25	26	24	89	99	108	115	114
Y	51	56	57	55	54	51	54	54	51	51	45	48	48	45
Zr	284	316	327	299	318	308	319	328	302	248	256	249	235	239

(*continued*)

Table A2.1. (*continued*)

Eruption	Cape Therma 3												
Analysis	29	30	31	32	33	34	35	36	37	38	39	40	41
Sample	8734	8791	8723	8729	8643	8728i	8728ii	8728iii	8731	8640	87107	8681	8635
Unit	B	B	B	A	A	A	A	A	A	A	A	A	A
Major elements recalculated dry (wt%)													
SiO_2	61.1	61.1	61.9	62.6	62.8	63.3	63.5	63.6	63.8	64.1	64.3	64.4	64.8
Al_2O_3	16.0	16.1	15.9	16.2	16.0	15.9	15.4	15.9	15.8	15.6	15.7	15.8	15.4
TiO_2	1.15	1.15	1.13	1.09	1.06	1.07	1.06	1.02	1.01	0.98	0.97	0.97	0.98
FeO(T)	7.05	7.02	6.90	6.48	6.36	6.20	6.29	6.10	5.95	5.76	5.75	5.78	5.75
MgO	2.27	2.30	1.96	1.70	1.74	1.59	1.62	1.56	1.45	1.46	1.38	1.29	1.40
CaO	5.15	5.16	4.65	4.44	4.51	4.10	4.08	4.03	3.95	3.91	3.69	3.64	3.59
Na_2O	4.46	4.43	4.58	4.52	4.49	4.60	4.75	4.64	4.77	4.85	4.81	4.75	4.63
K_2O	2.43	2.40	2.57	2.57	2.67	2.77	2.85	2.80	2.82	2.90	2.95	2.95	3.03
MnO	0.13	0.14	0.15	0.16	0.17	0.15	0.15	0.15	0.15	0.16	0.15	0.14	0.14
P_2O_5	0.30	0.29	0.24	0.26	0.25	0.25	0.25	0.26	0.24	0.26	0.25	0.25	0.27
Trace elements (ppm)													
Ba	412	404	390	442	445	470	427	460	484	456	500	486	491
Ce	70	62	20	39	46	33	61	54	63	56	46	60	61
Cr	8	15	17	19	11	10	10	5	14	10	11	16	bd
La	28	30	47	31	37	33	19	22	38	28	31	34	31
Ni	7	8	11	10	7	10	11	12	10	10	7	8	11
Nb	12	12	6	13	12	13	6	14	13	12	15	17	15
Rb	90	90	97	95	97	104	100	100	114	109	110	112	110
Sr	188	191	197	178	185	174	174	178	179	174	167	167	162
Th	21	17	19	17	17	18	20	19	19	17	19	21	24
V	116	111	88	71	68	55	62	57	51	43	45	46	45
Y	48	51	47	46	52	50	50	53	53	50	56	51	50
Zr	243	237	253	270	na	280	261	288	295	297	309	298	273

Eruption	Lower Pumice 1														
Analysis	42	43	44	45	46	47	48	49	50	51	52	53	54	55	56
Sample	8642	8736	S79-89	S82-14	S82-14	8697	8692	S82-15	8684	8649	8801	8691	8781	S79-49	S82-8
Unit	C	C	C	C	C	C	C	C	C	A	B	B	C	B	A
Major elements recalculated dry (wt%)															
SiO_2	53.5	53.8	53.9	54.4	55.8	57.9	58.0	58.1	62.3	66.3	66.8	67.2	68.1	68.4	68.4
Al_2O_3	18.9	19.6	19.0	19.7	17.6	17.7	17.7	17.9	16.9	15.6	14.9	15.1	15.4	15.0	15.0
TiO_2	1.32	1.20	1.28	1.20	1.75	1.24	1.08	1.04	0.84	0.71	0.64	0.54	0.58	0.54	0.56
FeO(T)	8.24	7.92	8.05	7.50	7.92	6.97	6.91	6.78	5.56	4.37	4.94	3.61	3.91	3.72	3.66
MgO	3.76	3.40	3.53	3.06	3.13	2.68	2.94	2.80	1.94	1.11	1.15	0.76	0.71	0.84	0.74
CaO	9.37	9.41	9.27	9.32	7.07	7.14	7.43	7.24	5.31	3.01	3.45	3.87	2.44	2.41	2.14
Na_2O	3.56	3.40	3.60	3.44	4.67	4.38	3.95	4.08	4.62	5.86	4.54	5.28	5.46	5.50	5.91
K_2O	0.86	0.90	0.90	0.96	1.13	1.55	1.52	1.60	2.23	2.67	3.31	3.38	3.15	3.36	3.46
MnO	0.15	0.14	0.18	0.16	0.22	0.16	0.12	0.15	0.13	0.17	0.11	0.13	0.12	0.14	0.12
P_2O_5	0.31	0.23	0.29	0.32	0.71	0.37	0.26	0.21	0.19	0.21	0.17	0.11	0.13	0.14	0.11
Trace elements (ppm)															
Ba	201	215	211	180	257	278	266	321	404	467	393	482	507	494	471
Ce	21	29	18	37	38	54	49	33	27	44	43	80	54	65	49
Cr	22	24	33	18	15	14	22	21	33	16	13	18	bd	3	3
La	25	15	17	10	22	9	20	25	29	33	24	26	42	27	35
Ni	4	5	7	1	6	6	7	8	10	14	13	13	14	3	3
Nb	12	10	15	8	8	6	12	9	11	4	10	10	9	14	13
Rb	32	28	31	32	41	52	53	58	77	100	120	111	117	101	118
Sr	296	296	274	283	308	243	231	215	173	143	135	106	117	110	105
Th	8	7	4	7	9	10	13	12	14	22	24	15	25	27	16
V	185	169	162	187	123	102	129	145	77	35	27	19	24	13	23
Y	27	26	27	33	46	39	35	40	43	51	51	52	58	56	58
Zr	95	99	115	104	130	153	145	171	227	284	276	310	321	310	345

(*continued*)

Table A2.1. (*continued*)

Eruption	Lower Pumice 1						Lower Pumice 2							
Analysis	57	58	59	60	61	62	63	64	65	66	67	68	69	70
Sample	S80-170	8662	8696	LS159-91	S82-13	S82-12	8636	8616A	S80-276	8742	8659	LS00-91	8743i	8743ii
Unit	A	B	A	A	C	C	A	A	A	D	A	A	D	D
Major elements recalculated dry (wt%)														
SiO_2	68.4	68.6	68.8	69.2	69.4	69.6	47.4	48.8	51.8	54.7	54.9	55.0	55.1	55.5
Al_2O_3	14.7	15.3	15.2	15.1	15.3	15.3	17.7	19.6	18.3	18.5	17.1	17.2	18.4	18.1
TiO_2	0.50	0.56	0.56	0.53	0.58	0.57	0.30	0.45	0.83	1.11	1.12	1.07	1.07	1.06
FeO(T)	3.52	3.76	3.67	3.29	3.80	3.87	6.54	5.90	7.78	7.90	8.38	7.17	7.86	7.87
MgO	0.83	0.62	0.62	0.71	0.67	0.67	11.29	8.07	6.54	3.73	4.31	4.71	3.66	3.60
CaO	2.17	2.27	2.20	2.09	2.23	2.38	15.35	15.25	11.05	9.12	8.82	8.68	8.96	8.78
Na_2O	6.21	5.50	5.26	5.22	4.41	4.13	1.10	1.58	2.82	3.54	4.04	3.98	3.47	3.62
K_2O	3.48	3.15	3.43	3.32	3.40	3.27	0.10	0.17	0.62	0.98	0.97	0.98	1.08	1.15
MnO	0.12	0.14	0.10	0.14	0.13	0.13	0.15	0.12	0.18	0.17	0.17	0.17	0.18	0.15
P_2O_5	0.11	0.12	0.11	0.11	0.10	0.11	0.03	0.04	0.17	0.22	0.24	0.24	0.22	0.18
Trace elements (ppm)														
Ba	423	523	516	493	514	536	48	84	133	247	199	242	250	243
Ce	58	55	65	73	56	59	0	0	19	40	bd	39	21	bd
Cr	4	10	9	16	7	11	188	79	89	36	62	38	37	28
La	21	32	39	33	31	38	bd	bd	3	10	11	9	21	13
Ni	bd	12	14	9	7	8	bd	bd	47	4	16	19	5	6
Nb	13	9	7	15	13	14	70	35	5	17	4	6	16	bd
Rb	103	123	117	112	124	117	1	7	16	32	26	26	35	37
Sr	111	114	107	98	109	111	200	238	256	268	260	239	258	251
Th	21	16	17	23	26	20	4	1	1	1	bd	8	6	4
V	13	22	17	20	28	27	97	114	203	161	182	160	162	192
Y	59	55	53	55	57	57	9	14	26	29	27	31	33	30
Zr	315	329	320	314	341	347	35	42	68	112	96	104	117	113

Eruption	Lower Pumice 2													
Analysis	71	72	73	74	75	76	77	78	79	80	81	82	83	84
Sample	8616B	8655	8660	S82-107	S82-109	8656	8673	S80-273	S82-106	8654	8650	LS103-91	8666	S82-111
Unit	A	A	A	A	A	A	A	A	A	A	A	A	B	C
Major elements recalculated dry (wt%)														
SiO_2	55.7	63.0	63.1	63.9	66.3	67.5	67.5	67.5	67.6	68.1	68.3	68.3	68.6	68.7
Al_2O_3	17.5	16.0	16.0	16.1	15.6	15.2	15.2	15.2	15.7	15.3	15.0	15.1	14.9	14.9
TiO_2	1.10	0.71	0.72	0.71	0.59	0.50	0.57	0.54	0.53	0.53	0.48	0.52	0.51	0.46
FeO(T)	7.76	5.09	5.21	5.05	4.25	3.75	3.97	3.72	3.85	3.53	3.26	3.24	3.77	3.04
MgO	4.03	2.22	2.21	2.09	1.48	1.26	1.19	1.13	1.22	0.84	0.90	0.95	0.94	0.66
CaO	8.25	5.03	5.23	4.52	3.68	3.03	2.84	3.90	2.97	2.72	2.18	3.50	2.58	2.53
Na_2O	4.10	5.67	5.04	5.13	5.01	5.67	5.52	4.79	4.88	5.75	6.54	4.76	5.18	6.06
K_2O	1.14	1.95	2.14	2.29	2.78	2.83	2.97	2.92	3.06	2.96	3.17	2.99	3.39	3.44
MnO	0.18	0.17	0.15	0.14	0.11	0.14	0.13	0.13	0.10	0.14	0.10	0.13	0.12	0.11
P_2O_5	0.27	0.21	0.18	0.15	0.13	0.12	0.12	0.16	0.10	0.12	0.11	0.16	0.10	0.11
Trace elements (ppm)														
Ba	267	390	385	407	460	467	408	451	489	477	460	432	424	529
Ce	18	30	54	42	57	34	59	49	44	44	38	70	47	56
Cr	56	22	21	12	11	12	13	6	12	9	16	16	11	7
La	16	23	25	22	29	23	32	26	23	26	43	33	28	30
Ni	6	8	10	10	6	13	8	2	6	14	11	6	8	3
Nb	15	16	11	10	12	11	11	12	12	9	3	12	11	11
Rb	29	67	65	74	93	91	93	79	99	90	96	88	99	111
Sr	244	166	157	151	124	113	123	126	114	113	116	110	106	93
Th	4	8	10	15	9	16	14	17	17	14	17	20	18	11
V	140	60	64	80	53	26	33	27	43	17	14	18	33	19
Y	31	45	44	45	51	52	51	58	49	53	55	52	52	57
Zr	119	217	226	234	287	284	268	272	298	281	297	276	294	331

(*continued*)

Table A2.1. (*continued*)

Eruption	Lower Pumice 2												Cape Thera	
Analysis	85	86	87	88	89	90	91	92	93	94	95	96	97	98
Sample	S82-112	8652	LS13-91	S82-10	LS55-91	S82-9	S82-110	8629	S82-108	S79-69	LS61-91	LS58-91	8632	85074
Unit	C	B	A	B	A	B	C	C	A	B	C	C	A	A
Major elements recalculated dry (wt%)														
SiO_2	69.0	69.0	69.2	69.3	69.3	69.4	69.5	69.5	69.6	70.3	70.3	70.8	61.1	61.2
Al_2O_3	14.9	15.0	14.6	15.0	15.3	15.0	15.2	15.2	15.4	14.9	14.7	14.8	15.6	15.6
TiO_2	0.44	0.46	0.46	0.49	0.51	0.47	0.46	0.45	0.49	0.45	0.42	0.43	1.16	1.16
FeO(T)	3.01	3.16	2.98	3.34	3.22	3.25	3.05	3.14	3.19	3.32	2.75	2.77	7.47	7.15
MgO	0.71	0.67	1.05	0.62	0.91	0.65	0.61	0.59	0.75	0.55	0.63	0.55	2.47	2.44
CaO	1.84	2.05	1.92	2.01	2.26	2.00	1.85	2.02	1.94	1.87	1.83	1.80	5.56	5.29
Na_2O	6.54	6.11	5.88	5.58	4.66	5.56	5.72	5.73	5.19	5.02	5.37	4.70	4.16	4.77
K_2O	3.39	3.34	3.40	3.44	3.20	3.47	3.42	3.26	3.24	3.38	3.50	3.67	2.06	2.00
MnO	0.11	0.11	0.12	0.12	0.13	0.11	0.09	0.10	0.11	0.12	0.11	0.10	0.16	0.17
P_2O_5	0.09	0.09	0.09	0.10	0.12	0.09	0.09	0.08	0.10	0.11	0.08	0.08	0.23	0.20
Trace elements (ppm)														
Ba	444	482	455	514	463	498	504	486	519	498	468	459	373	378
Ce	40	39	63	51	69	51	45	53	49	57	64	58	50	66
Cr	6	6	6	5	10	3	7	bd	bd	bd	9	9	8	6
La	22	45	26	29	27	30	29	31	28	27	21	35	25	21
Ni	8	12	2	5	7	6	8	11	bd	1	5	6	bd	bd
Nb	14	11	12	12	12	5	12	7	12	13	14	12	10	10
Rb	106	102	94	101	89	105	106	103	107	97	98	100	69	68
Sr	92	103	89	102	108	99	92	92	98	93	85	83	172	177
Th	16	17	20	23	18	19	23	19	20	19	23	17	13	11
V	20	15	16	24	21	15	18	9	22	5	16	9	146	139
Y	57	57	52	58	52	56	58	57	59	56	55	53	44	42
Zr	334	305	304	325	285	322	337	317	328	319	315	315	210	205

Eruption	Cape Thera													
Analysis	99	100	101	102	103	104	105	106	107	108	109	110	111	112
Sample	85075	8640	85073	86352	8637	86351	8647	S79-126	8641	85063	8638	8633	LS125-91	8636
Unit	A	B	A	A	B	A	B	B	B	B	B	A	A	B
Major elements recalculated dry (wt%)														
SiO_2	61.3	61.4	61.7	61.7	61.8	61.8	62.3	62.6	62.7	62.8	62.8	63.0	63.0	63.1
Al_2O_3	15.8	15.7	15.7	15.8	15.8	15.7	15.6	15.5	15.6	15.7	15.6	15.5	15.8	15.5
TiO_2	1.18	1.13	1.15	1.14	1.13	1.13	1.10	1.04	1.13	1.04	1.07	1.07	1.08	1.07
FeO(T)	7.20	7.25	7.12	7.16	7.20	7.17	6.85	6.36	7.02	6.45	6.64	6.64	6.03	6.60
MgO	2.43	2.30	2.29	2.23	2.21	2.24	2.18	2.22	2.16	2.00	2.00	1.93	2.09	1.92
CaO	5.29	5.38	5.18	5.25	5.11	5.19	4.94	4.29	5.02	4.63	4.76	4.77	4.83	4.69
Na_2O	4.49	4.40	4.42	4.20	4.32	4.20	4.41	5.06	3.97	4.81	4.43	4.41	4.54	4.45
K_2O	1.96	2.02	2.03	2.12	2.13	2.16	2.23	2.58	2.17	2.24	2.28	2.33	2.19	2.27
MnO	0.16	0.17	0.15	0.16	0.15	0.17	0.17	0.16	0.16	0.16	0.17	0.14	0.17	0.16
P_2O_5	0.22	0.22	0.20	0.22	0.23	0.25	0.23	0.24	0.23	0.21	0.22	0.24	0.23	0.24
Trace elements (ppm)														
Ba	365	349	407	356	388	373	379	315	381	401	391	387	368	384
Ce	44	61	55	47	52	66	65	58	66	53	39	63	68	61
Cr	0	10	5	7	6	6	5	11	4	0	4	0	18	0
La	19	28	22	26	33	27	27	22	26	27	34	35	27	22
Ni	bd	3	bd	bd	4	bd	bd	bd	bd	bd	4	bd	2	bd
Nb	10	9	10	10	11	10	12	11	11	12	11	12	11	11
Rb	70	72	71	69	72	72	76	72	74	80	77	78	73	78
Sr	174	174	170	172	167	169	163	153	166	164	160	161	160	158
Th	13	15	11	15	10	14	16	15	15	13	14	12	17	16
V	143	136	136	133	139	128	116	92	120	111	108	113	111	107
Y	41	44	43	45	45	44	47	51	44	43	45	45	47	48
Zr	208	219	210	220	224	216	230	239	228	230	234	234	233	241

(*continued*)

Table A2.1. (*continued*)

Eruption	Cape Thera		Middle Pumice											
Analysis	113	114	115	116	117	118	119	120	121	122	123	124	125	126
Sample	8634	8642	S82-103	S82-102	S82-45	S82-104	S82-92	S86-44	S82-114	S82-115	S82-105	S82-113	S82-93	S82-43
Unit	A	B	C	C	A	B	B	A	B	B	B	B	B	A
Major elements recalculated dry (wt%)														
SiO_2	63.1	63.5	62.4	62.4	62.7	62.9	62.9	62.9	63.0	63.1	63.1	63.1	63.2	63.4
Al_2O_3	15.5	15.4	15.9	15.9	16.0	16.1	15.7	15.9	16.1	16.1	16.0	16.2	15.8	15.8
TiO_2	1.07	1.05	1.07	1.05	1.09	1.03	1.04	1.03	1.04	1.01	1.02	1.02	1.03	1.00
FeO(T)	6.53	6.47	6.45	6.43	6.39	5.97	6.20	6.22	5.99	5.90	5.94	5.96	6.20	5.99
MgO	1.94	1.95	1.98	2.03	1.83	1.79	1.71	1.87	1.70	1.77	1.82	1.73	1.73	1.74
CaO	4.65	4.58	4.85	4.79	4.64	4.47	4.30	4.42	4.34	4.29	4.45	4.32	4.33	4.19
Na_2O	4.52	4.72	4.87	4.82	4.89	5.20	5.48	5.00	5.23	5.23	5.02	5.03	5.04	5.09
K_2O	2.32	1.91	2.13	2.12	2.10	2.21	2.27	2.27	2.22	2.21	2.27	2.25	2.26	2.35
MnO	0.14	0.16	0.15	0.17	0.16	0.15	0.16	0.14	0.15	0.15	0.15	0.15	0.16	0.16
P_2O_5	0.25	0.24	0.25	0.25	0.27	0.25	0.23	0.24	0.27	0.26	0.25	0.25	0.24	0.23
Trace elements (ppm)														
Ba	401	406	388	419	391	400	391	379	423	408	393	391	423	389
Ce	57	54	51	42	36	46	49	41	52	47	59	59	48	42
Cr	8	0	8	6	9	4	9	12	4	6	6	8	bd	11
La	21	33	21	22	24	27	21	32	21	26	29	21	21	24
Ni	bd	3	8	11	7	bd	9	2	3	bd	3	5	bd	4
Nb	10	10	11	9	11	12	11	10	10	9	11	11	11	11
Rb	77	74	83	83	79	85	82	83	87	83	84	87	87	85
Sr	159	156	174	175	178	171	166	170	173	165	168	171	170	168
Th	15	15	16	10	16	11	8	13	13	8	12	13	20	19
V	101	100	89	88	85	84	76	82	81	78	82	78	82	73
Y	46	49	52	54	55	53	52	56	54	54	56	55	51	56
Zr	237	245	250	253	249	257	262	266	272	261	264	272	271	271

Eruption	Middle Pumice								Vourvoulos					
Analysis	127	128	129	130	131	132	133	134	135	136	137	138	139	140
Sample	S80-244	S80-41	S80-240	LS177-91	S82-42	S82-41	S82-40	S82-39	861	86101	85010	8651	8698	85008
Unit	B	B	B	B	A	A	A	A	B	B	A	A	A	A
Major elements recalculated dry (wt%)														
SiO_2	63.5	63.7	63.7	63.9	64.9	65.0	65.4	65.4	56.8	57.8	62.6	63.3	65.4	65.4
Al_2O_3	15.6	15.8	15.8	15.9	15.6	15.6	15.5	15.6	15.7	15.5	15.4	15.0	14.9	15.1
TiO_2	1.01	1.00	0.97	1.01	0.86	0.88	0.85	0.85	1.49	1.41	1.10	1.00	0.84	0.81
FeO(T)	5.99	6.05	6.05	5.48	5.59	5.56	5.42	5.39	10.37	9.72	7.48	7.26	6.32	6.31
MgO	1.79	1.62	1.65	1.78	1.38	1.35	1.30	1.22	3.36	3.03	1.75	1.65	1.12	1.12
CaO	4.41	4.33	4.34	4.44	3.69	3.65	3.57	3.53	7.41	6.93	4.65	4.52	3.76	3.60
Na_2O	5.06	4.75	4.81	4.81	5.09	5.04	5.09	5.10	3.20	3.68	4.66	4.71	4.78	4.84
K_2O	2.26	2.29	2.29	2.30	2.55	2.52	2.57	2.61	1.29	1.51	1.99	2.17	2.49	2.50
MnO	0.18	0.18	0.17	0.16	0.16	0.17	0.16	0.15	0.18	2.20	0.16	0.16	0.17	0.18
P_2O_5	0.26	0.25	0.26	0.26	0.21	0.22	0.20	0.20	0.19	0.19	0.26	0.25	0.23	0.19
Trace elements (ppm)														
Ba	325	338	355	354	437	426	403	410	206	292	376	364	413	411
Ce	62	48	47	63	51	48	48	46	36	25	68	58	71	68
Cr	5	8	9	11	8	6	8	6	16	11	4	0	4	0
La	20	23	17	18	21	29	30	28	18	18	19	23	32	25
Ni	bd	3	bd	5	8	6	9	bd	3	3	bd	bd	bd	bd
Nb	10	9	11	11	12	11	12	11	7	7	10	10	12	11
Rb	71	75	74	80	94	93	91	93	51	52	77	77	85	88
Sr	168	163	165	164	154	153	151	150	197	188	176	163	146	150
Th	14	14	9	17	15	15	19	15	8	10	12	10	14	16
V	59	60	67	66	62	53	56	53	296	260	84	71	46	40
Y	55	55	54	51	58	59	62	59	41	43	58	53	60	62
Zr	250	245	247	254	283	290	300	298	170	181	250	259	285	292

(*continued*)

Table A2.1. (*continued*)

Eruption	Vourvoulos					Upper Scoriae 1								
Analysis	141	142	143	144	145	146	147	148	149	150	151	152	153	154
Sample	85068	LS131-91	8697	85007	8652	85233	85020	85022	LS134-91	LS9-91	85024	8303	860	S79-10
Unit	A	A	A	A	A	C	A	A	A	C	C	C	B	C
Major elements recalculated dry (wt%)														
SiO_2	65.6	65.6	65.8	65.8	65.9	58.1	58.3	58.4	58.6	58.6	58.6	58.7	58.7	58.8
Al_2O_3	14.8	14.8	14.8	15.1	14.8	16.0	16.0	16.0	15.9	15.9	16.1	15.9	15.7	15.8
TiO_2	0.77	0.83	0.80	0.79	0.79	1.27	1.32	1.33	1.31	1.33	1.27	1.31	1.34	1.29
FeO(T)	6.23	5.71	6.46	6.21	6.44	8.81	8.96	8.99	7.95	8.00	8.69	8.84	8.95	8.78
MgO	1.12	1.06	1.02	1.06	1.02	2.90	2.90	2.92	2.81	2.85	2.91	2.77	2.82	2.92
CaO	3.49	3.57	3.59	3.47	3.52	6.62	6.55	6.56	6.46	6.43	6.29	6.39	6.45	6.34
Na_2O	4.96	4.89	4.58	4.80	4.57	4.76	4.20	4.21	4.23	4.22	4.23	4.42	4.08	4.28
K_2O	2.63	2.47	2.53	2.54	2.64	1.25	1.37	1.38	1.42	1.39	1.45	1.37	1.52	1.33
MnO	0.19	0.19	0.19	0.17	0.16	0.19	0.20	0.22	0.19	0.18	0.19	0.18	0.19	0.20
P_2O_5	0.20	0.21	0.22	0.20	0.22	0.19	0.20	0.19	0.21	0.21	0.20	0.19	0.19	0.24
Trace elements (ppm)														
Ba	430	394	419	420	417	262	217	229	285	289	239	224	300	261
Ce	43	58	53	55	75	40	48	45	53	52	57	54	25	44
Cr	0	10	0	0	0	7	8	8	23	16	7	8	6	11
La	22	20	28	30	25	17	16	13	7	21	11	15	24	11
Ni	bd	5	bd	bd	2	5	bd	bd	5	3	bd	2	4	3
Nb	9	11	11	12	11	8	7	7	7	8	9	6	8	7
Rb	87	83	85	92	87	49	48	51	47	45	55	52	52	55
Sr	142	141	141	146	137	192	203	205	194	195	205	197	194	202
Th	17	15	16	16	17	7	10	10	10	10	10	10	10	2
V	31	30	41	30	42	174	191	198	173	172	175	178	171	175
Y	59	61	60	61	59	40	44	44	44	45	45	42	43	51
Zr	274	284	288	289	289	167	176	179	182	181	189	174	179	189

Eruption	Upper Scoriae 1					Upper Scoriae 2								
Analysis	155	156	157	158	159	160	161	162	163	164	165	166	167	168
Sample	85023	85110	85019	85016	85014	S82-101	85106	85048	85196	84004	8621	85241	85038	S79-113
Unit	B	C	A	A	A	D	D	C	C	D	B	D	B	C
Major elements recalculated dry (wt%)														
SiO_2	58.9	59.0	59.0	59.7	63.2	58.3	58.4	58.6	58.6	58.8	58.8	59.1	59.1	59.2
Al_2O_3	16.0	15.8	16.0	15.7	15.5	16.2	16.0	16.1	16.1	16.1	15.8	15.6	16.0	15.9
TiO_2	1.31	1.31	1.27	1.23	1.01	1.32	1.32	1.28	1.29	1.25	1.32	1.22	1.25	1.24
FeO(T)	8.62	8.81	8.77	8.65	7.20	8.78	8.77	8.62	8.62	8.16	8.84	8.31	8.35	8.20
MgO	2.86	2.73	2.77	2.60	1.58	2.90	3.03	2.90	2.95	2.71	2.96	2.67	2.80	2.71
CaO	6.35	6.31	6.28	6.09	4.48	6.51	6.64	6.52	6.52	6.29	6.55	6.42	6.27	6.22
Na_2O	4.17	4.24	4.01	4.06	4.65	4.13	3.95	4.22	3.99	4.70	3.74	4.41	4.22	4.39
K_2O	1.48	1.44	1.45	1.52	1.96	1.49	1.49	1.49	1.54	1.63	1.60	1.66	1.62	1.69
MnO	0.18	0.18	0.19	0.18	0.18	0.20	0.18	0.17	0.17	0.17	0.17	0.16	0.17	0.21
P_2O_5	0.18	0.20	0.20	0.21	0.26	0.23	0.20	0.19	0.19	0.21	0.23	0.24	0.20	0.24
Trace elements (ppm)														
Ba	257	255	261	324	370	322	201	220	212	271	287	277	286	238
Ce	40	55	44	56	56	48	41	43	49	46	48	30	44	44
Cr	13	7	6	6	4	12	6	11	5	15	7	0	4	15
La	12	16	19	13	28	18	19	21	20	12	22	11	13	16
Ni	bd	bd	bd	bd	bd	3	3	bd	bd	2	6	bd	2	1
Nb	7	6	8	8	10	7	7	8	8	7	8	9	7	8
Rb	52	51	53	55	70	67	58	60	61	bd	60	57	65	61
Sr	204	199	202	193	177	189	189	196	187	181	183	183	185	183
Th	11	8	9	12	12	5	11	11	8	13	13	14	8	9
V	179	172	182	171	69	170	211	200	200	144	199	174	183	202
Y	41	45	44	44	57	42	42	42	42	43	40	43	43	47
Zr	179	178	187	191	244	199	180	187	180	200	188	197	189	201

(*continued*)

Table A2.1. (*continued*)

Eruption	Upper Scoriae 2														
Analysis	169	170	171	172	173	174	175	176	177	178	179	180	181	182	183
Sample	85138	84001	8622	84002	85069	85052	LS184-91	88667	84003	8668	85042	LS174-91	8623	8666	85044
Unit	D	D	B	D	D	C	D	D	D	D	C	B	A	A	A
Major elements recalculated dry (wt%)															
SiO_2	59.2	59.3	59.5	59.5	59.6	59.8	60.0	60.0	60.3	60.5	60.5	61.3	65.7	66.8	67.0
Al_2O_3	16.0	16.2	15.8	16.0	16.0	16.0	16.0	15.5	16.2	15.7	15.9	16.0	15.3	15.2	15.3
TiO_2	1.25	1.24	1.30	1.24	1.20	1.20	1.22	1.18	1.22	1.20	1.19	1.20	0.90	0.73	0.72
FeO(T)	8.33	8.04	8.37	8.05	8.11	8.03	7.21	7.71	7.58	7.80	7.67	6.87	5.51	5.01	4.92
MgO	2.78	2.62	2.60	2.62	2.72	2.63	2.78	2.47	2.34	2.42	2.44	2.47	1.23	0.97	0.93
CaO	6.30	5.96	6.13	6.05	6.08	5.99	6.19	6.28	5.58	5.69	5.67	5.61	3.63	3.12	3.05
Na_2O	4.22	4.58	4.12	4.37	4.20	4.40	4.62	4.48	4.65	4.50	4.53	4.31	4.73	4.76	4.92
K_2O	1.57	1.72	1.69	1.73	1.65	1.67	1.59	1.94	1.84	1.88	1.78	1.84	2.59	3.09	2.88
MnO	0.16	0.16	0.18	0.16	0.19	0.16	0.17	0.16	0.16	0.18	0.18	0.15	0.16	0.14	0.14
P_2O_5	0.19	0.21	0.23	0.20	0.20	0.20	0.22	0.23	0.21	0.23	0.21	0.22	0.24	0.19	0.15
Trace elements (ppm)															
Ba	288	274	298	286	295	312	279	291	296	314	314	290	377	379	404
Ce	38	48	29	43	48	40	60	34	38	54	59	54	38	61	68
Cr	8	17	0	17	8	5	27	4	15	4	7	22	0	0	0
La	20	12	19	20	21	18	24	15	18	21	25	14	29	30	27
Ni	3	bd	bd	bd	bd	bd	2	bd	bd	2	2	2	bd	2	3
Nb	7	7	9	7	8	8	7	9	9	8	8	8	10	12	12
Rb	58	bd	62	bd	65	64	54	76	bd	72	71	67	95	128	111
Sr	190	176	179	176	177	182	175	179	174	175	181	175	141	126	132
Th	13	13	14	16	10	12	16	12	14	13	14	16	20	18	21
V	217	176	170	167	176	171	146	135	143	146	150	129	32	32	26
Y	42	43	44	43	43	46	45	43	46	47	47	47	55	58	60
Zr	191	200	192	198	192	201	200	203	218	215	215	216	284	319	310

Eruption	Cape Riva												
Analysis	184	185	186	187	188	189	190	191	192	193	194	195	196
Sample	S82-73	S82-54	S80-145	S82-53	S82-55	LS77-91	LS183-91	S82-72	S82-67	S80-11	S82-69	S82-66	S82-68
Unit	A	A	A	A	A	A	A	A	B	B	B	B	B
Major elements recalculated dry (wt%)													
SiO_2	60.5	60.7	60.9	61.1	61.7	61.7	62.8	64.3	64.4	64.7	65.4	65.5	65.7
Al_2O_3	16.7	16.5	16.7	16.1	16.3	16.1	16.0	16.0	15.8	15.8	15.6	15.5	15.6
TiO_2	0.85	0.87	0.80	0.82	0.84	0.81	0.79	0.81	0.81	0.79	0.79	0.77	0.74
FeO(T)	6.47	6.70	6.31	6.13	6.26	5.72	5.32	5.42	5.38	5.32	5.10	5.14	4.98
MgO	3.23	3.02	3.01	2.78	2.63	2.88	2.46	1.94	1.70	1.65	1.47	1.49	1.64
CaO	6.21	6.13	6.12	5.65	5.58	5.76	5.20	4.41	4.09	4.05	3.76	3.84	3.78
Na_2O	4.20	4.23	4.29	5.41	4.66	4.38	4.61	4.77	5.36	5.02	5.27	5.19	4.94
K_2O	1.61	1.63	1.61	1.72	1.78	1.72	1.88	2.10	2.13	2.30	2.28	2.23	2.30
MnO	0.14	0.14	0.16	0.15	0.15	0.16	0.14	0.12	0.17	0.16	0.12	0.12	0.12
P_2O_5	0.15	0.14	0.17	0.16	0.15	0.15	0.15	0.17	0.18	0.21	0.16	0.18	0.17
Trace elements (ppm)													
Ba	363	339	292	303	370	324	364	437	426	423	436	434	446
Ce	49	48	27	24	38	52	54	36	49	50	38	36	46
Cr	47	38	25	28	28	31	27	18	14	11	9	8	14
La	14	21	12	20	20	16	18	19	26	30	29	26	23
Ni	10	15	9	11	8	9	5	bd	8	4	7	7	9
Nb	7	7	8	8	8	8	9	9	7	9	10	9	9
Rb	50	52	45	53	57	51	57	68	70	64	71	70	71
Sr	181	185	180	179	182	164	160	157	161	146	148	153	148
Th	11	13	12	7	4	12	10	9	9	8	12	16	9
V	122	138	128	100	115	108	96	70	68	60	59	52	55
Y	43	49	41	45	49	42	45	49	57	52	55	56	55
Zr	200	181	185	196	205	190	212	247	241	238	258	252	260

(*continued*)

Table A2.1. (*continued*)

Eruption	Cape Riva													
Analysis	197	198	199	200	201	202	203	204	205	206	207	208	209	210
Sample	LS149-91	S82-23	S82-23	S82-60	S82-24	LS66-91	S82-62	S82-21	S82-50	S82-52	S80-142	S80-185	S80-278	S82-51
Unit	B	D	B	D	D	A	C	B	A	A	C	D	B	A
Major elements recalculated dry (wt%)														
SiO_2	66.0	66.3	66.4	66.5	66.5	66.6	66.6	66.6	66.7	66.8	66.9	66.9	66.9	66.9
Al_2O_3	15.1	15.3	15.5	15.5	15.3	15.1	15.4	15.5	15.6	15.5	15.4	15.5	15.3	15.4
TiO_2	0.71	0.73	0.75	0.75	0.74	0.70	0.75	0.74	0.74	0.74	0.67	0.71	0.68	0.75
FeO(T)	4.31	4.74	4.81	4.76	4.68	4.10	4.75	4.72	4.76	4.64	4.44	4.62	4.51	4.69
MgO	1.51	1.21	1.13	1.13	1.16	1.09	1.11	1.04	1.07	1.07	1.12	1.15	1.13	1.08
CaO	3.38	3.25	3.28	3.17	3.15	3.13	3.21	3.21	3.15	3.08	3.52	3.18	3.13	3.04
Na_2O	5.80	5.74	5.36	5.54	5.64	6.13	5.42	5.36	5.23	5.41	5.15	5.24	5.72	5.27
K_2O	2.41	2.43	2.36	2.33	2.47	2.44	2.42	2.48	2.47	2.48	2.55	2.43	2.40	2.54
MnO	0.15	0.15	0.15	0.16	0.14	0.15	0.15	0.14	0.14	0.13	0.14	0.14	0.16	0.15
P_2O_5	0.17	0.17	0.22	0.20	0.19	0.18	0.19	0.18	0.18	0.16	0.19	0.18	0.18	0.17
Trace elements (ppm)														
Ba	428	464	472	451	477	448	477	465	473	477	431	462	460	470
Ce	62	44	46	45	41	45	33	45	50	48	55	54	43	52
Cr	20	9	6	4	5	13	7	9	10	8	3	5	8	4
La	24	29	25	27	30	25	30	29	29	30	24	27	20	30
Ni	8	8	11	8	6	6	4	7	8	11	2	bd	2	3
Na	11	9	9	10	10	11	10	10	9	10	11	11	10	11
Rb	72	74	76	78	77	75	76	75	77	77	70	70	72	78
Sr	129	149	147	143	146	133	142	140	140	142	145	139	139	139
Th	14	14	14	13	13	14	12	6	10	14	16	14	11	15
V	40	41	49	46	38	30	46	42	46	39	31	28	32	37
Y	54	57	62	59	59	55	57	58	57	58	55	58	57	61
Zr	253	260	276	278	268	264	279	259	271	279	260	262	273	278

Eruption	Cape Riva						Minoan							
Analysis	211	212	213	214	215	216	217	218	219	220	221	222	223	224
Sample	S80-143	S82-49	S82-84	S82-88	S82-75	S80-136	S82-27	S80-25a	S82–33	S80-23	S80-22a	S80-22b	S80-26	S82-26
Unit	A	A	C	C	C	C	A	A	A	A	A	A	A	A
Major elements recalculated dry (wt%)														
SiO_2	67.0	67.1	67.1	67.3	67.3	67.4	52.5	53.7	54.2	58.1	58.3	58.5	58.7	59.1
Al_2O_3	15.3	15.4	15.3	15.3	15.3	15.7	17.7	17.4	17.7	17.3	17.2	17.1	17.7	17.1
TiO_2	0.69	0.73	0.74	0.74	0.76	0.70	1.03	1.04	1.04	0.83	0.84	0.85	0.83	0.90
FeI(T)	4.54	4.64	4.66	4.69	4.64	4.58	10.05	10.20	9.48	7.57	7.37	7.34	7.28	7.41
MgO	1.08	0.99	1.03	1.02	0.96	1.05	5.28	4.56	4.43	3.55	3.44	3.38	2.89	3.02
CaO	3.14	3.14	3.02	3.08	3.06	2.84	9.57	9.02	8.53	7.18	7.33	7.28	6.66	6.59
Na_2O	5.38	5.26	5.29	5.11	5.22	4.81	2.63	2.66	3.18	3.84	3.78	3.78	4.00	3.86
K_2O	2.44	2.41	2.50	2.50	2.47	2.58	0.96	1.17	1.22	1.27	1.45	1.48	1.58	1.67
MnO	0.18	0.16	0.15	0.15	0.16	0.15	0.16	0.18	0.18	0.16	0.16	0.15	0.15	0.15
P_2O_5	0.18	0.18	0.18	0.18	0.18	0.19	0.08	0.09	0.11	0.11	0.12	0.12	0.16	0.12
Trace elements (ppm)														
Ba	451	476	499	488	492	430	288	334	360	349	384	405	448	510
Ce	53	37	59	46	61	50	37	45	35	50	36	39	46	40
Cr	3	5	7	3	bd	1	21	21	19	7	14	15	8	15
La	23	28	25	28	24	25	20	19	17	23	15	16	23	26
Ni	bd	7	5	bd	2	2	5	bd	4	bd	bd	bd	bd	6
Nb	10	11	11	11	12	10	4	6	6	4	7	6	7	6
Rb	69	82	86	81	81	74	29	33	36	36	39	38	42	51
Sr	140	142	136	138	138	127	271	273	287	231	218	227	264	233
Th	12	14	20	14	8	13	7	9	9	7	10	6	10	9
V	28	44	43	40	47	30	285	360	249	185	204	211	168	165
Y	57	58	56	58	59	55	23	22	26	28	29	30	27	30
Zr	264	280	287	281	289	253	86	98	115	122	116	117	121	126

(*continued*)

Table A2.1. (*continued*)

Eruption	Minoan												
Analysis	225	226	227	228	229	230	231	232	233	234	235	236	237
Sample	LS124-91	S82-34a	S80-24	S80-25b	S82-31	S82-3	LS112-91	S82-28	S80-29	S82-30	S82-11	S82-2	S79-101
Unit	A	A	A	A	A	A	A	A	B	B	B	B	B
Major elements recalculated dry (wt%)													
SiO_2	59.7	61.2	62.5	63.6	67.6	69.1	70.0	70.3	70.5	70.6	70.8	70.9	70.9
Al_2O_3	16.8	17.0	16.9	16.3	15.1	15.0	14.8	14.8	14.7	14.6	14.7	14.7	14.6
TiO_2	0.81	0.84	0.79	0.79	0.54	0.53	0.47	0.46	0.44	0.46	0.44	0.47	0.43
FeO(T)	6.19	6.49	5.89	5.61	4.23	3.62	2.95	3.10	3.16	3.05	2.89	3.02	2.82
MgO	3.21	2.35	2.10	2.02	1.41	1.02	0.91	0.85	0.86	0.66	0.64	0.62	0.61
CaO	6.61	5.75	5.29	5.00	3.44	2.88	2.78	2.46	2.53	2.36	2.29	2.36	2.22
Na_2O	4.04	4.24	4.30	4.25	4.71	4.82	4.73	4.88	4.63	5.08	5.04	4.78	5.09
K_2O	1.68	1.90	1.91	2.14	2.72	2.86	2.93	2.98	3.03	3.00	3.03	3.05	3.12
MnO	0.14	0.16	0.13	0.14	0.09	0.08	0.09	0.08	0.10	0.08	0.07	0.07	0.08
P_2O_5	0.11	0.11	0.15	0.13	0.09	0.08	0.08	0.08	0.09	0.08	0.07	0.07	0.08
Trace elements (ppm)													
Ba	452	565	502	583	535	553	503	511	552	554	573	562	548
Ce	52	35	56	61	38	37	63	51	58	40	54	53	51
Cr	12	13	6	6	9	5	9	7	7	bd	6	5	6
La	19	27	24	30	36	29	28	30	25	30	29	30	27
Ni	3	3	bd	bd	bd	9	4	10	2	9	8	9	bd
Nb	7	7	7	6	9	9	11	8	11	10	10	11	11
Rb	49	54	53	59	86	96	86	93	86	98	99	98	88
Sr	219	230	218	211	136	124	107	102	105	103	87	103	96
Th	10	8	14	15	16	19	19	14	22	16	20	21	16
V	129	121	99	96	59	41	38	33	35	33	25	30	13
Y	28	36	36	34	45	46	45	43	48	45	47	48	48
Zr	146	144	167	176	274	295	277	278	291	294	306	312	296

Eruption	Minoan									
Analysis	238	239	240	241	242	243	244	245	246b	247
Sample	LS118-91	S82-78	LS172-91	S80-119	S80-28	S82-1b	LS112-91	LS104-91	S82-34	LS108-91
Unit	C	C	D	B	A	A	C	A	B	A
Major elements recalculated dry (wt%)										
SiO_2	70.9	71.1	71.1	71.2	71.2	71.2	71.2	71.4	71.4	71.4
Al_2O_3	14.4	14.5	14.5	14.8	14.5	14.4	14.5	14.6	14.6	14.4
TiO_2	0.42	0.45	0.43	0.41	0.41	0.44	0.43	0.41	0.42	0.41
FeO(T)	2.59	2.84	2.56	2.62	2.82	2.84	2.53	2.49	2.80	2.53
MgO	0.77	0.65	0.62	0.65	0.60	0.56	0.67	0.58	0.60	0.59
CaO	2.25	2.16	2.25	2.06	2.21	2.19	2.19	2.16	2.08	2.12
Na_2O	5.11	5.01	4.93	5.04	4.89	5.06	4.97	4.93	4.49	4.93
$K_{22}O$	3.12	3.07	3.10	3.09	3.16	3.10	3.10	3.06	3.19	3.13
MnO	0.09	0.08	0.07	0.07	0.08	0.08	0.08	0.08	0.08	0.09
P_2O_5	0.07	0.08	0.07	0.09	0.08	0.06	0.06	0.07	0.06	0.08
Trace elements (ppm)										
Ba	538	576	532	562	561	573	509	542	543	419
Ce	59	56	62	44	51	45	53	55	34	52
Cr	7	7	13	bd	3	7	8	24	7	5
La	30	28	25	24	28	31	29	30	29	27
Ni	2	7	9	bd	bd	8	2	7	8	2
Nb	10	11	9	11	10	11	10	11	10	10
Rb	95	106	94	106	88	104	94	94	101	91
Sr	96	99	94	91	98	96	92	95	95	85
Th	22	20	21	24	16	23	21	20	20	20
V	25	28	22	23	21	26	21	23	25	14
Y	44	49	45	47	51	51	45	47	47	43
Zr	299	333	292	320	299	328	298	301	319	282

Appendix 2.2 Plutonic blocks from the Thera pyroclastics

Cape Therma 3

1	86304	Altered diorite, Cape Plaka.
2	86302	Diorite, Cape Plaka.
3	86430	Altered diorite, Cape Plaka.
4	86301	Uralitized diorite, Cape Plaka.
5	86303	Uralitized diorite, Cape Plaka.

Middle Pumice

6	8424	Gabbro orthocumulate. Unit B, Balos.
7	84219	Oxidized gabbro cumulate. Unit B, east of Cape Balos.
8	8426	Altered gabbro cumulate. Unit B, Cape Akrotiri.
9	8423	Uralitized gabbro cumulate. Unit B, Balos.
10	8422	Gabbro orthocumulate. Unit B, Balos.
11	84216	Gabbro cumulate. Unit B, Cape Mavros.
12	8425	Sub-ophitic quartz gabbro. Unit B, Cape Akrotiri.
13	8429	Oxidized quartz gabbro. Unit B, Cape Akrotiri.
14	84214	Quartz gabbro. Unit B, Athinios.
15	84217	Augite-rich quartz gabbro. Unit B, Cape Mavros.
16	8428	Orthocumulate. Unit B, Cape Akrotiri.
17	84210	Hyperthene-rich quartz gabbro. Unit B, Cape Aspronisi.
18	8421	Plagioclase-rich quartz gabbro. Unit B, Balos.
19	84218	Oxidized quartz gabbro cumulate. Unit B, Cape Loumaravi.
20	84215	Quartz gabbro. Unit B, Athinios.
21	8427	Fine-grained orthocumulate. Unit B, Cape Aspronisi.
22	84212	Altered diorite orthocumulate. Unit B, Cape Aspronisi.
23	84211	Diorite orthocumulate. Unit B, Cape Aspronisi.

Upper Scoriae 1

24	84129	Glass-bearing quartz gabbro. Unit C, Cape Plaka.
25	84130	Quartz microgabbro. Unit C, Cape Mavros.
26	84128	Porphyritic quartz microgabbro. Unit C, Cape Aspronisi.
27	8645	Quartz microgabbro. Unit C, Cape Mavros.
28	8513	Quartz microgabbro. Unit B, Akrotiri quarry.

Upper Scoriae 2

29	84014	Mafic gabbro. Top of unit D, Ammoudi.
30	84015	Oxidized mafic gabbro. Unit D, Ammoudi.
31	84025	Sub-ophitic gabbro. Top of unit D, Ammoudi.
32	84018	Oxidized gabbro cumulate. Unit D, Ammoudi.
33	8401	Cumulate gabbro. Near base of unit D, Ammoudi.
34	84011	Oxidized porphyritic quartz gabbro. Unit D, Ammoudi.
35	84023	Oxidized porphyritic gabbro. Unit D, Oia.
36	84021	Sub-ophitic gabbro. Base of unit D, Ammoudi.
37	84017	Highly oxidized gabbro. Unit D, Ammoudi.
38	84016	Gabbro orthocumulate. Top of unit D, Ammoudi.
39	84010	Quartz gabbro orthocumulate. Top of unit D, Ammoudi.
40	8403	Quartz gabbro cumulate. Middle of unit D, Ammoudi.
41	8402	Quartz gabbro orthocumulate. Middle of unit D, Ammoudi.
42	84019	Quartz gabbro. Unit D, Ammoudi.
43	8405	Quartz gabbro orthocumulate. Unit D, Ammoudi.
44	84020	Oxidized quartz gabbro cumulate. Unit D, Ammoudi.
45	8406	Porphyritic quartz gabbro. Middle of unit D, Ammoudi.
46	85041	Quartz gabbro. Unit B, Alonaki quarry.
47	85255	Uralitized quartz gabbro. Unit C, Balos.
48	84026	Oxidized quartz gabbro. Unit D, Ammoudi.
49	84024	Quartz gabbro orthocumulate. Top of unit D, Ammoudi.
50	8407	Quartz gabbro orthocumulate. Middle of unit D, Ammoudi.
51	8409	Oxidized porphyritic quartz gabbro. Unit D, Ammoudi.

Cape Riva

52	84921	Leucocratic gabbro orthocumulate. Unit C, Cape Aspronisi.
53	84920	Uralitized quartz gabbro. Unit C, Cape Aspronisi.
54	S80-161b	Granitoid. Phreatomagmatic ash atop unit C, 700 m west of Cape Tinos.
55	S80-152b	Granitoid. Unit C, 1 km north of Cape Simandiri.

Minoan

56	S80-21e	Granitoid. Unit A, Phira quarry.
57	S80-21b	Granitoid. Unit A, Phira quarry.

Table A2.2. *Chemical analyses of plutonic blocks from the Thera pyroclastics*

Eruption	Cape Therma 3					Middle Pumice								
Analysis	1	2	3	4	5	6	7	8	9	10	11	12	13	14
Sample	86304	86302	86430	86301	86303	8424	84219	8426	8423	8422	84216	8425	8429	84214
Major elements recalculated dry (wt%)														
SiO_2	57.6	57.9	58.8	58.9	60.1	52.4	52.4	52.8	53.2	53.3	53.5	53.6	54.3	54.5
Al_2O_3	17.4	17.0	17.2	17.2	16.6	16.4	17.0	18.9	17.4	16.9	17.5	16.5	16.9	16.9
TiO_2	1.02	0.98	0.94	0.90	0.97	1.32	1.00	0.97	1.14	1.19	0.99	1.25	1.13	1.08
FeO	6.59	7.21	6.41	6.01	5.52	9.87	8.93	7.52	8.26	8.78	7.21	8.89	8.63	8.58
MgO	3.29	3.19	3.15	3.27	3.33	5.79	6.34	5.00	5.25	5.64	4.04	5.70	5.05	5.41
CaO	7.67	7.17	6.92	7.37	7.63	10.18	10.44	10.42	10.22	9.80	11.22	9.68	9.22	8.73
Na_2O	4.20	4.12	3.79	4.15	5.22	2.99	2.96	3.60	3.38	3.29	4.63	3.26	3.33	3.28
K_2O	1.93	2.03	2.45	1.93	0.36	0.72	0.68	0.54	0.85	0.85	0.64	0.84	1.12	1.15
MnO	0.08	0.11	0.11	0.09	0.08	0.18	0.16	0.14	0.16	0.18	0.11	0.17	0.16	0.15
P_2O_5	0.25	0.20	0.22	0.21	0.14	0.08	0.07	0.05	0.09	0.10	0.11	0.13	0.15	0.16
Trace elements (ppm)														
Ba	423	451	407	358	168	158	153	133	178	182	154	183	214	238
Ce	56	32	64	55	50	20	14	22	28	18	31	49	42	24
Cr	32	27	32	32	27	111	146	70	83	113	38	126	80	152
La	24	20	31	38	18	0	4	5	4	14	0	7	6	6
Ni	12	13	16	13	15	37	46	23	31	38	10	40	27	46
Nb	10	13	11	11	14	4	4	3	4	6	4	5	6	5
Rb	58	71	100	62	3	na	na	na	na	na	na	na	na	na
Sr	268	258	236	251	240	205	210	235	213	200	280	203	189	204
Th	12	12	17	12	16	6	2	3	8	7	3	5	10	6
V	139	132	119	124	121	305	267	309	293	229	279	241	219	221
Y	33	36	36	36	36	25	24	21	25	26	28	28	32	30
Zr	166	171	193	185	260	90	85	93	107	109	114	111	161	73

Eruption	Middle Pumice									Upper Scoriae 1				
Analysis	15	16	17	18	19	20	21	22	23	24	25	26	27	28
Sample	84217	8428	84210	8421	84218	84215	8427	84212	84211	84129	84130	84128	8645	8513
Major elements recalculated dry (wt%)														
SiO_2	54.5	54.8	54.8	55.5	56.0	56.2	57.5	57.6	59.3	54.4	54.9	55.5	55.6	56.4
Al_2O_3	17.5	16.4	17.5	17.5	17.8	19.6	16.3	16.8	18.1	17.0	17.2	16.6	16.5	16.5
TiO_2	1.09	1.20	0.74	1.10	1.11	0.83	1.23	1.22	1.16	1.27	1.32	1.41	1.27	1.27
FeO	4.47	8.71	7.20	8.09	7.59	5.97	8.20	7.98	6.28	9.52	9.42	9.54	9.63	9.41
MgO	5.04	5.01	5.83	3.75	3.81	2.94	3.36	3.10	2.19	4.02	3.46	3.31	3.73	3.31
CaO	12.47	8.41	9.55	8.46	8.35	8.74	7.49	7.20	5.65	8.91	8.57	8.02	8.49	7.97
Na_2O	4.27	3.59	3.18	3.74	3.80	3.93	3.99	4.24	5.46	3.42	3.65	4.05	3.28	3.49
K_2O	0.32	1.57	0.89	1.58	1.26	1.58	1.62	1.50	1.43	1.10	1.22	1.23	1.25	1.36
MnO	0.15	0.16	0.14	0.12	0.14	0.12	0.16	0.16	0.07	0.17	0.16	0.17	0.19	0.17
P_2O_5	0.15	0.15	0.09	0.16	0.15	0.12	0.19	0.18	0.36	0.14	0.14	0.18	0.12	0.14
Trace elements (ppm)														
Ba	133	280	164	264	212	234	284	286	295	208	258	263	257	274
Ce	26	39	20	36	40	17	50	31	43	25	39	25	20	46
Cr	101	111	151	63	65	44	48	28	13	33	26	25	14	8
La	6	9	0	14	9	11	16	19	20	13	15	13	20	14
Ni	23	32	33	19	22	14	12	8	0	11	3	3	5	5
Nb	4	8	4	5	5	6	7	8	8	5	5	5	6	7
Rb	na	na	na	na	na	na	na	na	na	na	na	na	44	49
Sr	256	185	219	199	198	222	198	203	281	204	212	210	203	204
Th	7	11	3	11	10	8	15	11	7	6	7	11	9	11
V	159	240	178	200	196	150	185	192	84	261	251	254	273	227
Y	33	36	22	35	34	25	40	38	38	33	36	40	37	36
Zr	105	170	98	142	147	143	185	178	141	134	149	156	149	139

(*continued*)

Table A2.2. (*continued*)

Eruption	Upper Scoriae 2													
Analysis	29	30	31	32	33	34	35	36	37	38	39	40	41	42
Sample	84014	84015	84025	84018	8401	84011	84023	84021	84017	84016	84010	8403	8402	84019
Major elements recalculated dry (wt%)														
SiO_2	48.2	48.6	51.2	51.8	51.8	52.3	52.6	52.7	53.2	53.2	53.2	53.5	54.0	54.2
Al_2O_3	18.9	17.4	18.9	17.5	20.6	18.3	16.9	17.2	17.4	18.7	17.9	17.1	17.3	17.2
TiO_2	1.21	1.01	1.05	1.38	0.59	1.34	1.00	1.30	1.07	1.35	1.25	1.13	1.11	1.33
FeO	10.60	9.62	8.20	8.76	6.74	9.96	9.13	9.88	8.21	9.33	9.01	9.13	8.72	8.37
MgO	5.39	6.69	4.89	4.91	4.82	3.83	5.93	5.09	5.33	3.38	4.29	4.84	4.76	3.52
CaO	12.43	13.80	12.10	10.89	11.81	9.42	10.71	9.84	10.59	9.38	9.44	9.56	9.02	10.09
Na_2O	2.25	2.42	3.17	4.23	2.94	3.72	2.81	3.09	3.24	3.57	3.80	3.79	3.87	4.79
K_2O	0.67	0.27	0.34	0.41	0.46	0.89	0.70	0.72	0.71	0.81	0.82	0.66	0.98	0.23
MnO	0.15	0.16	0.09	0.09	0.14	0.15	0.16	0.17	0.14	0.13	0.12	0.20	0.09	0.09
P_2O_5	0.17	0.04	0.07	0.06	0.06	0.08	0.09	0.03	0.10	0.14	0.16	0.12	0.10	0.15
Trace elements (ppm)														
Ba	127	83	114	107	88	189	139	168	156	197	217	167	183	132
Ce	11	8	25	20	22	26	8	20	37	25	40	26	40	17
Cr	68	75	56	28	52	27	91	53	92	29	41	38	46	27
La	12	bd	bd	bd	bd	7	bd	9	7	11	bd	13	5	7
Ni	25	24	12	7	21	5	29	12	43	6	9	15	23	5
Nb	3	bd	3	3	2	3	3	4	3	5	5	3	5	5
Rb	na	na	na	na	na	na	na	na	na	na	na	na	na	na
Sr	226	230	256	232	255	247	187	229	214	248	236	205	251	273
Th	4	4	1	5	4	4	3	4	4	5	7	7	9	11
V	393	367	331	228	138	343	246	323	201	268	249	225	289	232
Y	26	15	24	22	20	27	26	24	27	29	33	32	29	32
Zr	87	45	71	80	64	93	94	101	93	113	82	123	318	135

Eruption	Upper Scoriae 2									Cape Riva				Minoan	
Analysis	43	44	45	46	47	48	49	50	51	52	53	54	55	56	57
Sample	8405	84020	8406	85041	85255	84026	84024	8407	8409	84921	84920	S80-161b	S80-152b	S80-21e	S80-21b
Major elements recalculated dry (wt%)															
SiO_2	54.3	54.5	54.7	54.9	55.1	55.2	55.2	56.0	56.8	50.9	54.3	67.2	67.2	62.3	62.9
Al_2O_3	18.5	17.7	15.8	17.9	15.8	17.7	16.8	17.3	15.9	15.7	16.7	15.4	15.3	16.3	17.0
TiO_2	1.20	1.03	1.34	1.26	1.26	1.44	0.99	0.88	1.36	1.88	1.93	0.74	0.76	0.76	0.77
FeO	8.50	8.16	9.43	8.85	9.33	9.15	8.41	7.25	9.58	12.09	10.32	4.67	4.69	6.37	5.64
MgO	3.43	4.53	5.11	3.25	4.72	2.83	4.66	4.33	3.43	5.39	3.14	1	0.96	2.33	1.78
CaO	8.94	9.41	8.87	8.74	9.55	7.85	8.70	9.43	7.06	10.29	8.35	2.97	2.92	5.48	5
Na_2O	3.75	3.36	3.01	3.58	3.30	4.11	3.11	4.35	3.90	2.78	3.88	5.22	5.24	4.2	4.61
K_2O	1.16	0.97	1.34	1.13	0.69	1.36	1.52	0.25	1.76	0.65	1.03	2.56	2.6	1.98	2
MnO	0.14	0.15	0.17	0.17	0.13	0.15	0.16	0.09	0.09	0.19	0.14	0.14	0.13	0.13	0.14
P_2O_5	0.11	0.13	0.24	0.13	0.17	0.17	0.10	0.11	0.15	0.16	0.21	0.18	0.18	0.11	0.14
Trace elements (ppm)															
Ba	224	198	243	261	181	262	223	130	319	136	283	498	495	487	532
Ce	22	31	40	46	26	34	30	28	29	32	36	61	46	69	50
Cr	25	45	102	11	30	25	67	27	26	44	8	bd	4	7	5
La	12	11	15	15	5	11	7	11	20	14	4	21	26	27	25
Ni	8	14	23	4	11	3	21	8	4	14	2	bd	bd	bd	bd
Nb	5	4	6	7	6	7	6	5	6	6	6	11	12	9	9
Rb	na	na	na	75	49	na	na	na	na	23	30	87	84	61	53
Sr	246	218	343	249	214	233	189	279	224	219	252	133	134	209	226
Th	7	9	8	8	7	8	11	9	9	6	7	17	15	16	11
V	219	189	250	237	264	243	251	168	275	479	238	35	35	160	97
Y	29	30	35	34	37	37	32	24	35	30	35	56	59	36	37
Zr	134	128	130	96	126	155	132	93	161	90	126	297	288	157	257

Appendix 2.3 Juvenile components of the minor pyroclastic sequences

MS6

1	LS30-90	Scoria half-way down fall deposit CD 3, Thera quarry.
2	LS23-90	Pumice at base of CD3, Thera quarry.
3	LS22-90	Pumice clasts from 15 cm fall deposit CD4, Thera quarry.
4	LS21-90	Pumices from base of CD5, Thera quarry.
5	LS17-90C	Pumice from base of CD6, Thera quarry.
6	LS19-90	Pumice 100 cm from base of CD6, Thera quarry.
7	LS18-90	Pumice 40 cm from base of CD6, Thera quarry.
8	LS17-90A	Pumice from base of CD6, Thera quarry.
9	LS29-90	Pumice from base of 128 cm CD6, Thera quarry.
10	LS17-90B	Pumice from base of CD6, Thera quarry.
11	LS17-90D	Slightly banded pumice from base of CD6, Thera quarry.
12	LS27-90	Pumices from base of 70 cm fall deposit CD7, Thera quarry.
13	LS15-90	Pumices from CD8, Thera quarry.
14	LS26-90	Scoriae from 22 cm fall deposit CD9, Thera quarry.
15	LS14-90	Scoriae from fall deposit CD9, Thera quarry.
16	LS8-90	Scoriae from fall deposit CD10, Thera quarry.
17	LS25-90	Scoriae from fall deposit CD10, Thera quarry.
18	LS9-90	Scoriae from undesignated 10 cm scoria layer, Thera quarry.
19	LS6-90	Scoriae from undesignated 14 cm scoria layer, Thera quarry.
20	LS13-90	Scoriae from undesignated 6 cm scoria layer, Thera quarry.
21	LS12-90	Scoriae from undesignated 13 cm scoria layer, Thera quarry.
22	LS5-90	Pumices from undesignated 14 cm fall deposit, Thera quarry.
23	LS11-90	Scoriae from undesignated 10 cm scoria layer, Thera quarry.
24	LS4-90	Pumices from undesignated 33 cm fall deposit, Thera quarry.

MS7

25	LS42-91	Scoria from CD2, Thera quarry.
26	LS32-91	Scoria from CD2, Thera quarry.
27	LS24-91	Pumice from middle of CD4, Thera quarry.
28	LS26-91	Scoria from base of 28 CD4, Thera quarry.
29	LS64-91	Scoria from CD4, Cape Plaka.
30	LS31-91	Scoria from top of undesignated 33 cm fall deposit, Thera quarry.
31	LS23-91	Scoria from undesignated 21 cm deposit, Thera quarry.
32	LS29-91	Banded pumice from base of undesignated 17 cm deposit, Thera quarry.
33	LS30-91	Pumice from top of undesignated 17 cm deposit, Thera quarry.

MS8

34	LS175-91	Scoria from CD1, Thera Harbour.
35	LS46-91	Scoria from middle of CD1, Thera quarry.
36	LS49-91	Scoria from base of CD1, Thera quarry.
37	LS47-91	Scoria from top of CD1, Thera quarry.
38	LS48-91	Scoria from base of CD1, Thera quarry.
39	LS44-91	Scoria from base of undesignated 35 cm ash deposit, Thera quarry.
40	LS50-91	Scoria from undesignated 47 cm fall deposit, Thera quarry.
41	LS43-91	Scoria from undesignated 25 cm deposit, Thera quarry.
42	LS51-91	Scoria from undesignated 10 cm fall deposit, Thera quarry.
43	LS45-91	Pumice from undesignated 10 cm fall layer, Thera quarry.

Table A2.3. *Chemical analyses of juvenile components of the minor pyroclastic sequences*

Eruption	MS 6													
Analysis	1	2	3	4	5	6	7	8	9	10	11	12	13	14
Sample	LS30-90	LS23-90	LS22-90	LS21-90	LS17-90C	LS19-90	LS18-90	LS17-90A	LS29-90	LS17-90B	LS17-90D	LS27-90	LS15-90	LS26-90
Unit	CD 3	CD 3	CD 4	CD 5	CD 6	CD 6	CD 6	CD 6	CD 6	CD 6	CD 6	CD 7	CD 8	CD 9
Major elements recalculated dry (wt%)														
SiO_2	58.2	61.9	60.8	58.8	61.2	64.7	64.9	65.0	65.1	65.2	65.6	62.2	62.5	56.1
Al_2O_3	17.4	16.3	16.0	16.6	16.5	15.6	15.4	15.5	15.4	15.5	15.3	16.2	16.1	16.8
TiO_2	0.98	1.02	1.08	1.02	1.00	0.88	0.90	0.85	0.86	0.86	0.88	1.04	1.07	0.93
FeO(T)	7.37	6.58	7.43	7.68	6.89	5.79	5.76	5.70	5.63	5.60	5.53	6.69	6.65	7.96
MgO	3.13	1.97	2.50	3.04	2.02	1.53	1.37	1.43	1.40	1.34	1.27	1.92	1.96	4.91
CaO	7.38	5.14	5.68	7.16	5.78	4.15	4.04	4.00	3.99	3.86	3.77	5.00	4.92	8.94
Na_2O	3.86	4.88	4.17	3.79	4.30	4.59	4.70	4.64	4.67	4.73	4.64	4.59	4.38	2.89
K_2O	1.39	1.88	2.01	1.60	1.90	2.48	2.55	2.54	2.58	2.59	2.64	1.98	2.02	1.21
MnO	0.15	0.16	0.14	0.16	0.13	0.12	0.15	0.12	0.11	0.12	0.13	0.14	0.14	0.14
P_2O_5	0.17	0.22	0.20	0.17	0.20	0.23	0.22	0.23	0.23	0.24	0.24	0.23	0.23	0.12
Trace elements (ppm)														
Ba	293	338	340	289	339	395	380	399	405	351	399	352	327	231
Ce	18	48	45	29	49	53	40	61	51	53	48	49	51	21
Cr	22	13	35	37	19	34	14	38	16	44	14	28	10	64
La	4	14	31	10	18	15	26	18	30	32	20	8	14	7
Ni	6	2	4	12	3	13	9	2	5	8	9	3	8	21
Nb	6	8	8	6	9	9	12	10	10	11	11	8	9	6
Rb	40	50	65	51	61	75	82	79	81	79	82	61	61	37
Sr	241	213	174	188	185	152	148	145	147	139	139	181	158	196
Th	13	14	15	13	15	18	21	19	20	20	16	16	14	9
V	164	100	185	179	123	64	58	57	54	59	54	100	101	174
Y	30	41	39	35	39	46	47	48	47	46	49	42	41	31
Zr	135	173	197	164	196	235	236	242	247	239	247	204	202	131

Eruption	MS 6										MS 7			
Analysis	15	16	17	18	19	20	21	22	23	24	25	26	27	28
Sample	LS14-90	LS8-90	LS25-90	LS9-90	LS6-90	LS13-90	LS12-90	LS5-90	LS11-90	LS4-90	LS42-91	LS32-91	LS24-91	LS26-91
Unit	CD 9	CD 10	CD 10								CD 2	CD 2	CD 4	CD 4
Major elements recalculated dry (wt%)														
SiO_2	55.7	54.7	54.9	53.4	54.6	55.4	55.7	57.5	57.7	64.0	52.0	53.5	58.1	58.6
Al_2O_3	16.7	17.4	17.4	17.3	17.3	17.0	17.2	16.9	17.2	15.5	17.6	17.4	15.1	15.1
TiO	0.92	0.91	0.91	0.94	1.02	0.89	0.97	0.97	1.01	1.04	0.79	0.90	1.44	1.44
FeO(T)	8.18	8.00	8.08	8.65	8.58	7.83	8.05	7.55	7.53	5.97	8.48	8.20	9.36	9.04
MgO	5.04	5.13	5.27	5.58	4.83	5.21	4.87	4.07	3.40	1.63	6.45	5.92	3.07	2.87
CaO	9.24	10.06	9.43	10.64	9.36	9.47	8.87	8.07	7.98	4.19	12.06	10.73	7.18	7.17
Na_2O	2.88	2.59	2.72	2.56	2.89	2.95	3.00	3.03	3.32	4.47	1.82	2.22	3.53	3.44
K_2O	1.09	0.97	0.97	0.74	1.11	1.09	1.17	1.65	1.66	2.67	0.57	0.92	1.78	1.91
MnO	0.15	0.14	0.16	0.15	0.15	0.14	0.14	0.15	0.14	0.15	0.17	0.16	0.19	0.18
P_2O_5	0.11	0.11	0.11	0.11	0.15	0.12	0.13	0.16	0.16	0.29	0.07	0.12	0.23	0.26
Trace elements (ppm)														
Ba	208	163	193	154	232	196	199	276	258	447	89	139	286	284
Ce	19	40	20	7	21	40	39	44	31	63	18	18	37	38
Cr	27	64	83	67	49	37	38	35	52	5	33	52	13	14
La	18	11	8	8	6	9	11	15	11	18	8	12	17	11
Ni	24	23	31	25	25	29	24	20	20	2	32	38	4	5
Nb	5	5	5	4	5	5	5	7	7	13	3	4	6	8
Rb	35	30	28	22	32	36	34	53	56	84	19	32	62	69
Sr	197	211	209	222	220	200	205	189	200	155	171	189	173	168
Th	11	11	6	5	10	8	11	19	13	19	2	4	12	10
V	195	189	187	213	197	190	189	163	187	74	190	193	221	194
Y	29	27	29	25	31	27	31	38	34	53	21	28	41	42
Zr	120	110	115	90	121	123	125	172	170	259	84	118	199	206

(*continued*)

Table A2.3. (*continued*)

Eruption	MS 7					MS 8									
Analysis	29	30	31	32	33	34	35	36	37	38	39	40	41	42	43
Sample	LS64-91	LS31-91	LS23-91	LS29-91	LS30-91	LS175-91	LS46-91	LS49-91	LS47-91	LS48-91	LS44-91	LS50-91	LS43-91	LS51-91	LS45-91
Unit	CD 4					CD 1	CD 1	CD 1	CD 1	CD 1					
Major elements recalculated dry (wt%)															
SiO_2	59.3	53.5	58.2	62.8	64.2	55.8	56.0	56.1	56.8	57.7	52.7	53.1	53.1	53.4	54.0
Al_2O_3	15.1	15.7	15.7	14.8	14.8	16.6	16.1	16.1	16.3	15.8	17.2	17.2	17.4	17.1	16.5
TiO_2	1.42	0.92	1.33	1.15	1.02	1.05	1.22	1.18	1.17	1.19	0.85	0.87	1.04	0.92	1.04
FeO(T)	8.95	8.50	8.77	7.37	6.78	8.84	9.35	9.11	9.05	8.72	8.63	8.88	9.14	8.87	8.74
MgO	2.81	7.56	3.11	1.89	1.59	4.36	3.68	3.75	3.63	3.19	6.44	5.88	5.06	5.44	5.64
CaO	6.42	10.48	7.29	5.15	4.22	9.23	8.91	9.42	8.46	8.28	11.14	10.98	10.58	10.77	10.47
Na_2O	3.62	2.15	3.49	3.94	4.12	2.72	3.13	2.76	3.05	3.31	2.01	2.17	2.51	2.47	2.28
K_2O	1.92	0.92	1.76	2.53	2.84	1.15	1.25	1.22	1.27	1.48	0.71	0.65	0.83	0.76	1.00
MnO	0.19	0.16	0.18	0.15	0.19	0.17	0.18	0.18	0.19	0.18	0.17	0.18	0.17	0.16	0.16
P_2O_5	0.22	0.12	0.21	0.24	0.24	0.14	0.15	0.15	0.16	0.18	0.11	0.10	0.13	0.11	0.15
Trace elements (ppm)															
Ba	294	134	283	349	396	177	195	189	200	234	97	116	146	133	160
Ce	41	25	29	65	59	15	17	39	26	36	24	7	43	22	14
Cr	19	170	18	7	17	29	20	23	26	15	87	52	33	21	72
La	10	7	13	25	21	5	10	16	20	12	4	16	4	16	11
Ni	6	78	8	12	8	19	7	10	11	5	43	36	21	20	30
Nb	9	4	7	12	11	5	5	6	6	6	3	2	3	2	5
Rb	68	31	61	92	97	39	40	43	43	48	23	23	29	26	35
Sr	172	219	179	151	201	175	176	181	182	170	186	187	199	195	180
Th	17	6	13	17	21	9	6	7	8	8	7	3	9	3	5
V	201	191	196	103	71	229	252	235	239	209	209	217	234	212	220
Y	45	29	40	49	55	32	33	32	35	39	26	23	29	26	33
Zr	212	115	193	265	281	143	150	155	156	174	98	90	112	101	126

References

ABBEY, S. 1980. *Studies in 'standard samples' for use in the general analysis of silicate rocks and minerals. Part 6: 1979 edition of 'usable values'*. Geological Survey of Canada Papers, **80-14**.

ALLEN, J. C. & BOETTCHER, A. L. 1978. Amphiboles in andesite and basalt: II stability as a function of P-T-F_{H_2O}-fO_2. *American Mineralogist*, **63**, 1074–1087.

ALLEN, S. R. & CAS, R. A. F. 1998. Lateral variations within coarse co-ignimbrite lithic breccias of the Kos Plateau Tuff, Greece. *Bulletin of Volcanology*, **59**, 356–377.

ALLEGRE, C. J. 1968. ^{230}Th dating of volcanic rocks: a comment. *Earth and Planetary Science Letters*, **5**, 109–210.

—— & CONDOMINES, M. 1976. Fine chronology of volcanic processes using ^{238}U-^{230}Th systematics. *Earth and Planetary Science Letters*, **28**, 395–406.

ALTHERR, R. & SEIDEL, E. 1977. Speculations on the geodynamic evolution of the Attic-Cycladic Complex during Alpidic times. *In*: KALLERGIS, G. (ed.) *Proceedings of the 5th Colloqium on Geology of the Aegean Region*. Athens, 347–352.

——, HENJES-KUNST, F., MATTHEWS, A., FRIEDRICHSEN, H. & HANSEN, B. T. 1988. O-Sr isotope variations in Miocene granitoids from the Aegean: evidence for an origin by combined assimilation and fractional crystallization. *Contributions to Mineralogy and Petrology*, **100**, 528–541.

——, SCHLIESTEDT, M., OKRUSCH, M., SEIDEL, E., KREUZER, H., HARRE, W., LENZ, H., WENDT, I. & WAGNER, G. A. 1979. Geochronology of high-pressure rocks on Sifnos (Cyclades, Greece). *Contributions to Mineralogy and Petrology*, **70**, 245–255.

ANDERSEN, D. J. & LINDSLEY, D. H. 1988. Internally consistent solution models for Fe-Mg-Mn-Ti oxides. Part I. Fe-Ti oxides. *American Mineralogist*, **73**, 714–726.

——, —— & DAVIDSON, P. M. 1993. QUILF: A Pascal program to assess equilibria among Fe-Mg-Mn-Ti oxides, pyroxenes, olivines, and quartz. *Computers and Geosciences*, **19**, 1333–1350.

ANDRIESSEN, P. A. M. 1978. *Isotopic age relations within the polymetamorphic complex of the island of Naxos (Cyclades, Greece)*. PhD Thesis, Verhergen ZWO-Laboratotium Voor Isotopen Geologie, Amsterdam.

——, BANGA, G. & HEBEDA, E. H. 1987. Isotopic age study of Pre-Alpidic rocks in the basal units on Naxos, Sikinos and Ios, Greek Cyclades. *Geologishe en Mijnbouw*, **66**, 3–14.

——, BOELRIJK, N. A., I. M., HEBED, A., E. H., PRIEM, N. N. A., VERDUMEN, E. A.TH. & VERSCHURE, R. H. 1979. Dating the events of metamorphism and granite magmatism in the Alpine Orogen of Naxos (Cyclades, Greece). *Contributions to Mineralogy and Petrology*, **69**, 215–225.

ANGELIER, J., LYBERIS, N., LE PICHON, X., BARRIER, E. & HUCHON, P. 1982. The tectonic development of the Hellenic arc and the Sea of Crete: a synthesis. *Tectonophysics*, **86**, 159–196.

ARAMAKI, S. 1984. Formation of Aira Caldera, southern Kyushu, 22,000 years ago. *Journal of Geophysical Research*, **89**, 8485–8501.

ARCULUS, R. J. & WILLS, K. J. A. 1980. The petrology of plutonic blocks and inclusions from the Lesser Antilles island arc. *Journal of Petrology*, **21**, 743–749.

——, GUST, D. A. & KUSHIRO, I. 1991. The evolution of Fuji and Hakone volcanoes, Honshu, Japan. *Research and Exploration*, **7**, 276–309.

ARVANTIDES, N., BOSTROM, K., KALOGEROPOULOS, S., PARITSIS, S., GALANOPOULOS, V. & PAPAVASSILIOU, C. 1990. Geochemistry of lavas, pumice and veins in drill core GPK-1, Palaea Kameni, Santorini. *In*: HARDY, D. A. (ed.) *Thera and the Aegean World III*, **2**, London, 266–279.

BACON, C. R. 1992. Partially melted granodiorite and related rocks ejected from Crater lake caldera, Oregon. *Transactions of the Royal Society of Edinburgh: Earth Sciences*, **83**, 27–47.

——1986. Magmatic inclusions in silicic and intermediate rocks. *Journal of Geophysical Research*, **91B**, 6091–6112.

—— & DRUITT, T. H. 1988. Compositional evolution of the zoned calcalkaline magma chamber of Mount Mazama, Crater Lake, Oregon. *Contributions to Mineralogy and Petrology*, **98**, 224–256.

—— & HIRSCHMANN, M. M. 1988. Mg/Mn Partitioning as a Test For Equilibrium Between Coexisting Fe-Ti Oxides. *American Mineralogist*, **73**, 57–61.

BAILLIE, M. G. L. 1990. Irish tree rings and an event in 1628 BC. *In*: HARDY, D. A. (ed.) *Thera and the Aegean World III*, **3**. The Thera Foundation, London, 160–166.

—— & MUNROE, M. A. R. 1988. Irish tree-rings, Santorini and volcanic dust veils. *Nature*, **332**, 344–346.

BAKER, D. R. & EGGLER, D. H. 1987. Compositions of anhydrous and hydrous melts coexisting with plagioclase, augite, olivine or low-Ca pyroxene from 1 atm to 8 kbar: application to the Aleutian volcanic center of Atka. *American Mineralogist*, **72**, 12–28.

BARBERI, F. & CARAPEZZA, M. L. 1994. Helium and CO_2 soil gas emissions from Santorini (Greece). *Bulletin of Volcanology*, **56**, 335–342.

BARD, E., HAMELIN, B., FAIRBANKS, R. & ZINDLER, A. 1990. Calibration of the ^{14}C timescale over the last 30 000 years using mass spectrometric U-Th ages from Barbados corals. *Nature*, **345**, 405–410.

BARREIRO, B. A. 1983. Lead isotope compositions of South Sandwich Island volcanic rocks and their bearing on magmagenesis in intra-oceanic island arcs. *Geochimica et Cosmochimica Acta*, **47**, 817–822.

BARTON, M. & HUIJSMANS, J. P. P. 1986. Post-caldera dacites from the Santorini Volcanic Complex, Aegean Sea: An example of the eruption of lavas of near constant composition over a 2200 year period. *Contributions to Mineralogy and Petrology*, **94**, 472–495.

——, SALTERS, V. J. M. & HUIJSMANS, J. P. P. 1983. Sr isotope and trace element evidence for the role of continental crust in calc-alkaline volcanism on Santorini and Milos, Aegean Sea, Greece. *Earth and Planetary Science Letters*, **63**, 273–291.

BASSINOT, F. C., LABEYRIE, L. D., VINCENT, E., QUIDELLEUR, X., SHACKLETON, N. J. & LANCELOT, Y. 1994. The astronomical theory of climate and the age of the Bruhnes-Matuyama magnetic reversal. *Earth and Planetary Science Letters*, **126**, 91–108.

BENNETT, J. T., KRISHNASWAMI, S., TUREKIAN, K. K., MELSON, W. G. & HOPSON, C. A. 1982. The Uranium and Thorium Decay-Series Nuclides in Mt. St. Helens Effusives. *Earth and Planetary Science Letters*, **60**, 61–69.

BLAKE, S. & IVEY, G. N. 1986. Density and viscosity gradients in zoned magma chambers and their influence on withdrawal dynamics. *Journal of Volcanology and Geothermal Research*, **30**, 201–230.

BOND, A. & SPARKS, R. S. J. 1976. The Minoan eruption of Santorini, Greece. *Journal of the Geological Society of London*, **132**, 1–16.

BOSTRÖM, K., HALLBERG, A., ABERG, A. & MAGNET DE SAISSY, H. 1990*b*. Metallogenesis at Santorini: a subduction-zone related process. I: deposition of hydrothermal sediments. *In*: HARDY, D. A. (ed.) *Thera and the Aegean World III*, **2**. The Thera Foundation, London, 280–290.

——, INGRI, J., BOSTRÖM, B., ANDERSSON, P., ARVANITIDES, N., GALANOPOULOS, V., KALOGEROPOULOS, S., PAPAVASSILIOU, C. & PARITSIS, S. 1990*a*. Chemistry of hydrothermal solutions in Drill Hole GPK-1, Palea Kameni, Santorini, Greece. *In*: HARDY, D. A. (ed.) *Thera and the Aegean World III*, **2**. The Thera Foundation, London, 257–260.

BOTTINGA, Y. & WEILL, D. F. 1970. Densities of liquid silicate systems calculated from partial molar volumes of oxide components. *American Journal of Science*, **269**, 169–182.

BRIQUEU, L. & LANCELOT, J. R. 1984. A geochemical study of Nea-Kameni hyalodacites (Santorini volcano, Aegean Island Arc). Inferences concerning the origin and effects of solfataras and magmatic evolution. *Journal of Volcanology & Geothermal Research*, **20**, 41–54.

——, JAVOY, M., LANCELOT, J. R. & TATSUMOTO, M. 1986. Isotope geochemistry of recent magmatism in the Aegean arc: Sr, Nd, Hf and O isotopic ratios in the lavas of Milos and Santorini – geodynamic implications. *Earth and Planetary Science Letters*, **80**, 41–54.

BROPHY, J. G. 1991. Composition gaps, critical crystallinity, and fractional crystallization in orogenic (calc-alkaline) magmatic systems. *Contributions Mineralogy and Petrology*, **109**, 173–182.

BUDETTA, G., CONDARELLI, D., FYTIKAS, M., KOLIOS, N., PASCALE, G., RAPOLLA, A. & PINNA, E. 1984. Geophysical prospecting on the Santorini islands. *Bulletin of Volcanology*, **47**, 447–466.

BURNHAM, C. W. & DAVIS, N. F. 1971. The role of H_2O in silicate melts: I. P-V-T relations in the system $NaAlSi_3O_8$-H_2O to 10 kilobars and 1000°C. *American Journal of Science*, **270**, 54–79.

CASALE, R., FYTIKAS, M., SIGVALDASSON, G. & VOUGIOUKALAKIS, G. (eds) 1998. *The European Laboratory volcanoes. Proceedings of a second workshop, Santorini, Greece, 2 to 4 May 1996*. European Commission.

CAWTHORN, R. G. & O'HARA, M. J. 1976. Amphibole fractionation in calcalkaline magma genesis. *American Journal of Science*, **276**, 309–329.

CHEN, J., EDWARDS, L. & WASSERBURG, G. J. 1992. Mass spectrometry and applications to uranium-series disequilibrium. *In*: IVANOVICH, M. & HARMON, R. S. (eds) *Uranium-Series Disequilibrium: Applications To Earth, Marine And Environmental Sciences (Second Edition)*. Oxford University Press, 174–206.

CLAYTON, R. N. & MAYEDA, T. K. 1963. The use of bromine pentafluoride in the extraction of oxygen from oxides and silicates for isotopic analysis. *Geochimica et Cosmochimica Acta*, **27**, 43–52.

CLYNNE, M. A. 1990. Stratigraphic, lithologic and major-element geochemical constraints on magmatic evolution at the Lassen volcanic center, California. *Journal of Geophysical Research*, **95**, 19 651–19 669.

CONDOMINES, M. & SIGMARSSON, O. 1993. Why are so many arc magmas close to ^{238}U–^{230}Th radioactive equilibrium? *Geochimica et Cosmochimica Acta*, **57**, 4491–4497.

——, HEMOND, C. & ALLEGRE, C. J. 1988. U-Th-Ra radioactive disequilibria and magmatic processes. *Earth and Planetary Science Letters*, **90**, 243–262.

——, MORAND, P. & ALLEGRE, C. J. 1981. ^{230}Th-^{238}U radioactive disequilibria in tholeiites from the FAMOUS Zone (Mid-Atlantic Ridge, 36°50′N): Th and Sr isotopic geochemistry. *Earth and Planetary Science Letters*, **55**, 247–256.

——, ——, CAMUS, G. & DUTHOU, L. 1982. Chronological and geochemical study of lavas from the Chaines des Puys, Massif Central, France: evidence for crustal contamination. *Contributions to Mineralogy and Petrology*, **81**, 296–303.

CONTICELLI, S., FRANCALANCI, L., SANTO, A. P. & PETRONE, C. 1998. Mineral chemistry as a contribution to the understanding of the Post-Minoan magmatic system of Santorini, Greece. *In*: CASALE, R. *et al.* (eds) *Proceedings of the second workshop, Santorini, Greece, 2 to 4 May 1996*. European Commission, 157–174.

COTTRELL, E., GARDNER, J. E. & RUTHERFORD, M. J. 1999. Petrologic and experimental evidence for the movement and heating of the pre-eruptive Minoan rhydacite (Santorini, Greece). *Contributions to Mineralogy and Petrology*, **135**, 315–331.

COX, A. & DALRYMPLE, G. B. 1967. Statistical analysis of geomagnetic reversal data and the precision of potassium-argon dating. *Journal of Geophysical Research*, **72**, 2603–2614.

CRISP, J. A. 1984. Rates of magma emplacement and volcanic output. *Journal of Volcanology and Geothermal Research*, **20**, 177–211.

DALRYMPLE, G. B. 1989. The GLM continuous laser system for ^{40}Ar/^{39}Ar dating: description and performance characteristics. *US Geological Survey Bulletin*, **1890**, 89–96.

—— & LANPHERE, M. A. 1969. *Potassium-Argon Dating*. Freeman, New York.

——, ALEXANDER, E. C. JR., LANPHERE, M. A. & KRAKER, G. P. 1981. *Irradiation of samples for $^{40}Ar/^{39}Ar$ dating using the Geological Survey TRIGA reactor*. US Geological Survey Professional Papers, **1176**.

DAVIS, E. N. & BASTAS, C. 1978. Petrology and geochemistry of the metamorphic system of Santorini. *In*: DOUMAS, C. (ed.) *Thera and the Aegean World II*. The Thera Foundation, London, 61–79.

——, GARTZOS, E. & DIETRICH, V. J. 1998. Magmatic evolution of the Pleistocene Akrotiri volcanoes. *In*: CASALE, R. *et al.* (eds) *Proceedings of the second workshop, Santorini, Greece, 2 to 4 May 1996*. European Commission, 49–68.

DEER, W. A., HOWIE, R. A. & ZUSSMAN, J. 1966. *An Introduction to the Rock-Forming Minerals*. Longman Group Ltd, Harlow.

DELIBASIS, N., CHAILAS, S., LAGIOS, E. & DRAKOPOULOS, J. 1990. Surveillance of Thera Volcano, Greece: microseismicity monitoring. *In*: HARDY, D. A. (ed.) *Thera and the Aegean World III*, **2**. The Thera Foundation, London 199–206.

DE PAOLO, D. J. 1981. Trace element and isotopic effects of combined wall-rock – assimilation and fractional crystallization. *Earth and Planetary Science Letters*, **53**, 189–202.

——1988. *Neodymium Isotope Geochemistry: An Introduction*. Springer Verlag, New York.

DE SILVA, S. L. 1989. The origin and significance of crystal-rich inclusions in pumices from two Chilean ignimbrites. *Geological Magazine*, **126**, 159–175.

——1991. Styles of zoning in central Andean ignimbrites; Insights into magma chamber processes. *Geological Society of America Special Paper*, **265**, 217–232.

DEWEY, J. E., PITTMAN III, W. C., RYAN, W. B. F. & BONNIN, J. 1973. Plate tectonics and evolution of the Alpine system. *In*: HARMON, R. S. & RAPELA, C. W. (eds) *Andean Magmatism and its Tectonic Setting. Geological Society of America Bulletin*, **84**, 3137–3180.

DIETRICH, V. J., DAVIS, E. & GARTZOS, E. 1998. Amphibole in rhyodacites and dacites from the Akrotiri volcanoes and the complexity of discontinuous fractionation. *In*: CASALE, R. *et al.* (eds) *Proceedings of the second workshop, Santorini, Greece, 2 to 4 May 1996*. European Commission, 69–80.

DI PAOLO, G. M. 1974. Volcanology and petrology of Nisyros island (Dodecanese, Greece). *Bulletin of Volcanology*, **38**, 944–987.

DOUMAS, C. (ed.) 1978. *Thera and the Aegean World I*. The Thera Foundation. London.

—— (ed.) 1980. *Thera and the Aegean World II*. The Thera Foundation. London.

DRUITT, T. H. 1983. *Explosive volcanism on Santorini, Greece*. PhD Thesis, University of Cambridge.

——1985. Vent evolution and lag breccia formation during the Cape Riva eruption of Santorini, Greece. *Journal of Geology*, **93**, 439–454.

—— & BACON, C. R. 1986. Lithic breccia and ignimbrite erupted during the collapse of Crater Lake caldera, Oregon. *Journal of Volcanology and Geothermal Research*, **29**, 1–32.

—— & ——1989. Petrology of the zoned calcalkaline magma chamber of Mount Mazama, Crater Lake, Oregon. *Contributions to Mineralogy and Petrology*, **101**, 245–259.

—— & FRANCAVIGLIA, V. 1990. An ancient caldera cliff line in Phira and its significance for the topography and geology of pre-Minoan Santorini. *In*: HARDY, D. A. (ed.) *Thera and the Aegean World III*, **2**. The Thera Foundation, London, 362–370.

—— & ——1992. Caldera formation on Santorini and the physiography of the islands in the late Bronze Age. *Bulletin of Volcanology*, **54**, 484–493.

—— & SPARKS, R. S. J. 1982. A proximal ignimbrite breccia facies on Santorini, Greece. *Journal of Volcanology and Geothermal Research*, **13**, 147–171.

—— & ——1984. On the formation of calderas during ignimbrite eruptions. *Nature*, **310**, 679–681.

—— EDWARDS, L., LANPHERE, M., SPARKS, R. S. J. & DAVIES, M. 1998. Volcanic development of Santorini revealed by field, radiometric, chemical and isotopic studies. The European Laboratory Volcanoes. *In*: CASALE, R. *et al.* (eds) *Proceedings of the second workshop, Santorini, Greece, 2 to 4 May 1996*. European Commission, 37–48.

——, MELLORS, R. A., PYLE, D. M. & SPARKS, R. S. J. 1989. Explosive volcanism on Santorini, Greece. *Geology Magazine*. **126**, 95–126.

DUFFIELD, W. A. & DALRYMPLE, G. B. 1990. The Taylor Creek Rhyolite of New Mexico: A rapidly emplaced field of lava domes and flows. *Bulletin of Volcanology*, **52**, 475–487.

DURR, S., ALTHERR, R., KELLER, J., OKRUSCH, M. & SEIDEL, E. 1978. The median Aegean crystalline belt: stratigraphy, structure, metamorphism, magmatism, Alps, Appennines, Hellenides, Stuttgart. *In*: CLOSS, H., ROEDER, D. & SCHMIDT, K. (eds) *Inter-Union Commission on Geodynamics Scientific Report*, **38**, 537–564.

EDWARDS, L. 1994. *Magma cyclicity and isotopic variation on Santorini volcano, Aegean Sea, Greece*. PhD Thesis, University of Bristol.

EICHELBERGER, J. C. 1980. Vesiculation of mafic magma during replenishment of silicic magma reservoirs. *Nature*, **288**, 446–450.

ERIKSEN, U., FRIEDRICH, W. L., BUCHARD, T. B., TAUBER, H. & THOMSEN, M. S. 1990. The Stronghyle caldera: geological, palaeontological and stable isotope evidence from radiocarbon dated stromatolites from Santorini. *In*: HARDY, D. A. (ed.) *Thera and the Aegean World III*, **2**. The Thera Foundation, London, 362–370.

ESPERANCA, S., CRSICI, G. M., DE ROSA, R. & MAZZOULI, R. 1992. The role of crust in the evolution of the island of Lipari (Aeolian Islands, Italy). *Contributions to Mineralogy and Petrology*, **112**, 450–462.

FAURE, G. 1986. *Principles of Isotope Geology (2nd edition)*. John Wiley & Sons, Inc., New York.

FEDERMAN, A. N. & CAREY, S. N. 1980. Electron microprobe correlation of tephras from Eastern Mediterranean abyssal sediments and the island of Santorini. *Quaternary Research*, **13**, 160–171.

FEELEY, T. C. & DAVIDSON, J. P. 1994. Petrology of calcalkaline lavas at Volcan Ollague and the origin of compositional diversity at central Andean stratovolcanoes. *Journal of Petrology*, **35**, 1295–1340.

FERRARA, G., FYTIKAS, N., GUILIANI, O. & MARINELLI, G. 1980. Age of the formation of the Aegean active volcanic arc. *In*: DOUMAS, C. (ed.) *Thera and the Aegean World II*. The Thera Foundation, London, 37–41.

FLEMMING, N. C. 1978. Thera as the tectonic focus of the south Aegean: archaeological evidence from the Aegean margin. *In*: DOUMAS, C. (ed.) *Thera and the Aegean World I*. The Thera Foundation, London, 82–84.

FOUQUÉ, F. 1879. *Santorin et ses eruptions*. Masson, Paris.

——1998. *Santorini and its eruptions*. [Translated and annotated by A. R. McBirney). Johns Hopkins, University, Press, Baltimore.

FRANCALANCI, L., VOUGIOUKALAKIS, G., ELEFTHERIADES, G., PINARELLI, L., PETRONE, C., MANETTI, P. & CHRISTOFIDES, G. 1998. Petrographic, chemical and isotopic variations in the intra-caldera post-Minoan rocks of the Santorini volcanic field, Greece. *In*: CASALE, R. *et al.* (eds) *Proceedings of the second workshop, Santorini, Greece, 2 to 4 May 1996*. European Commission, 175–186.

FREUNDT, A. & TAIT, S. R. 1986. The entrainment of high-viscosity magma into low-viscosity magma in eruption conduits. *Bulletin of Volcanology*, **48**, 325–339.

FRIEDRICH, W. L. 1980. Fossil plants from Weichselian Interstadials, Santorini, (Greece) II. *In*: DOUMAS, C. (ed.) *Thera and the Aegean World II*. The Thera Foundation, London, 109–128.

——, PICHLER, H. & KUSSMAUL, S. 1977. Quaternary pyroclastics from Santorini, Greece amd their significance for the Mediterranean palaeoclimate. *Bulletin of the Geological Society of Denmark*, **A26**, 27–39.

——, WAGNER, P. & TAUBER, H. 1990. Radiocarbon dated plant remains from the Akrotiri excavation on Santorini, Greece. *In*: HARDY, D. A. (ed.) *Thera and the Aegean World III*, **3**. The Thera Foundation, London, 188–196.

FYTIKAS, M. & MARINELLI, G. 1976. Geology and geothermics of the island of Milos (Greece). *Proceedings of Geothermal Energy*, **1**, 516–524.

——, INNOCENTI, F., KOLIOS, N., MANETTI, P., MAZZUOLI, R., POLI, G., RITA, F. & VILLARI, L. 1986. Volcanology and petrology of volcanic products from the island of Milos and neighbouring islets. *Journal of Volcanology and Geothermal Research*, **28**, 297–317.

——, ——, MANETTI, P., MAZZUOLI, R., PECCERILLO, A. & VILLARI, L. 1984. Tertiary to Quaternary evolution of volcanism in the Aegean region. *In*: DIXON, J. E. & ROBERTSON, A. H. F. (eds) *The Geological Evolution of the Eastern Mediterranean*. Geological Society, London, Special Publications, **17**, 687–699.

——, KOLIOS, N. & VOUGIOUKALAKIS, G. 1990*a*. Post-Minoan volcanic activity of the Santorini volcano. Volcanic hazard and risk, forecasting possibilites. *In*: HARDY, D. A. (ed.) *Thera and the Aegean World III*, **2**. The Thera Foundation, London, 183–198.

——, KARYDAKIS, G., KAVOURIDIS, TH., KOLIOS, N. & VOUGIOUKALAKIS, G. 1990*b*. Geothermal research on Santorini *In*: HARDY, D. A. (ed.) *Thera and the Aegean World III*, **2**. The Thera Foundation, London, 241–249.

GALANOPOULOS, A. G. 1971. The eastern Mediterrranean trilogy in the Bronze Age. *In*: KALOUEROPOULOU, A. (ed.) *Acta of the First International Scientific Congress on the Volcano of Thera*, Athens, 184–210.

GARCIA, M. O. & JACOBSON, S. S. 1979. Crystal clots, amphibole fractionation, and the evolution of calc-alkaline magmas. *Contribributions Mineralogy and Petrology*, **69**, 319–327.

GARDEWEG, M. C., SPARKS, R. S. J. & MATTHEWS, S. J. 1998. Evolution of Lascar Volcano, Northern Chile. *Journal of the Geological Society, London*, **155**, 89–104..

GARDNER, J. E., THOMAS, R. M. E., JAUPART, C. & TAIT, S. R. 1996. Fragmentation of magma during Plinian volcanic eruptions. *Bulletin of Volcanology*, **58**, 144–162.

GARTZOS, E., DIETRICH, V. J. & DAVIS, E. 1998. Magma mixing in basaltic andesites of Cape Mavroorachidi (Akrotiri Volcanoes). *In*: CASALE, R. *et al.* (eds) *Proceedings of the second workshop, Santorini, Greece, 2 to 4 May 1996*. European Commission, 81–88.

GEORGALAS, G. C. 1953. L'éruption du volcan de Santorin en 1950. *Bulletin Volcanologique*, **13**, 39–55.

——1962. *Catalogue of the Active Volcanoes of the World Including Solfatara Fields, Greece*. International Association of Volcanology, Rome.

——1971. L'Eruption Minoenne du volcan de Santorin. *In*: KALOUEROPOULOU, A. (ed.) *Acta of the First International Scientific Congress on the Volcano of Thera*, Athens, 170–179.

GILL, J. B. 1981. *Orogenic Andesites and Plate Tectonics*. Springer-Verlag, Berlin, Heidelberg.

—— & CONDOMINES, M. 1992. Short-lived radioactivity and magma genesis. *Science*, **257**, 1368–1376.

—— & WILLIAMS, R. W. 1990. Th-isotope and U-series studies of subduction-related volcanic rocks. *Geochimica et Cosmochimica Acta*, **54**, 1427–1442.

——, PYLE, D. M. & WILLIAMS, R. W. 1992. Igneous rocks. *In*: IVANOVICH, M. & HARMON, R. S. (eds) *Uranium-Series Disequilibrium: Applications To Earth, Marine And Environmental Sciences (Second Edition)*. Oxford University Press, 207–258.

GROVE, T. L. & BAKER, M. B. 1984. Phase equilibrium controls on the tholeiitic versus calc-alkaline differentiation trends. *Journal of Geophysical Research*, **89**, 3253–3274.

—— & DONNELLY-NOLAN, J. M. 1986. The evolution of young silicic lavas at Medicine Lake Volcano, California: implications for the origins of compositional gaps in calcalkaline series lavas. *Contributions to Mineralogy and Petrology*, **92**, 281–302.

—— & KINZLER, R. J. 1986. Petrogenesis of andesites. *Annual Review of Earth Planetary Science*, **14**, 417–454.

GUICHARD, F., CAREY, S., ARTHUR, M. A., SIGURDSSON, H. & ARNOLD, M. 1993. Tephra from the Minoan eruption of Santorini in sediments of the Black Sea. *Nature*, **363**, 610–612.

HAMMER, C. U., CLAUSEN, H. B., FREIDRICH, W. L. & TAUBER, H. 1987. The Minoan eruption of Santorini dated to 1645 BC? *Nature*, **328**, 517–519.

HARDY, D. A. (ed.) 1990. *Thera and the Aegean World III*. 3 Volumes. The Thera Foundation, London.

HARMON, R. S., BARREIRIO, B., MOORBATH, S., HOEFS, J., FRANCIS, P. W., THORPE, R. S., DERUELLE, B., MCHUGH, J. & VIGLINO, J. A. 1984. Regional O-, Sr-, and Pb-isotope relationships in late Cenozoic calc-alkaline lavas of the Andean Cordillera. *Journal of the Geological Society, London*, **141**, 803–822.

HARVEY, P. K., TAYLOR, D. M., HENDRY, R. D. & BANCROFT, F. 1973. An accurate fusion method for the analysis of rocks and chemically related materials by X-ray Fluorescence Spectrometry. *X-Ray Spectrometry*, **2**, 33–44.

HAWKESWORTH, C. J. & POWELL, M. 1980. Magma genesis in the Lesser Antilles island arc. *Earth and Planetary Science Letters*, 51, 297–308.

——, GALLAGHER, K., HERGT, J. M. & MCDERMOTT, F. 1993. Trace element fractionation processes in the generation of island arc basalts. *Philosophical Transactions of the Royal Society, London*, **A342**, 179–191.

HEIKEN, G. & MCCOY, F. JR. 1984. Caldera development during the Minoan eruption, Thira, Cyclades, Greece. *Journal of Geophysical Research*, **89**, 8441–8462.

—— & ——1990. Precursory activity to the Minoan eruption, Thera. *In*: HARDY, D. A. (ed.) *Thera and the Aegean World III*, **2**. The Thera Foundation, London, 79–88.

HENJES-KUNST, F. & KREUZER, H. 1982. Isotopic dating of Pre-Alpidic rocks from the island of Ios (Cyclades, Greece). *Contributions to Mineralogy and Petrology*, **80**, 245–253.

HERZBERG, C. T. 1978. Pyroxene geothermometry and geobarometry: experimental and thermodynamic evalution of some subsolidus phase relations involving pyroxenes in the system CaO–MgO–Al_2O_3–SiO_2. *Geochimica et Cosmochimica Acta*, **42**, 945–957.

HICKEY, R. L., FREY, F. A., GERLACH, D. C. & LOPEZ-ESCOBAR, L. 1986. Multiple sources for basaltic arc rocks from the Southern Volcanic Zone of the Andes (34°–41°S): trace element and isotopic evidence for contributions from subducted oceanic crust, mantle and continental crust. *Journal of Geophysical Research*, **91**, 5963–5983.

HILDRETH, W. 1981. Gradients in silicic magma chambers: implications for lithospheric magmatism. *Journal of Geophysical Research*, **86**, 10 153–10 192.

—— & MOORBATH, S. 1988. Crustal contributions to arc magmatism in the Andes of Central Chile. *Contributions to Mineralogy and Petrology*, **98**, 455–489.

HOEFS, J. 1978. Oxygen isotope composition of volcanic rocks from Santorini and Christiani. *In*: DOUMAS, C. (ed.) *Thera and the Aegean World I*. The Thera Foundation, London, 163–170.

HUBBERTEN, H. W., BRUNS, M., CALAMIOTOU, M., APOSTOLAKIS, C., FILIPPAKIS, S. & GRIMANIS, A. 1990. Radiocarbon dates from the Akrotiri excavations. *In*: HARDY, D. A. (ed.) *Thera and the Aegean World III*, **3**. The Thera Foundation, London, 179–187.

HUIJSMANS, J. P. P. 1985. Calcalkaline lavas from the volcanic complex of Santorini, Aegean Sea, Greece. *Geologica Ultraiectina*, **41**, 1–316.

—— & BARTON, M. 1989. Polybaric geochemical evolution of two shield volcanoes from Santorini, Aegean Sea, Greece: evidence for zoned magma. *Journal of Petrology*, **30**, 583–625.

——, —— & SALTERS, V. J. M. 1988. Geochemistry and evolution of the calc-alkaline volcanic complex of Santorini, Aegean Sea, Greece. *Volcanology and Geothermal Research*, **34**, 283–306.

HUPPERT, H. E. & SPARKS, R. S. J. 1988. The generation of granite by intrusion of basalt into the continental crust. *Journal of Petrology*, **29**, 599–624.

——, —— & TURNER, J. S. 1982. Effect of volatiles on mixing in calcalkaline magma systems. *Nature*, **297**, 554–557.

——, —— & ——1984. Some effects of viscosity on the dynamics of replenished magma chambers. *Journal of Geophysical Research*, **89**, 6857–6877.

IMURA, R. 1993. A reconstruction of small-scale eruptions using pyroclastic deposits. *Geographical Reports of Tokyo University*, 17–78.

INGAMELLS, C. O. 1970. Lithium metaborate flux in silicate analysis. *Analytica Chimica Acta*, **52**, 323–334.

INNOCENTI, F., MANETTI, P., PECCERILLO, A. & POLI, G. 1979. Inner arc volcanism in NW Aegean arc: geochemical and geochronological data. *Neues Jahrbuch für Mineralogie Monashefte*, **H.4**, 145–158.

——, ——, —— & ——1981. South Aegean volcanic arc: geochemical variations and geotectonic implications. *Bulletin of Volcanology*, **44**, 377–391.

IRVINE, T. N. 1982. Terminology for layered intrusions. *Journal of Petrology*, **23**, 127–162.

—— & BARAGER, W. R. A. 1971. A guide to the chemical classification of the common rocks. *Canadian Journal of Earth Sciences*, **8**, 523–548.

IVANOVICH, M. & HARMON, R. S. 1982. *Uranium Series Disequilibria: Applications to Environmental Problems*. Oxford University Press, Oxford.

JACKSON, J. A. 1994. Active tectonics of the Aegean region. *Annual Reviews of Earth and Planetary Sciences*, **22**, 239–271.

——, KING, G. & VITA-FINZI, C. 1982. The neotectonics of the Aegean: an alternative view. *Earth and Planetary Science Letters*, **61**, 303–318.

JAMES, D. E. 1984. Quantitative models for crustal contamination in the Central and northern Andes. *In*: *Andean Magmatism: Chemical and Isotopic Constraints*. Shiva Geology Series, Shiva Publishing Ltd, Norwich, 124–138.

JANSEN, J. B. H. 1973. *Geological map of Naxos*. National Institute of Geological and Mineral Research, Greece.

—— & SCHUILING, R. D. 1976. Metamorphism on Naxos: petrology and geothermal gradients. *American Journal of Science*, **276**, 1225–1253.

——, VAN DER KRAATS, A. H., VAN DER RIJST, H. & SCHUILING, R. D. 1978. Metamorphism of siliceous dolomites at Naxos, Greece. *Contributions to Mineralogy and Petrology*, **67**, 279–288.

KALOGEROPOULOS, S. & PARITSIS, S. 1990. Geological and geochemical evolution of the Santorini volcano: a review. *In*: HARDY, D. A. (ed.) *Thera and the Aegean World III*, **2**. The Thera Foundation, London, 164–171.

KALOUEROPOULOU, A. (ed.) 1971. *Acta of the First International Scientific Congress on the Volcano of Thera*. Athens.

KELLER, J. 1982. Mediterranean island arcs. *In*: THORPE, R. S. (ed.) *Andesites*. J. Wiley & Sons, 307–325.

——1981. Quaternary tephrochronology in the Mediterranean region. *In*: SELF, S. & SPARKS, R. S. J. (eds) *Tephra Studies*. D. Riedel, 227–244.

KILIAS, A. A., MOUNTRAKIS, D. M., TRANOS, M. D. & PAVLIDES, S. B. 1998. The prevolcanic metamorphic rocks of Santorini island: structural evolution and kinematics during the Tertiary (South Aegean, Greece). *In*: CASALE, R. *et al.* (eds) *Proceedings of the second workshop, Santorini, Greece, 2 to 4 May 1996*. European Commission, 23–36.

KISKYRAS, D. A. 1978. The geotectonic state of the Greek region: vulcanism, intermediate earthquakes and plate tectonics. *In*: DOUMAS, C. (ed.) *Thera and the Aegean World I*. The Thera Fopundation, London, 86–96.

KOBAYASHI, T. 1986. Volcanic ash deposits formed by the intermittent eruption of the active volcano, Sakurajima. *Journal of the Institute of Earth Sciences*, Faculty of Science, Kagoshima University, 1–12.

KREUZER, H., HARRE, W., LENZ, H., WENDT, I. & HENJES-KUNST, F. 1978. K/Ar and Rb/Sr daten von mineralen aus dem polymetamorphen kristallen der Kykladen-insel Ios (Griechenland). *Fortschrau Minerology*, **56**, 69–70.

KTENAS, C. 1935. Le groupe d'Iles du Santorin. Contribution a l'etude des laves tertiaires et quaternaires de la mer Egee. *Pragam Academia Athens*, **A4**, 53–57.

KYSER, T. K., O'NEILL, J. R. & CARMICHAEL, I. S. E. 1982. Genetic relations among basic lavasa and ultramafic nodules: evidence from oxygen isotope compositions. *Contributions to Mineralogy and Petrology*, **81**, 88–102.

LAMARCHE, V. C. & HIRSCHBOECK, K. K. 1984. Frost rings in trees as records of major volcanic eruptions. *Nature*, **307**, 121–126.

LE PICHON, X., ANGELIER, J., AUBOUIN, J. & 11 OTHERS 1979. From subduction to transform motion: a seabeam survey of the Hellenic trench system. *Earth and Planetary Science Letters*, **44**, 441–450.

LIATSIKAS, N 1942. Mineralogie und chemismus der laven des ausbruches 1939–1941 des Santorin-vulkans. *Prakt Academia Athens*, **17**, 95–102.

LIMBERG, E. M. & VAREKAMP, J. C. 1991. Young pumice deposits on Nisyros, Greece. *Bulletin of Volcanology*, **54**, 68–77.

LINDSLEY, D. H. 1983. Pyroxene geothermometry. *American Mineralogy*, **68**, 477–493.

LINEWEAVER, J. L. 1963. Oxygen outgassing caused by electron bombardment of glass. *Journal of Applied Physics*, **34**, 1786–1791.

MAALOE, S. & MCBIRNEY, A. R. 1997. Liquid fractionation. Part IV: Scale models for liquid fractionation of calc-alkaline magmas. *Journal of Volcanology and Geothermal Research*, **76**, 111–125.

MACDOUGALL, J. D. 1995. Using short-lived U and Th series isotopes to investigate volcanic processes. *Annual Reviews in Earth and Planetary Sciences*, **23**, 143–167.

MAKRIS, J. 1978. The crust and upper mantle of the Aegean region from deep seismic soundings. *Tectonophysics*, **46**, 269–284.

——1980. Geodynamic considerations of the development of the Hellenides. *In*: DOUMAS, C. (ed.) *Thera and the Aegean World II*. The Thera Foundation, London, 43–44.

—— & STOBBE, C. 1980. The thermal regime of the Aegean area. *In*: DOUMAS, C. (ed.) *Thera and the Aegean World II*. The There Foundation, London, 45–48.

MANKINEN, E. A. & DALRYMPLE, G. B. 1972. Electron microprobe evaluation of terrestrial basalts for whole-rock dating. *Earth and Planetary Science Letters*, **17**, 159–168.

MANN, A. C. 1983. Trace element geochemistry of high-alumina basalt-andesite-dacite-rhyodacite lavas of the main volcanic series of Santorini volcano, Greece. *Contributions to Mineralogy and Petrology*, **84**, 43–57.

MARINATOS, S. 1939. The volcanic destruction of Minoan Crete. *Antiquity*, **13**, 425–439.

MARSH, B. D. 1988. Crystal capture, sorting, and retention in convecting magma. *Geological Society of America Bulletin*, **100**, 1720–1737.

——1990. Reply to discussion by Sparks, R. S. J. of 'Crystal capture, sorting and retention in convecting magma' by B. D. Marsh. *Bulletin of the Geological Society of America*, **102**, 850–853.

MATSUHISA, Y. 1979. Oxygen isotopic compositions of volcanic rocks from the East Japan island arcs and their bearing on petrogenesis. *Journal of Volcanology and Geothermal Research*, **5**, 271–296.

MATTHEWS, A. & SCHLIESTEDT, M. 1984. Evolution of the blueschist and greenschist facies rocks of Sifnos, Cyclades, Greece – a stable isotope study of subduction-related metamorphism. *Contributions to Mineralogy and Petrology*, **88**, 150–163.

MCBIRNEY, A. R, BAKER, B. H. & NILSON, R. H. 1985. Liquid fractionation. Part I. Basic principles and experimental simulations. *Journal of Volcanology and Geothermal Research*, **24**, 1–24.

MCCLELLAND, E. A. & DRUITT, T. H. 1989. Palaeomagnetic estimates of emplacement temperatures of pyroclastic deposits on Santorini, Greece. *Bulletin of Volcanology*, **51**, 16–27.

—— & THOMAS, R. M. E. 1990. A palaeomagnetic study of Minoan age tephra from Thera. *In:* HARDY, D. A. (ed.) *Thera and the Aegean World III*, **2**. The Thera Foundation, London, 129–138.

MCDERMOTT, F. & HAWKESWORTH, C. 1991. Th, Pb, and Sr isotopic variations in young island arc volcanics and oceanic sediments. *Earth and Planetary Science Letters*, **104**, 1–15.

——, ELLIOTT, T. R., VAN CALSTEREN, P. & HAWKESWORTH, C. J. 1993. Measurement of $^{230}Th/^{232}Th$ ratios in young volcanic rocks by single-sector thermal ionization mass-spectrometry. *Chemical Geology*, **103**, 283–292.

MCKENZIE, D. P. 1985. ^{230}Th-^{238}U disequilibrium and the melting process beneath ridge axes. *Earth and Planetary Science Letters*, **72**, 149–157.

——1970. Plate tectonics of the Mediterranean region. *Nature*, **226**, 239–243.
——1978. Active tectonics of the Alpine–Himalayan belt: the Aegean Sea and surrounding regions. *Geophysical Journal of the Royal Astronomy Society*, **55**, 217–254.
MELLORS, R. A. 1988. *Explosive volcanism on Santorini, Greece and Mt. St. Helens*. PhD Thesis, University of Cambridge.
—— & SPARKS, R. S. J. 1991. Spatter-rich pyroclastic flow deposits on Santorini, Greece. *Bulletin of Volcanology*, **53**, 327–342.
MERCIER, J. L., SOREL, D. & VERGELY, P. 1989. Extensional tectonic regimes in the Aegean basins during the Cenozoic. *Basin Research*, **2**, 49–71.
MÉSZÁROS 1978. Some words on the Minoan tsunami of Santorini. *In*: DOUMAS, C. (ed.) *Thera and the Aegean World I*. The Thera Foundation, London, 257–261.
MERZBACHER, C. & EGGLER, D. H. 1984. A magmatic geohygrometer: application to Mt. St. Helens and other dacite magmas. *Geology*, **12**, 587–590.
MITROPOULOS, P. & TARNEY, J. 1992. Significance of mineral composition variations in the Aegean Island Arc. *Journal of Volcanology and Geothermal Research*, **51**, 283–303.
——, ——, SAUNDERS, A. D. & MARSH, N. G. 1987. Petrogenesis of Cenozoic volcanic rocks from the Aegean island arc. *Journal of Volcanology and Geothermal Research*, **32**, 177–193.
MIYASHIRO, A. 1974. Volcanic rock series in island arcs and active continental margins. *American Journal of Science*, **274**, 321–355.
MO, X., CARMICHAEL, I. S. E., RIVERS, M. & STEBBINS, J. 1982. The partial molar volume of Fe_2O_3 in multicomponent silicate liquids and the pressure dependence of oxygen fugacity in magmas. *Mineralogical Magazine*, **75**, 237–245.
MOUNTRAKIS, D., PAVLIDES, S., CHATZIPETROS, A., MELETIDIS, S., TRANOS, M. M., VOUGIOUKALAKIS, G. & KILIAS, A. 1998. Active deformation of Santorini. *In*: CASALE, R. *et al.* (eds) *Proceedings of the second workshop, Santorini, Greece, 2 to 4 May 1996*, European Commission, 13–22.
MUELENBACHS, K. & BYERLY, G. 1982. ^{18}O enrichment of silicic magmas caused by crystal fractionation at the Galapagos spreading center. *Contributions to Mineralogy and Petrology*, **79**, 76–79.
NEUMANN VAN PADANG, M. 1936. Die geschichte des vukanismus Santorins von ihren Anafangen bis zum zerstoren Bimssteinausbruch um die mitte des 2. Jahrthausend v Chr. *In*: RECK, H. (ed.) *Santorin – Der Werdegang eines Inselvulkans und sein Ausbruch 1925–1928*, **1**. D. Reimer, Berlin, 1–72.
——1971. Two catastrophic eruptions in Indonesia, comparable with the plinian outburst of the volcano of Thera (Santorini) in Minoan time. *In*: KALOUEROPOULOU, A. (ed.) *Acta of the First International Scientific Congress on the Volcano of Thera*, Athens, 51–63.
NICHOLLS, I. A. 1971*a*. Petrology of Santorini volcano, Cyclades, Greece. *Journal of Petrology*, **12**, 67–119.
——1971*b*. Santorini volcano, Greece – Tectonic and petrochemical relationships with volcanics of the Aegean region. *Tectonophysics*, **11**, 377–385.
——1978. Primary basaltic magmas for the pre-caldera volcanic rocks of Santorini. *In*: DOUMAS, C. (ed.) *Thera and the Aegean World I*. The Thera Foundation, London, 109–120.
NIELSON, C. H. & SIGURDSSON, H. 1981. Quantitative methods for electron microprobe analysis of sodium in natural and synthetic glasses. *American Mineralogist*, **66**, 547–552.
NIELSEN, R. L. & DELONG, S. E. 1992. A numerical approach to boundary layer fractionation: application to differentiation in natural magma systems. *Contributions to Mineralogy and Petrology*, **110**, 355–369.
NILSON, R. H., MCBIRNEY, A. R. & BAKER, B. H. 1985. Liquid fractionation. Part II: Fluid dynamics and quantitative implications for magmatic systems. *Journal of Volcanology and Geothermal Research*, **24**, 25–54.
NINKOVICH, D & HEEZEN, B. C. 1965. Santorini tephra. *Proceedings of the Colston Research Society*, Butterworths, London, 413–453.
OKRUSCH, M., SEIDEL, E. & DAVIS, E. N. 1978. The assemblage jadeite-quartz in the glaucophane rocks of Sifnos (Cyclades, Greece). *Neues Jahrbuch für Mineralogie Abhandlungen*, **132**, 284–308.
PAPASTAMATIOU, J. 1956. Sur l'âge des calcaires cristillins de l'île de Théra (Santorin). *Bulletin of Geological Society of Greece*, **3:1**, 104–113.
PAPAZACHOS, B. C. 1990. Seismicity of the Aegean and the surrounding area. *Tectonophysics*, **178**, 287–308.
—— & PANAGIOTOPOULOS, D. G. 1993. Normal faults associated with volcanic activity and deep rupture zones in the southern Aegean volcanic arc. *Tectonophysics*, **220**, 301–308.
PE, G. G. 1972. Geochemistry and chemical mineralogy of the lavas of Crommyonia. *Annales Geologie des Pays Hellenes*, **24**, 257–275.
——1973. Petrology and geochemistry of volcanic rocks of Aegina, Greece. *Bulletin of Volcanology*, **37**, 491–514.
——1974. Volcanic rocks of Methana (South Aegean arc, Greece). *Bulletin of Volcanology*, **38**, 270–290.
——1975. Strontium isotope ratios in volcanic rocks from the northwestern part of the Hellenic arc. *Chemical Geology*, **15**, 53–60.
—— & GLEDHILL, A. 1975. Strontium isotope ratios in volcanic rocks from the southeastern part of the Hellenic arc. *Lithos*, **8**, 209–214.
PEARCE, J. A. & PEATE, D. W. 1995. Tectonic implications of the composition of volcanic arc magmas. *Annual Reviews of Earth and Planetary Sciences*, **23**, 251–285.
PECCERILLO, A. & TAYLOR, S. R. 1976. Geochemistry of Eocene calc-alkalic rocks from the Pègues L'Abbé (1842). *Histoire de Santorin ou Théra*, Paris, 667pp.
PE-PIPER, G. G., PIPER, D. J. W. & REYNOLDS, P. H. 1983. Paleomagnetic stratigraphy and radiometric dating of the Pliocene rocks of Aegina, Greece. *Bulletin of Volcanology*, **46–1**, 1–7.
PERISSORATIS, C. 1990. Marine geological research on Santorini: preliminary results. *In*: HARDY, D. A. (ed.) *Thera and the Aegean World III*, **2**. The Thera Foundation, London, 305–311.
——1995. The Santorini volcanic complex and its relation to the stratigraphy and structure of the Aegean arc, Greece. *Marine Geology*, **128**, 37–58.
PICHLER, H. & FRIEDRICH, W. L. 1976. Radiocarbon dates of Santorini volcanics. *Nature*, **262**, 373–374.
—— & ——1980. Mechanism of the Minoan eruption of Santorini. *In*: DOUMAS, C. (ed.) *Thera and the Aegean World II*. The Thera Foundation, London, 15–30.
—— & KUSSMAUL, S. 1972. The calc-alkaline rocks of the Santorini Group (Aegean Sea, Greece). *Neues Jahrbuch für Mineralogie Abhandlungen*, **116**, 268–307.
—— & ——1980. Comments on the geological map of the Santorini islands. *In*: DOUMAS, C. (ed.) *Thera and the Aegean World II*. The Thera Foundation, London, 413–427.
PUCHELT, H. 1978. Evolution of the volcanic rocks of Santorini. *In*: DOUMAS, C. (ed.) *Thera and the Aegean World I*. The Thera Foundation, London, 131–146.
—— & HOEFS, J. 1971. Preliminary geochemical and strontium isotope investigations on Santorini rocks. *In*: KALOUEROPOULOU, A. (ed.) *Acta of the First International Scientific Congress on the Volcano of Thera*, Athens, 318–327.
PYLE, D. M. 1990*a*. New estimates for the volume of the Minoan eruption. *In*: HARDY, D. A. (ed.) *Thera and the Aegean World III*, **2**. The Thera Foundation, London, 113–121.
——1990*b*. *Geological and radiochemical studies on young volcanoes*. PhD Thesis, University of Cambridge.
——, DAWSON, J. B. & IVANOVICH, M. 1991. Short-Lived Decay Series Disequilibria in the Natrocarbonatite Lavas of Oldoinyo Lengai, Tanzania: Constraints on The Timing of Magma Genesis. *Earth and Planetary Science Letters*, **105**, 378–396.
——, IVANOVICH, M. & SPARKS, R. S. J. 1988. Magma-Cumulate Mixing Identified By U-Th Disequilibrium Dating. *Nature*, **331**, 157–159.
REAGAN, M. K., VOLPE, A. M. & CASHMAN, K. V. 1992. ^{238}U And ^{232}Th Series Chronology Of Phonolite Fractionation At Mount Erebus, Antarctica. *Geochimica et Cosmochimica Acta*, **56**, 1401–1407.
RECK, H. 1936. *Santorini: Der Werdegang eines Inselvulkans und sein ausbruch 1925–1928*. Verlag Von Dietrich Reimer, Berlin (3 volumes).
ROEDER, P. L. & EMSLIE, R. F. 1970. Olivine-liquid equilibrium. *Contributions to Mineralogy and Petrology*, **29**, 275–289.
ROLLINSON, H. 1993. *Using Geochemical Data: evaluation, presentation, interpretation*. Longman Scientific and Technical, UK.
ROSI, M., VEZZOLI, L., ALEOTTI, P. & DE CENSI, M. 1996. Interaction between caldera collapse and eruptive dynamics during the Campanian ignimbrite eruption, Phleagrean Fields, Italy. *Bulletin of Volcanology*, **57**, 541–554.
RUTHERFORD, M. J. & DEVINE, J. D. 1988. The May 18 1980, eruption of Mount St. Helens 3. Stability and chemistry of amphibole in the magma chamber. *Journal of Geophysical Research*, **93**, 11949–11959.
RYE, R. O., SCHUILING, R. D., RYE, D. M. & JANSEN, J. B. H. 1976. Carbon, hydrogen and oxygen isotope studies of the regional metamorphic complex at Naxos, Greece. *Geochimica et Cosmochimica Acta*, **40**, 1031–1049.
SAKUYAMA, M. 1983. Petrology of arc volcanic rocks and their origin by mantle diapirs. *Journal of Volcanology and Geothermal Research*, **18**, 297–320.
SCANDONE, R. 1990. Chaotic collapse of calderas. *Journal of Volcanology and Geothermal Research*, **42**, 285–302.
SCARFE, C. M. & FUJII, T. 1987. Petrology of crystal clots in the pumice of Mount St. Helens, March 19, 1982 eruption: significant role of the Fe-Ti oxide crystallisation. *Journal of Volcanology and Geothermal Research*, **34**, 1–14.
SCHLIESTEDT, M. 1980. *Phasengleichgewichte in hochdruckgesteinen von Sifnos, Griechenland*. PhD Thesis, Technische Universitat, Braunschweig.
——, ALTHERR, R. & MATTHEWS, A. 1987. Evolution of the Cycladic Crystalline Complex: petrology, isotope geochemistry and geochronology. *In*: HELGESON, H. C. (ed.) *Chemical transport in metasomatic processes*. Reidel Pub. Co., 389–428.
SEIDENKRANZ, M.-S. 1992. *Foraminiferal analyses of shelf areas: Stratigraphy, ecology and taxonomy*. PhD Thesis, University of Aarhus.
SEWARD, D., WAGNER, G. A. & PICHLER, H. 1980. Fission track ages of Santorini volcanics. *In*: DOUMAS, C. (ed.) *Thera and the Aegean World II*. The Thera Foundation, London, 101–108.
SHACKLETON, N. J. 1987. Oxygen isotopes, ice volume and sea level. *Quaternary Science Reviews*, **6**, 183–190.
SIGURDSSON, H., CAREY, S. & DEVINE, J. D. 1990. Assessment of the mass, dynamics, and environmental effects of the Minoan eruption of Santorini Volcano. *In*: HARDY, D. A. (ed.) *Thera and the Aegean World III*, **2**. The Thera Foundation, London, 100–112.
SISSON, T. W. & GROVE, T. L. 1993. Experimental investigations of the role of H_2O in calc-alkaline differentiation and subduction zone magmatism. *Contributions to Mineralogy and Petrology*, **113**, 143–166.
SKARPELIS, N. & LIATI, A. 1990. The prevolcanic basement of Thera at Athinios: metamorphism, plutonism and mineralization. *In*: HARDY, D. A. (ed.) *Thera and the Aegean World III*, **2**. The Thera Foundation, London, 172–182.
——, KYRIAKOPOULOS, K & VILLA, I. M. 1988. Dating a drilled granitic intrusion at Thera (Santorini, Greece) (Abstract). *In*: *Annual Meeting – Society of Italy, Mineralogy and Petrology*.
——, KYRIAKOPOULOS, K. & VILLA, I. M. 1992. Occurrence and ^{40}Ar ^{39}Ar dating of a granite in Thera (Santorini, Greece). *Geologishes Rundschau*, **81**, 729–735.
SMITH, R. L. 1979. Ash-flow magmatism. *In*: CHAPIN, C. E. & ELSTON, W. E. (eds) *Ash-Flow Tuffs*. Geological Society of America, Special Papers, **180**, 5–27.
SNYDER, D. & TAIT, S. R. 1996. Magma mixing by convective entrainment. *Nature*, **379**, 529–531.
SPAKMAN, W., WORTEL, M. J. R. & VLAAR, N. J. 1988. The Hellenic subduction zone: A tomographic image and its geodynamic implications. *Geophysical Research Letters*, **15**, 60–63.

SPARKS, R. S. J. 1990. Discussion of 'Crystal capture, sorting and retention in convecting magma' by, B. D. Marsh. *Bulletin of the Geological Society of America*, **102**, 847–850.

—— & MARSHALL, L. A. 1986. Thermal and mechanical constraints on mixing between mafic and silicic magmas. *Journal of Volcanology and Geothermal Research*, **29**, 99–124.

—— & WILSON, C. J. N. 1990. The Minoan deposits: a review of their characteristics and interpretation. *In*: HARDY, D. A. (ed.) *Thera and the Aegean World III*, **2**. The Thera Foundation, London, 89–99.

—— & WRIGHT, J. V. 1979. Welded air-fall tuffs. *In*: CHAPIN, C. E. & ELSTON, W. E. (eds) *Ash-Flow Tuffs*. Geological Society of America, Special Papers, **180**, 155–166.

——, HUPPERT, H. E. & TURNER, J. S. 1984. The fluid dynamics of evolving magma chambers. *Philosophical Transactions of the Royal Society, London*, **A310**, 511–534.

——, SIGURDSSON, H. & WILSON, L. 1977. Magma mixing: mechanism of triggering explosive acid eruptions. *Nature*, **267**, 315–318.

SPIEGELMAN, M. & ELLIOTT, T. 1993. Consequences of melt transport for uranium-series disequilibrium in young lavas. *Earth And Planetary Science Letters*, **118**, 1–20.

STACEY, J. S., SHERRILL, N. D., DALRYMPLE, G. B., LANPHERE, M. A. & CARPENTER, N. V. 1981. A five-collector system for the simultaneous measurement of argon isotope ratios in a static mass spectrometer. *International Journal of Mass Spectroscopy and Ion Physics*, **39**, 167–180.

STAMATELOPOULOU-SEYMOUR, K. & VLASSOPOULOS, D. 1992. Magma mixing at Nisyros volcano, as inferred from incompatible trace-element systematics. *Journal of Volcanology and Geothermal Research*, **50**, 273–299.

——, VLASSOPOULOS, D., PEARCE, T. H. & RICE, C. 1990. The record of magma chamber processes in plagioclase phenocrysts at Thera Volcano, Aegean Volcanic Arc, Greece. *Contributions to Mineralogy and Petrology*, **104**, 73–84.

STOLPER, E. & NEWMAN, S. 1994. The role of water in the petrogenesis of Mariana trough magmas. *Earth And Planetary Science Letters*, **121**, 293–325.

STURCHIO, N. C., BINZ, C. M & LEWIS, C. H. 1987. Thorium-uranium disequilibrium in a geothermal discharge zone at Yellowstone. *Geochimica et Cosmochimica Acta*, **51**, 2025–2034.

——, BOHLKHE, J. K. & BINZ, C. M. 1989. Radium-Thorium disequilibrium and zeolite-water ion exchange in a Yellowstone hydrothermal environment. *Geochimica et Cosmochimica Acta*, **53**, 1025–1035.

SULLIVAN, D. G. 1988. The discovery of Santorini Minoan tephra in western Turkey. *Nature*, **333**, 552–554.

SUN, S. S. 1980. Lead isotope study of young volcanic rocks from mid-ocean ridges, ocean islands and island arcs. *Philosophical Transactions of the Royal Society London*, **A297**, 409–445.

SWEATMAN, T. R. & LONG, J. V. P. 1969. Quantitative electron-probe microanalysis of rock-forming minerals. *Journal of Petrology*, **10**, 332–379.

TARNEY, J., BARR, S., MITROPOULOS, P. SIDERIS, K., KATERINOPOULOS, A. & STOURAITI, C. 1998. Santorini: geochemical constraints on magma sources and eruption mechanisms. *In*: CASALE, R. *et al.* (eds) *Proceedings of the second workshop, Santorini, Greece, 2 to 4 May 1996*, European Commission, 89–112.

TATARIS, A. A. 1956. The Eocene in the semimetamorphosed basement of Thera island. *Bulletin of the Geological Society of Greece*, **III: 1**, 232–238.

TAYLOR, H. P. 1968. The oxygen isotope geochemistry of igneous rocks. *Contributions to Mineralogy and Petrology*, **19**, 1–71.

—— & TURI, B. 1976. High ^{18}O igneous rocks from the Tuscan Magmatic Province, Italy. *Contributions to Mineralogy and Petrology*, **55**, 33–54.

——, —— & CUNDARI, A. 1984. $^{18}O/^{16}O$ and chemical relationships in K-rich volcanic rocks from Australia, East Africa, Antarctica and San Venanzo – Cupaello, Italy? *Earth and Planetary Science Letters*, **69**, 263–276.

TAYLOR, J. R. 1982. *An Introduction to Error Analysis*. University Science Books, Mill Valley, California.

TAYLOR, S. R. & MCCLELLAN, S. M. 1985. *The Continental Crust: Its Composition and Evolution*. Blackwell Scientific Publications, Oxford.

THOMAS, N. & TAIT, S. R. 1997. The dimensions of magmatic inclusions as a constraint on the physical mechanism of mixing. *Journal of Volcanology and Geothermal Research*, **75**, 167–178.

——, —— & KOYAGUCHI, T. 1993. Mixing of stratified liquids by the motion of gas bubbles with application to magma mixing. *Earth and Planetary Science Letters*, **115**, 161–175.

THOMAS, R. M. E. 1993 *Determination of the emplacement temperature of the pyroclastic deposits by theoretical and paleomagnetic methods*. PhD Thesis, University of Bristol.

THUNELL, R. C., WILLIAMS, D., FEDERMAN, A. & SPARKS, R. S. J. 1977. Late Quaternary tephra chronology of Eastern Mediterranean sediments. *Geological Society of America Abstracts with Programs*, **9**, 1200.

VAN BEMMELEN, R. W. 1971. Four volcanic outbursts that influenced human history. Toba, Sunda, Merapi and Thera. *In*: KALOUEROPOULOU, A. (ed.) *Acta of the First International Scientific Congress on the Volcano of Thera*, Athens, 5–50.

VAN DER MAAR, P. A. 1980. The geology and petrology of Ios, Cyclades, Greece. *Annales Geologie Pays Helleniques*, **XXX/I**, 206–224.

—— & JANSEN, J. B. H. 1983. The geology of the polymetamorphic complex of Ios, Cyclades, Greece, and its significance for the Cycladic Massif. *Geologishes Rundschau*, **72**, 283–299.

——, FEENSTRA, A., MANDERS, B. & JANSEN, J. B. H. 1981. The petrology of the island of Sikinos, Cyclades, Greece, in comparison with that of the adjacent island of Ios. *Neues Jahrbuch für Mineralogie Monadshefte*, 459–469.

VEIZER, J. & COMPSTON, W. 1974. $^{87}Sr/^{86}Sr$ composition of seawater during the Phanerozoic. *Geochimica et Cosmochimica Acta*, **38**, 1461–1484.

VITALIANO, D. B & VITALIANO, C. J. 1971. Plinian eruptions, earthquakes and Santorin a review. *In*: KALOUEROPOULOU, A. (ed.) *Acta of the First International Scientific Congress on the Volcano of Thera*, Athens, 88–108.

VOLPE, A. M. & HAMMOND, P. E. 1991. ^{238}U-^{230}Th-^{226}Ra Disequilibria In Young Mount St Helens Rocks: Time Constraint For Magma Formation And Crystallisation. *Earth And Planetary Science Letters*, **107**, 475–486.

WAGER, L. R. & BROWN, G. M. 1968. *Layered Igneous Rocks*. Oliver and Boyd, Edinburgh.

WAGNER, T. P., DONNELLY-NOLAN, J. M. & GROVE, T. L. 1995. Evidence of hydrous differentiation and crystal accumulation in the low-MgO, high-Al_2O_3 Lake Basalt from Medicine Lake volcano, California. *Contributions to Mineralogy and Petrology*, **121**, 201–216.

WALLMAN, P. C., MAHOOD, G. A. & POLLARD, D. D. 1988. Mechanical models for correlation of ring-fracture eruptions at Pantelleria, Strait of Sicily, with glacial sea-level. *Bulletin of Volcanology*, **5**, 327–339.

WASHINGTON, H. S. 1926. Santorini eruption of 1925. *Bulletin of the Geological Society of America*, **37**, 349–384.

WATKINS, N. D., SPARKS, R. S. J., SIGURDSSON, H., HUANG, T. C., FEDERMAN, A., CAREY, S. & NIKOVITCH, D. 1978. Volume and extent of the Minoan tephra from Santorini volcano: new evidence from deep-sea sediment cores. *Nature*, **271**, 122–126.

WELLS, P. R. A. 1977. Pyroxene thermometry in simple and complex systems. *Contributions to Mineralogy and Petrology*, **62**, 129–139.

WHITE, W. M. 1984. Hf-Nd-Sr isotopes and incompatible element abundances in island arcs: implications for magma origins and crust-mantle evolution. *Earth and Planetary Science Letters*, **67**, 167–185.

——1989. Geochemcial evidence for crust-to-mantle recycling in subduction zones. *In*: *Crust Mantle Recycling at Converged Zones*. NATO ASI Series C, **258**, 43–58.

—— & DUPRE, B. 1986. Sediment subduction and magma genesis in the Lesser Antilles: Isotopic and trace element constraints. *Journal of Geophysical Research*, **91**, 5927–5941.

—— & PATCHETT, J. 1984. Hf-Nd-Sr isotopes and incompatible element abundances in island arcs: implications for magma origins and crust-mantle evolution. *Earth and Planetary Science Letters*, **67**, 167–185.

WIJBRANS, J. R. & MCDOUGALL, I. 1988. Metamorphic evolution of the Attic-Cycladic metamorphic belt on Naxos (Cyclades, Greece) utilizing $^{40}Ar/^{39}Ar$ age spectrum measurements. *Journal of Metamorphic Geology*, **6**, 571–594.

WILLIAMS, R. W. & GILL, J. B. 1989. Effects of partial melting on the Uranium Decay Series. *Geochimica et Cosmochimica Acta*, **53**, 1607–1619.

WILSON, C. J. N. & HOUGHTON, B. F. 1990. Eruptive mechanisms in the Minoan eruption: evidence from pumice vesicularity. *In*: HARDY, D. A. (ed.) *Thera and the Aegean World III*, **2**. The Thera Foundation, London, 122–128.

WILSON, L. 1978. Energetics of the Minoan eruption. *In*: DOUMAS, C. (ed.) *Thera and the Aegean World I*. The Thera Foundation, London, 221–228.

——1980. Energetics of the Minoan eruption: some revisions. *In*: DOUMAS, C. (ed.) *Thera and the Aegean World II*. The Thera Foundation, London, 31–35.

WILSON, M. 1989. *Igneous Petrogenesis: A Global Tectonic Approach*. Harper Collins Academic, London.

WOOD, B. J. & HOLLOWAY, J. R. 1982. Theoretical prediction of phase relationships in planetary mantle. *Journal of Geophysical Research*, **87**, A19–A30.

WOODHEAD, J. D. & FRASER, D. G. 1985. Pb, Sr and ^{10}Be isotopic studies of volcanic rocks from the northern Mariana islands: implications for magma genesis and crustal recycling in the Western Pacific. *Geochimica et Cosmochimica Acta*, **49**, 1925–1930.

WRIGHT, J. V. 1978. Remanent magnetism of poorly-sorted deposits from the Minoan eruption of Santorini. *Bulletin of Volcanology*, **41**, 131–135.

—— & WALKER, G. P. L. 1977. The ignimbrite source problem: significance of a co-ignimbrite lag-fall deposit. *Geology*, **5**, 729–732.

WYERS, G. P. 1987. *Petrogenesis of calc-alkaline and alkaline magmas from the southern and eastern Aegean Sea, Greece*. PhD Thesis, Ohio State University.

—— & BARTON, M. 1989. Polybaric evolution of calc-alkaline magmas from Nisyros, southeastern Hellenic Arc, Greece. *Journal of Petrology*, **30**, 1–37.

YOKOYAMA, I. 1978. The tsunami caused by the prehistoric eruption of Thera. *In*: DOUMAS, C. (ed.) *Thera and the Aegean World I*. The Thera Foundation, London, 277–283.

ZELLMER, G. 1998. *Petrogenetic processes and their times scales beneath Santorini, Aegean Volcanic Arc, Greece*. PhD Thesis, Open University, UK.

——, BLAKE, S., VANCE, D., HAWKESWORTH, C. & TURNER, S. 1999. Plagioclase residence times at two island arc volcanoes (Kameni Islands, Santorini, and Soufiere, St Vincent) determined by Sr diffusion systematics. *Contributions to Mineralogy and Petrology*, in press.

——, HAWKESWORTH, C. & TURNER, S. 1998. U–Th–Ra isotope evidence for rates of fluid transport and magmatic proceesses beneath Santorini, Aegean Volcanic Arc, Greece. *Mineralogical Magazine*, **62**, 1685–1686.

Index

Page numbers in *italics* refer to Figures and page numbers in **bold** refer to Tables

actinolite 81
Aegean Island arc 10
Aegean microplate 5
Aegean Sea 3 5
Aegina 10, *11*
AFC models 112–116, 131
AFM diagrams *11*, *92*
agglomerates
  Middle Pumice 30
  Upper Scoriae 2 39
Akrotiri, Cape 17, *21*
  see also Early Centres of Akrotiri *also* Cinder Cones of Akrotiri
Akrotiri-Thera Series 90
Al_2O_3/SiO_2
  Cape Thera pyroclastics *93*
  Early Centres of Akrotiri *91*
  minor pyroclastics *97*
Alai, Cape, first explosive cycle *15*, *17*, 22–23, *33*
Aleutian Islands, isotope analyses compared 103, *104*, *105*, *106*
alkali feldspar 11, 81
allanite 81
Alonaki, Cape, rhyodacites *17*, 25, *33*, **120**
Alpine orogeny 8–9, 129
Amorgos 8
amphibole 1 81
Anatolian trough 5 *6*
Andes Volcanic Zones, isotope analyses compared 103, *104*
andesites 58, 82–83
  Akrotiri Cinder Cones 20, 129
  Cape Alai 22–23, *33*, 59
    $^{40}Ar/^{39}Ar$ ages **19**
    K/Ar ages **18**
  Cape Riva 65, 92
  Cape Simandiri *17*, 27
  Cape Skaros *17*, 37
  Cape Therma 1 92
  Cape Therma 3 96
  Lower Pumice 1 65, 92, 96
  Lower Pumice 2 60–64
  Middle Pumice 68, 71
  Middle Tuffs series 28
  Minoan Tuff 60–64
  Mt Loumaravi 17
  Oia 41, 59
  Peristeria 19, 59
  Skaros shield 59, **120**
  Upper Scoriae 2 39
  Vourvoulos 71
apatite 58–59, 68, 81
$^{40}Ar/^{39}Ar$ geochronology **19**, *51*, 134
  basement 8 9
  Cinder Cones of Akrotiri 20
  first explosive cycle 23, 25
  Peristeria volcano 19, 127
  rhyodacites of Early Centres of Akrotiri 17–18
  second explosive cycle 28, 35, 37, 40
Archangelos, Mt 14, 17, *21*
Aspronisi, Cape *21*, 30, 34
Aspronisi, Island of 14, *15* *17*
Aspronisi tuff ring *17*, 28, 32
assimilation 106, 110–116, 130–131
Athinios, Cape *20*
Athinios metapelites 16, *17*, *20*
Atlanti-Volos Group 10
augite 37, 68, 70, 71, 82
Ayios Nikolaos, Cape 37

Ba geochemistry
  Cape Thera pyroclastics *94*
  Early Centres of Akrotiri *91*
  minor pyroclastics *98*
Balos, Cape 20, *21*
Balos cone 20, 65
basalt 58, 110, 129
  Akrotiri Cinder Cones 20
  Cape Simandiri *17*, 27
  Cape Skaros *17*, 37, 59
  Lower Pumice 2 60, 92
  Peristeria volcano 19, 59
basement 5–8, 10
Basement Formation 16, *17*, *20*, *30*
Bimstein Oberer 1
Bimstein Unterer 1
biotite 11, 58–59, 81
blueschist facies 8 16, 129
bombs *32*
Bouguer anomaly map *16*
breccias
  Lower Pumice sequence 25, 26
  Middle Pumice 30
  Peristeria volcano 19
Bronze Age eruptions 1 13, 14

^{14}C dating of second explosive cycle 35, 41, 46
calderas *2*, 13, 14–16, *33*, 52–53, 129, 130
  caldera 1 27
  caldera 2 37
  caldera 3 41–43, 44
  caldera 4 48
CaO/SiO_2 in Cape Thera pyroclastics *93*
Cape Alai Centre *15*, *17*, 22–23, *33*
Cape Alonaki rhyodacites *17*, 25, *33*, **120**
Cape Columbos Tuff Ring 35–37
Cape Riva Tuff *17*, 41, *55*, 129, 130
  andesitic components 65–67
  crystal content **62**
  geochronology **19**
  glass composition **66**
  isotope analyses **120**, **121**
  isotopes analyses 100, *101*, *102*, *103*, *104*
    juvenile components 140
    major element analyses 148–149
  trace element analyses 148–149
  major element analyses **61**, **64**, 92, *93*, 107, 108
  mixing data **70**
  petrogenetic modelling 109, *111*, *113*, *114*, *115*, *116*
  plagioclase composition *68*
  plutonic blocks 151
    major element analyses 153
    trace element analyses 153
  pyroxene and olivine composition *69*
  silica percentage *58*
  trace element analyses **61**, **64**, 92, *93*, 107, 108
Cape Thera Tuff *17*, 28, 68
  crystal content **62**
  glass composition **72**
  isotopes analyses *101*, *102*, *103*, *104*
  juvenile components 139
    major element analyses 145–146
    trace element analyses 145–146
  major element analyses **61**, *93*
  petrogenetic modelling *111*, *112*, *113*, *116*
  pyroxene and olivine composition *69*
  silica percentage *58*
  trace element analyses **61**, *93*
Cape Therma 1 *17*, 25, *30*, *33*
  crystal content **62**
  isotope analyses 100, *101*, *102*, *103*, *104*, **120**
  juvenile components 138
    major element analyses 142
    trace element analyses 142
  major element analyses **59**, **61**, 92, *93*, 107
  petrogenetic modelling 109, *111*, *112*, *113*, *114*, *115*, *116*
  pyroxene and olivine composition *69*
  silica percentage *58*
  trace element analyses **59**, **61**, 92, *93*, 107
Cape Therma 2 *17*, 25, **120**, **121**
  crystal content **62**
  isotope analyses *101*, *102*, *103*, *104*, **120**, **121**
  juvenile components 138
    major element analyses 142
    trace element analyses 142
  major element analyses **59**, **61**, 92, *93*
  petrogenetic modelling *111*, *113*, *114*, *115*, *116*
  pyroxene and olivine composition *69*
  silica percentage *58*
  trace element analyses **59**, **61**, 92, *93*
Cape Therma 3 *17*, 25, *30*, *33*
  crystal content **62**
  isotope analyses 100, *101*, *102*, *103*, *104*, **120**, **121**
  juvenile components 138
    major element analyses 142–143
    trace element analyses 142–143
  major element analyses **59**, **61**, *93*
  nodules 81
  petrogenetic modelling 109, *111*, *112*, *113*, *114*, *115*, *116*
  plutonic blocks 151
    major element analyses 152
    trace element analyses 152
  pyroxene and olivine composition *69*
  silica percentage *58*
  trace element analyses **59**, **61**, *93*
Central Aseismic Plateau 5
Central trough 5
Christiana Islands *13*, 14, 129
Cinder Cone of Megalo Vouno **18**, 32, 35, *36*
Cinder Cones of Akrotiri 16, *17*, **18**, **19**, 20, *21*
clinopyroxene 11, 58–59, 60, 64, 67, 68, 71, 79–81, 82, 83, 84, 85
Columbos, Cape *15*, 35–37, 129
Columbos Bank volcano *13*, 14
compositional zoning *see* zoning
conglomerate 1
Cr geochemistry 107
Crommyonia 10
crust 13
  assimilation 130–131
  thickness 5
  thinning 129
crystal fractionation 107, 110–116
cummingtonite 81
cumulate nodules of Thera pyroclastics
  geochemistry 85–87
  links to host rock 82–85
  mineralogy 79–81
  P–T of formation 85
  petrogenesis 87
  petrology 79
  texture 79
cumulus crystals 79
Cycladic Crystalline Complex 5 *8*
cycles of vulcanicity 132–133

δD analyses *101*, *103*
dacites 58, 60, 129
  Cape Mavros 17
  Cape Riva 65
  Cape Skaros 37
  Cape Therma 1 92
  Early Centres of Akrotiri 58
  Kameni Islands 59
  Middle Pumice 60, 68, 70
  Middle Tuffs series 28
  Peristeria volcano 19
  Upper Scoriae 1 71
  Upper Scoriae 2 71
  Vourvoulos Tuff 60
digital elevation model *14*
diorite nodules *see* cumulate nodules
dune bedding 41
dykes 35
dykes of Peristeria 19

Early Centres of Akrotiri 16, 17–19, *20*, *21*, *22*
$^{40}Ar/^{39}Ar$ geochronology **19**
geochemistry 89–90
geochronology **19**
K/Ar geochronology **18**
phenocryst composition 58–59
earthquakes 5
electron microprobe analysis 134
Eocene metamorphism 129
epicentres 5
epidote 81
European Laboratory Volcano 4
evolution of magma 130–131
extensional regime 5 129

faults and faulting 5 *6*, 129
geometry 43
maps *13*, *42*
role in magma channelling 51
feldspar *see* alkali feldspar *also* plagioclase
FeO/SiO_2
Cape Thera pyroclastics *93*
Early Centres of Akrotiri *91*
minor pyroclastics *97*
fiamme 25
First Explosive Cycle 16, *17*, 20–27
Folegandros 8
fractional crystallisation 110–116, 130
fractionation 107, 109–110

gabbro fragments 64
gabbroic nodules *see* cumulate nodules
Gavrillos 14, *15*
geochemistry of magma
evolution 130–131
secular variation 131–132
see also isotope geochemistry *also* major element analyses *also* trace element analyses
geological maps *15*
Akrotiri Peninsula *21*
Kameni islands *49*
Peristeria *24*
Phira *29*
Thera *20*
geothermometry 4 73
glass composition **66**, 70, **72**, 74, **119**
granite porphyry 16
granitoids 9–10, 129
greenschist facies 8 129

haematite 81
Hellenic arc *7*
Hellenic trench 5
Heptapedio, Cape 19, 37, *38*
Hercynian orogeny 129
$^{176}Hf/^{177}Hf$ 92
hornblende 1 11, 58–59, 81
hyaloclastites 1 17, 19, 129
hybridism 131
hydrogen isotope analyses 135–136
hypersthene 81

I type granite 9 16
ignimbrites
Cape Therma 25
Middle Tuffs series 28
Minoan eruption *45*, *46*
ilmenite 58–59, 70, 71, 81
intermediate eruptions 67–73, 74–75
Ionian trench 5 *6*
Ios 8 *9*
isopach maps *28*
isotope geochemistry
history of research 91–92
Thera pyroclastics 100–106, 108–109
see also under named isotopes

Jacomo I Crispo of Naxos, Duke 1
Japan arc, isotope analyses compared 103, *104*, *105*

K feldpsar *see* alkali feldspar
K_2O/SiO_2 *10*
Cape Thera pyroclastics *93*
minor pyroclastics *97*
K/Ar geochronology 8 9, **18**, *51*, 134
Cinder Cones of Akrotiri 20
first explosive cycle 23, 25–26
Peristeria volcano 19, 127
rhyodacites of Early Centres of Akrotiri 17–18
second explosive cycle 27–28, 40
Kameni Islands 14, *15*, 130
geological map *49*
stratigraphy *17*
volcanism 48–49
Kameni lavas 16, *17*, 48–49, 129
geochemistry 90–91
geochronology **19**
isotope analyses **121**
major and trace element analyses 108
phenocryst composition 59
U/Th disequilibrium studies 126–127
Kameni Line 129
Kokkino Vouno cinder cone 32, 35, *36*
Kokkinopetra, Cape 21, *31*
Kos 10
Kos granodiorite isotope analyses *104*, *105*, *106*

large ion lithophile (LIL) plots, Thera pyroclastics *95*, 100, 131
Laurium granite isotope analyses *104*, *105*, *106*
Lesser Antilles, isotope analyses compared 103, *104*, *106*
limestones of Mt Profitis Ilias 16, *17*, *20*
Loumaravi, Cape *15*
Loumaravi, Mt 14, 17, *21*
Loumaravi–Archangelo Series 89
Lower Pumice 1 *17*, 25–26, *30*, *33*, 129, 130
andesitic components 65–67
crystal content **62**
geochronology **19**
glass analysis **66**
isotope analyses 100, *101*, *102*, *103*, *104*, **120**, **121**
juvenile components 138
major element analyses 143–144
trace element analyses 143–144
K/Ar geochronology **18**
major element analyses **59**, **61**, **64**, 92, *93*, 107, 108
petrogenetic modelling 109, *111*, *112*, *113*, *114*, *115*, *116*
plagioclase composition *68*
pyroxene and olivine composition *69*
silica percentage *58*
trace element analyses **59**, **61**, **59**, **64**, 92, *93*, 107, 108
Lower Pumice 2 *17*, 26–27, *30*, *33*, 60–64, 129, 130
crystal content **62**
geochronology **19**, 124–125
glass composition **66**
isotope analyses 100, *101*, *102*, *103*, *104*, **120** **121**, 124–125
juvenile components 138–139
major element analyses 144–145
trace element analyses 144–145
major element analyses **59**, **61**, **64**, 92, *93*, 108
petrogenetic modelling 109, *111*, *112*, *113*, *114*, *115*, *116*
phenocryst composition 64
plagioclase composition *68*
pyroxene and olivine composition *69*
scoria composition **70**
silica percentage *58*
trace element analyses **59**, **61**, **64**, 92, *93*, 108

maar 20
mafic defined 58
magma evolution 130–131
magma mixing 107–108
magnetite 11, 58–59, 67, 68, 71, 81, 82, **119**
Main Series 90
major element analyses of Thera pyroclastics
history of research 89–91
methods 134, **135**, **136**
petrogenetic modelling 109–116
results
cumulate nodules 85–87
major units 92–100
minor units 100
results discussed 106–108
Manolas Bay 27
Marianas, Pb isotope analyses compared *105*
Mavrorachidi, Cape *15*
Mavrorachidi cone 20
Mavros, Cape *15*, 17, 18, 20, *21*
Meagalo Vouno 129
Megalo cinder cone 32, 35, *36*
Megalo Vouno, Mt 14, *15*, 19, *24*, 37
Megolodontidae 16
Mesa Vouno, Cape *20*
metamorphism 8 129
metapelites of Athinios 16, *17*, *20*, *30*
Methana 10, *11*
Mexican Volcano Belt, isotope analyses compared 103, *104*
MgO/SiO_2
Cape Thera pyroclastics *93*
Early Centres of Akrotiri *91*
Micros Profitis Ilias 14, 19, *23*, 37, 129
Middle Pumice 3 *17*, 28–31, *33*, *34*, 68–71
compositional zoning *73*
crystal content **62**
geochronology **19**
glass composition **72**, *74*
isotope analyses **120**, **121**
isotopes analyses *101*, *102*, *103*, *104*
juvenile components 139
major element analyses 146
trace element analyses 146
major element analyses **61**, *93*
petrogenetic modelling *111*, *112*, *113*, *116*
plutonic blocks 151
major element analyses 152
trace element analyses 152
pyroxene and olivine composition *69*
silica percentage *58*
trace element analyses **61**, *93*
Middle Tuffs series *17*, 28–35, 130
Miliolidae 16
Milos 8 10, *11*
mineralogy of cumulate nodules 79–81
Minoan Tuff *17*, 43–48, 60–64, 129, 130
crystal content **62**
crystal rich pumice 67
eruption phases 2 4
geochronology **19**
glass composition **66**
isotope analyses 100, *101*, *102*, *103*, *104*, 118–124
juvenile components 140–141
major element analyses 149–150
trace element analyses 149–150
major element analyses **61**, **64**, 92, *93*, *94*, *95*, 96, 107, 108
petrogenetic modelling *111*, *113*, *114*, *115*, *116*
phenocryst composition 64
plagioclase composition *68*
plutonic blocks 151
major element analyses 153
trace element analyses 153
pyroxene and olivine composition *69*
scoria composition **70**
silica percentage *58*
trace element analyses **61**, **64**, 92, *93*, *94*, *95*, 96, 107, 108
Minoan Civilization 1 13, 14
minor pyroclastics 108
isotope analyses **121**
juvenile components 152, 155–156
major element analyses *97*, *98*, *99*, 100
trace element analyses *97*, *98*, *99*, 100

Miocene
  intrusions 9–10, 16, 129
  metamorphism 129
mixing of magma 130–1
Modern Series 90

Na_2O/SiO_2 *93*
Naxos 8 *9*
$^{143}Nd/^{144}Nd$
  history of research 92
  methods of analysis 135
  Thera pyroclastics 100, *101*, *102*, 103, *104*, *106*, 131
Nea Kameni 14, *15*, 25, 26, 39
Nisyros 10, *11*
nodules of Thera pyroclastics
  geochemistry 85–87
  links to host rock 82–85
  mineralogy 79–81
  P–T of formation 85
  petrogenesis 87
  petrology 79
  texture 79

δ^{18} 9 10
  history of research 92
  methods of analysis 135
  Thera pyroclastics *101*, *103*, 105–106, *116*, 131
obsidian
  Lower Pumice sequence 25
  Vourvoulos Tuff 71
Oia 14, *15*, 19, 26, *31*, *40*, 41
olivine 11, 37, 81, *84*
  iron rich 130
    Middle Pumice 60
    Minoan Tuff 64
    Vourvoulos Tuff 60, 71
  magnesium rich
    Cape Riva 65
    Lower Pumice 67
olivine gabbro fragments 64
orthopyroxene 11, 58–59, 60, 64, 67, 68, 71, 81, 82, 83, 84, 85

P_2O_5/SiO_2
  Cape Thera pyroclastics *93*
  Early Centres of Akrotiri *91*
  minor pyroclastics *98*
P–T of formation of cumulate nodules 85
Palaea Kameni 14, *15*
palaeomagnetism 2
Patagonia, isotope analyses compared 103, *104*
Pb isotope systematics 100, *101*, *102*, *105*, *106*, 131, 135
Pègues 1
Peristeria volcano and lavas 14, 16, 19–20, *24*, 129
  $^{40}Ar/^{39}Ar$ geochronology **19**, 127
  geochemistry 90–91
  geochronology **19**
  K/Ar geochronology **18**, 127
  petrogenetic modelling 109, *111*
  phenocryst composition 59
  U/Th disequilibrium studies 127
Perivola, Cape *15*, 25, 26, 28, *32*
petrogenesis
  cumulate nodules 87
  lavas 58–60
petrogenetic modelling 109–116
petrology
  cumulate nodules 79
  lavas 58–60
  nodules and lavas compared 82–85
phenocrysts
  compositions 58–60
  disequilibria of isotopes 103–105
Phira 3 *15*, 27, 28, *29*, *33*
phreatomagmatic eruption 2
phreatomagmatic surge 130
phreatomagmatic tuffs of Akrotiri Cinder Cones 20
plagioclase 11, 58–59, 60, 64, 65, 67, 68, 70, 71, 79, 106, **119**
Plaka, Cape *20*, *30*, *34*
Plinian phase 2 25, 26, 41, *42*, 129
Pliny trench 5 *6*
Pliocene
  arc development 129
  foraminifera 18
Poros 10, *11*
porphyritic texture 11
Pre-Cape Therma tuff **120**
pre-volcanic history *see* basement
primocrysts 79
Profitis Ilias Mt 14, *15*, 16
pumice breccia 1
pumices
  crystal rich 67
  Lower Pumice sequence 25–27
pyroclastic flows 2 *27*
  emplacement 54–56
  proximal 53–54

quartz 11, 81

Ra isotope analysis 136, 137
radiometric dating methods *see under named isotopes*
Rayleigh fractionation 109–110
Rb geochemistry
  Cape Thera pyroclastics *94*
  Early Centres of Akrotiri *91*
  minor pyroclastics *99*
Rb/Sr geochronology 6
rhyodacites 58, 60, 129
  Cape Alonaki *17*, **18**, 25, *33*, 130
  Cape Riva 92
  Cape Therma 1 92
  Early Centres of Akrotiri 17, 58
  Lower Pumice 2 124–125
  NE Thera **18**, 25
  Therasia Dome 41, 59
rhyolite 58, 60
Riva *see* Cape Riva Tuff

S-type plutons 9
Samos 10
sanidine 11
Santorini 10, *11*
Santorini marble *104*
Santorini metavolcanics *104*
Santorini schist *104*, *105*, *106*
Santorini–Amorgos Ridge 13
scoriae
  Cape Riva 65
  Lower Pumice 1 65
  Lower Pumice 2 63, **70**
  Middle Pumice 68
  Minoan Tuff 60, 64, **70**
  see also Upper Scoriae 1 *also* Upper Scoriae 2
sea floor bathymetry *13*
Second Explosive Cycle 16, *17*, 27–48
seismic profile *15*
Sierifos 8
Sifnos 8 9
Sikinos *9*
silicic eruptions 58, 60–67, 75–78
Simandiri, Cape *15*, *17*, 27
Simandiri lavas 90–91
Simandiri shield 14, **18**, **19**, 27
Skaros, Cape *15*, 37
Skaros lavas **120**, 130
  geochemistry 90–91
  in petrogenetic modelling 109, *111*
  phenocryst composition 59
Skaros shield 14, **19**, 37–39
slump structures *22*
South Sandwich Islands, isotope analyses compared 103, *104*, *106*
spatter agglomerate 67
spatter rags *36*, 39, *56*
sponge spicules 1
Sr geochemistry
  Cape Thera pyroclastics *94*
  Early Centres of Akrotiri *91*
  minor pyroclastics *99*
$^{87}Sr/^{86}Sr$ *11*, 131
  basement 6 8, 9
  granitoids 10
  history of research 91–92
  method of analysis 135
  Thera pyroclastics 100, *101*, *102*, 103, *104*, *106*
Strabo 1
Strabo trench 5 *6*
stratigraphy *17*
stromatolites 43
strombolian eruptions 20
submarine volcanic products 129
subsidence v. uplift 129
Superficial Formation 16
Syros 8

Taiwan, isotope analyses compared *105*
tectonic environment 3 5, 51
temperature of eruption 4 73
textural analysis 79
Th isotope analysis 131, 136–137
Thera 14, *15*, *17*, *20*
  Cape *34*
  First International Science Congress on the Volcano 1–2
  see also Cape Thera Tuff
Thera pyroclastics 14, 16, *30*, 48, 129, 130
  cumulate nodules
    geochemistry 85–87
    links to host rock 82–85
    mineralogy 79–81
    P–T of formation 85
    petrogenesis 87
    petrology 79
    texture 79
  geochemical analyses
    results 92–100
    results discussed 106–109
  see also under named units
Therasia 14, *15 17*
  lava geochemistry 90–91, **120**
Therasia Dome Complex 14, *37*, *39*, 41, 130
Therma *see* Cape Therma
TiO_2/SiO_2
  Cape Thera pyroclastics *93*
  minor pyroclastics *98*
titanite 81
Tourlos, Cape *15*, *23*, 37, *38*, 41
trace element analyses of Thera pyroclastics
  history of research 89–91
  methods 134, **135**, **136**
  results
    cumulate nodules 85–87
    major units 92–100
    minor units 100
  results discussed 8
travertine 43
Triassic limestones 16
Tuff Ring of Aspronisi *17*, 28, 32
tuffs
  Akrotiri 17
  Cape Therma 25, *33*
  Peristeria Volcano 19

U isotope analysis
  methods 118, 136–137
  results
    Kameni lavas 126–127
    Lower Pumice 2 124–125
    Minoan tuff 118–124
    minor pyroclastics 125, 128
    Peristeria volcanics 127
U/Th geochronology 19
uplift v. subsidence 129
Upper Scoriae 1 *17*, 28, 34–35, 37, *56*, 71–73, 130
  crystal content **62**
  geochronology **19**
  glass composition **72**

isotope analyses 100, *101*, *102*, *103*, *104*, **120**, **121**
juvenile components 140
major element analyses 147
trace element analyses 147
major element analyses **61**, *93*
petrogenetic modelling 109, *111*, *113*, *114*, *115*, *116*
plutonic blocks 151
major element analyses 152
trace element analyses 152
pyroxene and olivine composition *69*
silica percentage *58*
trace element analyses **61**, *93*
Upper Scoriae 2 *17*, 39–41, *56*, 71–73, 130
$^{40}Ar/^{39}Ar$ geochronology **19**
crystal content **62**
geochronology **19**
glass composition **72**
isotope analyses 100, *101*, *102*, *103*, *104*, **120**, **121**
juvenile components 140
major element analyses 147–148
trace element analyses 147–148
K/Ar geochronology **18**
major element analyses **61**, *93*
petrogenetic modelling *111*, *113*, *114*, *115*, *116*
plutonic blocks 151
major element analyses 153
trace element analyses 153
pyroxene and olivine composition *69*
silica percentage *58*
trace element analyses **61**, *93*
V geochemistry *94*
Viglos, Mt 14, *15*
vitric tuffs of Akrotiri 17, 20, *22*
volcanic field
description 13–16
summary **50**
Volcanic Formation 16
Vounia, Cape 17, 21
Vourvoulos Tuff *17*, 28, 32, 71, 130
crystal content **62**
glass composition **72**
isotope analyses 100, *101*, *102*, *103*, *104*
juvenile components 139–140
major element analyses 146–147
trace element analyses 146–147
major element analysis **61**, 92, *93*
petrogenetic modelling 109, *111*, *113*, *116*
pyroxene and olivine composition *69*
silica percentage *58*
trace element analyses **61**, 92, *93*
vulcanian activity 129

water content, Thera pyroclastics 73–74

xenocrysts 64, 67, 73, 79
XRD analysis *109*
XRF analysis
major elements 134, **135**, **136**
trace elements 134, **135**, **136**

Y geochemistry *94*

zircon 58–59
zircon fission track age 18–19
zoning 130
description 58–60
intermediate products 60–67
silicic products 67–73
interpretation for magma chamber 74–78
origins 78
Zr geochemistry
Cape Thera pyroclastics *94*
Early Centres of Akrotiri *91*
minor pyroclastics *99*